

# **Soil Mechanical Systems and Related Farming Machinery**





# Soil Mechanical Systems and Related Farming Machinery

Editors

**Ju-Seok Nam**

**Yongjin Cho**



Basel • Beijing • Wuhan • Barcelona • Belgrade • Novi Sad • Cluj • Manchester

*Editors*

Ju-Seok Nam  
Kangwon National  
University  
Chuncheon  
Republic of Korea

Yongjin Cho  
Jeonbuk National University  
Jeonju  
Republic of Korea

*Editorial Office*

MDPI AG  
Grosspeteranlage 5  
4052 Basel, Switzerland

This is a reprint of articles from the Special Issue published online in the open access journal *Agriculture* (ISSN 2077-0472) (available at: [https://www.mdpi.com/journal/agriculture/special\\_issues/HJ176P7057](https://www.mdpi.com/journal/agriculture/special_issues/HJ176P7057)).

For citation purposes, cite each article independently as indicated on the article page online and as indicated below:

Lastname, A.A.; Lastname, B.B. Article Title. <i>Journal Name</i> <b>Year</b> , Volume Number, Page Range.
--

**ISBN 978-3-7258-2349-9 (Hbk)**

**ISBN 978-3-7258-2350-5 (PDF)**

[doi.org/10.3390/books978-3-7258-2350-5](https://doi.org/10.3390/books978-3-7258-2350-5)

© 2024 by the authors. Articles in this book are Open Access and distributed under the Creative Commons Attribution (CC BY) license. The book as a whole is distributed by MDPI under the terms and conditions of the Creative Commons Attribution-NonCommercial-NoDerivs (CC BY-NC-ND) license.

# Contents

<b>About the Editors</b> . . . . .	<b>vii</b>
<b>Preface</b> . . . . .	<b>ix</b>
<b>Yongjin Cho and Ju-Seok Nam</b> Soil Mechanical Systems and Related Farming Machinery Reprinted from: <i>Agriculture</i> <b>2024</b> , <i>14</i> , 1661, doi:10.3390/agriculture14091661 . . . . .	<b>1</b>
<b>Hyo-Geol Kim, Jin-Woong Lee, Su-Chul Kim, Jooseon Oh and Sung-Bo Shim</b> Development of a Modified Method for Measuring the Actual Draft Force Using a Tractor-Attached Dynamometer Reprinted from: <i>Agriculture</i> <b>2024</b> , <i>14</i> , 544, doi:10.3390/agriculture14040544 . . . . .	<b>6</b>
<b>Bo-Min Bae, Yeon-Soo Kim, Wan-Soo Kim, Yong-Joo Kim, Sang-Dae Lee and Taek-Jin Kim</b> The Development of a Draft Force Prediction Model for Agricultural Tractors Based on the Discrete Element Method in Loam and Clay Loam Reprinted from: <i>Agriculture</i> <b>2023</b> , <i>13</i> , 2205, doi:10.3390/agriculture13122205 . . . . .	<b>18</b>
<b>Juwon Shin, Jinho Won, Seong-Min Kim, Dae-Cheol Kim and Yongjin Cho</b> Fertilization Mapping Based on the Soil Properties of Paddy Fields in Korea Reprinted from: <i>Agriculture</i> <b>2023</b> , <i>13</i> , 2049, doi:10.3390/agriculture13112049 . . . . .	<b>35</b>
<b>Yi-Seo Min, Yeon-Soo Kim, Ryu-Gap Lim, Taek-Jin Kim, Yong-Joo Kim and Wan-Soo Kim</b> The Influence of Soil Physical Properties on the Load Factor for Agricultural Tractors in Different Paddy Fields Reprinted from: <i>Agriculture</i> <b>2023</b> , <i>13</i> , 2073, doi:10.3390/agriculture13112073 . . . . .	<b>49</b>
<b>Ryu-Gap Lim, Wan-Soo Kim, Young-Woo Do, Md. Abu Ayub Siddique and Yong-Joo Kim</b> Performance Evaluation of a Virtual Test Model of the Frame-Type ROPS for Agricultural Tractors Using FEA Reprinted from: <i>Agriculture</i> <b>2023</b> , <i>13</i> , 2004, doi:10.3390/agriculture13102004 . . . . .	<b>65</b>
<b>Woo-Jae Cho and Myongkyoon Yang</b> High-Throughput Plant Phenotyping System Using a Low-Cost Camera Network for Plant Factory Reprinted from: <i>Agriculture</i> <b>2023</b> , <i>13</i> , 1874, doi:10.3390/agriculture13101874 . . . . .	<b>80</b>
<b>Donggeun Kim, Jisu Song and Jaesung Park</b> Quantifying Soil Particle Settlement Characteristics through Machine Vision Analysis Utilizing an RGB Camera Reprinted from: <i>Agriculture</i> <b>2023</b> , <i>13</i> , 1674, doi:10.3390/agriculture13091674 . . . . .	<b>100</b>
<b>Yeon-Soo Kim, Bo-Min Bae, Wan-Soo Kim, Yong-Joo Kim, Sang-Dae Lee and Taek-Jin Kim</b> Working Load Analysis of a 42 kW Class Agricultural Tractor According to Tillage Type and Gear Selection during Rotary Tillage Operation Reprinted from: <i>Agriculture</i> <b>2023</b> , <i>13</i> , 1556, doi:10.3390/agriculture13081556 . . . . .	<b>117</b>
<b>Hyoung-Jong Ahn, Young-Jun Park, Su-Chul Kim and Chanho Choi</b> Theoretical Calculations and Experimental Studies of Power Loss in Dual-Clutch Transmission of Agricultural Tractors Reprinted from: <i>Agriculture</i> <b>2023</b> , <i>13</i> , 1225, doi:10.3390/agriculture13061225 . . . . .	<b>133</b>

<b>Dongu Im, Ho-Seop Lee, Jae-Hyun Kim, Dong-Joo Moon, Tae-Ick Moon, Seung-Hwa Yu and Young-Jun Park</b> Bucket Size Optimization for Metering Device in Garlic Planter Using Discrete Element Method Reprinted from: <i>Agriculture</i> <b>2023</b> , <i>13</i> , 1199, doi:10.3390/agriculture13061199 . . . . .	<b>149</b>
<b>Anatoliy Lebedev, Mykhailo Shuliak, Stanislav Khalin, Sergei Lebedev, Katarzyna Szwedziak, Krzysztof Lejman, et al.</b> Methodology for Assessing Tractor Traction Properties with Instability of Coupling Weight Reprinted from: <i>Agriculture</i> <b>2023</b> , <i>13</i> , 977, doi:10.3390/agriculture13050977 . . . . .	<b>166</b>
<b>Sri Markumningsih, Seok-Joon Hwang, Jeong-Hun Kim, Moon-Kyeong Jang, Chang-Seop Shin and Ju-Seok Nam</b> Comparison of Consumed Power and Safety of Two Types of Semi-Automatic Vegetable Transplanter: Cam and Four-Bar Link Reprinted from: <i>Agriculture</i> <b>2023</b> , <i>13</i> , 588, doi:10.3390/agriculture13030588 . . . . .	<b>177</b>
<b>Gholamhossein Shahgholi, Abdolmajid Moinfar, Ali Khoramifar, Sprawka Maciej and Mariusz Szymanek</b> Investigating the Effect of Tractor's Tire Parameters on Soil Compaction Using Statistical and Adaptive Neuro-Fuzzy Inference System (ANFIS) Methods Reprinted from: <i>Agriculture</i> <b>2023</b> , <i>13</i> , 259, doi:10.3390/agriculture13020259 . . . . .	<b>196</b>
<b>Seok-Joon Hwang, Moon-Kyeong Jang and Ju-Seok Nam</b> Development of Autofeeding Device Applicable to a Biodegradable Pot Tray Reprinted from: <i>Agriculture</i> <b>2022</b> , <i>12</i> , 2097, doi:10.3390/agriculture12122097 . . . . .	<b>211</b>

# About the Editors

## **Ju-Seok Nam**

Ju-Seok Nam received his B.S., M.S., and Ph.D. in Biosystems Engineering from Seoul National University, the Republic of Korea, in 2007, 2009 and 2014, respectively. He has been a Professor in the Department of Biosystems Engineering at Kangwon National University and a Principal Investigator of the Agricultural Field Machine Laboratory since 2016. His interests relate to the areas of design and reliability tests for agricultural machinery, simulation studies to prevent the overturning and rollover of agricultural machinery, agricultural ergonomics to reduce the work stress of farmers, and cultivating models to increase the mechanization rate of agricultural work. He won the Best Professor Award from Kangwon National University in 2021 and has published 24 papers in international journals in the past three years.

## **Yongjin Cho**

Yongjin Cho received his B.S., M.S., and Ph.D. in Bio-Mechatronics Engineering from Sungkyunkwan University, the Republic of Korea, in 2006, 2008, and 2013, respectively. Since 2018, he has been a Professor at the Department of Bioindustrial Machinery Engineering at Jeonbuk National University. His research focuses on precision agriculture using smart agricultural machinery, including agriculture sensors, automation package technology for farming, and the development of a 110kW tractor for large agricultural applications. He also works on developing models to increase the mechanization rate of various agricultural tasks. In 2018, he received the Superior Paper Award from the ASABE (the American Society of Agricultural and Biological Engineers), and since 2020, and he has published 15 papers in international journals.



# Preface

Farming machinery has a long history of development. However, the rate of farming mechanization is still low in many countries, and technological advances are needed to develop optimal machinery for specific agricultural work. This requires an in-depth understanding of both soil and mechanical systems as most farming machinery work on soil. This reprint aims to expand knowledge about soil and mechanical systems by introducing the latest related research.

The studies presented in this reprint include research on advanced machinery technology, soil-machine interactions, and soil characteristics. It contains original and advanced research with novel analytical and experimental methods. Most farming machine applications such as agricultural tractors for multi-purposed works, rotavators for soil preparation, planters and transplanters for planting crops, pot-seeding machines for seeding in pot trays, and machine vision systems for crop phenotyping information were covered in this reprint. It also includes research on soil-machine interactions pertaining to traction force, load factor, tillage workload, and soil compaction as well as soil characteristics regarding fertilization effect and soil particle size distribution.

We believe that the research published in this reprint will be helpful to related researchers and contribute to expanding knowledge in this field. We appreciate all of the authors and reviewers for publishing their significant research results and providing excellent suggestions to improve the quality of this reprint.

**Ju-Seok Nam and Yongjin Cho**

*Editors*





# Soil Mechanical Systems and Related Farming Machinery

Yongjin Cho <sup>1</sup> and Ju-Seok Nam <sup>2,\*</sup>

<sup>1</sup> Department of Bioindustrial Machinery Engineering, Jeonbuk National University, Jeonju 54896, Republic of Korea; choyj@jbnu.ac.kr

<sup>2</sup> Department of Biosystems Engineering, Kangwon National University, 1 Kangwondaehak-gil, Chuncheon 24341, Republic of Korea

\* Correspondence: njsg1218@kangwon.ac.kr

The mechanization of agricultural work has contributed significantly to the improvement of agricultural productivity and reduced production costs. Recently, its importance has been highlighted owing to the shortage of agricultural labor, especially in developing countries where urbanization is progressing rapidly [1,2]. Since the beginning of mechanization, various types of farming machinery related to soil preparation, sowing, fertilization, pest control, harvesting, and post-harvesting have been developed. In addition, customized farming machines suitable for the cultivation type and soil characteristics of each country and region have been developed [3]. Unlike other industrial machinery, farming machinery targets living organisms and operates on the soil; therefore, it should be designed considering its interaction with the soil. Thus, it is essential to understand the characteristics of both the soil and mechanical systems to optimize the design of farming machinery. This Special Issue covers the design, analysis, and testing of all types of farming machinery, with an in-depth understanding of soil and mechanical systems.

This Special Issue contains 14 papers, with 12 research articles, one communication article, and one technical note. The authors are from five countries: Indonesia, Iran, Poland, South Korea, and Ukraine. In terms of machines, agricultural tractors, rotavators, garlic planters, vegetable transplanters, pot-seeding machines, and machine vision systems were included. Design, measurement, simulation, and theoretical analyses were conducted to develop advanced farming machinery techniques and to extend the understanding of the interaction between soil and mechanical systems in farming machine applications. The papers in this Special Issue can be grouped into three categories: advanced farming machinery techniques, soil–machine interaction research, and soil property research.

The first category includes advanced farming machine techniques. This includes the development of novel or improved mechanical systems, advanced measurement and simulation methods, and the investigation of the characteristics of farming machines using theoretical or experimental methods. Eight papers were included in this category, half of which were related to agricultural tractors.

Kim et al. presented a modified method to improve the accuracy of a three-point hitch dynamometer, also known as a six-component load cell, for measuring the precise traction force of agricultural tractors [4]. They suggested modified force and moment equations that could consider the geometry and tilt of the dynamometer under real installation conditions. The accuracy of the modified method was verified through an actual field test. This study is important because accurate knowledge of the operating force is crucial for the application of smart farming technology that requires the precise control of attached implements, as well as for the optimal design and efficient use of agricultural tractors.

Unlike Kim et al. [4], who focused on measuring the traction force, Lebedev et al. analyzed the effect of a coupling weight to increase the traction efficiency of agricultural tractors by reducing the uneven distribution of vertical reactions between the wheels [5]. They employed theoretical and comparative analyses by incorporating existing scientific findings related to agricultural tractors operating in traction mode. This study revealed

**Citation:** Cho, Y.; Nam, J.-S. Soil Mechanical Systems and Related Farming Machinery. *Agriculture* **2024**, *14*, 1661. <https://doi.org/10.3390/agriculture14091661>

Received: 23 July 2024

Accepted: 26 July 2024

Published: 23 September 2024



**Copyright:** © 2024 by the authors. Licensee MDPI, Basel, Switzerland. This article is an open access article distributed under the terms and conditions of the Creative Commons Attribution (CC BY) license (<https://creativecommons.org/licenses/by/4.0/>).

that agricultural tractors with a center of mass offset to the front or rear axles had the highest probability of equal distribution of vertical reactions between the wheels of one axle, and agricultural tractors with a center of mass in the middle between the axles had the lowest probability. In addition, this study found that agricultural tractors can operate with maximum traction efficiency when the front and rear axles are locked during plowing work, with an uneven load distribution on the sides. Although further verification is required under conditions with various installed implements, this study provides good insights into the effect of an agricultural tractor's coupling weight and center of mass on traction performance.

Lim et al. developed a finite element (FE)-based simulation model of an agricultural tractor's frame-type rollover protective structure (ROPS) to replace a real ROPS test with a virtual simulation [6]. This study presents methods for developing 3D models of ROPS and setting the load and boundary conditions to accurately simulate the force and deformation applied to the ROPS. The accuracy of the proposed method was verified using actual test results. Virtual simulation technology for the ROPS of agricultural tractors can make significant savings in time and cost, and is also very important in terms of safety. Many developed countries are conducting research to develop this technology, and this study provides important technical information.

Ahn et al. investigated power loss in the dual-clutch transmission (DCT) of agricultural tractors using theoretical and experimental approaches considering the oil circulation effect [7]. Power losses in all of the components of the DCT, such as gears, shafts, bearings, clutches, and brakes, were calculated using the ISO standard and viscous fluid theory, and the theoretical analysis result was verified through an experiment using a three-axis dynamometer system. This study revealed that the oil level of the transmission system, oil circulation conditions, and operating characteristics of the transmission components, such as rotation speed, are important factors for power loss and transmission efficiency. This study has important implications as the interest in DCT and energy conservation is increasing worldwide.

Cho and Yang developed a real-time, low-cost, and high-throughput plant phenotyping system for commercial plant factories that can determine crop growth information, such as fresh weight, leaf length, leaf width, and number of leaves [8]. The developed system is composed of a low-cost phenotype sensor network with an integrated Raspberry Pi board and a camera module that allows easy modification depending on the crop growth environment. The applicability of the system is validated through experiments on Batavia lettuce cultivated in a plant factory. The cost-effective and highly productive characteristics of the developed system can be distinguished from those of existing phenotyping systems. The ripple effect of this research is significant, as it can be applied to all types of crop cultivation facilities, including smart farms.

Lim et al. studied garlic planters [9]. This study presented a simulation method using the discrete element method (DEM) to optimize the bucket size of the finger-type metering device. For highly accurate simulation results, techniques for creating 3D models of garlic cloves and buckets, deriving the physical and mechanical properties of garlic cloves, and setting the contact conditions between the garlic cloves and bucket were presented. The simulation method presented in this study was validated through experiments using an actual garlic clove and bucket. As a result of this study, the authors were able to obtain the optimal bucket size with a plant rate of 97.5%. Recently, DEM have been widely used in simulations of the interaction effects between farming machinery and soil or agricultural products, and this study provides important information for correctly applying DEM.

In countries such as Korea and Japan, where the per capita cultivation area is not large, vegetable transplantation is often performed using semi-automatic vegetable transplanters. Markunningsih et al. investigated the power consumption, static safety factor, and fatigue life characteristics of cam- and four-bar link-type transplanters during operation [10]. Each characteristic was measured and analyzed through extensive field tests using numerous sensors attached to the transplanter components. This study expands the understanding

of the operating characteristics of semi-automatic vegetable transplanters, as well as the measurement and analysis techniques for the consumed power and static and dynamic safety of farming machines.

A mechanical pot-seeding machine was used to sow seeds into pot trays for transplanted crops. Plastic pot trays are currently being used, but are known to cause environmental problems. Hwang et al. developed an auto-feeding device for a mechanical pot-seeding machine applicable to paper-based biodegradable pot trays [11]. An auto-feeding device is used to supply pot trays individually in the first part of the mechanical pot-seeding machine, and a design appropriate for the physical and mechanical properties of the pot tray is essential. The authors designed and manufactured an auto-feeding device using mechanical and kinematic theories after measuring the properties of biodegradable pot trays. The performance of the developed device was evaluated through an actual test. The results of this study can be applied to technology for future environmental conservation.

The second category is soil-machine interaction research. It deals with the interaction effect between soil and mechanical systems, including the performance of machines that vary depending on the soil properties or the properties of soil that vary depending on the machine characteristics. Four studies were included in this category, all of which were related to agricultural tractors.

Bae et al. developed a traction force prediction model for agricultural tractors as part of a simulation study using DEM [12]. They presented a technique for modeling virtual soil environments in a simulation based on measured soil properties to obtain accurate simulation results. The traction force of an agricultural tractor during moldboard plow operations was simulated by considering the interaction between the soil and the plow blade. The simulation results were validated through an actual field test, which revealed higher accuracy than the existing empirical equation. Although the authors noted that further research is required to improve the prediction accuracy, this study provides good insight for simulating the interaction between soil and mechanical systems using DEM. This study can also be used as a reference for future digital twin modeling techniques for agricultural machinery.

Emission regulations for agricultural tractors are becoming stricter worldwide as concerns about environmental pollution increase. The load factor (LF) of agricultural tractors, which is the ratio of the actual engine power to the rated engine power, is an important indicator of air pollutant emissions. To obtain a more realistic LF in agricultural tractors, Min et al. investigated the effects of soil physical properties on the LF through extensive experiments under various soil conditions [13]. The results confirmed that soil variables had a significant influence on the LF, although the impact varied depending on the soil type. The authors noted that further research is needed to collect LF data under a wider range of tractor operating and soil conditions to improve reliability. This study has important implications related to environmental regulations of agricultural tractors.

Tillage is an essential agricultural task for the preparation of proper soil environments for crop growth. It is usually conducted by agricultural tractors with implements such as plows and rotavators, and the interaction between the soil and implementation has a decisive impact on tillage performance. Kim et al. analyzed the effects of the tillage type and gear selection on the workload of agricultural tractor-implement systems during rotary tillage [14]. The soil properties and mechanical operating characteristics were simultaneously considered to derive conclusions through extensive field experiments. The authors concluded that both the soil and mechanical conditions significantly influenced the tillage workload. The quantitative measurement results of this study can be used as reference data for designing agricultural tractors and implements as well as for understanding the workload characteristics during tillage operations.

Soil compaction caused by the passage of agricultural tractors has long been a subject of interest because of its significant effect on crop growth. Shahgholi et al. investigated the effects of the tire parameters of agricultural tractors on soil compaction through experiments and mathematical analysis [15]. The authors revealed that the tire size, tire inflation

pressure, and number of passages are significant influencing factors of soil compaction, and their effects vary depending on the tire type and soil depth. A narrow tire is more effective for soil compaction because its soil bulk density changes significantly more than that of a normal tire under the same external offset condition. This study provides insight into the interaction between soil compaction and the mechanical or operating characteristics of agricultural tractors.

The final subject area was soil property research. It focuses on the quantification of soil properties for agricultural applications, with two papers in this category.

In precision agriculture, which minimizes the amount of input resources and maximizes production, spot-specific fertilization or variable control based on soil and crop characteristics is essential. Shin et al. developed a map of expected fertilization rates for nitrogen (N) and phosphorus (P<sub>2</sub>O<sub>5</sub>) based on quantified soil properties in salt-affected paddy fields [16]. The predicted N fertilization rate for the entire field was within 10.0 g to 25.7 g for each lot, whereas that of P<sub>2</sub>O<sub>5</sub> was in the range of 0.68 g to 8.46 g. This large deviation indicates significant savings in resources compared to fertilizing the same amount overall. The technique used in this study can be applied to any type of fertilizer for precision agriculture.

Soil particle size distribution has a significant impact on the mechanical characteristics of the soil and its interaction with farming machines. Standard sieves were used to determine the size distribution of relatively large particles. However, for very small particles (less than approximately 5 mm in diameter), a hydrometer test is needed to determine the size distribution, which requires a considerable amount of labor and time. Kim et al. proposed a new method to determine the size distribution of small particles using a machine vision system with a red–green–blue (RGB) camera to overcome the shortcomings of hydrometer tests [17]. The experimental results demonstrate the reliability and accuracy of the proposed system, with only a 2.3% deviation from the actual particle size distribution. This study presents a novel and promising technique for assessing soil particle size distribution, which can be an alternative to traditional methods.

The papers in this Special Issue of Soil Mechanical Systems and Related Farming Machinery contain excellent research results that reflect the latest trends in the field. We are confident that this Special Issue will inspire researchers in the field and serve as excellent research reference data. We sincerely thank all of the authors who submitted their papers to this Special Issue and the reviewers of these papers for their constructive comments and thoughtful suggestions.

**Author Contributions:** Conceptualization, Y.C. and J.-S.N.; investigation, Y.C.; writing—original draft preparation, Y.C.; writing—review and editing, J.-S.N.; and visualization, Y.C. and J.-S.N. All authors have read and agreed to the published version of the manuscript.

**Funding:** This work was supported by Korea Institute of Planning and Evaluation for Technology in Food, Agriculture, and Forestry (IPET) through Machinery Mechanization Technology Development Program for Field Farming Program funded by Ministry of Agriculture, Food, and Rural Affairs (MAFRA) (RS-2023-00236201).

**Conflicts of Interest:** The authors declare no conflicts of interest.

## References

1. Kim, S.J.; Lee, H.S.; Hwang, S.J.; Kim, J.H.; Jang, M.K.; Nam, J.S. Development of Seeding Rate Monitoring System Applicable to a Mechanical Pot-Seeding Machine. *Agriculture* **2023**, *13*, 2000. [CrossRef]
2. Choudhary, V.; Machavaram, R. Need of Automation in Paddy Nurseries for Raising Paddy Seedlings in India: A Review. *J. Biosyst. Eng.* **2022**, *47*, 209–222. [CrossRef]
3. Bagherpour, H.; Talab, M.M.S. Design, Construction, and Evaluation of a Precision Vegetable Reaper to Use in Small Plots. *J. Biosyst. Eng.* **2024**, *49*, 41–51. [CrossRef]
4. Kim, H.G.; Lee, J.W.; Kim, S.C.; Oh, J.; Shim, S.B. Development of a Modified Method for Measuring the Actual Draft Force Using a Tractor-Attached Dynamometer. *Agriculture* **2024**, *14*, 544. [CrossRef]
5. Lebedev, A.; Shuliak, M.; Khalin, S.; Lebedev, S.; Szwedziak, K.; Lejman, K.; Niedbała, G.; Łusiak, T. Methodology for Assessing Tractor Traction Properties with Instability of Coupling Weight. *Agriculture* **2023**, *13*, 977. [CrossRef]

6. Lim, R.G.; Kim, W.S.; Do, Y.W.; Siddique, M.A.A.; Kim, Y.J. Performance Evaluation of a Virtual Test Model of the Frame-Type ROPS for Agricultural Tractors Using FEA. *Agriculture* **2023**, *13*, 2004. [CrossRef]
7. Ahn, H.J.; Park, Y.J.; Kim, S.C.; Choi, C. Theoretical Calculations and Experimental Studies of Power Loss in Dual-Clutch Transmission of Agricultural Tractors. *Agriculture* **2023**, *13*, 1225. [CrossRef]
8. Cho, W.J.; Yang, M. High-Throughput Plant Phenotyping System Using a Low-Cost Camera Network for Plant Factory. *Agriculture* **2023**, *13*, 1874. [CrossRef]
9. Im, D.; Lee, H.S.; Kim, J.H.; Moon, D.J.; Moon, T.I.; Yu, S.H.; Park, Y.J. Bucket Size Optimization for Metering Device in Garlic Planter Using Discrete Element Method. *Agriculture* **2023**, *13*, 1199. [CrossRef]
10. Markumningsih, S.; Hwang, S.J.; Kim, J.H.; Jang, M.K.; Shin, C.S.; Nam, J.S. Comparison of Consumed Power and Safety of Two Types of Semi-Automatic Vegetable Transplanter: Cam and Four-Bar Link. *Agriculture* **2023**, *13*, 588. [CrossRef]
11. Hwang, S.J.; Jang, M.K.; Nam, J.S. Development of Autofeeding Device Applicable to a Biodegradable Pot Tray. *Agriculture* **2022**, *12*, 2097. [CrossRef]
12. Bae, B.M.; Kim, Y.S.; Kim, W.S.; Kim, Y.J.; Lee, S.D.; Kim, T.J. The Development of a Draft Force Prediction Model for Agricultural Tractors Based on the Discrete Element Method in Loam and Clay Loam. *Agriculture* **2023**, *13*, 2205. [CrossRef]
13. Min, Y.S.; Kim, Y.S.; Lim, R.G.; Kim, T.J.; Kim, Y.J.; Kim, W.S. The Influence of Soil Physical Properties on the Load Factor for Agricultural Tractors in Different Paddy Fields. *Agriculture* **2023**, *13*, 2073. [CrossRef]
14. Kim, Y.S.; Bae, B.M.; Kim, W.S.; Kim, Y.J.; Lee, S.D.; Kim, T.J. Working Load Analysis of a 42 kW Class Agricultural Tractor According to Tillage Type and Gear Selection during Rotary Tillage Operation. *Agriculture* **2023**, *13*, 1556. [CrossRef]
15. Shahgholi, G.; Moinfar, A.; Khoramifar, A.; Maciej, S.; Szymanek, M. Investigating the Effect of Tractor's Tire Parameters on Soil Compaction Using Statistical and Adaptive Neuro-Fuzzy Inference System (ANFIS) Methods. *Agriculture* **2023**, *13*, 259. [CrossRef]
16. Shin, J.; Won, J.; Kim, S.M.; Kim, D.C.; Cho, Y. Fertilization Mapping Based on the Soil Properties of Paddy Fields in Korea. *Agriculture* **2023**, *13*, 2049. [CrossRef]
17. Kim, D.; Song, J.; Park, J. Quantifying Soil Particle Settlement Characteristics through Machine Vision Analysis Utilizing an RGB Camera. *Agriculture* **2023**, *13*, 1674. [CrossRef]

**Disclaimer/Publisher's Note:** The statements, opinions and data contained in all publications are solely those of the individual author(s) and contributor(s) and not of MDPI and/or the editor(s). MDPI and/or the editor(s) disclaim responsibility for any injury to people or property resulting from any ideas, methods, instructions or products referred to in the content.

## Article

# Development of a Modified Method for Measuring the Actual Draft Force Using a Tractor-Attached Dynamometer

Hyo-Geol Kim <sup>1</sup>, Jin-Woong Lee <sup>2</sup>, Su-Chul Kim <sup>3</sup>, Jooseon Oh <sup>4,5,\*</sup> and Sung-Bo Shim <sup>6,7,8,\*</sup><sup>1</sup> TYM Co., Ltd., Seoul 06053, Republic of Korea; zion.kim@tym.world<sup>2</sup> Specialized Machinery and Robotics Group, Korea Institute of Industrial Technology, Gimje 54325, Republic of Korea; reallybear@kitech.re.kr<sup>3</sup> Department of Industrial Machinery DX, Korea Institute of Machinery and Materials, Daejeon 34103, Republic of Korea; sckim@kimm.re.kr<sup>4</sup> Department of Convergence Biosystems Engineering, Chonnam National University, Gwangju 61186, Republic of Korea<sup>5</sup> BK21 Interdisciplinary Program in IT-Bio Convergence System, Chonnam National University, Gwangju 61186, Republic of Korea<sup>6</sup> Department of Bio-Industrial Machinery Engineering, Kyungpook National University, Daegu 41566, Republic of Korea<sup>7</sup> Smart Agri Innovation Center, Kyungpook National University, Daegu 41566, Republic of Korea<sup>8</sup> Upland Field Machinery Research Center, Kyungpook National University, Daegu 41566, Republic of Korea

\* Correspondence: jooseon.oh@jnu.ac.kr (J.O.); sbs80@knu.ac.kr (S.-B.S.); Tel.: +82-62-530-2155 (J.O.); +82-53-950-5793 (S.-B.S.)

**Abstract:** In this study, crank-locker kinematic equations were used to analyze the three-point hitch behavior when the dynamometer was connected to the work machine. The dynamometer was statically tested with a hydraulic actuator, and the accuracy of the three-way force and the moment was confirmed to be 96–99%. The calibrated dynamometer was put to the test on a real farm field, and data were collected using a data acquisition system. Using the transport pitch correction equation, the collected data can be transformed into more realistic data. International standards were used to determine the point of connection between the tractor, dynamometer, and implement. The results of this study made it possible to accurately measure force and moment, which will have an important role in future agricultural technologies such as autonomous agricultural operation.

**Keywords:** three-point hitch; tractor-attached dynamometer; force–moment equation; force measurement accuracy

**Citation:** Kim, H.-G.; Lee, J.-W.; Kim, S.-C.; Oh, J.; Shim, S.-B. Development of a Modified Method for Measuring the Actual Draft Force Using a Tractor-Attached Dynamometer. *Agriculture* **2024**, *14*, 544. <https://doi.org/10.3390/agriculture14040544>

Academic Editors: Jin He and Caiyun Lu

Received: 25 October 2023

Revised: 15 March 2024

Accepted: 25 March 2024

Published: 29 March 2024



**Copyright:** © 2024 by the authors. Licensee MDPI, Basel, Switzerland. This article is an open access article distributed under the terms and conditions of the Creative Commons Attribution (CC BY) license (<https://creativecommons.org/licenses/by/4.0/>).

## 1. Introduction

Modern agriculture is highly specialized and mechanized, and the agricultural work-force is decreasing as rural populations decline and age. As a result, the use of a tractor that can be equipped with a variety of agricultural implements to increase the labor force is becoming more common [1].

The tractor generates forces in various directions during operation. The generated force affects operation performance, the life of the implement, and tractor parts [2]. The tractor interacts with the soil during operation, and the force is changed by various variables, such as the soil properties and the tractor's shift level.

The traction force generated by the tractor can be estimated from the Wismer–Luth, Brixius equations, etc., which are registered in the ASABE test specification [3,4]. However, since these estimation methods are empirical formulas rather than theory-based methods, the prediction result cannot be considered accurate. Furthermore, because variables such as the soil cone index (CI) cannot be used in real-time formulas, predicting the traction force in real time is inaccurate. As a result, measuring the force with a sensor such as a load cell or strain gage yields the most accurate traction results. To address these issues,

dynamometers with sensors have recently been developed to measure the force generated during operation [4].

An adjustable three-point hitch dynamometer with a draft capacity of 50 kN to measure forces on the tractor and mounted implements were developed [5]. With this dynamometer, it was confirmed that all mounted tillage implements in categories II and III such as plows, cultivators, and harrows could be tested [6]. And a bi-axial direct-mount strain gage lower link system calibrated for coincident and perpendicular loads up to 10 kN for measuring tractor–implement forces were developed [7]. The strain gage test method was confirmed to be the most appropriate when medium-type equipment is used with a tractor. However, because all of the tests were conducted in a lab, field validation is required.

A mathematical model was developed to determine the forces and the moments at the different couplers between bodies of the tractor–dynamometer–implement system, taking into account the mechanical characteristics of the dynamometer as well as the inclination of the terrain on which the tractor is working [8]. This model allows you to evaluate the dynamometer’s destructive effect on the forces acting on the tractor. However, the effect of the connection between the dynamometer and the power take-off (PTO) was not considered. To measure traction forces, a dynamometer made up of three telescopic beams connected to a central T-shaped box was developed [9]. A three-point hitch-attached dynamometer basic conceptual diagram was presented. Different strain gage sets can be attached and arranged in the bridge to measure only lateral or vertical forces. However, because it was developed for use in a specific region, the use of the device presented is bound to be limited. Additionally, there is a lack of evidence that the measured force was exact using dynamometer.

A six-component load cell was developed to measure the tractor’s traction force, and the accuracy of the load measurement using a six-component load cell was validated using a static load test [10]. In addition, a field test was conducted by installing the developed six-component load cell on the multi-tasking agricultural implement and measuring the working load. A method was presented for acquiring and post-processing traction force data while performing tillage operations using a three-point hitch [11]. The developed system is capable of running a large number of carried and partially carried machines in the II and III categories. In two past studies, a research was conducted to measure forces and moments using a hitch dynamometer, but it cannot be considered that accurate forces and moments were analyzed because changes in size and angle due to installation of the dynamometer were not considered.

Many research cases support the use of a three-point hitch dynamometer to measure the force applied to a three-point hitch during agricultural work confirmed [12,13]. To increase the precision of force measurement, the three-point hitch dynamometer primarily employs a six-component load cell. However, there are only a few cases where the geometrical change caused by the installation of the dynamometer is considered. Furthermore, no research has been conducted on how to correct the actual data that change depending on the angle of the dynamometer.

In this study, a modified method was presented to increase the accuracy of traction force prediction for tractors equipped with dynamometers. Using the existing equations, a modified equation considering the geometry of the dynamometer was developed. The equation’s accuracy has been demonstrated through static load tests and a field test. By correcting the error of the measurement data that may occur due to the installation of the dynamometer, a modified method that can obtain data close to the actual is presented.

Securing realistic traction force data enables accurate measurement of the traction force. And it will enable the development of algorithms for performing autonomous agricultural operation through accurate traction measurement.

## 2. Materials and Methods

### 2.1. Three-Point Hitch

As shown in Figure 1, the three-point hitch is the most representative method used to connect the tractor and various implements [14]. The three-point hitch consists of two lower links and one upper link, and there are other devices to drive these links. The lift arm rotates by hydraulic power and is connected to the lift rod. The lift rod is connected to the lower link to pull up the lower link. The upper link moves dependently as the lower link moves up and down. The upper link is adjustable in length, and the upper and lower links each have a link point attached to the tractor and a hitch point attached to the implement. ISO 730 [15] defines mast height as the height of the triangle formed by the three hitch points.

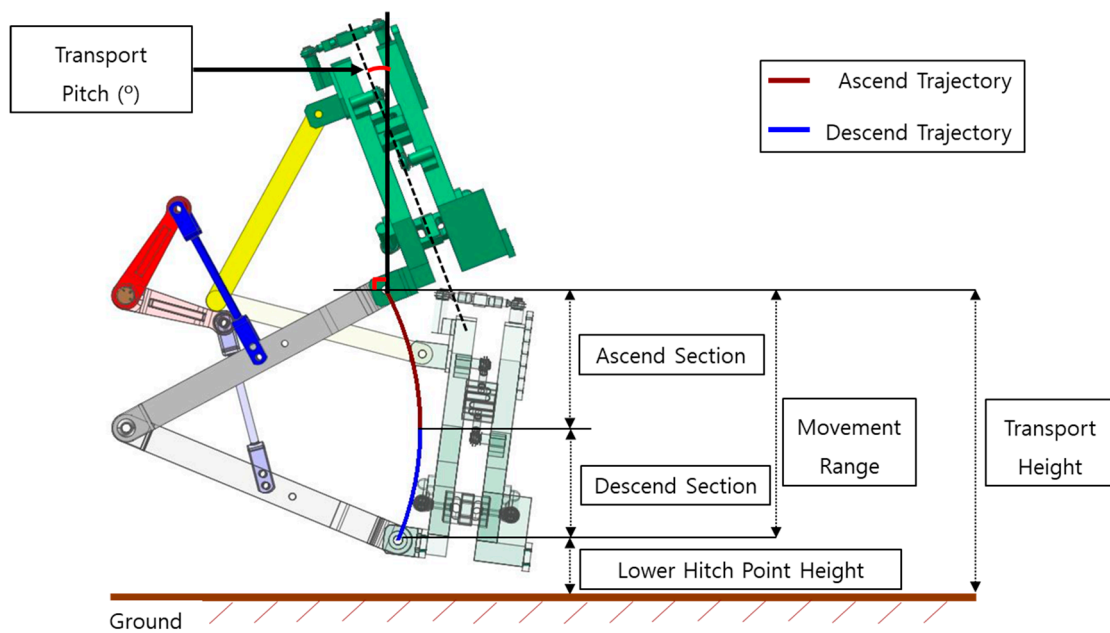


**Figure 1.** Element of three-point hitch.

When the three-point hitch ascends and descends, a height element with the ground and transport pitch of the implement occur. The transport pitch is defined as the angle between the working machine and the virtual vertical line. Transport pitch is determined by the range of use of the implement, which has a significant impact on load and traction. The transport pitch is measured when the minimum transport height is reached. The transport height is the vertical distance from the ground to the lower hitch point when the three-point hitch is ascended. The lower hitch point height is the vertical distance between the ground and the lower hitch point when the hitch descends. The movement range is actually the vertical displacement of the three-point hitch and is the transport height minus the lower hitch point height [16–19]. Transport pitch, transport height, lower hitch point height, and mast height are all specified by the ISO 730.

### 2.2. Three-Point Hitch-Type Dynamometer

#### 2.2.1. Specification of Load Cell and DAQ

The dynamometer used in this study is a combination of triangular frame and one-axis load cell. The triangular shape was chosen for this study because it is known to be more structurally stable and easy to design. Because each link of the three-point hitch is connected one to one, the triangular geometry is relatively stable in terms of dynamics.

Single-axis load cells (CAS, SBA-2) are installed in 6 locations. Three load cells mounted in the tractor driving direction measure only the traction force. Two load cells mounted on the slope of a triangle measure longitudinal and vertical forces. Load cells



mounted in the horizontal direction measure only longitudinal forces. The specifications of the load cell used in this study are shown in Table 1.

**Table 1.** Specification of the load cell used in this study.

Specification	Value
Max capacity (kgf)	2000
Rated output (mV/V)	$3.0 \pm 0.3$
Zoro balance (mV/V)	$0 \pm 0.03$
Combined error (%)	0.03
Repeatability (%)	0.01
Recommended excitation (V)	10
Maximum excitation (V)	15

Six load cells connected to the dynamometer are connected to the data acquisition system (DAQ) with a Wheatstone bridge. The data from each measured load cell are independently output and finally converted into target elements via equations. Output data are transferred to a PC via Ethernet and stored. The specifications of DAQ used for data acquisition are shown in Table 2. Each load cell is connected to the switch box by a connector and then from the switch box to the DAQ.

**Table 2.** Specification of DAQ used in this study.

Specification	Value
Model Name	Q.Brixx A108
Manufacturer	Gantner, Germany
Input Voltage (V)	Max 30
Input Current (mA)	Max 0.5
Upper Threshold (V)	>10
Lower Threshold (V)	<2
Analog Input Accuracy (%)	0.01–0.05
Repeatability (%)	0.003

2.2.2. Dynamometer Component Force and Moment

Because the dynamometer’s load cell can only detect force in one direction, it must be converted to the needed factor using the combined load cell. The traction force is measured on  $F_a$ ,  $F_b$  and  $F_c$  load cells mounted in the tractor’s driving direction. Figure 2 shows a free body diagram of the load cell’s three-direction force.

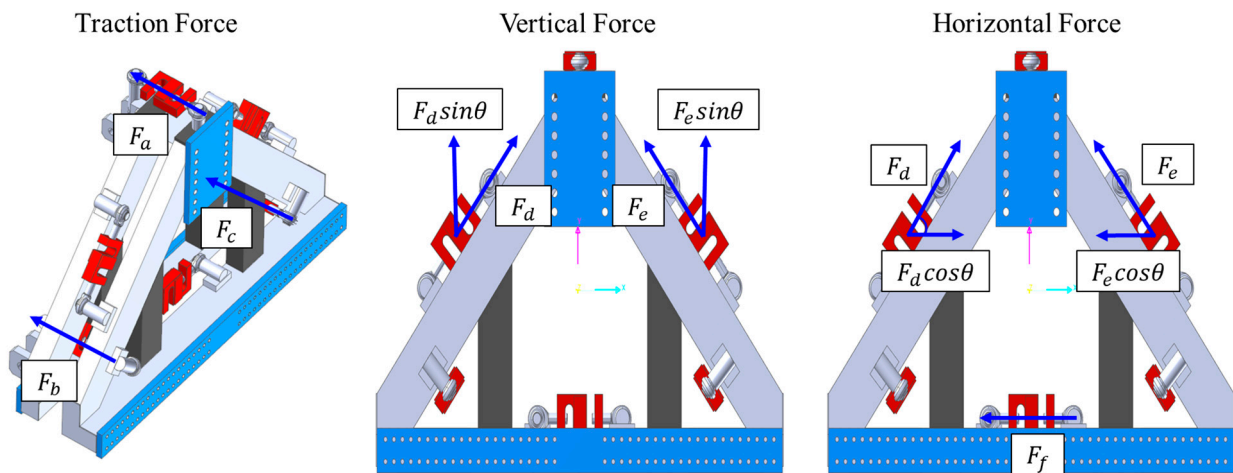


**Figure 2.** Component force direction of load cells.

Vertical force is calculated by multiplying the value measured by the  $F_d$  and  $F_e$  load cells mounted on the inclined plane of the triangle and the sine of the triangle. The longitudinal force is calculated by multiplying the values of the load cells  $F_d$  and  $F_e$  by the cosine of the triangle, and adding  $F_f$  which measures the longitudinal force.

The traction moment is calculated from the front of the dynamometer's geometric center. Forces  $F_d$  and  $F_e$  are converted to perpendicular components and recalculated as moments. Forces of  $F_a$ ,  $F_b$  and  $F_c$  in the same moment, direction does not affect the traction moment. Force  $F_f$  is added to the moment in the tension direction.

The vertical direction moment is calculated based on the center of the dynamometer from above.  $F_a$ ,  $F_f$ , which make up the center, and  $F_d$  and  $F_e$ , which are not in the plane, do not affect the vertical direction moment. Vertical moments are calculated simply with  $F_b$  and  $F_c$ , as well as a horizontal distance away from the center.

The horizontal direction moment is also calculated based on the side of the dynamometer from above.  $F_d$ ,  $F_e$ , which make up the center, and  $F_f$  not in the plane, do not affect the horizontal direction moment. Horizontal moments are calculated only with  $F_a$ ,  $F_b$  and  $F_c$ , and with a vertical distance away from the center.

Once the component force and moment are determined, the component force and moment may be calculated using the dynamometer shape and center point.  $P_h$  is the sum of the traction forces.  $P_v$  is the sum of the vertical forces, and  $P_s$  is the sum of the horizontal forces.  $M_h$  is the torsional moment acting in the traction direction?  $M_v$  is the torsional moment acting in the vertical direction,  $M_s$  is the torsional moment acting in the horizontal direction.

### 2.3. Tractor and Implement

The dynamometer was mounted on the 26 kW tractor and linked to the 2440 mm-long plows. Figure 3 shows the dynamometer and associated components attached to the tractor. The implement used in this study was category 1 type, and detailed information was omitted.



**Figure 3.** Dynamometer and instrumentation components.

### 2.4. Test

Static load tests and field tests were performed to compare the results measured by the dynamometer with those calculated by modified equation.

In the static load tests, the method was used to apply static load and moment through a hydraulic actuator to compare the input value with the actual input load. In field tests,

the force was measured by performing the plow operation while maintaining the operating depth of the plow constant [20].

### 3. Results and Discussion

#### 3.1. Modified Equation

The component force–moment equation for the triangular three-point hitch dynamometer was developed based on these considerations. Figure 4 summarizes the direction and magnitude of moments. The location information where the load cells are mounted on the dynamometer is shown in Figure 4. This is very important information regarding moment calculations. The location values in this study are as follows.

$$l_1 = 0.0506 \text{ m}$$

$$l_2 = 0.2878 \text{ m}$$

$$l_3 = 0.2461 \text{ m}$$

$$l_4 = 0.3081 \text{ m}$$

$$l_5 = 0.3233 \text{ m}$$

$$l_6 = 0.1938 \text{ m}$$

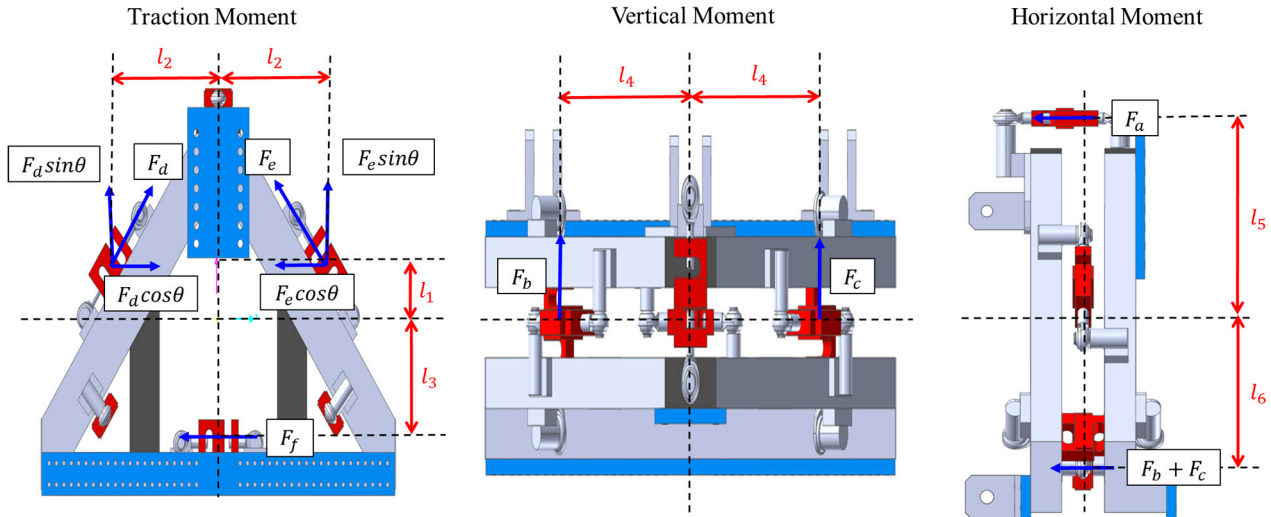


Figure 4. Moment direction of load cells.

Figure 5 shows the direction of each force and moment, and the dynamometer equation developed is represented by Equations (1)–(6). The coordinate system for calculation was set based on the end point of the dynamometer axis connected to the PTO axis. The tractor’s forward direction was set to the x-axis, the left and right directions were set to the y-axis, and the vertical direction was set to the z-axis. This system is local coordinate system [21].

$$F_x = F_a + F_b + F_c \tag{1}$$

$$F_z = F_d \sin\theta + F_e \sin\theta \tag{2}$$

$$F_y = F_e \cos\theta - F_d \cos\theta + F_f \tag{3}$$

$$M_x = (F_d - F_e) \times [l_2 \sin\theta + l_1 \cos\theta] + l_3 \times F_f \tag{4}$$

$$M_z = (F_b - F_c) \times l_4 \tag{5}$$

$$M_y = F_a l_5 - (F_b + F_c) \times l_6 \tag{6}$$

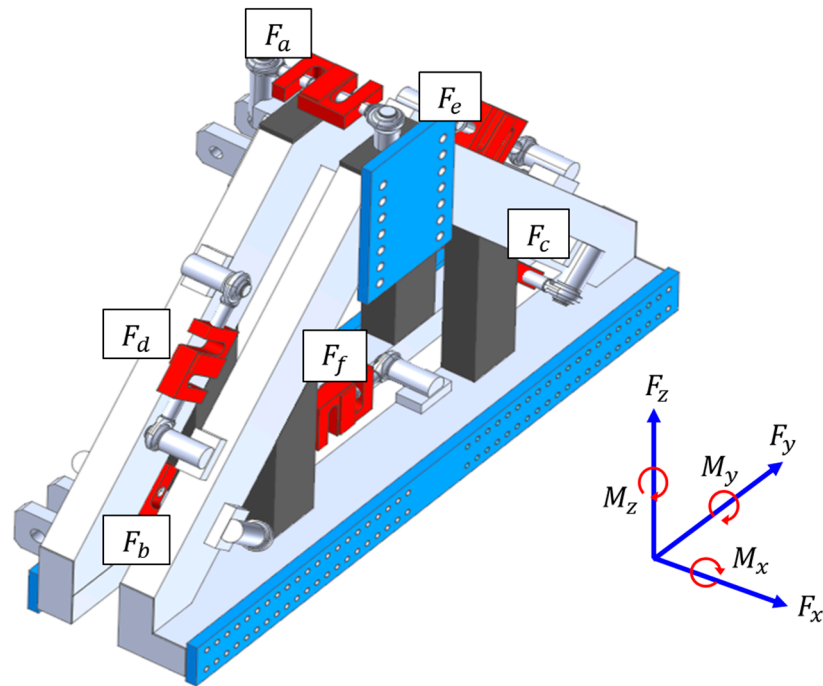


**Figure 5.** The force–moment direction of the dynamometer.

The dynamometer consists of a single-axis load cell, its value should be modified according to the pitch angle of the dynamometer. Since the dynamometer was initially connected vertically to the lower link, the transport pitch is the dynamometer’s angle.

Let the  $x'y'z'$  coordinate system move and rotate with the dynamometer such that the load cells are always in the  $y'z'$  plane and with the same  $y'z'$  coordinates ( $x'$  coordinate of all load cells is zero since all load cells are in the  $y'z'$  plane). Since the  $x'y'z'$  coordinate system moves with the dynamometer, any forces and moments measured by the dynamometer load cells will be expressed in the  $x'y'z'$  coordinate system by Equations (1)–(6), irrespective of the orientation of the dynamometer, even if it is upside down. The  $xyz$  coordinate system and  $x'y'z'$  coordinate system can be simplified through Figure 6.

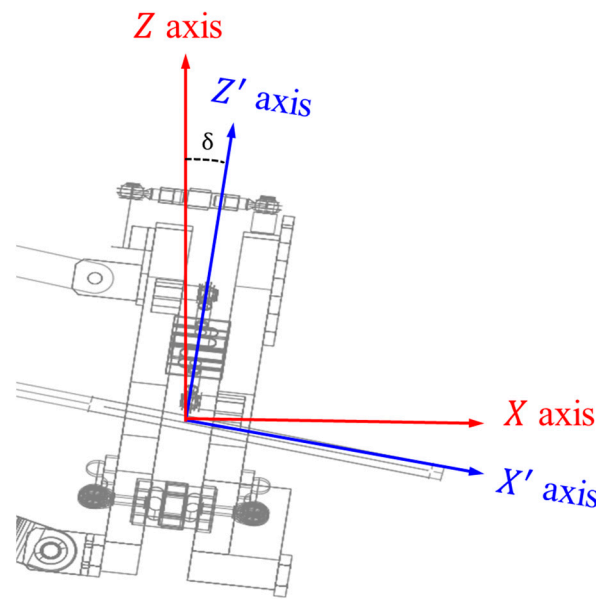


Figure 6. New coordinate system.

Transform these forces and moments in the  $x'y'z'$  coordinate system at transport pitch,  $\delta$ , to the global coordinate system,  $xyz$ . The transport pitch used in this study is  $-7.52^\circ$  at lowest hitch point. All that is required to achieve this is to pre-multiply the force and moment vectors by a standard 2-D coordinate transformation matrix.

Equation (7) rotates the  $x'y'z'$  coordinate system about the  $y'$  axis by an angle  $\delta$ . Whether the signs for  $\sin\delta$  are positive or negative depends on whether the rotation angle is measured from  $x'y'z'$  to  $xyz$ , or from  $xyz$  to  $x'y'z'$  coordinate systems. The same rotation matrix can be used to transform the three moments,  $M_{x'}$ ,  $M_{y'}$  and  $M_{z'}$  to  $M_x$ ,  $M_y$  and  $M_z$  in the global  $xyz$  coordinate system. In fact, the three orthogonal forces and moments as measured by the dynamometer load cells, can be combined into a six dimensional load vector, and transformed from the  $x'y'z'$  coordinate system by pre-multiplying by a single  $6 \times 6$  partitioned transformation matrix.

$$\begin{bmatrix} F_x \\ F_y \\ F_z \end{bmatrix} = \begin{bmatrix} \cos\delta & 0 & \sin\delta \\ 0 & 1 & 0 \\ -\sin\delta & 0 & \cos\delta \end{bmatrix} \begin{bmatrix} F_{x'} \\ F_{y'} \\ F_{z'} \end{bmatrix} \tag{7}$$

### 3.2. Result of the Static Load Test

Tables 3 and 4 show the calculated force and moment when the static force and moment are applied. The moment is calculated by multiplying the vertical distance between the hydraulic actuator and the center of the dynamometer. And the error rate was calculated by comparing the calculated data and the input data.

Table 3. Calculated force and input force.

Specification	Calculated Force (kN)	Input Force (kN)	Error Rate (%)
Traction Force	14.709	14.551	1.1
Vertical Force	9.806	9.732	0.8
Lateral Force	4.903	5.032	2.6

**Table 4.** Calculated moment and input moment.

Specification	Calculated Moment (kN·m)	Input Moment (kN·m)	Error Rate (%)
Traction Moment	3.912	3.983	1.8
Vertical Moment	3.912	3.807	2.7
Lateral Moment	2.535	2.619	3.5

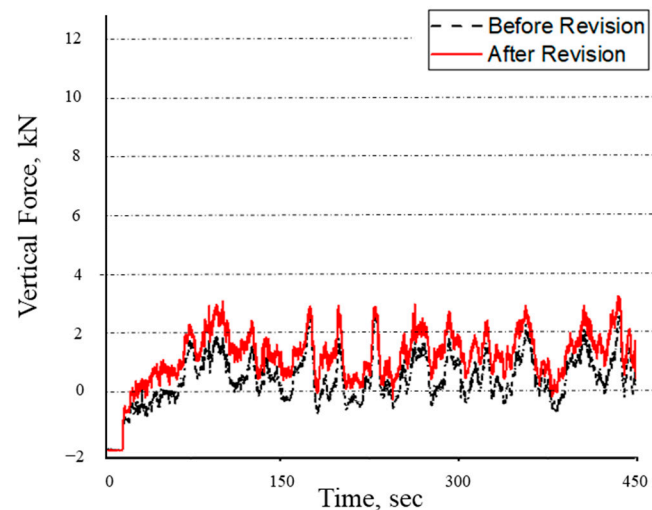
The component force test yielded an accuracy of 97.4% or higher in all regions, as well as satisfactory reliability. The component force tests have modest errors, which are predicted to be caused by manufacturing errors and misalignment when attaching the surface plates.

The error of the moment test is expected to be the measurement error and the moment arm length. The maximum accuracy of 98.2% and the minimum accuracy of 96.5% were calculated for the whole test, and the dynamometer is considered reliable even considering the error rate.

### 3.3. Result of the Field Test

To ensure that the dynamometer operates accurately in the field, the dynamometer was tested in the field. The test site is a test field located in Gimje-si, Korea. The force was measured by performing the plow operation while maintaining the operating depth of the plow constant. The operation velocity was set to 3 km/h, and the hitch height lever was set to the same value during all test conditions. During plow work, the power of the tractor was mainly consumed by the traction force, and the vertical force supporting the machine was second. Horizontal forces occurred insignificantly, and the effects of torsion were not considered in this study.

Figure 7 shows the traction force corrected by dynamometer installation, while Figure 8 shows the vertical force. When the implement descends due to the horizontal connection condition of the initial implementation, the transport pitch occurs in the negative direction, so the traction force decreases by the transport pitch sine value of the vertical force.

**Figure 7.** Traction data before and after revision.



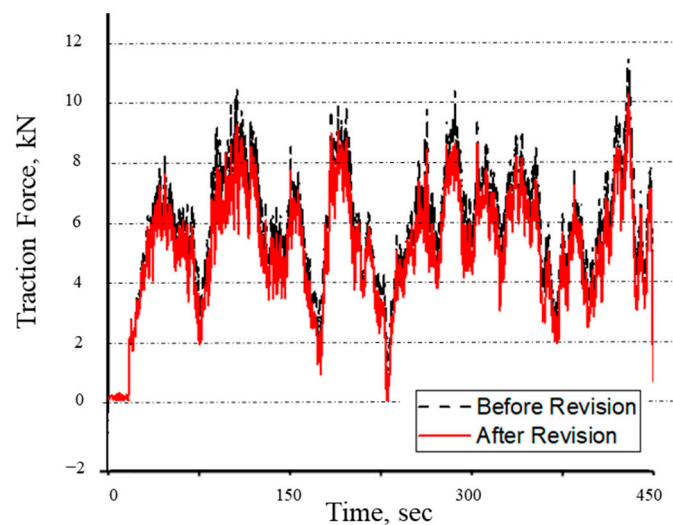


**Figure 8.** Vertical force data before and after revision.

The measured values of the traction force and vertical force itself are also changed by the transport pitch, but the transport pitch generated at the actual working depth is 0.994–0.99, and the difference value is insignificant, 0.06–1%, so there is virtually no difference.

When the transport pitch value occurs anticlockwise when the implement is lowered, the traction force increases in part with the vertical force and decreases in part with the traction force, resulting in a traction-vertical component force that differs from the initial measured force. The larger the transport pitch, the larger the difference between the correction value and the measured value is because the value of the traction force to be converted to the vertical force is greater than the vertical force to be converted to the traction force. When lowering the implement to the desired operation depth, the transport pitch affects this difference. In addition, the initial connection angle is thought to be important. As a result, net traction increased by approximately 11.4%.

As a result, the difference in vertical force is greater while operating with plows, cultivators, and sub-soilers, which demand a high traction force. When working with a rotavator or agricultural roller under conditions that demand little traction or have a high vertical force due to the weight of the implement itself, the difference in the traction force is expected to be greater.

Through this study, a method to accurately measure traction forces and moments was proposed. Static tests were performed in which known values were applied to the dynamometer, and the effectiveness of the method was proven as a result of low errors. It was confirmed that the results of applying this method to the field test showed a difference of 11.4% compared to the value measured using the existing method.

In order to realize open-field smart farms, which are in the spotlight as one of future agriculture, autonomous farming must be carried out. For autonomous agricultural operation, it is necessary to accurately measure the load applied to the three-point hitch during agricultural operation, and this study can contribute. In addition, it is necessary to correct the measurement results using a dynamometer and verify the effectiveness of this study through various field tests.

#### 4. Conclusions

This study was conducted to design a three-point hitch dynamometer with an easy connection to the implement and to propose a calibration equation to obtain realistic data. The conclusions obtained in this study are as follows.

- (1) The force–moment equation was developed considering the geometrical position of the load cell constituting the dynamometer and, as a result of static load testing using a hydraulic actuator, confirmed more than 97% accuracy in all sections.

- (2) The plow work data were collected in the field with a dynamometer and verified in a static environment. A modified equation based on transport pitch was used to modify the measured data. The actual traction force is slightly less than the measured traction force, and the actual vertical force is 11.7% greater than the measured vertical force. Because the dynamometer is a single-axis load cell, the correction data using the transport pitch are thought to be closer to the actual data.
- (3) Because traction is primarily used in plowing, a significant difference between the actual vertical force and the measured vertical force was confirmed because the traction force to be converted into vertical force was large. In contrast, in roller and landscape work, where vertical force is primarily used, the vertical force to be converted into the traction force is greater, so a significant difference between the actual traction force and the measured traction force is expected.
- (4) This study can be used as a basis for open-field smart farm research. The core of open-field smart farm technology is autonomous agricultural operation, and for this, it is most important to accurately analyze the traction force required for agricultural operation. The significance of this study is that it enabled precise traction analysis for autonomous agricultural operation. In addition, it is expected that further research will be needed, such as real-time traction analysis and traction force prediction for real-time autonomous agricultural operation.

**Author Contributions:** Conceptualization and methodology, H.-G.K.; validation, J.O.; formal analysis, J.-W.L.; data curation, S.-C.K.; writing—original draft preparation, H.-G.K. and J.O.; writing—review and editing, J.O. and S.-B.S.; funding acquisition, S.-B.S. All authors have read and agreed to the published version of the manuscript.

**Funding:** This research was supported by Kyungpook National University Research Fund, 2021. This research was conducted with the support of the “Development of Safety Evaluation and Management Technology for High-Risk Construction Machinery (Project No. RS-2023-00244879)” implemented by the Ministry of Land, Infrastructure and Transport/Korea Agency for Infrastructure Technology Advancement and overseen by the Korea Construction Equipment Safety Institute.

**Institutional Review Board Statement:** Not applicable.

**Data Availability Statement:** Data is contained within the article.

**Conflicts of Interest:** Author Hyo-Geol Kim is employed by the company TYM Co., Ltd. The remaining authors declare that the research was conducted in the absence of any commercial or financial relationships that could be construed as a potential conflict of interest.

## References

1. Koo, Y.M. PTO Torque and draft analyses of an integrated tractor-mounted implement for round ridge preparation. *J. Biosyst. Eng.* **2022**, *47*, 330–343. [CrossRef]
2. Beigi, M.; Ghazavi, M.A.; Ahmadi, I. Design and construction of load cell of a three point hitch dynamometer for tractor John Deere 3140. *J. Mod. Process. Manufacturing Prod.* **2014**, *3*, 47–58.
3. Wismer, R.D.; Luth, H.J. Off-road traction prediction for wheel vehicles. *Trans. ASAE* **1974**, *17*, 8–14. [CrossRef]
4. Alimardani, R.; Fazel, A.; Akram, A.; Mahmoudi, A.; Varnamkhsati, M.G. Design and Development of a three-point hitch dynamometer. *J. Agric. Technol.* **2008**, *4*, 37–52.
5. Brixius, W.W. *Traction Prediction Equations for Bias Ply Tires*; Transaction of the ASAE, 87-1622; American Society of Agricultural Engineers: St. Joseph, MI, USA, 1987.
6. Askari, M.; Komarizade, M.H.; Nikbakht, A.M.; Nobakht, N.; Teimourlou, R.F. A novel three-point hitch dynamometer to measure the draft requirement of mounted implements. *Res. Agric. Eng.* **2011**, *57*, 128–136. [CrossRef]
7. Khan, J.; Godwin, R.J.; Kilgour, J.; Blackmore, B.S. Design and calibration of a direct mounted strain gauged lower links system for measurement of tractor-implement force. *J. Eng. Appl. Sci.* **2006**, *1*, 22–25.
8. Roca, J.; Comellas, M.; Pijuan, J.; Nogués, M. Development of an easily adaptable three-point hitch dynamometer for agricultural tractors. Analysis of the disruptive effects on the measurements. *J. Soil Tillage* **2019**, *194*, 104323. [CrossRef]
9. Al-Jalil, H.F.; Khdair, A.; Mukahal, W. Design and performance of and adjustable three-point hitch dynamometer. *J. Soil Tillage* **2001**, *62*, 153–156. [CrossRef]
10. Kim, E.K.; Moon, S.G.; Oh, C.M.; Han, J.W. Working load measurement using 6-component load cell and fatigue damage analysis of composite working implement. *J. Agric. Life Environ. Sci.* **2017**, *29*, 225–236.



11. Kostic, M.; Rakic, D.Z.; Licen, H.H.; Malinovic, N.C. Design and construction of three point hitch device for measuring draft of tillage implement—Data acquisition and post processing analysis. *J. Food Agric. Environ.* **2014**, *12*, 1300–1307.
12. Kumari, A.; Raheman, H. Development of a Novel Draft Sensing Device with Lower Hitch Attachments for Tractor-Drawn Implements. *J. Biosyst. Eng.* **2024**, 1–9. [CrossRef]
13. Tewari, V.K.; Ravi, N.; Jha, K.R.; Ashok, A. Design and development of a three-Point-linkage dynamometer for tillage research. *Agric. Eng. Today* **2012**, *36*, 33–38.
14. *ASABE Standard S217*; Three-Point Free-Link Attachment for Hitching Implements to Agricultural Wheel Tractors. American Society of Agricultural and Biological Engineers: St. Joseph, MI, USA, 2001.
15. *ISO Standard 730*; Agricultural Wheeled Tractors—Rear-Mounted Three-Point Linkage—Part 1: Categories 1, 2, 3 and 4. ISO: Geneva, Switzerland, 2009.
16. *ISO Standard 11001-1*; Agricultural Wheeled Tractors and Implements—Three-Point Hitch Couplers—Part 1: U-Frame Coupler. ISO: Geneva, Switzerland, 2016.
17. *ISO Standard 11001-2*; Agricultural Wheeled Tractors and Implements—Three-Point Hitch Couplers—Part 2: A-Frame Coupler. ISO: Geneva, Switzerland, 2017.
18. *ISO Standard 11001-3*; Agricultural Wheeled Tractors and Implements—Three-Point Hitch Couplers—Part 3: Link coupler. ISO: Geneva, Switzerland, 1993.
19. *ISO Standard 11001-4*; Agricultural Wheeled Tractors and Implements—Three-Point Hitch Couplers—Part 4: Bar Coupler. ISO: Geneva, Switzerland, 1994.
20. Bentaher, H.; Hamza, E.; Kantchev, G.; Maalej, A.; Arnold, W. Three-point hitch-mechanism instrumentation for tillage power optimization. In Proceedings of the 14th Annual Conference of the Misr Society of Agricultural Engineering; 2006; Volume 22, pp. 923–936. Available online: <https://citeseerx.ist.psu.edu/document?repid=rep1&type=pdf&doi=f470dc69970f41d2d6790174b64237c823e6ee35> (accessed on 14 March 2024).
21. *ISO Standard 5673-2*; Agricultural Tractors and Machinery—Power Take-Off Drive Shafts and Power-Input Connection—Part 2: Specification for Use of PTO Drive Shafts, and Position and Clearance of PTO Drive Line and PIC for Various Attachments. ISO: Geneva, Switzerland, 2017.

**Disclaimer/Publisher’s Note:** The statements, opinions and data contained in all publications are solely those of the individual author(s) and contributor(s) and not of MDPI and/or the editor(s). MDPI and/or the editor(s) disclaim responsibility for any injury to people or property resulting from any ideas, methods, instructions or products referred to in the content.

## Article

# The Development of a Draft Force Prediction Model for Agricultural Tractors Based on the Discrete Element Method in Loam and Clay Loam

Bo-Min Bae <sup>1</sup>, Yeon-Soo Kim <sup>1,\*</sup>, Wan-Soo Kim <sup>2,3</sup>, Yong-Joo Kim <sup>4,\*</sup>, Sang-Dae Lee <sup>5</sup> and Taek-Jin Kim <sup>6</sup>

<sup>1</sup> Department of Bio-Industrial Machinery Engineering, Pusan National University, Miryang 50463, Republic of Korea; qhals806@pusan.ac.kr

<sup>2</sup> Department of Bio-Industrial Machinery Engineering, Kyungpook National University, Daegu 41566, Republic of Korea; wansoo.kim@knu.ac.kr

<sup>3</sup> Upland Field Machinery Research Center, Kyungpook National University, Daegu 41566, Republic of Korea

<sup>4</sup> Department of Biosystems Machinery Engineering, Chungnam National University, Daejeon 34134, Republic of Korea

<sup>5</sup> Smart Agricultural R&D Group, Korea Institute of Industrial Technology (KITECH), Gimje 54325, Republic of Korea; sdlee96@kitech.re.kr

<sup>6</sup> Department of Drive System Team, TYM R&D Center, Iksan 54576, Republic of Korea; taek.kim@tym.world

\* Correspondence: yskim23@pusan.ac.kr (Y.-S.K.); babina@cnu.ac.kr (Y.-J.K.); Tel.: +82-55-350-5422 (Y.-S.K.); +82-42-821-6716 (Y.-J.K.)

**Abstract:** In the field of agricultural machinery, various empirical field tests are conducted to measure design loads for the optimal design and implementation of tractors. However, conducting field tests is costly and time-consuming, with many constraints on weather and field soil conditions, and research utilizing simulations has been proposed as an alternative to overcome these shortcomings. The objective of this study is to develop a DEM-based draft force prediction model that reflects differences in soil properties. For this, soil property measurements were conducted in two fields (Field A in Daejeon, Republic of Korea, and Field B in Chuncheon, Republic of Korea). The measured properties were used as parameters for DEM-based particle modeling. For the interparticle contact model, the EPPA contact model was used to reflect the compressibility and stickiness of cohesive soils. To generate an environment similar to real soil, particle mass and surface energy were calibrated based on bulk density and shear torque. The soil property measurements showed that Field B had a higher shear strength and lower cone index and moisture content compared to Field A. The actual measured draft force was 19.47% higher in Field B than in Field A. In this study, this demonstrates the uncertainty in predicting draft force by correlating only one soil property and suggests the need for a comprehensive consideration of soil properties. The simulation results of the tillage operation demonstrated the accuracy of the predicted shedding force compared to the actual field experiment and the existing theoretical calculation method (ASABE D497.4). Compared to the measured draft force in the actual field test, the predictions were 86.75% accurate in Field A and 74.51% accurate in Field B, which is 84% more accurate in Field A and 37.32% more accurate in Field B than the theoretical calculation method. This result shows that load prediction should reflect the soil properties of the working environment, and is expected to be used as an indicator of soil–tool interaction for digital twin modeling processes in the research field of bio-industrial machinery.

**Keywords:** draft force; agricultural tractor; moldboard plow tillage; soil property

**Citation:** Bae, B.-M.; Kim, Y.-S.; Kim, W.-S.; Kim, Y.-J.; Lee, S.-D.; Kim, T.-J. The Development of a Draft Force Prediction Model for Agricultural Tractors Based on the Discrete Element Method in Loam and Clay Loam. *Agriculture* **2023**, *13*, 2205. <https://doi.org/10.3390/agriculture13122205>

Academic Editor: Kenshi Sakai

Received: 15 October 2023

Revised: 19 November 2023

Accepted: 24 November 2023

Published: 27 November 2023



**Copyright:** © 2023 by the authors. Licensee MDPI, Basel, Switzerland. This article is an open access article distributed under the terms and conditions of the Creative Commons Attribution (CC BY) license (<https://creativecommons.org/licenses/by/4.0/>).

## 1. Introduction

Among various agricultural operations, soil tillage operations such as moldboard plow generate the most soil resistance, which caused various dynamic stresses on the tractor. In addition, this is widely used as an indicator to evaluate the performance of agricultural machinery [1]. These tillage operations are performed in a wide range of soil environments

and directly contribute to soil resistance and working load size. These factors act in combination and exhibit an atypical correlation with the working load, making it difficult to predict the working load in the soil environment [2]. Therefore, the design optimization of agricultural equipment typically relies on iterative prototyping and evaluation using soil bins and field experiments.

A number of studies have been performed on the various factors that affect the draft force of agricultural tractors, either through field experiments in soil bin test beds or in real agricultural environments. Raper [3] studied an analysis of minimum draft force generation as a function of subsoil geometry through soil bin tests, and the results showed that, the lesser the resistance of a bent shank compared to a straight shank, the more soil breakdown occurs. Kim et al. [4] conducted a study to analyze the effects of tillage depth and gear selection on the mechanical load and fuel efficiency of agricultural tractors during plow tillage. Typically, the working load increased as the travel speed increased, and there were different trends in production versus fuel usage depending on the type of agricultural machinery. Kim et al. [5] carried out a study for the progress of a real-time tillage depth measurement system. The development of an improved real-time tillage depth measurement system was to quantitatively confirm the increasing draft force with tillage depth. Development and design processes by the means of field testing have the advantage of reflecting actual field conditions, however they have a lot of disadvantages, including cost, time, the labor of building an instructional system, lower replicability, space constraints, and the effects of weather and soil conditions.

As an alternative to actual field experiments, simulation-based virtual field experiments can reduce the number of prototypes and accelerate design and product development by facilitating the creation of targeted work environments in any climate [6]. Virtual field experiments can be performed in two representative numerical methods. One method of virtual field experiments, the finite element method (FEM), is a stress analysis method that divides a structure into elements of virtually finite size and analyzes the structure as a collection of these elements. Analyses using FEM models use complex geometries as simple geometries, providing values that clearly indicate the location of high stresses or displacements. Fielke [7] carried out a soil–tool interaction analysis study of the cutting edges of tillage tools based on FEM. In Fielke’s study, the effects of Poisson’s ratio and cutting-edge geometry on tillage forces and soil flow were determined through FEM simulations. A study of soil–tool interaction was conducted by Ucgul et al. [8] by comparing discrete and finite element methods. The study showed that a better vertical force prediction was obtained using DEM software (EDEM 2.7<sup>TM</sup>), whereas forward soil movements below the tillage depth were simulated more accurately using FEM. The prediction accuracy of the FEM simulation model was verified by soil bin experiments. A follow-up study analyzed the effects of the cutting angle and tool lift angle of the moldboard plow through FEM simulations using an elasto-plastic model [9,10]. However, numerical studies using FEM have the disadvantage that it is difficult to predict the flow of granular materials and is not suitable for modeling materials with large displacements, such as soil.

Another representative numerical analysis method, the discrete element method (DEM), has been used worldwide in agricultural machinery research because it can calculate the interaction of each granular material. In a study analyzing the analysis time and accuracy of fine-grained material sizes in relation to the computational power of the computer, Wang et al. [11] conducted a study on the effect of modeling particle size on the interaction between soil and subsoiler. The results, models with a radius of 4 to 7 mm, provided relatively accurate predictions. They also reported that, when modeling simulations were reduced from a radius of 5 mm to 3 mm, the solution time increased by about seven times. Obermayr et al. [12] carried out DEM simulations to forecast the draft force of a simple tool in a cohesionless powdery material, and validated the simulation consequences with small-scale laboratory tests, which showed that the draft force was predicted within a reasonable range despite the outdated particle modeling. Ucgul et al. [13] performed DEM modeling using a hysteretic spring contact model based on cohesion and

adhesion. The results showed that the proposed contact model could be used to predict both tillage aeration and vertical tillage force for different speeds, operating depths, moisture contents, and compaction levels. Tekeste et al. [14] utilized DEM simulations to investigate the impact of tiller sweep–soil interaction, worn and hardened edges on soil–tool forces, and soil flow. Their findings revealed that carbide-treated worn sweeps exhibited comparable soil gradient forces and soil forward failure distances to those of new sweeps. However, most previous studies have been conducted in soil bin testing facilities under granular material or cohesionless soil conditions. [15] The soil within soil bin test facilities exhibits a lower cohesion compared to the natural paddy field, attributed to frequent indoor tillage operations; consequently, soil modeling in a soil bin test facility commonly employs a hysteretic spring contact model [16]. However, the DEM modeling of agricultural soils involves a nonlinear hysteretic spring model and employs the Edinburgh elasto-plastic adhesion (EEPA) contact model [17], which considers the compressible, adhesive, and nonlinear behavior of cohesive solids between particles and between particle shapes. Recently, a study predicted the working performance of agricultural machinery in response to DEM simulations of the properties of cohesive soil, a real agricultural soil. Kim et al. [18] conducted a study to predict the draft force with tillage depth by using the EEPA contact model to implement the modulus of compression and stickiness of cohesive soil in a DEM simulation program. In the same soil environment, draft force prediction studies have been conducted, but draft force prediction studies based on soil properties have not yet been conducted.

The specific objective of this study is to elucidate the soil–implement interaction by predicting the draft force in two soil working environments with different properties during moldboard plowing operations, and demonstrating the prediction accuracy by comparing the draft force predicted by traditional theoretical prediction equations and actual field experiment results.

## 2. Materials and Methods

### 2.1. Measurement of Field Soil Properties

To simulate the properties of the two fields and select them as modeling parameters, soil property measurement tests were performed respectively. Field A is located in Daejeon, Republic of Korea, and Field B is located in Chuncheon, Republic of Korea. The soil properties were calculated based on the uniformed grid (3 m × 3 m) sampling method in the field [19]. Each field was divided into 10 uniformed grids, each of which was sampled to measure the physical properties of the soil and vane shear and cone penetration tests to measure the mechanical properties. An actual field has different soil properties according to the depth [5]. Therefore, in this study, the target tillage depth of 20 cm was divided into several layers and the soil properties of each layer were measured. According to the depth of the blade of the ring-type vane shear tester (5 cm), the soil layer was divided into four layers: Layer 1 (0~5 cm), Layer 2 (5~10 cm), Layer 3 (10~15 cm), and Layer 4 (15~20 cm), and 10 times of soil sampling and shear vane tests were performed for each layer. Figure 1 displays the positions of the two examined fields and the soil property measurements obtained through uniform grid sampling.

For physical properties of the soil, soil sampling was conducted in both test fields, A and B, utilizing a 100 mL soil sampling tube (DIK-1801, Daiki Rika Kogyo Co., Ltd., Konosu, Japan) in conjunction with a soil sampling tool (DIK-1815, Daiki Rika Kogyo Co., Ltd., Konosu, Japan). To determine the soil moisture content, each soil sample underwent a 24 h drying process at 110 °C [20] using the oven drying method (SH-DO-100FGB, Samheung Energy, Sejong, Republic of Korea). The compaction of soil occurs due to the exclusion of air or water from void spaces, rearrangement of soil particles, and compaction of water and air within the voids. Soil texture is also an important indicator for soil modeling because it determines the degree to which soil particles rearrange and many other properties, such as water permeability [21]. The soil texture at the field site was analyzed using the USDA soil classification method [22] with a sieve shaker (HJ-4560, Heungjin, Gimpo,

Republic of Korea) [23]. The soil model’s plasticity index value, a determinant for its plastic characteristics and compressibility [24], was assessed through the Atterberg limit test encompassing liquid and plastic limits [25].

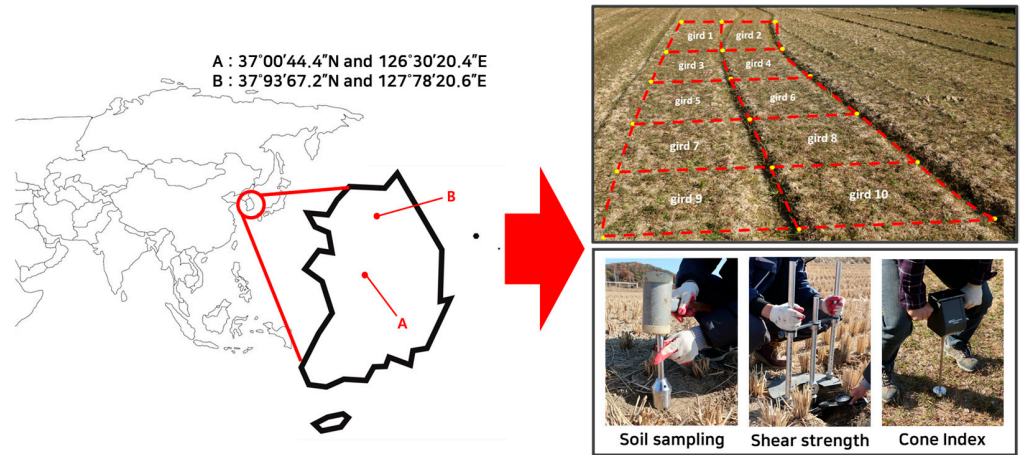


**Figure 1.** Location of test fields and uniformed grid sampling methods.

Shear strength and cone index are mechanical properties of soil that have a significant impact on working load [26,27]. These two properties were measured using a cone penetration tester (DIK-5532, Daiki Rika Kogyo Co., Ltd., Konosu, Japan) [28,29] and a ring-type vane shear tester (DIK-5503, Daiki Rika Kogyo Co., Ltd., Konosu, Japan). Shear strength was obtained from Equation (1) [30]:

$$\tau = \frac{3M}{2\pi(r_1^3 - r_2^3)} \tag{1}$$

where  $\tau$  is the shear strength of the soil (Pa),  $M$  is the soil resistance torque that caused the vane shear test (Nm), and  $r_1$  and  $r_2$  are the inner and the outer radii of the shear box (m).

2.2. Modeling Cohesive Soil with DEM

Modeling the virtual soil environment for simulation can be broadly divided into particle modeling and contact modeling. The modeling process proceeded as shown in Figure 2.

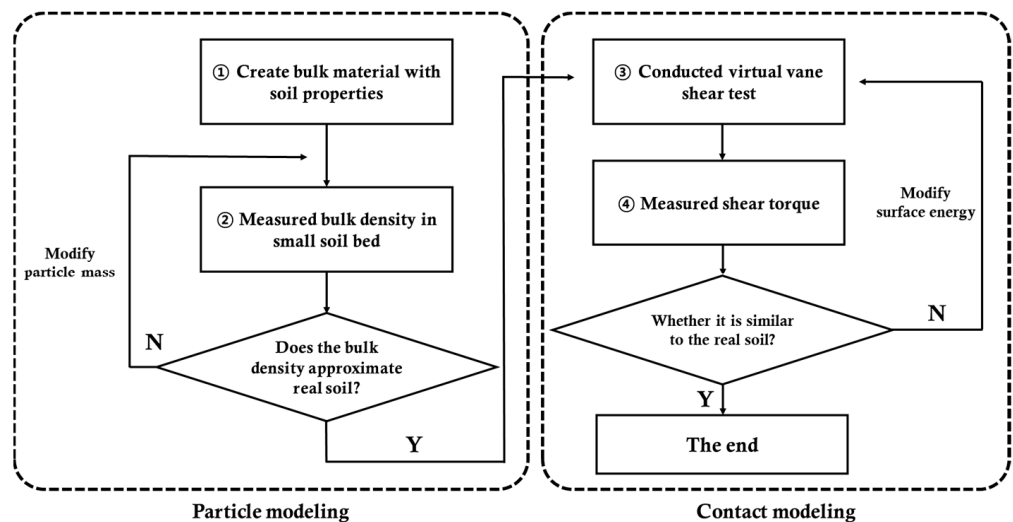


**Figure 2.** Modeling Procedures for Virtual Soil Environments.

The first step in conducting a DEM simulation is to model the particles. Modeling soil particles requires entering parameters such as solid density, Poisson’s ratio, shear modulus, Young’s modulus, and friction coefficient for both soil and steel. Table 1 shows the major particle model parameters in the DEM software (EDEM, 2022, Altair, Troy, MI, USA). The particle size of the soil was set based on past studies to reduce the simulation time without adversely affecting the prediction accuracy [18]. An increase in particle size leads to an increase in voids, so the process of calibrating the mass of the particles based on the actual measured bulk density was performed. The shear modulus and Young’s modulus, which have a direct and significant impact on the draft force, were set based on measured values from field properties experiments. In prior work, Wang et al. [11] investigated subsoiler interaction with soil using DEM and they made a clear distinction between the friction coefficients of ploughed soil and soil beneath the subsoiler when selecting modeling parameters. In this study, the parameters used in Wang et al.’s study were selected to reflect the change in soil properties with depth. The restitution coefficients for soil–soil and soil–steel were selected from values widely used in DEM studies [31,32].

**Table 1.** Major particle model parameters in EDEM.

Properties	Value
Particle size of soil	Radii 5 mm
Particle mass of soil	Calibrated
Shear modulus	Measured
Young’s modulus	Measured
Static friction coefficient of soil–soil	0.4
Rolling friction coefficient of plough layer	0.58
Rolling friction coefficient of hardpan layer	0.25
Static friction coefficient of soil–steel	0.24
Rolling friction coefficient of plough layer–steel	0.34
Rolling friction coefficient of hardpan layer–steel	0.14
Restitution coefficient of soil–soil	0.2
Restitution coefficient of soil–steel	0.3

The second step in conducting a DEM simulation is contact modeling. EDEM (EDEM, 2022, Altair, Troy, MI, USA) provides several contact models to reproduce various particle-to-particle contact behaviors. Soil with clay content exhibits a greater capacity for retaining water when compared to sandy soil [33]. This enhanced water retention capability creates a conducive environment for the flourishing of crops. Consequently, it is common to find clay-rich agricultural soils in Korea. This study employed the EEPA contact model to simulate the compressibility and stickiness of agricultural soil. The EEPA contact model is organized into various equations for numerical analysis. The vertical normal force of the EEPA model is given by Equation (2)

$$F_n = (f_{hys} + f_n^d)u, \tag{2}$$

where  $F_n$  is the total contact normal force,  $f_{hys}$  is the hysteretic spring stiffness,  $f_n^d$  is the damping force, and  $u$  is the unit normal vector pointing to the center of the particle at the contact point.

$$f_{sys} = \begin{cases} f_0 + k_1\delta^n & \text{if } k_2(\delta^n - \delta_p^n) \geq k_1\delta^n \\ f_0 + k_2(\delta^n - \delta_p^n) & \text{if } k_1\delta^n > -k_{adh}\delta^x \\ f_0 - k_{adh}\delta^x & \text{if } -k_{adh}\delta^x > k_2(\delta^n - \delta_p^n) \end{cases} \tag{3}$$

where  $f_0$  is the initial contact normal force,  $\delta^n$  is the initial overlap,  $-k_{adh}$  is the adhesive stiffness, and  $\delta^x$  is the overlap due to adhesive force.

$$f_n^d = 2\sqrt{\frac{5}{6}}\beta_{NL}\sqrt{K_n m^*}v_n \tag{4}$$

$$K_n = 2E * \sqrt{R * \delta^n} \tag{5}$$

$$\beta_{NL} = \frac{\ln e}{\sqrt{\ln e^2 + \pi^2}} \tag{6}$$

where  $\beta_{NL}$  is the coefficient of the normal dashpot in the nonlinear model,  $K_n$  is the Hertzian stiffness,  $m^*$  is the equivalent mass of the particle, and  $e$  is the user-defined restoration factor in the simulation.

Additionally, the contact tangential force ( $F_t$ ) was obtained from Equation (7):

$$F_t = f_{ts} + f_{ds} \tag{7}$$

where  $f_{ts}$  is the tangential spring force and  $f_{td}$  is the tangential damping force.

$$f_{ts} = f_{ts(n-1)} + \Delta f_{ts} \tag{8}$$

$$\Delta f_{ts} = k_t \delta_t \tag{9}$$

$$k_t = \zeta_{tm} 8G^* \sqrt{R^* \delta_n} \tag{10}$$

$$f_t^d = -2\sqrt{\frac{5}{6}}\beta_{NL}\sqrt{k_t m^*}v_t^r \tag{11}$$

$$\beta_t = \sqrt{\frac{4m^*k_t}{1 + (\frac{\pi}{\ln e})^2}} \tag{12}$$

where  $f_{ts(n-1)}$  is the tangential spring force at the previous time step,  $\Delta f_{ts}$  is the increment in the tangential force,  $k_t$  is the tangential normal stiffness,  $\delta_t$  is the tangential displacement,  $\zeta_{tm}$  is the tangential stiffness multiplier,  $G^*$  is the equivalent shear modulus,  $R^*$  is the equivalent radius,  $v_t$  is the relative tangential velocity between the two particles, and  $\beta_t$  is the linear tangential dashpot coefficient, which depend on the tangential stiffness.

$$\tau_i = -\mu_t f_{hys} R_i \omega_i \tag{13}$$

Finally, the rolling friction torque  $\tau_i$  was obtained from Equation (9),  $\mu_t$  is the rolling friction,  $R_i$  is the distance from the contact point to the center of the particle, and  $\omega_i$  is the vector of the unit angular velocity of the particle at the contact point. Equations (2)–(13), used for particle force calculations in EDEM, show that the contact force, which consists of normal and tangential forces, is a function of the particle mass, particle overlap, particle size, Young’s modulus, shear modulus, friction coefficient, and restitution coefficient.

Table 2 presents the key input parameters for the EEPA contact model. In this paper, the input parameters were determined by referring to a soil model with compressibility and adhesion from the Soil Starter Pack provided by DEM software (EDEM, 2022, Altair, Troy, MI, USA). The surface energy was calibrated with a virtual simulation using a ring-type vane shear tester to set the value. For cohesionless soils, the calibration is most often performed with a repose angle experiment. Cohesive soils sometimes exhibit non-flowing characteristics in certain areas. Hence, when calibrating cohesive soils, relying on vane shear test outcomes and comparisons proves more suitable than utilizing the repose angle for calibration. Repeated calibration through virtual vane shear tests was conducted for every soil layer to accurately anticipate the loads induced by tillage activities.

**Table 2.** Major contact model parameters in EDEM.

Properties	Value
Constant pull-off force	0
Surface energy	Calibrated
Tensile exponent	5
Tangential stiff multiplier	0.28571
Slope exponent	1.5
Contact plasticity ratio	0.75

### 2.3. Design a Working Load Measurement System

#### 2.3.1. Tractor-Implement System

A 42 kW tractor (TX58, TYM, Iksan, Republic of Korea) was selected for this study considering the tillage load. Table 3 shows the specific specifications of the tractors utilized. Moldboard plows are commonly used in soil mechanization research due to their high working stability and soil resistance. In the field experiment, a six-row moldboard plow (WJSP-6S, Woongjin, Gimje, Republic of Korea) with a maximum working depth of 200 mm was used to perform the tillage test. The detailed specifications of the machine are presented in Table 4. The moldboard plow was reverse engineered in a 1:1 ratio using a 3D scanner for the virtual draft force prediction test.

**Table 3.** Specifications of the agricultural tractor used in this study.

Item	Specification
Company	TYM
Model	TX58
Wheel base (mm)	2155
Length × width × height (mm)	3695 × 1848 × 2560
Engine	Rated power (kW) Max torque (Nm)
	42 @ 2000 rpm 211.8 @ 1600 rpm
Transmission gear selection	Main 4 stage/Sub 6 stage
PTO gear selection	1st 540 rpm 2nd 750 rpm 3rd 1000 rpm
Tire (inch)	Front 11.2–20 Rear 14.9–30
Maximum travel speed (km/h)	33.8

**Table 4.** Specifications of the moldboard plow used in this study.

Item	Specification
Product name	WJSP-6S
Manufacturing company	Woongjin
Type	Moldboard plow
Length × width × height (mm)	1930 × 1800 × 1235
Rake angle (deg)	30.76
Tillage width (mm)	270
Share length (mm)	360



Table 4. Cont.

Item	Specification
Share form	Pointed
Required power (kW)	40–52
Maximum tillage depth (mm)	Up to 200
Coulter type	Skid jig/Plain coulter with spring
Coulter diameters (mm)	340
Number of furrows	3
Required travel speed (km/h)	5–8

### 2.3.2. Working Load Measurement System

The load generated during tillage operations using a moldboard plow is strongly influenced by tillage depth and travel speed. For a comparative analysis of the effects of soil properties, it is requisite to verify the draft force at a constant tillage depth and travel speed with a device that accurately measures tillage depth and travel speed. The working load measurement system consists of a draft force measurement part, a tillage depth measurement part, and a real-time kinematic global positioning system (RTK-GPS) Mini Survey Antenna GPS1000, Swift Navigation, San Francisco, CA, USA). Figure 3 illustrates the load measurement system along with the installation positions of each measurement component. The part of draft force measurement consisted of a triangular jig with load cells (UU-T2, DACELL, Cheongju, Republic of Korea) to measure the draft force. The draft force ( $D$ ) was obtained as the sum of the loads measured on the three load cells that measure tangential forces ( $F_A$ ,  $F_B$ ,  $F_C$ ).

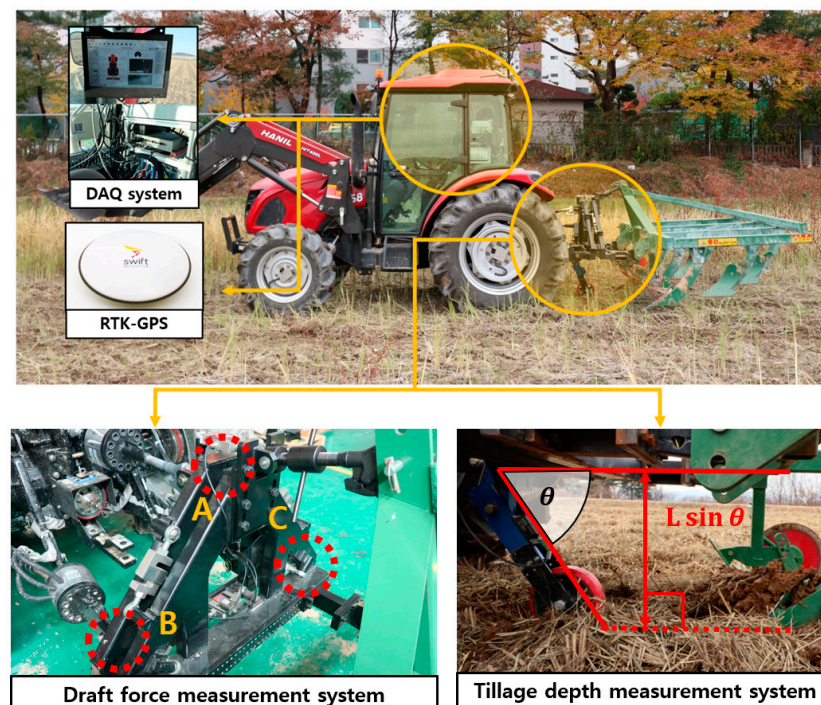


Figure 3. Configuration of field load measurement system.

$$D = F_A + F_B + F_C \quad (14)$$

The segment dedicated to tillage depth measurement facilitates the real-time tracking of the moldboard plow's vertical penetration depth that was achieved by affixing a

custom-designed jig, housing an inclinometer (IS2MA090-U-BL, GEMACsensors, Chemnitz, Germany), at the base of the draft force measurement system [5].

$$d = L \sin \theta_1 - L \sin \theta_2 \quad (15)$$

where  $d$  is the tillage depth (cm),  $L$  is the length of the lower link of tillage depth measurement system (cm),  $\theta_1$  is the initial angle of the lower link measured using the inclination sensor when tillage depth is zero (deg), and  $\theta_2$  is the angle of the lower link measured using the inclination sensor when tillage depth occurs (deg).

The RTK-GPS is designed to attach to the tractor's center of gravity and measure the speed at which it is reduced by slip during tillage operations. The data acquisition system, Dewesoft X (Dewesoft 3X, Dewesoft, Trbovlje, Slovenia), was employed for concurrent field data measurements, operating at a sampling frequency of 1 kHz.

#### 2.4. Field Experimental Design

The predicted draft force from the DEM simulation was compared to field tests to demonstrate its accuracy. Load measurement tests were performed on two fields in different locations to compare the draft force due to differences in soil properties. Field A was located at 37°00'44.4" N and 126°30'20.4" E and Field B was located at 37°93'67.2" N and 127°78'20.6" E. The tillage operation was performed by speeding the M3 gear (theoretical speed is 7.9 km/h) in four-wheel drive mode on a 100 m straight course with a moldboard plow. The measuring tractor's results from each field, including the travel speed, tillage depth, and draft force, were recorded across three drives and subsequently organized in ascending order based on tillage depth.

#### 2.5. Theoretical Method for Draft Force Prediction

Typically, the validation of the predicted draft force from tillage operations involves comparing these values against those derived from traditional theoretical calculation methods [34]. For the theoretical calculations, ASAE Standard D.497.4 was used [35]. This method stands out as the simplest and most prevalent due to its reliance on soil texture details, tillage depth, implement geometry, and travel speed to make predictions.

$$D = F_i[A + BV + CV^2]bd \quad (16)$$

where  $F_i$  is the dimensionless soil texture adjustment with different values (if soil has fine texture  $F_i = 1$ , medium texture  $F_i = 0.7$ , and coarse texture  $F_i = 0.45$ ),  $A$ ,  $B$ , and  $C$  are machine-specific parameters determined by the implement type. In the case of moldboard flow,  $A$  is 652,  $B$  is 0, and  $C$  is 5.1.

### 3. Results

#### 3.1. Result of Soil Properties Measurement

The results of the soil's physical and mechanical properties measured in the field according to the soil layer are presented in Table 5.

Atterberg limits testing showed that the plastic and liquid limits for Field A were  $21.1 \pm 1.55\%$  and  $34.59 \pm 0.81\%$ , respectively, and the plastic and liquid limits for Field B were  $19.62 \pm 1.22\%$  and  $32.31 \pm 0.64\%$ . The contact modeling parameters were selected based on the assumption that all soil layers were classified as plastic, which has a similar behavior to the compressible sticky model in the soil starter pack of DEM software (EDEM, 2022, Altair, Troy, MI, USA). A soil particle analysis revealed that Field A exhibited a loam texture composed of 40% sand, 48% silt, and 12% clay, while Field B demonstrated a clay loam texture comprising 40% sand, 28% silt, and 32% clay. The shear strength obtained based on the vane shear torque increased with depth, with Field A increasing by about 1.67 times to 25.19 kPa at Layer 1 and 42.25 kPa at Layer 4, and Field B increasing by about 1.43 times to 65.32 kPa at Layer 1 and 93.10 kPa at Layer 4. Identifying the hardpan layer's formation site is crucial, as tillage operations aim to disrupt this layer. Figure 4 shows the

results of the cone penetration test for Field A and Field B. For the cone penetration test in Field A, the cone index is 491.5, 586.8, 706.4, and 2008.9 kPa, in the order of the layers. The cone index for field B is 548.96, 731.81, 824.75, and 1090.59 kPa, in the order of each layer. For both Field A and Field B, the cone index increases from Layer 3 to Layer 4 by 64.8% and 24.4%, respectively, indicating that the hardpan is located in Layer 4.

**Table 5.** Measured on-field soil properties according to soil layer.

Field	Properties	Soil Layer			
		Layer 1 (0~5 cm)	Layer 2 (5~10 cm)	Layer 3 (10~15 cm)	Layer 4 (15~20 cm)
A	Bulk density ( $\text{g}/\text{cm}^3$ )	1.50	1.60	1.72	1.90
	Moisture contents (%)	32.21	34.20	28.72	24.23
	Cone index (kPa)	465.48	547.92	636.96	1900.2
	Shear strength (kPa)	25.19	30.87	32.90	42.25
B	Bulk density ( $\text{g}/\text{cm}^3$ )	1.90	1.91	1.96	2.02
	Moisture contents (%)	26.56	23.81	22.49	20.24
	Cone index (kPa)	707.56	868.44	1063.16	2153.64
	Shear strength (kPa)	65.32	68.24	72.14	93.10

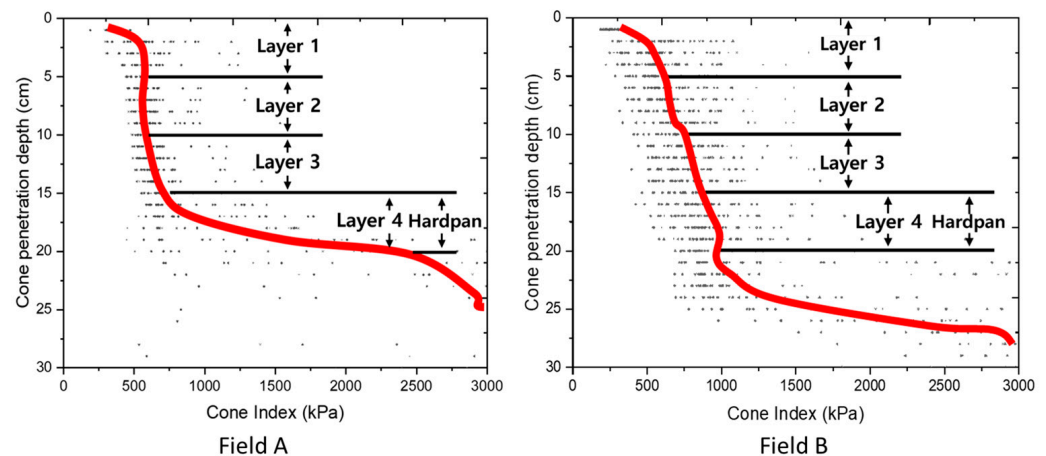


**Figure 4.** Results of cone penetration test.

### 3.2. Soil Modeling and Calibration Using DEM

Considering the computational power of the computer, a particle size of a 5 mm radius was selected for the soil modeling. The soil modeled using the discrete element method had more voids than the real soil due to the larger particle size. Therefore, the mass of the particles was calibrated based on the measured bulk density for a realistic draft force prediction. Soil particles were produced within a small soil bin (700 mm  $\times$  700 mm  $\times$  120 mm) and the total number of particles generated was 20,684. The calibration results are shown in Table 6.

Following the bulk density calibration, the interparticle surface energy was calibrated based on the shear torque obtained from the vane shear test. The vane shear tester was modeled as a CAD step file, as shown in Figure 5, and imported into DEM software (EDEM, 2022, Altair, Troy, MI, USA) to measure the shear torque generated by rotating the vane blades at the same angular speed as the field test. The generated particles were standardized with a radius of 5 mm, mirroring the simulation used for predicting draft force. The shear torque was measured by setting the vane shear tester to penetrate only the vane part to minimize the impact of vertical loading on the measurement. The surface energy values calibrated using shear torque are shown in Table 7. The shear strength error in Field A ranged from 8.51% to 54.9%, and the calibration process reduced the error by 0.16% to 0.89%. In the calibration process for Field A, the input surface energy values were

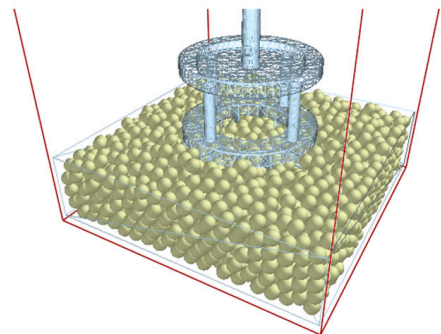
130, 150, 260, and 330 J/m<sup>2</sup> allocated to Layer 1, Layer 2, Layer 3, and Layer 4. For Field B, the error in the shear strength ranged from 9.4% to 39.53%, and the calibration process reduced the error from 0.52% to 1.35%. In the calibration of Field B, the input surface energy values allocated to Layer 1, Layer 2, Layer 3, and Layer 4 were 100, 300, 500, and 900 J/m<sup>2</sup> respectively.

**Table 6.** Calibration results of bulk density.

Field	Soil Layer	Procedure	Particle Mass (kg)	Bulk Density (kg/m <sup>3</sup> )		Calibration Error (%)
				Simulated	Measured	
A	Layer 1	Initial	0.00144	1538.90	1496.58	2.83
		Calibrated	0.00138	1508.42		0.79
	Layer 2	Initial	0.00144	1559.09	1597.01	2.37
		Calibrated	0.00147	1597.44		0.03
	Layer 3	Initial	0.00144	1557.89	1715.29	9.18
		Calibrated	0.00159	1714.88		0.02
	Layer 4	Initial	0.00144	1565.49	1904.46	17.80
		Calibrated	0.00175	1904.81		0.02
B	Layer 1	Initial	0.00144	1269.91	1899.8	33.16
		Calibrated	0.00174	1901.43		0.09
	Layer 2	Initial	0.00144	1269.91	1905.64	33.36
		Calibrated	0.00175	1912.36		0.35
	Layer 3	Initial	0.00144	1905.69	1955.48	35.05
		Calibrated	0.00179	1956.07		0.03
	Layer 4	Initial	0.00144	1269.91	2021.54	37.18
		Calibrated	0.00185	2021.64		0.005



(a)



(b)

**Figure 5.** Calibration of shear torque using vane shear test: (a) field experiments and (b) ED-EM simulation.

### 3.3. Prediction of Draft Force Based on DEM Simulations

#### 3.3.1. Results of Draft Force Measurements from Actual Field Tests

The actual field tests were conducted three times with the gear selection of the M3 for each field following the draft force measurement procedure. Table 8 shows travel speed and draft force for each tillage depth. The target tillage depth was 15–20 cm, and the average tillage depth was 16.28 cm in Field A and 16.9 cm in Field B. The actual travel speed measured through RTK-GPS was reduced by slip, showing Field A at 5.63 km/h and Field B at 5.43 km/h in gear M3. In order to determine the difference in draft force based on the soil properties, it was necessary to uniformize the tillage depth, which has a large impact on the draft force. Based on the tillage depth, the most data were recorded at 16–17 cm and the draft force was averaged at that depth. The results showed that the measured draft force was 12.38 kN in Field A and 14.79 kN in Field B.

**Table 7.** Calibration results for shear torque in small soil bin using field measurements values.

Field	Soil Layer	Procedure	Surface Energy (J/m <sup>2</sup> )	Shearing Torque (Nm)		Calibration Error (%)
				Simulated	Measured	
A	Layer 1	Initial	100	4.73		8.51
		Calibrated	130	5.13	5.17	0.77
	Layer 2	Initial	100	5.11		19.27
		Calibrated	150	6.32	6.33	0.16
	Layer 3	Initial	100	3.81		43.56
		Calibrated	260	6.69	6.75	0.89
	Layer 4	Initial	100	3.91		54.9
		Calibrated	330	8.64	8.67	0.35
B	Layer 1	Initial	100	12.14		9.4
		Calibrated	100	13.55	13.4	1.19
	Layer 2	Initial	100	12.56		10.29
		Calibrated	300	13.84	14	1.14
	Layer 3	Initial	100	11.93		19.39
		Calibrated	500	15	14.8	1.35
	Layer 4	Initial	100	11.55		39.53
		Calibrated	900	19.2	19.1	0.52

**Table 8.** Draft force measurement results from actual field experiment.

Field A			Field B		
Tillage Depth (cm)	Travel Speed (km/h)	Draft Force (kN)	Tillage Depth (cm)	Travel Speed (km/h)	Draft Force (kN)
15	5.89 ± 0.35	11.61	15	5.83 ± 0.51	13.71
16	5.85 ± 0.31	12.11	16	5.68 ± 0.65	14.72
17	5.77 ± 0.33	12.64	17	5.47 ± 0.59	14.86
18	5.62 ± 0.34	13.29	18	5.61 ± 0.51	15.18
19	5.41 ± 0.39	13.53	19	4.99 ± 0.80	17.80
20	5.25 ± 0.48	14.30	20	4.97 ± 0.71	16.81

### 3.3.2. Creating a Virtual Soil Bed for Simulation

Figure 6 shows a large soil bed that represents the properties of the soil measured in this study. Considering the 1:1 ratio in full-scale moldboard plow geometry and the target tillage depth, the large soil bed size was set to 5000 mm × 2500 mm × 300 mm (length × width × depth) to minimize the interaction between the walls and the particles. The height of each soil layer in the virtual large soil bed was set to 50 mm for Layers 1, 2, and 3 and 150 mm for Layer 4. The total number of particles in the large soil bed was 4,004,939.

The simulation time was 3.2 s to ensure that the moldboard plow was sufficiently penetrated to represent a constant working load. The tillage depth in the simulation was set to 16.5 cm to compare with the actual field test conducted for the purpose of breaking the hardpan layer.

### 3.3.3. Accuracy Verification of DEM Simulation for Draft Force Prediction

Draft force is a force generated in the same axis as the working direction when the implement is towed by a tractor. To predict the draft force in this study, the total force generated in the Y-axis, the working direction, was analyzed through EDEM (EDEM, 2022, Altair, Troy, MI, USA). Then, the accuracy of the predicted draft force was demonstrated by comparing it to measured values from actual field experiments and to values obtained from the traditional theoretical method. As shown in Table 9, the simulation results show that Field A has a predicted draft force of 14.02 kN and Field B has a predicted draft force of 18.56 kN. The predicted draft forces obtained through the theoretical calculation method are 24.42 kN in Field A and 24.08 kN in Field B. Comparing the draft force measured in



the actual field test to the draft force predicted by the simulation, the error for Field A is 13.25% and the error for Field B is 25.49%. The draft force predicted by the theoretical calculation method was 24.42 kN in Field A and 24.08 kN in Field B. Figure 7 shows a graph of the measured draft force from an actual field trial and predicted draft force based on simulation. Savitsky–Golay has the advantage of preserving the shape of the peaks when smoothing [36], so the graph of the draft force recorded in the form of a waveform was fitted with the Savitsky–Golay method. Figure 8 shows a comparison of Field A and Field B, which includes the actual measured draft force, the draft force predicted by the DEM simulation, and the values obtained using traditional theoretical methods. The actual measured draft force was 13.28% higher in Field B than in Field A, while the DEM simulation predicted that the draft force in Field B was 32.38% higher than that in Field A. Despite the errors, the increasing trend of the draft force could be demonstrated through the discrete element method.

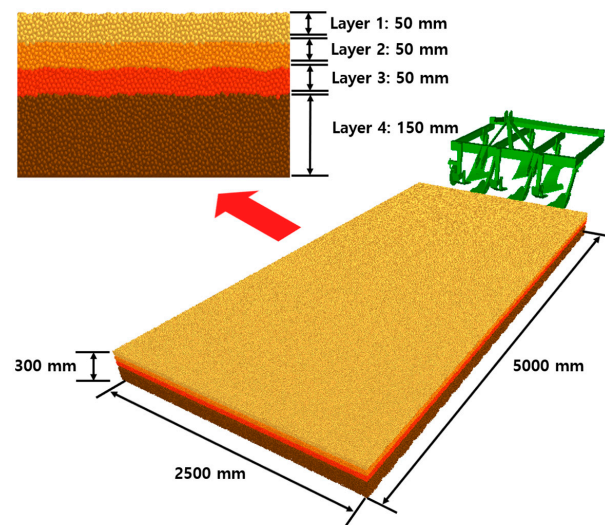


Figure 6. Virtual large soil bed made based on measured soil properties by soil layer.

Table 9. Result of draft force predict simulation.

Field	Tillage Depth (cm)	Travel Speed (km/h)	Draft Force (kN)		Predicted Error (%)
			Simulated	Measured	
A	16.5	5.63	14.02	12.38	13.25
B		5.43	18.56	14.79	25.49

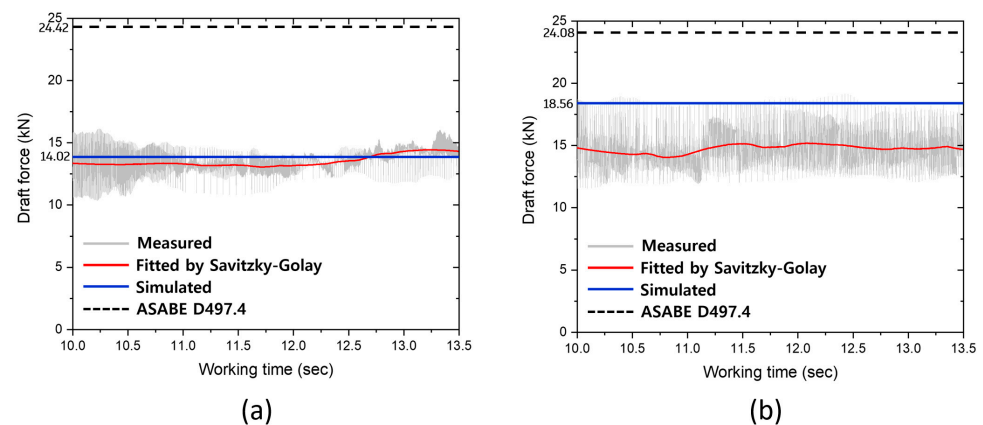


Figure 7. Comparison of draft force between actual field test and DEM simulation at 16.5 cm tillage depth. (a) Field A and (b) Field B.

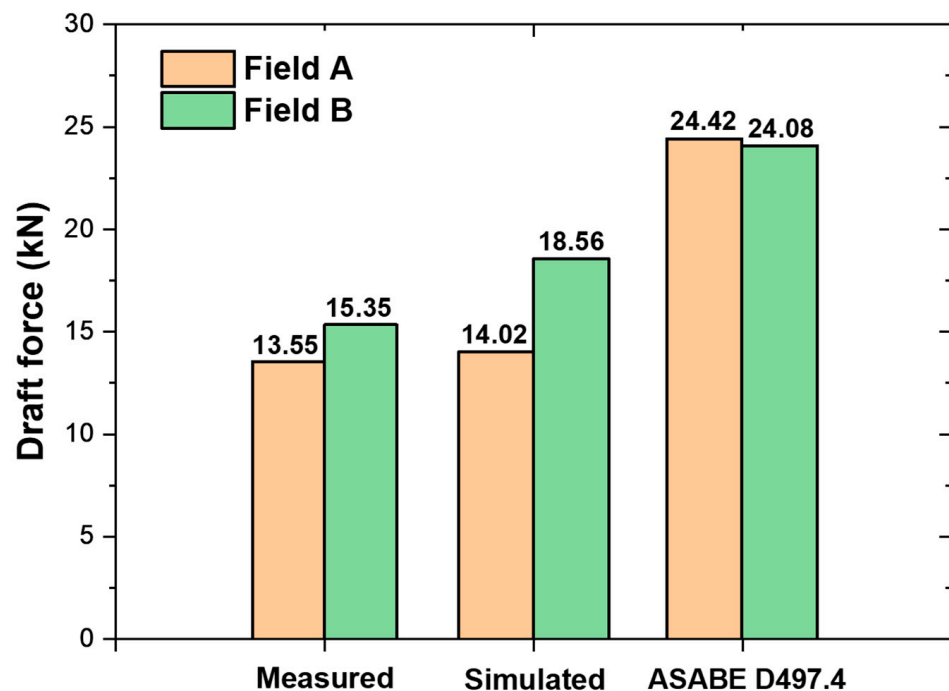


Figure 8. Comparison of draft force between Field A and Field B.

#### 4. Discussion

In this study, a procedure for measuring soil properties was established, and property measurement tests were conducted at different depths of the soil in two cohesive fields with different properties. Measured properties include soil texture, moisture content, bulk density, shear strength, cone index, plastic limit, and liquid limit. First, the soil texture of the two fields was determined, with Field A as loam and Field B as clay loam. To determine the difference in draft force based on the properties of the working environment, the cone index of the soil was first compared. The cone index is one indicator of soil compaction, and past research has shown that the cone index is proportional to the workload of a tractor [26]. Compared to Field A, Field B was 1.52 times higher in Layer 1, 1.58 times higher in Layer 2, and 1.62 times higher in Layer 3, while in Layer 4, Field A was 1.84 times higher than Field B. In terms of shear strength, Field B measured higher than Field A in all soil layers: 2.59 times in Layer 1, 2.21 times in Layer 2, 2.19 times in Layer 3, and 2.2 times in Layer 4. For moisture content, Field A had a higher measured moisture content in all layers compared to Field B: 1.21 times at Layer 1, 1.44 times at Layer 2, 1.28 times at Layer 3, and 1.2 times at Layer 4. Rashidi et al. [37] reported that the draft force was the highest at 484 kgf in soil with 11.27% moisture content and the lowest was at 427 kgf in soil with 22.87% moisture content. In addition, S.A. Al-Suhaibani et al. [38] confirmed that the draft force decreases as the moisture content increases in soil at 5.08%, 5.14%, and 6.82%. Based on these past studies, for the two fields that were found to be plastic state by the Atterberg limit test, it can be assumed that the lower moisture content in Field B experienced more draft force. In the actual field test, the measured draft force was 12.38 kN in Field A and 14.79 kN in Field B, with Field B being 19.47% higher than Field A. Based on these results, the analysis of soil properties for draft force prediction should be treated comprehensively, and it is difficult to relate only one factor to draft force.

To reflect the properties of the measured soil in the particle modeling, two steps of calibration were performed. Since this process results in more voids than in real soil, the mass of the particles was calibrated based on the bulk density. As a result, the error was reduced to a range of 0.005–0.79%. In addition, unlike cohesionless soil, the cohesive soil modeling was calibrated for surface energy by performing a vane shear test rather than an angle of repose test. As a result, the virtual test closely reproduced the measured shear

torque with an error from 0.16 to 1.35%. Despite calibrating the values of bulk density and shear torque to within 1.5% of each other, there was a prediction error of 13.25% for Field A and 25.49% for Field B. This indicates the need for more precise soil property measurements for modeling parameters that were not addressed, such as the coefficient of restitution and plasticity ratio. The fact that more prediction errors occurred in Field B compared to Field A is also an important discussion point. In this study, in the process of reflecting the measured soil properties into the particle modeling, a virtual vane shear test was performed to calibrate the surface energy based on the shear torque. As a result, Field A showed an error in shear torque of less than 1%, while Field B was calibrated with an error of up to 1.35%. It can be seen that an error in the calibration step led to more error in predicting the draft force.

The DEM-simulation-based predicted draft force was 14.02 kN in Field A and 18.56 kN in Field B, differences of 13.25% and 25.49%, respectively, when compared to the actual field test. Compared to the traditional theoretical calculation method, the DEM-simulation-based draft force prediction was 84% more accurate for Field A and 37.32% more accurate for Field B. Since the existing theoretical calculation method comprehensively classified soil texture into three categories (fine, medium, and coarse) and did not reflect other soil properties except soil texture, it could not show the difference in predicted draft force under the same type of implement and almost similar working conditions (tillage depth and travel speed, etc.). On the other hand, DEM-simulation-based draft force predictions were significant even under similar operating conditions (same tillage depth and similar travel speed), reflecting the soil properties that affect draft force.

## 5. Conclusions

In this study, a draft force prediction model using DEM was developed to verify the effect of soil properties on draft force through simulation. The soil textures of the two fields were loam and clay loam, and the difference in draft force due to the difference in the physical properties of the two fields could be seen. The developed prediction model was also verified by comparing the actual field experiment with the existing theoretical calculation method. Soil property measurements were conducted at each depth in two fields with different physical properties. The Atterberg limit test revealed that both soils were cohesive soil in a plastic state. Past studies have shown that, the higher the shear strength and cone index, and the lower the moisture content in a certain section, the higher the draft force. However, Field B had a higher shear strength, lower moisture content, and lower cone index compared to Field A. Therefore, it is difficult to relate to a single factor when predicting the draft force, and many factors must be considered together. The precision of the predicted draft force from DEM simulations was confirmed by juxtaposing it with the measured draft force obtained from real-field experiments. In Field A, the draft force prediction from DEM simulations demonstrated an accuracy rate of 86.75%, while, in Field B, it reached 74.51%. The process of calibrating the surface energy based on shear torque resulted in more errors in Field B than in Field A, which led to a larger error in the draft force prediction. In future research, it is recommended to further study the modeling of various agricultural soil environments to improve the accuracy of design load prediction for soil-machine systems. The developed DEM-based draft force prediction model is up to 84% more accurate than the existing theoretical method by ASABE D497.4. This demonstrated the importance of reflecting the physical and mechanical characteristics of the working environment when assessing the performance of agricultural machinery. Performance evaluations of soil tillage machines include not only the workload, but also the degree of soil crushing and the flow of soil to invert and properly drain the soil. Future research should focus on enhancing the initial prediction accuracy of workload by employing precise soil property measurements based on modal modeling parameters. Furthermore, it is anticipated that the acceleration of simulation-based design optimization will be achieved through the establishment of a comprehensive database encompassing diverse soil environments. This will enable a more thorough study of load predictions for



various types of working machines beyond moldboard plow. For virtual simulation-based performance evaluations, it is important to obtain a database for defining various farming environments and analyzing loads. The results of this study are expected to be used as indicators of soil–tool interaction in future soil–tractor and soil–tire interaction studies for agricultural operations.

**Author Contributions:** Conceptualization, Y.-S.K. and Y.-J.K.; methodology, Y.-S.K. and W.-S.K.; software, B.-M.B. and T.-J.K.; validation, Y.-S.K. and B.-M.B.; formal analysis, Y.-S.K. and B.-M.B.; investigation, Y.-J.K. and S.-D.L.; data curation, Y.-S.K. and B.-M.B.; writing original, B.-M.B.; writing—review and editing, Y.-S.K. and W.-S.K.; supervision, Y.-J.K. and S.-D.L.; project administration, Y.-J.K. and S.-D.L.; funding acquisition, Y.-J.K. and S.-D.L. All authors have read and agreed to the published version of the manuscript.

**Funding:** This work was supported by the Industrial Strategic Technology Development Program (20014649, Development of intelligent technology and standard integrated controller for tractor attached implement) funded By the Ministry of Trade, Industry & Energy (MOTIE, Republic of Korea).

**Institutional Review Board Statement:** Not applicable.

**Data Availability Statement:** Data are contained within the article.

**Conflicts of Interest:** The authors declare no conflict of interest.

## References

- Mahatale, Y.V.; Tathod, D.V.; Chavan, V.K. Performance of Reversible Mold Board Plow. In *Emerging Technologies in Agricultural Engineering*; Apple Academic Press: Palm Bay, FL, USA, 2017; pp. 137–163.
- Kim, W.-S.; Kim, Y.-J.; Park, S.-U.; Nam, K.-C.; Choi, C.-H. Analysis of Traction Performance for an Agricultural Tractor According to Soil Moisture Content during Plow Tillage. In Proceedings of the 2019 ASABE Annual International Meeting, Boston, MA, USA, 7–9 July 2019; pp. 2–7.
- Raper, R.L. Force requirements and soil disruption of straight and bentleg subsoilers for conservation tillage systems. *Appl. Eng. Agric.* **2005**, *21*, 787–794. [CrossRef]
- Kim, Y.S.; Kim, W.S.; Baek, S.Y.; Baek, S.M.; Kim, Y.J.; Lee, S.D.; Kim, Y.J. Analysis of Tillage Depth and Gear Selection for Mechanical Load and Fuel Efficiency of an Agricultural Tractor Using an Agricultural Field Measuring System. *Sensors* **2020**, *20*, 2450. [CrossRef] [PubMed]
- Kim, Y.S.; Kim, T.J.; Kim, Y.J.; Lee, S.D.; Park, S.U.; Kim, W.S. Development of a Real-Time Tillage Depth Measurement System for Agricultural Tractors: Application to the Effect Analysis of Tillage Depth on Draft Force during Plow Tillage. *Sensors* **2020**, *20*, 912. [CrossRef] [PubMed]
- Aikins, K.A.; Ucgul, M.; Barr, J.B.; Awuah, E.; Antille, D.L.; Jensen, T.A.; Desbiolles, J.M.A. Review of Discrete Element Method Simulations of Soil Tillage and Furrow Opening. *Agriculture* **2023**, *13*, 541. [CrossRef]
- Fielke, J.M. Finite Element Modelling of the Interaction of the Cutting Edge of Tillage Implements with Soil. *J. Agric. Eng. Res.* **1999**, *74*, 91–101. [CrossRef]
- Ucgul, M.; Saunders, C.; Fielke, J.M. Comparison of the Discrete Element and Finite Element Methods to Model the Interaction of Soil and Tool Cutting Edge. *Biosyst. Eng.* **2018**, *169*, 199–208. [CrossRef]
- Bentaher, H.; Ibrahmi, A.; Hamza, E.; Hbaieb, M.; Kantchev, G.; Maalej, A.; Arnold, W. Finite Element Simulation of Moldboard–Soil Interaction. *Soil Tillage Res.* **2013**, *134*, 11–16. [CrossRef]
- Ibrahmi, A.; Bentaher, H.; Hbaieb, M.; Maalej, A.; Mouazen, A.M. Study the Effect of Tool Geometry and Operational Conditions on Mouldboard Plough Forces and Energy Requirement: Part 1. Finite Element Simulation. *Comput. Electron. Agric.* **2015**, *117*, 258–267. [CrossRef]
- Wang, X.; Zhang, S.; Pan, H.; Zheng, Z.; Huang, Y.; Zhu, R. Effect of Soil Particle Size on Soil-Subsoiler Interactions Using the Discrete Element Method Simulations. *Biosyst. Eng.* **2019**, *182*, 138–150. [CrossRef]
- Obermayr, M.; Dressler, K.; Vrettos, C.; Eberhard, P. Prediction of Draft Forces in Cohesionless Soil with the Discrete Element Method. *J. Terramech.* **2011**, *48*, 347–358. [CrossRef]
- Ucgul, M.; Fielke, J.M.; Saunders, C. Three-Dimensional Discrete Element Modelling (DEM) of Tillage: Accounting for Soil Cohesion and Adhesion. *Biosyst. Eng.* **2015**, *129*, 298–306. [CrossRef]
- Tekeste, M.Z.; Balvanz, L.R.; Hatfield, J.L.; Ghorbani, S. Discrete Element Modeling of Cultivator Sweep-to-Soil Interaction: Worn and Hardened Edges Effects on Soil-Tool Forces and Soil Flow. *J. Terramech.* **2019**, *82*, 1–11. [CrossRef]
- Bravo, E.L.; Tijskens, E.; Suárez, M.H.; Gonzalez Cueto, O.; Ramon, H. Prediction Model for Non-Inversion Soil Tillage Implemented on Discrete Element Method. *Comput. Electron. Agric.* **2014**, *106*, 120–127. [CrossRef]
- DEM Solutions Ltd. *Theory Reference Guide, Version 2.6*; DEM Solutions Ltd.: Edinburgh, UK, 2014.

17. Morrissey, J.P.; Thakur, S.C.; Ooi, J.Y. EDEM Contact Model: Adhesive Elasto-Plastic Model. *Granul. Matter* **2014**, *16*, 383–400.
18. Kim, Y.S.; Siddique, M.A.A.; Kim, W.S.; Kim, Y.J.; Lee, S.D.; Lee, D.K.; Hwang, S.J.; Nam, J.S.; Park, S.U.; Lim, R.G. DEM Simulation for Draft Force Prediction of Moldboard Plow According to the Tillage Depth in Cohesive Soil. *Comput. Electron. Agric.* **2021**, *189*, 106368. [CrossRef]
19. Tan, K.H. *Soil Sampling, Preparation, and Analysis*; CRC Press: New York, NY, USA, 1995; ISBN 0-8247-9675-6.
20. O’Kelly, B.C.; Sivakumar, V. Water Content Determinations for Peat and Other Organic Soils Using the Oven-Drying Method. *Dry. Technol.* **2014**, *32*, 631–643. [CrossRef]
21. Klute, A.; Bradford, J.M.; Gupta, S.C. Compressibility. Methods Soil Anal. Part 1—Physical Mineral. Methods. *Soil Sci. Soc. Am. Am. Soc. Agron.* **1986**, 377–382. [CrossRef]
22. Ditzler, C.; Scheffe, K.; Monger, H.C. *USDA Handbook 18*; Government Printing Office: Washington, DC, USA, 2017.
23. Thien, S.J. A Flow Diagram for Teaching Texture-by-Feel Analysis. *J. Agron. Educ.* **1979**, *8*, 54–55. [CrossRef]
24. Ibrahim, N.M.; Rahim, N.L.; Amat, R.C.; Salehuddin, S.; Ariffin, N.A. Determination of Plasticity Index and Compression Index of Soil at Perlis. *APCBEE Procedia* **2012**, *4*, 94–98. [CrossRef]
25. *D4318-10*; Test Methods for Liquid Limit, Plastic Limit, and Plasticity Index of Soils (D4318-10), Report. ASTM International Standard: West Conshohocken, PA, USA, 2010.
26. Kim, W.S.; Kim, Y.J.; Baek, S.M.; Baek, S.Y.; Moon, S.P.; Lee, N.G.; Kim, T.J.; Siddique, A.A.; Jeon, H.H.; Kim, Y.S. Effect of the Cone Index on the Work Load of the Agricultural Tractor. *J. Drive Control* **2020**, *17*, 9–18. [CrossRef]
27. Benjamin, J.G.; Cruse, R.M. Tillage Effects on Shear Strength and Bulk Density of Soil Aggregates. *Soil Tillage Res.* **1987**, *9*, 255–263. [CrossRef]
28. *ASABE Standards EP542*; Procedure for Using and Reporting Data Obtained with the Soil Cone Penetrometer. ASAE: St. Joseph, MI, USA, 2009; Volume 1999.
29. *ASABE Standards S313.3*; Soil Cone Penetrometer. ASAE: St. Joseph, MI, USA, 2005; Volume 1999.
30. Srivastava, A.K.; Goering, C.E.; Rohrbach, R.P.; Buckmaster, D.R. *Engineering Principles of Agricultural Machines*, 2nd ed.; The American Society of Agricultural and Biological Engineers: St. Joseph, MI, USA, 2006.
31. Hang, C.; Gao, X.; Yuan, M.; Huang, Y.; Zhu, R. Discrete Element Simulations and Experiments of Soil Disturbance as Affected by the Tine Spacing of Subsoiler. *Biosyst. Eng.* **2018**, *168*, 73–82. [CrossRef]
32. Saunders, C.; Ucgul, M.; Godwin, R.J. Discrete Element Method (DEM) Simulation to Improve Performance of a Mouldboard Skimmer. *Soil Tillage Res.* **2021**, *205*, 104764. [CrossRef]
33. Bolotov, A.G.; Shein, E.V.; Makarychev, S.V. Water Retention Capacity of Soils in the Altai Region. *Eurasian Soil Sci.* **2019**, *52*, 187–192. [CrossRef]
34. Ahmadi, I. Development and Assessment of a Draft Force Calculator for Disk Plow Using the Laws of Classical Mechanics. *Soil Tillage Res.* **2016**, *163*, 32–40. [CrossRef]
35. Palmer, R.A. American Society of Agricultural Engineers. *Science* **1953**, *118*, 3. [CrossRef]
36. Savitzky, A.; Golay, M.J.E. Smoothing and Differentiation of Data. *Anal. Chem.* **1964**, *36*, 1627–1639. [CrossRef]
37. Ranjbar, I.; Rashidi, M.; Lehmal, H.F.; Mirmoradi, M.; Abdolalizadeh, E. Modeling of Double Action Disc Harrow Draft Force Based on Tillage Depth and Forward Speed. *Middle East J. Sci. Res.* **2013**, *17*, 1061–1067.
38. Al-Suhaibani, S.A.M.F.; Wahby, A.M.; Aboukarima, I.S.T. Study on the Effect of Soil Moisture Content and Plowing Speed on Draft Requirements of a Moldboard Plow. *J. Adv. Agric.* **2015**, *4*, 477–486.

**Disclaimer/Publisher’s Note:** The statements, opinions and data contained in all publications are solely those of the individual author(s) and contributor(s) and not of MDPI and/or the editor(s). MDPI and/or the editor(s) disclaim responsibility for any injury to people or property resulting from any ideas, methods, instructions or products referred to in the content.

## Article

# Fertilization Mapping Based on the Soil Properties of Paddy Fields in Korea

Juwon Shin <sup>1</sup>, Jinho Won <sup>1</sup>, Seong-Min Kim <sup>1,2</sup>, Dae-Cheol Kim <sup>1,2</sup> and Yongjin Cho <sup>1,2,\*</sup>

<sup>1</sup> Department of Bioindustrial Machinery Engineering, Jeonbuk National University, Jeonju 54896, Republic of Korea; jw970429@naver.com (J.S.); wjh9446@jbnu.ac.kr (J.W.); smkim@jbnu.ac.kr (S.-M.K.); dckim12@jbnu.ac.kr (D.-C.K.)

<sup>2</sup> Institute of Agricultural Machinery ICT Convergence, Jeonbuk National University, Jeonju 54896, Republic of Korea

\* Correspondence: chojy@jbnu.ac.kr

**Abstract:** The purpose of this study was to construct a map of expected fertilization rates for nitrogen (N) and phosphorus (P<sub>2</sub>O<sub>5</sub>) based on measurements of components in soil samples and to identify the spatial variabilities of four lots of a salt-affected paddy field in Korea. Four salt-affected paddy field lots in Korea were divided into 30 sectors for collecting soil samples. They were then analyzed for soil organic matter (SOM), silicon dioxide (SiO<sub>2</sub>), total nitrogen (TN), and available phosphorus (Av.P<sub>2</sub>O<sub>5</sub>) in accordance with international standards. Expected fertilization rates of N and P<sub>2</sub>O<sub>5</sub> were developed as prescription standards for the application of fertilizer to paddy fields. They were derived using a model of the fertilization rates of N and P<sub>2</sub>O<sub>5</sub>. To determine the presence of spatial correlation and continuity in the given fields, a spherical variogram was used. Based on the spherical model with the application of a regular kriging interpolation, maps of the contents of TN and Av.P<sub>2</sub>O<sub>5</sub> as well as the expected fertilization rates of N and P<sub>2</sub>O<sub>5</sub> at each sector of 1 × 1 m<sup>2</sup> were developed. The expected fertilization rate of N at each sector appeared in the range of min. 10.0 g to max. 25.7 g, while that of P<sub>2</sub>O<sub>5</sub> appeared in the range of min. 0.68 g to max. 8.46 g.

**Keywords:** fertilization rate; kriging; soil mapping; variogram

**Citation:** Shin, J.; Won, J.; Kim, S.-M.; Kim, D.-C.; Cho, Y. Fertilization Mapping Based on the Soil Properties of Paddy Fields in Korea. *Agriculture* **2023**, *13*, 2049. <https://doi.org/10.3390/agriculture13112049>

Academic Editor: Mojtaba Zeraatpisheh

Received: 4 October 2023

Revised: 19 October 2023

Accepted: 23 October 2023

Published: 26 October 2023



**Copyright:** © 2023 by the authors. Licensee MDPI, Basel, Switzerland. This article is an open access article distributed under the terms and conditions of the Creative Commons Attribution (CC BY) license (<https://creativecommons.org/licenses/by/4.0/>).

## 1. Introduction

Soil is regarded as an essential element for agriculture. It not only provides necessary nutrients and moisture needed for the growth of crops but also provides a stable foundation for the habitat. To produce agricultural products of good quality through an improvement in productivity and in the quality of crops, a sustainable management of soil is essential [1–3].

Fertilizer for soil is an important element that affects the growth of crops. It consists of nitrogen, phosphorus, potassium, and so on. Some farmers tend to exceed the level of reasonable fertilization rates needed for the growth of crops to maximize the yield of crops [4]. Conventional fertilization with excess manuring disturbs sustainable agriculture. An excess supply of nitrogen results in an exceeded reasonable level of nutrient needed for the growth of crops and reduces the resistance of crops against insect pests. Furthermore, it accelerates the acidification of the soil, leading to soil contamination [5]. An excess supply of phosphorus could disturb the absorption of nutrients by crops, reduce the level of the pH of the soil, and bring about eutrophication of the soil by creating an insoluble compound bound with either aluminum or iron. Excessive application of fertilizer could create various environmental problems, such as salt accumulation, overnutrition, accumulation of heavy metal and nitrate in the soil, and so on, resulting in adverse effects such as deteriorated growth of crops and consequential decrease in productivity [6]. Thus, the physicochemical properties of soils need to be considered for sustainable management of soil.

On the other hand, due to the geographical characteristics of Korea, the country is surrounded by the sea on three sides, and more than 66% of the country's land area is covered by mountains and lakes, leaving only about 26% of the land area available for agriculture. Therefore, reclamation projects were carried out to maximize land use and develop agricultural areas [7]. Reclamation refers to the conversion of water surfaces such as oceans, rivers, and lakes into arable land. About 81% of the reclaimed land in Korea is used for paddies, and about 21.9% of it is used as salt-affected paddies [8]. "Salt-affected paddy" refers to soil that has been recently reclaimed and has a high salt concentration. Compared to normal soils, salt-affected paddy soil has a lower fertility and a higher salt concentration, which reduces the availability of moisture to crops and can lead to an imbalance of nutrients needed for crop growth. In addition, salt-affected paddy soils have poorly developed soil structure, resulting in poor particle cohesion and low water-holding capacity [9]. Therefore, soil management technology that improves crop quality and yield while considering the chemical and physical properties of the soil is required [10], and sustainable agriculture and high-quality crop production are possible through proper fertilizer input [11].

Precision agriculture is a term describing the agricultural approach to maximize the level of productivity and quality by minimizing the input of resources such as water, fertilizer, manpower, and so on. It is also a term describing the technique to control the specified space of each site for the stable growth of crops [12]. Accordingly, a decision support system that takes spatial and temporal variabilities into account can be provided to keep reasonable levels of harvest and quality of crops. This could realize a safe production system in terms of the environment [13]. A technology that is capable of reducing uneven effects on crop growth is needed, utilizing the efficient processing of information of varying soil properties in the spaces of each lot of a field [14]. Variable rate technology has been introduced to solve such a problem. It could control the fertilization rate by considering spatial variabilities of corresponding factors in soils. To apply variable rate technology effectively, the identification of soil properties by considering spatial variabilities in the soil is essential [15].

To solve potential economic and environmental problems due to an excessive or deficient input of soil fertilizer, the development of a map of soils to design the application of variable rate technology is essential [16]. After developing a spatial statistics model of soil properties, a map of soil properties can be created by applying the spatial statistics model to a geographical database [17]. Rabi [18] has reported that unsampled data could be estimated using kriging interpolation in a variogram model developed based on sample data of soil collected at each site. Zhang and Kovacs [19] have developed a map of predicted soil components by employing sensor data applied to a spatial statistics model. Diacano and Castrignano [20] have applied variable rate technology to each location by employing a developed map of soil components. Aggelopoulou and Pateras [21] have developed a map of nitrogen content in soil through collected samples of soil, applied the fertilization of nitrogenous fertilizer to each lot, and reduced the fertilization rate of nitrogenous fertilizer by approximately 38%. Hong and Kim [22] have introduced variable rate technology to rice and reduced the fertilization rate by approximately 32% compared to conventional fertilization. The map of soil components can be utilized as an important tool for producing crops of uniform quality by taking spatial variability of soil into account.

Identification of soil composition is essential for soil mapping for variable rate technology. However, there is currently no active research on salt-affected paddies in Korea, and it is time to conduct research on salt-affected paddy soil for the realization of precise agriculture.

The purpose of this study is to analyze the soil composition of salt-affected paddies in Korea and to develop a variable rate technology application map for nitrogen and phosphate fertilizers. The specific objectives are as follows.

1. Collect soil samples from salt-affected paddies in South Korea and characterize the soil composition.
2. Derive expected nitrogen and phosphate rates based on the analyzed chemical composition.

3. Create a map of the total nitrogen and available phosphorus content of salt-affected paddies and a map of the expected nitrogen and phosphorus rates for variable rate technology through a variogram and kriging.

## 2. Materials and Methods

### 2.1. Analysis of Soil Components and Model of Fertilization Rate

The soil samples used in this study were collected from four places of a salt-affected paddy field (126°52'28" E, 37°05'09" N and 3 m elevation) in Suchon-ri, Jangan-myeon, Hwaseong-si, Gyeonggi-do Province in Korea during the period from 19 April 2022 to 23 April 2022 (Figure 1). Temperature and humidity in the ambient environment were 15.1 °C and 45%, respectively. The soil texture was silty clay. Silty clay is grayish in color, soft in texture, and abundant in organic matter, with a clay content of more than 50%, and is mainly distributed in ocean current areas. For the sampling of soils, the paddy field was divided into 30 sectors. The size of each sector was set as 11 × 9 m, 13 × 8 m, 13 × 9 m, and 13 × 9 m, respectively. A dedicated “Soil Sampler (Edelman Auger, Eijkelkamp, The Netherlands)” was used for the sampling of soils. A depth of 5 cm of surface soil was removed for sampling soils. A total of 120 soil samples were collected from the plough layer with a depth of 15 cm. Five samples were collected from each sector. Collected samples were mixed into a single lump to minimize potential deviations in the compositions of components in the soil sample.

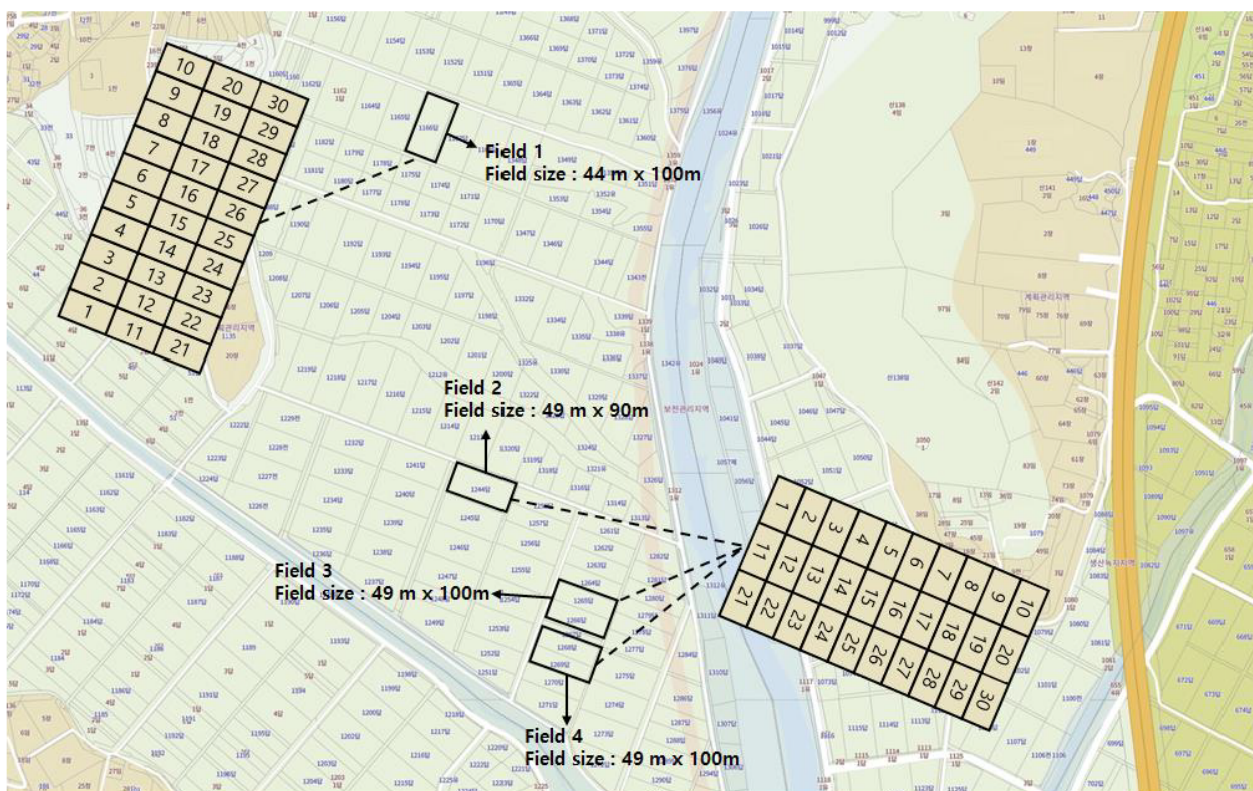


**Figure 1.** Location of soil sampling point in Hwaseong-si, Gyeonggi-do, Republic of Korea. All fields were divided into 30 sections. Each number was a soil sampling number.

The collected samples of the soil were forwarded to the “Center of Soil Verification” in the “Korea Agriculture Technology Promotion Agency” for analysis of the components in the soil samples. The “Manual of analysis procedures for comprehensive test lab [23]” and the “Method for Chemical Analysis of Soils [24]” of the “Rural Development Administration” in Korea were employed for analyses of soil organic matter (SOM), silicon dioxide (SiO<sub>2</sub>), total nitrogen (TN), available phosphorus (Av.P<sub>2</sub>O<sub>5</sub>), and so on in the soil

samples. The soil samples were pulverized finely and sifted through a 0.5 mm screen. The components of SOM, SiO<sub>2</sub>, Av.P<sub>2</sub>O<sub>5</sub>, and TN in the soil samples were then analyzed by utilizing the Tyurin method, the method of stationary fresh water incubation, the Lancaster method, and the Dumas method, respectively.

The Tyurin method is an externally heated method of analysis, in which the soil sample is finely ground and sieved through a 0.5 mm sieve, and then 0.3 g of the homogenized soil sample and 10 mL of 0.4 N potassium dichromate sulfate-mixed solution are added to a 250 mL glass triangular flask. In our study, the mixture was then heated on a heating plate at 200 °C and boiled for 5 min from the beginning of bubbling, then removed from the heating plate; the potassium dichromate sulfate mixture was washed with distilled water, and about 5 mL of 85% phosphoric acid (H<sub>3</sub>PO<sub>4</sub>) and 5–6 drops of the indicator diphenylamine solution were added. Then, it was titrated with 0.2 M ferric ammonium sulfate solution, and the end point was measured when the color of the solution changed from black-brown to indigo-blue to green.

The fresh water constant temperature method was performed by placing 10 g of air-dried fine earth into a 100 mL centrifuge tube, shaking it in 60 mL of distilled water, removing the air, and sealing it. After that, it was placed in a thermostat at 40 °C for 7 days, and the supernatant was filtered through filter paper No. 6. Then, 10 mL of the filtered supernatant was placed in a test tube; 0.25 M HCl solution and 5 mL of ammonium molybdate solution were added; and 10 mL of sodium sulfite solution was added after standing for about 3 min. The treated supernatant was measured at an absorbance of 700 nm after about 10 min of incubation.

The Lancaster method was carried out by placing 5 g of air-dried fine earth in a triangular flask, dissolving 400 mL of HOAC and 300 mL of 10 M lactic acid in 6 L of distilled water, then adding 22.2 g of NH<sub>4</sub>F, 133.3 g of ammonium sulfate, and 170 g of NaOH. Then, 20 mL of leachate adjusted to pH 4.25 by adding distilled water was added, shaken for 10 min, and filtered through No. 2 filter paper. Color development and determination were performed by the molybdenum (MO) method with ascorbic acid and the MO method with 1-amino-2-naphtol-4-sulfonic acid.

The Dumas method is a method for quantifying N<sub>2</sub>O by reducing it to N<sub>2</sub> and measuring the volume of N<sub>2</sub> gas. The soil sample is oxidized by heating CuO to a high temperature of more than 600 °C; the resulting combustion gas is reduced to N<sub>2</sub> gas by contact with pure CO<sub>2</sub> and hot Cu, and CO is converted to CO<sub>2</sub> by contacting CuO again. The N<sub>2</sub>–CO<sub>2</sub> mixture is passed through a nitrometer in a concentrated alkaline solution, and after the CO<sub>2</sub> is captured, the volume of N<sub>2</sub> gas is measured to quantify the nitrogen content.

The model of fertilization rate for N and P<sub>2</sub>O<sub>5</sub>, which was developed as a fertilization standard of rice [25], was also used for the analysis. The fertilization rate of N corresponds to the components of the soil of SOM and SiO<sub>2</sub>. It can be calculated through Formula (1), whereas the fertilization rate of P<sub>2</sub>O<sub>5</sub> corresponds to the soil component of Av.P<sub>2</sub>O<sub>5</sub>. It can be calculated by using Formula (2). Formulas (3) and (4) are transformations wherein a unit area of 10a is converted into 1 m<sup>2</sup> to be compatible with the scale of the lot.

$$N(\text{kg}/10\text{a}) = 9.05 - 0.108 \times \text{OM} + 0.020 \times \text{SiO}_2 \quad (1)$$

$$\text{P}_2\text{O}_5 (\text{kg}/10\text{a}) = (100 - \text{Av.P}_2\text{O}_5) \times 0.1 \quad (2)$$

$$N(\text{kg}/\text{m}^2) = (9.05 - 0.108 \times \text{OM} + 0.020 \times \text{SiO}_2) \times 0.001 \quad (3)$$

$$\text{P}_2\text{O}_5 (\text{kg}/\text{m}^2) = (100 - \text{Av.P}_2\text{O}_5) \times 0.1 \times 0.001 \quad (4)$$

where N is nitrogen (kg/10a); OM is organic matter (g/kg); SiO<sub>2</sub> is silicon dioxide (mg/kg); P<sub>2</sub>O<sub>5</sub> is phosphorus (kg/10a); and Av.P<sub>2</sub>O<sub>5</sub> is available phosphorus (100 mg/kg).



## 2.2. Spatial Statistics Model

A variogram generally uses measured data to predict unknown data, to determine the presence of correlation and continuity between data, and to estimate the interdependent distance between data [26,27]. “Correlation” and “variance” are measures to determine the presence of correlation between data. Autocorrelation represents a correlation between different variables at the point of measurement, given that only one datum is known at each point. Thus, it was regarded that it could be employed as a quantitative measure [28,29]. According to Lee and Jung [28], the autocovariance that expresses the quantitative measure of interrelationship between data points, which are distant from the point of specified data, is used. Autocovariance increases in accordance with decreasing distance between two data points. Therefore, it decreases in accordance with increasing distance between two data points [30]. In general, the semivariogram, which is half (1/2) of the variogram, is used. It provides the correlation length (range), threshold (sill), and nugget, which are necessary information for the kriging interpolation (Figure 2). Correlation length refers to the maximum distance of separation that represents the correlation between data points, whereas the threshold indicates the degree of variance of data. The nugget represents a constant value at the separation distance of 0. The selection of the model of the variogram is very important since the identified spatial correlation obtained through using the variogram would validate continuity in the interpolation of spatial data. Thus, the spherical model, which could be employed as an excellent one to determine the spatial variability and continuity of the soil, was used.

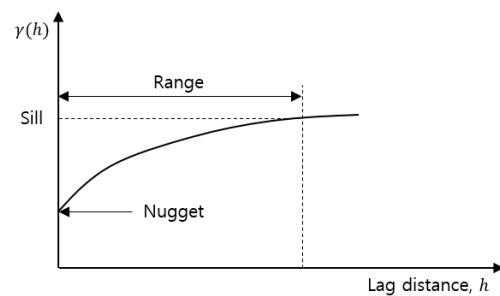


**Figure 2.** Sill, range, and nugget on variogram.

In this study, a regular kriging interpolation was applied to develop a soil map of the expected N and P<sub>2</sub>O<sub>5</sub> fertilization amount suitable for salt-affected paddies, and the mentioned variogram and regular kriging interpolation were performed through Surfer ver. 22 (Golden Software, Golden, CO, USA).

Kriging interpolation renders expected differences between actual and estimated values to be 0 by using the BLUE (best linear unbiased estimator) of the minimum variance for the periphery or zone of given data in an arbitrary spatial space. Simultaneously, it renders dispersion of difference as minimized. A spherical model renders the tangential line at the point of 0 separation distance to intersect the threshold at the point of 2/3 of the correlation length, thereby enabling the derivation of threshold and correlation length.

## 3. Results and Discussion

### 3.1. Derivation of Expected Fertilization Rates Accordant with Soil Components

Table 1 presents the soil properties of collected soil samples from each field. Mean and standard deviation of the SOM of the entire field were 20.6 g/kg and 4.482 g/kg, respectively. Those of SiO<sub>2</sub> were 471.6 mg/kg and 72.80 mg/kg, respectively. Mean and standard deviation of Av.P<sub>2</sub>O<sub>5</sub> were 44.24 mg/kg and 12.73 mg/kg, respectively. Those of TN were 0.12% and 0.02%, respectively. There were approximately less than 15% of differences compared to the average of the entire field in the statistics of SOM, SiO<sub>2</sub>, and Av.P<sub>2</sub>O<sub>5</sub>. TN showed a difference of less than 20% compared to the average of the entire field. However, the SOM and Av.P<sub>2</sub>O<sub>5</sub> in Field 2 and Field 4 exhibited respective values

higher than the average of the entire field. In the case of SOM, its value in Field 2 was approximately 24% higher than the average of the entire field, while that of Field 4 was approximately 19% lower than the average of the entire field. With regard to Av.P<sub>2</sub>O<sub>5</sub>, the value of Field 2 was approximately 19% lower than the average of the entire field, while the value of Field 4 was approximately 37% higher than the average of the entire field. Such variability of the chemical components in the soils of each field was due to environmental factors comprising climate conditions, soil management approaches, and so on. According to Park [31], the variability in the chemical composition of soil could be created by various environmental factors such as the properties of specific soils, the size of the land area, and functions of time factors, consistent with the results of the analysis of soil components in the present study.

**Table 1.** Soil properties of collected soil samples.

		Min.	25%	Median	75%	Max.	Mean	* S.D.
All Fields (n = 120)	SOM [g/kg]	11.37	16.89	19.96	24.33	31.29	20.60	4.48
	SiO <sub>2</sub> [mg/kg]	300.88	414.60	466.04	524.30	637.40	471.60	72.80
	Total Nitrogen [%]	0.06	0.10	0.12	0.14	0.19	0.12	0.02
	Av.P <sub>2</sub> O <sub>5</sub> [mg/kg]	15.39	35.20	41.84	52.35	75.43	44.24	12.73
Field 1 (n = 30)	SOM [g/kg]	11.37	16.74	21.98	23.68	29.91	20.90	4.38
	SiO <sub>2</sub> [mg/kg]	300.88	410.51	450.74	509.21	629.48	456.00	70.47
	Total Nitrogen [%]	0.06	0.10	0.13	0.15	0.19	0.13	0.03
	Av.P <sub>2</sub> O <sub>5</sub> [mg/kg]	28.58	33.80	37.81	42.67	48.64	38.10	5.72
Field 2 (n = 30)	SOM [g/kg]	20.43	24.33	25.90	27.39	31.29	25.50	3.09
	SiO <sub>2</sub> [mg/kg]	327.74	387.23	421.58	481.50	565.71	437.40	68.03
	Total Nitrogen [%]	0.11	0.13	0.14	0.15	0.17	0.14	0.02
	Av.P <sub>2</sub> O <sub>5</sub> [mg/kg]	15.39	29.31	35.61	41.74	48.78	35.70	9.63
Field 3 (n = 30)	SOM [g/kg]	15.25	17.21	19.05	21.08	24.74	19.20	2.47
	SiO <sub>2</sub> [mg/kg]	409.49	442.02	474.28	533.05	637.40	488.50	52.92
	Total Nitrogen [%]	0.9	0.10	0.11	0.12	0.15	0.11	0.01
	Av.P <sub>2</sub> O <sub>5</sub> [mg/kg]	32.43	36.54	41.54	47.65	60.23	42.70	8.00
Field 4 (n = 30)	SOM [g/kg]	11.58	15.39	16.71	18.53	21.98	16.80	2.39
	SiO <sub>2</sub> [mg/kg]	375.14	438.22	505.41	571.92	696.36	504.60	80.42
	Total Nitrogen [%]	0.08	0.09	0.10	0.12	0.14	0.10	0.01
	Av.P <sub>2</sub> O <sub>5</sub> [mg/kg]	48.36	54.78	58.53	64.75	75.43	60.60	9.06

\* S.D. = Standard Deviation.

Fertilization rates for N and P<sub>2</sub>O<sub>5</sub> were derived by using Formulas (3) and (4) (Table 2, Figures 3 and 4) to alleviate variability in soil composition and to obtain a reasonable fertilization rate for each field. According to the fertilization standards for crops in Korea, the optimal nitrogen fertilization rate is 11 to 18 kg/10a, and the optimal phosphorus fertilization rate is 4.5 kg/10a. Derivation of the expected fertilization rate of N for each sector used both SOM and SiO<sub>2</sub>, while the derivation of the expected fertilization rate of P<sub>2</sub>O<sub>5</sub> used Av.P<sub>2</sub>O<sub>5</sub>. Mean expected fertilization rates of N for Fields 1–4 were 15.9 kg/10a, 15.1 kg/10a, 16.8 kg/10a, and 17.4 kg/10a, respectively, while those of P<sub>2</sub>O<sub>5</sub> were 6.1 kg/10a, 6.4 kg/10a, 5.7 kg/10a, and 4.3 kg/10a, respectively. The predicted fertilization rate of N exhibited a difference of less than 20% compared to the average of each field. The expected fertilization rate of N for Fields 3 and 4 should be set higher than those of Fields 1 and 2 (Figure 3). The difference in fertilization rate of P<sub>2</sub>O<sub>5</sub> was insignificant except for that of Field 4.



**Table 2.** Means and standard deviations (SD) of expected fertilizer.

	All Fields		Field 1		Field 2		Field 3		Field 4	
	Mean (n = 120)	SD (n = 120)	Mean (n = 30)	SD (n = 30)	Mean (n = 30)	SD (n = 30)	Mean (n = 30)	SD (n = 30)	Mean (n = 30)	SD (n = 30)
Nitrogen fertilizer [kg/10a]	16.3	0.27	15.9	0.15	15.1	0.17	16.8	0.12	17.4	0.12
P <sub>2</sub> O <sub>5</sub> fertilizer [kg/10a]	5.6	0.12	6.1	0.06	6.4	0.10	5.7	0.09	4.3	0.11

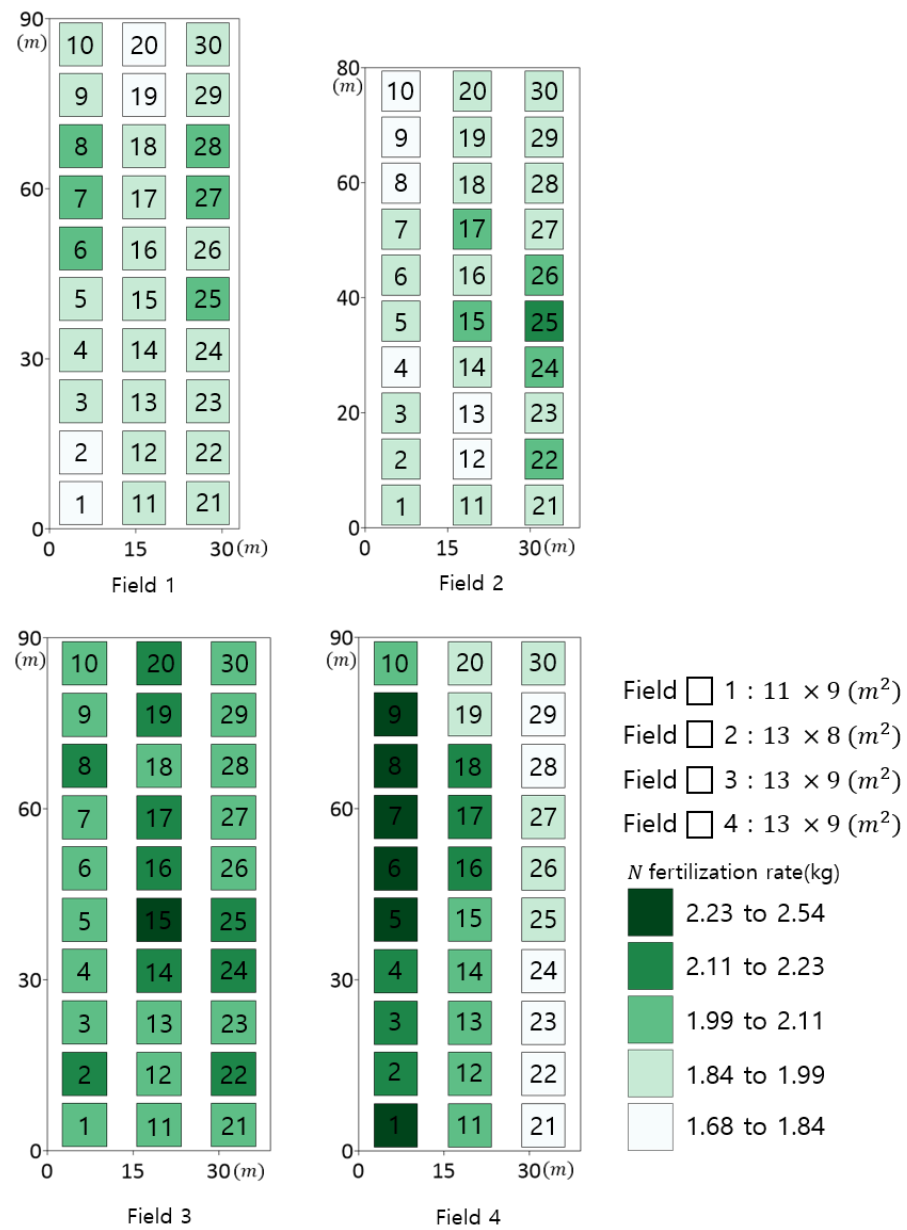


**Figure 3.** Expected N fertilization rate by section. All fields were divided into 30 sections. Each section size of field 1 to 4 was 11 × 9, 13 × 8, 13 × 9, and 13 × 9 m<sup>2</sup>, respectively.

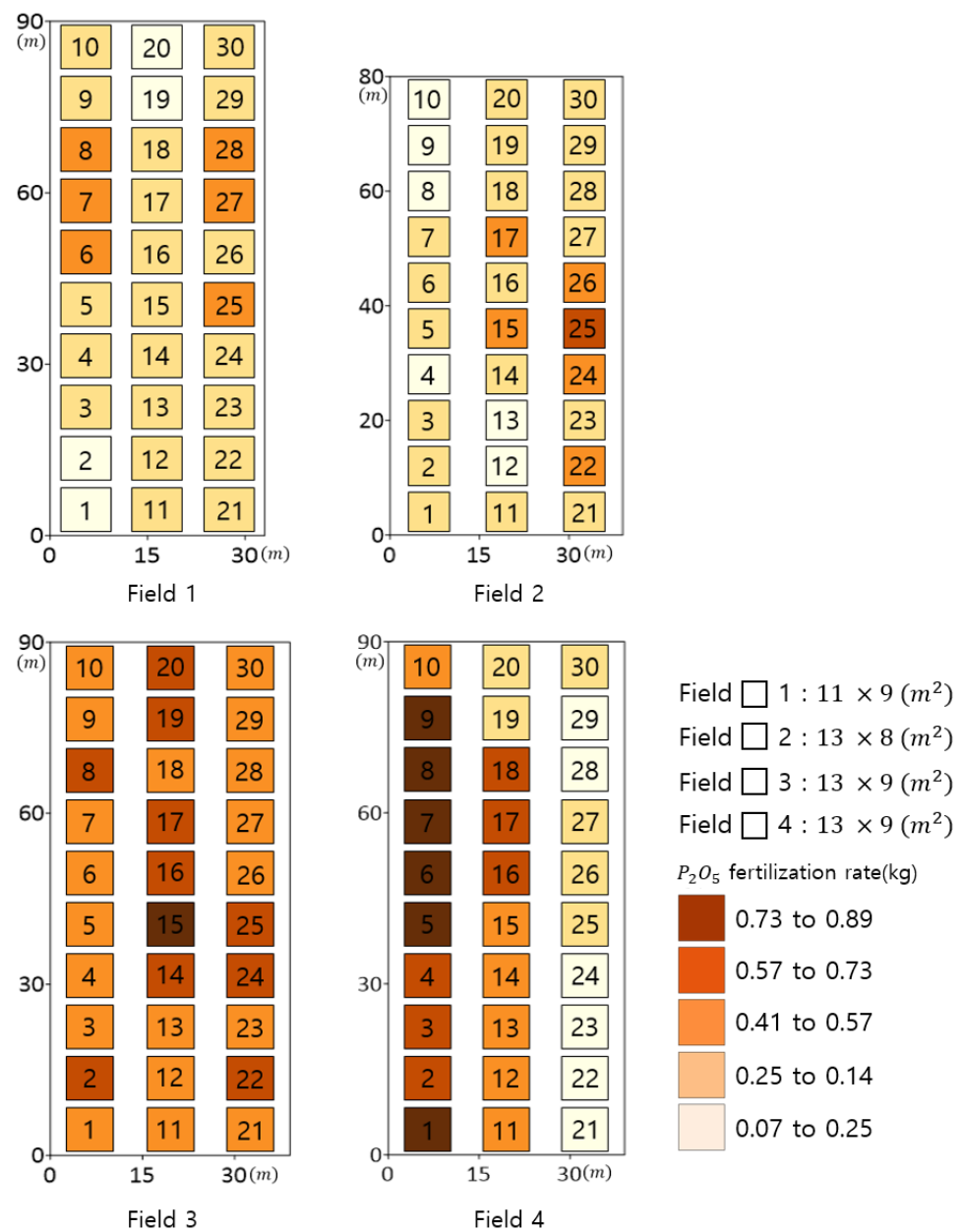


**Figure 4.** Expected P<sub>2</sub>O<sub>5</sub> fertilization rate by section. All fields were divided into 30 sections. Each section size of field 1 to 4 was 11 × 9, 13 × 8, 13 × 9, and 13 × 9 m<sup>2</sup>, respectively.

### 3.2. Spatial Statistics Analysis of Expected Fertilization Rate to Develop a Map of Variable Fertilization

The spherical model of the variogram was employed to construct a map of the variable fertilization of the expected fertilization rate of N and P<sub>2</sub>O<sub>5</sub> for each field. The threshold (sill) and correlation length (range) of TN, Av.P<sub>2</sub>O<sub>5</sub>, N, and P<sub>2</sub>O<sub>5</sub> are as presented in Table 3. Figure 5 represents the spherical model of the variogram of N and P<sub>2</sub>O<sub>5</sub>. The N fertilizer for Field 4 and the P<sub>2</sub>O<sub>5</sub> fertilizer for Fields 2 and 3 exhibit a trend of larger spatial variability compared to those of other fields; the value of N fertilizer for Field 4 appeared as 43.26 m, which was higher than 20.43 m and 27.54 m for Fields 2 and 3. Contrarily, a higher value of the sill and a lower value of the range, compared to those of other fields, appeared in the cases of N fertilizer and Av.P<sub>2</sub>O<sub>5</sub> fertilizer for Field 2. This was attributed to the lower spatial dependence of N fertilizer and Av.P<sub>2</sub>O<sub>5</sub> fertilizer for Field 2 compared to the higher spatial variability in the given space.

**Table 3.** Sill and range for soil properties and expected fertilizer using variogram.

		Field 1		Field 2		Field 3		Field 4	
		Sill (m)	Range (m)	Sill (m)	Range (m)	Sill (m)	Range (m)	Sill (m)	Range (m)
Soil properties	TN in soil (%)	0.0051	276.60	0.0009	124.00	0.0006	220.00	0.0008	182.90
	Av.P <sub>2</sub> O <sub>5</sub> in soil (mg/kg)	33.32	36.31	89.01	27.08	100	99.90	66.26	30.85
Expected fertilizer	N fertilizer (kg/Sector *)	0.0199	28.42	0.0220	20.43	0.0189	27.54	0.0614	43.26
	P <sub>2</sub> O <sub>5</sub> fertilizer (kg/Sector *)	0.0033	36.31	0.0104	31.19	0.0112	73.68	0.0088	26.13

Sector \* = Division of the entire field into 30 (Each sector size of fields 1–4 is 99 m<sup>2</sup>, 104 m<sup>2</sup>, 127 m<sup>2</sup>, and 127 m<sup>2</sup>).

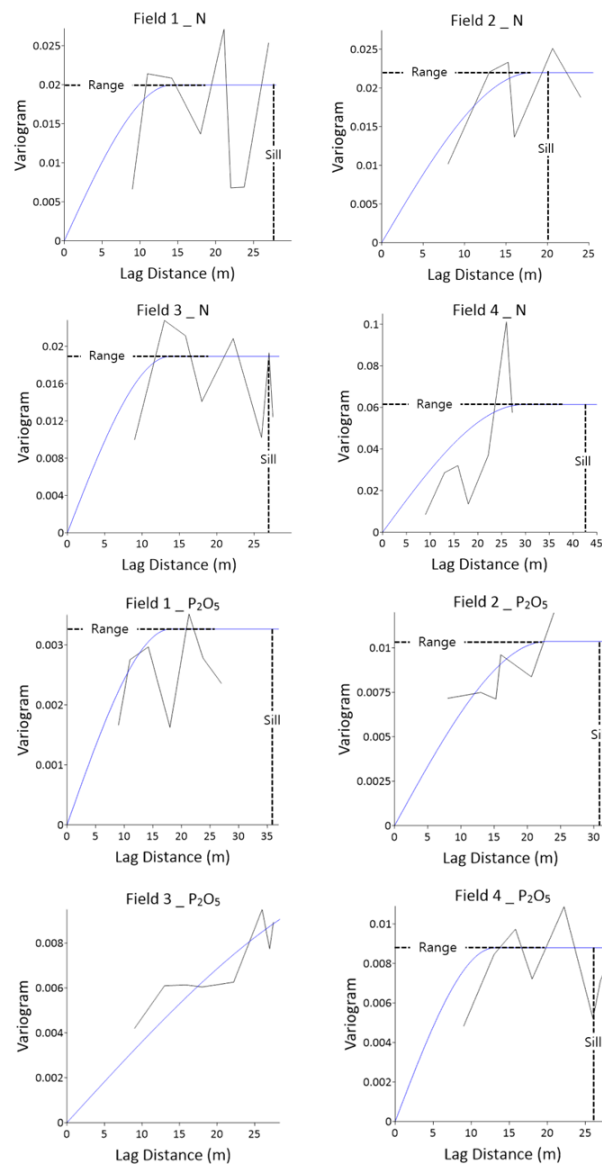


**Figure 5.** Variogram of N and P<sub>2</sub>O<sub>5</sub> using spherical model. The blue and gray lines mean the spherical model and measured data, respectively.

### 3.3. Map of Variable Fertilization Developed by the Application of Interpolation

A map of soil components was developed by employing the regular kriging interpolation, the known spatial statistics technique, based on the spherical variogram model to obtain variable fertilization rates suitable for rice in the paddy fields of Korea. The soil map is divided into ( $1 \times 1 \text{ m}^2$ ), taking into account the speed and working radius of the developing variable rate fertilizer applicator for accurate and precise variable rate fertilization. The expected fertilization map can show the appropriate fertilization amount for each compartment in the field (Figures 6 and 7). Figure 6 represents the map illustrating the predicted fertilization rate of TN (upper end of Figure 6) and N (lower end of Figure 6) in the soil for each field. Figure 7 represents the map illustrating the predicted fertilization rate of Av.P<sub>2</sub>O<sub>5</sub> (upper end of Figure 7) and P<sub>2</sub>O<sub>5</sub> (lower end of Figure 7) in soils for each field. In the map, the parts that correspond to less content or less predicted fertilization rate are painted in white color, and by way of contrast, the parts corresponding to more content or more predicted fertilization rate are painted in either green or orange color. In the case of the fertilization rate of N, the predicted fertilization rate per unit sector ( $1 \times 1 \text{ m}^2$ ) appeared as 12 g to 26 g for Field 1 and Field 2 and 10.0 g to 21.7 g for Fields 3 and 4. With regard to the case of the fertilization rate of Av.P<sub>2</sub>O<sub>5</sub>, the predicted fertilization rate per unit sector ( $1 \times 1 \text{ m}^2$ ) appeared as 5.15 g to 7.27 g for Field 1, 3.07 g to 8.46 g for Field 2, 3.16 g to 6.83 g for Field 3, and 0.68 g to 5.21 g for Field 4. The trends in the maps of the Av.P<sub>2</sub>O<sub>5</sub> content and predicted fertilization rate of P<sub>2</sub>O<sub>5</sub> in the soil for each field appeared oppositely (Figure 7). And the maps of the TN content and predicted fertilization rate of N in the soil for each field appeared with partially contrasting trends. This was attributed to the difference in the content levels of the SOM and SiO<sub>2</sub>. It appears that with the utilization of the expected fertilization maps (N and P<sub>2</sub>O<sub>5</sub>) in the development of the variable rate fertilizer applicator, more precise variable rate fertilization will be achievable in the future. This is believed to enable environmentally friendly and sustainable agriculture, specifically, precision farming, by minimizing the input of fertilizer and increasing crop yields. Thus, it is presumable that the minimization of the input of fertilizer and the increase in production of crops would be enabled by utilizing the map of the predicted fertilization rate (of N and P<sub>2</sub>O<sub>5</sub>) in a way of realizing an environmentally friendly and sustainable agriculture, precision agriculture.

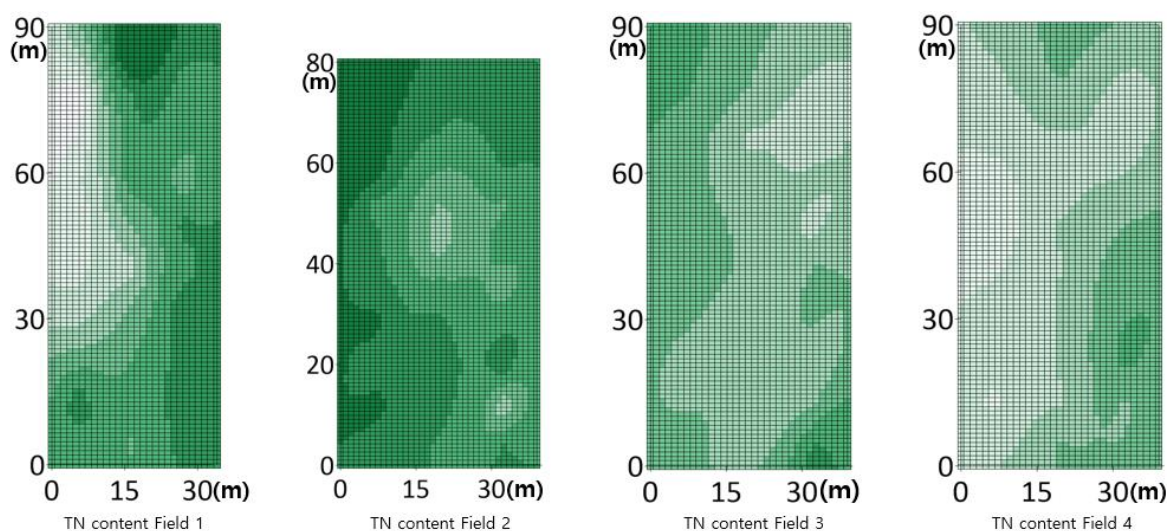


Figure 6. Cont.



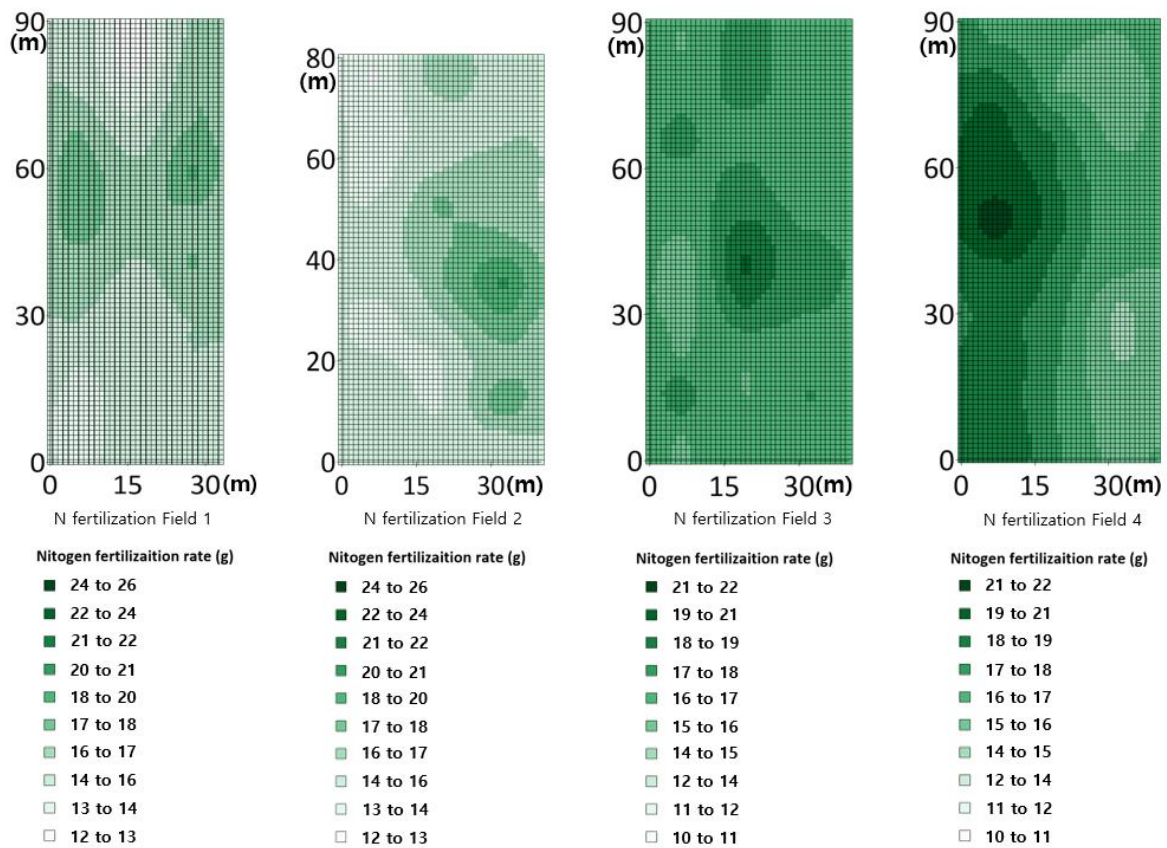


Figure 6. Mapping of TN content in soil and estimated N fertilization rate. Each square color represents the appropriate N fertilization rate for a 1 m<sup>2</sup> divided field.

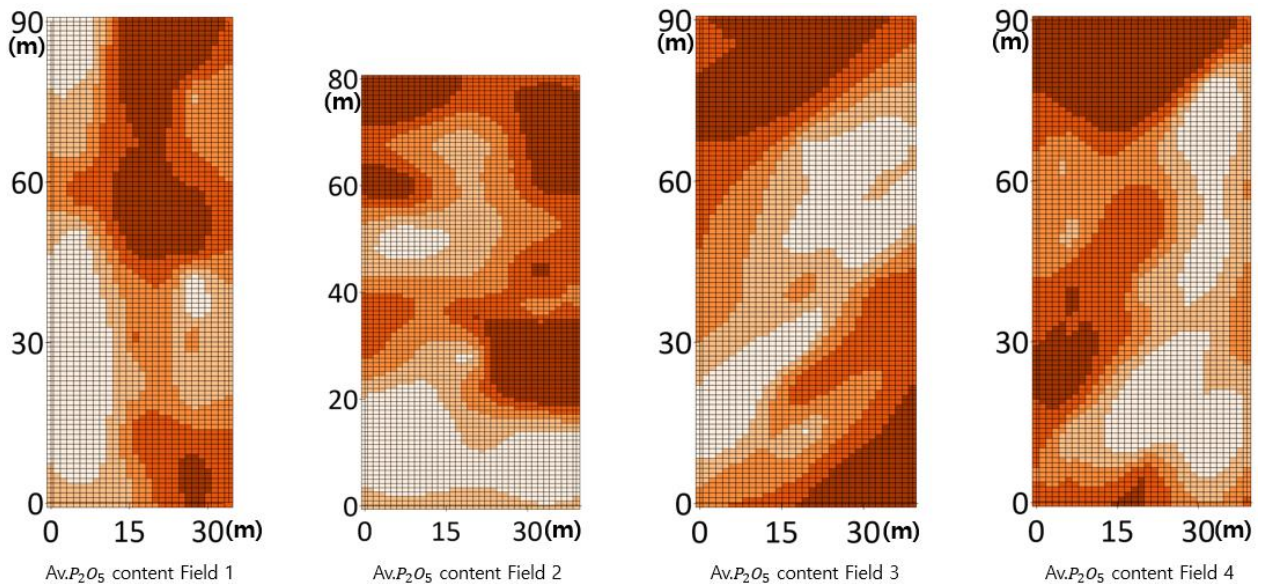
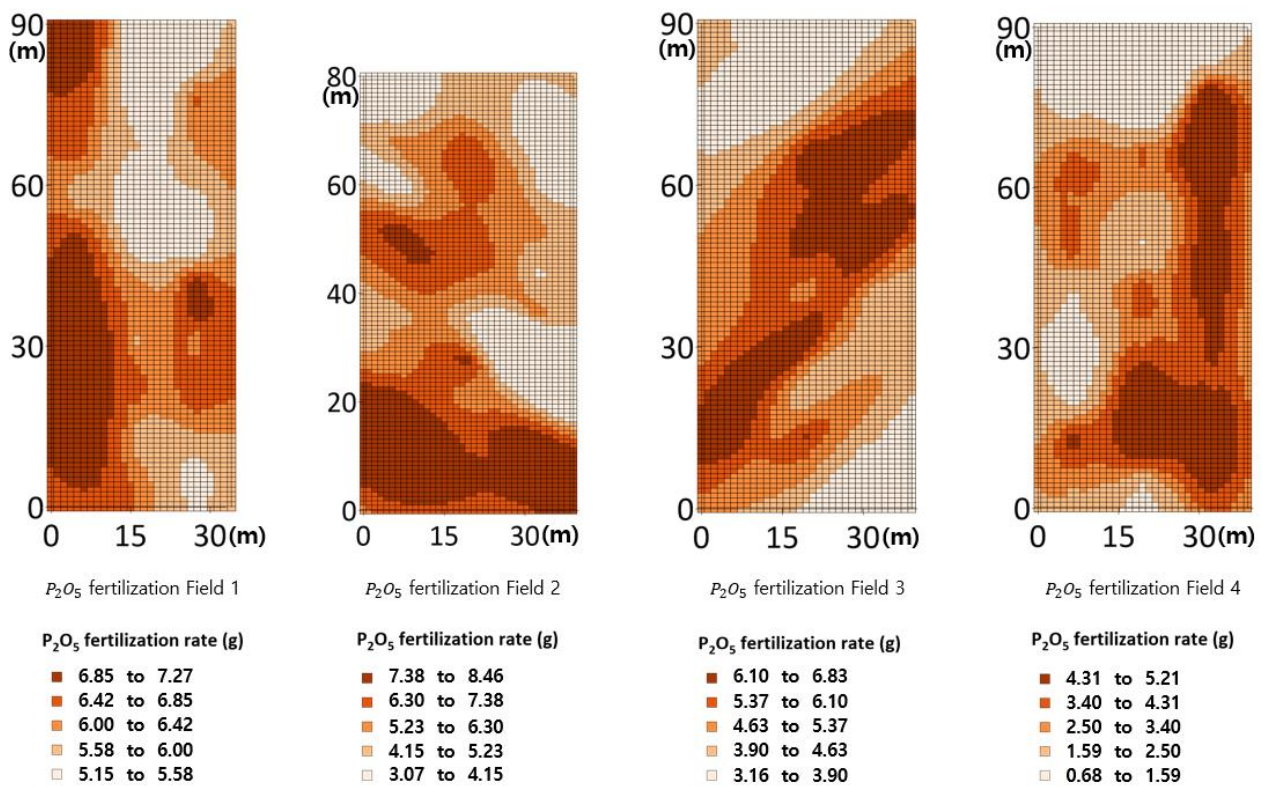


Figure 7. Cont.



**Figure 7.** Mapping of Av.P<sub>2</sub>O<sub>5</sub> content in soil and estimated P<sub>2</sub>O<sub>5</sub> fertilization rate. Each square color represents the appropriate P<sub>2</sub>O<sub>5</sub> fertilization rate for a 1 m<sup>2</sup> divided field.

#### 4. Conclusions

The present paper intended to develop a map of the expected fertilization rate of N and P<sub>2</sub>O<sub>5</sub> through the measurement of chemical components and the identification of spatial variability in soil samples collected from four lots of a paddy field in Korea. The paddy field was divided into 30 lots for the sampling of soils collected for the analysis. SOM, SiO<sub>2</sub>, and Av.P<sub>2</sub>O<sub>5</sub> manifested differences of less than 15% compared to the overall average of the field, while the TN exhibited a difference of less than 20% from the overall average of the field.

According to the prescription standard of fertilization for each crop based on chemical components comprising SOM, SiO<sub>2</sub>, and Av.P<sub>2</sub>O<sub>5</sub>, the modeling for the expected fertilization rate of N and P<sub>2</sub>O<sub>5</sub> was carried out, from which the predicted average of the fertilization rate of N and P<sub>2</sub>O<sub>5</sub> per each lot appeared as 1.78 kg and 0.60 kg, respectively. The spherical model was employed to develop a map of soil components for the application of variable fertilization suitable for crops in Korean paddy fields. In addition, the map of the expected fertilization rate of N and P<sub>2</sub>O<sub>5</sub> was developed through the application of regular kriging interpolation based on the spherical model for which the total field was divided into sectors of 1 × 1 m<sup>2</sup> to achieve precise variable fertilization. The predicted fertilization rate of N for each lot in the entire field appeared in the range from min. 10.0 g to max. 25.7 g, whereas that of P<sub>2</sub>O<sub>5</sub> appeared in the range from min. 0.68 g to max. 8.46 g. The map of the predicted fertilization rate of N exhibited a trend partially contrasting with the map of the predicted fertilization rate of TN, whereas the map of the predicted fertilization rate of P<sub>2</sub>O<sub>5</sub> manifested a fully contrasting trend with the map of Av.P<sub>2</sub>O<sub>5</sub> content. This kind of map of the predicted fertilization rate can minimize the input of resources by enabling a reasonable application of N and P<sub>2</sub>O<sub>5</sub> necessary for crops. The map of the expected fertilization rate of P<sub>2</sub>O<sub>5</sub> and N developed in the present study needs to be validated through verifying the actual yield and evaluating the quality of rice resulting from its use.

**Author Contributions:** Methodology, S.-M.K.; Validation, D.-C.K.; Formal analysis, J.W.; Writing—original draft, J.S.; Writing—review and editing, Y.C. All authors have read and agreed to the published version of the manuscript.

**Funding:** This research was supported by the Rural Development Administration of Korea (PJ01710005) and the National Institute of Agriculture, Forestry, and Food Technology Planning and Evaluation (RS-2023-00236201).

**Institutional Review Board Statement:** Not applicable.

**Data Availability Statement:** Not applicable.

**Conflicts of Interest:** The authors declare no conflict of interest.

## References

- Kim, D. Development and Accuracy Evaluation of Field Soil Temperature Prediction Model by Depth Using Artificial Intelligence and Meteorological Parameters. Master's thesis, The Seoul National University, Seoul, Republic of Korea, 2002.
- Passioura, J. Soil conditions and plant growth. *Plant Cell Environ.* **2002**, *25*, 311–318. [CrossRef] [PubMed]
- Tahat, M.M.; Alananbeh, K.M.; Othman, Y.A.; Leskovar, D.I. Soil health and sustainable agriculture. *Sustainability* **2020**, *12*, 4859. [CrossRef]
- Lemaire, G.; Gastal, F. N uptake and distribution in plant canopies. In *Diagnosis of the Nitrogen Status in Crops*; Springer: Berlin/Heidelberg, Germany, 1997; pp. 3–43.
- Wei, W.; Yang, M.; Liu, Y.; Huang, H.; Ye, C.; Zheng, J.; Guo, C.; Hao, M.; He, X.; Zhu, S. Fertilizer N application rate impacts plant-soil feedback in a sanqi production system. *Sci. Total Environ.* **2018**, *633*, 796–807. [CrossRef] [PubMed]
- Savci, S. An agricultural pollutant: Chemical fertilizer. *Int. J. Environ. Sci. Dev.* **2012**, *3*, 73. [CrossRef]
- Jeong, K.S. Sihwa Construction Project. *J. Korean Water Resour. Assoc.* **1996**, *29*, 106–115.
- Kim, H.; Kim, S.; Lee, D. The effects of irrigation water salinity levels on growth of rice by growth stage. *J. Korean Soc. Agric. Eng.* **2019**, *2019*, 73.
- Lee, S.H.; Yoo, S.H.; Seol, S.I. Assessment of Salt Damage for Upland-Crops in Dae-Ho Reclaimed Soil. *J. Korean Environ. Agric.* **2000**, *19*, 358–363.
- Monzon, J.P.; Calviño, P.; Sadras, V.O.; Zubiaurre, J.; Andrade, F.H. Precision agriculture based on crop physiological principles improves whole-farm yield and profit: A case study. *Eur. J. Agron.* **2018**, *99*, 62–71. [CrossRef]
- Khuang, T.; Huan, T.; Hach, C. Study on fertilizer rates for getting maximum grain yield and profitability of rice production. *Omonrice* **2008**, *16*, 93–99.
- Stafford, J.V. Essential technology for precision agriculture. In Proceedings of the Third International Conference on Precision Agriculture, Minneapolis, MN, USA, 23–26 June 1996; Wiley Online Library: New York, NY, USA; pp. 593–604.
- Van Rees, H.; McClelland, T.; Hochman, Z.; Carberry, P.; Hunt, J.; Huth, N.; Holzworth, D. Leading farmers in South East Australia have closed the exploitable wheat yield gap: Prospects for further improvement. *Field Crops Res.* **2014**, *164*, 1–11. [CrossRef]
- Cho, S.I.; Chang, Y.C.; Yeo, W.Y. Construction of a Spatioal Database for Realizing Precision Farming. *J. Biosyst. Eng.* **2002**, *27*, 161–172.
- Sawyer, J.E. Concepts of variable rate technology with considerations for fertilizer application. *J. Prod. Agric.* **1994**, *7*, 195–201. [CrossRef]
- Fu, W.; Tunney, H.; Zhang, C. Spatial variation of soil nutrients in a dairy farm and its implications for site-specific fertilizer application. *Soil Tillage Res.* **2010**, *106*, 185–193. [CrossRef]
- Scull, P.; Franklin, J.; Chadwick, O.A.; McArthur, D. Predictive soil mapping: A review. *Prog. Phys. Geogr.* **2003**, *27*, 171–197. [CrossRef]
- Sahoo, R.N. *Geostatistics in Geoinformatics for Managing Spatial Variability*; Indian Agricultural Research Institute: Pusa, India, 2003.
- Zhang, C.; Kovacs, J.M. The application of small unmanned aerial systems for precision agriculture: A review. *Precis. Agric.* **2012**, *13*, 693–712. [CrossRef]
- Diacono, M.; Castrignanò, A.; Troccoli, A.; De Benedetto, D.; Basso, B.; Rubino, P. Spatial and temporal variability of wheat grain yield and quality in a Mediterranean environment: A multivariate geostatistical approach. *Field Crops Res.* **2012**, *131*, 49–62. [CrossRef]
- Aggelopoulou, K.; Pateras, D.; Fountas, S.; Gemtos, T.; Nanos, G. Soil spatial variability and site-specific fertilization maps in an apple orchard. *Precis. Agric.* **2011**, *12*, 118–129. [CrossRef]
- Hong, Y.; Kim, G.; Kim, S.; Kang, T. Development of a soil sensor-based variable rate fertilizer applicator. In Proceedings of the KSAM 2013 Spring Conference, Jeju, Republic of Korea, 31 October–1 November 2013; Volume 18, pp. 139–140.
- NAAS. *Manual of Analysis Procedures for Comprehensive Test Lab*; National Academy of Agricultural Science, Rural Development Administration: Suwon-si, Republic of Korea, 2017.
- NAAS. *Methods of Soil Chemical Analysis*; National Academy of Agricultural Science, Rural Development Administration: Suwon-si, Republic of Korea, 2010.

25. NASS. *Fertilization Standard of Crops*; National Academy of Agricultural Science, Rural Development Administration: Suwon-si, Republic of Korea, 2017.
26. Ver Hoef, J.M.; Cressie, N. Multivariable spatial prediction. *Math. Geol.* **1993**, *25*, 219–240. [CrossRef]
27. Yang, F.-g.; Cao, S.-y.; Liu, X.-n.; Yang, K.-j. Design of groundwater level monitoring network with ordinary kriging. *J. Hydrodyn.* **2008**, *20*, 339–346. [CrossRef]
28. Lee, K.S.; Lee, D.H.; Jung, I.K.; Chung, S.O.; Sudduth, K.A. Sampling and calibration requirements for optical reflectance soil property sensors for Korean paddy soils. *J. Biosyst. Eng.* **2008**, *33*, 260–268.
29. Gringarten, E.; Deutsch, C.V. Teacher's aide variogram interpretation and modeling. *Math. Geol.* **2001**, *33*, 507–534. [CrossRef]
30. Hwang, S.H.; Ham, D.H. Evaluation of spatial downscaling methods for enhancement of spatial precipitation estimation. *J. Korean Soc. Hazard Mitig.* **2013**, *13*, 149–164. [CrossRef]
31. Park, N.-W. Integration of categorical data using multivariate kriging for spatial Interpolation of ground survey data. *Spat. Inf. Res.* **2011**, *19*, 81–89.

**Disclaimer/Publisher's Note:** The statements, opinions and data contained in all publications are solely those of the individual author(s) and contributor(s) and not of MDPI and/or the editor(s). MDPI and/or the editor(s) disclaim responsibility for any injury to people or property resulting from any ideas, methods, instructions or products referred to in the content.



## Article

# The Influence of Soil Physical Properties on the Load Factor for Agricultural Tractors in Different Paddy Fields

Yi-Seo Min <sup>1</sup>, Yeon-Soo Kim <sup>2</sup>, Ryu-Gap Lim <sup>3</sup>, Taek-Jin Kim <sup>4</sup>, Yong-Joo Kim <sup>5,6,\*</sup> and Wan-Soo Kim <sup>1,7,\*</sup>

<sup>1</sup> Department of Bio-Industrial Machinery Engineering, Kyungpook National University, Daegu 41566, Republic of Korea; msg337@gmail.com

<sup>2</sup> Department of Bio-Industrial Machinery Engineering, Pusan National University, Miryang 50463, Republic of Korea; yskim23@pusan.ac.kr

<sup>3</sup> Department of Smart Agriculture, Korea Agriculture Technology Promotion Agency, Iksan 54667, Republic of Korea; limso@koat.or.kr

<sup>4</sup> Department of Drive System Team, TYM R&D Center, Iksan 54576, Republic of Korea; taek.kim@tym.world

<sup>5</sup> Department of Smart Agriculture Systems, Chungnam National University, Daejeon 34134, Republic of Korea

<sup>6</sup> Department of Biosystems Machinery Engineering, Chungnam National University, Daejeon 34134, Republic of Korea

<sup>7</sup> Upland Field Machinery Research Center, Kyungpook National University, Daegu 41566, Republic of Korea

\* Correspondence: babina@cnu.ac.kr (Y.-J.K.); wansoo.kim@knu.ac.kr (W.-S.K.)

**Abstract:** The load factor (LF) of a tractor represents the ratio of actual engine power and rated engine power, and is an important indicator directly used in calculating national air pollutant emissions. Currently, in the Republic of Korea, a fixed value of 0.48 is used for the LF regardless of the working conditions, making it difficult to establish a reliable national air pollutant inventory. Since tractors perform work under soil conditions, soil physical properties directly affect the tractor LF. Therefore, it is expected that more accurate LF estimation will be possible by utilizing soil physical properties. This study was conducted to assess the impact of soil physical properties on the LF. Experimental data were collected in ten different soil conditions. Correlation analysis revealed that the LF exhibited strong correlations with SMC, soil texture, and CI, in that order. The coefficient of determination for the regression model developed using soil variables ranged from 0.678 to 0.926. The developed regression models generally showed higher accuracy when utilizing multiple soil variables, as compared to using a single soil variable. Therefore, an effective estimation of the LF through non-experimental methods can be achieved by measuring various soil properties.

**Keywords:** agricultural tractor; load factor; engine characteristic; soil physical properties; tillage operation

**Citation:** Min, Y.-S.; Kim, Y.-S.; Lim, R.-G.; Kim, T.-J.; Kim, Y.-J.; Kim, W.-S. The Influence of Soil Physical Properties on the Load Factor for Agricultural Tractors in Different Paddy Fields. *Agriculture* **2023**, *13*, 2073. <https://doi.org/10.3390/agriculture13112073>

Academic Editor: Jin He

Received: 27 September 2023

Revised: 24 October 2023

Accepted: 26 October 2023

Published: 29 October 2023



**Copyright:** © 2023 by the authors. Licensee MDPI, Basel, Switzerland. This article is an open access article distributed under the terms and conditions of the Creative Commons Attribution (CC BY) license (<https://creativecommons.org/licenses/by/4.0/>).

## 1. Introduction

Recently, there has been a significant amount of international interest in addressing environmental pollution problems [1]. The Korean government provides a clean air policy support system (CAPSS) for the management of national air pollutant emissions to analyze emissions and uses it to utilize national air conservation policies [2]. NRMS by non-road mobile machinery (NRMM), including agricultural machinery and construction machinery, is one of the key categories among the various sectors managed by CAPSS [3]. The Republic of Korea's NO<sub>x</sub> emissions from NRMMs were 311,748 tons in 2019, which is 28.7% of the country's annual NO<sub>x</sub> emissions [4].

Among the various machinery industries included in NRMM, agricultural machinery is essential for the production of high-efficiency and high-quality agricultural products. Tractors are among the most useful agricultural machinery. In 2019, the annual working area of tractors in the Republic of Korea was 21.7 ha/year, and the annual usage time was 139.9 h/year [5]. They can be specifically employed to perform multi-purpose agricultural tasks by attaching various pieces of working equipment [6].

In the Republic of Korea, national air pollutant emissions from agricultural machinery are calculated using the following formula [3,7], which takes into account the number of units owned, rated power, load factor (LF), and emission factor:  $\text{Emission (g/y)} = \text{Number of machinery} \times \text{Rated power (kW)} \times \text{Load factor} \times \text{Working hours (h/y)} \times \text{Emission factor (g/kWh)}$ . LF is one of the most important factors in the above formula [8]. It is a quantitative indicator of the average power rating of the engine [9,10]. Currently, in the Republic of Korea, LF is used as a fixed value of 0.48 regardless of various conditions, such as the agricultural machinery type, model, power range, and operating conditions [11]. This greatly reduces the reliability of the national emissions inventory for agricultural machinery, and it is necessary to secure an LF generated under actual agricultural working conditions for an accurate representation.

In the domain of construction machinery, there have been studies aimed at quantifying the LF and emissions under actual operational conditions. Previous studies have indicated that the LF and emissions during actual operations are contingent on the specific type of construction equipment [12]. The conclusions of this study propose the potential for devising an emission factor model based on the LF. However, due to the influence of diverse emission control devices, the linear relationship between LFs and emission factors has proven elusive [13]. Barati and Shen (2016) developed an LF estimation model and an emission estimation model [14]. The LF model was developed using three operating parameters, including machine acceleration, road inclination, and machine speed, and the model demonstrated a high  $R^2$  range of 0.973 to 0.986. And the emission model for  $\text{CO}_2$ , Co, HC, and  $\text{NO}_x$  emission based on the LF exhibited a substantial  $R^2$  range of 0.904 to 0.954. The conclusion of this study was that the LF and emissions have a strong linear relationship, and operational parameters have a high linear relationship with the LF, which suggests that emissions can be accurately estimated through operating parameters. As these operational parameters are crucial to the accuracy of the model, they should be selected taking into consideration the machine's characteristics.

Tractors are mainly operated in soil conditions, and the tractor's load (i.e., the LF) varies greatly depending on the soil conditions [15,16]. Numerous previous studies have indicated that the engine load differs depending on the soil physical properties. Inchebron et al. (2012) evaluated the traction performance of a tractor equipped with a moldboard plow at various tillage depths and SMC conditions [17]. It was demonstrated that elevated soil moisture content (SMC) led to increased rolling resistance and wheel slippage and decreased traction efficiency. Kim et al. (2021) analyzed the effect of SMC on tractor traction performance during moldboard plow operations [18]. The results of the study highlighted that the tractor's traction load varied in accordance with SMC levels. Rasool and Raheman (2018) conducted a study on improving the traction performance of mobile tractors according to the cone index (CI) [19]. The traction performance was assessed by towing a load tractor on the experimental tractor. It was identified that soils with a large CI increased the drawbar force and traction efficiency. Battiato and Diserens (2017) performed the simulation and validation of tractor traction performance under different soil texture conditions [20]. Traction tests were performed using a second tractor as a braking machine. As a result, the traction power of the tractor was found to be different in soils with different soil textures.

In previous studies, the emphasis was primarily on tractor wheel slip and traction force. Multiple soil variables were employed to describe the LF of the tractor. The soil physical properties have intricate interactions with the soil–tractor system, making it challenging to mathematically resolve these relationships. Consequently, numerous studies in terramechanics have been conducted based on empirical experimental values, primarily focusing on individual soil variables. While individual soil physical characteristics can influence the LF, employing a broader range of soil variables could provide a more comprehensive explanation of the engine load of the tractor [21,22]. Previous research indicates that SMC, CI, and soil texture are interrelated, and this relationship appears to be nonlinear [23]. In specific soil conditions, an increase in SMC can initially lead to an increase in CI, followed

by a decrease, which is influenced by the soil's particle composition. These characteristics make it challenging to predict the impact of unaccounted soil conditions on the LF. Therefore, estimating tractor load based on various combinations of soil conditions can enhance a model's reliability. However, this approach has limitations due to the difficulty of obtaining soil and engine load data. Consequently, comprehensive studies that evaluate tractor LF based on diverse combinations of soil conditions are relatively scarce.

Research on the influence of soil physical properties on tractor LFs can aid in the appropriate estimation of the LF based on soil variables. Due to the highly diverse and challenging-to-control nature of soil conditions, it is impractical to experimentally evaluate the LF across all soil conditions. Estimating the LF using tractor specifications and soil variables could lead to more accurate exhaust gas emission calculations compared to applying a fixed value of 0.48. This may help to improve the reliability of emission data from tractors in the Republic of Korea.

Therefore, the aim of this study is to evaluate the effect of soil physical properties on the LF of tractors. This study is expected to provide useful information as a foundational study for estimating the tractor LF based on soil physical properties in the future. The specific objectives of this study are as follows: (1) the measurement of tractor engine data using a load measurement system, (2) the measurement of soil physical properties, (3) an evaluation of the influence of soil physical properties on the tractor LF, and (4) the development of an LF estimation model according to soil properties.

## 2. Materials and Methods

### 2.1. Experimental Equipment

#### 2.1.1. Agricultural Tractor

In this study, a 78 kW agricultural tractor (S07, TYM, Gongju, Republic of Korea) was utilized. Table 1 details the specific tractor specifications utilized in this study. Figure 1 depicts the engine performance curve of the tractor.

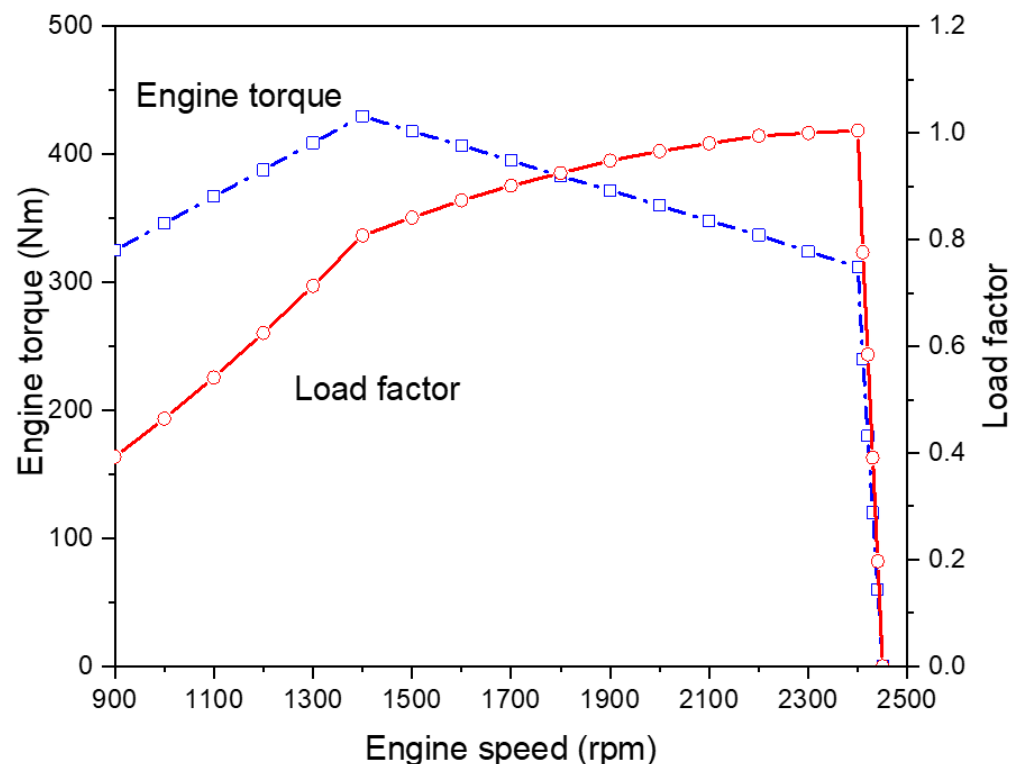


**Figure 1.** The engine performance curve of the tractor used in this study.

**Table 1.** Specification of the 78 kW agricultural tractor used in this study.

Item		Specifications
Engine	Dimensions (length × width × height) (mm)	4225 × 2140 × 2830
	Empty weight (kg)	3985
	Make	DOOSAN INFRACORE
	Type	In-line, 4-cycle
	Aspiration	Turbocharged and intercooler
	Rated torque (Nm)	324 @2300 rpm
	Rated power (kW)	78 @2300 rpm
	Max. torque (Nm)	430 @1400 rpm
	Torque rise (%)	31.3
	Maximum speed (rpm)	2450
	Bore × Stroke (mm)	98 × 113
	Total displacement (cc)	3409
	Compression ratio	17:1
	Dry weight (kg)	500
Transmission	Emission Compliance	TIER4-Final/EU STAGE IV
	Type	Power shuttle
	Gear stage (Forward/Reverse)	32/32

### 2.1.2. Measurement Equipment

In this study, a tractor equipped with a Tier-4 compliant electronic control unit was utilized. Engine torque and engine rotational speed during field operations were measured using a data measurement device (QuantumX MX840B, HBM, Darmstadt, Germany) through controller network area (CAN) communication. Among various soil physical properties, we selected three representative attributes: SMC, CI, and soil texture. SMC was measured through a soil moisture sensor (TDR350; Spectrum Technology, Aurora, IL, USA) with two rods, each 20 cm in length. CI was measured with a cone penetrometer (SC900; Spectrum Technology, Aurora, IL, USA). The average CI value, calculated from measurements obtained every 25 mm at a depth of 150 mm, was employed [24]. Table 2 demonstrates the specifications of the soil measurement equipment. Soil samples were collected at a depth of 150 mm. The soil particle proportion was determined using the hydrometer method of the Soil Environment Analysis Center of Chungnam National University, and soil texture was classified according to the USDA soil classification system.

**Table 2.** Specification of the soil measurement equipment used in this study.

Item	Specification
Soil moisture sensor	Measurement units: percentage of volumetric water content (VWC)
	Range: 0% VWC to saturation
	Accuracy: ±3.0% VWC
Cone penetrometer	Measurement units: cone index (kPa)
	Range: 0 to 45 cm, 0 to 7000 kPa
	Accuracy: ±1.25 cm, ±103 kPa

## 2.2. Field Experiment

### 2.2.1. Field Site

The field experiment was conducted at 10 sites in the Republic of Korea, as illustrated in Figure 2. All sites were paddy fields where rice was the primary crop, and only stubble remained at the time of the experiment. The experiments were conducted in March of the experimental year, just before the rice was transplanted, following the November harvest of the previous year. Information for each site is presented in Table 3.

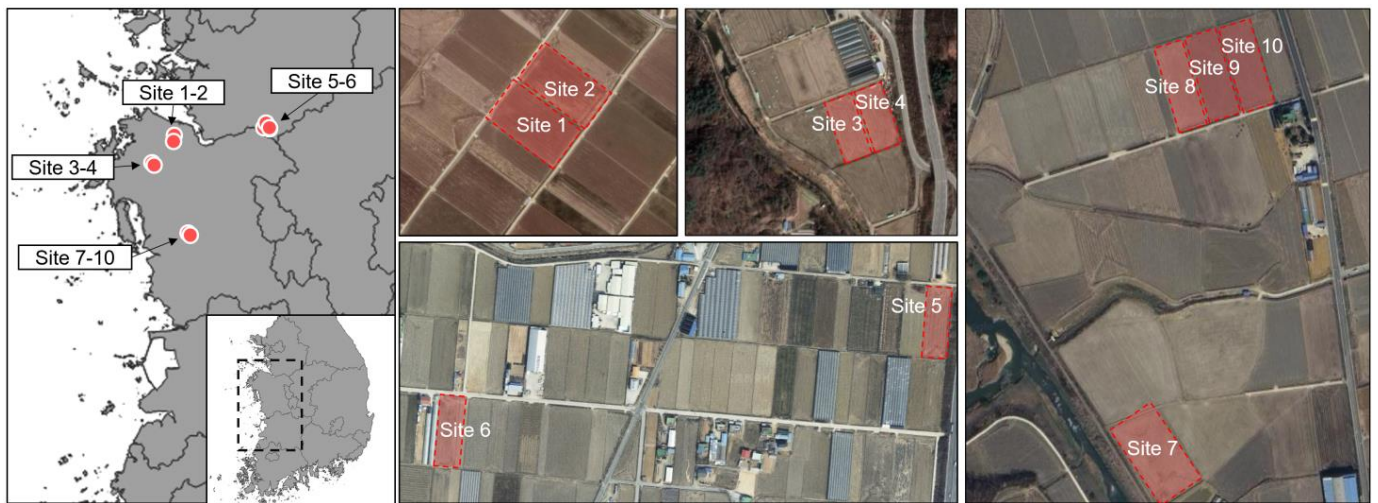


Figure 2. Geospatial information of each experimental site.

Table 3. Information about the field experiment sites.

Sites	Field Size (m)	Location	Latitude	Longitude	Experimental Year
1	60 × 100	Seosan	36°46'44.4" N	126°33'27.0" E	2017
2	60 × 100	Seosan	36°46'46.2" N	126°33'28.8" E	2017
3	40 × 100	Cheongyang	36°30'35.3" N	126°47'27.5" E	2017
4	40 × 100	Cheongyang	36°30'35.9" N	126°47'29.1" E	2017
5	30 × 100	Anseong	36°56'42.7" N	127°14'33.2" E	2019
6	40 × 100	Anseong	36°56'37.8" N	127°14'04.5" E	2019
7	60 × 100	Dangjin	36°55'50.0" N	126°37'57.5" E	2019
8	40 × 100	Dangjin	36°56'04.1" N	126°37'58.3" E	2019
9	40 × 100	Dangjin	36°56'04.3" N	126°37'59.8" E	2019
10	40 × 100	Dangjin	36°56'04.8" N	126°38'01.5" E	2019

### 2.2.2. Soil Environment Measurement

Soil sampling can be carried out using various methods, including simple random sampling, systematic sampling, and stratified sampling. Samples are collected according to a regularized pattern in systematic sampling [25]. This method is often more accurate than simple random sampling because it guarantees uniform spatial coverage [26]. Therefore, in this study, soil samples were collected using a systematic sampling method. A total of ten soil samples were collected from each of the ten field sites, and SMC and CI were measured at the same points.

### 2.2.3. Field Experiment Conditions

In this study, the tractor implement used was an eight-blade moldboard plow (WJSP-8; Woongjin Machinery, Gimje, Republic of Korea). The dimensions of the moldboard plow were 2150 mm × 2800 mm × 1250 mm (length × width × height), with a weight of 790 kg. The tractor’s driving gear stage was set to M3 low (7.09 km/h) during plow tillage [8]. The tillage depth was set to be in the range of 13 to 17 cm through the tractor’s automatic tilling depth control system, and tillage work was performed with an average tillage depth of 15 cm.

## 2.3. Data Analysis

### 2.3.1. Load Factor Analysis

Engine torque and rotational speed data collected during tractor operations in the ten sites were analyzed to determine the LF. The engine power was calculated as in Equation (1), using time-based engine torque and rotational speed. Then, the average of engine power

was calculated using time-based engine power. The analysis process of the engine power involved removing outliers using boxplot-based whisker analysis. In particular, this process was used to remove engine power values that were higher than the engine's rated power. The average of engine power data for each site was used in calculating the LF, as shown in Equation (2). One-way analysis of variance (ANOVA) was performed using IBM SPSS Statistics (SPSS 25, SPSS Inc., New York, NY, USA) to evaluate whether soil physical property and engine characteristic data from each site showed significant mean differences between groups.

$$EP = \frac{2\pi TN}{60,000}, \quad (1)$$

$$LF = \frac{EP_m}{EP_r}, \quad (2)$$

where EP represents the engine power, T is the engine torque, N is the engine rotational speed, LF is the load factor,  $EP_m$  is the measured engine power in real time, and  $EP_r$  is the rated engine power.

### 2.3.2. Correlation Analysis

A correlation analysis was conducted to analyze the impact of soil physical properties on the LF. The linearity between two variables was assessed using the Pearson correlation coefficient ( $r$ ), as illustrated in Equation (3). The range of  $r$  values is from  $-1$  to  $1$ , where an absolute value of  $1$  indicates a perfect linear relationship and a value of  $0$  signifies no linear relationship. Each soil variable is considered to have a linear relationship with the LF when the absolute value of  $r$  is  $0.7$  or higher and the significance level of  $p < 0.05$ .

$$r = \frac{\sum_{i=1}^n (X_i - \bar{X})(Y_i - \bar{Y})}{\sqrt{\sum_{i=1}^n (X_i - \bar{X})^2 \sum_{i=1}^n (Y_i - \bar{Y})^2}} \quad (3)$$

where  $\bar{X}$  is the mean of sample group X, and  $\bar{Y}$  is the mean of sample group Y.

### 2.3.3. Regression Analysis

The data collected from field experiments were used to develop regression models. Since the tractor and equipment conditions were consistent throughout the experiments, only soil variables were considered in the regression models. Considering the ease of data collection for each soil variable, regression models were constructed using both individual functions and combinations of functions. Equation (4) can be utilized in cases when only a soil moisture sensor is accessible. Equation (5) can be utilized in cases when only a soil strength sensor is accessible. Soil moisture sensors and soil strength sensors have been widely used as important tools for soil monitoring due to their affordability and ease of measurement. Equation (6) can be utilized when analyzing soil texture of an experimental field. The soil texture incorporates the proportions of sand, silt, and clay, but we only considered the sand proportion, which has the most significant impact on the LF. Using multiple soil texture variables had a detrimental effect on the model's performance, as stated in the paper. Typically, soil texture analysis involves several processes, such as sample collection, drying, and classification, making data measurement more challenging. Furthermore, in order to investigate whether the estimation performance of the model was enhanced by combining multiple soil variables, we employed all possible combinations of these variables ( $f_1, f_2, f_3, f_1 + f_2, f_1 + f_3, f_2 + f_3, f_1 + f_2 + f_3$ ), as stated in the study.

$$LF = f_1(\text{SMC}) \quad (4)$$

where SMC is the soil moisture content.

$$LF = f_2(\text{CI}), \quad (5)$$

where CI is the cone index.

$$LF = f_3(S_a) \tag{6}$$

where  $S_a$  is the sand proportion.

The performance of the estimative model based on regression analysis was evaluated by referring to previous studies. For the assessment of model performance, four statistical metrics were chosen: the coefficient of determination ( $R^2$ ), mean absolute percentage error (MAPE), root mean square error (RMSE), and relative deviation (RD) [27]. Each of these model performance metrics was calculated using Equations (7)–(10), based on the actual and estimated engine loads.

$$R^2 = \frac{\sum_{i=1}^N (y_i - y_a) - \sum_{i=1}^N (y_i - \hat{y}_i)}{\sum_{i=1}^N (y_i - y_a)}, \tag{7}$$

$$MAPE = \frac{1}{N} \sum_{i=1}^N \left| \frac{1}{y_i} (y_i - \hat{y}_i) \right| \times 100(\%), \tag{8}$$

$$RMSE = \sqrt{\frac{1}{N} \sum_{i=1}^N (\hat{y}_i - y_i)^2}, \tag{9}$$

$$RD = \frac{RMSE}{Mean} \times 100, \tag{10}$$

where  $y_a$  is the mean actual load factor,  $y_i$  is the actual load factor, and  $\hat{y}_i$  is the estimated load factor.

### 3. Results

#### 3.1. Soil Physical Properties

The collected CI and SMC from a total of ten sites are displayed in Figure 3. The CI and SMC exhibited large variations across ten measurements for each site. In terms of the CI, the largest variation was observed at site 9, ranging from 640.6 to 2085.0 kPa. As for the SMC, the most extensive range was observed at site 1, ranging from 24.2 to 41.0%. Additionally, in general, the CI exhibited a wider range than the SMC. The minimum value for CI was observed at site 4, measuring 236.6 kPa, while the maximum value was observed at site 9, measuring 2085.0 kPa. For SMC, the minimum value was noted at site 4, measuring 18.42%, while the maximum value was noted at site 8, measuring 45.90%.

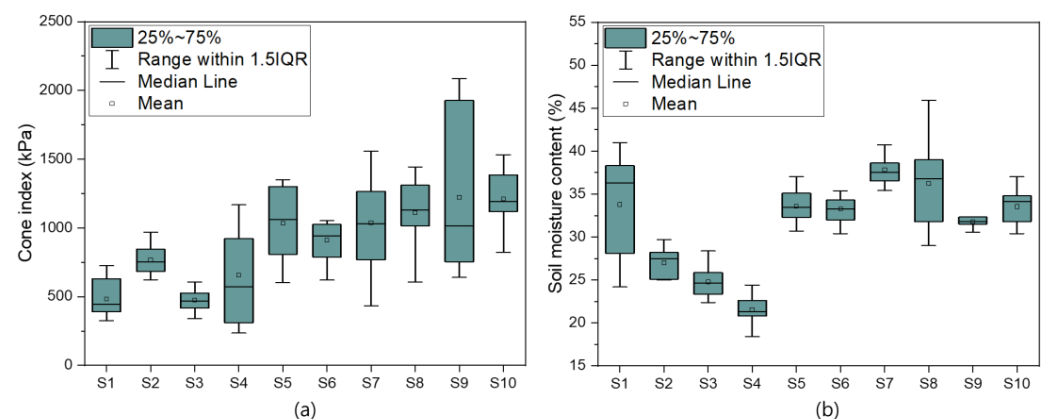


**Figure 3.** Results of box plot analysis of soil physical properties measured on field experiment sites (e.g., S1 refers to site 1): (a) cone index (CI) and (b) soil moisture content (SMC).

Figure 4 illustrates the results of the particle distribution proportion analysis for each particle type in the context of soil texture analysis. The sand proportion ranged from 24% to 85% across all sites, with Groups S1 to S4 exhibiting a sand proportion of over 70%. The



silt proportion ranged from 13% to 57% across all sites, while Groups S5 to S10 displayed higher silt proportions, exceeding 35%. Clay ranged from 2% to 27%, with Groups S1 to S4 demonstrating a low clay proportion of less than 8%, and Groups S5 to S10 demonstrating a high clay proportion of over 18%. Sites with a high sand proportion exhibited relatively low CI values. These results are consistent with findings reported in previous studies [28].

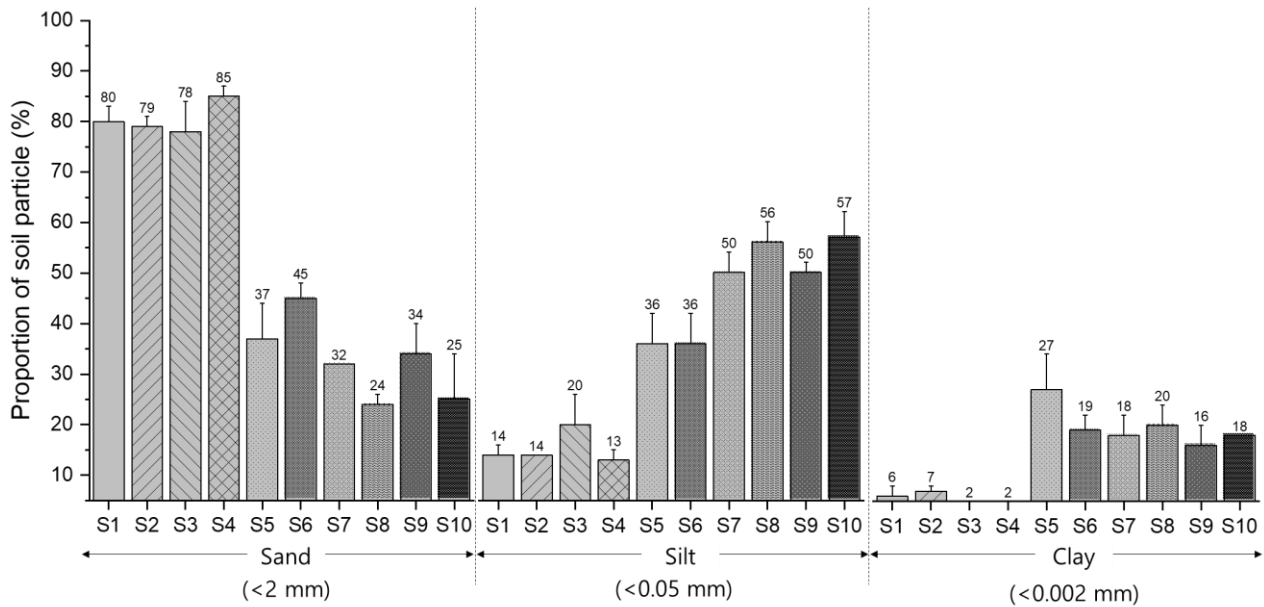


**Figure 4.** Results of sand, silt, and clay proportion analysis of soil particles by field experiment sites, where S# refers to the number of sites (i.e., S1 = Site 1).

Table 4 presents the analysis results of the soil physical properties of the ten sites used in this study. Soil textures were categorized as loamy sand in four sites, clay loam in one site, loam in two sites, and silt loam in three sites. An ANOVA analysis was conducted to determine whether there were significant differences in the means of soil physical properties data across different sites. The analysis results indicated statistically significant differences between sites, with the exception of a few sites with comparable values. Furthermore, in all cases except for the comparison between sites 8 and 10, each site exhibited statistically significant mean differences in at least one soil physical property. This suggests that data measurements were taken from sites with varying soil physical properties.

**Table 4.** Analysis results of averaged soil physical properties, including soil moisture content, cone index, soil particle proportions, and soil texture (N = 10).

Sites	SMC (%)	CI (kPa)	Soil Particle Proportions (%)			Soil Texture
			Sand (<2 mm)	Silt (<0.05 mm)	Clay (<0.002 mm)	
1	33.79 <sup>b,c</sup>	483 <sup>e</sup>	80.00 <sup>b</sup>	14.00 <sup>e</sup>	6.00 <sup>d</sup>	Loamy sand
2	27.01 <sup>d</sup>	768 <sup>c,d</sup>	79.00 <sup>b</sup>	14.00 <sup>e</sup>	7.00 <sup>d</sup>	Loamy sand
3	24.79 <sup>d</sup>	476 <sup>e</sup>	78.00 <sup>b</sup>	20.00 <sup>d</sup>	2.00 <sup>e</sup>	Loamy sand
4	21.55 <sup>e</sup>	656 <sup>d,e</sup>	85.00 <sup>a</sup>	13.00 <sup>e</sup>	2.00 <sup>e</sup>	Loamy sand
5	33.60 <sup>b,c</sup>	1034 <sup>a,b,c</sup>	37.00 <sup>d</sup>	36.00 <sup>c</sup>	27.00 <sup>a</sup>	Clay loam
6	33.27 <sup>c</sup>	910 <sup>b,c,d</sup>	45.00 <sup>c</sup>	36.00 <sup>c</sup>	19.00 <sup>b</sup>	Loam
7	37.84 <sup>a</sup>	1038 <sup>a,b,c</sup>	32.00 <sup>e</sup>	50.00 <sup>b</sup>	18.00 <sup>b,c</sup>	Loam
8	36.24 <sup>a,b</sup>	1111 <sup>a,b</sup>	24.00 <sup>f</sup>	56.00 <sup>a</sup>	20.00 <sup>b</sup>	Silt loam
9	31.77 <sup>c</sup>	1223 <sup>a</sup>	34.00 <sup>e</sup>	50.00 <sup>b</sup>	16.00 <sup>c</sup>	Silt loam
10	33.54 <sup>b,c</sup>	1212 <sup>a</sup>	25.00 <sup>f</sup>	57.00 <sup>a</sup>	18.00 <sup>b,c</sup>	Silt loam

Mean values within same column showing different superscripts are significantly different ( $p < 0.05$ ). Duncan's least significant multiple-range test was employed to compare the means.



Figure 5 displays the results of mapping the 10 study sites onto the USDA soil texture classification triangle. Overall, sites 1–4 are predominantly situated within the loamy sand region, characterized by high sand proportions and low clay proportions. The remaining sites exhibited a balanced mixture of soil particles.

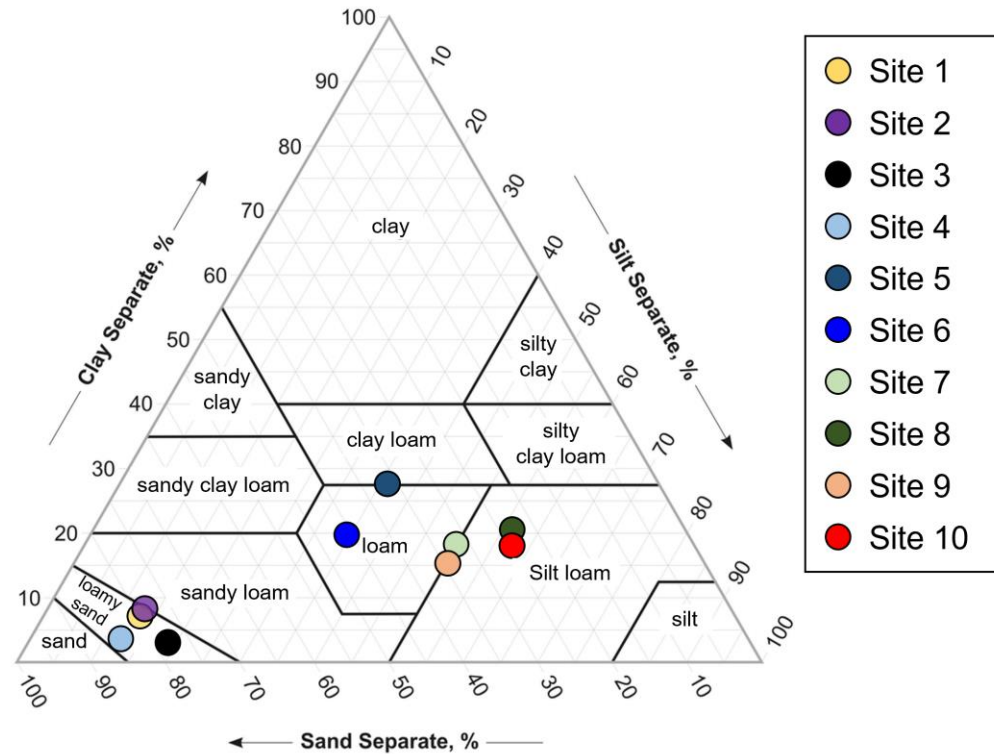


**Figure 5.** Classification results of the sampled soil by ten field experiment study sites mapped to the USDA soil texture triangle.

### 3.2. Engine Load Characteristics

The measurement results of the engine load characteristics at each site are depicted in Figure 6. Site 4 had the lowest average engine torque of 127.1 Nm, while site 7 had the highest average engine torque of 359.1 Nm. Site 6 had the lowest average engine rotational speed at 1967 rpm, while site 4 had the highest at 2450 rpm. The average engine power and average LF were lowest at site 4, measuring 32.60 kW and 0.418, respectively, and highest at site 10, measuring 78.33 kW and 1.004, respectively. The engine power and LF exhibited a similar box plot pattern to that of engine torque. Therefore, engine torque is estimated to have a greater effect on LF than engine rotation speed.

The statistical analysis results of the engine load characteristics are presented in Table 5. The average values of the engine load characteristics across all sites ranged as follows: engine rotation speed from 2148 to 2419 rpm, engine torque from 227.2 to 329.7 Nm, engine power from 57.52 to 76.76 kW, and LF from 0.737 to 0.984. According to the ANOVA results, both engine rotation speed and engine torque exhibited statistically significant mean differences across all sites. Conversely, there were no statistically significant differences observed in engine power and LF between sites 7 and 8 or between sites 5 and 9.

Figure 7 displays the results of mapping the average LF for each site to the engine performance curve. During soil tillage operations, tractors are generally operated at an engine rotational speed of 2400 rpm; however, when there is a demand for a higher load than the LF that can be output at this time, the engine rotational speed is reduced to output a higher LF [29]. Therefore, site 4, which has a low LF requirement, performs work in the range of 2400 rpm, whereas sites with a higher LF requirement have an engine operating point in a lower range of engine rotation speed.

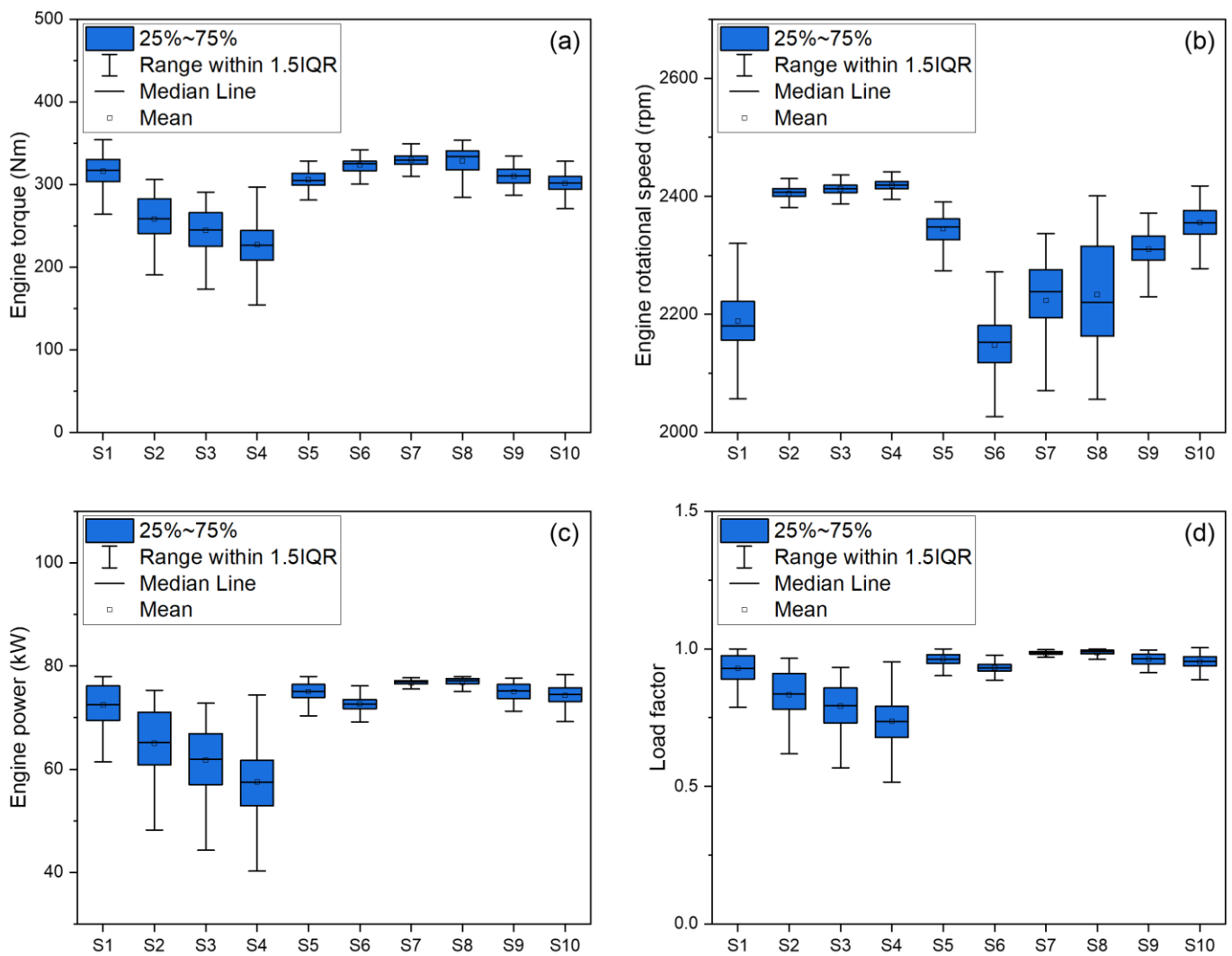


**Figure 6.** Results of box plot analysis of engine load measured on field experiment sites (e.g., S1 refers to site 1): (a) engine torque (ET), (b) engine rotation speed, (c) engine power (EP), and (d) load factor (LF).

**Table 5.** Results of engine load characteristics.

Sites	Engine Rotational Speed (rpm)	Engine Torque (Nm)	Engine Power (kW)	Load Factor
1	2189 <sup>i</sup>	316.4 <sup>d</sup>	72.47 <sup>e</sup>	0.929 <sup>e</sup>
2	2405 <sup>c</sup>	258.3 <sup>h</sup>	65.03 <sup>f</sup>	0.834 <sup>f</sup>
3	2413 <sup>b</sup>	244.6 <sup>i</sup>	61.77 <sup>g</sup>	0.792 <sup>g</sup>
4	2419 <sup>a</sup>	227.2 <sup>j</sup>	57.52 <sup>h</sup>	0.737 <sup>h</sup>
5	2345 <sup>e</sup>	305.8 <sup>f</sup>	75.07 <sup>b</sup>	0.962 <sup>b</sup>
6	2148 <sup>j</sup>	323.4 <sup>c</sup>	72.70 <sup>d</sup>	0.932 <sup>d</sup>
7	2224 <sup>h</sup>	329.7 <sup>a</sup>	76.71 <sup>a</sup>	0.983 <sup>a</sup>
8	2233 <sup>g</sup>	328.8 <sup>b</sup>	76.76 <sup>a</sup>	0.984 <sup>a</sup>
9	2310 <sup>f</sup>	310.3 <sup>e</sup>	75.05 <sup>b</sup>	0.962 <sup>b</sup>
10	2356 <sup>d</sup>	301.4 <sup>g</sup>	74.32 <sup>c</sup>	0.953 <sup>c</sup>

Means ( $\pm$ standard deviation) within same column showing different superscripts are significantly different ( $p < 0.05$ ). Duncan's least significant multiple-range test was applied to compare the means.

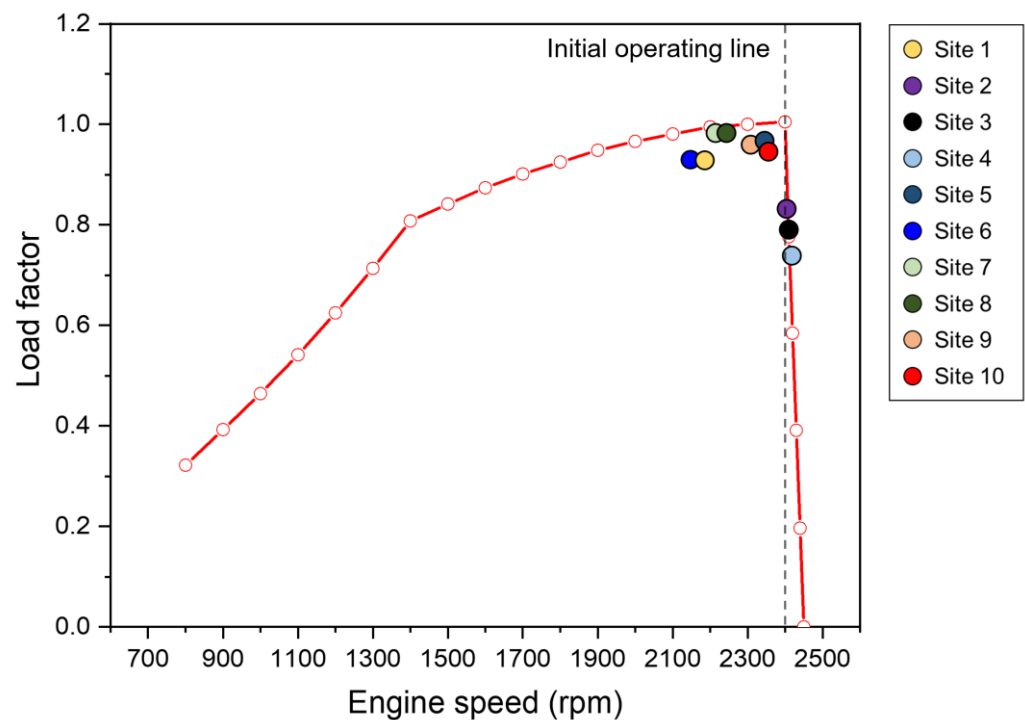


**Figure 7.** Load factor analysis results for each site on the engine performance curve.

### 3.3. Effect of Soil Physical Properties on Engine Load

Figure 8 presents the correlation matrix depicting the relationship between soil physical properties and engine load characteristics. The top portion of the matrix features bivariate scatterplots along with fitted lines, while the bottom section displays Pearson correlation coefficients. The engine speed exhibited a significance level of  $p > 0.05$  between soil texture (sand, silt, and clay proportions) and the CI. Therefore, the correlation coefficients between engine speed and soil parameters are considered unreliable. In contrast, engine torque, engine power, and LF exhibited a significance level of  $p < 0.05$  for all soil variables in the study. The LF exhibited correlation coefficients ranging from absolute values of 0.79 to 0.91 for soil parameters. Excluding engine power, the variables that had the most significant impact on the LF were engine torque ( $r = 0.96$ ), SMC ( $r = 0.91$ ), sand proportion ( $r = -0.85$ ), and clay proportion ( $r = 0.84$ ). Except for silt proportion and SMC, five of the soil variables mostly demonstrated a significance level of  $p < 0.05$ . The sand proportion and silt proportion displayed a very strong correlation coefficient of  $-0.98$ . Therefore, to address the issue of multicollinearity in the regression model, only sand proportion, one of the two soil variables with a higher correlation coefficient with load, was selected as the soil variable for developing the regression model.

Table 6 presents the developed regression models. The adjusted  $R^2$  ranges from 0.638 to 0.902, indicating that each model can estimate the load rate with an accuracy ranging from 63.8% to 90.2%.

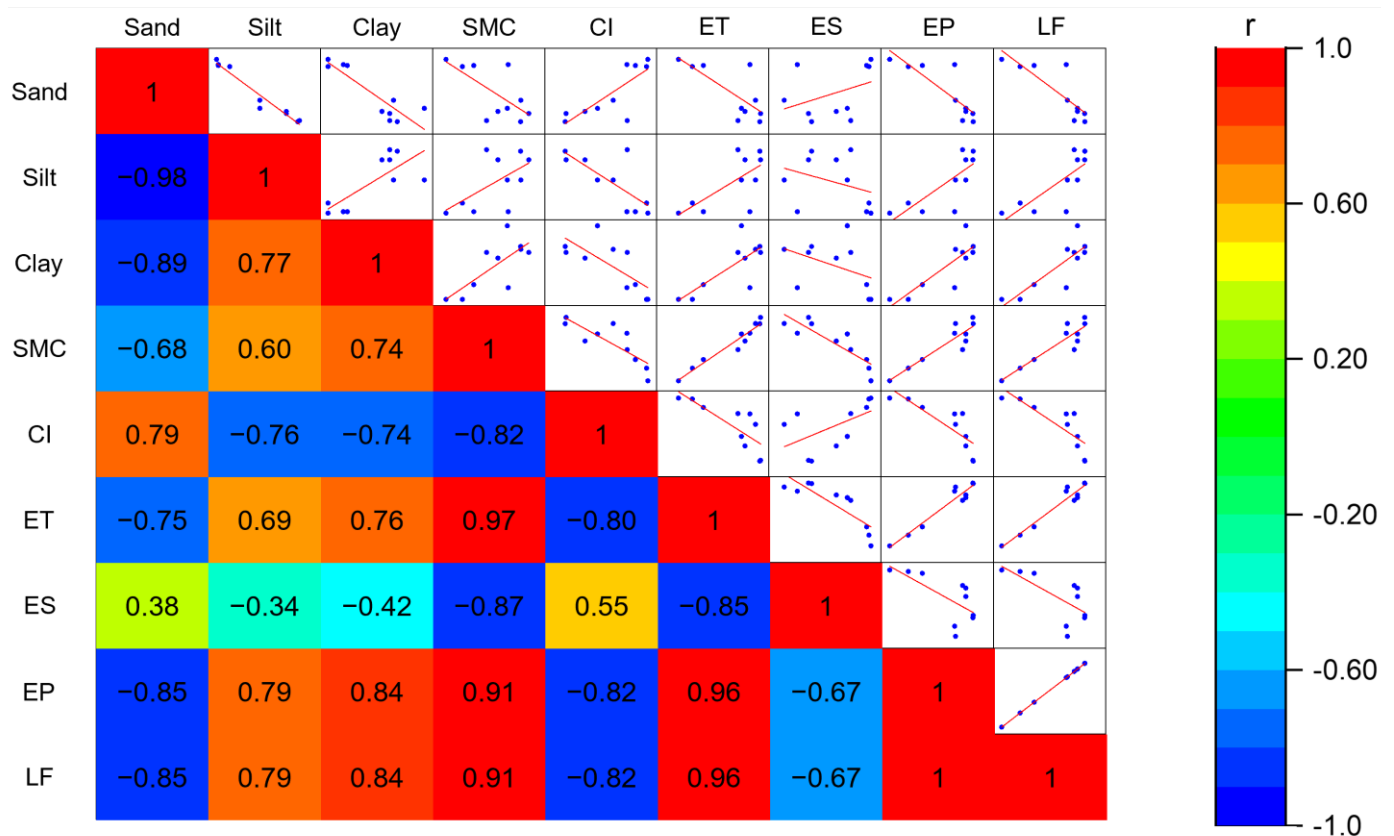
Models A–C represent single-variable regression models for soil physical properties. Model A had the highest  $R^2$  at 0.824, while Model B had the lowest  $R^2$  at 0.678. Model D used SMC and CI as soil variables. The combination of these two soil variables is significant because they can be relatively easily obtained through field sensors. However, Model D's adjusted  $R^2$  of 0.800 was slightly lower than Model A's adjusted  $R^2$  of 0.803, which solely used SMC as a variable. Thus, using both SMC and CI for load estimation may potentially reduce model accuracy. Models E and F utilized soil texture variables. Model E exhibited a higher adjusted  $R^2$  value compared to Model A, while Model F outperformed Model B. Hence, incorporating the sand proportion variable can enhance the accuracy of the regression model. Model G incorporated all soil variables, displaying an adjusted  $R^2$  value of 0.888, which was lower than Model E but higher than Model F. When comparing

Models E and G, the reason for the decrease in model accuracy can be attributed to the fact that the dependent variable is already well explained solely by the SMC variable. A high correlation between the SMC and CI variables can, in fact, decrease model accuracy. Therefore, it is crucial to choose a model with the appropriate number of variables.

**Table 6.** Regression model for estimating the load factor of the tractor.

Model	Source	Regression Model	R <sup>2</sup>	R <sup>2</sup> Adj	S.E.
A	f <sub>1</sub>	LF = 0.0147SMC + 0.4487	0.824	0.803	0.0388
B	f <sub>2</sub>	LF = -0.000255CI + 1.1343	0.678	0.638	0.0525
C	f <sub>3</sub>	LF = -0.00292S <sub>p</sub> + 1.0582	0.718	0.683	0.0491
D	f <sub>1</sub> + f <sub>2</sub>	LF = 0.0114SMC - 0.000076CI + 0.6168	0.844	0.800	0.0391
E	f <sub>1</sub> + f <sub>3</sub>	LF = 0.00997SMC - 0.00147S <sub>p</sub> + 0.6719	0.924	0.902	0.0274
F	f <sub>2</sub> + f <sub>3</sub>	LF = -0.000126CI - 0.001804S <sub>p</sub> + 1.1130	0.780	0.717	0.0465
G	f <sub>1</sub> + f <sub>2</sub> + f <sub>3</sub>	LF = 0.0108SMC + 0.000030CI - 0.00162S <sub>p</sub> + 0.6282	0.926	0.888	0.0291

Note: SMC = soil moisture content (%), CI = cone index (kPa), S<sub>p</sub> = sand proportion (%).



Note: SMC = soil moisture content, CI = cone index, ET = engine torque, ES = engine speed, EP = engine power, LF = load factor. The blue dots in the figure represent each data from 10 sites.

**Figure 8.** Results of correlation analysis of soil physical properties and engine load characteristics.

Table 7 displays the results of ANOVA analysis for each regression model, showcasing the degrees of freedom (Df), sum of squares (SS), and mean squares (MS). A higher F-value implies that the regression model better explains the variability in the dependent variable. Models E and A exhibited higher F-values of 42.278 and 37.381, respectively, indicating strong explanatory power. In contrast, Models F and B demonstrated lower F-values of 12.375 and 16.848, respectively, indicating relatively weaker explanatory capabilities. Consequently, the SMC is significantly more effective in explaining the load rate compared to the CI. Model G, which utilized all soil variables, yielded an F-value of 24.881. The *p*-value, calculated using the F-value and Df, indicates the probability that the model's

dependent variable and independent variable have no significant correlation. All models demonstrated statistical significance with  $p < 0.01$ . Variance inflation factor (VIF) is used for diagnosing multicollinearity, and it is the reciprocal of tolerance. VIF values closer to 1 indicate that there is no correlation between independent variables. Typically, a VIF of 10 or higher suggests multicollinearity [30]. The VIF for each model ranged between 1.854 and 4.435. Therefore, all models did not exhibit multicollinearity issues.

**Table 7.** ANOVA results for each regression model.

Model		Degrees of Freedom (Df)	Sum of Squares (SS)	Mean Squares (MS)	F-Value	p-Value	Variable	Tolerance	Variance Inflation Factor (VIF)
A	Regression	1	0.0565	0.0565	37.381	0.000 *	SMC		
	Residual	8	0.0120	0.0015					
B	Regression	1	0.0464	0.0464	16.848	0.003 *	CI		
	Residual	8	0.0221	0.0028					
C	Regression	1	0.0492	0.0492	20.370	0.002 *	Sand		
	Residual	8	0.0193	0.0024					
D	Regression	2	0.0578	0.0289	18.964	0.001 *	SMC	0.331	3.201
	Residual	7	0.0107	0.0015			CI	0.331	3.201
E	Regression	2	0.0633	0.0316	42.278	0.000 *	SMC	0.539	1.854
	Residual	7	0.0052	0.0007			Sand	0.539	1.854
F	Regression	2	0.0534	0.0267	12.375	0.005 *	CI	0.370	2.703
	Residual	7	0.0151	0.0022			Sand	0.370	2.703
G	Regression	3	0.0634	0.0211	24.881	0.001 *	SMC	0.329	3.042
	Residual	6	0.0051	0.0008			CI	0.225	4.435
							Sand	0.367	2.722

\* Significant at  $p < 0.01$ .

#### 4. Discussion

The data obtained from previous studies were utilized to validate the regression models derived in this study [31]. The study evaluated the tractor's operational performance using the same tractor–moldboard plow combination. In contrast to this study, the moldboard plow had six blades and the tractor had a rated power of 42 kW. The soil physical properties were determined by measuring the SMC in the 150 to 200 mm layer and the CI as the average value in the 0 to 150 mm range, aligning with our data collection methodology for this study. The LF used measurements obtained under the condition of a working depth of 16 cm. The average LF for each soil physical characteristic reported in the previous studies is presented in Table 8.

**Table 8.** Average LF by soil physical properties for model validation [31].

Site	SMC (%)	CI (kPa)	Soil Texture			LF
			Sand (%)	Silt (%)	Clay (%)	
1	19.45	689.69	68	20	21	0.793
2	24.50	563.21	40	48	12	0.852
3	20.24	864.67	40	28	32	0.921

Table 9 illustrates the estimation value and analysis result of error for the model. The estimated average LF ranged from 0.734 to 0.956 at site 1, 0.808 to 0.991 at site 2, and 0.746 to 0.942 at site 3. MAPE, RMSE, and RD were used as an indicator to evaluate the model performance. The MAPE ranges of models A to G varied from 5.36% to 12.55%. With the exception of one case, Models D to G, which employed multiple soil variables, exhibited lower MAPEs compared to models A to C that utilized single soil variables. This suggests that employing multiple soil variables can enhance the estimative accuracy of the models. However, in the case of Model F, which used CI and sand proportion as variables, its MAPE was higher compared to the model C concerning the sand proportion. This underscores the fact that not all variables hold equal importance, and the choice of specific soil variables can significantly impact the model's performance. Furthermore, this emphasizes the conclusions drawn from the research in the Results section.

**Table 9.** Analysis of errors in validation data for each regression model.

	Items	Model A	Model B	Model C	Model D	Model E	Model F	Model G
Site 1	Average LF (Kim et al. [31])				0.793			
	Estimated LF	0.734	0.956	0.860	0.787	0.766	0.902	0.748
	Error (%)	7.43	20.58	8.47	0.80	3.44	13.79	5.64
Site 2	Average LF (Kim et al. [31])				0.852			
	Estimated LF	0.808	0.991	0.942	0.855	0.857	0.970	0.844
	Error (%)	5.20	16.21	10.47	0.26	0.57	13.77	1.00
Site 3	Average LF (Kim et al. [31])				0.921			
	Estimated LF	0.746	0.914	0.942	0.783	0.815	0.932	0.807
	Error (%)	19.09	0.84	2.19	15.02	11.58	1.11	12.43
Average	MAPE (%)	10.57	12.55	7.04	5.36	5.19	9.56	6.35
	RMSE	0.110	0.124	0.065	0.080	0.064	0.093	0.071
	RD (%)	12.87	14.44	7.66	9.35	7.44	10.85	8.31

The analysis result of RMSE and RD differed somewhat from MAPE. Model C demonstrated the second lowest values for RMSE and RD. This is the result of RMSE and RD being more responsive to outliers compared to MAPE. In practice, Models D, F, and G, which employed multiple soil variables, exhibited higher errors at specific sites. These results underscore the need for a more diverse dataset of LF data collected under various soil conditions to enhance the model's stability and applicability.

## 5. Conclusions

In this study, the effect of soil physical properties on LF of tractor engine was analyzed. A correlation analysis was performed between LF and five soil variables: SMC, CI, sand proportion, silt proportion, and clay proportion, and all soil variables were found to have a strong correlation with LF. However, the correlation coefficients between each soil variable and LF were different, indicating that the soil variables had different impacts. The LF estimation model was developed through a regression model using soil variables. The objective of developing this estimation model was to estimate the LF more accurately and compare the accuracy of models using a single soil variable and models using multiple soil variables. In many cases, models using multiple soil variables demonstrated higher accuracy compared to those using a single soil variable. Therefore, adding soil variables allows us to encompass the complexity and variability caused by soil conditions during actual tractor operations, leading to an improvement in model accuracy. However, in some instances, the addition of soil variables led to a decrease in model accuracy. This occurred due to the added soil variable having a relatively low correlation with LF, which increased the error of the model, or the increase in outlier values due to the high correlation between the added variables. Consequently, it was concluded that selecting an appropriate level of model complexity is crucial.

Kim et al.'s (2022) model validation was performed using soil physical properties and LF data reported in [31]. The MAPE of the models varied between 5.19 and 12.55%, with models using multiple soil variables tending to have lower errors. This supports the conclusions of this study. However, there was no correlation between the model's high  $R^2$  value and the error in the verification results. Differences in tractor power, soil consolidation tools, range of soil conditions, etc., can affect the accuracy of the model. Therefore, LF data collected under a wider range of operating conditions and soil conditions are needed to improve the model's reliability and versatility. Research on data collection for these various conditions will continue to be conducted in future studies.

**Author Contributions:** Conceptualization, W.-S.K. and Y.-J.K.; methodology, W.-S.K.; software, Y.-S.M., Y.-S.K. and R.-G.L.; validation, Y.-S.K.; formal analysis, Y.-S.M. and T.-J.K.; investigation, Y.-S.M. and T.-J.K.; data curation, W.-S.K. and R.-G.L.; writing—original draft preparation, Y.-S.M. and W.-S.K.; writing—review and editing, Y.-S.M. and W.-S.K.; supervision, W.-S.K. and Y.-J.K.; project administration, Y.-J.K. and R.-G.L.; funding acquisition, Y.-J.K. All authors have read and agreed to the published version of the manuscript.

**Funding:** This work was carried out with the support of "Cooperative Research Program for Agriculture Science and Technology Development (Project No. PJ0156952022)" Rural Development Administration, Republic of Korea.

**Institutional Review Board Statement:** Not applicable.

**Informed Consent Statement:** Not applicable.

**Data Availability Statement:** The data presented in this study are available within the article.

**Conflicts of Interest:** The authors declare no conflict of interest.

## References

- Zhang, L.; Xu, M.; Chen, H.; Li, Y.; Chen, S. Globalization, green economy and environmental challenges: State of the art review for practical implications. *Front. Environ. Sci.* **2022**, *10*, 870271. [CrossRef]
- National Institute of Environmental Research Center (NIER). *Standard Operations Procedure for the Construction of Supporting Data for National Air Pollutant Emissions*; NIER: Incheon, Republic of Korea, 2019; Available online: <https://www.air.go.kr/article/view.do?boardId=8&articleId=89&boardId=8&menuId=49&currentPageNo=1> (accessed on 25 September 2023).
- National Air Emission Inventory and Research Center (NAIR). *Handbook of Estimation Methods for National Air Pollutant Emissions V*; NAIR: Cheongju, Republic of Korea, 2022; Available online: <https://www.air.go.kr/article/view.do?boardId=8&articleId=238&boardId=8&menuId=49&currentPageNo=1> (accessed on 25 September 2023).
- National Air Emission Inventory and Research Center (NAIR). *2019 National Air Pollutant Emissions*; NAIR: Cheongju, Republic of Korea, 2022; Available online: <https://www.air.go.kr/article/view.do?boardId=7&articleId=145&boardId=7&menuId=48&currentPageNo=1> (accessed on 25 September 2023).
- National Institute of Agricultural Sciences (NIAS). *2019 Investigation of Agricultural Machinery Usage*; NIAS: Wanju, Republic of Korea, 2020.
- Kim, W.S.; Lee, S.E.; Baek, S.M.; Baek, S.Y.; Jeon, H.H.; Kim, T.J.; Lim, R.G.; Choi, J.Y.; Kim, Y.J. Evaluation of exhaust emissions factor of agricultural tractors using portable emission measurement system (PEMS). *J. Drive Control* **2023**, *20*, 15–24.
- Zhang, G.; Sandanayake, M.; Setunge, S.; Li, C.; Fang, J. Selection of emission factor standards for estimating emissions from diesel construction equipment in building construction in the Australian context. *J. Environ. Manag.* **2017**, *187*, 527–536. [CrossRef] [PubMed]
- Lee, J.H.; Jeon, H.H.; Baek, S.Y.; Baek, S.M.; Kim, W.S.; Siddique, M.A.A.; Kim, Y.J. Analysis of Emissions of Agricultural Tractor according to Engine Load Factor during Tillage Operation. *J. Drive Control* **2022**, *19*, 54–61.
- Tan, D.; Tan, J.; Peng, D.; Fu, M.; Zhang, H.; Yin, H.; Ding, Y. Study on real-world power-based emission factors from typical construction machinery. *Sci. Total Environ.* **2021**, *799*, 149436. [CrossRef] [PubMed]
- Lee, S.E.; Kim, T.J.; Kim, Y.J.; Lim, R.G.; Kim, W.S. Analysis of Engine Load Factor for Agricultural Cultivator during Plow and Rotary Tillage Operation. *J. Drive Control* **2023**, *20*, 31–39.
- Baek, S.M.; Kim, W.S.; Baek, S.Y.; Jeon, H.H.; Lee, D.H.; Kim, H.K.; Kim, Y.J. Analysis of engine load factor for a 78 kW class agricultural tractor according to agricultural operations. *J. Drive Control* **2022**, *19*, 16–25.
- Lee, D.I.; Park, J.; Shin, M.; Lee, J.; Park, S. Characteristics of Real-World Gaseous Emissions from Construction Machinery. *Energies* **2022**, *15*, 9543. [CrossRef]
- Shin, D.H.; Park, Y.S.; Yoo, C.; Park, S.H. Study on Real-Work NOx Emission Characteristics according to Load Factor of Excavator. *J. Drive Control* **2023**, *20*, 1–8.
- Barati, K.; Shen, X. Operational level emissions modelling of on-road construction equipment through field data analysis. *Autom. Constr.* **2016**, *72*, 338–346. [CrossRef]
- Koo, Y.M. PTO torque and draft analyses of an integrated tractor-mounted implement for round ridge preparation. *J. Biosyst. Eng.* **2022**, *47*, 330–343. [CrossRef]
- Kim, J.T.; Im, D.; Cho, S.J.; Park, Y.J. A Study on the Prediction of Driving Performance of Agricultural Tractors Driving on Dry Sand. *J. Biosyst. Eng.* **2022**, *47*, 502–509. [CrossRef]
- Inchebron, K.; Seyedi, S.M.; Tabatabaekolour, R. Performance evaluation of a light tractor during plowing at different levels of depth and soil moisture content. *Int. Res. J. Appl. Basic Sci.* **2012**, *3*, 626–631.
- Kim, W.S.; Kim, Y.J.; Park, S.U.; Kim, Y.S. Influence of soil moisture content on the traction performance of a 78-kW agricultural tractor during plow tillage. *Soil Tillage Res.* **2021**, *207*, 104851. [CrossRef]

19. Rasool, S.; Raheman, H. Improving the tractive performance of walking tractors using rubber tracks. *Biosyst. Eng.* **2018**, *167*, 51–62. [CrossRef]
20. Battiato, A.; Diserens, E. Tractor traction performance simulation on differently textured soils and validation: A basic study to make traction and energy requirements accessible to the practice. *Soil Tillage Res.* **2017**, *166*, 18–32. [CrossRef]
21. Han, G.; Kim, K.D.; Ahn, D.V.; Park, Y.J. Comparative Analysis of Tractor Ride Vibration According to Suspension System Configuration. *J. Biosyst. Eng.* **2023**, *48*, 69–78. [CrossRef]
22. Choudhary, S.; Upadhyay, G.; Patel, B.; Naresh; Jain, M. Energy requirements and tillage performance under different active tillage treatments in sandy loam soil. *J. Biosyst. Eng.* **2021**, *46*, 353–364. [CrossRef]
23. Ayers, P.D.; Perumpral, J.V. Moisture and density effect on cone index. *Trans. ASAE* **1982**, *25*, 1169–1172. [CrossRef]
24. *ASABE Standards EP542; Procedure for Using and Reporting Data Obtained with the Soil Cone Penetrometer*. American Society of Agricultural and Biological Engineers: St. Joseph, MO, USA, 2019.
25. Reicosky, D. *Managing Soil Health for Sustainable Agriculture Volume 2: Monitoring and Management*; Burleigh Dodds Science Publishing: Cambridge, UK, 2018.
26. Tan, K.H. *Soil Sampling, Preparation, and Analysis*; CRC Press: New York, NY, USA, 1995; ISBN 0-8247-9675-6.
27. Kim, W.S.; Lee, D.H.; Kim, Y.J.; Kim, Y.S.; Park, S.U. Estimation of Axle Torque for an Agricultural Tractor Using an Artificial Neural Network. *Sensors* **2021**, *21*, 1989. [CrossRef]
28. Kim, W.S.; Kim, Y.J.; Baek, S.Y.; Baek, S.M.; Kim, Y.S.; Choi, Y.; Kim, Y.K.; Choi, I.S. Traction performance evaluation of a 78-kW-class agricultural tractor using cone index map in a Korean paddy field. *J. Terramechanics* **2020**, *91*, 285–296. [CrossRef]
29. Chancellor, W.; Thai, N. Automatic control of tractor transmission ratio and engine speed. *Trans. ASAE* **1984**, *27*, 642–0646. [CrossRef]
30. Salmerón Gómez, R.; Rodríguez Sánchez, A.; García, C.G.; García Pérez, J. The VIF and MSE in Raise Regression. *Mathematics* **2020**, *8*, 605. [CrossRef]
31. Kim, Y.S.; Lee, S.D.; Baek, S.M.; Baek, S.Y.; Jeon, H.H.; Lee, J.H.; Kim, W.-S.; Shim, J.Y.; Kim, Y.J. Analysis of the effect of tillage depth on the working performance of tractor-moldboard plow system under various field environments. *Sensors* **2022**, *22*, 2750. [CrossRef]

**Disclaimer/Publisher’s Note:** The statements, opinions and data contained in all publications are solely those of the individual author(s) and contributor(s) and not of MDPI and/or the editor(s). MDPI and/or the editor(s) disclaim responsibility for any injury to people or property resulting from any ideas, methods, instructions or products referred to in the content.



## Article

# Performance Evaluation of a Virtual Test Model of the Frame-Type ROPS for Agricultural Tractors Using FEA

Ryu-Gap Lim <sup>1</sup>, Wan-Soo Kim <sup>2,3</sup>, Young-Woo Do <sup>2</sup>, Md. Abu Ayub Siddique <sup>4</sup> and Yong-Joo Kim <sup>4,5,6,\*</sup>

<sup>1</sup> Department of Smart Agriculture, Korea Agriculture Technology Promotion Agency, Iksan 54667, Republic of Korea; limso@koat.or.kr

<sup>2</sup> Department of Bio-Industrial Machinery Engineering, Kyungpook National University, Daegu 41566, Republic of Korea; wansoo.kim@knu.ac.kr (W.-S.K.); duddn3372@naver.com (Y.-W.D.)

<sup>3</sup> Upland Field Machinery Research Center, Kyungpook National University, Daegu 41566, Republic of Korea

<sup>4</sup> Department of Agricultural Machinery Engineering, Chungnam National University, Daejeon 34134, Republic of Korea; ayub@cnu.ac.kr

<sup>5</sup> Department of Biosystems Machinery Engineering, Chungnam National University, Daejeon 34134, Republic of Korea

<sup>6</sup> Department of Smart Agriculture Systems, Chungnam National University, Daejeon 34134, Republic of Korea

\* Correspondence: babina@cnu.ac.kr

**Abstract:** In this study, a model of the frame-type ROPS (rollover protective structure) for an agricultural tractor was developed using FEA (finite-element analysis). Various boundary conditions were applied as input variables to replace the actual test of the ROPS with a virtual test. An optimization study was carried out based on the boundary conditions of the bolt, considering the ROPS part directly mounted on the tractor and the folding connection to the ROPS. The results of the virtual test were compared with those of the actual test, and the error was determined. The maximum error of the evaluation model was 7.0% for the force applied on the load and 9.6% for the corresponding ROPS deformation. All mounting bolts of the ROPS required modeling. In particular, we had to establish free boundary conditions for axial rotation to implement the folding connection. In addition, a simulation of the frame-type ROPS was conducted according to the mesh size. A convenient simulation time was obtained for a mesh size of 8~10 mm. Compared with the actual test, the accuracy was the highest with a mesh size of 6~8 mm.

**Keywords:** agricultural tractor; ROPS; virtual test; FEA

**Citation:** Lim, R.-G.; Kim, W.-S.; Do, Y.-W.; Siddique, M.A.A.; Kim, Y.-J. Performance Evaluation of a Virtual Test Model of the Frame-Type ROPS for Agricultural Tractors Using FEA. *Agriculture* **2023**, *13*, 2004. <https://doi.org/10.3390/agriculture13102004>

Academic Editor: Jin He

Received: 14 September 2023

Revised: 12 October 2023

Accepted: 13 October 2023

Published: 15 October 2023



**Copyright:** © 2023 by the authors. Licensee MDPI, Basel, Switzerland. This article is an open access article distributed under the terms and conditions of the Creative Commons Attribution (CC BY) license (<https://creativecommons.org/licenses/by/4.0/>).

## 1. Introduction

According to a survey on agricultural machinery accidents in Korea, tractor accidents due to a lack of safety measures account for 16.1% of all farming accidents, and overturning and fall accidents account for 43.3% of all tractor accidents [1]. According to a fatal accident investigation by the Ministry of Agriculture, Forestry and Fisheries of Japan conducted in 2005, about 70% of tractor fatal accidents were caused by tractor tipping or falls. This may be related to the fact that, in Japan, the installation rate of rollover protection structure (ROPS) is 69%, and only 48% of these frames are certified ROPSs, ensuring the required performance [2]. In 2002, approximately 52% of fatal accidents during tractor operation in the United States were caused by tipping, and the ROPS installation rate was 38% [3]. In Portugal, over the past 10 years, tractor accidents accounted for 79% of all deaths caused by farming accidents, and 38.6% of these accidents were caused by the overturning; the application rate of the ROPS for tractors was only 4.1% [4]. In Korea, the installation rate of the ROPS is 80.1%, but 15.6% of the ROPSs are then removed due to the conditions of the working environment [5]. It thus appears that, in most countries, tractor accidents are often fatal, which makes crucial the installation of the tractor ROPS with certified safety performance [6–8].

When a tractor overturns, the ROPS, which is intended to protect the driver, is subjected to external forces inducing crushing and deformation [9]. The tests performed to evaluate ROPS crushing and deformation resistance involve applying static loads to the tractor-installed ROPS to assess its efficiency in protecting the driver's safety zone. However, when changes are introduced in ROPS, even minor design changes such as thickness variations to improve its strength or changes in the location of bolt holes, the ROPS must be tested again and obtain a safety certification, which is time-consuming and expensive. For this reason, during the 2018 OECD (Organization for Economic Cooperation and Development) Tractor Technical Meeting, the OECD Tractor Division proposed to replace actual tests with virtual tests when assessing ROPS performance. Accordingly, the OECD Tractor Division is developing a virtual test for the ROPS. In technologically advanced countries, the importance of tractor ROPS virtual test technology is recognized through various studies.

Karakulak and Yetkin [10] argued that virtual testing can prevent wasting time and money in test repetitions whenever a minor change is introduced in a tractor ROPS design, and Blanco and Martin [11] confirmed that simulation tests required before ROPS certification tests are convenient in these respects [11]. Fabbri and Wards (2002) successfully simulated the test conditions defined in the OECD code to verify the effectiveness of FEA in reverse engineering of the tractor ROPS [12]. In Korea, Ha et al. [13] used finite-element analysis to design the ROPS that met the certification conditions and compared their results with those of an actual test, confirming that their method allowed satisfying the OECD code. Kim et al. [14] used the finite-element method to achieve the OECD certification of agricultural tractor cabin structures [14]. Additionally, Jang and Lee [15] obtained an optimal ROPS design using finite-element analysis, reducing the manufacturing time and cost and satisfying the performance requirements.

In this way, finite-element analysis can be applied in various conditions, allowing the optimization of various aspects such as object performance and reverse engineering [16–18]. It also has the great advantage of being able to repeatedly check load test results that cannot be repeated in reality. As mentioned earlier, the importance of ROPS performance certification is increasing, and at the same time, a simplification of the existing test methods is continuously required. One way to simplify the test methods is to introduce virtual testing, which has the advantages of being less expensive and time-consuming as well as more suitable for complex structure installations. However, a specific method for virtual testing has not been established yet, and most previous studies used empirical methods. In addition, as ROPS behavior is nonlinear, performance testing has to be conducted in conditions very similar to the real ones to increase accuracy; therefore, setting boundary conditions and constraints for the examined finite elements is very important.

The aim of this study was to develop a model for virtual testing as efficient as the performance test method recommended by the OECD tractor code and reflecting the structural characteristics of the ROPS. We propose a simplified model to validate the data obtained by virtual tests based on real-vehicle tests. We verified our model with data collected through repeated tests using a simplified ROPS model in previous research [19].

## 2. Materials and Methods

### 2.1. Experimental Design

In order to improve accuracy when performing finite-element analysis of the ROPS, it is important to select the most appropriate hardening model for the ROPS material. The stiffness of the model can be reduced by including soft deformable elements [20]. Since the shape of the joint portion of bolts is complex, it is difficult to establish it according to the joint conditions. That is why, depending on the purpose of the analysis, it is necessary to select a precise, practical, and simple model. The FE models can be developed for various conditions and can yield results similar to those obtained with actual tests only when suitable elements and constraints are set. Therefore, in this study, a virtual test was conducted by developing an FE model considering the characteristics of the tractor ROPS.

Rather than developing a new virtual test software, we verified it with an actual test using a dynamic commercial tool so that users can easily access it. The possibility of virtual testing was confirmed by modeling boundary conditions suitable for the frame-type ROPS and load plates considering actual tests. The procedure for developing the model is shown in Figure 1.

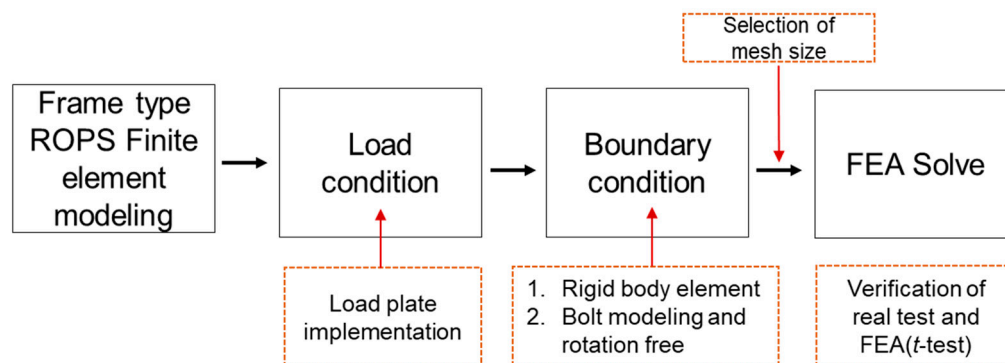


**Figure 1.** Procedure to develop the virtual test model for ROPS described in this study.

The required energy and forces for the ROPS performance test were calculated using the reference mass of an agricultural tractor of 1650 kg based on OECD code 4. The required energy and force were calculated as 2.310 kJ rear, 2.888 kJ side, and 0.578 kJ front and 33.0 kN crush, respectively. The loading sequence should be as follows: rear, primary crush, lateral, secondary crush, front. The crushing test was performed in both real and virtual tests. However, the crushing test was not analyzed in this study because it is a vertical load, not a concept of force direction and energy absorption.

## 2.2. Software

In general, various software packages are used for structural analysis. In this study, Marc ver. 2020 (MSC software Corp., Newport Beach, CA, USA), which is widely used for the structural analysis of the tractor ROPS in Korea, was chosen [21]. This is a general-purpose, commercial analysis software package that is compatible with various FE model files and has auto-remeshing and refinement functions useful for the analysis of the nonlinear behavior of the ROPS in load tests. Marc has the advantage of being able to model the behavior according to nonlinear physical properties and environmental characteristics, considering the passage of time, by simply defining a contact model and providing a re-mesh function.

## 2.3. Simulation Conditions

### 2.3.1. FE Model for the Frame-Type ROPS

For a certification test of ROPS performance, the manufacturer must submit a drawing including detailed information, such as the tractor's basic characteristics, specifications for each ROPS component, the material used, and the type of assembly and mounting bolts, to an authorized testing agency. The submitted detailed drawings by the tractor manufacturer were used to create the initial FE model for virtual testing. In this study, a 3D model of each ROPS component was developed using Solidworks ver. 2019 (Dassault systems SolidWorks Corp., Waltham, MA, USA) based on a drawing of the tractor, as shown in Figure 2a. The main frame material of the ROPS model was square steel-pipe SPSR, and the folding and mounting portions were made of steel-plate SS400. The FE model used automatic meshing, and local corrections were made for mesh breaks and element shapes. In addition, each component was named and grouped to facilitate finding the requested information for the analysis. A grid was made based on the adaptive FE method for each part, and the shape of each part was accordingly presented. Its advantages allow us to predict and redesign the mesh breaks, shape, etc. for each assembly. Table 1

summarizes the mesh information for the nodes and elements of the entire ROPS and the geometric and material information for each part. The FE model of the ROPS included upper and lower frames, with 26,474 nodes and 25,951 elements. With respect to the shape, there were 24,654 square elements, 217 triangular elements, 792 hexagonal elements, and 276 octagonal elements. The FE model of the generated ROPS is shown in Figure 2b,c. The mainframe, steel plates, pins and mounting plates, and bolts are configured in the same way as the real thing. Therefore, it has the advantage of being able to analyze the FE model by various contact condition methods compared with the real one. In terms of geometry, the mainframe was a 3D shell with upper, middle, and lower parts, and the bolts for folding and mounting the ROPS were 3D solid. Based on previous research, as shown in Figure 3, the true stress–strain values of SS400 and SPSR were used in the simulation. As for the material properties of S45C bolts, the linear properties entered for automatic provision in the analysis software were used.

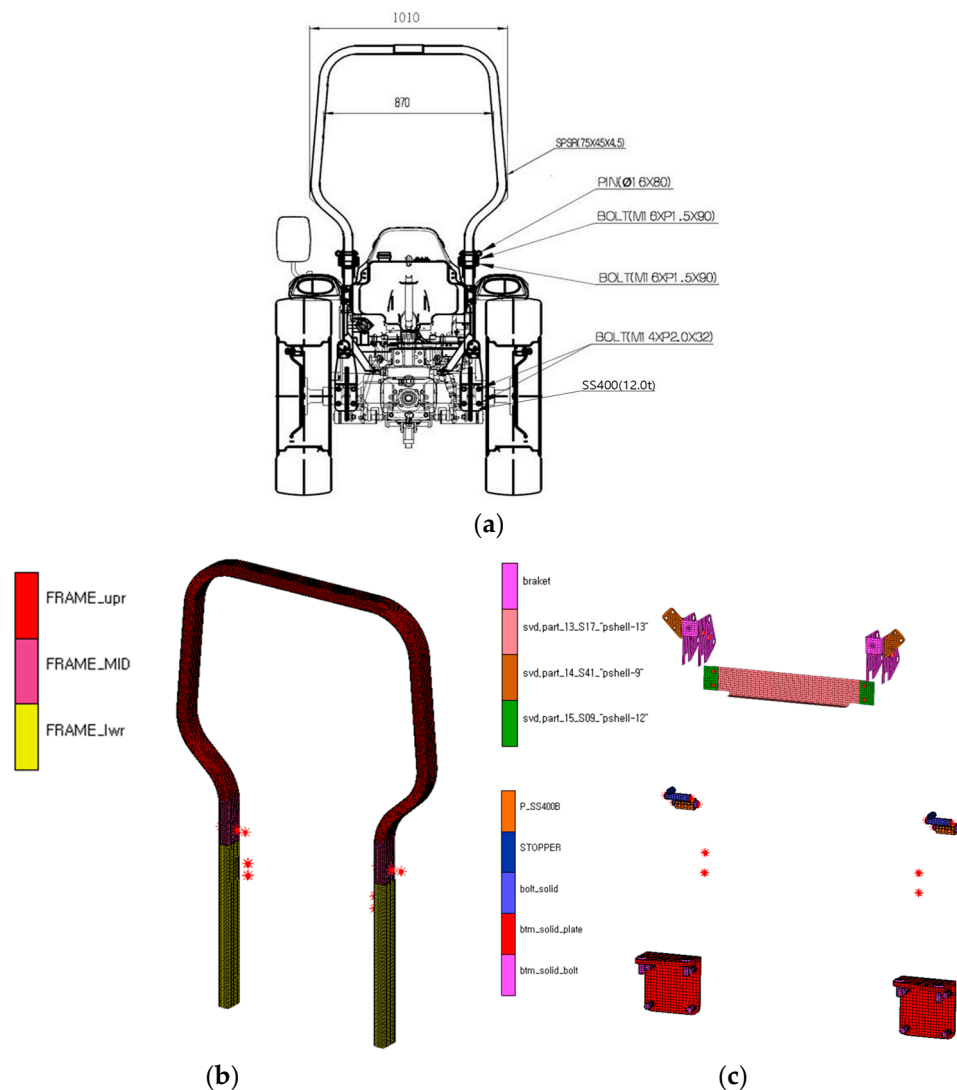


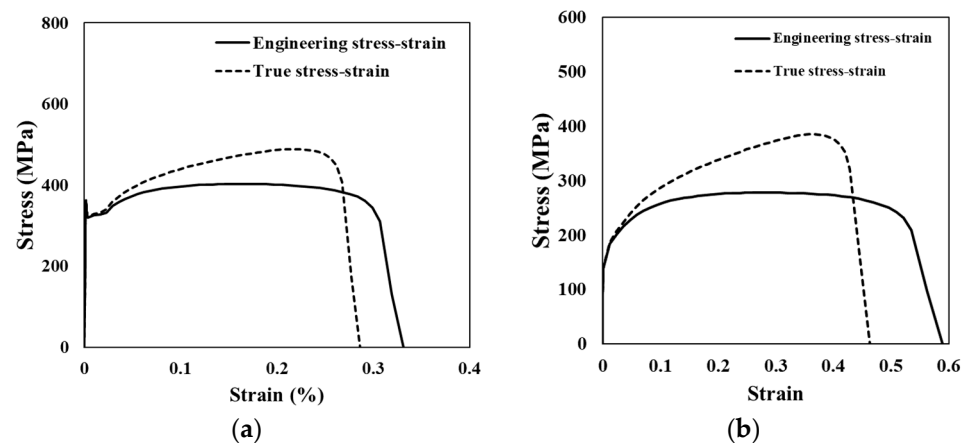
**Figure 2.** Collimation between the FE model and real model for frame-type ROPS: (a) drawing of frame-type ROPS; (b) frame of FE model; (c) folding part, plate, pin, and bolt of FE model. \* Boundary conditions of contact area.

**Table 1.** Specifications of the FE model for ROPS proposed in this study.

Mesh		Geometric		
Components	Specification (Number)	Components	Properties	No. of Elements
Nodes	26,474	Frame upper part	3D Shell	14,565
Elements	25,951	Frame mid part	3D Shell	1518
		Frame lower part	3D Shell	5786
Quad	24,654	Frame weld	3D Shell	142
		Bolt case	3D Solid	144
Tria	217	Stopper bolt	3D Solid	72
		Bolt	3D Solid	652
Hexa	792	Bottom plate	3D Solid	2336
		Bottom bolt	3D Solid	1576
Octagon	276	Folding part bolt	3D thin walled	4

Material Properties				
Components	Mass Density (kg/m <sup>3</sup> )	Elastic Modulus (GPa)	Poisson's Ratio	No. of Elements
SPSR	7900	200	0.28	42,348
SS400	7900	200	0.28	8529
S45C Stopper	7850	205	0.29	76
S45C Bolt	7850	205	0.29	652



**Figure 3.** True stress–strain of material used in this study. (a) SS400; (b) SPSR.

2.3.2. Load Conditions

In the simulation, the load was applied in the rear, side, and front of the ROPS, and the point contact condition was set at the same location as that in the actual test [22]. The evaluation of the ROPS was performed by applying loads with the energy required to simulate real conditions. However, there was no function available in the analysis program to estimate the required energy. Therefore, the representative deformation value for the required energy was selected based on the trail-error method and simulated the model. The load conditions including load direction and point in the ROPS FE model are shown in Figure 4. The ROPS test is a sequential analysis and should take into account the behavior changes caused by the previous test. In particular, the results of the ROPS test can be expressed in a strain–force graph obtained by determining strain energy, displacement, and force over time. The forces applied to the rear, side, and front of the ROPS are represented on the minus Y axis, minus X axis, and Y-axis, respectively.

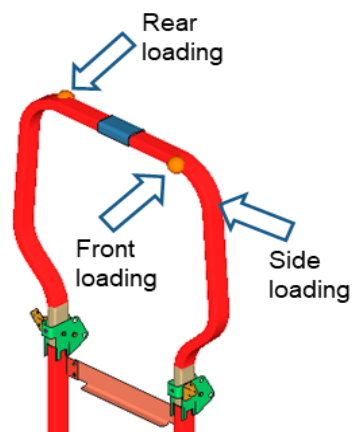
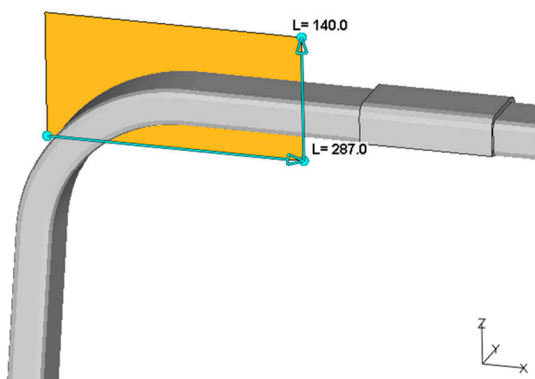


**Figure 4.** Loading conditions in the ROPS FE model.

In the actual test process, as shown in Figure 5a, a load plate of a certain size was attached to the front of the cylinder, and a load was applied. However, since the point of contact was set in the analysis, 2D plate elements were implemented by directly measuring the actual size of the load plate. The number of nodes for the central contact position of the plate element implemented in the analysis was 12,461 for the rear load and 26,475 for the front load, as shown in Figure 5b. As shown in Figure 6a, a load plate was installed to prevent the slipping and separation of the cylinder in order to apply the side load, and after measuring its size, a 2D plate element was introduced in the model, as shown in Figure 6b.



(a)



(b)

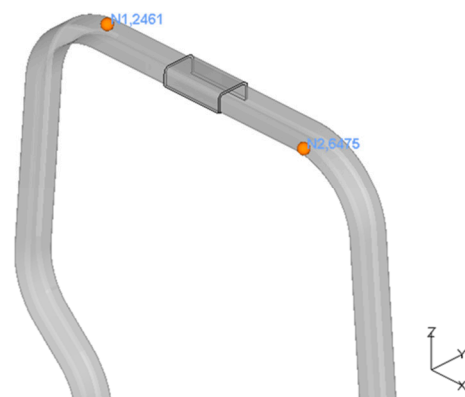


**Figure 5.** Load plate of the ROPS, for rear and front loading. (a) Actual plate; (b) 2D load plate size and node identification in the FE model.



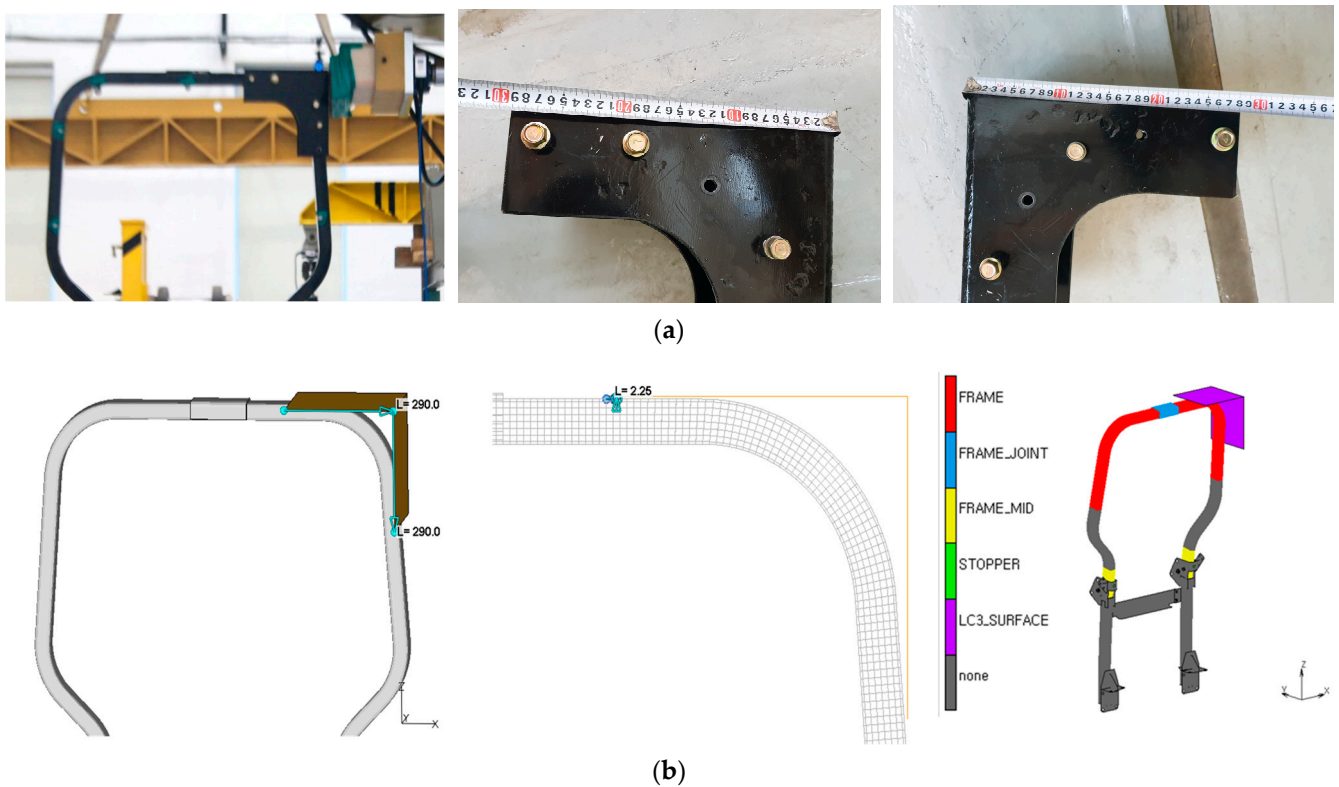


**Figure 6.** Load plate of the ROPS for side loading. (a) Actual; (b) 2D load plate size in the FE model.

### 2.3.3. Boundary Conditions

In the FE model, the mounting and folding parts of the ROPS consist of three-dimensional elements (3D shell, solid) connected to plate elements (2D plate). Therefore, when connecting solid elements and plate elements as well as beam elements in the normal direction of the plate elements, a hinge may be introduced. Therefore, a detailed analysis is required. The 3D solid elements have 3 degrees of freedom per node, while the shell plate elements have 6 degrees of freedom per node and generally are not stiff in the normal direction. The ROPS has a relatively complex shape in which solids and shell plates are geometrically connected. The boundary conditions regarded (1) the portion of the ROPS attached to the tractor and (2) the folding portion of the ROPS; the model was developed with two variables. As shown in Figure 7a, instead of 10 bolts for ROPS mounting, it was applied as a rigid body element (except for the bolt modeling process). For the second condition, we modeled the bolts as shown in Figure 7b and then constrained the displacement of the bolts on the x, y, and z axes on a rigid body, as shown in Figure 7c.

The ROPS upper frame can be folded for work convenience. As shown in Figure 8, it was difficult to model a behavior similar to the actual one when a load was applied because in the folding region, a solid element and a plate element were bound and had different degrees of freedom. Therefore, in this study, boundary conditions were set so that the FE model could obtain results that were as close to reality as possible. The boundary conditions were set as follows: (1) the bolts in the folding part were set to rigid restraints, (2) all fastening parts outside the bolts were connected, and (3) the fastening part inside the bolts was set free to rotate in the axial direction. In this study, boundary conditions were defined according to the Korean national standard [23]. This study focused on developing and verifying a virtual test model, and because too much content had to be covered to provide all mathematical equations, it was omitted, which can be confirmed in the standard. Table 2 shows the comparison between the existing methods and this study. The existing method, which did not consider the physical properties of the mounting bolt and the behavior of the connection, and the method of this study, which considered the physical

properties of the modeled bolt and the contact condition of the connection, were compared. In addition, we compared it with the virtual test based on data from previous studies such as ROPS actual test, which did not exist until now.

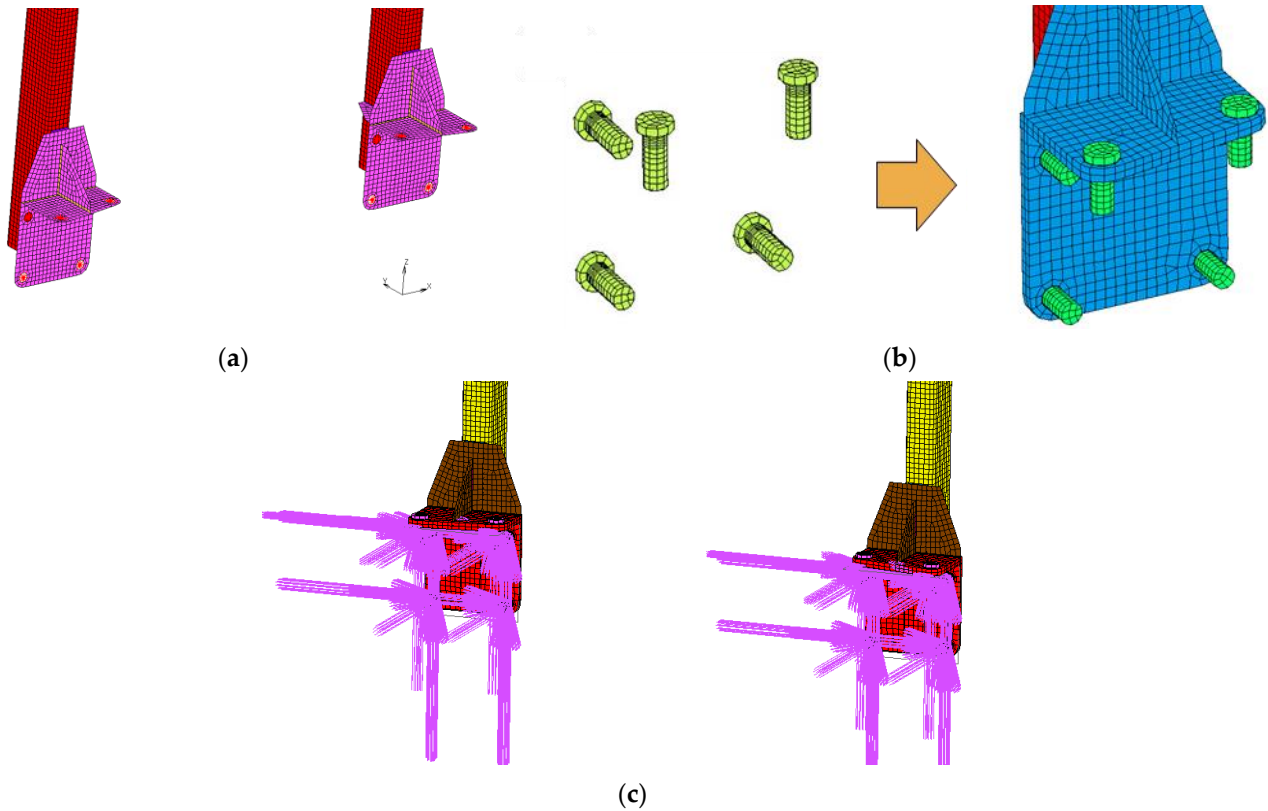


**Figure 7.** Boundary conditions of the mounting parts. (a) Constraints for bolt hole; (b) bolt modeling; (c) constraints for modeled bolts.

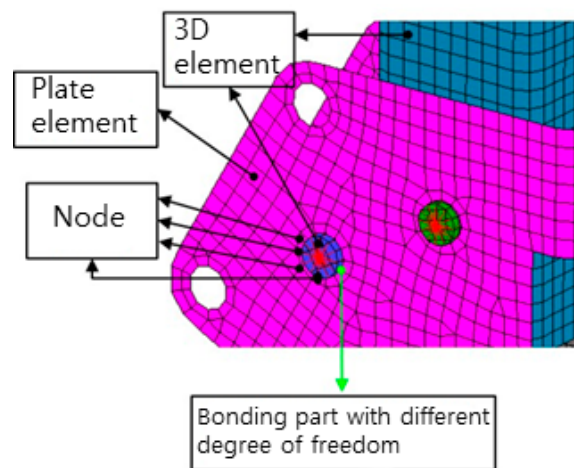


**Figure 8.** Model of the 3D shell and 2D plate of the folding portion of a tractor ROPS.



**Table 2.** Comparison of existing methods and this study.

Division	Existing Methods (FEA 1)	Study Methods (FEA 2)
ROPS mounting part	Rigid restraints	Bolts modeled Reflection physical property
ROPS folding part	Rigid restraints	Between plate element and 3D element was set rotation-free in the axial direction
Mesh size	Simple selection of large or small meshes	Apply mesh after performing simulation tests for each mesh size

#### 2.3.4. Selection of the Mesh Size

If the same mesh is applied throughout the analysis, and deformation occurs in various parts during the structural analysis, some serious errors may occur, making it difficult to guarantee reliability. To reduce these errors, engineers often locally use fine meshes over the entire finite-element model. This is inefficient in terms of computing resources and time required for the analysis [24]. Also, the meshes of small size do not prevent excessive deformation in an unpredictable dynamics analysis. Therefore, it is important to find the optimal mesh size rather than simply choose a large or a small mesh size [25]. Therefore, in order to evaluate the effect of the mesh size on the FEA of the performance of the ROPS, five mesh sizes, i.e., 4, 6, 8, 10, and 15 mm, were selected using the re-meshing function, as shown in Figure 9. The optimal mesh size was selected by evaluating the difference between the actual test results and those of the FE model.

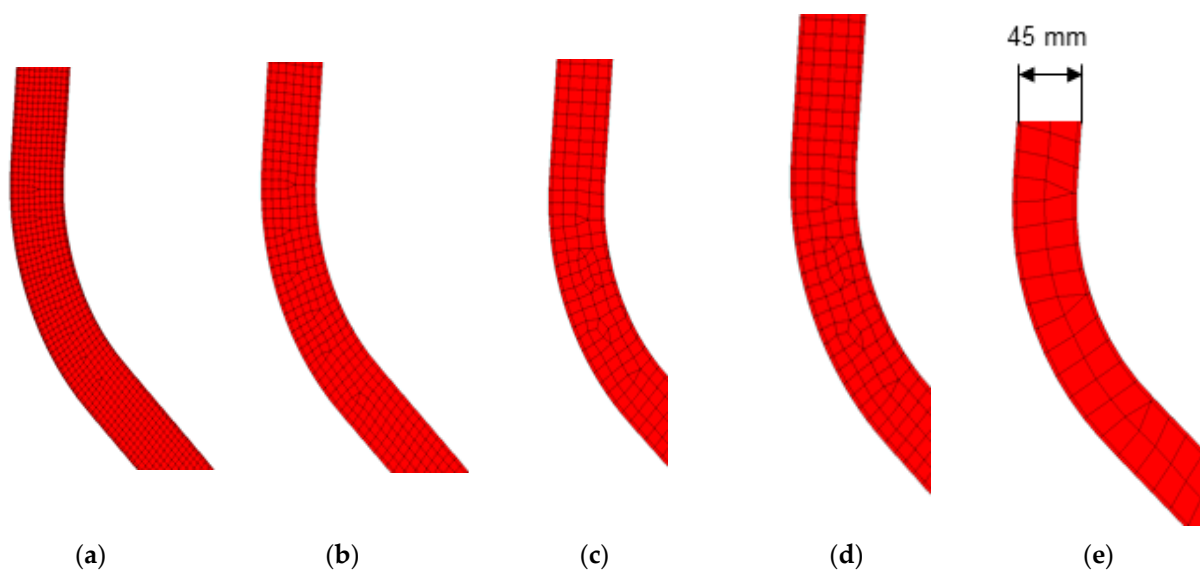


**Figure 9.** Mesh size of the ROPS in the FE model. Chosen mesh sizes: (a) 4 mm; (b) 6 mm; (c) 8 mm; (d) 10 mm; (e) 15 mm.

### 3. Results and Discussion

#### 3.1. Performance of ROPS Simulation Test

##### 3.1.1. Results by Boundary Conditions Rigid Body Element (FEA 1)

The automatic meshing with a mesh size of 6 mm was applied in the simulation. As a result of the simulation, we measured a force of 12.301 kN on the rear load, 19.515 kN on the side load, and 9.267 kN on the front load, and the corresponding values of maximum deformation were 253.9, 180.6, and 96.9 mm, respectively. Figure 10 shows a force–deformation graph that compares the obtained actual test values from a previous study with the virtual test values. It is evident that, in the simulation, the force sharply increased in each loading

direction at the beginning, after the application of the load. This was not observed in the actual test. Because the folding part and the bolt mounting part of the ROPS were set to rigid constraints, a stress stiffening effect occurred. Therefore, it was measured to have higher rigidity and smaller deformation than the actual test.

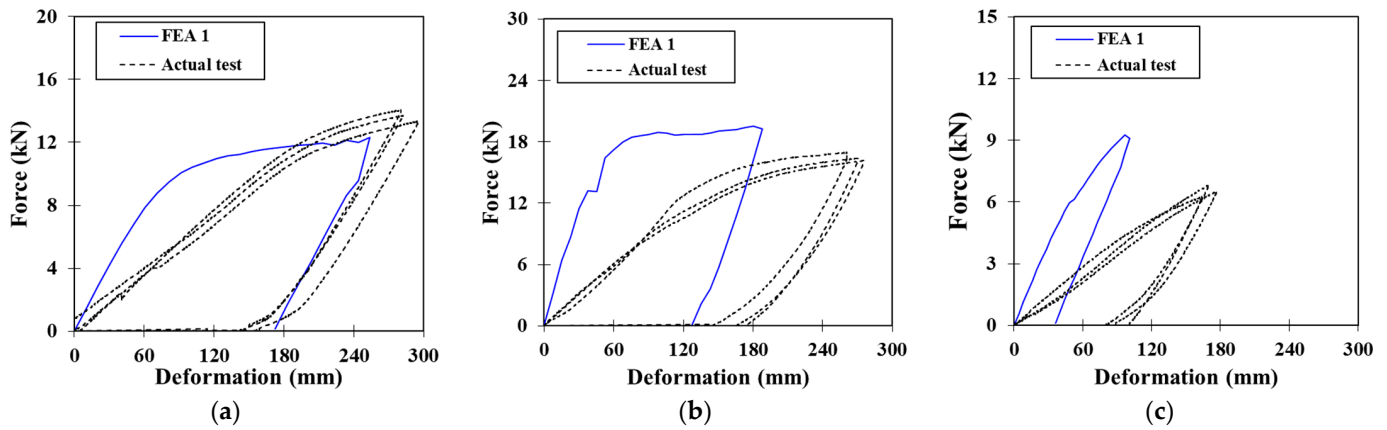


**Figure 10.** Force–deformation curve; results of FEA 1. (a) Rear loading, (b) side loading, and (c) front loading.

The errors and simulation results of FEA 1 are summarized in Table 3. The force and maximum deformation in the different loading directions were significantly different. In particular, the force error at the front load reached 43.4%. One-sample *t*-tests were performed comparing the mean force and the mean deformation measured in the actual test and in the simulation. As shown in Table 4, we found significant differences according to the *p* values at the confidence level of 95%.

**Table 3.** Results of the force and maximum deformation for ROPS FEA 1 by load direction.

Load Direction	Force (kN)			Maximum Deformation (mm)		
	Simulated (FEA 1)	Measured	Error (%)	Simulated (FEA 1)	Measured	Error (%)
Rear	12.301	13.681	10.1	253.9	285.9	11.2
Side	19.515	16.308	19.7	180.6	269.2	32.9
Front	9.267	6.461	43.4	96.9	170.2	43.1

**Table 4.** One-sample *t*-test on the results from FEA 1 and the actual analysis ( $\alpha = 0.05$ , two-tailed).

Test	N	Mean	SD	SE	t	df	<i>p</i>	Mean Difference	
Actual rear/ FEA rear	Force	3	13.7	0.353	0.204	6.77	2.00	0.021 *	1.38
	Deformation	3	286	8.11	4.68	6.85	2.00	0.021 *	32.1
Actual side/ FEA side	Force	3	16.3	0.0402	0.0232	−138	2.00	0.001 *	−3.21
	Deformation	3	269	7.46	4.31	20.6	2.00	0.002 *	88.6
Actual front/ FEA front	Force	3	6.46	0.195	0.112	−25.0	2.00	0.002 *	−2.81
	Deformation	3	170	6.46	3.73	19.7	2.00	0.003 *	73.3

\*  $\alpha = 0.05$ , *p* value <  $\alpha$ ; Therefore, there is a significant difference.

### 3.1.2. Results by Bolt Modeling and Free Axial Rotation (FEA 2)

External conditions such as load plates were implemented in the same way as in the actual test. In addition, the characteristics of the ROPS contact site were reflected in the

FEA boundary conditions. The test of the FE model was performed by setting the contact conditions of the mounting bolt and the folding steel plate. Figure 11 shows the FEA 2 stress distribution and deformation results of ROPS loading. A comparison between the simulation and the actual test is shown in the graphs in Figure 12. The graph obtained with the simulation appeared similar in shape to that obtained with the actual test. As before, a stress stiffening effect was seen at the beginning of the test. In fact, when compared with the actual test, the force at the beginning linearly increased as the deformation reached about 70 mm. But the errors were smaller overall. Table 5 shows the results for each load direction and the corresponding errors. We measured a force of 12.789 kN on the rear load, 17.135 kN on the side load, and 6.911 kN on the front load. The maximum deformation was 298.5 mm at the rear, 243.8 mm at the side, and 153.9 mm at the front. In summary, we found that the errors of load force and corresponding deformation were as follows: rear force 6.5%, deformation 4.4%; side force 5.1%, deformation 9.4%; front force 7.0%, deformation 9.6%. Overall, it showed significantly better performance than FEA 1. The results of one-sample *t*-tests comparing the actual and the FEA test results are shown in Table 6. We found significant differences only for the forward load deformation and the lateral load force and deformation, as indicated by the small *p*-value at a confidence level of 95%.

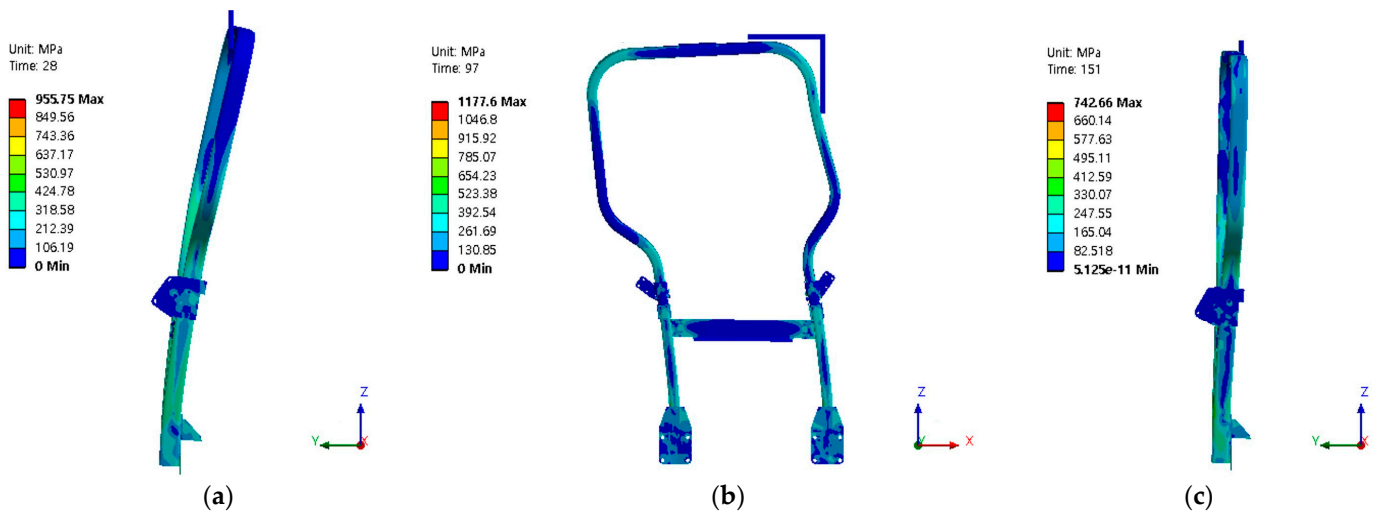


**Figure 11.** Evaluation of the distribution stress and deformation on ROPS according to the loading direction. (a) Rear loading; (b) side loading; and (c) front loading.

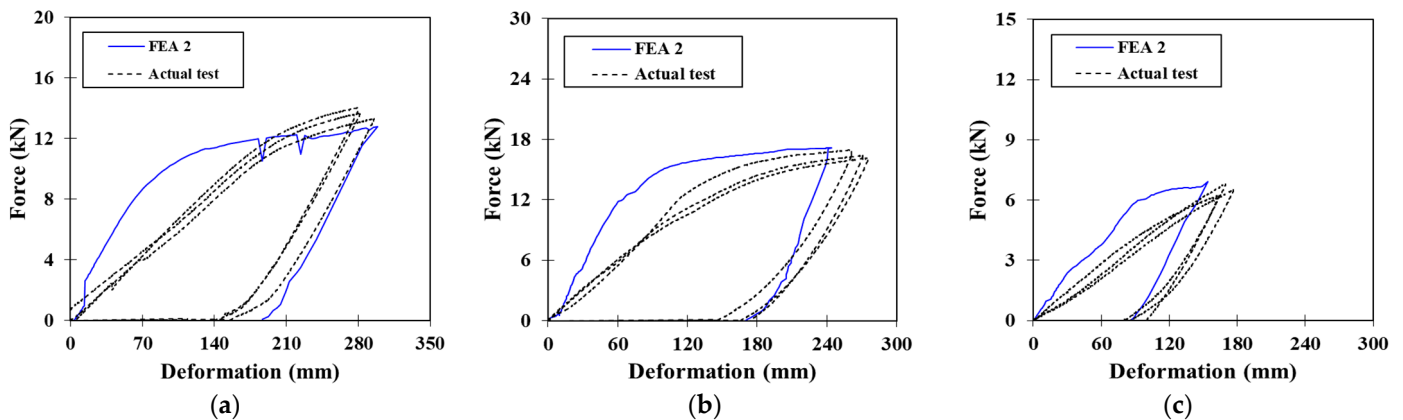


**Figure 12.** Force–deformation curve; FEA 2 results. (a) Rear loading, (b) side loading, and (c) front loading.

**Table 5.** Results of the force and maximum deformation for ROPS FEA 2 by load direction.

Load Direction	Force (kN)			Maximum Deformation (mm)		
	Simulated (FEA 2)	Measured	Error (%)	Simulated (FEA 2)	Measured	Error (%)
Rear	12.789	13.681	6.5	298.5	285.9	4.4
Side	17.135	16.308	5.1	243.8	269.2	9.4
Front	6.911	6.461	7.0	153.9	170.2	9.6

**Table 6.** One-sample *t*-test on the results from FEA 2 and the actual analysis ( $\alpha = 0.05$ , two-tailed).

Test	N	Mean	SD	SE	t	df	<i>p</i>	Mean Difference	
Actual rear/ FEM rear	Force	3	13.7	0.353	0.204	4.38	2.00	0.054	0.892
	Deformation	3	286	8.11	4.68	−2.68	2.00	0.116	−12.5
Actual side/ FEM side	Force	3	16.3	0.0402	0.0232	−35.7	2.00	0.001 *	−0.827
	Deformation	3	269	7.46	4.31	0.028	2.00	0.028 *	25.4
Actual front/ FEM front	Force	3	6.46	0.195	0.112	−4.01	2.00	0.057	−0.450
	Deformation	3	170	6.46	3.73	4.37	2.00	0.049 *	16.3

\*  $\alpha = 0.05$ , *p* value <  $\alpha$ ; Therefore, there is a significant difference.

### 3.2. Simulation Test Results by Mesh Size

The mesh sizes in the ROPS FE model were set differently, and a test was performed on the rear load. The results showing the actual and FEA test results according to the mesh size are shown in Figure 13. The results are shown in Table 7. The time for solving the ROPS finite-element model was 21,285 s for an element size of 4 mm, 8315 s for an element size of 6 mm, 3383 s for an element size of 8 mm, 2540 s for an element size of 10 mm, and 4605 s for an element size of 15 mm. When the size of the element was 8 or 10 mm, the model was solved in a relatively short time, whereas when the element size was 4 mm, it took about 6 h to solve it. The largest error in the force value when comparing the results with those of the actual test was found for the element size of 10 mm and was 21.9%. In addition, the error in the force value was 19.3% and 18.8%, respectively, for the element sizes of 4 mm and 15 mm. Although the mesh size 6 mm showed the lowest error, this condition still required the second highest simulation time among the five mesh conditions. Therefore, the user must select the mesh size considering the appropriate simulation time and error. These results are similar to those presented in the previous research results of Kim and Jung (2012), who studied the relationship between element size, effective characteristics, and analysis time [26]. To replace a real-test ROPS performance, the virtual test is required to be highly accurate. It was observed that the lowest error in the virtual test compared with the actual test was for the mesh size of 6 mm.

**Table 7.** FEA results and errors for the ROPS FE model according to the mesh size.

Mesh Size (mm)	4	6	8	10	15
Simulation time (s)	21,285	8315	3383	2540	4605
Force (kN)	11.045	12.687	11.830	10.684	11.147
Error (%)	19.3	7.3	13.5	21.9	18.8

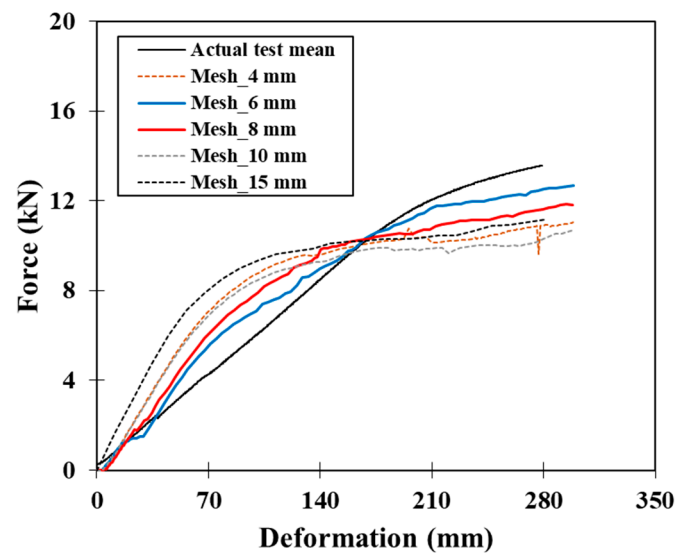


**Figure 13.** Comparison of the force–deformation curves obtained with the ROPS FE model and the actual test according to the mesh size.

#### 4. Conclusions

The ROPS for the tractor driver’s rollover safety must be subjected to load performance tests even when only minor design changes are introduced, such as changes in the position of bolts and in frame thickness. Tractors and the ROPS need to be examined and certified through actual testing, which is costly and requires manpower and money. Therefore, in this study, the characteristics of the tractor frame-type ROPS were considered to develop a simulation as a valid alternative to actual testing. In addition, an FE model was developed considering different boundary conditions. Simulations were performed, and the results were compared with those obtained with the actual test; the corresponding errors were then calculated. The main findings of this study were as follows:

- (1) For the virtual test of the frame-type ROPS, the stress stiffening effect of the tractor and its mounted area must be considered. Therefore, all bolts should be modeled rather than using rigid body constraints. Additionally, the boundary condition of the bolt finite-element model must be set to rotation-free for the bolt itself.
- (2) The size of the load plate in the actual performance test was taken into consideration and reflected in the load conditions. In addition, the boundary conditions of the ROPS part directly mounted on the tractor were simulated by applying bolt 3D modeling and free axial rotation rather than rigid body restraints. As a result, the slope of the force–deformation curve was improved. The measurement error with respect to the actual test measurement was reduced by up to 38.3%.
- (3) A simulation was conducted to identify the mesh size suitable for the ROPS. As for the simulation time, when the mesh size was 8 or 10 mm, the simulation was relatively short. The error with respect to the measurement from the actual test was the smallest, i.e., at 7.3%, when the mesh size was 6 mm.
- (4) We expect that the results of this study will soon allow the establishment of a secure virtual test technology for domestic ROPS. In addition, we expect that it will be possible to propose a domestic virtual test technology to the OECD tractor group. The manufacturers can thus verify ROPS design changes to improve ROPS quality through convenient virtual tests. This is expected to help ensure excellent ROPS quality by reducing costs and saving time.

In this study, the FE model for frame-type ROPS performance was proposed. The results of this study suggested the possibility of replacing real tests with virtual tests. In future research, in order to improve the accuracy of virtual testing, we would like to

implement full virtual testing as a replacement for actual testing through advanced research such as individual research on the physical properties of materials.

**Author Contributions:** Conceptualization, R.-G.L. and Y.-J.K.; methodology, R.-G.L., Y.-J.K. and W.-S.K.; software, R.-G.L.; validation, R.-G.L. and W.-S.K.; formal analysis, R.-G.L. and W.-S.K.; investigation, R.-G.L., W.-S.K., Y.-W.D. and M.A.A.S.; data curation, R.-G.L.; writing—original draft preparation, R.-G.L., W.-S.K. and Y.-W.D.; writing—review and editing, R.-G.L., W.-S.K., Y.-W.D. and M.A.A.S.; supervision, R.-G.L. and Y.-J.K.; project administration, R.-G.L.; funding acquisition, R.-G.L. and Y.-J.K. All authors have read and agreed to the published version of the manuscript.

**Funding:** This work was supported by Korea Institute of Planning and Evaluation for Technology in Food, Agriculture and Forestry (IPET) through Technology Commercialization Support Program, funded by Ministry of Agriculture, Food and Rural Affairs (MAFRA) (821014-03 and 821053-03).

**Institutional Review Board Statement:** Not applicable.

**Data Availability Statement:** The data presented in this study are available within the article.

**Conflicts of Interest:** The authors declare no conflict of interest.

## References

1. Rural Development Administration (RDA). *Current Status of Damage for Farmers Related to Agricultural Machinery*; RDA: Jeonju, Republic of Korea, 2019; pp. 20–38.
2. Muneki, T. Survey on the accident caused by agricultural machinery and its protective equipment. In Proceedings of the Japan-Korea Joint Seminar on the Safety of Agricultural Machinery, Saitama, Japan, 31 October 2006.
3. Rautiainen, R.H.; Reynolds, S.J. Mortality and morbidity in agriculture in the United States. *J. Agric. Saf. Health* **2002**, *8*, 259–276. [CrossRef] [PubMed]
4. Antunes, S.M.; Cordeiro, C.; Teixeira, H.M. Analysis of fatal accidents with tractors in the centre of Portugal: Ten years analysis. *Forensic Sci. Int.* **2018**, *287*, 74–80. [CrossRef] [PubMed]
5. Kim, H.J.; Kim, K.W.; Choi, S.; Kim, J.S.; Kim, Y.Y.; Kim, J.O.; Kim, H.K.; Kwon, S.H. A Study on Improving the Tractor ROPS and Seatbelt use of Korean Farmers. *J. Biosyst. Eng.* **2010**, *35*, 294–301. [CrossRef]
6. Kim, J.H.; Hwang, S.J.; Nam, J.S. Simulation study on the safety of a fastening device of agricultural by-product collector. *J. Drive Control* **2023**, *20*, 42–49. [CrossRef]
7. Lee, D.; Yoo, H.J.; Shin, M.; Oh, J.; Shim, S.B. Analysis of overturning stability of small off-road vehicle. *J. Biosyst. Eng.* **2023**, *48*, 309–318. [CrossRef]
8. Iqbal, M.Z.; Islam, M.N.; Ali, M.; Kiraga, S.; Kim, Y.J.; Chung, S.O. Theoretical overturning analysis of a 2.6-kW two-row walking-type automatic pepper transplanter. *J. Biosyst. Eng.* **2022**, *47*, 79–91. [CrossRef]
9. Lim, R.G.; Kang, Y.S.; Kim, T.J. Measurement uncertainty calculation for improving test reliability of agricultural tractor ROPS test. *J. Drive Control* **2023**, *20*, 34–40. [CrossRef]
10. Karakulak, S.S.; Yetkin, E. Agricultural tractor cabin safety analysis and test correlation. *Int. J. Automot. Sci. Technol.* **2002**, *4*, 1–9. [CrossRef]
11. Blanco, D.; Martin, C.; Ortalde, A. Virtual ROPS and FOPS testing on agricultural tractors according to OECD standard code 4 and 10. In Proceedings of the 14th International LS-DYNA Users Conference, Detroit, MI, USA, 12–14 June 2016.
12. Fabbri, A.; Ward, S. Validation of a finite element program for the design of roll-over protective framed structures (ROPS) for agricultural tractors. *Biosyst. Eng.* **2002**, *81*, 287–296. [CrossRef]
13. Ha, C.W.; Kim, H.J.; Goo, N.S.; Kwon, Y.D. Finite element analysis of an agricultural cabin based on the OECD standard (code 4). *J. Biosyst. Eng.* **2003**, *28*, 431–436. [CrossRef]
14. Kim, H.J.; Goo, N.S.; Kwon, Y.D.; Ha, C.W.; Jung, H.K. Structural analysis of an agricultural tractor cabin for OECD certification. In Proceedings of the Korean Society of Mechanical Engineers Autumn Conference, Jeju, Republic of Korea, 27–29 June 2001.
15. Jang, H.; Lee, B. Optimal design of tractor cabin frame using design of experiment of taguch. *J. Korea Acad.-Ind. Coop. Soc.* **2015**, *16*, 7377–7384. [CrossRef]
16. Won, J.G.; Yoon, J.I.; Lee, H.A.; Chung, S.G.; Jeong, J.S. Simulation analysis on static safety of 55Hp-servo-based hydrostatic transmission. *J. Drive Control* **2022**, *19*, 34–42. [CrossRef]
17. Yu, Y.J.; An, Y.C.; Lee, K.H.; Park, J.H.; Lee, D.; Lee, C.H. Fatigue and severity analysis of drive axle parts according to forklift driving environment. *J. Drive Control* **2023**, *20*, 24–30. [CrossRef]
18. Kumar, N.; Tewari, V.K. Modification of reactive muffler in farm tractor to reduce noise level using finite element method. *J. Biosyst. Eng.* **2023**, *48*, 165–177. [CrossRef]
19. Lim, R.G.; Kang, Y.S.; Lee, D.H.; Kim, W.S.; Lee, J.H.; Kim, Y.J. Agricultural tractor roll over protective structure (ROPS) test using simplified ROPS model. *Korea J. Agric. Sci.* **2023**, *49*, 771–783. [CrossRef]
20. Agius, D.J.; Kourousis, K.I.; Takla, M.; Subic, A. Enhanced non-linear material modelling for analysis and qualification of rollover protective structures. *Proc. Inst. Mech. Eng. Part D J. Automob. Eng.* **2015**, *230*, 1558–1568. [CrossRef]

21. Song, H.S.; Kim, Y.Y.; Lim, R.G. Determination of the properties of structural steel for agricultural tractor roll-over protective structure by tensile test and finite element analysis. *J. Korean Soc. Mech. Technol.* **2019**, *21*, 567–576. [CrossRef]
22. OECD (Organization for Economic Cooperation and Development). *OECD Standard Code for the Official Testing of Protective Structures on Agricultural and Forestry Tractors (Statics Test)*; Tractor Standard Code 4-OECD; OECD Headquarters: Paris, France, 2021.
23. *KS B 7950*; Tractors for Agriculture and Forestry-Two-Post Roll-Over Protective Structures-Virtual Statistic Test Method and Acceptance Conditions. Korea Standards Association: Seoul, Republic of Korea, 2022.
24. Yoon, C.Y. Efficient adaptive finite element mesh generation for dynamics. *Comput. Struct. Eng. Inst. Korea* **2013**, *26*, 385–392. [CrossRef]
25. Heo, J.H.; Kim, H.S. Bending moment calculation method and optimum element size for finite element analysis with continuum elements. *Comput. Struct. Eng. Inst. Korea* **2018**, *31*, 9–16. [CrossRef]
26. Kim, S.W.; Jung, H.C. Investigation on the effect of mesh density in FE analysis for prediction of mechanical behavior of a PCM. In Proceedings of the Korean Society for Technology of Plasticity Conference, Jeju, Republic of Korea, 10–11 May 2012.

**Disclaimer/Publisher’s Note:** The statements, opinions and data contained in all publications are solely those of the individual author(s) and contributor(s) and not of MDPI and/or the editor(s). MDPI and/or the editor(s) disclaim responsibility for any injury to people or property resulting from any ideas, methods, instructions or products referred to in the content.

## Article

# High-Throughput Plant Phenotyping System Using a Low-Cost Camera Network for Plant Factory

Woo-Jae Cho <sup>1,2</sup> and Myongkyoon Yang <sup>3,4,\*</sup>

<sup>1</sup> Department of Bio-Industrial Machinery Engineering, College of Agriculture & Life Sciences, Gyeongsang National University, Jinju 52828, Republic of Korea; woojae56@gnu.ac.kr

<sup>2</sup> Institute of Smart Farm, Gyeongsang National University, Jinju 52828, Republic of Korea

<sup>3</sup> Department of Bioindustrial Machinery Engineering, Jeonbuk National University, Jeonju 54896, Republic of Korea

<sup>4</sup> Institute of Agricultural Machinery & ICT Convergence, Jeonbuk National University, Jeonju 54896, Republic of Korea

\* Correspondence: yangmk@jbnu.ac.kr

**Abstract:** Plant phenotyping has been widely studied as an effective and powerful tool for analyzing crop status and growth. However, the traditional phenotyping (i.e., manual) is time-consuming and laborious, and the various types of growing structures and limited room for systems hinder phenotyping on a large and high-throughput scale. In this study, a low-cost high-throughput phenotyping system that can be flexibly applied to diverse structures of growing beds with reliable spatial-temporal continuities was developed. The phenotyping system was composed of a low-cost phenotype sensor network with an integrated Raspberry Pi board and camera module. With the distributed camera sensors, the system can provide crop imagery information over the entire growing bed in real time. Furthermore, the modularized image-processing architecture supports the investigation of several phenotypic indices. The feasibility of the system was evaluated for Batavia lettuce grown under different light periods in a container-type plant factory. For the growing lettuces under different light periods, crop characteristics such as fresh weight, leaf length, leaf width, and leaf number were manually measured and compared with the phenotypic indices from the system. From the results, the system showed varying phenotypic features of lettuce for the entire growing period. In addition, the varied growth curves according to the different positions and light conditions confirmed that the developed system has potential to achieve many plant phenotypic scenarios at low cost and with spatial versatility. As such, it serves as a valuable development tool for researchers and cultivators interested in phenotyping.

**Keywords:** plant phenotyping; phenotypic index; low-cost system; camera network; online monitoring; plant factory

**Citation:** Cho, W.-J.; Yang, M. High-Throughput Plant Phenotyping System Using a Low-Cost Camera Network for Plant Factory.

*Agriculture* **2023**, *13*, 1874. <https://doi.org/10.3390/agriculture13101874>

Academic Editor: Signe Marie Jensen

Received: 31 August 2023

Revised: 15 September 2023

Accepted: 20 September 2023

Published: 25 September 2023



**Copyright:** © 2023 by the authors. Licensee MDPI, Basel, Switzerland. This article is an open access article distributed under the terms and conditions of the Creative Commons Attribution (CC BY) license (<https://creativecommons.org/licenses/by/4.0/>).

## 1. Introduction

Stressful situations cause morphological, physiological, and biochemical changes in crops. Thus, research on crop phenomics has been conducted to measure and utilize these changes in order to increase productivity, improve quality, and reduce energy and resource consumption through optimal control [1]. In the early stage, a specific stimulus was provided in a controlled environment, such as a smart farm, and response analysis and growth modeling were performed. In particular, to obtain characteristic information about crops, direct measurement, observation, or destructive methods are used. However, although these methods are generally simple and reliable, they require considerable time and labor because of the small number of activities that can be performed at one time [2,3]. In addition, when destructive methods are applied, the sample is damaged, and subsequent analysis is difficult.



To overcome these difficulties, various analyses using non-destructive methods have been conducted. Data available for analysis include images, environmental (temperature, humidity, light intensity, and nutrients) values, and physical (length and weight) values to quantify the genotype and phenotype [4]. Among them, image-based methods are used to analyze the external characteristics or growth of crops using two- (2D) or three-dimensional (3D) images or to indirectly explain internal phenomena through spectral images [5]. As several samples can be easily and automatically obtained using a camera, the time and cost required to acquire feature information can be reduced [6]. In addition, a large amount of information can be obtained using several images, broadening the scope of the analysis. This development coincides with the creation of integrated and mass crop production facilities; moreover, with the development of information communication technology (ICT) convergence technology, high-throughput analysis has been developed into a high-speed, mass-phenotypic method with high efficiency [7]. A high-throughput phenotyping platform refers to a system that integrates the storage of crop data, data analysis, robotics, and decision making. Growing demand, along with the development of numerous types of applicable data and technologies, has led to the requirement of several research studies for this platform and improvement of standardization, experimental methods, and analysis [8–10].

The process of stably collecting and analyzing images is important for analyzing the overall growth of crops through images. The process of acquiring the image should place no additional stress on the crop, and there should be no other influences such as noise or color distribution changes on the image. Several cameras can be utilized to acquire images. In addition, automatically moving and saving the images according to the conditions in a specific storage space can be advantageous because shooting is conducted over several days depending on the growth process. A system with continuity in which the characteristics of crops are automatically analyzed using various image processing and machine learning algorithms for each image and where model development and updates are performed is considered ideal. Thus, the entire process from image acquisition to analysis must be organically connected to enable high-speed mass-phenotypic analysis. However, most of the previously developed systems are very expensive and use algorithms applicable only to a specific environment, hindering their broad application. For example, in a previous study, when examining the number and area of leaves in the growth chamber to investigate the development of Arabidopsis, there were differences in the absence of various application; in addition, the study was soil-based [11]. Similarly to this study, in a 2D-based phenotyping system using a fixed camera, automatic water supply adjustment and area and color characteristics were analyzed. This study was conducted in a soil environment and applied to relatively small crops [12]. In some studies, 3D images and spectroscopy were applied by performing growth monitoring through individual moving ports. However, a limited number of parameters were used, and there were difficulties in system configuration using built-in software [13,14].

A plant factory is a mass crop production facility that can provide a more uniform growth environment than the open field through artificial lighting and complex environmental control in an enclosed space for the year-round production of crops [15]. However, even within these plant factories, spatial variations exist in micro-environmental conditions, such as light, temperature, and humidity, resulting in growth differences [3,16]. Moreover, it is necessary to capture and analyze at minimum hundreds of plant images per day to follow the rapid and intensive progression of growth in plant factories [4,17]. If the analysis is not accomplished in a real-time manner, the data will be accumulated and delay the response to the crop status. In the context, high-speed mass phenotyping approach can be a practical solution to provide location-specific information on crops growing in the cultivation bed, thereby allowing precise environmental control and growth management in plant factories such as yield estimation, crop harvest, or disease treatment.

Methods for acquiring image information according to location include acquiring multiple images while moving one camera and acquiring multiple data at a time by arranging

multiple cameras at a certain location. When using a single mobile camera system, it is possible to use a high-cost camera with good performance rather than purchasing several cameras. Good performance provides high resolution and facilitates obtaining images of depth sensors or other wavelength bands rather than simple colors. Because the image is acquired with one device, there is no need to consider the error of the hardware itself. However, this method is relatively expensive and has limitations in repeatability, data acquisition time, and movement section restrictions because the camera position must be moved manually unless an additional automation device is employed in a situation where multiple crops need to be photographed. For example, Jiang et al. [18] developed an on-the-go monitoring platform to measure crop-growth variation according to the location; however, this system could only be moved for the first applied bed structure, and the configuration of the system became more complicated as the cultivation area increased. Yeh et al. [19] created a moving-image monitoring system using a moving arm. Its effectiveness was verified only on a small vertical bed, and rapid analysis was difficult because the growth information was confirmed via image processing through post-processing. Rossi et al. [20] reported a low-cost sliding platform for high-resolution plant phenotyping, but the processing time of more than 1 h would limit the application of the system to the level of laboratory analysis. A greenhouse-based low-cost phenotyping platform reported by Yassue et al. [21] is noteworthy since it proved its effectiveness in a greenhouse-level environment. However, it would not be applicable for vertical plant factories due to height problems. Bari et al. [22] applied a moving-cart embedded camera to the rails for monitoring growing peas in greenhouse, but the large area of the greenhouse meant that it was necessary to analyze the image via post-processing after the collection of images.

By contrast, as the method using several inexpensive cameras can secure a large amount of simultaneous image data, it is easy to analyze changes in the same location without additional correction processes. In addition, it can be flexibly configured for plant factories with relatively large and diverse production structures. However, there is a non-uniformity of information depending on the type and quality of images and the use of various hardware; therefore, it is necessary to develop an image processing technique to overcome this problem. Although An et al. [23] adopted the calibration of multiple-camera array and utilized it for plant phenotyping, the post-data collection and -processing made it difficult to access and analyze data in real time. Thrash et al. [24] also proposed a low-cost wireless phenotyping system, but it was only developed for a single index and a horizontal space. Gang et al. [25] developed a novel convolutional neural network-based model that can estimate various morphologic indices for plants grown in greenhouses, but its feasibility was not validated in an integrated phenotyping platform.

Considering the aforementioned limitations, it is necessary to develop a low-cost phenotyping system capable of collecting and processing data in real time while being structurally more flexible for crop monitoring in vertical plant factories. Furthermore, for phenotyping modeling aimed at analyzing the behaviors of various crops, it is necessary to simplify the determination of new indices or code modifications for correlation analysis.

For the purpose, in this study, a multi-camera network using an inexpensive image sensor and processor was developed. It was designed to have flexible space applicability through a wireless, miniaturized camera node configuration, and to make it easy to collect and analyze various phenotypic indices through a modularized image processing algorithm structure. Based on this, a system capable of performing high-speed mass-phenotypic analysis was constructed. Specifically, the developed system continuously and stably collected crop growth images from camera devices installed at different locations, classified them according to location and time, and stored them in an independent space of the computer server. The stored images were configured to analyze diverse crop characteristics through various image processing algorithms and to output the results. Additionally, the analyzed crop characteristics were used as data for a growth model for a specific situation, and the model was updated according to the data generation. The feasibility of the developed system was evaluated by collecting 2D images of lettuces for the entire

growth cycle at various locations. To verify the applicability of the obtained phenotypic indices, growth information of lettuces growing under two different photo-environmental conditions within the plant factory were analyzed and compared.

## 2. Materials and Methods

### 2.1. Plant Growth Conditions

The camera system could be applied to any leafy vegetables with low heights, which are usually cultivated in the commercial plant factories [26]. In this study, Batavia lettuce (*Lactuca sativa* L.) was cultivated for the growth experiment, which is a type of lettuce that originated in Europe. Lettuce is one of the most important leafy vegetables in plant factories because of its popularity, with the highest consumption and economic importance throughout the world [27,28]. Individuals with similar weight, size, and shape were selected by direct sowing, and a monitoring experiment was conducted on the growth of the entire cycle from the second day after planting.

Cultivation was conducted in a container environment system located in Yongin, Gyeonggi-do, Republic of Korea (Figure 1). This container, a system that has an environment independent of the outside environment, is suitable for conducting reaction experiments of crops to a target factor. Crops were grown independently in a sponge medium serving as artificial soil, and the necessary nutrients were provided through a closed nutrient film technique system where the electrical conductivity and pH values without a separate nutrient solution supply device. Generally, EC and pH values below or above the optimal range can impede water and nutrient uptake in crops, thereby inhibiting growth and potentially inducing diseases [29]. Therefore, the nutrient solution was manually managed to maintain an appropriate concentration by measuring the EC and pH values at 2-day intervals through standard sampling. During cultivation, the temperature inside the container plant factory was maintained at an average of 22.1 °C in the range of 21–23 °C, and the humidity was maintained at an average of 65% in the range of 50% to 80%. CO<sub>2</sub> was maintained at 400–700 ppm as a factor relating to plant respiration.



**Figure 1.** Crop-growth container system with controlled environment.

### 2.2. Photoperiod Condition

Photoperiod is one of the most important variables affecting the plants' growth process, thereby inspiring researchers or industries to explore the effective light/dark cycle for leafy vegetable productivity [30,31]. Specifically, it was reported that differing pulse width modulation of light would be an important factor in the photosynthesis. Chen and Yang [32] reported that intermittent light irradiation could enhance the biomass and taste of lettuces. Therefore, not only to evaluate the applicability of the developed system but also to confirm the effect of different light/dark cycles on the growth of lettuces, an experiment was conducted to establish a camera network for two cultivation beds and to check the growth

difference by varying the photoperiod conditions for each zone. The control (con) group was irradiated with light for 16 h and maintained in the dark for 8 h; for the pulse (pul) group, light–dark conditions were set at intervals of 2 h and 1 h, respectively. Accordingly, the daily light irradiation time of the two groups was 16 h, and the total irradiation time and the total incident light amount were the same under the two photoperiod conditions. However, it was expected that improved growth would appear for pul group due to the different light/dark cycles. A total of 14 Batavia lettuces were cultivated for each group, and 4 lettuces were used for acquiring destructive test data (Figure 2). Specifically, 12 camera systems were installed for each control and experimental group to acquire images, while each camera was installed to be located in the center of each target crop. With regard to the extra two cameras for each group, they were used to validate the phenotypic analysis during the cultivation. Growth characteristics such as fresh weights of shoots, leaf length, leaf width, and leaf numbers were measured for four samples every week. Fresh weights of shoots of lettuces were measured using a digital scale (Si-234, Denver Instrument, Denver, CO, USA), and the length and the width of leaves were measured using a ruler. The measured values were used to analyze the differences in data and to compare means among the treatments, respectively.

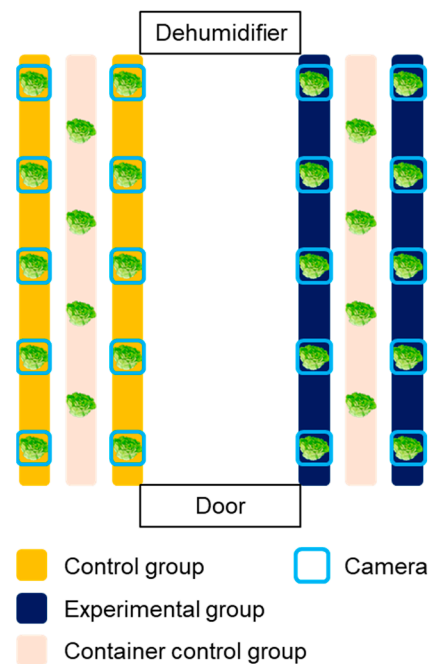


**Figure 2.** Experimental layout of growing bed and camera network installation.

### 2.3. Low-Cost Camera Network

For high-speed, mass-phenotypic analysis targeting plant factories, the narrow cultivation interval between crops and the restriction of height should be considered. Accordingly, the proposed system was configured in the form of a multi-point camera network that could freely attach and detach small camera modules and provide integrated access to information on each image collection node through a web connection. Moreover, the building cost of the camera network system is about 5% level compared to the on-the-go monitoring system by Jiang, Kim, and Cho [18] (Table 1). Although the cost will be increased as the number of camera nodes increases, it is still more reasonable than the on-the-go monitoring system when considering the scan area.

**Table 1.** Comparison of the camera network system with the on-the-go monitoring system by Jiang, Kim, and Cho [18].

Item	Camera Network System	On-the-Go System
Cost	~USD 50 per node	~USD 2200
Setup	Light and compact (~50 g L96 mm × W71 mm × D26 mm per node)	Bulky (~8 kg for conveyer belts, controllers, motors, and actuators)
Scan area (height of 0.45 m)	0.54 m × 0.4 m	0.94 m × 1.8 m
Plant scan time	<1 ms	~127 s
Ease of installation	Easy (due to the node's compact size and individual modularity)	Difficult (due to the complexity of conveyer belts and frames)
External equipment	Wi-Fi router	Linear actuators, a motor servo driver, and step motors

A Raspberry Pi 3B+ (Raspberry Pi Foundation, Cambridge, UK) was used as a low-cost microprocessor that can acquire images of crops for the experiment and transmit them to the server. It was selected because it is small, light, and inexpensive, has good compatibility with various equipment, and has good accessibility compared to other commercial products.

Various cameras, including a USB webcam, can be connected to the Raspberry Pi to take pictures. The Raspberry Pi Camera v2 (Raspberry Pi Foundation, UK) was selected and used to compare the stability, convenience, and image quality. This camera is composed of a module with a resolution of 3280 × 2464 and a performance of approximately eight megapixels. For the stability of data collection, the board and camera modules were configured in a one-to-one connection. The Raspberry Pi and camera module used in this study are not essential parts and can be replaced with other products depending on the experimental environment conditions.

Because the monitoring of crops is conducted remotely, the information obtained on the local Raspberry Pi has to be grasped remotely. Moreover, as mentioned above, an external system is needed to solve the problems associated with the use of multiple processors and limited local capacity. To this end, a computer acting as a server and multiple Raspberry Pi devices were connected to form a system to automatically import data. The computer acting as a server played an overall role in storing and analyzing data. The computer was configured with a Linux operating system environment of core i7-7700k CPU @4.2 GHz (Intel Corp., Santa Clara, CA, USA) and 32 GB RAM for continuity with Raspberry Pi.

Figure 3 shows the network diagram for system setup. This network diagram is an example for the photoperiod experiment of this study, and it is possible to add or remove a server, router, Raspberry Pi, etc., depending on the researcher's experimental environment. Several Raspberry Pi devices for shooting were connected to a single local router via Wi-Fi. A port forwarding method replaces the internal IP between the local router and the Raspberry Pi connected to the lower internal network and creates a new address that can be accessed remotely. Therefore, it was possible to remotely access the Raspberry Pi containing the image information for each location and transmit and receive real-time monitoring and image information. The external server was connected to several Raspberry Pi devices through the local router and used the secure shell (SSH) protocol to access and issue remote commands. Thus, the SSH class was implemented, and the image data were transmitted to the server at a specific period after creating a session using the port forwarding access address. In the server, there were folders designated for each Raspberry Pi, and images were saved in each folder with a name set using date and time information.

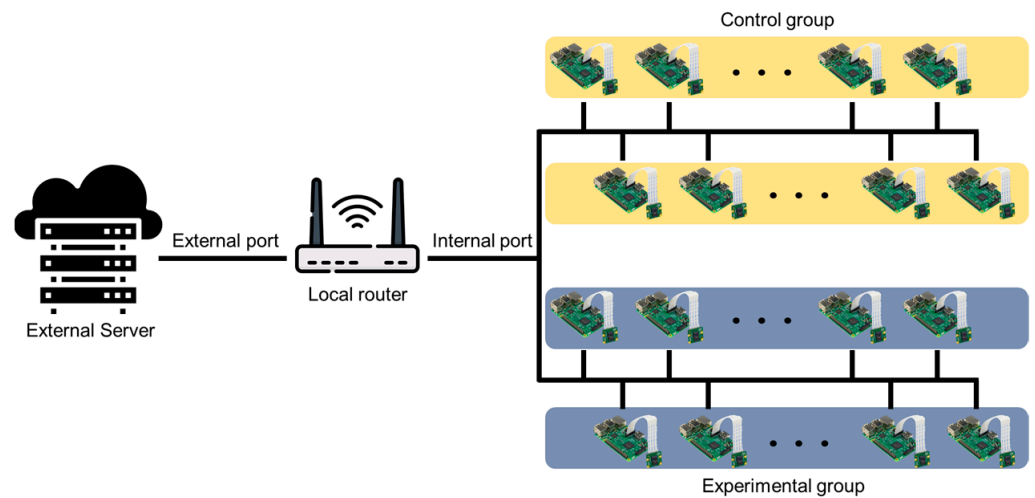


**Figure 3.** Diagram of network structure of the system.

#### 2.4. Crop Image Collection

As described in the following passages, image data taken according to time conditions were saved in the Raspberry Pi and configured to be transmitted to the server at a specific point in time to enable continuous image shooting. When an image acquisition signal was transmitted to the Raspberry Pi according to the time condition (20 min intervals), a process for stabilizing the image sensor was performed, and the image shooting was performed after acquiring the local time required for phenotypic analysis. To stably acquire image data, the data transmission operation was interrupted during the acquisition process. Since it did not take much time to transmit one image, the data were transmitted when a certain number of images were accumulated in consideration of the system load in the transmission process. Accordingly, data collection to the server was performed once daily. The code for image acquisition was written using Python, and camera control was performed with a Python library called “PiCamera.” The use of crontab provided a reduction in the system load, as the system was run only when necessary, rather than continuously.

As the images acquired have high resolution, one file has a size of approximately 4 MB. This is not a problem in short-term monitoring, but in the case of long-term experiments, there may be a problem of insufficient capacity inside the processor. Accordingly, flags for the number of consecutive shooting days, or the number of stored files can be configured to enable continuous monitoring by deleting previous files when the limit is exceeded. In addition, in the process of transmitting the image to the server, it was implemented to record and display logs such as connection errors, image errors, and transmission completion of the local Raspberry Pi to promptly respond to users.

The imaging system consisted of a top-view image acquisition system that could secure crop-growth images in container environmental conditions. The system was configured so that only one crop was placed in the center of one image. Camera modules were installed in the space between the LED lamps to obtain an accurate top-view image and to prevent light intensity interference. Each camera module was calibrated using a classic color checker (X-Rite, Grand Rapids, MI, USA) to compensate the spatial variability. Image acquisition was performed for additional 10 s to stabilize the shooting. Figure 4 shows the multi-camera network installed for multi-point growth image monitoring.



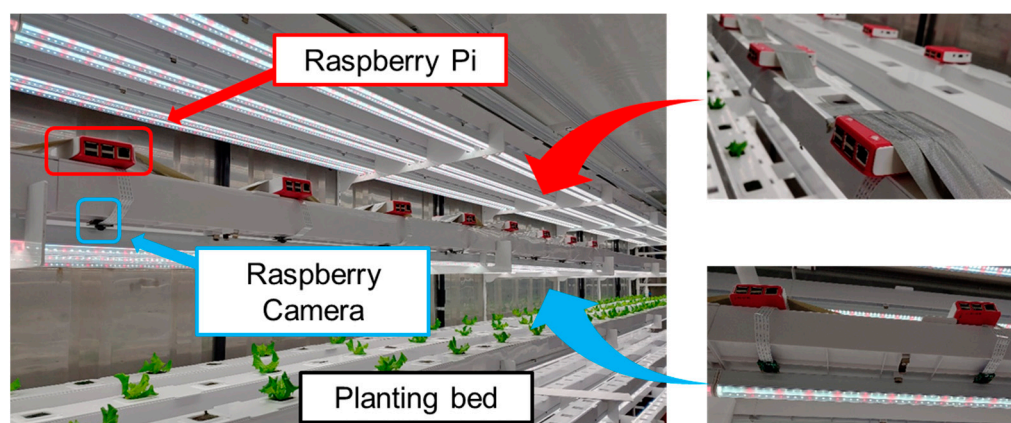


**Figure 4.** Views of multi-camera network-based high-throughput phenotyping system.

### 2.5. Phenotypic Index Processing Algorithms

An automatic extraction process of the phenotypic index required for analysis was performed on crop images stored in each folder of the server. Crop images acquired by our system consisting of a camera network contain various noises depending on the environmental conditions of the plant factory. Depending on the system configuration conditions, an image contains only one crop, but the image also includes several types of surrounding environments, such as planting bed, media, and other modules, as noise. The image processing steps to counter these issues are shown in Figure 5. Several algorithms were combined to extract the region of interest (ROI) corresponding to the crop parts required for analysis. ROI are initially extracted from the acquired images using the vegetation index and Otsu threshold method. Because small errors appear in these results, the final binary ROI was extracted through the intersection of colorimetric changes and small space filling methods. For the extracted ROI, the contour and pixel area were obtained, the center was found, the shortest and longest lengths were measured, and the average color information was identified. The extracted index formed a data frame with the structure of the crop, date, time, index 1, index 2, . . . , index n, which was stored in a comma-separated values (csv) format. It was also possible to check the image for specific results. The image processing was configured to be performed on the entire folder when a certain number of image data were added, including files that were not analyzed. The default value was set at daily intervals; thus, when the daily data transmission was completed, index extraction was performed only on new data. The newly created indicator data were stored cumulatively in the previously saved csv file to enable continuous analysis. For the storage and management of data, it is possible to consider a method of using a database rather than a simple csv format storage. In this study, a database was not considered because a simple configuration was sufficient. However, if the system grows in size, the use of a database would be necessary. OpenCV and PlantCV libraries were mainly used in the image processing.

For accurate analysis of crop image phenotypic indices, some aspects were considered on the images obtained. First, image distortion was considered [33]. Usually, in the case of an image containing several crops, errors occur in the center and edges of the image owing to the hardware characteristics of the camera lens. This phenomenon is called distortion. In the case of the configured system, only one crop was placed in the center of one camera to avoid distortion. Second, even by precisely positioning the camera and crop, physical skew occurs [34]. This can cause problems in image tracking because movement may occur as the crop grows; in addition, it depends on the characteristics of hydroponics. In this regard, an analysis method not affected by skew was used. Specifically, two methods were applied to avoid the effect of skew: first, one camera was placed for each crop so that the crop was located in the center of the image, thereby minimizing the effects of skew, which typically occurs in the corners of the image. Second, the projected area viewed from the

top instead of the actual leaf area to extract phenotyping features because it could reduce skew interference caused by leaves growing in various directions. Lastly, because multiple cameras were used, the colors appeared slightly different for each camera, even when shooting the same subject. This was solved by performing a calibration process using a separate color panel as a hardware characteristic.

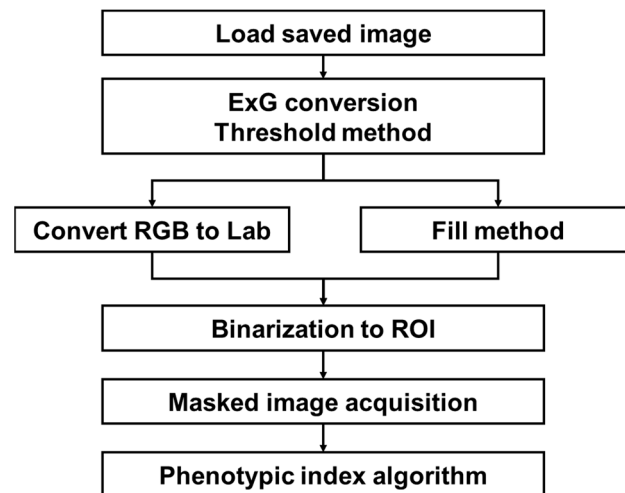


**Figure 5.** Overall flowchart for crop ROI extraction and phenotypic index.

The first step of the analysis of crops is the extraction of a ROI through background separation. If ROI extraction is not performed adequately, values calculated in the subsequent process become useless. Accordingly, several algorithms were combined and utilized. The target part was a crop, and the image to be analyzed was in the form of 2D red–green–blue (RGB). Thus, Excess Green (ExG), an image extraction method [35], was applied among the available vegetation indices [36]. As shown in Equation (1),  $R$ ,  $G$ , and  $B$  color channels were used, normalized values divided by the maximum values ( $R_m$ ,  $G_m$ ,  $B_m$ ) of each channel were employed, and the equation was derived by assigning weights to the green part.

$$R^* = \frac{R}{R_m}, G^* = \frac{G}{G_m}, B^* = \frac{B}{B_m}$$

$$r = \frac{R^*}{R^*+G^*+B^*}, g = \frac{G^*}{R^*+G^*+B^*}, b = \frac{B^*}{R^*+G^*+B^*}$$

$$ExG = 2g - r - b \quad (1)$$

ExG uses only RGB colors and is an index affected by green; therefore, large and small noises could be included, as shown in Figure 6. Although the noise of small particles is also an issue, the artificial medium, which is usually used in plant factories, has a larger role in noises. The artificial medium is artificial soil constructed to enable crops to absorb and support the nutrient solution. In commercial plant factories, an empty artificial medium is sometimes placed to control the planting distance, but it could be recognized as a crop part in the image and included as noise. These noises cannot be distinguished by using ExG, so additional image processing is required.

In this study, the hydroponic system in plant factory was considered as the target field. Therefore, noise filtering for plant factory condition was established to extract the crop parts, excluding noise from the image extracted through the vegetation index. After converting the image masked with ExG to the Lab color system, the green-magenta and blue-yellow channels were extracted, and a threshold value determined based on the trial-and-error method was set to remove the noise. Since the lab color space reflects the uniformity of colors, thereby allowing more robustness for the illumination effect [37,38]. Relating to binarization for crop segmentation, by combining the two methods and performing an additional fill process on a small part, a sophisticated binary image of the ROI was extracted. The final target image was obtained by masking the original image on the binary image (Figure 7).





**Figure 6.** Results of applying ExG conversion to crop images: (A) RGB and (B) ExG binary images.



**Figure 7.** Additional image processing to acquire images of the ROI: (A,B) noise removal through Lab color system, (C) binary image, and (D) mask image.

Although more sophisticated segmentation techniques such as a multilevel thresholding or combination of other color spaces such as hue–saturation–value (HSV), and hue–saturation–intensity (HSI) used for detecting the diseased leaf area could be used, the techniques require more processing time for one image, thereby inducing considerable delay for entire growing bed monitoring [37–39]. Therefore, in this study, the proposed image processing algorithm was simply constructed to achieve the real-time analysis of the morphological growth characteristics.

A process was performed to determine a phenotypic index that could be used for analysis with respect to the extracted ROI image. The center, contour, length, central axis, color space distribution, growth distortion, and color histogram were selected by referring to the useful phenotypic indices related to crop morphology in previous studies [19,40–42]. Table 2 shows a description of each indicator and the automatic acquisition algorithm.

All processes such as image acquisition, save, image processing, and phenotypic index extraction were modularized through classes and functions. Modularity facilitated the modification and addition of content. Although some parameters needed to be modified according to the experimental environment conditions, it was possible to easily change them according to the user environment through the modularization of the image processing algorithm. Since it was possible to remove only a specific part and add a sub-list of new functions and classes, it could be flexibly applied according to various experimental purposes and growing environments.

Although these various phenotypic indices can have meaning by themselves, they enable further analysis through correlation with actual crop characteristics or addition of an algorithm. To check this possibility, the manually measured values were used for analysis. In the process of conducting the experiment, crop characteristics such as fresh weight, leaf length, leaf width, and leaf number were manually measured and compared with the extracted phenotypic indices. After identifying the correlation, a trend line was drawn through a regression equation, and the coefficient of determination and root mean square error (RMSE) were obtained to verify the indices.

Table 2. Phenotypic index description and computation method.



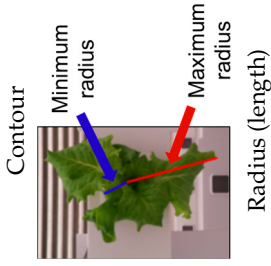
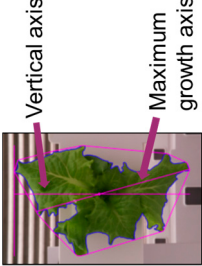
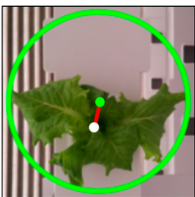
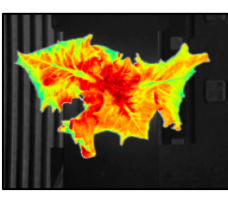
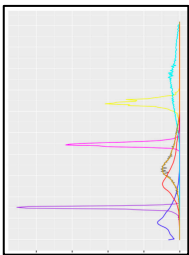
Phenotypic Index	Description	Equation	Equation Number
 <p>Center</p>	<ul style="list-style-type: none"> <li>Obtained by using the moment value to find the coordinates of the center of mass <math>p_{cm}</math></li> <li>Reference point for radius and growth skew calculation</li> </ul>	$m_{ij} = \sum_{x,y} (array(x,y) \cdot x^i \cdot y^j)$ $\bar{x} = \frac{m_{10}}{m_{00}}, \quad \bar{y} = \frac{m_{01}}{m_{00}}$	(2)
 <p>Contour</p>	<ul style="list-style-type: none"> <li>Point data acquired using the boundary of the binary mask image through ROI extraction</li> <li>Used for projected leaf area calculation</li> </ul>	$l_{contour} = \sum  p_c^i - p_c^{i-1} $ <p><math>p_c^i</math>: <math>i</math>-th point of the contour</p>	(3)
 <p>Contour</p> <p>Minimum radius</p> <p>Maximum radius</p> <p>Radius (length)</p>	<ul style="list-style-type: none"> <li>Minimum and maximum radii (length) from the central index to the contour using Euclidean distance</li> <li>Available for estimation of leaf length and volume index</li> </ul>	$l_{max\ radius} = \max \left\{ \overbrace{p_{cm} - p_c^i} \right\}$ $l_{min\ radius} = \min \left\{ \overbrace{p_{cm} - p_c^i} \right\}$ <p><math>p_{cm}</math>: center point</p>	(4)
 <p>Vertical axis</p> <p>Maximum growth axis</p> <p>Central axis</p>	<ul style="list-style-type: none"> <li>Vertical axis in space with respect to the center of the crop and the axis showing maximum growth</li> <li>Alignment of the obtained crop image; evaluation of the crop growth behavior</li> </ul>	$Axis_{max\ growth} = \max \left\{ \overbrace{p_c^i - p_c^j} \right\}$	(5)

Table 2. Cont.

Phenotypic Index	Description	Equation	Equation Number
	<ul style="list-style-type: none"> <li>• Degree of deviation of the center of the crop from the center of both the circumscribed circle and the circumscribed rectangle with respect to the crop</li> <li>• Evaluation of the crop growth behavior</li> </ul>	$I_{growth\ skew} = \left  \frac{P_{cm} - P_{cc}}{P_{cm} - P_{cc}} \right $	(6)
<p>Growth skew</p> 	<ul style="list-style-type: none"> <li>• Degree of color intensity for the crop image (depth image: spatial map)</li> <li>• Available for estimation of crop height, volume index</li> </ul>	-	-
<p>Color space distribution</p> 	<ul style="list-style-type: none"> <li>• Histogram for each color coordinate system of RGB, Lab, and HSV for the masked crop part</li> <li>• Color indices-based plant disease or stress evaluation</li> </ul>	-	-
<p>Color histogram</p>			

### 3. Results

#### 3.1. Evaluation of Camera Network

It was confirmed that the developed system can easily identify and solve various problems that may occur in the process of image acquisition and processing through the log generated during the image transmission process. This detected several errors in the artificially generated data port, capturing data, and in the transmission process. Accordingly, it was possible to respond appropriately to the problems that arose, and the validity of subsequent analysis of the transmitted data could be secured.

The phenotypic index extraction algorithm was evaluated by performing the analysis on nine items, including center, contour, minimum radius, maximum radius, spatial vertical axis, maximum growth axis, color space distribution, growth distortion, and color histogram. As a result of performing automatic index extraction on a total of 35,000 image data, the total analysis time was approximately 2.43 s per image and included index values and image result output. The time required for analysis may vary depending on the number and type of indicators to be analyzed.

Figure 8 shows the analysis results using the phenotypic indices selected by the developed system for one crop. ROI extraction was performed through background separation, and the phenotypic index was automatically extracted according to a previously defined algorithm. The background was adequately removed using the vegetation index, color system conversion, and additional algorithms and by providing visualization information for all indices such as center, contour, and maximum/minimum radius. As a result of applying the original image and the phenotypic index, the entire growth cycle can be analyzed for approximately two weeks with an interval of two days for the image. This can provide a better understanding of the acquired information, such as the growth level of crops, growth status, and product quality. In addition, it is possible to access the saved analysis result and analyze it in the form of a data frame. In the developed system environment, the data frame can access each index value by using a “key” corresponding to the column, and it is possible to separate data for each crop by specifying a “value” condition of the key. Accordingly, it is possible to analyze individual crops to perform intensive analysis on crops of different growth by location.

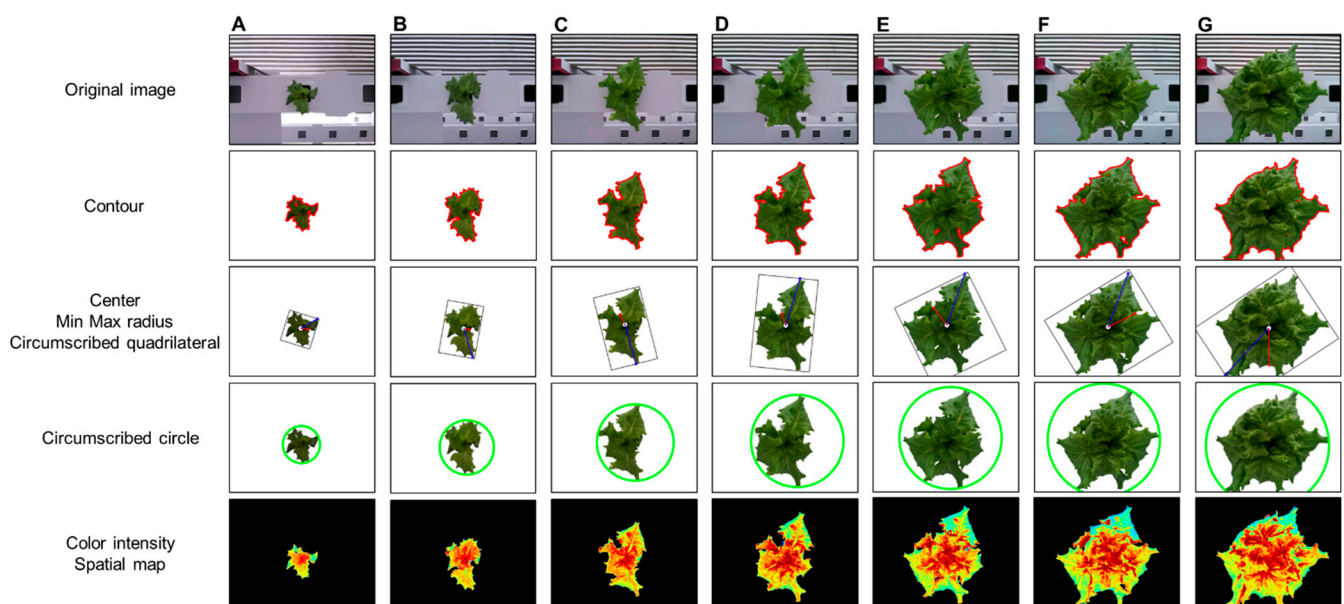


**Figure 8.** Changes in phenotypic indices according to crop growth: days (A) 1, (B) 3, (C) 5, (D) 7, (E) 9, (F) 11, and (G) 13.

### 3.2. Growth Analysis for Lettuces under Different Light Conditions

Figure 9 shows the area index changes for the pul group with a change in the photoperiod and for the “con group” with no change. In the pul group, as the light period during image acquisition and the dark period when acquisition was interrupted were short, the data appeared continuously, whereas the con group showed a step-like graph because the dark period was long. The two groups had the same duration of the entire light period; thus, the total number of images acquired in one day was the same, even though there were differences in the acquisition time. That is, the data of the two groups were compared for each day, not for the point value corresponding to the x-axis value of the graph.

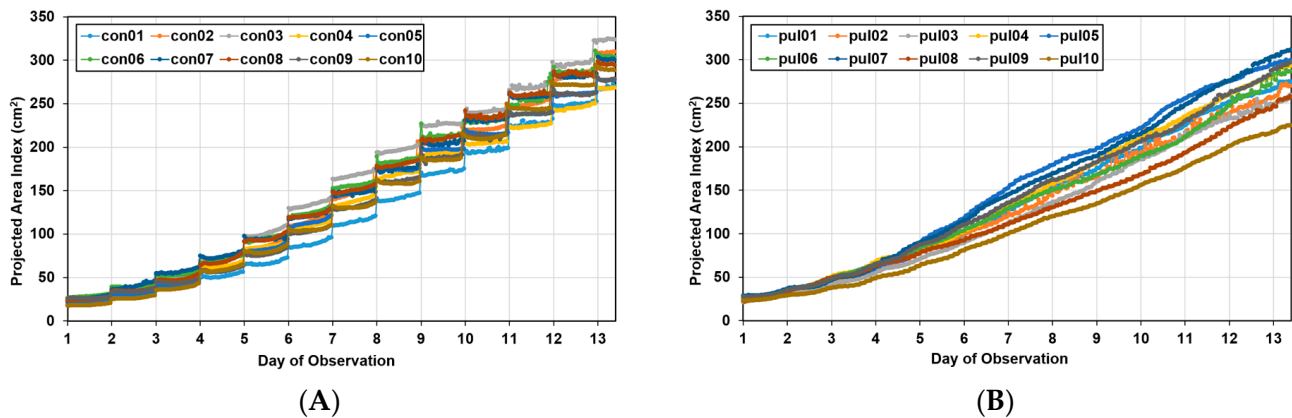
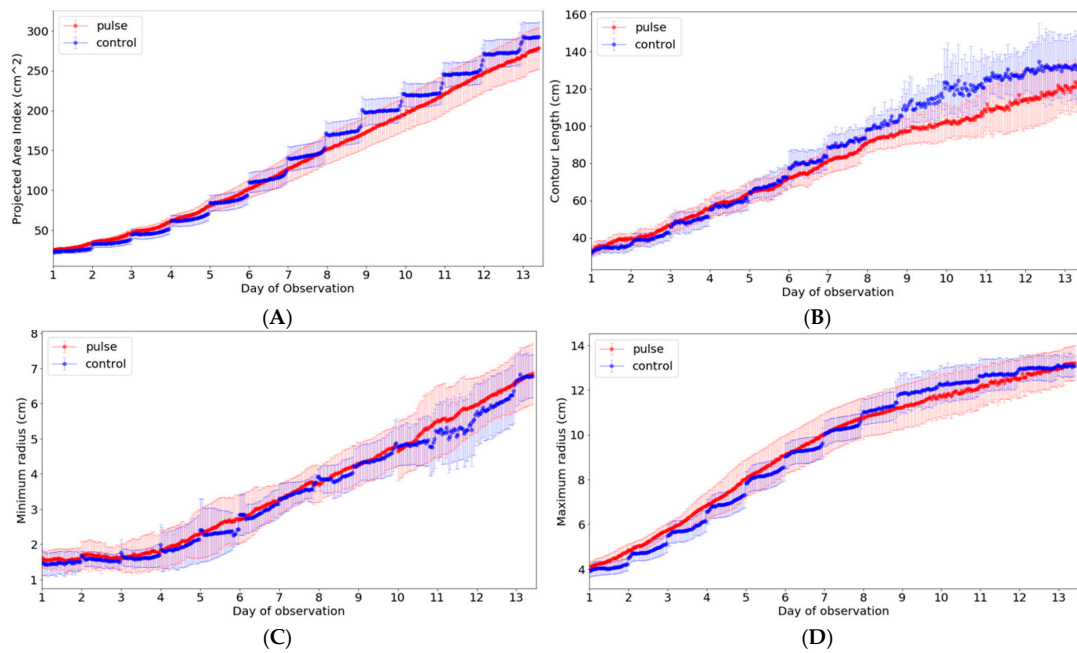


**Figure 9.** Growth curves for Batavia lettuces in different light periods: (A) control group (con) and (B) pulse group (pul).

In the growth curve, the growth pattern according to the growth location was different in both groups, indicating that there was spatial variation. Approximately 13 days after transplantation, the maximum area of lettuce was approximately 18% larger than the minimum area in the control group, whereas in the pulse group, it was 38% larger, confirming that the spatial variation was larger in the pulse group.

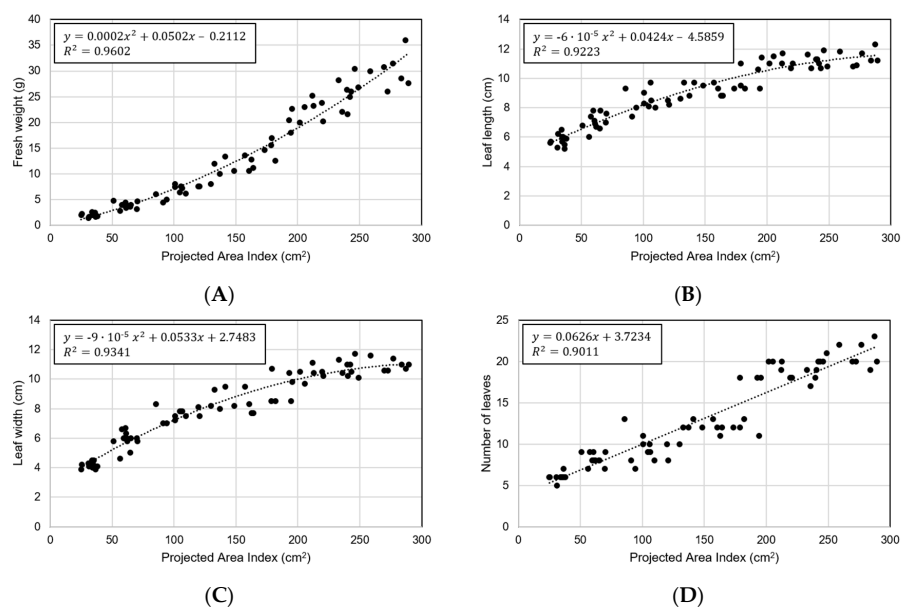
Among the ten phenotypic indices that can be extracted from our system, the indices that can be analyzed meaningfully in light condition experiments include contour, length, minimum radius, and maximum radius in addition to area. These phenotypic indices were closely analyzed to examine the growth difference according to the light period (Figure 10). Thus, a new data frame was created by calculating the average value and standard deviation of each indicator in the developed system interface, and it was expressed as a graph. In the graph, there was no significant difference in the minimum and maximum radius, but the growth was higher in the control group in both area and contour length.

Figure 10 shows the index change for one crop during the experimental period. As observed, it is possible to monitor the growth status, including the phenotypic indices selected for the crop growth of the entire period, using the developed system. However, based on the indices, additional considerations were identified in the analysis. In the case of the contour, it was possible to find a part showing a difference due to the complexity expressed in the growing process of the crop or the change in the crop shape according to the light/dark period. Accordingly, the maximum length from the center was measured by moving the position according to a specific period rather than a single point according to the passage of time. Although it was shown continuously on the graph, the actual measurement position changed significantly. The minimum length was considerably affected even by slight differences in these morphological characteristics; thus, this index showed the greatest change.



**Figure 10.** Analysis of phenotypic indices for Batavia lettuces in different light periods: (A) area, (B) contour length, (C) minimum radius, and (D) maximum length. The colored area indicates the standard deviations.

In order to verify the phenotypic index, the analysis was performed using the area index as a representative. Figure 11 shows the results of performing predictions using area index for the four characteristics of manually measured crops. Each regression formula was set to have the highest coefficient of determination. The area index showed the best correlation with fresh weight ( $R^2 = 0.9602$  and  $RMSE = 2.23$  g) (Figure 11A). In the early stages of small size, it was small with  $RMSE = 0.83$  g, but it was confirmed that the error also increased as the size increased (Figure 11B–D). A comparison with the other three characteristics showed a low coefficient of determination compared to the fresh weight, and no specific characteristics were found.



**Figure 11.** Predicting crop ground truth data through area index: (A) fresh weight, (B) leaf length, (C) leaf width, and (D) number of leaves.



#### 4. Discussion

Among the phenotypic indices, the area that was the most intuitive index for crop growth was a part of the projected pixel points obtained from the top view. Although the area index would be different from the actual area because the index was calculated based on the top projection image without considering the lateral information, it can be used to provide spatial-temporal information of growing lettuces. Specifically, the site-specific growth monitoring might be feasible for the small number of plants because the variations in growth are displayed from the images for all growth periods [19,42]. In fact, this index enabled us to clearly identify both spatial variation in growth and differences in the photoperiods (Figures 9 and 10). In particular, looking at the control condition graph in Figure 10A, it can be seen that the y-axis value decreases at the beginning of the change from the dark period to the light period, and then it gradually increases thereafter. This is considered to be a phenomenon that occurs because the leaf area is expanded due to the horizontal decrease in the leaf during the dark period [31,43]. It can be seen from the graph that it decreases again as the light period begins, but it gradually increases again with plant growth. Meanwhile, another analysis was possible. Under the experimental conditions, when the light period was twice that of the dark stage, and considering the length of the x-axis expressed in the graph, it can be judged that the growth of the crop mainly occurred during the dark stage (Figure 10A). At the beginning of the experiment, the difference was less than two times, but on day 7, the difference in area was slightly larger. Initially, the control group showed similar or slightly smaller values, but 7 days after planting, it showed a larger value than the pulse group. In fact, even in the destruction data, the group with a change in the photoperiod had poor growth, and the final weight showed a difference of 13.89 g when comparing the average value based on the fresh weight of the above-ground part; thus, it was interpreted that this part was revealed by the area index. The initial hypothesis was that the efficiency could be increased by changing the photoperiod, but it was judged that the efficiency was rather low due to the short light period. The length of the contour was similar to that of the area, indicating a difference between the two groups. However, unlike the area index, where the difference gradually increased, the length of the contour showed an initial large difference, which gradually decreased (Figure 10B). As the crop grew, the edge of the leaf flattened, and the curvature seemed to disappear due to overlapping. Therefore, a different tendency from the continuously increasing area index was observed. In particular, a relatively fast saturation phenomenon was observed in the control group. The minimum and maximum radii from the center were also projected values, and the minimum length index was not suitable for analysis of the photoperiod (Figure 10C,D). This was because the minimum radius showed a large change depending on the growth of new leaves and the effect of the light period. The maximum radius showed a tendency similar to that of the area at the beginning, but with saturation at a relatively early period, and the two groups reached the same value in the second half of the experiment. Unlike the area and contour length indices that could increase in various directions on the image, the maximum radius index could not be measured beyond the measurable range; therefore, this point is shown in the graph. Moreover, researchers or growers can add new phenotypic indices based on the camera network system. Then, the system could be used for building a new phenotyping model by building a new model between the phenotypic indices and plant physiological behaviors such as nutrient deficiencies, diseases, or pests.

When referring to studies relating to fresh weight, it was found that the analysis using the area index extracted from this study has explanatory power, and it can be said that the low error shows the accuracy of the measurement (Figure 11A) [3,44]. Similarly, it was confirmed that the maximum radius index and the contour index had a high coefficient of determination in each leaf length and leaf width (Figure 11B,C). The results show the usefulness of the system for monitoring and determining the phenotypic indices of growing plants.

From the index, the growth of different light/dark cycle were observed and compared. The growth of the pul group was lower than that of the con group, indicating the longer

light/dark cycle would be more beneficial for vegetative growth of lettuces. Specifically, lettuce biomass did not change unidirectionally with the extension or shortening of the light/dark cycle, but only specific light/dark cycle can strengthen root growth and water absorption of lettuces [32,45]. Therefore, it is important to find the optimal cycle of the illumination on growing lettuces. The results show the developed system would provide the continuous monitoring of growing lettuces, thereby allowing more effective and rapid analysis on such variables.

Table 3 shows the comparison of the high-throughput plant phenotyping system developed in this study with other existing systems. The most expensive system using a 3D camera array showed a highly accurate measurement performance with a slope of 1.01 and  $R^2$  of 0.99 in the comparison with the actual values [46]. The automated growth measurement system using a conveyer also showed a highly linear predictability for the fresh weight, with a slope near 1.0 and  $R^2$  of 0.95 [18]. Although the predictability of the developed system is lower than those systems (Figure 11), it is comparable to other systems with  $R^2$  of 0.6–0.8 [20,21]. Considering the performance, a total cost of USD 1200 is quite reasonable. The system also can measure various phenotypic characteristics and has a high degree of freedom in analysis compared to other systems. Moreover, the use of other devices might be limited due to their high costs or spatial reasons in densely growing environment such as plant factories. In contrast, the proposed system has excellent space efficiency through a small-sized camera module and a network-based multi-connection protocol. Continuous monitoring of phenotypic indices relating to height, leaf area, volume and biomass are effective parameters that could allow farmers to conduct better fertilizer and water management as well as scheduling of their harvest [47,48]. In plant factories, leafy vegetables are usually harvested when the leaves reach full vegetative growth; thus, it is important to monitor the growth during the vegetative stage. Accordingly, in this paper, lettuce observation was continued from two days after transplantation until the end of the first harvest, and usable phenotypic indices were successfully presented.

**Table 3.** Comparison of the camera network system with the on-the-go monitoring system by Jiang, Kim and Cho [18].

System	Plant	No. of Plants	Phenotypic Characteristics	Code Availability	Cost	Ref.
Camera array HTPP *	Arabidopsis	1050	3	Commercial + Not open	~USD 43,200 (including camera)	[46]
Greenhouse-based HTPP *	Maize	756	3	Open	~USD 5000 (including camera)	[21]
An automated growth measurement system	Boston lettuce	45	4	Not open	~USD 2200 (including camera)	[18]
Sliding phenotyping platform	Maize, Tomato, Olive	1	8	Commercial	~USD 1300 (without camera)	[20]
Our system	Batavia lettuce	24	10	Open	~USD 1200 (including camera)	-

\* HTPP: high-throughput plant phenotyping.

From the above results, it is demonstrated that the developed system can be applied to the real-time analysis of growth differences by group for various growth condition changes in plant factories, as well as spatial variation analyses according to the visualization of growth distribution. In future research, we will improve the measurement performance of the system by adding a side-view camera to collect information about crop height and areas that cannot be observed from the top view. In particular, we intend to apply a machine learning algorithm to the various phenotypic indices collected from the system to understand more complex crop-growth information and to develop a web-based interface, such that users can freely select and modify functions for each process.



## 5. Conclusions

In this study, we developed an analysis system for high-speed mass phenotyping based on a multi-point camera network using low-cost cameras and processor boards. To ensure its applicability to various cultivation structures and environments, a server computer was configured for several image collection modules to automatically import data from multiple points. Transmission stabilization conditions were applied for data collection stability, and a large amount of image information was transmitted from the local to the main server at daily intervals. When the transmission was completed, an ROI image was obtained through background separation, and 10 phenotypic indices were calculated using an image processing algorithm. The processing time of approximately 2.43 s per image confirmed the real-time analysis performance of the developed system. By applying the system to a commercial plant factory environment, it was possible to determine the growth distribution information and the influence of the growth environment for each individual based on various phenotypic indices through the data frame, confirming its feasible application. The projected area index-based estimation for fresh weight, leaf length, leaf width, and the number of leaves shows a high  $R^2$  over than 0.9, indicating the system would be feasible for monitoring the growth information of growing lettuces. In addition, the high scalability of easily removing or adding programming parts through modularization of the calculation and analysis structure of the phenotypic index can be useful for growers or researchers who are concerned. In future research, we intend to introduce a side-view camera for crop height analysis and strengthen the field usability by adding machine learning algorithms. Overall, the developed system is expected to effectively help crop-growth management, as it can respond to changes in the dense plant factory cultivation environment and structural changes through low-cost camera installation and network connection configuration.

**Author Contributions:** Conceptualization, M.Y.; methodology, M.Y. and W.-J.C.; software, M.Y. and W.-J.C.; validation, M.Y.; formal analysis, M.Y. and W.-J.C.; writing—original draft preparation, M.Y. and W.-J.C.; writing—review and editing, M.Y. and W.-J.C.; visualization, M.Y. and W.-J.C.; supervision, M.Y.; project administration, M.Y.; funding acquisition, M.Y. All authors have read and agreed to the published version of the manuscript.

**Funding:** This work was supported by the National Research Foundation of Korea (NRF) grant funded by the Korea government (MSIT) (No. 2022R1C1C2005959), and the Technology development Program funded by the Ministry of SMEs and Startups (G21S325921401).

**Institutional Review Board Statement:** Not applicable.

**Data Availability Statement:** The data and code used in this study are available from the corresponding author upon request.

**Acknowledgments:** The authors would like to thank n.thing Inc. Republic of Korea for providing a container-type vertical farm.

**Conflicts of Interest:** The funders had no role in the design of the study; in the collection, analyses, or interpretation of data; in the writing of the manuscript; or in the decision to publish the results.

## References

1. Li, L.; Zhang, Q.; Huang, D. A review of imaging techniques for plant phenotyping. *Sensors* **2014**, *14*, 20078–20111. [CrossRef] [PubMed]
2. Chen, D.; Neumann, K.; Friedel, S.; Kilian, B.; Chen, M.; Altmann, T.; Klukas, C. Dissecting the Phenotypic Components of Crop Plant Growth and Drought Responses Based on High-Throughput Image Analysis. *Plant Cell* **2014**, *26*, 4636–4655. [CrossRef]
3. Chen, W.-T.; Yeh, Y.-H.F.; Liu, T.-Y.; Lin, T.-T. An automated and continuous plant weight measurement system for plant factory. *Front. Plant Sci.* **2016**, *7*, 392. [CrossRef]
4. Fahlgren, N.; Gehan, M.A.; Baxter, I. Lights, camera, action: High-throughput plant phenotyping is ready for a close-up. *Curr. Opin. Plant Biol.* **2015**, *24*, 93–99. [CrossRef]
5. Kacira, M.; Ling, P. Design and development of an automated and Non-contact sensing system for continuous monitoring of plant health and growth. *Trans. ASABE* **2001**, *44*, 989. [CrossRef]
6. Sonnentag, O.; Hufkens, K.; Teshera-Sterne, C.; Young, A.M.; Friedl, M.; Braswell, B.H.; Milliman, T.; O’Keefe, J.; Richardson, A.D. Digital repeat photography for phenological research in forest ecosystems. *Agric. Meteorol.* **2012**, *152*, 159–177. [CrossRef]

7. Jiang, Y.; Li, C.; Paterson, A.H. High throughput phenotyping of cotton plant height using depth images under field conditions. *Comput. Electron. Agric.* **2016**, *130*, 57–68. [CrossRef]
8. Barker III, J.; Zhang, N.; Sharon, J.; Steeves, R.; Wang, X.; Wei, Y.; Poland, J. Development of a field-based high-throughput mobile phenotyping platform. *Comput. Electron. Agric.* **2016**, *122*, 74–85. [CrossRef]
9. Ge, Y.; Bai, G.; Stoerger, V.; Schnable, J.C. Temporal dynamics of maize plant growth, water use, and leaf water content using automated high throughput RGB and hyperspectral imaging. *Comput. Electron. Agric.* **2016**, *127*, 625–632. [CrossRef]
10. Naik, H.S.; Zhang, J.; Lofquist, A.; Assefa, T.; Sarkar, S.; Ackerman, D.; Singh, A.; Singh, A.K.; Ganapathysubramanian, B. A real-time phenotyping framework using machine learning for plant stress severity rating in soybean. *Plant Methods* **2017**, *13*, 23. [CrossRef]
11. Granier, C.; Aguirrezabal, L.; Chenu, K.; Cookson, S.J.; Dauzat, M.; Hamard, P.; Thioux, J.J.; Rolland, G.; Bouchier-Combaud, S.; Lebaudy, A. PHENOPSIS, an automated platform for reproducible phenotyping of plant responses to soil water deficit in *Arabidopsis thaliana* permitted the identification of an accession with low sensitivity to soil water deficit. *New Phytol.* **2006**, *169*, 623–635. [CrossRef] [PubMed]
12. Tisné, S.; Serrand, Y.; Bach, L.; Gilbault, E.; Ben Ameer, R.; Balasse, H.; Voisin, R.; Bouchez, D.; Durand-Tardif, M.; Guerche, P. Phenoscope: An automated large-scale phenotyping platform offering high spatial homogeneity. *Plant J.* **2013**, *74*, 534–544. [CrossRef] [PubMed]
13. Hartmann, A.; Czauderna, T.; Hoffmann, R.; Stein, N.; Schreiber, F. HTPheno: An image analysis pipeline for high-throughput plant phenotyping. *BMC Bioinform.* **2011**, *12*, 148. [CrossRef] [PubMed]
14. Shankar, T.; Malik, G.C.; Banerjee, M.; Dutta, S.; Praharaj, S.; Lalichetti, S.; Mohanty, S.; Bhattacharyay, D.; Maitra, S.; Gaber, A. Prediction of the effect of nutrients on plant parameters of rice by artificial neural network. *Agronomy* **2022**, *12*, 2123. [CrossRef]
15. Joo, H.-J.; Jeong, H.-Y. Growth analysis system for IT-based plant factory. *Multimed. Tools Appl.* **2017**, *76*, 17785–17799. [CrossRef]
16. Kang, W.H.; Zhang, F.; Lee, J.W.; Son, J.E. Improvement of canopy light distribution, photosynthesis, and growth of lettuce (*Lactuca sativa* L.) in plant factory conditions by using filters to diffuse light from LEDs. *Hortic. Sci. Technol.* **2016**, *34*, 84–93. [CrossRef]
17. Moriyuki, S.; Fukuda, H. High-Throughput Growth Prediction for *Lactuca sativa* L. Seedlings Using Chlorophyll Fluorescence in a Plant Factory with Artificial Lighting. *Front. Plant Sci.* **2016**, *7*, 394. [CrossRef]
18. Jiang, J.-s.; Kim, H.-J.; Cho, W.-J. On-the-go image processing system for spatial mapping of lettuce fresh weight in plant factory. *IEAC-Pap.* **2018**, *51*, 130–134. [CrossRef]
19. Yeh, Y.-H.F.; Lai, T.-C.; Liu, T.-Y.; Liu, C.-C.; Chung, W.-C.; Lin, T.-T. An automated growth measurement system for leafy vegetables. *Biosyst. Eng.* **2014**, *117*, 43–50. [CrossRef]
20. Rossi, R.; Leolini, C.; Costafreda-Aumedes, S.; Leolini, L.; Bindi, M.; Zaldei, A.; Moriondo, M. Performances Evaluation of a Low-Cost Platform for High-Resolution Plant Phenotyping. *Sensors* **2020**, *20*, 3150. [CrossRef]
21. Yassue, R.M.; Galli, G.; Borsato, R., Jr.; Cheng, H.; Morota, G.; Fritsche-Neto, R. A low-cost greenhouse-based high-throughput phenotyping platform for genetic studies: A case study in maize under inoculation with plant growth-promoting bacteria. *Plant Phenome J.* **2022**, *5*, e20043. [CrossRef]
22. Bari, M.A.A.; Fonseka, D.; Stenger, J.; Zitnick-Anderson, K.; Atanda, S.A.; Morales, M.; Worrall, H.; Piche, L.; Kim, J.; Johnson, J. A greenhouse-based high-throughput phenotyping platform for identification and genetic dissection of resistance to *Aphanomyces* root rot in field pea. *Plant Phenome J.* **2023**, *6*, e20063. [CrossRef]
23. An, N.; Palmer, C.M.; Baker, R.L.; Markelz, R.J.C.; Ta, J.; Covington, M.F.; Maloof, J.N.; Welch, S.M.; Weinig, C. Plant high-throughput phenotyping using photogrammetry and imaging techniques to measure leaf length and rosette area. *Comput. Electron. Agric.* **2016**, *127*, 376–394. [CrossRef]
24. Thrash, T.; Lee, H.; Baker, R.L. A low-cost high-throughput phenotyping system for automatically quantifying foliar area and greenness. *Appl. Plant Sci.* **2022**, *10*, e11502. [CrossRef]
25. Gang, M.-S.; Kim, H.-J.; Kim, D.-W. Estimation of Greenhouse Lettuce Growth Indices Based on a Two-Stage CNN Using RGB-D Images. *Sensors* **2022**, *22*, 5499. [CrossRef]
26. Kozai, T. Current status of plant factories with artificial lighting (PFALs) and smart PFALs. In *Smart Plant Factory: The Next Generation Indoor Vertical Farms*; Springer: Singapore, 2018; pp. 3–13.
27. Coelho, A.F.S.; Gomes, É.P.; Sousa, A.d.P.; Glória, M.B.A. Effect of irrigation level on yield and bioactive amine content of American lettuce. *J. Sci. Food Agric.* **2005**, *85*, 1026–1032. [CrossRef]
28. Liu, Z.; Xu, Q. An Automatic Irrigation Control System for Soilless Culture of Lettuce. *Water* **2018**, *10*, 1692. [CrossRef]
29. Wortman, S.E. Crop physiological response to nutrient solution electrical conductivity and pH in an ebb-and-flow hydroponic system. *Sci. Hortic.* **2015**, *194*, 34–42. [CrossRef]
30. Shao, M.; Liu, W.; Zha, L.; Zhou, C.; Zhang, Y.; Li, B. Altering light–dark cycle at pre-harvest stage regulated growth, nutritional quality, and photosynthetic pigment content of hydroponic lettuce. *Acta Physiol. Plant.* **2021**, *43*, 9. [CrossRef]
31. Fricke, W. Night-time transpiration–favouring growth? *Trends Plant Sci.* **2019**, *24*, 311–317. [CrossRef]
32. Chen, X.-l.; Yang, Q.-c. Effects of intermittent light exposure with red and blue light emitting diodes on growth and carbohydrate accumulation of lettuce. *Sci. Hortic.* **2018**, *234*, 220–226. [CrossRef]
33. Ma, X.; Zhu, K.; Guan, H.; Feng, J.; Yu, S.; Liu, G. High-throughput phenotyping analysis of potted soybean plants using colorized depth images based on a proximal platform. *Remote Sens.* **2019**, *11*, 1085. [CrossRef]

34. Sinoquet, H.; Thanisawanyangkura, S.; Mabrouk, H.; Kasemsap, P. Characterization of the light environment in canopies using 3D digitising and image processing. *Ann. Bot.* **1998**, *82*, 203–212. [CrossRef]
35. Riehle, D.; Reiser, D.; Griepentrog, H.W. Robust index-based semantic plant/background segmentation for RGB-images. *Comput. Electron. Agric.* **2020**, *169*, 105201. [CrossRef]
36. Woebbecke, D.M.; Meyer, G.E.; Von Bargen, K.; Mortensen, D. Color indices for weed identification under various soil, residue, and lighting conditions. *Trans. ASAE* **1995**, *38*, 259–269. [CrossRef]
37. Hassanein, M.; Lari, Z.; El-Sheimy, N. A New Vegetation Segmentation Approach for Cropped Fields Based on Threshold Detection from Hue Histograms. *Sensors* **2018**, *18*, 1253. [CrossRef] [PubMed]
38. Jiao, Y.; Luo, R.; Li, Q.; Deng, X.; Yin, X.; Ruan, C.; Jia, W. Detection and Localization of Overlapped Fruits Application in an Apple Harvesting Robot. *Electronics* **2020**, *9*, 1023. [CrossRef]
39. Sibiya, M.; Sumbwanyambe, M. An Algorithm for Severity Estimation of Plant Leaf Diseases by the Use of Colour Threshold Image Segmentation and Fuzzy Logic Inference: A Proposed Algorithm to Update a “Leaf Doctor” Application. *AgriEngineering* **2019**, *1*, 205–219. [CrossRef]
40. Upadhyaya, H.D.; Ortiz, R.; Bramel, P.J.; Singh, S. Phenotypic diversity for morphological and agronomic characteristics in chickpea core collection. *Euphytica* **2002**, *123*, 333–342. [CrossRef]
41. Li, D.; Li, C.; Yao, Y.; Li, M.; Liu, L. Modern imaging techniques in plant nutrition analysis: A review. *Comput. Electron. Agric.* **2020**, *174*, 105459. [CrossRef]
42. Lee, U.; Chang, S.; Putra, G.A.; Kim, H.; Kim, D.H. An automated, high-throughput plant phenotyping system using machine learning-based plant segmentation and image analysis. *PLoS ONE* **2018**, *13*, e0196615. [CrossRef]
43. Zweifel, R.; Sterck, F.; Braun, S.; Buchmann, N.; Eugster, W.; Gessler, A.; Häni, M.; Peters, R.L.; Walthert, L.; Wilhelm, M.; et al. Why trees grow at night. *New Phytol.* **2021**, *231*, 2174–2185. [CrossRef]
44. Jung, D.-H.; Park, S.H.; Han, X.Z.; Kim, H.-J. Image processing methods for measurement of lettuce fresh weight. *J. Biosyst. Eng.* **2015**, *40*, 89–93. [CrossRef]
45. Chen, X.-l.; Li, Y.-l.; Wang, L.-c.; Yang, Q.-c.; Guo, W.-z. Responses of butter leaf lettuce to mixed red and blue light with extended light/dark cycle period. *Sci. Rep.* **2022**, *12*, 6924. [CrossRef] [PubMed]
46. An, N.; Welch, S.M.; Markelz, R.J.C.; Baker, R.L.; Palmer, C.M.; Ta, J.; Maloof, J.N.; Weinig, C. Quantifying time-series of leaf morphology using 2D and 3D photogrammetry methods for high-throughput plant phenotyping. *Comput. Electron. Agric.* **2017**, *135*, 222–232. [CrossRef]
47. Buelvas, R.M.; Adamchuk, V.I.; Leksono, E.; Tikasz, P.; Lefsrud, M.; Holoszkiwicz, J. Biomass estimation from canopy measurements for leafy vegetables based on ultrasonic and laser sensors. *Comput. Electron. Agric.* **2019**, *164*, 104896. [CrossRef]
48. Hu, Y.; Wang, L.; Xiang, L.; Wu, Q.; Jiang, H. Automatic Non-Destructive Growth Measurement of Leafy Vegetables Based on Kinect. *Sensors* **2018**, *18*, 806. [CrossRef] [PubMed]

**Disclaimer/Publisher’s Note:** The statements, opinions and data contained in all publications are solely those of the individual author(s) and contributor(s) and not of MDPI and/or the editor(s). MDPI and/or the editor(s) disclaim responsibility for any injury to people or property resulting from any ideas, methods, instructions or products referred to in the content.

## Article

# Quantifying Soil Particle Settlement Characteristics through Machine Vision Analysis Utilizing an RGB Camera

Donggeun Kim <sup>1</sup>, Jisu Song <sup>2</sup> and Jaesung Park <sup>2,\*</sup><sup>1</sup> Graduate School of Agriculture, Kyoto University, Kyoto 606-8502, Japan; fty3000@snu.ac.kr<sup>2</sup> Department of Bio-Industrial Machinery Engineering, Pusan National University, Miryang 50463, Republic of Korea; jisu9380@pusan.ac.kr

\* Correspondence: jaesung.park@pusan.ac.kr

**Abstract:** Soil particle size distribution is a crucial factor in determining soil properties and classifying soil types. Traditional methods, such as hydrometer tests, have limitations in terms of time required, labor, and operator dependency. In this paper, we propose a novel approach to quantify soil particle size analysis using machine vision analysis with an RGB camera. The method aims to overcome the limitations of traditional techniques by providing an efficient and automated analysis of fine-grained soils. It utilizes a digital camera to capture the settling properties of soil particles, eliminating the need for a hydrometer. Experimental results demonstrate the effectiveness of the machine vision-based approach in accurately determining soil particle size distribution. The comparison between the proposed method and traditional hydrometer tests reveals strong agreement, with an average deviation of only 2.3% in particle size measurements. This validates the reliability and accuracy of the machine vision-based approach. The proposed machine vision-based analysis offers a promising alternative to traditional techniques for assessing soil particle size distribution. The experimental results highlight its potential to revolutionize soil particle size analysis, providing precise, efficient, and cost-effective analysis for fine-grained soils.

**Keywords:** soil particle size analysis; machine vision; RGB camera; settling characteristic; image analysis

**Citation:** Kim, D.; Song, J.; Park, J. Quantifying Soil Particle Settlement Characteristics through Machine Vision Analysis Utilizing an RGB Camera. *Agriculture* **2023**, *13*, 1674. <https://doi.org/10.3390/agriculture13091674>

Academic Editor: Ju-Seok Nam

Received: 4 July 2023

Revised: 21 August 2023

Accepted: 22 August 2023

Published: 24 August 2023



**Copyright:** © 2023 by the authors. Licensee MDPI, Basel, Switzerland. This article is an open access article distributed under the terms and conditions of the Creative Commons Attribution (CC BY) license (<https://creativecommons.org/licenses/by/4.0/>).

## 1. Introduction

Soil is composed of particles with varying sizes [1], and its properties vary depending on the particle size distribution. Soil texture is determined by its sand, silt, and clay content, and it is divided into coarse- and fine-grained soils based on the particle size distribution. These soil classifications are crucial because they facilitate the easy identification of general soil characteristics.

Particle size analysis separates soil by size to determine the particle size distribution [1]. Particle size analysis is one of the most basic and important soil property tests because soils can be classified according to their particle size distributions [2–4]. Using this method, the particle size distribution curve, which is the relationship curve of the percent finer (P) as a function of the particle size (D) of the soil, can be obtained. In addition to soil classification, the results of particle size analysis can be used for purposes such as index testing, profiling, and compliance [5]. They can also be used to estimate various soil properties such as permeability, shear strength, compressibility, conductivity, and consolidation [2,3].

In the particle size analysis tests, the particles with a diameter of 0.075 mm or more are analyzed via sieve analysis, and those with smaller diameters are analyzed using hydrometer testing [1–4,6–8]. Hydrometer testing is a test method for determining the particle size distribution of soil particles by measuring the change in density in a soil–water suspension over time as the soil particles settle in the suspension [2].

Hydrometer tests are widely used but have some limitations [9]. For example, they can be time- and labor-consuming [10] and exhibits operator and instrument dependency [3].

The hydrometer test involves multiple steps, including soil dispersion, sedimentation, and reading the hydrometer scale at specific time intervals. This makes it difficult to analyze a multitude of soil samples within a short period. Moreover, the accuracy of the hydrometer test depends on the skills and experience of the operator. Appropriate sample preparation, handling, and accurate hydrometer scale are critical for obtaining reliable results. Reading the hydrometer scale can be challenging because of several factors. The scale is often small and requires precise measurement. Variations in technique between different operators may introduce inconsistencies and affect the accuracy of the analysis. Despite these drawbacks, hydrometer testing is widely used for particle size analysis of fine-grained soils owing to its moderate cost, wide availability, and extensive existing references [5].

There are many alternatives to hydrometer testing, including laser diffraction (LD), X-ray absorption, and gamma-ray attenuation methods [8]. The aforementioned methods afford faster analysis and higher accuracy compared to hydrometer tests. However, they require specialized equipment for experimentation, which can be expensive to purchase, operate, and maintain. In particular, compared to experimental methods such as sieve analysis or pipette method, the test cost per sample is approximately 3 to 10 times more expensive, and the equipment cost is approximately 10 to 25 times more expensive [5]. As a result, these alternative methods have limitations that make them difficult to use except in specialized labs. It is also worth noting that hydrometer tests typically use 50 g of sample, whereas the aforementioned methods use much smaller amounts of sample; this can lead to problems concerning the representativeness of the test results [8]. In this regard, the sieve-hydrometer method is still widely used as the most representative method of soil particle size analysis.

Digital image analysis essentially entails analysis based on features found in a digital image of an object [11,12]. The process of analyzing digital images to quickly make a desired decision is referred to as machine vision. Digital image analysis is fast, inexpensive, and repeatable and has a wide range of applications [13–17]. As regards soils, digital image analysis is also being used to predict various soil properties such as water content [12,18–20], density [12,20], soil cracks [21,22], permeability [23,24], settling velocity [25,26] and strength [27,28].

Analyzing particle size distribution is also possible via digital image analysis. Soil particle size analysis through digital image analysis can be divided into two methods: measuring the size of individual particles in images and predicting the particle size distribution based on the features in the images. Measuring the size of individual particles is a widely used method for aggregates. Mora et al. [29] performed particle size analysis of coarse aggregates from 6.3 to 28 mm with high accuracy by digital image analysis. Ohm and Hryciw [16] developed a new image-based test called “sedimaging” to analyze particle sizes in the range of 0.075–2.0 mm, which has been typically performed by sieve analysis. Sudarsan et al. [30] characterized soil particle sizes using image analysis of microscope images. Bittelli et al. [31] conducted a comparative analysis of the pipette method, SediGraph method, LD method, and automated digital image analysis to determine the appropriate test method for particle size analysis of fine-graded soil and recommended the LD method as the standard method. Sun et al. [32] proposed a minimum image quality to obtain reliable results in image-based soil particle shape characterization. However, in the case of fine-grained soils with particle sizes of 0.075 mm or less, the size distribution is difficult to predict with typical digital image analysis because of the extremely small size of the particles and the difficulty of separating individual particles. As a result, the particle size analysis of fine-grained soils using digital image analysis is still limited. Thus, it is necessary to develop a particle size analysis method based on digital image analysis to analyze the particle size of fine-grained soil affordably and quickly.

Therefore, this study devised a machine vision-based analysis method to replace the hydrometer test to perform particle size analysis of fine-grained soil. The test method was developed by applying the principles of the hydrometer test. To reduce operator dependency and errors in the readings, an experimental method that does not use a

hydrometer was proposed. A digital camera was used to analyze the settling properties of the soil, replacing the hydrometer. In particular, the analysis was performed based on digital images acquired using a conventional digital camera meant for general use. This enables efficient soil particle size analysis and affords the advantage of real-time analysis and automation.

This paper follows a structured approach to introduce a machine vision-based method for analyzing fine-grained soil particle sizes, aimed at replacing traditional hydrometer testing. It begins by outlining the rationale for the study and the development of the experimental technique, which eliminates the need for a hydrometer reading. The soil properties under investigation are detailed, and the methodology for particle size analysis, including sieve analysis and a particle size analyzer, is explained. The image acquisition process using a specially designed settling tank and digital camera is then elucidated. The core of the paper focuses on image analysis, establishing relationships between settling distance, particle size, and average image intensity, which replaces hydrometer readings. Results showcase the method's success in predicting particle size distribution across various soil types, followed by a discussion of practical considerations and limitations.

## 2. Hydrometer Test

The hydrometer test is a test method for obtaining the particle size distribution by measuring the density of soil–water suspension over time and obtaining the percent finer ( $P$ ) by particle diameter ( $D$ ) of the soil sample [7,33]. The hydrometer test calculates the diameter of a soil particle based on Stoke's law [3,4,34]. The settling velocity ( $v$ ) of a particle having diameter  $D$ , according to Stoke's law, is as follows:

$$v = \frac{g(\rho_s - \rho_w)}{18\mu} D^2, \quad (1)$$

where  $g$  is the gravitational acceleration,  $\rho_s$  is the density of the soil particle,  $\rho_w$  is the density of water, and  $\mu$  is the viscosity of water at  $T$  ( $^{\circ}\text{C}$ ). A particle having diameter  $D$  settles at a distance equal to the settling distance ( $L$ ) in an elapsed time ( $t$ ); therefore,  $v = L/t$ . Therefore,  $D$  can be determined as follows:

$$D = \sqrt{\frac{18\mu}{g(\rho_s - \rho_w)} \frac{L}{t}}. \quad (2)$$

$L$  at time  $t$  is measured on the basis of the hydrometer reading ( $\gamma$ ). When the hydrometer and measuring cylinder are tested as a pair,  $L$  and  $\gamma$  are in a linear relationship.

$$L = a\gamma + b. \quad (3)$$

Here,  $a$  and  $b$  are the slope and intercept, respectively. Assuming that at time  $t = 0$ , a particle of mass  $m_{s1}$  is uniformly suspended in a volume  $V$ , the mass of the particle contained is  $m_{s1}/V$  and the volume is  $m_{s1}/(V\rho_s)$  in a unit volume of suspension. Thus, the volume and mass of water in a unit volume of suspension are  $1 - m_{s1}/(V\rho_s)$ ,  $\rho_w(1 - m_{s1}/(V\rho_s))$ , respectively. Therefore, the density of the suspension ( $\rho$ ) is as follows:

$$\rho = \frac{m_{s1}}{V} + \left( \rho_w - \frac{m_{s1}\rho_w}{V\rho_s} \right) = \rho_w + \frac{m_{s1}}{V} \left( \frac{\rho_s - \rho_w}{\rho_s} \right) \quad (4)$$

At time  $t = t$ , only particles having diameters smaller than  $D$  are present at depths smaller than  $L$ . Therefore, if the ratio of the mass of the particles having diameters smaller than  $D$  to the total mass is denoted  $P(D)$ , the density of the suspension at  $L$  is

$$\rho = \rho_w + \frac{m_{s1}}{V} \left( \frac{\rho_s - \rho_w}{\rho_s} \right) \frac{P(D)}{100} \quad (5)$$

In this case,  $\rho$  has the following relationship to the hydrometer reading ( $\gamma$ ):

$$\frac{\rho_s - \rho_w}{\rho_w} = \gamma + C_m + F, \tag{6}$$

where  $C_m$  is meniscus correction and  $F$  is the temperature correction coefficient. Thus, using Equations (5) and (6),  $P(D)$  can be calculated as follows:

$$P(D) = \frac{V}{m_{s1}} \frac{\rho_s}{\rho_s - \rho_w} (\gamma + C_m + F) \rho_w \times 100. \tag{7}$$

### 3. Materials and Methods

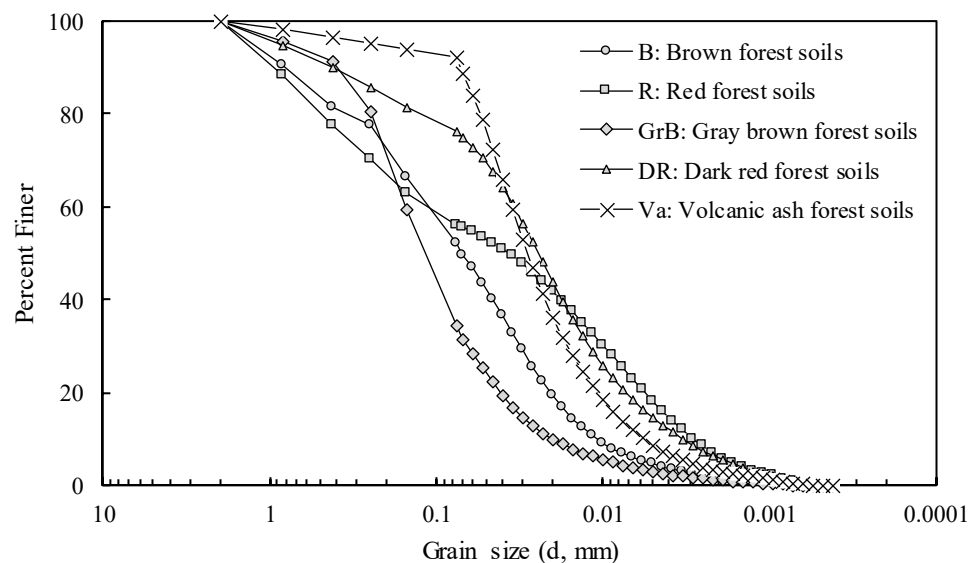
#### 3.1. Soil Properties

Table 1 summarizes an overview of the soil types used in the present study and their corresponding sampling locations. The investigation focused on five forest soils, namely, B, R, GrB, DR, and Va. These are representative soils in the Korean forest soil group.

**Table 1.** Description and sampling location of soil samples.

Soil Group (Subgroup)	Symbol	Latitude	Longitude
Brown forest soils	B	37.309404	127.30986
Red & yellow forest soils (Red forest soils)	R	37.23417	126.80021
Gray brown forest soils	GrB	35.98825	127.63727
Dark red forest soils	DR	37.28844	126.84164
Volcanic ash forest soils	Va	33.414417	126.48421

Particle size analysis and soil property tests were carried out on a set of five soil samples. The tests included a specific gravity test, as well as liquid and plastic limit tests (LL and PL), along with a loss of ignition (LOI) test. These experiments focused on particles measuring 2 mm or smaller. Furthermore, particle size analysis was performed on particles measuring 0.075 mm or larger using sieve analysis, while a particle size analyzer Malvern Mastersizer 2000 (Malvern Panalytical Ltd., Worcestershire, UK) was employed to analyze the smaller particles. The resulting particle size distribution curve for each soil sample, which combines the outcomes from the sieve analysis and particle size analyzer, is shown in Figure 1.



**Figure 1.** Particle size distribution curve of soil samples obtained using sieve analysis and a particle size analyzer.



Table 2 summarizes findings obtained from the particle size analysis and soil property tests. The specific gravity measurements for soil samples B, R, GrB, and DR were within the typical range for soils, while Va stood out with notably low specific gravity. Additionally, Va exhibited a significant LOI value of 32.6%, indicating a substantially higher organic matter content than the other soils examined. In terms of plasticity, B, GrB, and Va were classified as non-plastic, whereas R and DR showed low plasticity. Moving on to the particle size analysis results, GrB was identified as a coarse-grained soil, with 34.3% of particles passing through a 0.075 mm sieve, while the remaining were classified as fine-grained soils. Determining soil texture based on the sand, silt, and clay content proportions revealed that B, R, and GrB soils could be categorized as sandy loam, while DR and Va could be categorized as silt loam and silt, respectively.

**Table 2.** Result of soil property tests and particle size analysis.

Symbol	G <sub>s</sub> *	LL *	PI *	LOI *	<0.075 mm (%)	Sand (%)	Silt (%)	Clay (%)	USDA *
B	2.53	N.P. *	N.P.	12.9	52.1	52.2	46.1	1.7	Sandy Loam
R	2.59	36.64	20.67	6.8	56.0	45.2	48.6	6.2	Sandy Loam
GrB	2.61	N.P.	N.P.	6.9	34.3	70.6	28.2	1.2	Sandy Loam
DR	2.57	28.78	11.79	9.0	76.3	26.4	67.8	5.8	Silt Loam
Va	2.07	N.P.	N.P.	32.6	92.0	14.5	82.2	3.3	Silt

\* G<sub>s</sub>: Specific gravity, LL: Liquid limit (%), PI: Plastic index, N.P.: Non plastic. LOI: Loss of ignition (%), USDA: US Department of Agriculture.

### 3.2. Image Acquisition during Settlement of Soil Particles

In this study, we aimed to predict the particle size distribution of fine-grained soil with a diameter of 0.075 mm or less based on digital image analysis. For this purpose, it is necessary to acquire a series of digital images of the soil–water suspension during settlement. The particle size analysis of fine-grained soils was performed using the hydrometer test as aforementioned. The hydrometer test employs a measuring cylinder with an external scale for measuring the volume. In addition, measuring cylinders are typically made of glass, which can reflect light and result in low-quality images when used for capturing soil images. Hence, to overcome this issue, a settling tank was devised to replace the measuring cylinder, as illustrated in Figure 2.

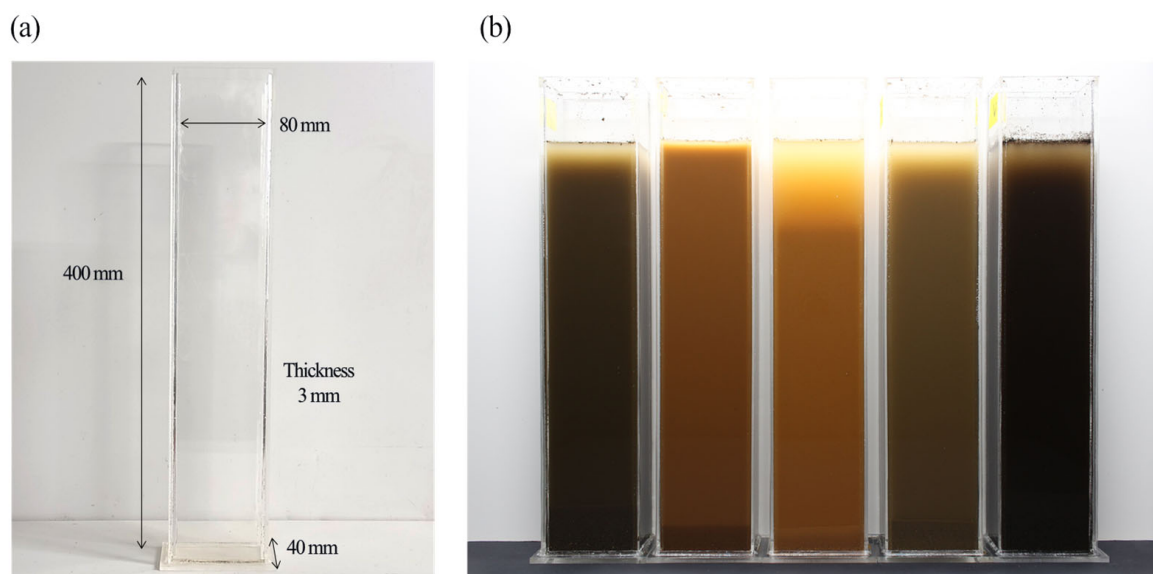


**Figure 2.** Settling tank for soil particle size analysis: (a) dimensions of settling tank; (b) experimental setup.

The settling tank used in the study has the following dimensions: a height of 400 mm, a width of 80 mm, and a depth of 40 mm. It is constructed using acrylic material having

a thickness of 3 mm. Each soil–water suspension in the settling tank weighs 100 g, and the total volume of the suspension is 1000 mL. Before adding the soil to the tank, it was thoroughly dried, and only the portion that passed through the 2 mm sieve was used, consistent with the particle size analysis test.

To capture digital images of the soil–water suspension during the settling process, a Canon EOS 100d camera (Canon Inc., Tokyo, Japan) was used. The photographs were acquired from the front of the settling tank, and a white matte plate was positioned at the back of the tank to eliminate color distortion caused by the background. The photography sessions were conducted in an indoor studio to maintain consistent lighting conditions. The camera settings were configured as follows: a shutter speed of 0.125 s, an aperture value of 5.6, and an ISO setting of 200.

For automated continuous shooting, the camera's shooting time was controlled by a computer. Canon's EOS Utility program was employed for this purpose. The elapsed time from the initiation of the settling process to the moment the  $n$ -th photograph was taken was defined as  $T_n$ .

In the hydrometer test, readings from the hydrometer are recorded at specific time intervals: around 1, 2, 4, 15, 30, 60, 240, and 1440 min, with the option for more readings to enhance accuracy. In this study, photographs were acquired every 10 s within the first 20 min, followed by intervals of one minute until 1520 min, and then at ten-minute intervals up to 2980 min. From this collection of images, those taken within the initial 120 s, as well as at 3, 4, 6, 8, 12, 15, 30, 60, 120, 240, 480, 960, and 1440 min, were chosen for in-depth analysis. As a result, a total of 25 images were utilized for the image analysis and particle size analysis.

### 3.3. Image Analysis

In Figure 3, a specific region of interest (ROI) is highlighted within the digital image. The ROI corresponds to the area spanning the top to the bottom of the soil–water suspension in each settling tank. This area was designated as the ROI for analysis purposes. The dimensions of the ROI are 400 pixels in width and 2400 pixels in height.

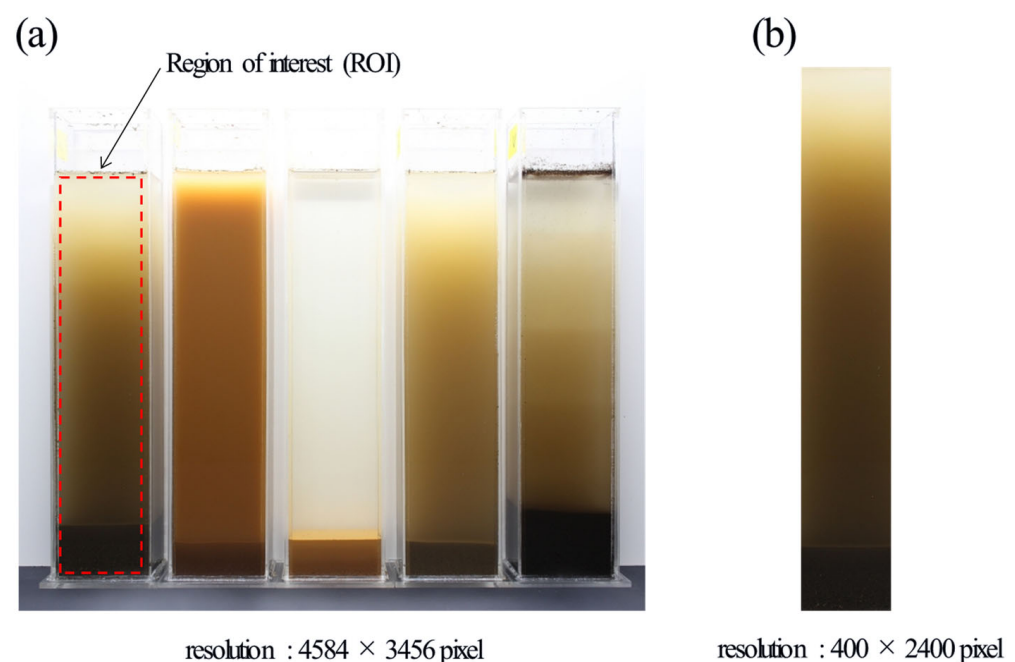


**Figure 3.** Region of interest in settling tank: (a) position of the region of interest; (b) cropped image of the region of interest.

Figure 4 illustrates the proposed concept of machine vision-based soil particle size analysis (MVSPSA). In the settling tank, the soil particles within the soil–water suspension gradually settle over time. As the particles settle, the color distribution within the suspension changes.

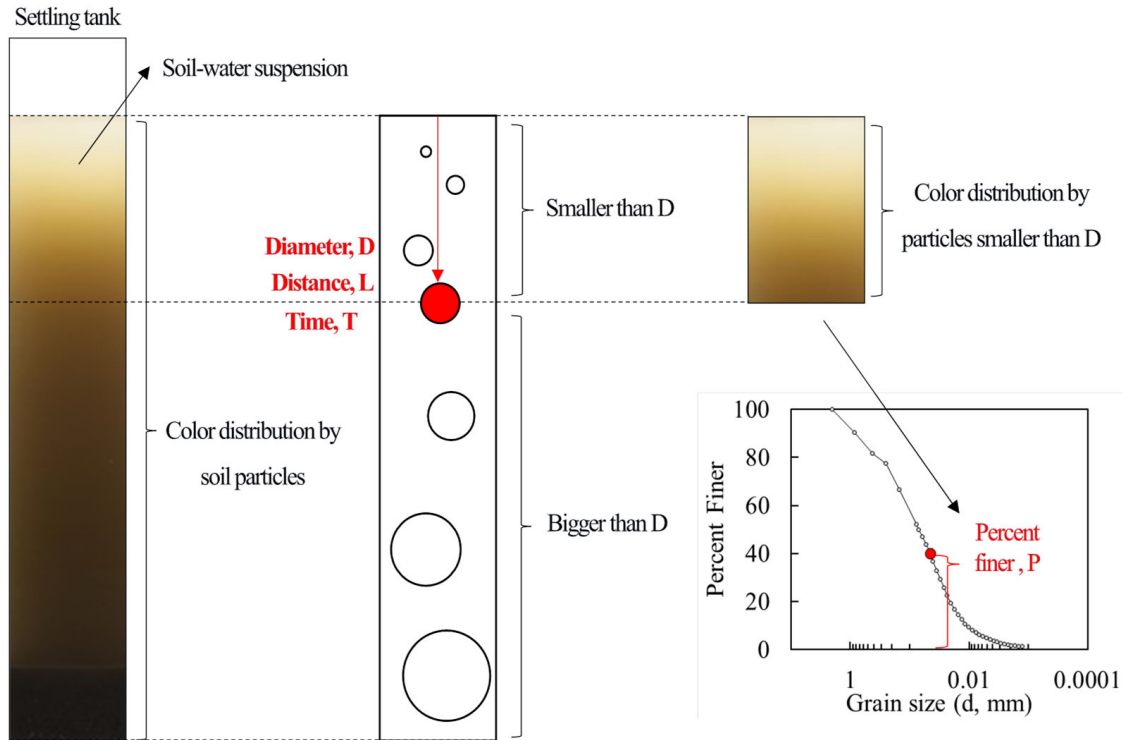


**Figure 4.** Conceptual diagram of machine vision-based soil particle size analysis.

The settling distance ( $L$ ), at time  $T$  for a particle having a diameter  $D$ , can be determined using Equation (2).  $L$  is directly proportional to the square of  $D$ . Consequently, particles that have settled below the distance  $L$  have sizes larger than  $D$ , whereas particles above the distance  $L$  have sizes smaller than  $D$ . Consequently, the color distribution in the image, specifically within the range of  $L$ , is primarily influenced by particles having diameters smaller than  $D$ .

In the hydrometer test, the hydrometer reading ( $\gamma$ ) at a particular value of  $L$  is measured using the hydrometer. This reading  $\gamma$  represents the density of the soil–water suspension, including particles having diameters smaller than  $D$  that have settled above  $L$ . According to Equation (7),  $\gamma$  is proportional to the percent finer ( $P$ ). Thus,  $\gamma$  serves as a measure of the weight of particles with sizes smaller than  $D$ . In this study, instead of using a hydrometer, we sought to represent the weights of the particles smaller than  $D$  by using image features.

Figure 5 depicts a schematic diagram of the movement of a particle of diameter  $D$  over time and its color change in a soil–water suspension. When the end of settlement of a particle with diameter  $D$  is  $T_i$ ,  $i$  images from  $T_1$  to  $T_i$  each contain images  $L_1$  to  $L_i$ . Each of these images represents the  $P$  values of particles smaller than  $D$ . Therefore,  $I_D$ , which is the average of the gray value of the  $i$ -th images ( $I_{D,i}$ ) taken from  $T_1$  to  $T_i$ , was calculated and used as a factor to predict the percent finer  $P$  of particles smaller than  $D$ .

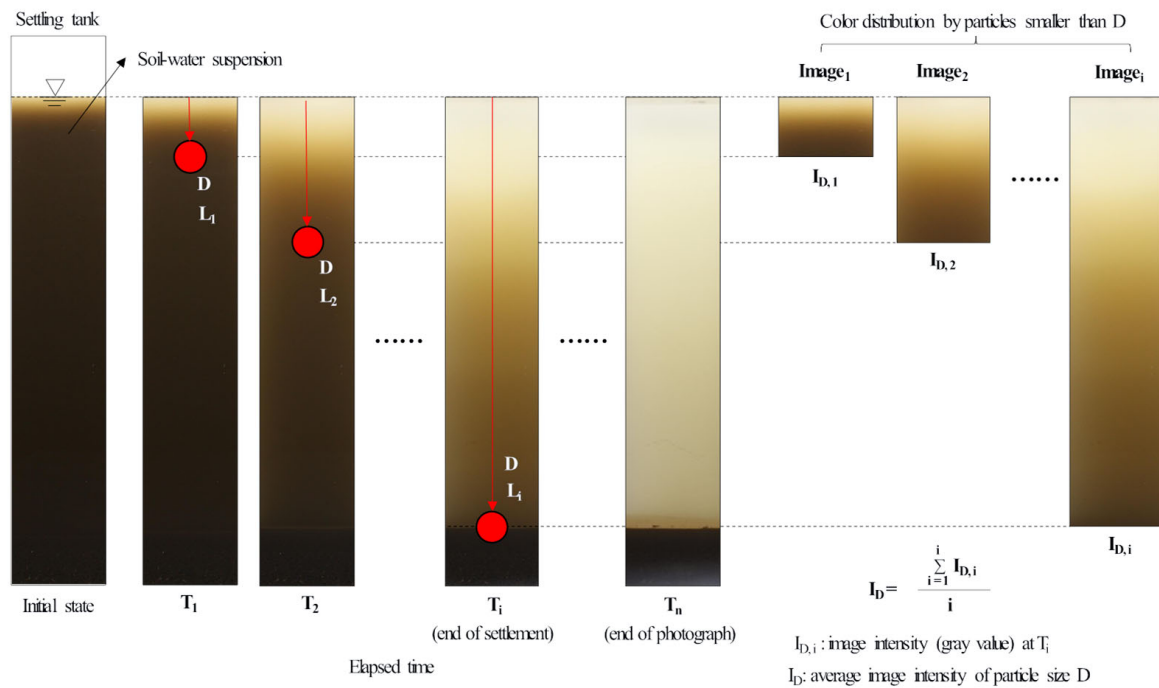


**Figure 5.** Calculation process of machine vision-based soil particle size analysis.

Python was utilized for performing image processing tasks, including crop and color extraction. Various libraries such as NumPy, pandas, pillow, OpenCV, and matplotlib, among others, were employed for this purpose. The ROI was extracted by cropping it from the original image. Subsequently, the ROI was converted into a grayscale image. To analyze the grayscale image, the average gray value was calculated from the top of the image up to a specific value of  $L$ .

Root mean squared error (RMSE) is used as a metric to evaluate the accuracy of image-based particle size analysis. RMSE is calculated as follows:

$$RMSE = \sqrt{\frac{1}{n} \sum_{i=1}^n (Predicted_i - Actual_i)^2} \tag{8}$$

where  $Predicted_i$  is the predicted  $i$ -th percent finer and  $Actual_i$  is the observed  $i$ -th percent finer.  $n$  is the number of data points.

#### 4. Results

##### 4.1. Image Analysis of Soil–Water Suspension during Settlement

Figure 6 shows the change in soil–water suspension and hydrometer reading during soil settlement over time. As time progresses, an observable trend emerges wherein the average color of the soil–water suspension gradually lightens. Specifically, in a soil–water suspension, the color tends to become lighter from the top downward. This phenomenon can be attributed to the gradual reduction in the concentration of suspended soil particles within the suspension. As settling occurs, the soil particles gradually settle down, leading to a decrease in their presence in the suspension. Consequently, the overall color of the suspension becomes lighter. Among the different soil types analyzed, Soil DR exhibited the most rapid color change, while Soil R exhibited the slowest. Within the initial 30-min period, most of the color change for Soil DR took place, with minimal additional color alteration thereafter.

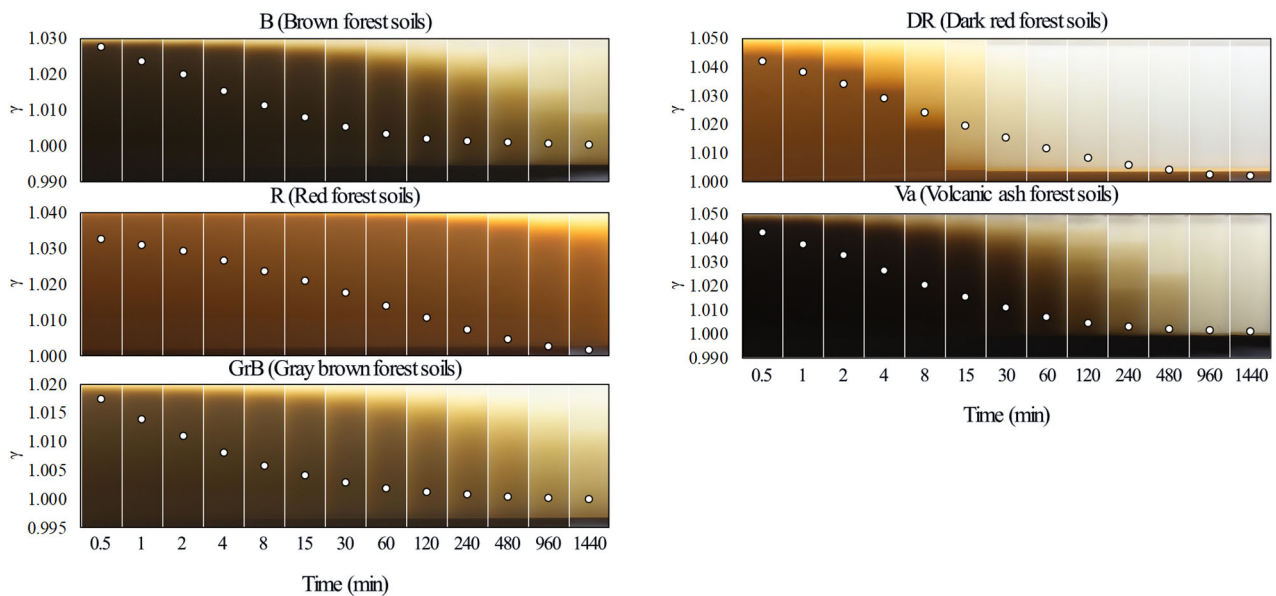


**Figure 6.** Changes in the hydrometer ( $\gamma$ ) reading and color in soil–water suspension according to time.

The presence of dark areas at the top of the region of interest (ROI) can be attributed to the settling of organic matter that was initially present on the water surface. During the settling process, these organic particles tend to migrate downward and accumulate in the upper portion of the ROI, resulting in the observed dark areas. On the other hand, at the bottom of the settling tank, particles that have completed the settling process are observed. It's important to note that the volume of settled particles after the settling process varies for each soil type. This discrepancy arises due to differences in particle size distribution, organic content, and other soil-specific characteristics. These variations result in differences in the volume of settled particles among different soil samples.

Additionally,  $\gamma$  gradually decreases over time in the settling process. The initial  $\gamma$  values differ among the soils due to variations in fine content (0.075 mm sieve passage). However, as the settling process progresses, the hydrometer readings ( $\gamma$ ) tend to converge towards a value close to 1. In hydrometer tests,  $\gamma$  is measured to calculate  $P$ , as expressed by Equation (7). Given this correlation between  $\gamma$  and particle sizes, it becomes feasible to explore whether certain image features of the soil change similarly to  $\gamma$ . By identifying image features that exhibit similar variations, the particle size distribution can be analyzed using image processing techniques.

Figure 7 shows the changes in gray value observed in a soil–water suspension as the settling process occurs. Over time, the gray value gradually increases, indicating a lightening of the soil–water suspension as the soil particles settle. The color change within the soil–water suspension varies across different elevations within ROI. Notably, the upper section of the soil–water suspension (0–10% range) exhibits significant color change initially but eventually converges towards a constant value after the completion of the settling process. In contrast, the lower section of the soil–water suspension (90–100% range) is where the sedimentation of the soil occurs. Consequently, the color value trend in this area differs from the rest of the ROI. For soil Va, it is worth noting that a relatively large volume of soil deposition occurs compared to the other soils. In fact, deposited soil is observed even within the 80–90% range of the suspension. As a result, subsequent analyses were performed within the 0–80% range of the ROI, excluding potential soil deposition, to ensure accurate color measurements in soil–water suspension.



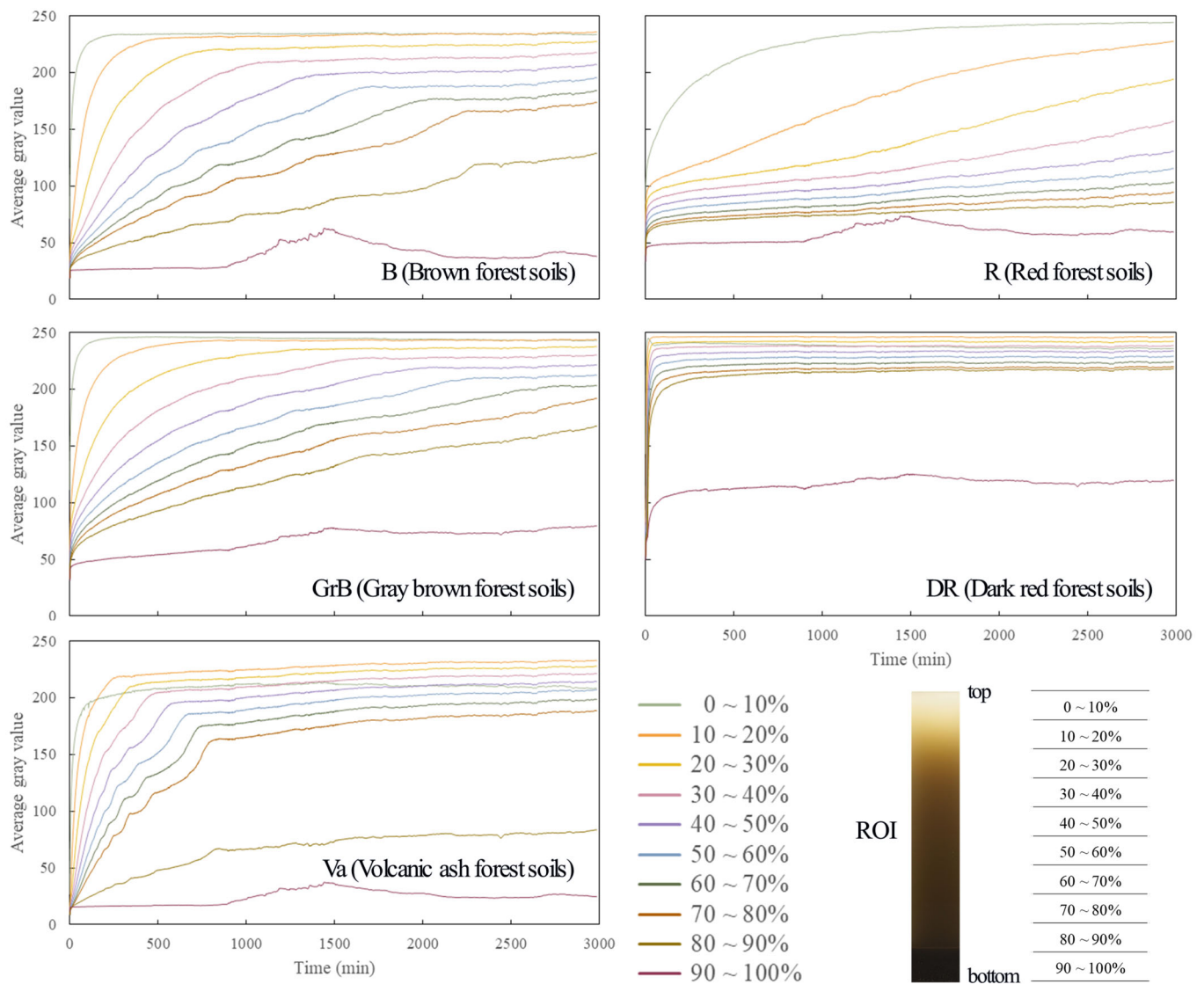


**Figure 7.** Changes of average gray value in soil–water suspension according to time.

#### 4.2. Prediction of Particle Size Distribution by MVSPSA

Figure 8 shows the relationship between  $L$  and  $D$  for soil B. According to Equation (3),  $L$  is proportional to the square of  $D$ . Hence, larger diameter particles exhibit increasingly rapid settlement. Considering that the height of the soil–water suspension in the settling tank is 38.4 cm, it can be observed that a particle with a diameter of 0.075 mm takes approximately 1.6 min to completely settle. In contrast, a particle with a diameter of 0.038 mm takes approximately 6 min. Furthermore, a smaller particle with a diameter of 0.002 mm settles a distance of 23.9 cm after 1440 min, while a particle with a diameter of 0.001 mm settles a distance of 6.0 cm. Using this approach, the value of  $L$ , based on the  $D$ , can be calculated for each soil type.  $L$  is also influenced by the specific gravity ( $G_s$ ) of the soil particles. This is because heavier particles tend to settle relatively faster. Consequently, soil types such as R, GrB, and DR, which have  $G_s$  approximately 1.5–3% higher than that of soil B, would exhibit increased values of  $L$  compared to soil B. In contrast, soil Va, with  $G_s$  approximately 18% smaller than that of soil B, shows a slower settling velocity compared to other soils, resulting in a decrease in  $L$  over the same period.

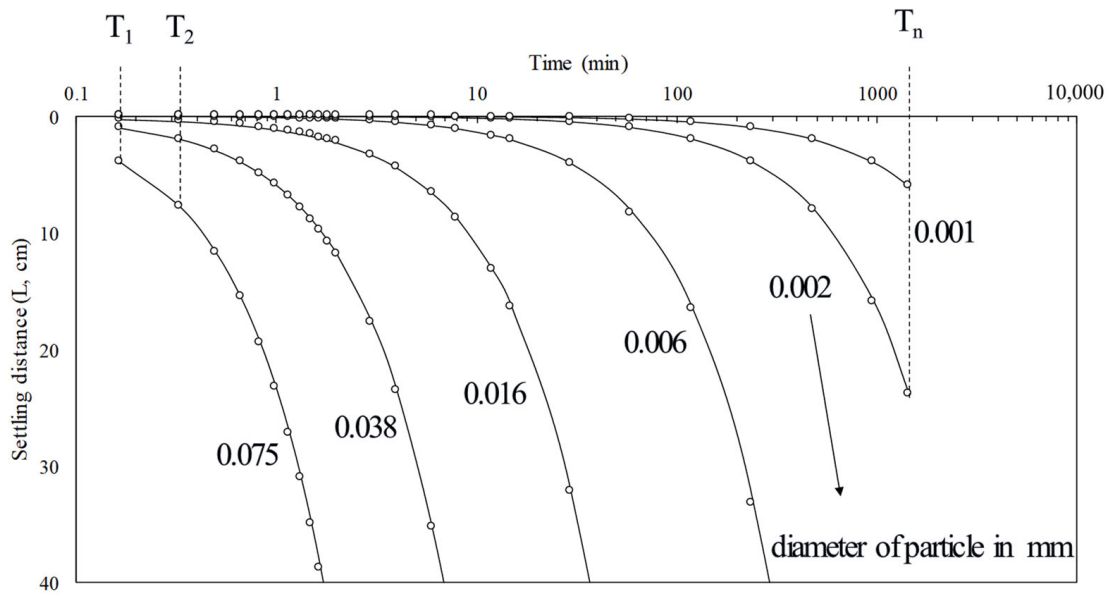


Figure 8. Relationship of settling distance ( $L$ ) and time ( $T$ ) for soil B.

Figure 9 illustrates the calculated values of  $I_D$  based on the particle diameter ( $D$ ). In an 8-bit grayscale image, the pixel intensity or gray value is represented by a value ranging from 0 (black) to 255 (white). Consequently, when the soil content within the soil–water suspension is high, the corresponding gray value of the image tends to be closer to 0. Conversely, if there is a minimal amount of soil present, the gray value tends to be closer to 255. For ease of interpretation, the scale of gray values has been adjusted to range from 0 (white) to 1 (black) rather than the original 0 (black) to 255 (white). Therefore, an  $I_D$  value closer to 1 signifies a darker image with a higher concentration of soil particles, whereas an  $I_D$  value closer to 0 represents a lighter image with a lower concentration of soil particles.  $I_D$  shows a decreasing trend as the diameter of the particle decreases, similarly to  $\gamma$ . This indicates the possibility of replacing  $\gamma$  with  $I_D$ .

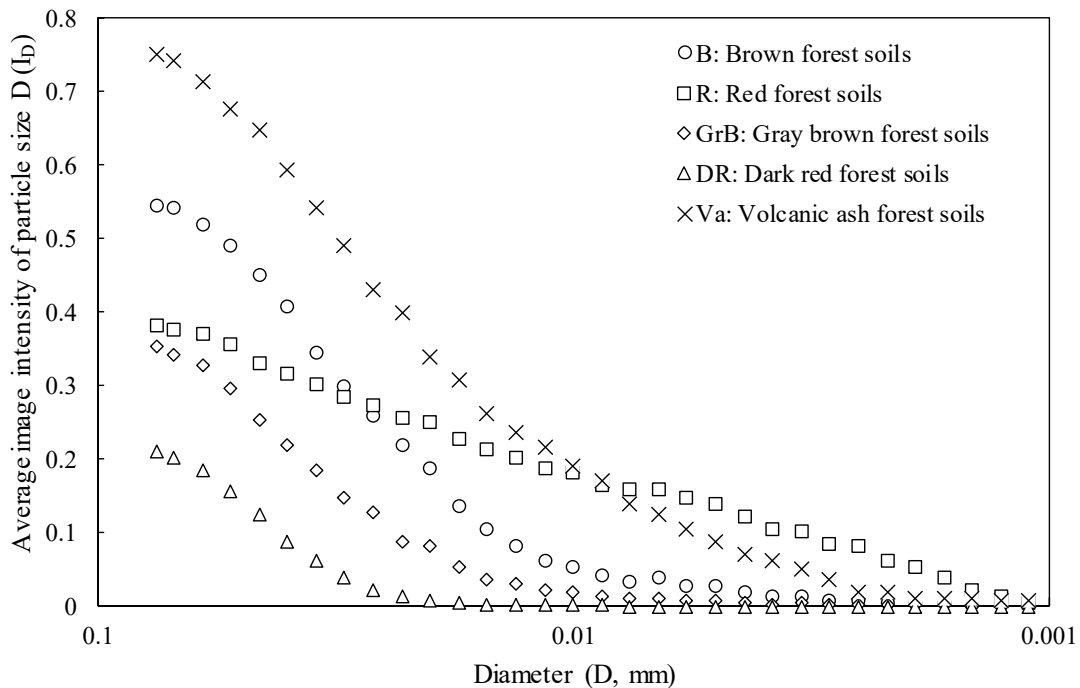
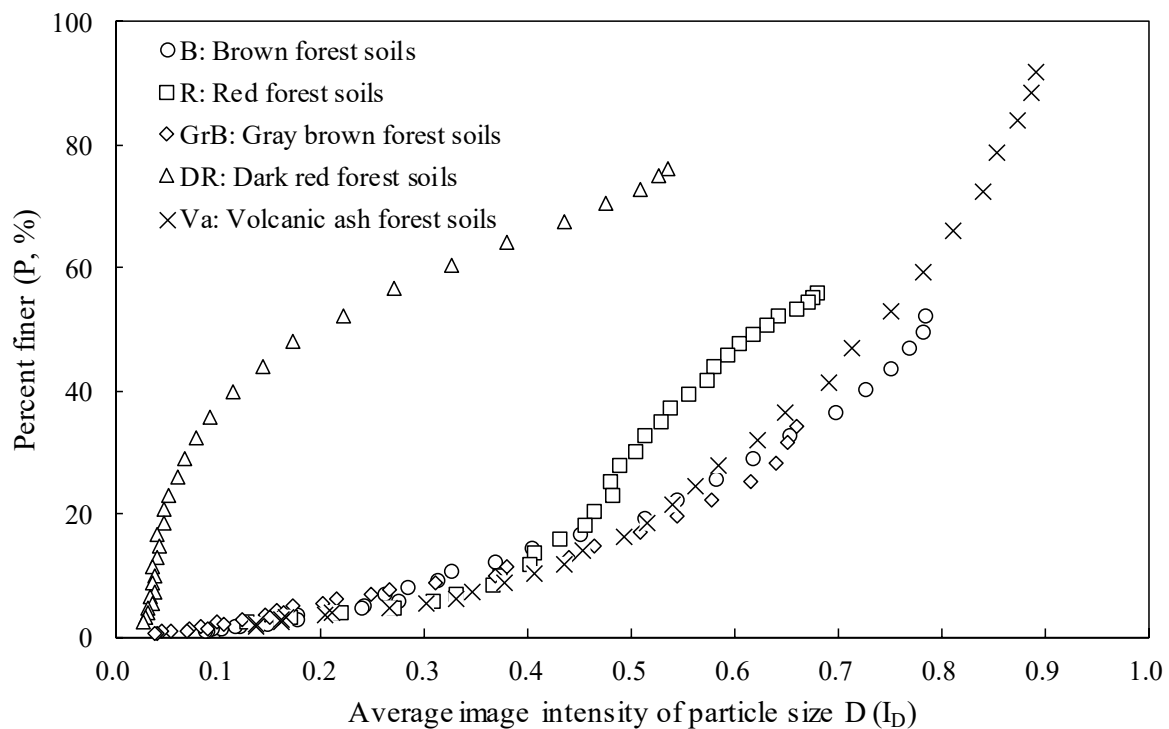


Figure 9. Calculation result of  $I_D$  for various diameter of soil particles.



Figure 10 shows the relationship between  $I_D$  and  $P$ . This indicates that  $P$  has an exponential tendency to increase with  $I_D$ . Depending on the value of  $I_D$ ,  $P$  tended to increase exponentially. Consequently, it is inferred that by applying a suitable exponent to  $I_D$ , it is feasible to accurately predict  $P$ . However, it is important to note that Soil DR exhibited a distinct trend compared with the other four soil types. The relationship between  $I_D$  and  $P$  for Soil DR deviated from the expected exponential behavior observed in the remaining soils.



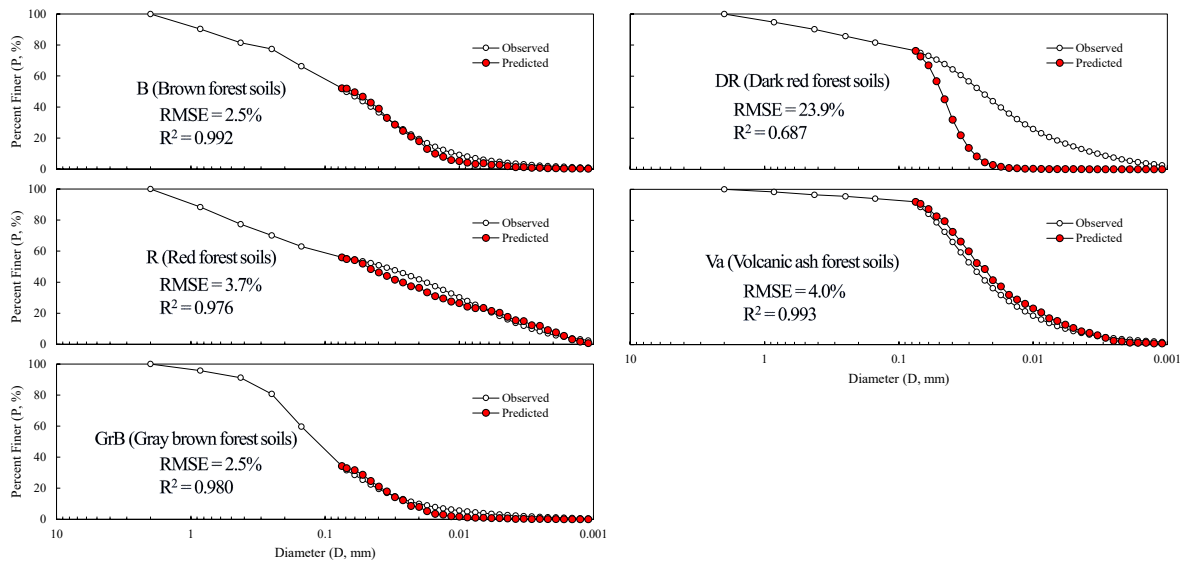
**Figure 10.** Relationship between average image intensity of particle size  $D$  and percent finer.

Considering the relationship between  $I_D$  and  $P$  shown in Figure 10, the prediction formula of  $P$  based on  $I_D$  is as follows:

$$P_D = I_D^m \times \frac{P_{0.075}}{I_{0.075}} \quad (9)$$

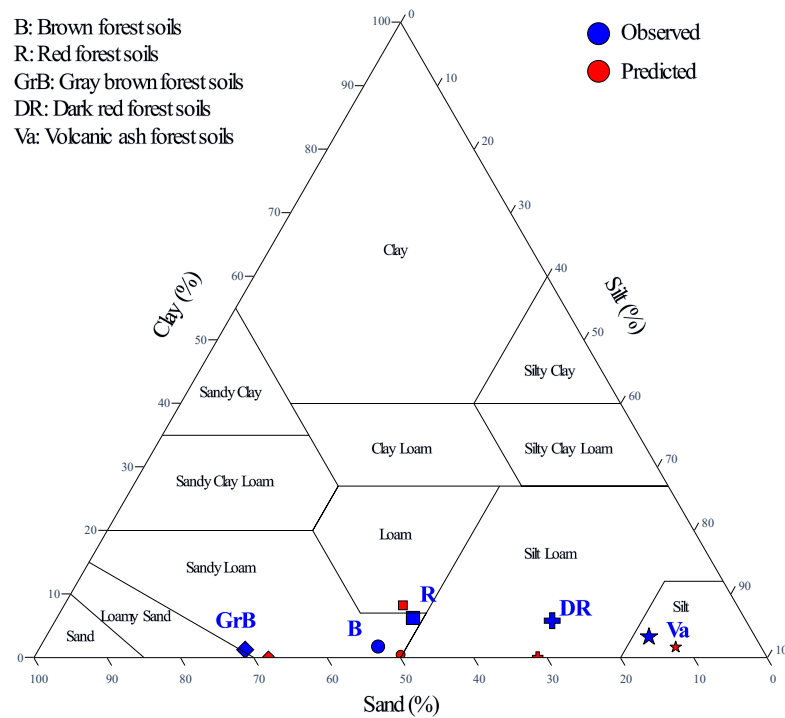
where  $m$  is exponent of  $I_D$ ,  $P_{0.075}$  is percent finer at  $D = 0.075$  mm,  $I_{0.075}$  is average image intensity of particle size = 0.075 mm.  $P_{0.075}$  and  $I_{0.075}$  were introduced to align the initial values of the image-based analysis results with the results of the sieve analysis. Depending on the value of  $m$ , the accuracy of the analysis results can vary. The optimal  $m$  for each soil was found to be different, but with the exception of DR, the other soils were found to be highly correlated when  $m$  ranged from 2 to 3. For Soil DR, the  $I_D$  did not exhibit an exponential relationship with  $P$ , resulting in a gradual decrease in correlation coefficient as  $m$  increased. On average, the highest correlation was found when  $m$  was 2.5. Therefore, it was decided to utilize  $m$  of 2.5 for predicting  $P$  using  $I_D$  across all soil types.

Figure 11 shows the results of the particle size analysis predicted using the proposed method. Except for Soil DR, the four remaining soil types yielded particle size distribution curves that closely matched the experimental results obtained from the laser particle size analyzer. Moreover, the root mean squared error (RMSE) of the prediction results, excluding Soil DR, demonstrated a high level of accuracy, ranging from 2.5 to 4.0%. This indicates that the proposed method provides reliable particle-size predictions for the analyzed soils, offering an effective alternative to hydrometer tests.



**Figure 11.** Particle size distribution curve predicted by machine vision-based soil particle analysis method for soil samples.

Figure 12 shows the USDA soil texture triangle depicting the sand, silt, and clay content calculated from the particle size analysis results. By utilizing the soil texture prediction derived from the image analysis, it becomes evident that the predicted soil texture closely corresponds to the soil texture determined from the actual particle size tests. This alignment between the predicted and calculated soil textures indicates the reliability and accuracy of the image analysis method for determining soil texture. The results confirm that the proposed approach successfully captures the essential characteristics of soil particles and enables the accurate prediction of soil texture based on particle size analysis.



**Figure 12.** Soil texture triangle predicted by machine vision-based soil particle analysis method for soil samples.

## 5. Discussion

### 5.1. Practical Considerations and Limitations

There are important considerations when implementing the machine vision-based soil particle analysis method proposed in this study.

Firstly, the analytical method relies on the average color of the image. However, it should be noted that color values in digital images can vary based on camera settings and lighting conditions. This means that the analysis results for the same sample can differ due to external factors affecting image color. To address this issue, establishing standardized lighting and shooting conditions or developing appropriate measures for correction when variations in shooting conditions occur is crucial. By ensuring consistency in image acquisition, the reliability and comparability of the analysis results can be enhanced.

Additionally, the analysis of the DR sample was not conducted appropriately, leading to different results compared with the other soil samples (B, R, GrB, and Va). This discrepancy is attributed to the rapid color change observed in the DR images within a very short period. While the other soils exhibited gradual color changes over a duration of 1440 min (1 day), the DR sample underwent significant color change within the initial 30 min, followed by a minimal color change afterward. However, it should be considered that the sedimentation of particles in the DR sample may still be occurring during periods when color changes are not observed. This discrepancy could be due to inadequate lighting or camera settings, which may have hindered proper observation of the settling process of small particles. To address these issues and ensure accurate and reliable results, optimizing the experimental setup, lighting conditions, and camera settings is recommended to capture the full range of particle settlement. Additionally, further investigations and adjustments specific to the DR sample may be necessary to improve the analysis methodology for this particular soil type.

### 5.2. Advantages of Proposed Method

This study introduces a machine vision-based soil particle analysis method utilizing a standard digital camera, presenting it as a viable alternative to the hydrometer test. The method offers several notable advantages.

Firstly, it enables experimentation on many samples. In this study, a single test successfully predicted the particle size of five samples. Although the resolution of commercial cameras imposes limitations on sample size, future improvements in camera technology and test setup optimizations can increase the number of simultaneous tests.

Additionally, the proposed method offers simplicity compared to hydrometer testing. Unlike the labor-intensive process of ongoing measurements required in hydrometer testing, the test described in this study can be automated after the initial setup, enhancing efficiency and reducing manual labor.

Furthermore, advancements in camera technology can further enhance the results. While a common commercial digital camera was utilized in this study, specialized cameras such as NIR or hyperspectral cameras allow for the observation of wavelengths beyond RGB. This opens possibilities for analyzing samples like DR that were challenging to study in this particular research. However, a notable strength of this study lies in its reliance on commonly available cameras, ensuring wider accessibility and distribution.

The proposed machine vision-based sedimentation test offers advantages such as the ability to experiment on larger sample sizes, simplicity compared to hydrometer testing, and potential enhancements with the progression of camera technology. Notably, this method utilizes widely accessible cameras, making it practical for various applications.

For the automation of hydrometer testing, Murad et al. [35] presented an automated hydrometer testing system for about \$70 using Time of Flight Distance (ToF). The system measures the distance between the hydrometer and the ToF sensor and converts it into a hydrometer reading. The study reported an  $R^2$  of percent finer of 0.857 to 0.896 when comparing the results of the automated system to the results of the pipette method. In this study,  $R^2$  at  $m = 2.5$  was 0.976 to 0.993 for the soils except DR. The clay content of

the soils in this study ranged from 1.2 to 6.2%, which is lower than the clay content of the soils used by Murad et al. [35], which ranged from 24.5 to 73.8%, which may explain the relatively high correlation. Compared to the above study, this study is considered to have the advantages of relatively simple system configuration and easy testing of a large number of samples. It is also significant that this study proposed a new method to analyze particle size by applying the principle of hydrometer test based on Stoke's law without using a hydrometer.

In particular, in this study, the percent finer was predicted based on the color change of the digital image, but in the further research, the hydrometer reading can be obtained directly by tracking the change of the position of the hydrometer in the digital image. In this regard, Souza et al. [36] applied machine vision technology to calibrate hydrometers that can be utilized in various industrial sites. Therefore, it is expected that machine vision-based hydrometer reading automation will be possible through further research.

## 6. Conclusions

This study focused on predicting the particle size distribution of fine-grained soil using digital image analysis. The study utilized a settling tank instead of a measuring cylinder to acquire digital images of soil–water suspensions during settlement. Image analysis techniques were applied to extract relevant features and predict the percent finer of particles smaller than a given diameter. The results showed a correlation between the average gray value of the images and the percent finer, indicating the potential of image-based analysis for particle size prediction.

The study investigated five forest soils, namely B, R, GrB, DR, and Va. The image analysis process involved cropping the region of interest (ROI) from the acquired images and calculating the average gray value up to a settling distance. The gray value decreased with decreasing particle diameter, similar to the hydrometer reading. The obtained gray values were then used to predict the percent finer of particles smaller than a given diameter.

The prediction results showed that the proposed method could closely align with the experimental results from a laser particle size analyzer for four out of five soil types. The RMSE of the prediction results ranged from 2.5% to 4.0%, indicating a high level of accuracy in particle size prediction.

Overall, this study demonstrates the potential of digital image analysis for predicting particle size distribution in fine-grained soils. The proposed method can provide a convenient and efficient alternative to traditional particle size analysis techniques, offering insights into soil properties and aiding in soil classification and characterization.

**Author Contributions:** Conceptualization, D.K. and J.P.; methodology, D.K. and J.P.; software, D.K. and J.S.; validation, D.K.; formal analysis, D.K. and J.S.; data curation, D.K. and J.P.; writing—original draft preparation, D.K. and J.S.; writing—review and editing, D.K., J.S. and J.P.; visualization, D.K. and J.S.; supervision, J.P.; funding acquisition, J.P. All authors have read and agreed to the published version of the manuscript.

**Funding:** This research was supported by the Basic Science Research Program of the National Research Foundation of Korea (NRF) and funded by the Ministry of Education (2021R111A1A01058373).

**Institutional Review Board Statement:** Not applicable.

**Informed Consent Statement:** Not applicable.

**Data Availability Statement:** Not applicable.

**Conflicts of Interest:** The authors declare no conflict of interest.

## References

1. Kaur, A.; Fanourakis, G.C. Effect of sodium carbonate concentration in calgon on hydrometer analysis results. *Period. Polytech. Civ. Eng.* **2018**, *62*, 866–872. [CrossRef]
2. Ghalib, A.M.; Hryciw, R.D. Soil particle size distribution by mosaic imaging and watershed analysis. *J. Comput. Civ. Eng.* **1999**, *13*, 80–87. [CrossRef]

3. Faroughi, S.; Huber, C. A theoretical hydrodynamic modification on the soil texture analyses obtained from the hydrometer test. *Geotechnique* **2016**, *66*, 378–385. [CrossRef]
4. Kaur, A.; Fanourakis, G. Effect of hydrometer type on particle size distribution of fine grained soil. In Proceedings of the 1st Southern African Geotechnical Conference, Sun City, South Africa, 5–6 May 2016; pp. 1–8.
5. Abbireddy, C.O.; Clayton, C.R. A review of modern particle sizing methods. *Proc. Inst. Civ. Eng.-Geotech. Eng.* **2009**, *162*, 193–201. [CrossRef]
6. Wen, B.; Aydin, A.; Duzgoren-Aydin, N.S. A comparative study of particle size analyses by sieve-hydrometer and laser diffraction methods. *Geotech. Test. J.* **2002**, *25*, 434–442.
7. Al-Hadidi, M.T.; Al-Adhamii, R.; Ali, B. Estimate the ratio of total dissolved salts from the hydrometer test results. *Appl. Res. J. (Eng.)* **2015**, *1*, 444–450.
8. Kakuturu, S.P.; Kinzel, M.; Xiao, M. *Effects of Maximum Particle Size on the Results of Hydrometer Tests on Soils*; ASTM International: West Conshohocken, PA, USA, 2019.
9. Stott, P.; Monye, P.; Theron, E. Assessment of reliability of the hydrometer by examination of sediment. In Proceedings of the Proceedings of the first Southern African Geotechnical Conference, Sun City, South Africa, 5–6 May 2016; pp. 281–286.
10. Barman, U.; Choudhury, R.D. Soil texture classification using multi class support vector machine. *Inf. Process. Agric.* **2020**, *7*, 318–332. [CrossRef]
11. Ravikumar, R.; Arulmozhi, V. Digital image processing-a quick review. *Int. J. Intell. Comput. Technol. (IJICT)* **2019**, *2*, 11–19.
12. Kim, D.; Kim, T.; Jeon, J.; Son, Y. Soil-Surface-Image-Feature-Based Rapid Prediction of Soil Water Content and Bulk Density Using a Deep Neural Network. *Appl. Sci.* **2023**, *13*, 4430. [CrossRef]
13. O'Donnell, T.K.; Goyne, K.W.; Miles, R.J.; Baffaut, C.; Anderson, S.H.; Sudduth, K.A. Identification and quantification of soil redoximorphic features by digital image processing. *Geoderma* **2010**, *157*, 86–96. [CrossRef]
14. Prats-Montalbán, J.M.; de Juan, A.; Ferrer, A. Multivariate image analysis: A review with applications. *Chemom. Intell. Lab. Syst.* **2011**, *107*, 1–23. [CrossRef]
15. Chitradevi, B.; Srimathi, P. An overview on image processing techniques. *Int. J. Innov. Res. Comput. Commun. Eng.* **2014**, *2*, 6466–6472.
16. Ohm, H.-S.; Hryciw, R.D. Size distribution of coarse-grained soil by sedimenting. *J. Geotech. Geoenviron. Eng.* **2014**, *140*, 04013053. [CrossRef]
17. Ren, J.; Li, X.; Zhao, K. Quantitative analysis of relationships between crack characteristics and properties of soda-saline soils in Songnen Plain, China. *Chin. Geogr. Sci.* **2015**, *25*, 591–601. [CrossRef]
18. dos Santos, J.F.; Silva, H.R.; Pinto, F.A.; de Assis, I.R. Use of digital images to estimate soil moisture. *Rev. Bras. de Eng. Agrícola e Ambient.* **2016**, *20*, 1051–1056. [CrossRef]
19. Kim, D.; Son, Y.; Park, J.; Kim, T.; Jeon, J. Evaluation of calibration method for field application of UAV-based soil water content prediction equation. *Adv. Civ. Eng.* **2019**, *2019*, 2486216. [CrossRef]
20. Kim, D.; Kim, T.; Jeon, J.; Son, Y. Convolutional Neural Network-Based Soil Water Content and Density Prediction Model for Agricultural Land Using Soil Surface Images. *Appl. Sci.* **2023**, *13*, 2936. [CrossRef]
21. Peng, X.; Horn, R.; Peth, S.; Smucker, A. Quantification of soil shrinkage in 2D by digital image processing of soil surface. *Soil Tillage Res.* **2006**, *91*, 173–180. [CrossRef]
22. Abd El-Halim, A. Image processing technique to assess the use of sugarcane pith to mitigate clayey soil cracks: Laboratory experiment. *Soil Tillage Res.* **2017**, *169*, 138–145. [CrossRef]
23. Yan, L.; Meng, Q.-X.; Xu, W.-Y.; Wang, H.-L.; Zhang, Q.; Zhang, J.-C.; Wang, R.-B. A numerical method for analyzing the permeability of heterogeneous geomaterials based on digital image processing. *J. Zhejiang Univ. Sci. A* **2017**, *18*, 124–137. [CrossRef]
24. Bryk, M.; Kołodziej, B. Suitability of Image Analysis in Evaluating Air and Water Permeability of Soil. *Agronomy* **2021**, *11*, 1883. [CrossRef]
25. Smith, S.J.; Friedrichs, C.T. Image processing methods for in situ estimation of cohesive sediment floc size, settling velocity, and density. *Limnol. Oceanogr. Methods* **2015**, *13*, 250–264. [CrossRef]
26. Kim, D.; Son, Y.; Park, J. Prediction of settling velocity of nonspherical soil particles using digital image processing. *Adv. Civ. Eng.* **2018**, *2018*, 4647675. [CrossRef]
27. Wang, S.-N.; Xu, W.-Y.; Shi, C.; Zhang, Q. Numerical simulation of direct shear tests on mechanical properties of talus deposits based on self-adaptive PCNN digital image processing. *J. Cent. South Univ.* **2014**, *21*, 2904–2914. [CrossRef]
28. Li, H.-D.; Tang, C.-S.; Cheng, Q.; Li, S.-J.; Gong, X.-P.; Shi, B. Tensile strength of clayey soil and the strain analysis based on image processing techniques. *Eng. Geol.* **2019**, *253*, 137–148. [CrossRef]
29. Mora, C.; Kwan, A.; Chan, H. Particle size distribution analysis of coarse aggregate using digital image processing. *Cem. Concr. Res.* **1998**, *28*, 921–932. [CrossRef]
30. Sudarsan, B.; Ji, W.; Adamchuk, V.; Biswas, A. Characterizing soil particle sizes using wavelet analysis of microscope images. *Comput. Electron. Agric.* **2018**, *148*, 217–225. [CrossRef]
31. Bittelli, M.; Andrenelli, M.; Simonetti, G.; Pellegrini, S.; Artioli, G.; Piccoli, I.; Morari, F. Shall we abandon sedimentation methods for particle size analysis in soils? *Soil Tillage Res.* **2019**, *185*, 36–46. [CrossRef]

32. Sun, Q.; Zheng, J.; Coop, M.R.; Altuhafi, F.N. Minimum image quality for reliable optical characterizations of soil particle shapes. *Comput. Geotech.* **2019**, *114*, 103110. [CrossRef]
33. Baghban, A.; Bahadori, M.; Bahadori, A. Prediction of particle size distribution in hydrometer test analysis using LSSVM algorithm. In Proceedings of the Asia Pacific Confederation of Chemical Engineering Congress 2015: APCCChE 2015, Incorporating CHEMECA 2015, Melbourne, Australia, 27 September–1 October 2015; pp. 1–13.
34. Özgan, E.; Öztürk, A. Genetic Algorithm Application for Hydrometer Tests. *Asian J. Chem.* **2009**, *21*, 6857–6868.
35. Murad, M.O.F.; Jones, E.J.; Minasny, B. Automated soil particle-size analysis using time of flight distance ranging sensor. *Soil Sci. Soc. Am. J.* **2020**, *84*, 690–699. [CrossRef]
36. De Souza, J.B.; Maio, M.F.; Belan, P.A. A Machine Vision for Automatic Hydrometers Calibration. *Int. J. Comput. Appl.* **2021**, *975*, 8887. [CrossRef]

**Disclaimer/Publisher’s Note:** The statements, opinions and data contained in all publications are solely those of the individual author(s) and contributor(s) and not of MDPI and/or the editor(s). MDPI and/or the editor(s) disclaim responsibility for any injury to people or property resulting from any ideas, methods, instructions or products referred to in the content.

## Article

# Working Load Analysis of a 42 kW Class Agricultural Tractor According to Tillage Type and Gear Selection during Rotary Tillage Operation

Yeon-Soo Kim <sup>1</sup>, Bo-Min Bae <sup>1</sup>, Wan-Soo Kim <sup>2</sup>, Yong-Joo Kim <sup>3,\*</sup>, Sang-Dae Lee <sup>4</sup> and Taek-Jin Kim <sup>5,\*</sup>

- <sup>1</sup> Department of Bio-Industrial Machinery Engineering, Pusan National University, Miryang 50463, Republic of Korea; yskim23@pusan.ac.kr (Y.-S.K.); qhals806@pusan.ac.kr (B.-M.B.)
- <sup>2</sup> Department of Bio-Industrial Machinery Engineering, Kyungpook National University, Daegu 41566, Republic of Korea; wansoo.kim@knu.ac.kr
- <sup>3</sup> Department of Biosystems Machinery Engineering, Chungnam National University, Daejeon 34134, Republic of Korea
- <sup>4</sup> Smart Agricultural R&D Group, Korea Institute of Industrial Technology (KITECH), Gimje 54325, Republic of Korea; sdlee96@kitech.re.kr
- <sup>5</sup> Department of Drive System Team, TYM R&D Center, Iksan 54576, Republic of Korea
- \* Correspondence: babina@cnu.ac.kr (Y.-J.K.); taek.kim@tym.world (T.-J.K.); Tel.: +82-42-821-6716 (Y.-J.K.); +82-63-723-7753 (T.-J.K.)

**Abstract:** The objective of this study was to analyze the effect of tillage type (i.e., primary and secondary tillage) and gear selection (P1L2 to P1L4) on the working load of tractor–implement systems during rotary tillage. Soil properties change with depth, and differences in properties along the depth distribution, such as the location of formation of the hardpan layer, internal friction angle, and moisture content, affect the load of rotary tillage operations. Therefore, the physical properties of soil along the field depth distribution were measured to analyze the effect of tillage type and gear selection on workload in rotary tillage. In addition, a load measurement system equipped with PTO torque meter, axle torque meter, proximity sensor, and RTK-GPS were configured on the 42 kW agricultural tractor. The experimental results show that the combination of tillage type and gear selection has a wide-ranging effect on the tractor’s workload and performance when the rotavator operated at the same tilling depth. Overall working load was higher by up to 14% (engine) and 29.1% (PTO shaft) in primary tillage compared to secondary tillage when the gear selection was the same. When the tillage type is the same, it was analyzed that the overall average torque increased by up to 35.9% (engine) and 33.9% (PTO shaft) in P1L4 compared to P1L2 according to gear selection. Based on load analysis results, it was found that the effect of gear selection (Engine: 4–14%, PTO: 12.1–28.6%) on engine and PTO loads was higher than that of tillage type (Engine: 31.6–35.1%, PTO: 31.9–32.8%), and the power requirement tended to decrease in secondary tillage. Therefore, working load should be considered according to the soil environment and tillage type when designing agricultural machinery system.

**Citation:** Kim, Y.-S.; Bae, B.-M.; Kim, W.-S.; Kim, Y.-J.; Lee, S.-D.; Kim, T.-J. Working Load Analysis of a 42 kW Class Agricultural Tractor According to Tillage Type and Gear Selection during Rotary Tillage Operation. *Agriculture* **2023**, *13*, 1556. <https://doi.org/10.3390/agriculture13081556>

Academic Editor: Jin He

Received: 28 June 2023

Revised: 1 August 2023

Accepted: 2 August 2023

Published: 3 August 2023

**Keywords:** working load; agricultural tractor; rotary tillage; soil property; tillage type



**Copyright:** © 2023 by the authors. Licensee MDPI, Basel, Switzerland. This article is an open access article distributed under the terms and conditions of the Creative Commons Attribution (CC BY) license (<https://creativecommons.org/licenses/by/4.0/>).

## 1. Introduction

In Korea, agricultural tractors have a working area of 18.9 ha per unit and an operation rate of 74.3%. Tractors not only simply pull attached implements, but also deliver the required power to drive attached implements through a power take-off (PTO) shaft [1]. In particular, agricultural power using PTO is mainly used for high-load agricultural work such as powered disc plow, rotary, and baler operation. Because tractors are subjected to large and irregular working load fluctuations depending on the type of agricultural work performed, it is necessary to analyze the largest fluctuation load on the tractor to ensure reliability [2,3].



For the optimal design of agricultural tractors and implements, it is necessary to measure and analyze the load data generated during agricultural work [4]. Basically, various load measurement tests were conducted for plow tillage. The initial working load analysis study was conducted mainly in the soil bin test bed to analyze soil–tool interaction. Raper [5] conducted a study related to the analysis of minimum draft force generation according to subsoiler geometry via a soil bin test. As a result, it was confirmed that the soil disruption was better with less resistance in the bentleg shanks than in the straight shanks. Other studies have conducted various types of soil–tool interaction study related to working conditions and load influence parameters on the basis of field experiments. Naderloo et al. [6] analyzed the tillage depth and travel speed effect on draft force using three types of plow treatment under clay loam soil conditions. Additionally, Moenifar [7] conducted field experiments to analyze the influence of tillage depth and penetration angle on soil–thin blade interaction. In addition, Aday and Ramadhan [8] conducted draft force and distribution area analysis studies with respect to single-tine and double-tine conditions in the subsoiler. In another study, Kichler et al. [9] conducted field tests to analyze the effect of transmission gear selection on tractor performance and fuel cost as a function of the geometric shape of the subsoiler during deep tillage operations. The field test results showed that the productivity rate increased as the appropriateness of gear selection increased, while the fuel cost decreased. In another study, Kim et al. [10] analyzed the effect of soil water content on the traction performance of agricultural tractors during tillage operation. On the basis of the results of the test, it was concluded that overall tractor traction performance parameters such as axle torque, slip and traction increased proportionally with increasing soil water content. In addition, Kim et al. [11,12] conducted field tests to analyze the field environment (i.e., soil texture and soil properties) and the effect of tillage depth and gear selection on the working load of tractors during tillage operations.

In addition, some studies have conducted field load measurement tests for agricultural operations using PTO power. Lee et al. [13] conducted field tests to measure the PTO working load during rotary tillage and baler operation in Korean upland fields. In another study, Behera et al. [14] analyzed the effects of tillage depth and travel speed on PTO torque, draft force and fuel consumption in rota-cultivators. Additionally, Kim et al. [15,16] conducted a load analysis study on the effect of different gear combinations on the PTO working load during rotary tillage. In another study, Kim et al. [17] conducted field measurement testing of the PTO working load of a multi-purpose cultivator in order to identify the weak part of the PTO gear train.

Rotary tillage is used in both primary and secondary tillage operations. It is also useful for puddling the field before paddy transplantation. However, load analysis studies with respect to the soil working environments and tillage types used in primary and secondary methods have not been performed. Therefore, this study was conducted to evaluate the working load of 42 kW class agricultural tractor with respect to tillage type and gear selection during rotary tillage, which is the most widely used agricultural operation that uses tractor PTO power. The main purposes were to (1) develop a field load measurement system with an experimental design, (2) measure and analyze the working load data during rotary tillage, and (3) perform an analysis of the effect of tillage type and gear selection on tractor working load.

## 2. Materials and Methods

### 2.1. Measurement of Field Soil Properties

Basically, all working loads of agricultural machinery originate from the soil environment. Since the rotary work was performed in two fields with different physical properties, soil property measurement tests were performed. Figure 1 shows the soil sampling procedure of the field soil properties. Soil properties were measured using the uniform grid (3 m × 3 m) sampling method in the field [18]. The test field was divided into 10 uniform grid squared, and soil sampling was performed in each grid square to measure the physical

properties of the soil, and in the case of the cone penetration test and vane shear test, which were performed to measure the engineering properties of the soil, 10 tests were performed in each grid, for a total of 100 tests.

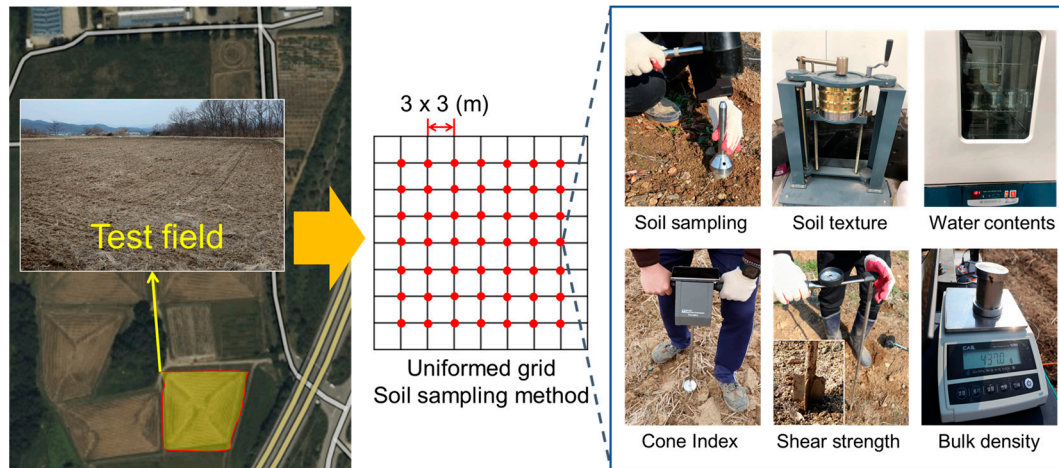


**Figure 1.** Sampling procedure of field soil property using uniformed grid method.

First, soil sampling was performed in each test field, A and B, using a 100 mL soil sampling tube (DIK-1801, Daiki Rika Kogyo Co., Ltd., Akagidai, Japan) and a soil sampling device (DIK-1815, Daiki Rika Kogyo Co., Ltd., Akagidai, Japan). To measure the soil water content, the soil specimen was dried at a temperature of 110 °C for 24 h [19] using the oven-drying method (SH-DO-100FGB, Samheung Energy, Sejong, Republic of Korea). The soil texture of field site was analyzed using the USDA soil classification method [20] using a sieve shaker (HJ-4560, Heungjin, Gimpo, Republic of Korea) [21].

Additionally, cone index and shear strength, which are the most important parameters among soil mechanical properties, and have the greatest impact on agricultural workload, were measured using a cone penetrometer (DIK-5532, Daiki Rika Kogyo Co., Ltd., Akagidai, Japan) [22,23] and a shear ring-type soil resistance meter (DIK-5503, Daiki Rika Kogyo Co., Ltd., Saitama, Japan), respectively.

In this study, the soil properties measured in this study were obtained using Equations (1)–(3) [24,25]:

$$W = \frac{100W_w}{W_s}, \quad (1)$$

where  $W$  is the soil water content (%),  $W_w$  is the water weight of the soil specimen, and  $W_s$  is the weight of solids in the soil specimen.

$$\gamma = \frac{W}{V}, \quad (2)$$

where  $\gamma$  is the bulk density ( $\text{g}/\text{cm}^3$ ),  $W$  is the total weight of the soil specimen (kg),  $V$  is the total volume of the soil specimen ( $\text{cm}^3$ ).

$$\tau = \frac{3M}{28\pi r^3}, \quad (3)$$

where  $\tau$  is the shear strength of soil (kPa),  $M$  is the soil resistance torque that caused the on-field vane shear test (Nm), and  $r$  is the radius of shear box.

## 2.2. Tractor–Implement System

Figure 2a shows a rotavator (WJ185A, Woongjin Machinery, Gimje, Republic of Korea), often used in studies on soil–machine interactions to analyze working load using PTO power. The rotavator undertakes a high-load operation compared to other agricultural operations,

such as plowing. Therefore, it is suitable for soil–tool interaction studies of agricultural machinery using PTO power. The rotavator has a maximum tillage depth of 200 mm, and the dimensions are 810 mm × 2020 mm × 1130 mm (length × width × height). In addition, it has 7 flanges and 42 tillage blades, with a working width of 1820 mm. The detailed specifications of the attachment implement are shown in Table 1.



**Figure 2.** Tractor–implement system used in this study: (a) rotavator (WJ185A, Woongjin, Republic of Korea); (b) 42 kW class agricultural tractor (TX58, TYM, Gongju, Republic of Korea).

**Table 1.** Specifications of the rotavator.

Item	Specification
Company	Woongjin
Model	WJ185A
Required power (kW)	35~45
Length (mm) × width (mm) × height (mm)	810 × 2020 × 1130
Tillage width (mm)	1820
Weight (kg)	405
Max. tillage depth (mm)	200
Number of flanges	7
Number of blades	42

In this study, a 42 kW tractor (TX58, Tong Yang Moolsan, Gongju, Republic of Korea) was used, considering that the specifications of the rotavator indicate that a power source of 35–45 kW is required, as shown in Figure 2b. The overall dimensions of the agricultural tractor body were 3695 mm × 1848 mm × 2560 mm (length × width × height), with a rated power of 35.6 kW and a maximum torque of 211.8 Nm. The test tractor’s total weight was 3894 kg, and with the inclusion of the DAQ system (229 kg) and a front loader (450 kg) (HIT400 L, Hanil Industry Co., Ltd., Gyeongsan, Republic of Korea). The agricultural tractor used in the field experiment was equipped with a mechanical transmission power shuttle, and through a combination of 4 main gears and 6 subgears, a total of 48 gears (24 forward gears, 24 reverse gears) could be shifted, depending the tilling work, and the maximum speed was 33.8 km/h. In addition, the PTO power train is a three-stage power train, and has rotational speeds of 540, 750, and 1000 rpm, respectively. The specifications of the agricultural tractor are shown in Table 2.



**Table 2.** Results of measured soil properties of test field according to soil depth.

Parameters	Soil Depth: 0 to 10 cm	Soil Depth: 10 to 20 cm
Water contents (WC, %)	20.6 ± 1.2	17.7 ± 1.1
Bulk density ( $\gamma$ , kg/m <sup>3</sup> )	1571.7 ± 75.2	1830 ± 30.6
Cone index (CI, kPa)	801.8 ± 277.6	2065.9 ± 643.1
Shear strength ( $\tau$ , kPa)	25.1 ± 7.2	64.3 ± 14.4

### 2.3. Working Load Measurement System

Figure 3 shows the overall measurement system of a 42 kW agricultural tractor for measuring working load during the rotary tillage. The DAQ (data acquisition) system was Dewesoft X (Dewesoft 3X, Dewesoft, Trbovlje, Slovenia), and the working load was measured simultaneously during rotary tillage at a sampling rate of 1 kHz. The working load measurement system used to analyze the effect of soil properties on the design load of the tractor–implement system during tillage operations is as follows:

$$V_{th} = \frac{\pi D_{rw} N_{rw} GR 3.6}{60} \quad (4)$$

where  $V_{th}$  is the theoretical speed of the tractor in the working direction (km/h),  $D_{rw}$  is the diameter of the rear wheel axle (m),  $N_{rw}$  is the wheel axle rotational speed as calculated by proximity sensors (rpm), and GR is the gear ratio,

$$S = \left( \frac{V_{th} - V_a}{V_{th}} \right) \times 100 \quad (5)$$

where  $S$  is the slip ratio (%) and  $V_a$  is the travel speed as the actual working speed of the tractor, as measured by RKT-GPS (km/h).

**Figure 3.** Configuration of the field load measurement system.

The engine load measuring unit featured a 5 kNm strain gauge torque transducer mounted on the flex plate to measure the engine torque ( $T_e$ ), which measured the torque data with non-contact sensor telemetry through an amplifier. The engine rotational speed ( $N_e$ ) was measured by sampling at 100 Hz based on wireless CAN (Controller Area Net-

work) communication and then synchronized with other working load data at 1 kHz using DAQ system. In addition, the engine power requirement can be obtained as follows:

$$P_e = \frac{2\pi T_e N_e}{60,000} \quad (6)$$

where  $P_e$  is the power requirement of the engine (kW),  $T_e$  is the engine torque (Nm) measured by the flex plate torque transducer, and  $N_e$  is the engine rotational speed (rpm) measured by controller area network (CAN) communication.

The torque of the wheel axle and the PTO shaft was measured using a flange-type torque transducer (Sensor telemetrie GmbH PCM16, MANNER, Spaichingen, Germany). The wheel axle torque and PTO torque data from each torque transducer were amplified by internal amplifiers. The torque range of the transducer was 15–30 kNm. In addition, a proximity sensor (CYGTS211B-PO2, Chen Yang Technologies GmbH & Co. KG, Finsing, Germany) was installed on the inner side of each wheel axle in order to measure wheel axle rotational speed. This method of measuring rotational speed has been used in previous studies [26,27]. An antenna integrating a torque transducer, a proximity sensor and an amplifier was installed inside and outside each wheel axle shaft to precisely measure the wheel axle load and the PTO axle load simultaneously. In the case of the proximity sensor, the measuring range was up to 20,000 rpm with a response frequency of 1–20 kHz. In addition, the power requirements of the agricultural tractor were analyzed in order to evaluate the working load of wheel axles and PTO shafts during rotary tillage operations, as follows:

$$P_w = \frac{2\pi T_w N_w}{60,000}, \quad (7)$$

where  $P_w$  is the power requirement of the wheel axle (kW),  $T_w$  is the wheel axle torque (Nm), as measured by the wheel torque meter, and  $N_w$  is the wheel axle rotational speed (rpm), as measured by the proximity sensor.

$$P_{PTO} = \frac{2\pi T_{pto} N_{pto}}{60,000}, \quad (8)$$

where  $P_{PTO}$  is the power requirement of the PTO shaft (kW),  $T_{PTO}$  is the PTO shaft torque (Nm), as measured by the PTO torque transducer, and  $N_{PTO}$  is the rotational speed of the PTO shaft (rpm), as measured by CAN communication.

To measure fuel consumption, an oval gear flowmeter (OG2-SS5-VHQ-B, Titan Enterprises, Sherborne, UK) was installed at the fuel injection inlet and outlet. Specific fuel consumption (SFC), which is often used as a performance indicator for fuel consumption, can be obtained using the following equation. The fuel cost was also calculated using the method described in another study [9].

$$FC = \frac{60(F_{in} - F_{out})}{0.83}, \quad (9)$$

$$SFC = \frac{FC}{P_e}, \quad (10)$$

$$PR = \frac{TS \times WW}{10}, \quad (11)$$

$$\text{Fuelcost} = FC \times \frac{1}{PR} \times FP, \quad (12)$$

where  $FC$  is the fuel consumption of the engine (kg/h),  $F_{in}$  is the flow rate (L/min) measured by the flow meter installed at the fuel inlet of the engine,  $F_{out}$  is the flow rate (L/min) measured by the flow meter installed at the fuel outlet of the engine,  $SFC$  is the specific fuel consumption (g/kWh),  $PR$  is the productivity rate (ha/h),  $TS$  is the travel speed measured

by RTK-GPS (km/h),  $WW$  is the working width (m), fuel cost (USD/ha), and  $FP$  is the fuel price (1.31 USD/kg).

#### 2.4. Field Experimental Design

In this study, field experiments were conducted to analyze the effect of tillage type and gear selection on the working load of agricultural tractors during rotary tillage. The field test site was located at  $37^{\circ}93'67.2''$  N and  $127^{\circ}78'20.6''$  E. After carrying out the soil property measurements using the equipment and method described in Section 2.1, rotary tillage was repeatedly performed using a tractor equipped with a field load measurement system.

The test was performed on the basis of the  $3 \times 2$  split-plot design under three different gear selection (combinations of a PTO stage 1 and transmission gear stages L2 to L4 (i.e., P1L2, P1L3, and P1L4)) and two tillage types (primary and secondary tillage), as shown in Figure 4. Under no-load conditions, the first PTO gear stage had a PTO shaft rotational speed of 540 rpm, and the L2, L3, and L4 transmission gear stages had theoretical travel speeds of about 1.57, 2.25, and 3 km/h, respectively, at rated engine rotational speed. However, a load measurement test for rotary tillage was performed under full-throttle conditions in four-wheel-drive mode, taking into consideration the driving propensities of farmers. In addition, the plowing depth was set to about 10–12 cm, and the engine, axle, PTO, travel speed, and slip were measured three times with each test condition as the target measurement parameter.



**Figure 4.** Load measurement test during rotary tillage: (a) primary tillage; (b) secondary tillage.

### 3. Results

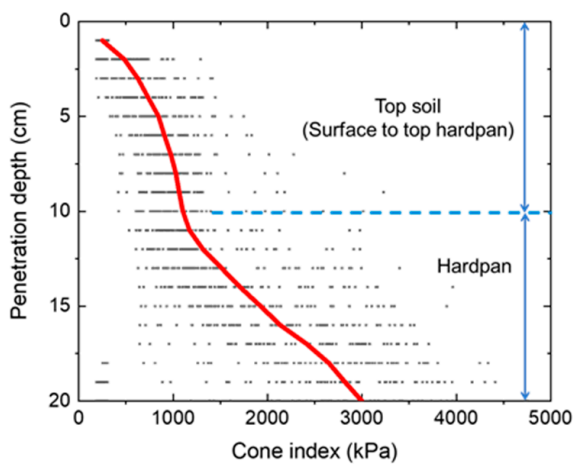
#### 3.1. Analysis of Soil Properties

In general, soil compaction in agricultural soils increases with the repeated use of heavy machinery such as tractors. Therefore, the distribution tendency of soil properties varies depending on the soil depth [28]. First, from the results of the cone penetration test analysis performed to see the distribution of mechanical properties of the soil, it was found that the cone index value rapidly increased at around 10 cm, as shown in Figure 5. Specifically, it showed an average value of  $801.8 \pm 277.6$  kPa at a depth of about 0–10 cm and an average value of 2065.9 kPa at a depth of 10–20 cm. The average values at a depth of 10–20 cm were found to be 2.57 times higher than those measured at 0–10 cm.

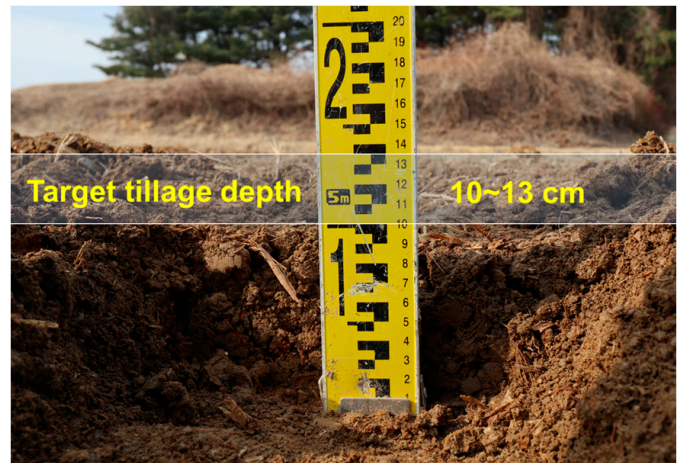
Based on the results of the cone penetration test, the field soil properties were measured by dividing it into two depths. Table 3 shows the results of field measurement of soil quality divided into two depth sectors according to the soil depth, top soil (0–10 cm) and hardpan (10–20 cm). As a result, of soil analysis, the test field site was analyzed as loam (sand 46%, silt 34%, clay 20%). In general, it is known that the deeper the soil layer, the higher the soil compaction and the lower the porosity, and the lower the water content than the topsoil. This field test site also showed that the topsoil had an overall average soil water content of  $20.6 \pm 1.2\%$ , which was 10% higher than that of the hardpan depth ( $17.7 \pm 1.1\%$ ). As for



the overall average bulk density result, the hardpan was analyzed to have an average of  $1830 \pm 30.6 \text{ kg/m}^3$ , 16.4% higher than the top soil ( $1571.7 \pm 75.2 \text{ kg/m}^3$ ), which showed similar bulk density results to the range of  $1500\text{--}2100 \text{ kg/m}^3$  reported in studies using actual field experiments for tillage operations [29,30]. Additionally, as a comparison group, the bulk density of soil failure by each of the primary (rotary tillage) and secondary tillage (rotary tillage after plowing) was measured, and the results showed  $1483.2 \pm 10.9 \text{ kg/m}^3$  and  $1431.2 \pm 17.2 \text{ kg/m}^3$ , respectively. Finally, in the case of shear strength, the average value of  $64.3 \pm 14.4 \text{ kPa}$  in hardpan was 2.56 times significantly larger than top soil value ( $25.1 \pm 7.2 \text{ kPa}$ ).



(a)



(b)

**Figure 5.** (a) Analysis of cone penetration test results; and (b) target tillage depth.

**Table 3.** Results of overall average travel speed and slip ratio according to driving conditions.

Driving Conditions	Theoretical Speed (km/h)	Travel Speed (km/h)	Slip Ratio (%)
Primary × P1L2	$1.73 \pm 0.03$	$1.7 \pm 0.14$	$1.42 \pm 5.31$
Primary × P1L3	$2.47 \pm 0.04$	$2.44 \pm 0.16$	$1.27 \pm 6.21$
Primary × P1L4	$3.29 \pm 0.06$	$3.26 \pm 0.25$	$0.51 \pm 6.54$
Secondary × P1L2	$1.73 \pm 0.02$	$1.68 \pm 0.08$	$2.43 \pm 4.63$
Secondary × P1L3	$2.47 \pm 0.02$	$2.42 \pm 0.12$	$2.04 \pm 4.81$
Secondary × P1L4	$3.29 \pm 0.05$	$3.24 \pm 0.17$	$1.43 \pm 4.99$

### 3.2. Travel Speed with Wheel Slippage

The overall average results of tillage depth and slip ratio are shown in Table 4. Since the travel speed was about 5–6% higher than the travel speed at the rated engine rotation speed in all gear stages, it was confirmed that the engine rpm was slightly higher than the rated speed. This was attributed to the fact that high loads such as plow tillage did not occur to such an extent that the engine load caused the engine rotational speed to drop below the rated engine rotational speed. In addition, the travel speed showed a very low slip ratio of 0.51~2.43%, considering the full-throttle condition of 2300 rpm. It was found that the harder the road surface (primary tillage) and the higher the travel speed (high transmission gear stage), the lower the overall average slip ratio, but the more frequent the negative slip based on larger data oscillation.



**Table 4.** Results of fuel efficiency by tillage type and gear selection.

Driving Conditions	FC <sup>1</sup> (kg/h)	SFC <sup>2</sup> (g/kWh)	PR <sup>3</sup> (ha/h)	Fuel Cost (\$/ha)
Primary × P1L2	7.19	358.07	0.31	30.38
Primary × P1L3	7.56	336.10	0.44	22.51
Primary × P1L4	7.84	326.73	0.59	17.41
Secondary × P1L2	6.87	396.58	0.31	29.03
Secondary × P1L3	7.73	338.62	0.44	23.01
Secondary × P1L4	7.85	329.73	0.59	17.43

<sup>1</sup> FC: fuel consumption; <sup>2</sup> SFC: specific fuel consumption; <sup>3</sup> PR: productivity rate.

### 3.3. Engine Load

The overall measured results of engine torque are shown in Figure 6. In the case of engine rotation speed, only a difference of less than 1% was observed as a result of whether primary (within 0.83%) or secondary tillage (within 0.65%) conditions were employed under full-throttle (about 2300 rpm). In the case of engine torque, average engine torques of the working sections of  $84.06 \pm 7.24$  Nm (P1L2),  $95.67 \pm 5.54$  Nm (P1L3), and  $111.55 \pm 9.92$  Nm (P1L4) were observed as a function of gear selection in primary tillage, and average engine torques of the working sections of  $73.69 \pm 6.86$  Nm (P1L2),  $91.88 \pm 6.59$  Nm (P1L3), and  $100.15 \pm 4.06$  Nm (P1L4) were observed in secondary tillage. Under the same gear selection condition, the engine torque increased by 4.12% (P1L3) to 14.07% (P1L2) as a function of the tillage type. In addition, it was found that the engine torque increased by up to 32.7% (primary tillage) or 35.9% (secondary tillage) under the same tillage type. Basically, the overall average engine torque showed higher values in primary tillage under the same gear selection conditions, while there was a difference in engine torque of up to 51.37% as a function of the combination of tillage type and gear selection.

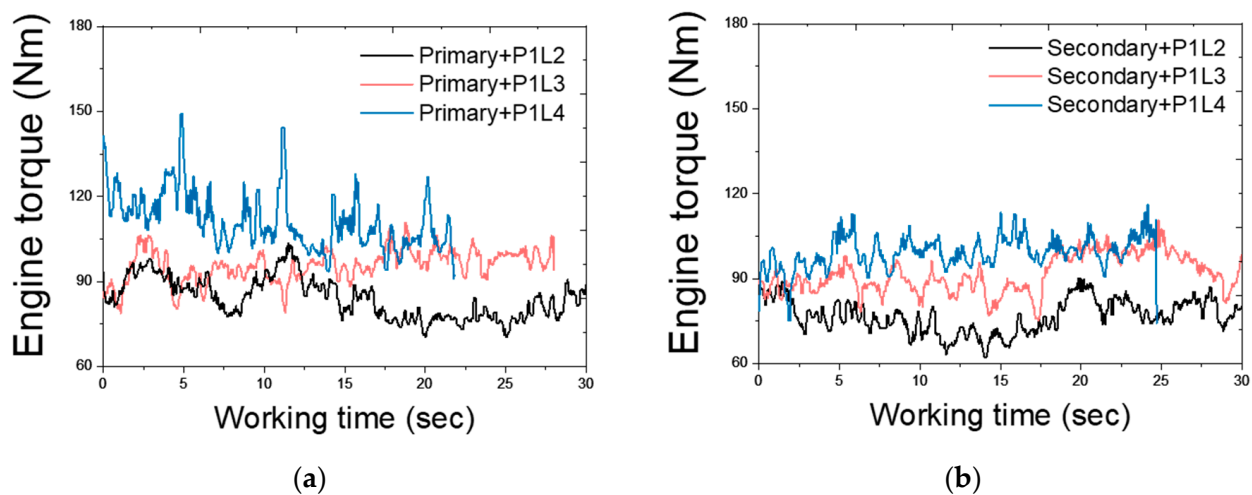


**Figure 6.** Results of engine torque data according to tillage type and gear selection during rotary tillage: (a) primary tillage; (b) secondary tillage.

### 3.4. PTO Shaft Load

The overall measured results of PTO shaft torque are shown in Figure 7. In the case of primary tillage, the overall average PTO shaft torque for the working section with respect to gear selection was  $256.1 \pm 36.8$  Nm (P1L2 at 564.5 rpm),  $286.2 \pm 32.1$  Nm (P1L3 at 563 rpm), and  $343.1 \pm 42.7$  Nm (P1L4 at 559.8 rpm). In the case of secondary tillage, the results of PTO shaft torque were  $200 \pm 28.3$  Nm (P1L2 at 565.4 rpm),  $255 \pm 29.7$  Nm (P1L3 at 563.4 rpm), and  $265.7 \pm 22.2$  Nm (P1L4 at 561.8 rpm). In the field test, the data measured for the secondary tillage method showed an average PTO torque value that was 10.1–22.6% lower than that of the primary tillage method due to the influence of the physical properties of soil, which changed rapidly with primary tillage, despite the rotary operation being

performed at the same travel speed, gear selection, and tillage depth. This phenomenon of increasing PTO shaft torque with increasing forward speed and decreased PTO shaft torque for secondary tillage was also observed in a 2018 study analyzing performance using a combined offset disc harrow [31].

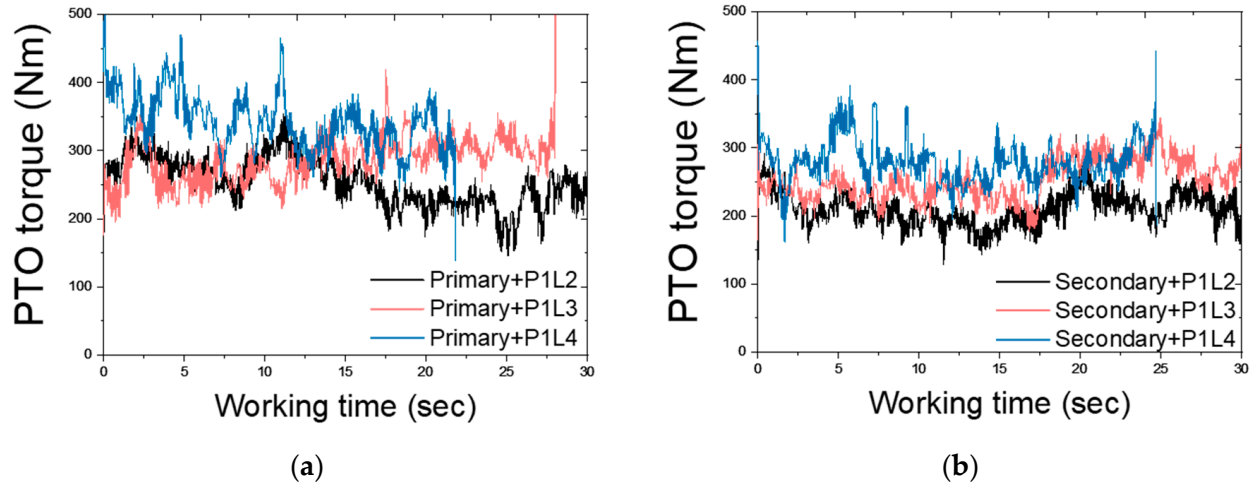


**Figure 7.** Results of PTO shaft torque as a function of tillage type and gear selection during rotary tillage: (a) primary tillage; (b) secondary tillage.

### 3.5. Axle Shaft Load

#### 3.5.1. Front Wheel Axle

The overall measurement results for front wheel torque are shown in Figure 8. In the case of primary tillage, the overall average front axle torques for the working section according to each gear selection were  $487.5 \pm 124$  Nm (P1L2 at 9.57 rpm),  $566.6 \pm 157$  Nm (P1L3 at 13.73 rpm), and  $541.2 \pm 213.5$  Nm (P1L4 at 18.16 rpm), respectively. In the case of secondary tillage, the results of front wheel axle torque were  $823.9 \pm 134.8$  Nm (P1L2 at 9.73 rpm),  $869.5 \pm 173.1$  Nm (P1L3 at 13.7 rpm), and  $878.7 \pm 108.7$  Nm (P1L4 at 18.2 rpm), respectively. Overall, secondary tillage showed average values for each gear selection that were 1.55–1.69 times higher than those for primary tillage, which was attributed to the fact that the power distribution in the engine was affected by the higher PTO load in primary tillage. However, it was confirmed that the pitch angle at the center of gravity of the tractor continuously occurred due to the soil–tool interaction in primary tillage, resulting in unstable load transfer. The standard deviation of the tractor’s torque was also higher by 23% at P1L4 than that for secondary tillage.

#### 3.5.2. Rear Wheel Axle

The overall results measured for rear wheel torque are shown in Figure 9. Basically, the rear wheel axle load, like the front wheel axle torque, did not show a linear relationship according to gear selection. However, it was analyzed that the rear axle load under secondary tillage conditions was 21% (P1L2) to 49% (P1L3) higher for all gear selections than under primary tillage conditions. In the case of primary tillage, the overall average rear axle torque for the working section according to each gear selection was  $555.9 \pm 127$  Nm (P1L2 at 6.41 rpm),  $622 \pm 167.8$  Nm (P1L3 at 9.18 rpm), and  $549.3 \pm 213.1$  Nm (P1L4 at 12.18 rpm), respectively. In the case of secondary tillage, the results of rear wheel axle torque were  $673.7 \pm 136.8$  Nm (P1L2 at 6.42 rpm),  $930.3 \pm 195$  Nm (P1L3 at 9.19 rpm),  $772.7 \pm 278.1$  Nm (P1L4 at 12.2 rpm), respectively. Based on these results, it was also concluded that the power requirements distributed to the axles were relatively high, as the power requirements in the engine and PTO shaft were relatively reduced in the rear wheels as well.

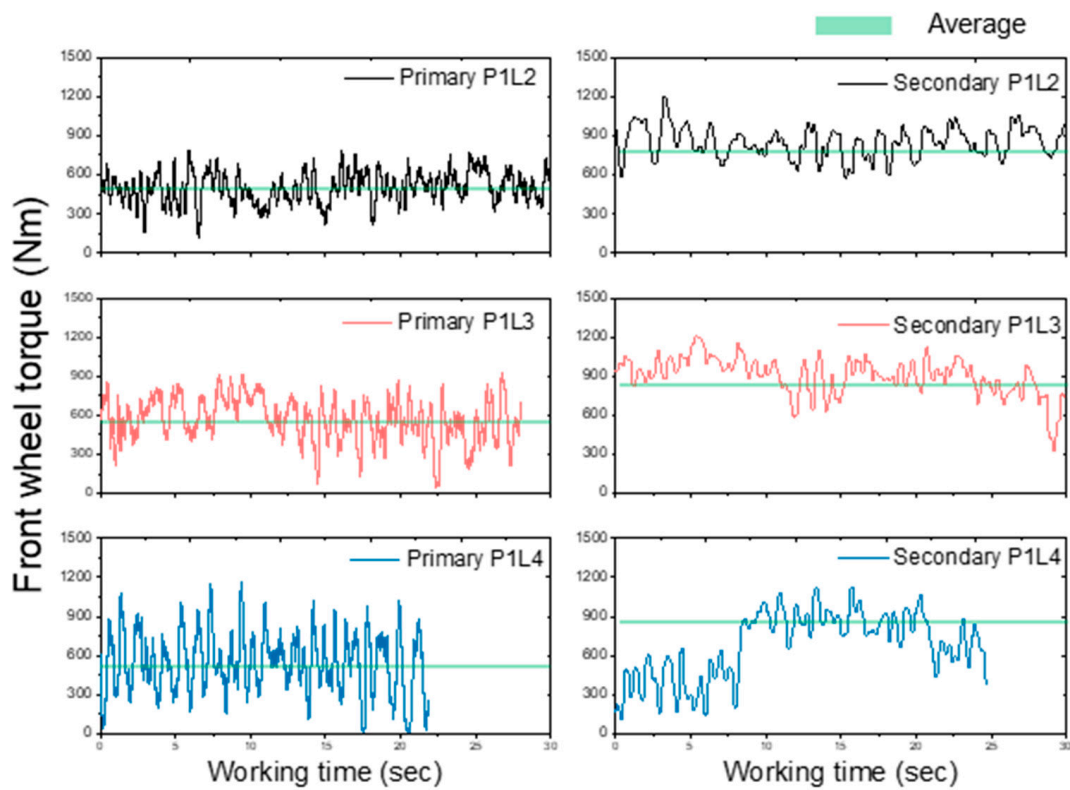


Figure 8. Results of front wheel axle torque data according to tillage type and gear selection during rotary tillage.

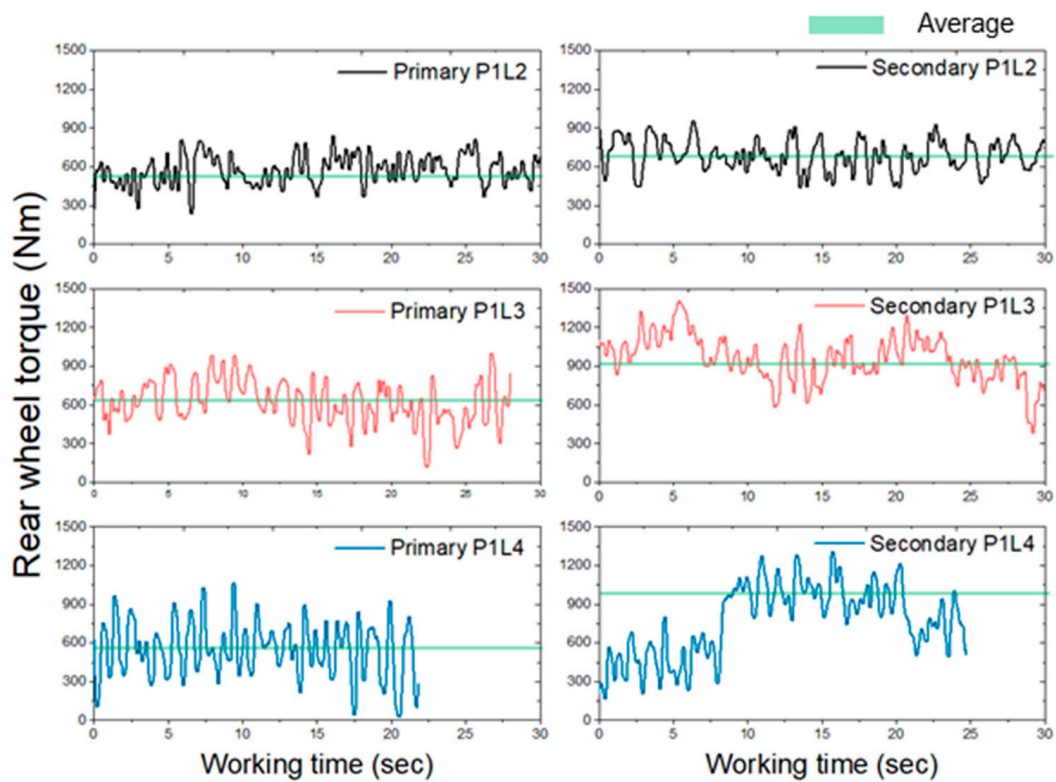


Figure 9. Results of rear wheel axle torque data according to tillage type and gear selection during rotary tillage.

### 3.6. Fuel Efficiency

The fuel efficiency of a 42 kW agricultural tractor depending on tillage type and gear selection is shown in Table 4. In terms of fuel usage, the FC when working with P1L4 was up to 1.09 times higher than the FC when working with P1L2. In terms of fuel efficiency, the SFC when working with P1L2 was up to 1.2 times higher than the SFC when working with P1L4. From a cost perspective, the fuel cost of working with P1L2 was up to 1.74 times higher than that when working with P1L4. In general, it has been reported that in order to obtain maximum fuel efficiency during tillage operations, it is required that the work be performed under the conditions of using the high torque ranges in the appropriate slip range [32]. Therefore, in the case of this test, where the slip rate did not change significantly when increasing the number of gears, the higher the torque value at a higher gear ratio, the better the fuel efficiency.

## 4. Discussion

In this study, the influence of soil–tool interaction (i.e., tillage type, gear selection, soil properties) during rotary plowing work was investigated. Based on a report on the effect of soil compaction on crop root growth from the USDA [33,34], test soil from an agricultural field was analyzed before the tillage operation in order to evaluate the degree to which the physical properties of the field affect (over 1630 kg/m<sup>3</sup>) or limit crop root growth (over 1800 kg/m<sup>3</sup>). The results of the test showed that the bulk density measured from 1571 to 1830 kg/m<sup>3</sup> decreased to a level of 1431 to 1480 kg/m<sup>3</sup>. This was judged as indicating that tillage type directly affects the soil–tool interaction.

In general, there are reports suggesting that the rear axle load is 3 to 8 times greater than the front axle load during plowing [11,12]. However, unlike plowing, the load transfer increased toward the front wheel, and the front wheel axle torque showed a similar level to the rear wheel axle torque. In other words, the rotavator increases the soil thrust in the working direction, giving the same effect as pushing the vehicle forward. This was found to be the same as the effect of strengthening the soil–tyre interaction with an auxiliary iron wheel. In addition, for the same reason, it was found that negative slip, which momentarily produces a higher travel speed than the theoretical speed of the vehicle, partly and momentarily occurs in some sections.

Figure 10 shows the relative histogram results of power requirements as a function of tillage type and gear selection. On the basis of the results of power requirement analysis, it can be seen that engine and PTO power have tendencies that are different from the wheel axle power requirements. In the case of wheel axle power under the same gear selection conditions, it was found that the required power in secondary tillage was 21–81% higher than in primary tillage. The reason for this phenomenon is that primary tillage reduces the internal friction of the soil [35]. In another study by Kim et al. [36], it was reported that with increasing value of the slip ratio range, the axle torque also increased. Table 4 shows that the slip ratio increased more during secondary tillage than during primary tillage, overall. Therefore, it seems that the power requirement of the wheel axle increased more during secondary tillage than during primary tillage in this study. In the case of the rotary tillage performed in this study, it was found that the effect of tillage method was greater than the effect of gear selection for the axle load, which is in contrast to the engine and PTO load. Conversely, it was analyzed that the effect of gear selection (Engine power: 4–14%, PTO power: 12.1–28.6%) on engine and PTO loads was greater than that of tillage type (Engine power: 31.6–35.1%, PTO power: 31.9–32.8%), and the load tended to decrease in secondary tillage.

Compared to the test conditions in the specifications of the actual rotavator, considering that only up to 62.1% of the maximum engine capacity (42 kW) was used, it was deemed that this work could be performed in a harder and stickier environment than the loam soil in which this study was conducted. In addition, it was concluded that the work efficiency will increase more when rotary tillage is performed under the conditions of a

tillage depth deeper than 12–13 cm, a wider work width (over 1820 mm), and a work speed faster than 3.24 km/h in the same working environment.

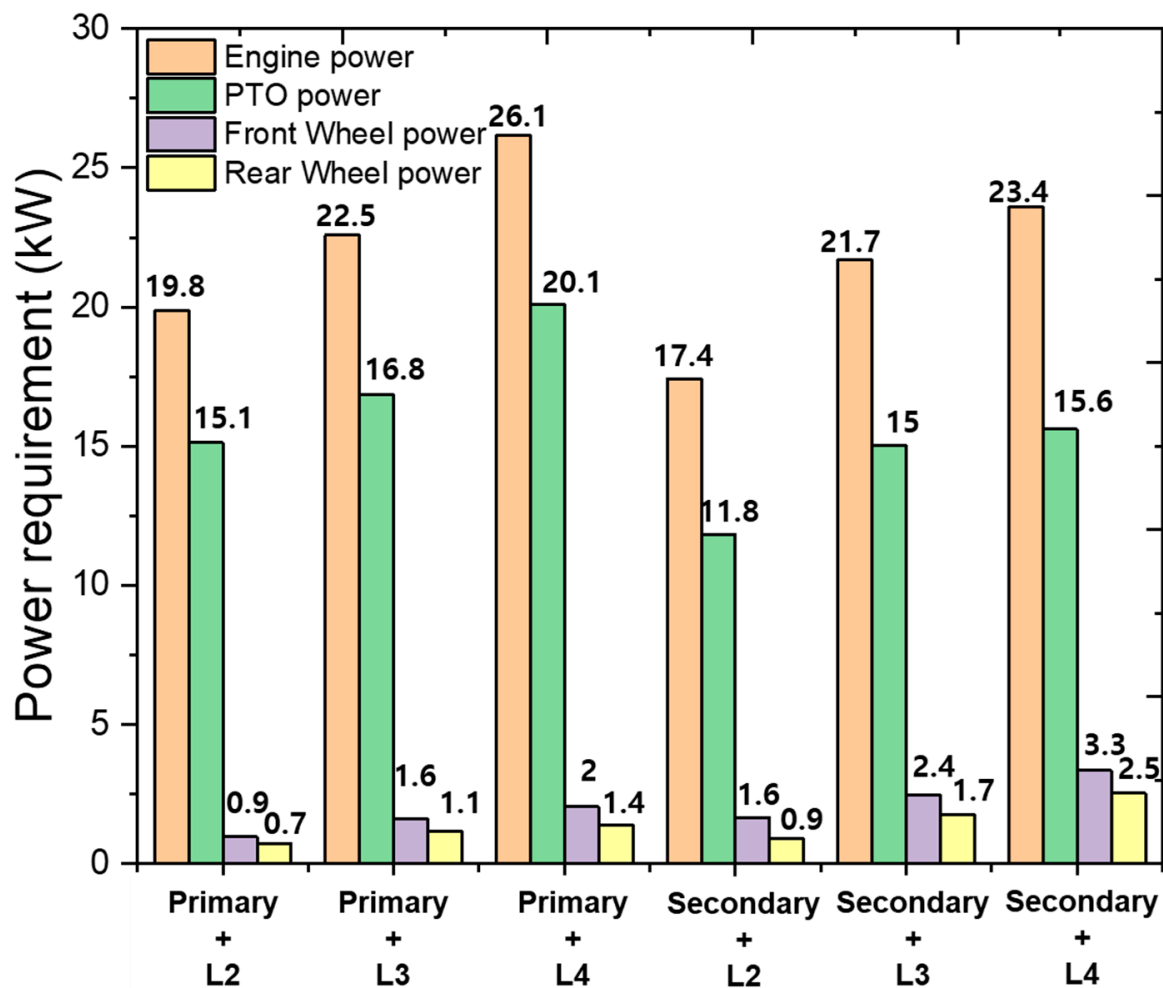


Figure 10. Analysis of power requirement as a function of tillage type and gear selection.

## 5. Conclusions

In this study, a field load measurement test was conducted to analyze the effect of tillage type (i.e., primary tillage or secondary tillage) and gear selection (i.e., P1L2, P1L3, or P1L4) on the tractor working load (i.e., engine load, wheel axle load, and PTO shaft load, as well as travel speed) during rotary tillage operations. The major conclusions obtained were as follows.

1. By measuring the soil properties according to depth, it was confirmed that the core index, shear strength, and water content, which are the main properties that affect the load of cultivation work, changed in accordance with the change in depth. In particular, soil bulk density was measured to decrease by 9–19% under rotary operation. Therefore, soil properties as a function of tillage type, which is a typical soil–tool interaction process, should be considered first when evaluating the performance of the operation of agricultural machinery or in field tests.
2. Overall average torque was higher by up to 14% (engine) and 29.1% (PTO shaft) in primary tillage than in secondary tillage when the selected gear was the same. When the tillage type was the same, it was found that the overall average torque increased as a result of gear selection by up to 35.9% (engine) and 33.9% (PTO shaft) in P1L4 compared to P1L2.

3. In the case of fuel efficiency, it was revealed that the effect of gear selection was greater than the effect of the tillage type. When working on loam field (soil water content of 17–20%, bulk density of 1571–1830 kg/m<sup>3</sup>, and cone index of 801–2065 kPa), the most suitable gear for reducing fuel consumption was found to be P1L4.
4. In addition, based on the power requirement results, from the perspective of the machine, when working on loamy soil with a tillage depth of 10 to 13 cm, 66.7–77% of the power generated by the engine was consumed by the PTO shaft. This shows that the force applied to the implements during rotary operation is greater than the traction load.
5. In the case of the power requirements, the power required on the same tillage type increased with increasing gear ratio. During secondary tillage, the overall power required decreased due to changes in key soil properties such as bulk density, cone index, and vane shear torque. Therefore, it was judged that design modification is necessary in order to have a wide working width, and that in some cases, rotary tillage will be possible at a deeper tillage depth or at a higher travel speed. It is expected that performance evaluation and optimal design of soil operation machinery in various working environments will be possible through similar field verification procedures in future studies.

Recently, various agricultural work environments have been defined, and virtual agricultural performance evaluation or load prediction simulation studies are being conducted through modeling. It is important to secure a database for the definition of agricultural work environments and load analysis. The results of this study are expected to be of use in future studies for designing loads in research on modeling and the verification of agricultural machinery systems such as soil–tool and soil–tyre interaction during agricultural operation.

**Author Contributions:** Conceptualization, Y.-S.K. and T.-J.K.; methodology, Y.-S.K. and W.-S.K.; software, B.-M.B. and T.-J.K.; validation, Y.-S.K. and W.-S.K.; formal analysis, Y.-S.K. and W.-S.K.; investigation, Y.-J.K. and T.-J.K.; data curation, Y.-S.K. and B.-M.B.; writing—original draft preparation, Y.-S.K.; writing—review and editing, B.-M.B.; supervision, Y.-J.K. and S.-D.L.; project administration, Y.-J.K. and T.-J.K.; funding acquisition, Y.-J.K. All authors have read and agreed to the published version of the manuscript.

**Funding:** This work was supported by the Korea Institute of Planning and Evaluation for Technology in Food, Agriculture, Forestry (IPET) through the Eco-Friendly Power Source Application Agricultural Machinery Technology Development Program, funded by Ministry of Agriculture, Food and Rural Affairs (MAFRA) (322047-5), and it was also supported by the Korea Institute of Planning and Evaluation for Technology in Food, Agriculture, Forestry (IPET) through the Technology Commercialization Support Program, funded by the Ministry of Agriculture, Food and Rural Affairs (MAFRA) (821014-03).

**Institutional Review Board Statement:** Not applicable.

**Data Availability Statement:** Data sharing not applicable.

**Conflicts of Interest:** The authors declare no conflict of interest.

## References

1. Kim, W.S.; Kim, Y.J.; Park, S.U.; Hong, S.J.; Kim, Y.S. Evaluation of PTO Severeness for 78 KW-Class Tractor According to Disk Plow Tillage and Rotary Tillage. *J. Drive Control* **2019**, *16*, 23–31. [CrossRef]
2. Lim, S.; Kwon, H.; Kang, Y.; Lee, P.; Kim, T.; Kim, Y.; Kim, Y. Power Analysis of a 3-KW Class Motor-Driven Multipurpose Walking-Type Transplanter. *J. Biosyst. Eng.* **2019**, *44*, 135–145. [CrossRef]
3. Kim, Y.J.; Chung, S.O.; Park, S.J.; Choi, C.H. Analysis of Power Requirement of Agricultural Tractor by Major Field Operation. *J. Biosyst. Eng.* **2011**, *36*, 79–88. [CrossRef]
4. Han, K.H.; Kim, K.U.; Wu, Y.G. Severeness of Transmission Loads of Agricultural Tractor for Rotary Operations in Poorly Drained Paddy Field. *J. Biosyst. Eng.* **1999**, *24*, 293–300.
5. Raper, R.L. Force requirements and soil disruption of straight and bentleg subsoilers for conservation tillage systems. *Appl. Eng. Agric.* **2005**, *21*, 787–794. [CrossRef]

6. Naderloo, L.; Alimadani, R.; Akram, A.; Javadikia, P.; Zeinali Khanghah, H. Tillage Depth and Forward Speed Effects on Draft of Three Primary Tillage Implements in Clay Loam Soil. *J. Food Agric. Environ.* **2009**, *7*, 382–385.
7. Moeenifar, A.; Mousavi-Seyedi, S.R.; Kalantari, D. Influence of Tillage Depth, Penetration Angle and Forward Speed on the Soil/Thin-Blade Interaction Force. *Agric. Eng. Int. CIGR J.* **2014**, *16*, 69–74.
8. Aday, S.H.; Ramadhan, M.N. Comparison between the Draft Force Requirements and the Disturbed Area of a Single Tine, Parallel Double Tines and Partially Swerved Double Tines Subsoilers. *Soil Tillage Res.* **2019**, *191*, 238–244. [CrossRef]
9. Kichler, C.M.; Fulton, J.P.; Raper, R.L.; McDonald, T.P.; Zech, W.C. Effects of Transmission Gear Selection on Tractor Performance and Fuel Costs during Deep Tillage Operations. *Soil Tillage Res.* **2011**, *113*, 105–111. [CrossRef]
10. Kim, W.S.; Kim, Y.J.; Park, S.U.; Kim, Y.S. Influence of Soil Moisture Content on the Traction Performance of a 78-KW Agricultural Tractor during Plow Tillage. *Soil Tillage Res.* **2020**, *207*, 104851. [CrossRef]
11. Kim, Y.S.; Kim, W.S.; Baek, S.Y.; Baek, S.M.; Kim, Y.J.; Lee, S.D.; Kim, Y.J. Analysis of Tillage Depth and Gear Selection for Mechanical Load and Fuel Efficiency of an Agricultural Tractor Using an Agricultural Field Measuring System. *Sensors* **2020**, *20*, 2450. [CrossRef]
12. Kim, Y.S.; Lee, S.D.; Baek, S.M.; Baek, S.Y.; Jeon, H.H.; Lee, J.H.; Kim, W.S.; Shim, J.Y.; Kim, Y.J. Analysis of the Effect of Tillage Depth on the Working Performance of Tractor-Moldboard Plow System under Various Field Environments. *Sensors* **2022**, *22*, 2750. [CrossRef]
13. Lee, D.H.; Kim, Y.J.; Chung, S.O.; Choi, C.H.; Lee, K.H.; Shin, B.S. Analysis of the PTO Load of a 75 KW Agricultural Tractor during Rotary Tillage and Baler Operation in Korean Upland Fields. *J. Terramech.* **2015**, *60*, 75–83. [CrossRef]
14. Behera, A.; Raheman, H.; Thomas, E.V. A Comparative Study on Tillage Performance of Rota-Cultivator (a Passive—Active Combination Tillage Implement) with Rotavator (an Active Tillage Implement). *Soil Tillage Res.* **2021**, *207*, 104861. [CrossRef]
15. Kim, Y.J.; Chung, S.K.; Choi, C.H.; Lee, D.H. Evaluation of Tractor PTO Severeness during Rotary Tillage Operation. *J. Biosyst. Eng.* **2011**, *36*, 163–170. [CrossRef]
16. Kim, Y.J.; Chung, S.O.; Choi, C.H. Effects of Gear Selection of an Agricultural Tractor on Transmission and PTO Load during Rotary Tillage. *Soil Tillage Res.* **2013**, *134*, 90–96. [CrossRef]
17. Kim, Y.S.; Lee, P.U.; Kim, W.S.; Kwon, O.W.; Kim, C.W.; Lee, K.H.; Kim, Y.J. Strength Analysis of a PTO (Power Take-Off) Gear-Train of a Multi-Purpose Cultivator during a Rotary Ditching Operation. *Energies* **2019**, *12*, 1100. [CrossRef]
18. Tan, K.H. *Soil Sampling, Preparation, and Analysis*; CRC Press: New York, NY, USA, 1995; ISBN 0-8247-9675-6.
19. O’Kelly, B.C.; Sivakumar, V. Water Content Determinations for Peat and Other Organic Soils Using the Oven-Drying Method. *Dry. Technol.* **2014**, *32*, 631–643. [CrossRef]
20. Ditzler, C.; Scheffe, K.; Monger, H.C. *USDA Handbook 18*; Government Printing Office: Washington, DC, USA, 2017.
21. Thien, S.J. A Flow Diagram for Teaching Texture-by-Feel Analysis. *J. Agron. Educ.* **1979**, *8*, 54–55. [CrossRef]
22. *ASABE Standards EP542*; Procedure for Using and Reporting Data Obtained with the Soil Cone Penetrometer. ASAE, Ed.: St. Joseph, MI, USA, 2009; Volume 1999.
23. *ASABE Standards S313.3*; Soil Cone Penetrometer. ASAE, Ed.: St. Joseph, MI, USA, 2005; Volume 1999.
24. Park, J.G. *Bio-Production Machinery Engineering*, 1st ed.; CIR: Seoul, Republic of Korea, 2008.
25. Srivastava, A.K.; Goering, C.E.; Rohrbach, R.P.; Buckmaster, D.R. *Engineering Principles of Agricultural Machines*, 2nd ed.; American Society of Agricultural and Biological Engineers (ASABE): St. Joseph, MI, USA, 2006.
26. Nataraj, E.; Sarkar, P.; Raheman, H.; Upadhyay, G. Embedded Digital Display and Warning System of Velocity Ratio and Wheel Slip for Tractor Operated Active Tillage Implements. *J. Terramech.* **2021**, *97*, 35–43. [CrossRef]
27. Rasool, S.; Raheman, H.; Upadhyay, G. Development of an Instrumentation System for Evaluating the Tractive Performance of Walking Tractors. *Int. J. Curr. Microbiol. Appl. Sci.* **2017**, *6*, 759–770. [CrossRef]
28. Chung, S.O.; Sudduth, K.A. Soil Failure Models for Vertically Operating and Horizontally Operating Strength Sensors. *Trans. ASABE* **2006**, *49*, 851–863. [CrossRef]
29. Farid Eltom, A.E.; Ding, W.; Ding, Q.; Ali, A.B.B.; Eisa Adam, B. Effect of Trash Board on Moldboard Plough Performance at Low Speed and under Two Straw Conditions. *J. Terramech.* **2015**, *59*, 27–34. [CrossRef]
30. Kim, Y.S.; Kim, W.S.; Siddique, A.A.; Baek, S.Y.; Baek, S.M.; Cheon, S.H.; Lee, S.D.; Lee, K.H.; Hong, D.H.; Park, S.U.; et al. Power Transmission Efficiency Analysis of 42 KW Power Agricultural Tractor According to Tillage Depth during Moldboard Plowing. *Agronomy* **2020**, *10*, 1263. [CrossRef]
31. Upadhyay, G.; Raheman, H. Performance of Combined Offset Disc Harrow (Front Active and Rear Passive Set Configuration) in Soil Bin. *J. Terramech.* **2018**, *78*, 27–37. [CrossRef]
32. Grisso, R.; Pitman, R.; Perumpral, J.V.; Vaughan, D.; Roberson, G.T.; Hoy, R.M. *“Gear up and Throttle down” to Save Fuel*; Virginia Cooperative Extension Publication: Blacksburg, VA, USA, 2011; pp. 442–450.
33. Nyéki, A.; Milics, G.; Kovács, A.J.; Neményi, M. Effects of Soil Compaction on Cereal Yield: A Review. *Cereal Res. Commun.* **2017**, *45*, 1–22. [CrossRef]
34. USDA. *Soil Mechanics Level I. Module 3—USDA Textural Soil Classification. Study Guide*; USDA, Soil Conservation Service: Stillwater, OK, USA, 1987.



35. Park, J.G.; Lee, K.S.; Cho, S.C.; Noh, K.M.; Chung, S.O.; Chang, Y.C. Analysis of Variations in Mechanical Properties of Soil by Tillage Operations. *J. Biosyst. Eng.* **2007**, *32*, 215–222.
36. Kim, W.S.; Kim, Y.S.; Kim, Y.J. Development of Prediction Model for Axle Torque of Agricultural Tractors. *Trans. ASABE* **2020**, *63*, 1773–1786. [CrossRef]

**Disclaimer/Publisher’s Note:** The statements, opinions and data contained in all publications are solely those of the individual author(s) and contributor(s) and not of MDPI and/or the editor(s). MDPI and/or the editor(s) disclaim responsibility for any injury to people or property resulting from any ideas, methods, instructions or products referred to in the content.

## Article

# Theoretical Calculations and Experimental Studies of Power Loss in Dual-Clutch Transmission of Agricultural Tractors

Hyoung-Jong Ahn <sup>1,2</sup>, Young-Jun Park <sup>2</sup>, Su-Chul Kim <sup>3</sup> and Chanho Choi <sup>1,\*</sup>

<sup>1</sup> Tractor Advanced Development Group, LS Mtron, Anyang 14118, Republic of Korea; hyoungjong.ahn@lsmtron.com

<sup>2</sup> Department of Biosystems Engineering, Seoul National University, 1 Gwanak-ro, Gwanak-gu, Seoul 08826, Republic of Korea; yjpark95@snu.ac.kr

<sup>3</sup> Department of Smart Industrial Machinery, Korea Institute of Machinery & Materials, Daejeon 34103, Republic of Korea; sckim@kimm.re.kr

\* Correspondence: chance.choi@lsmtron.com; Tel.: +82-31-8045-0494

**Abstract:** Recent carbon neutrality policies have led to active research in the agricultural tractor sector to replace internal combustion engines, making it imperative to minimize power losses to improve efficiency. Dual-clutch transmissions (DCTs) have been employed in agricultural tractors primarily due to their short shift time and smooth shift feel. However, DCTs have a relatively large number of components and complex structures owing to spatial constraints, making it challenging to predict power losses. Therefore, to predict DCT power losses, this study defined oil churning by considering the structural characteristics and oil circulation and comparing and analyzing the theoretical calculation and test results of power losses at different oil levels. Power loss was calculated based on ISO standards and fluid viscosity theory, and tests were performed to verify. We calculated power losses based on the defined oil churning of a DCT in agricultural tractors and confirmed that their consistency in test results improved when reflecting the lubrication state, considering the structural features and oil circulation. In addition, the factors contributing to power loss under low- and high-speed conditions were analyzed by calculating the power loss for each component.

**Keywords:** dual-clutch transmission; power loss; agricultural tractor

**Citation:** Ahn, H.-J.; Park, Y.-J.; Kim, S.-C.; Choi, C. Theoretical Calculations and Experimental Studies of Power Loss in Dual-Clutch Transmission of Agricultural Tractors. *Agriculture* **2023**, *13*, 1225. <https://doi.org/10.3390/agriculture13061225>

Academic Editor: Kenshi Sakai

Received: 20 May 2023

Revised: 5 June 2023

Accepted: 9 June 2023

Published: 10 June 2023



**Copyright:** © 2023 by the authors. Licensee MDPI, Basel, Switzerland. This article is an open access article distributed under the terms and conditions of the Creative Commons Attribution (CC BY) license (<https://creativecommons.org/licenses/by/4.0/>).

## 1. Introduction

Agricultural tractors perform various farming tasks using the vehicle's rotational power or traction, such as plowing, transportation, and rotary work. Traditionally, diesel engines, particularly with manual transmissions, have been widely used owing to their high torque characteristics relative to engine output. Recently, demand for improved driver convenience and work efficiency, as well as technological pressure to replace fossil fuels in the agricultural tractor sector due to carbon neutrality policies, has been increasing.

Prominent alternative power sources for agricultural tractors being discussed include hydrogen fuel cells, batteries, and biodiesel. Research on small electrically driven tractors using batteries and motors, and studies exploring the technical and economic feasibility of small farms, are actively underway [1–3]. Other studies have proposed new energy management strategies for applying hybrid systems, comprising fuel cells and battery packs, to agricultural tractors [4,5]. Moreover, energy, economic, and environmental life-cycle assessment analyses have been conducted for applying biodiesel fuel to agricultural tractors [6]. However, alternative power sources generate less energy per unit volume and mass compared to diesel [7,8]. Consequently, when using alternative power sources, the continuous working time is reduced, making power losses in transmission systems an even more critical issue owing to their direct impact on production efficiency.

Furthermore, researchers are actively studying automatic transmission systems in response to market demand for improved driver convenience and work efficiency [9–12].

Automated transmissions (ATs) allow drivers to operate without a gear lever and can improve transmission productivity via the selection of the optimal gear ratio for farming tasks through control algorithms. Dual-clutch transmissions (DCTs), a type of AT, use two clutches responsible for even and odd gear steps in power transmission. Considering DCTs preselect the target gear shift stage and engage the clutch when shifting, they have a short shift time with no power interruption, resulting in a smooth shifting experience. However, due to the increased number of mechanical components needed to select even and odd gears—such as wet multi-plate clutches—and the complex supporting structures for components owing to spatial constraints within the transmission, power losses in the transmission must be considered.

Research on power loss in transmissions has been conducted primarily at the component level. Many studies have investigated the drag torque caused by oil viscosity between friction surfaces to calculate the power loss of wet multi-plate clutches [13,14]. The shear stress caused by oil viscosity between the ring and cone was considered for calculating the power loss of synchronizers, friction coefficients obtained through testing were proposed to predict bearing power loss [15,16]. In addition, research comparing analytical models and test results has been conducted to predict the power loss caused by oil churning in gears [17,18]. Moreover, researchers have conducted studies to calculate the power loss due to gear load transfer and conducted experimental verifications [19,20].

Power loss research on DCTs has primarily been conducted in the automotive sector, predicting power loss through theoretical predictions and experimental verifications [21,22]. Additionally, research considering power loss in transmissions has also been conducted in the agricultural tractor sector. The efficiency and energy consumption of tractor transmissions have been examined primarily in relation to operating conditions using vehicle tests [23,24]. Studies have also been conducted to predict transmission efficiency by examining the power loss generated by each component of agricultural DCTs through theoretical calculations [25].

Considering policy reasons driven by carbon neutrality requirements and consumer demand, a systematic study on the power transmission efficiency of agricultural transmissions is necessary. However, research on the efficiency of tractors has focused primarily on vehicle-level experimental verification, while no studies have examined the contribution of each component to the total power loss and compared theoretical calculations with actual test results. Moreover, the oil-churning state of the mechanical components must be defined to accurately predict the power loss of a transmission system. However, in transmissions such as the DCT—which has many components and circulates oil through hydraulic systems—oil levels change locally; hence, the structural characteristics must be considered. Moreover, studies on efficiency considering oil level changes due to the structural characteristics of agricultural DCTs remain insufficient.

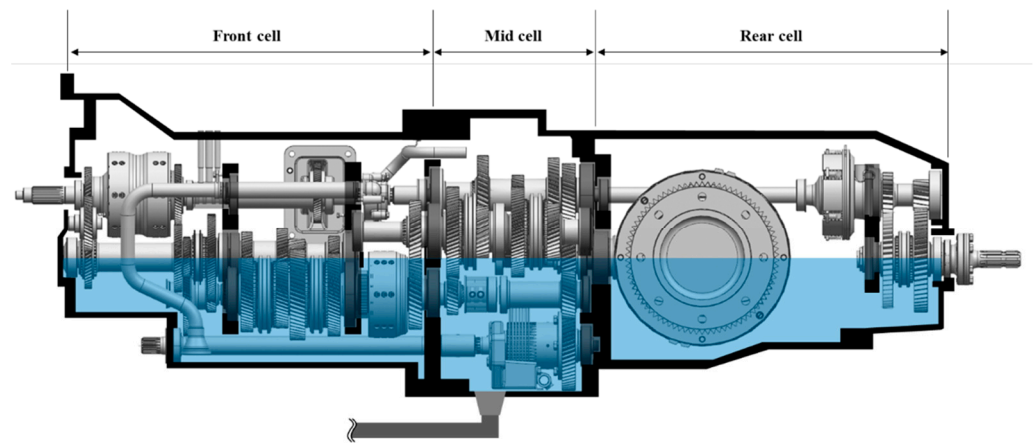
Accordingly, this study compared the theoretical predictions of power loss in a DCT applied to agricultural tractors with power loss measurements obtained through laboratory tests. Considering the oil circulation for DCT lubrication, two power loss models, which considered the average oil level and oil circulation, respectively, were proposed, with theoretical predictions performed for each case. We used the ISO standard and viscosity fluid theory to calculate the power loss of components making up the transmission and constructed a measurement system using a 3-axis dynamometer to measure them. The power losses considering oil circulation and the average oil level were compared and the test results were analyzed.

## 2. Materials and Methods

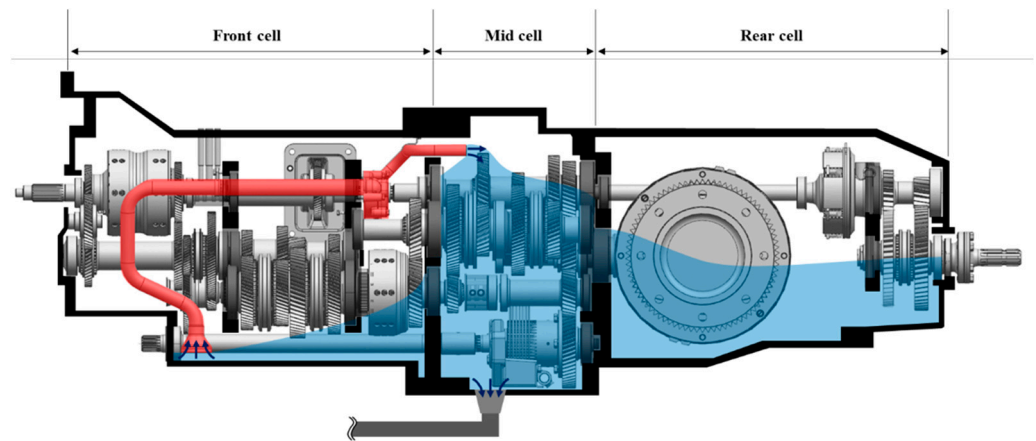
### 2.1. DCTs for Agricultural Tractors

In this study, a 24-speed full-power shift DCT for 100-kW agricultural tractors was applied to 5-ton tractors (without attachments) and shifted by alternately engaging the left and right odd and even shaft clutches. This DCT comprises three parts—input, even, and odd shafts—which is relatively more components than other transmissions.

As shown in Figure 1, the target DCT comprises 64 shafts, 58 gears, 95 bearings, 5 clutches, 14 synchronizers, and 2 dog clutches, and includes 2 rear axle brakes and 1 parking brake within the transmission. However, the transmission system is assembled by dividing it into sections because it is challenging to arrange the numerous components that make up the DCT in a single case. Each section has a partition wall supported by housing and bearings, with empty spaces being left to allow free oil movement when designing the partition wall. However, the rear partition wall has a relatively thick wall and a narrow space to support the amplified load of the gear train, hindering oil circulation and isolating the space. Nonetheless, these spaces can be divided into three cells based on the partition walls isolating them.



(a) Case I: Considering average oil level.



(b) Case II: Considering oil circulation.

**Figure 1.** Oil levels of a dual-clutch transmission (DCT) in full-power shift.

Figure 1 shows the structure and oil level of the DCT used in this study. The DCT is divided into three cells based on the partition walls supporting the rear part of the power transmission system: the front cell, where gears of the forward/reverse shift and main shift parts are arranged; the mid cell, where gears of the range shift and 4WD parts are arranged; and the rear cell, where the spiral bevel gear connected to the rear axle and PTO (power take-off) gears are arranged. As shown in Figure 1a, the transmission oil level is maintained at the height of the rear axle center.

The oil in agricultural tractors simultaneously performs the roles of lubrication for the components and hydraulic fluid for the hydraulic system. The transmission oil is churned by the immersed rotating components and circulated by the hydraulic system simultane-

ously. Therefore, the oil levels in each cell are dynamic and differ considerably. The DCT used in this study has an intake line at the bottom to supply oil to the hydraulic system. Moreover, to secure a stable oil supply flow when driving on a slope, forward/reverse and dual clutches are used, which forcibly supply oil from the front cell—where relatively more flow is discharged—to the mid cell through a pump. Figure 1b shows an oil-level application model reflecting the partition walls and oil circulation of the hydraulic system.

Theoretical power-loss predictions were performed for Case I, considering the average oil level of the transmission, and for Case II, considering the partition walls and hydraulic system, both verified through testing.

### 2.2. Power Loss Calculations

The ISO TR 14179-1 standard and drag torque due to viscous fluid were considered to calculate the power loss caused by the components making up the powertrain, with gears, bearings, shafts, clutches, and brakes considered for these calculations [26,27].

The total power loss can be expressed as the sum of fundamental, load-dependent, and speed-dependent power losses. The fundamental power loss is the power consumed to drive the tractor, a representative example being the power loss of the pump used to drive the hydraulic line. The measured fundamental power loss was 3.0 kW, applied equally to all gear steps. The load-dependent power loss occurs in the friction surfaces under load, resulting in a corresponding load-dependent power loss of gears and bearings. Speed-dependent power loss is the power loss due to motion resistance when components of the power transmission system rotate, implying that the power loss due to drag is caused by the oil applied for lubrication and cooling. For speed-dependent power loss, the power loss of clutches, bearings, gears, shafts, and brakes was considered. The total power loss ( $P_L$ ) of the power transmission system can be calculated using Equation (1), with the factors considered for each power loss shown in Table 1.

$$P_L = \sum P_{HP} + \sum P_{GL} + \sum P_{GS} + \sum P_{BL} + \sum P_{BS} + \sum P_S + \sum P_{CL} + \sum P_{BR} \quad (1)$$

**Table 1.** Composition of the total power loss.

Power Loss	Component
Fundamental power loss	Hydraulic pump [ $P_{HP}$ ]
Load-dependent power loss	Gear [ $P_{GL}$ ], Bearing [ $P_{BL}$ ]
Speed-dependent power loss	Gear [ $P_{GS}$ ], Bearing [ $P_{BS}$ ], Clutch [ $P_{CL}$ ], Shaft [ $P_S$ ], Brake [ $P_{BR}$ ]

#### 2.2.1. Power Losses of the Gear and Shaft

The load-dependent power loss of the gear ( $P_{GL}$ ) can be expressed as follows:

$$P_{GL} = \frac{f_m T_1 n_1 \cos^2 \beta}{9549M} \quad (2)$$

where  $f_m$  denotes the mesh coefficient of friction (determined by the pitch line speed, lubricating oil viscosity, load size, and gear size), and  $M$  denotes the mesh mechanical advantage (a coefficient influenced by the gear size, pressure angle, and gear step).

The speed-dependent power loss of the gear ( $P_{GS}$ ) and speed-dependent power loss of the shaft ( $P_S$ ) can be expressed as the sum of power losses owing to the outer diameter ( $P_{GW1}$ ), lateral part ( $P_{GW2}$ ), and tooth surface ( $P_{GW3}$ ).  $P_{GW1}$ ,  $P_{GW2}$ , and  $P_{GW3}$  can be calculated using Equations (3)–(5), respectively, as follows:

$$P_{GW1} = \frac{7.37 f_g v n^3 D^{4.7} L}{A_g 10^{26}} \quad (3)$$

$$P_{GW2} = \frac{1.474f_gvn^3D^{5.7}}{A_g10^{26}} \tag{4}$$

$$P_{GW3} = \frac{7.37f_gvn^3D^{4.7}F\left(\frac{R_f}{\sqrt{\tan\beta}}\right)}{A_g10^{26}} \tag{5}$$

where  $R_f$  denotes the roughness factor (which is influenced by the transverse module).

### 2.2.2. Power Loss of the Bearing

The load-dependent power loss of the bearing ( $P_{BL}$ ) can be expressed as follows:

$$P_{BL} = \frac{(M_1 + M_2)n}{9549} \tag{6}$$

where  $M_1$  denotes the bearing-load-dependent torque (calculated using the load rating of the bearing, dynamic load, coefficient of friction, and bearing size) and  $M_2$  denotes the cylindrical-roller-bearing axial-load-dependent moment (determined by the friction coefficient of the lubrication surface, axial bearing load, and bearing size).

The speed-dependent power loss of the bearing ( $P_{BS}$ ) can be expressed as follows:

$$P_{BS} = \frac{(M_0 + M_3)n}{9549} \tag{7}$$

where  $M_0$  denotes the load-independent frictional moment (influenced by the dynamic viscosity coefficient, dip factor, rotation speed, and size), and  $M_3$  is the frictional moment of seals (a factor influenced by the size and type of the bearing).

### 2.2.3. Power Loss of the Clutch and Brake

Clutch drag torque occurs owing to the shear stress caused by the viscosity of the lubricating oil between the friction surfaces. The clutch power loss can be calculated by correcting the drag torque based on the supplied flow area, while the drag torque can be calculated using Equation (8) [27]. The oil is supplied from the shaft center, causing a ruptured section where the oil flow breaks into mist and steam. As a result, three flow sections are generated— $T_{fa}$ ,  $T_{ra}$ , and  $T_m$ ; their relationships are expressed in Equations (9)–(11). The oil used was ISO VG 46; in addition, oil viscosity properties of 46 cSt at 40 °C and 6.7 cSt at 100 °C were considered. The viscosity of the lubricating oil in the mist state can be assumed to be 1/10 of the oil viscosity.

$$T_{CL} = (1 - r_{ag}) \cdot (T_{fa} + T_{ra} + T_m) \tag{8}$$

$$T_{fa} = \frac{\pi\mu\Delta\omega N}{2h} \cdot (r_c^4 - r_i^4) \tag{9}$$

$$T_{ra} = \frac{\pi\mu\Delta\omega N}{h} \cdot \Phi \cdot (r_o^2 - r_c^2) \tag{10}$$

$$T_m = \frac{2\pi\mu_{mist}\Delta\omega N}{h} \cdot \left[ \frac{(r_o^4 - r_c^4)}{4} - \frac{\Phi}{2} \cdot (r_o^2 - r_c^2) \right] \tag{11}$$

The power loss of the clutch ( $P_{CL}$ ) considering the drag torque of each section can be expressed as follows:

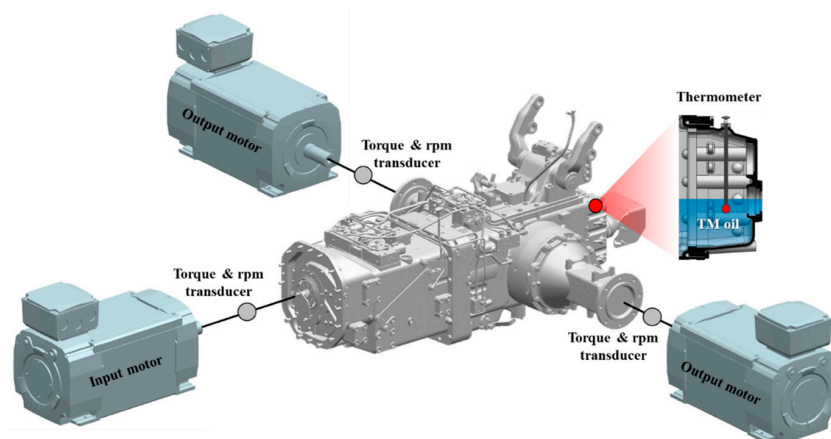
$$P_{CL} = T_{CL}\Delta n \frac{2\pi}{60 \times 1000} \tag{12}$$

Similarly, the power loss of the brake ( $P_B$ ), which occurs owing to the shear stress caused by the fluid viscosity, can be expressed as follows:

$$P_B = (1 - r_{ag}) \frac{N\mu\alpha}{h} \left( \frac{2\pi n}{60} \right)^2 \left[ \frac{r_o^4}{4} - \frac{r_i^4}{4} \right] \frac{1}{1000} \quad (13)$$

### 2.3. Power Loss Measurement of DCT

Figure 2 shows the system constructed for power loss measurement using a 3-axis dynamometer to control the rotation speed and torque. Sensors for measuring the rotation speed and torque are installed at the connection between the motor and the transmission to measure the input and output power. The input speed to the transmission is controlled at the input section, while the load applied to the transmission is controlled by controlling the torque at the output section. Additionally, a thermometer is installed inside the transmission system to monitor the oil temperature during the test. The test procedure is as follows. The speed of the input motor is slowly increased over 120 s from 0 to 2200 rpm. When the speed reaches 2200 rpm, the torque of the output motor is increased by 200 Nm to reach the target load level. While maintaining the target load for 1 min, the torque and rotation speed of the input and output sections are measured by the sensor. The oil temperature is maintained in the range of 50 to 90 °C, which is the normal operating temperature of the tractor. Motor and sensor specifications are shown in Table 2.



(a) layout of the 3-axis dynamometer system



(b) photograph of the 3-axis dynamometer system

**Figure 2.** Power loss measurement system.



**Table 2.** Specifications of sensor and motor applied to 3-axis dynamometer.

Component	Specifications
Input motor	Rated voltage: 360 V, rated speed: 3090 rpm, rated power: 282 kW
Output motor	Rated voltage: 360 V, rated speed: 1800 rpm, rated power: 246 kW
Torque and rpm sensor	Nominal torque: 30 kNm, nominal rotational speed: 4000 rpm Magnetic rotational speed measuring system: 1024 pulses/revolution

For the test, the input rotation speed was set to the engine’s rated rotation speed of 2200 rpm across all gear steps. The torque level applied to the transmission was determined separately for the two sections. In the max. traction force range, traction force was determined using the vehicle weight, with the engine’s output not fully utilized. In the rated engine power range, the engine’s rated output could be used, with the output torque of the rear axle decreasing as the vehicle speed increased. Figure 3 shows the test conditions, applying the wheel torque, vehicle speed, and input power at the rated rotation speed of the engine for the tractor used in this study. Tests were conducted in gear steps 2nd–24th, with the load conditions for each point shown in Figure 3.

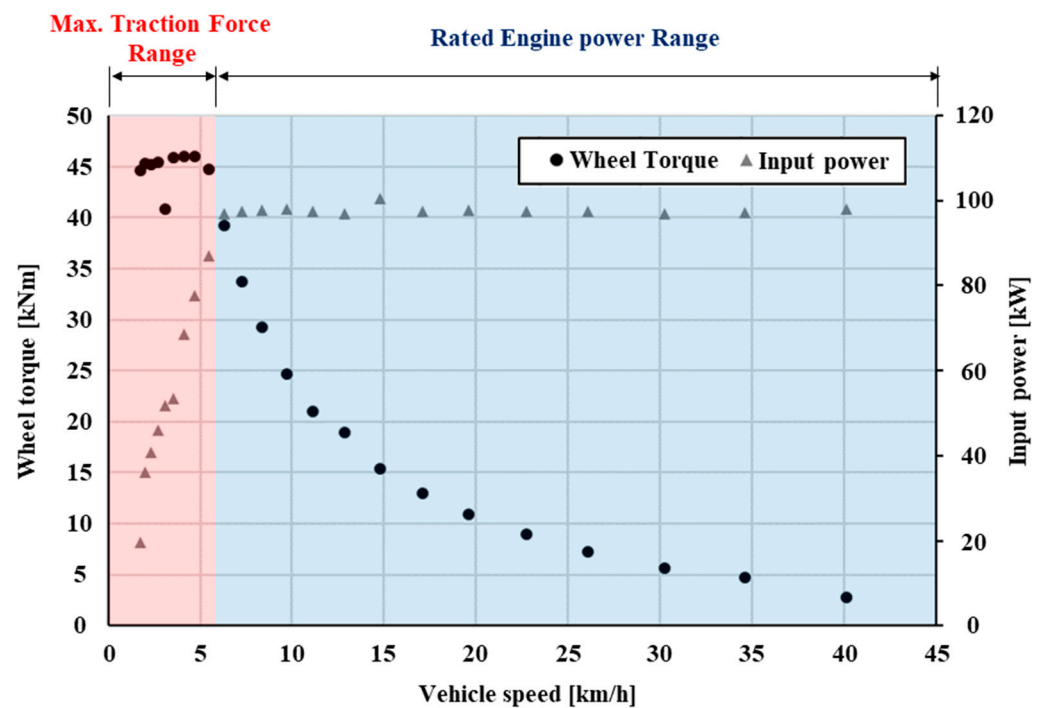
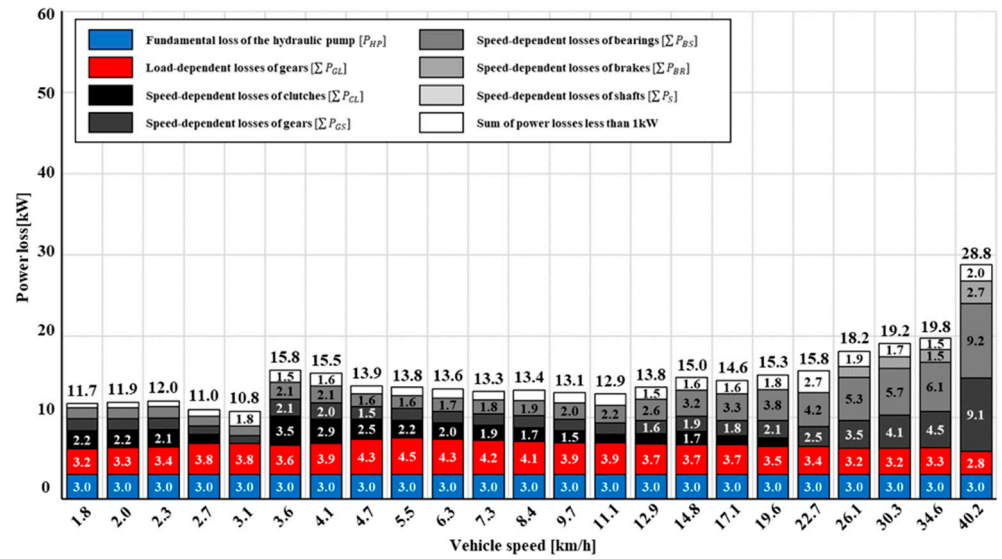


**Figure 3.** Input load conditions for experimental studies.

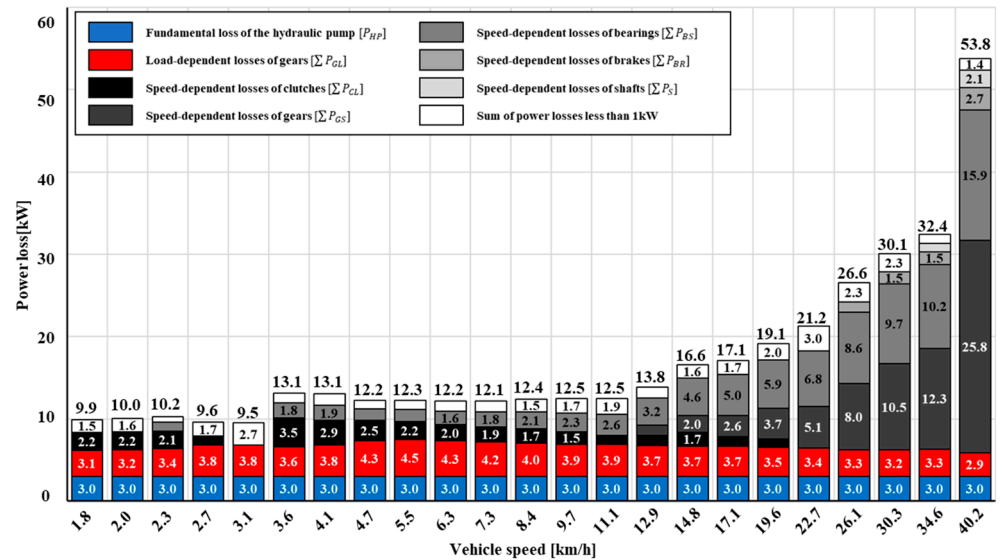
### 3. Results

#### 3.1. Theoretical Power Loss Calculations

Figure 4 shows the theoretical calculation results of the power loss based on the equations presented in Section 2.1. The horizontal axis represents the vehicle speed at the engine’s rated rotation speed for each gear step. For Case I and Case II, the total power loss can be calculated by adding the power loss of the DCT components, with power losses of less than 1 kW being combined and represented as a single item.



(a) Case I: Considering average oil level



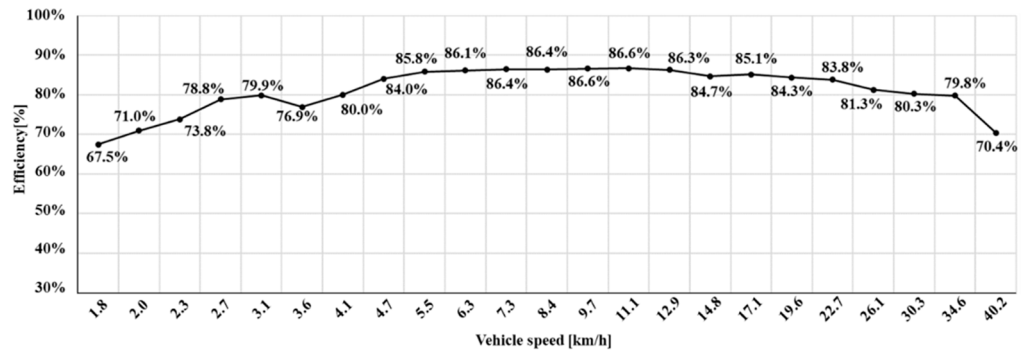
(b) Case II: Considering oil circulation

Figure 4. Theoretical calculation results of the power losses.

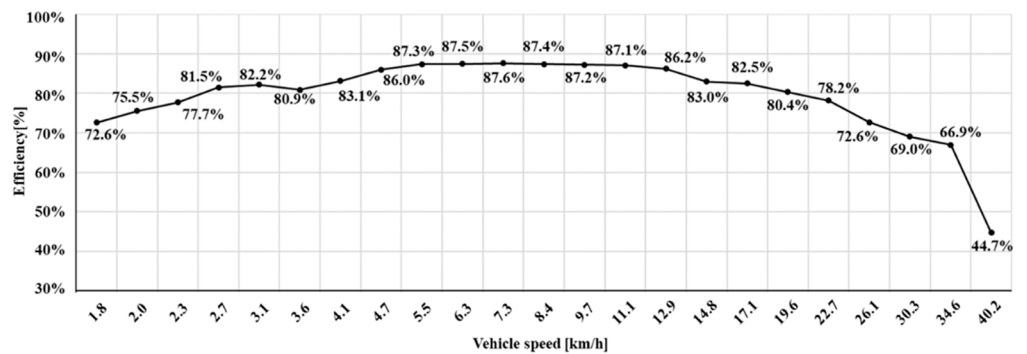
The components comprising the largest portion of overall power loss are the gears and bearings. Most of the load-dependent power loss occurs owing to the gears, the largest power loss occurring at 5.5 km/h for Cases I and II of 4.51 and 4.50 kW, respectively. As the vehicle speed increases at gear steps above 12 km/h, the speed-dependent power loss of the gears and bearings increases proportionally. Furthermore, the speed-dependent power loss of the gears and bearings is the highest at the top gear step of 40.2 km/h. In Case I, the speed-dependent power loss of the gears and bearings is 9.1 and 9.2 kW, respectively, while in Case II, it is 25.8 and 15.9 kW, respectively. The highest power loss occurs at the top speed of 40.2 km/h for both Cases I and II, with total power losses of 28.8 and 53.8 kW, respectively. This is because the speed-dependent power loss of each component is calculated to be higher in high-speed gear steps for Case II compared to Case I.

Figure 5 shows the power transmission efficiency calculated for Cases I and II. The power transmission efficiency for Cases I and II tends to increase as the vehicle speed

increases in the max. traction force range (0–5.5 km/h) owing to the contribution of fundamental and load-dependent power losses relative to the total power. In the rated engine power range (5.5–40.2 km/h), the efficiency is maintained up to a speed of 11.1 km/h, but drops sharply as the speed increases in high-speed gear steps above 12.9 km/h. The maximum efficiency is 86.6% at 9.7 km/h for Case I and 87.6% at 7.3 km/h for Case II, while the minimum efficiency is calculated to be 70.4% for Case I and 44.7% for Case II at 40.2 km/h.



(a) Case I: Considering average oil level



(b) Case II: Considering oil circulation

**Figure 5.** Power transmission efficiencies obtained by theoretical calculation.

### 3.2. Experimental Studies of Power Loss

Figure 6 shows the measurement results of power loss for each gear step of the DCT obtained through lab tests.

As the vehicle speed increases, the power loss of the transmission tends to increase. The power loss is lowest at 1.8 km/h (10.16 kW), and highest at 40.2 km/h (60.06 kW). Conversely, at lower gear steps with low vehicle speeds, the efficiency increases as the speed increases, it being highest at 5.5 km/h (83.2%). At gear steps with vehicle speeds above 5.5 km/h, the efficiency tends to decrease as the speed increases, the efficiency being the lowest at 40.2 km/h (37.2%).

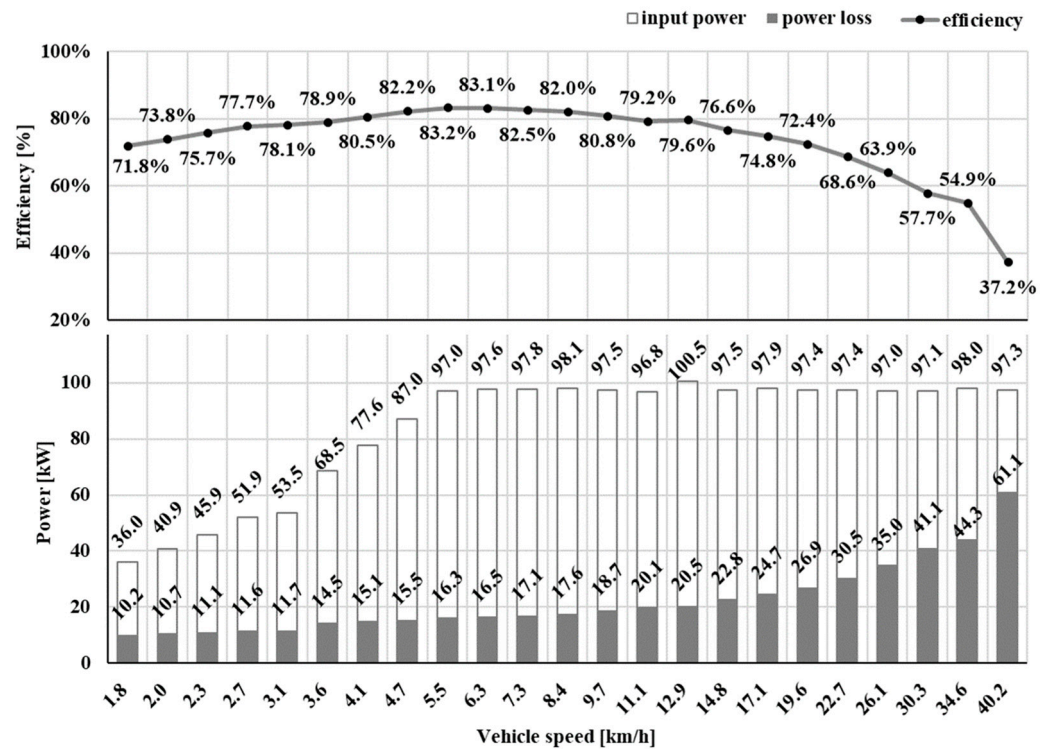


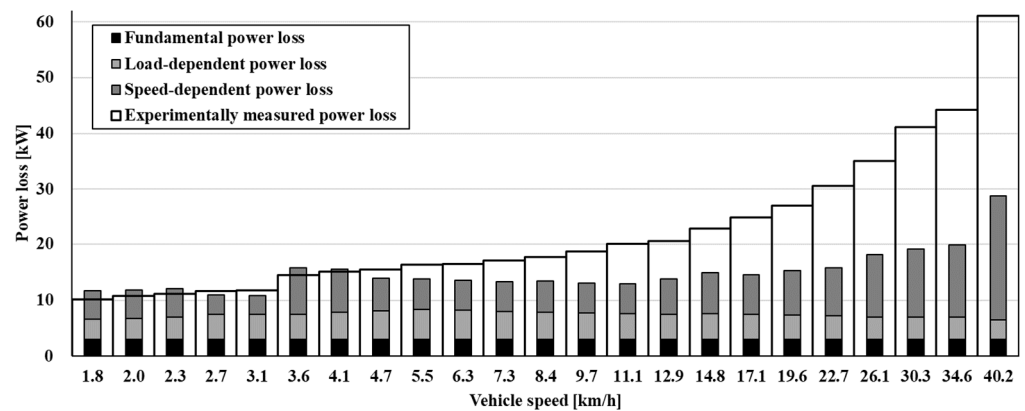
Figure 6. Power loss measurement results of the DCT.

#### 4. Discussion

##### Comparison between Theoretical Calculations and Experimental Studies

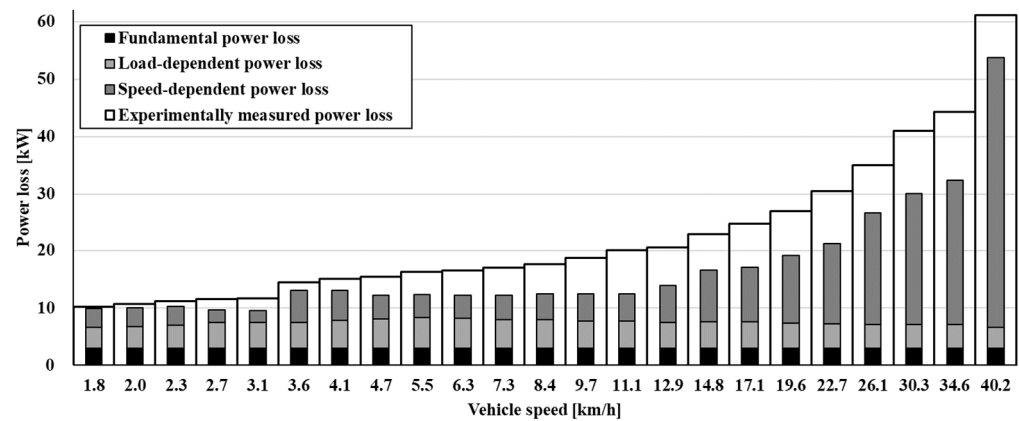
Figure 7 compares the theoretical calculations and experimental studies of the power losses for Cases I and II. The tendency for power loss to increase as vehicle speed increased is the same for both Cases I and II, but the absolute level of power loss differs more as the speed increases.

As shown in Figure 7a, in Case I the theoretical calculations tend to be higher than the test results. However, as the speed increases in the high-speed gear steps, the measured power loss increases; at 40.2 km/h, the measured power loss is 60.06 kW, while the calculated total power loss is 28.80 kW, the error being as much as 31.26 kW.



(a) Case I: Considering average oil level

Figure 7. Cont.



(b) Case II: Considering oil circulation

**Figure 7.** Comparison between calculations and measurements of the power loss.

As shown in Figure 7b, in Case II the load-dependent power loss is similar to that of Case I, where the speed-dependent power loss increases rapidly with the vehicle speed. The maximum power loss is 47.21 kW at 40.2 km/h, and the total power loss is 53.79 kW, exhibiting an error of 12.85 kW compared to the experimentally measured power loss of 60.06 kW. That is, the power loss error in high-speed gear steps is smaller than that of Case I.

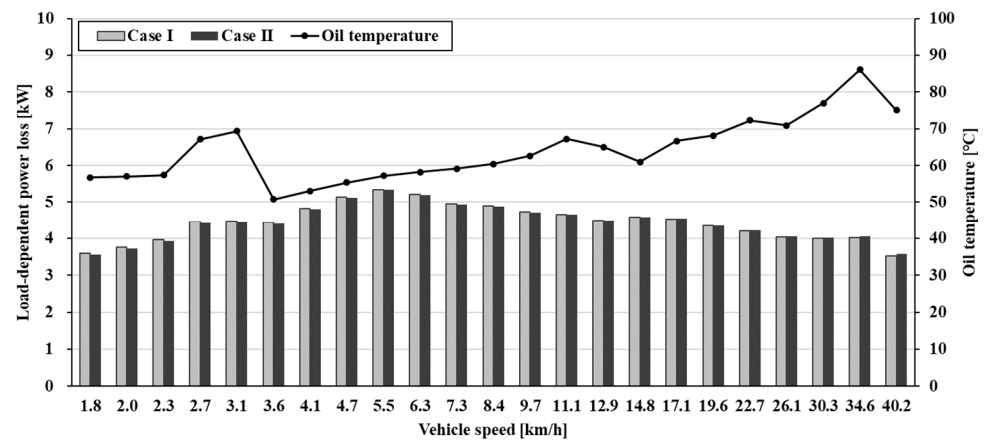
To analyze the effects of the oil level on load-dependent and speed-dependent power losses, the theoretical calculation results for the power loss in Cases I and II were compared, as shown in Figure 8.

Figure 8a shows the comparison of load-dependent power losses for Cases I and II, which are similar regardless of the oil levels. The load-dependent power loss is the highest at 5.5 km/h, corresponding to the fastest gear step in the max. traction force range for agricultural tractors.

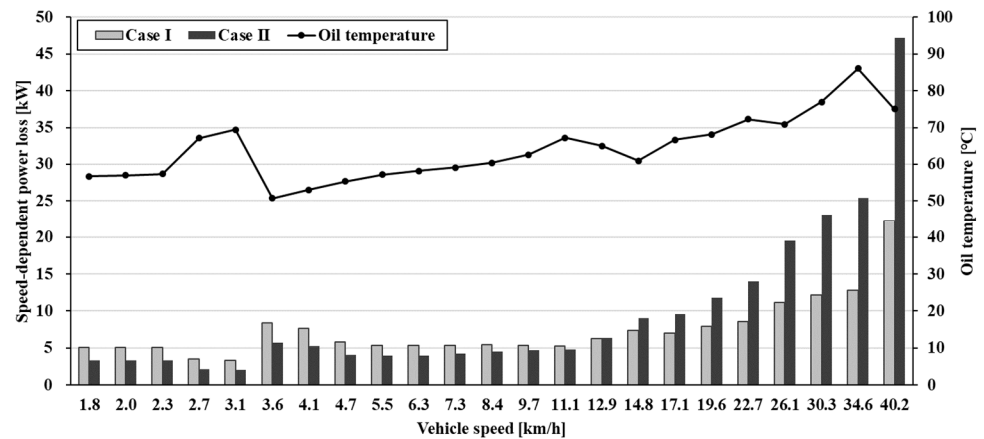
Figure 8b compares the speed-dependent power losses for Cases I and II. For both cases, the speed-dependent power loss tends to increase with vehicle speed. However, a local peak value is evident at 3.6 km/h owing to the considerable influence of temperature on the speed-dependent power loss. In the tests of 3.1 km/h and 3.6 km/h, the oil temperatures were 69.3 °C and 50.7 °C, respectively, showing a difference of 18.6 °C. As a result of calculating viscosity by the ASTM D341 method, the kinematic viscosity of the oil is 33.2 cSt and 63.61 cSt, respectively, for the tests of 3.1 km/h and 3.6 km/h. As the viscosity increases, it can be seen that the drag torque increases and results in a larger speed-dependent power loss.

According to the results shown in Figure 8b, at vehicle speeds below approximately 11.1 km/h, the power loss in Case I is greater; conversely, at speeds above 14.8 km/h, the power loss in Case II is greater. The differences in power loss between Cases I and II in each speed range are related to the structural features of the DCT used in the study.

The DCT used in the study comprises a gear train made up of 58 gears to implement 24 gear shift stages. The gears in the forward/reverse and main shift parts—including the dual clutches—are in the front cell, while gears in the range shift part are in the mid cell. The vehicle speed range for the primary work of agricultural tractors is defined by the range shift part, the transmission used in this study being divided into 0–4.1 km/h (low-speed range), 4.7–12.9 km/h (mid-speed range), and 14.8–40.2 km/h (high-speed range) depending on the applicable gear ratio. Consequently, the gears in the range shift part have larger gear ratio differences than other gears, the speed deviation of idle gears that do not transmit power also being greater.



(a) Simulated load-dependent power loss.



(b) Simulated speed-dependent power loss.

**Figure 8.** Power loss analysis results.

Figure 9 shows the average rotation speed and distribution of gears in the front and mid cells at the engine’s rated rotation speed. The gears in the front cell—which are closer to the engine—determine the forward/reverse direction and perform the role of primary reduction in the engine’s rotation speed. Consequently, their average rotation speed and deviation are similar. Therefore, the speed-dependent power loss of the gears in the front cell is not greatly affected by the vehicle speed.

By contrast, the rotation speed of the gears in the mid cell is similar to or lower than that of the gears in the front cell in the 1.8–12.9 km/h vehicle-speed range, the average rotation speed and deviation increasing sharply at speeds above 14.8 km/h compared to the gears in the front cell.

The rotation speed of the gears in the mid cell is more greatly influenced by driving speed than those in the front cell. Therefore, the speed-dependent power loss of the gears in the mid cell is affected by the driving speed, showing a similar tendency to the results shown in Figure 7b, where the speed-dependent power loss increases sharply at speeds above 14.8 km/h. Consequently, speed-dependent power loss has a greater impact on the components located in the front cell at low-speed gear steps and the mid cell at high-speed gear steps.

As in Case II of Figure 7b, when the oil level in the front cell is lowered and the oil level in the mid cell is raised, the speed-dependent power loss in the front cell decreases, reducing the total power loss at low speeds. Owing to the increased influence of speed-dependent power loss in the mid cell, the total power loss at high speeds increases. This

trend is consistent with the test results, where power loss decreases at low speeds and increases sharply at high speeds.

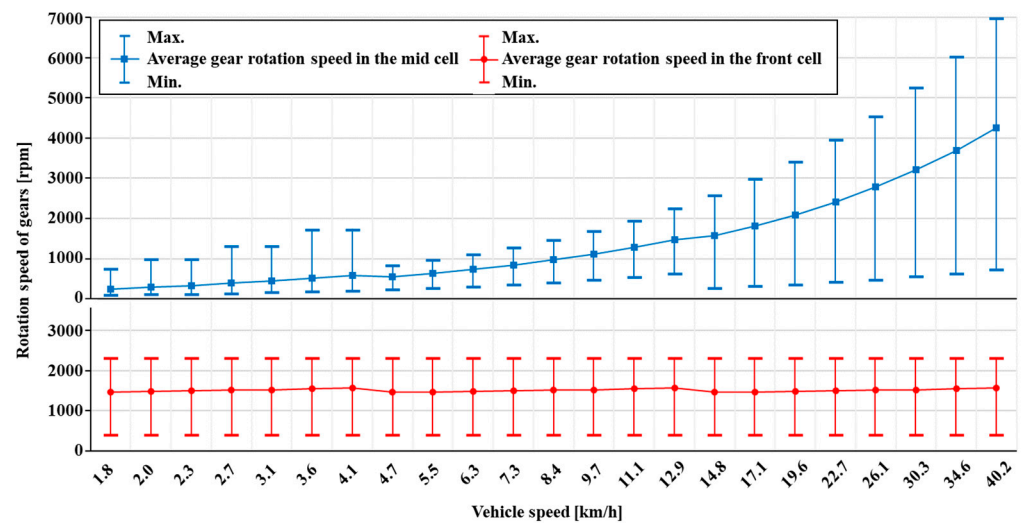


Figure 9. Rotation speed variation of each gear step.

Through this study, it was confirmed that the error between the theoretical calculation and the measured value of power loss was reduced by considering the oil level change caused by the oil circulation of the transmission. Therefore, in order to improve the efficiency of the transmission, the rotation speed of the internal components and the oil lubrication condition must be considered together. For example, gears with high rotation speeds should be located in positions that are not submerged in oil. Rotating components that are inevitably immersed in oil need to be designed with a small outer diameter and width to minimize power loss.

## 5. Conclusions

In this study, we calculated the power loss of an agricultural tractor DCT using the ISO standard and viscous fluid theory and measured the power loss of the DCT for each gear step using a 3-axis dynamometer measurement system. The calculated power loss and measurement results were compared and analyzed with the calculation results reflecting the oil levels considering the characteristics of the agricultural tractor DCT reviewed. The results of this study can be summarized as follows:

1. We calculated the power loss for each gear shift stage of a DCT applied to agricultural tractors using the ISO standard and the viscous fluid theory. The components accounting for the largest portion of the total power loss were the gears and bearings, with the efficiency calculated to be highest at 5.5 km/h, the fastest speed in the max. traction force range.
2. We confirmed that the theoretical calculation results of power loss in Case II were more consistent with the test results compared to Case I. Additionally, while the load-dependent power loss was not significantly affected by the oil level, the speed-dependent power loss was affected by the locally varying oil level owing to oil circulation.
3. The transmission components closer to the engine exhibited smaller speed deviations for each gear step, while the gears of the transmission components closer to the output shaft exhibited greater rotation speed and speed deviation between gears at higher gear steps. Owing to these driving characteristics, when the oil level in the cell closer to the output shaft rose, the power loss was lower at low-speed gear shift stages, while it increased sharply at high-speed gear steps.



4. Thus, we confirmed that, to predict the efficiency of agricultural transmissions, the oil level reflecting the transmission structure characteristics, oil circulation, and the operating characteristics of the transmission component—such as rotation speed and deviation—must be considered.

**Author Contributions:** Conceptualization, H.-J.A. and C.C.; methodology, H.-J.A. and S.-C.K.; investigation, Y.-J.P.; writing—original draft preparation, H.-J.A. and S.-C.K.; writing—review and editing, C.C. All authors have read and agreed to the published version of the manuscript.

**Funding:** This work was supported by the Technology Innovation Program (Development of common type dual-clutch transmission system and standardized control platform, No. 20011428), funded by the Ministry of Trade, Industry & Energy, Republic of Korea.

**Institutional Review Board Statement:** Not applicable.

**Data Availability Statement:** Not applicable.

**Conflicts of Interest:** The authors declare no conflict of interest.

## Nomenclature

$P_L$	Total power loss, kW
$P_{HP}$	Fundamental power loss of the hydraulic pump, kW
$P_{GL}$	Load-dependent power loss of the gear, kW
$P_{GS}$	Speed-dependent power loss of the gear, kW
$P_{BL}$	Load-dependent power loss of the bearing, kW
$P_{BS}$	Speed-dependent power loss of the bearing, kW
$P_S$	Speed-dependent power loss of the shaft, kW
$P_{CL}$	Speed-dependent power loss of the clutch, kW
$P_{BR}$	Speed-dependent power loss of the brake, kW
$f_m$	Mesh coefficient of friction
$M$	Mesh mechanical advantage
$T_1$	Pinion torque, Nm
$n_1$	Pinion rotation speed, rpm
$\beta$	Operating helix angle/mean spiral angle, degrees
$P_{GW1}$	Gear windage and churning losses associated with smooth outside diameters, kW
$P_{GW2}$	Gear windage and churning losses associated with smooth sides of the disc, kW
$P_{GW3}$	Gear windage and churning losses associated with tooth surfaces, kW
$f_g$	Gear dip factor
$\nu$	Kinematic oil viscosity, m <sup>2</sup> /s
$n$	Rotating speed, rpm
$L$	Length of element for gearing windage and churning, mm
$A_g$	Arrangement constant
$F$	Total face width, mm
$R_f$	Roughness factor for gear teeth
$M_0$	Load-independent frictional moment, Nm
$M_1$	Bearing load-dependent torque, Nm
$M_2$	Cylindrical roller bearing axial load-dependent moment, Nm
$M_3$	Frictional moment of seals, Nm
$T_{CL}$	Clutch torque loss, Nm
$r_{ag}$	Percentage value of the groove area to the friction material area
$T_{fa}$	Torque loss due to oil film in continuous section, Nm
$T_{ra}$	Torque loss due to oil film in ruptured section, Nm
$T_m$	Torque loss due to mist in ruptured section, Nm
$r_c$	Critical radius, m
$r_i$	Inner radius of the disk, m
$r_o$	Outer radius of the disk, m
$N$	Number of friction surfaces
$\mu$	Fluid absolute viscosity, Pa·s

$\mu_{mis}$	Absolute viscosity of mist, Pa·s
$\Delta\omega$	Difference in clutch rotation speed, rad/s
$h$	Clearance between plate and disc, m
$\Phi$	Critical radius square, m <sup>2</sup>
$\alpha$	Angle of the area of brake caliper, rad

## References

1. Ueka, Y.; Yamashita, J.; Sato, K.; Doi, Y. Study on the development of the electric tractor: Specifications and traveling and tilling performance of a prototype electric tractor. *Eng. Agric. Environ. Food* **2013**, *6*, 160–164. [CrossRef]
2. Vogt, H.H.; de Melo, R.R.; Daher, S.; Schmuelling, B.; Antunes, F.L.M.; dos Santos, P.A.; Albiero, D. Electric tractor system for family farming: Increased autonomy and economic feasibility for an energy transition. *J. Energy Storage* **2021**, *40*, 102744. [CrossRef]
3. Moreda, G.P.; Muñoz-García, M.A.; Barreiro, P.J. High voltage electrification of tractor and agricultural machinery—A review. *Energy Convers. Manag.* **2016**, *115*, 117–131. [CrossRef]
4. Martini, V.; Mocera, F.; Somà, A. Numerical Investigation of a Fuel Cell-Powered Agricultural Tractor. *Energies* **2022**, *15*, 8818. [CrossRef]
5. Yang, H.; Sun, Y.; Xia, C.; Zhang, H. Research on Energy Management Strategy of Fuel Cell Electric Tractor Based on Multi-Algorithm Fusion and Optimization. *Energies* **2022**, *15*, 6389. [CrossRef]
6. Hosseinzadeh-bandbafha, H.; Rafiee, S.; Ghobadian, B.; Mohammadi, P. Exergetic, economic, and environmental life cycle assessment analyses of a heavy-duty tractor diesel engine fueled with diesel–biodiesel–bioethanol blends. *Energy Convers. Manag.* **2021**, *241*, 114300. [CrossRef]
7. Madovi, O.; Hoffrichter, A.; Little, N.; Foster, S.N.; Isaac, R. Feasibility of hydrogen fuel cell technology for railway intercity services: A case study for the Piedmont in North Carolina. *Railw. Eng. Sci.* **2021**, *29*, 258–270. [CrossRef]
8. Bergthorson, J.M. Recyclable metal fuels for clean and compact zero-carbon power. *Prog. Energy Combust. Sci.* **2018**, *68*, 169–196. [CrossRef]
9. Kim, W.-S.; Kim, Y.-J.; Kim, Y.-S.; Baek, S.-M.; Baek, S.-Y.; Lee, D.-H.; Nam, K.-C.; Kim, T.-B.; Lee, H.-J. Development of Control System for Automated Manual Transmission of 45-kW Agricultural Tractor. *Appl. Sci.* **2020**, *10*, 2930. [CrossRef]
10. Kim, J.; Lee, H. Motor position control algorithm for an automated manual transmission of the agricultural tractor. *Proc. Inst. Mech. Eng. Part C J. Mech. Eng. Sci.* **2015**, *229*, 3341–3349. [CrossRef]
11. Brenninger, M.M. Fendt VariocVT in Agricultural Tractors. *SAE Tech. Pap.* 2007. [CrossRef]
12. Tanelli, M.; Panzani, G.; Savaresi, S.M.; Pirola, C. Transmission control for power-shift agricultural tractors: Design and end-of-line automatic tuning. *Mechatronics* **2011**, *21*, 285–297. [CrossRef]
13. Pahlovy, S.A.; Mahmud, S.F.; Kubota, M.; Ogawa, M.; Takakura, N. Prediction of Drag Torque in a Disengaged Wet Clutch of Automatic Transmission by Analytical Modeling. *Tribol. Online* **2016**, *11*, 121–129. [CrossRef]
14. Yuan, Y.; Liu, E.A.; Hill, J.; Zou, Q. An Improved Hydrodynamic Model for Open Wet Transmission Clutches. *J. Fluids Eng.* **2007**, *129*, 333–337. [CrossRef]
15. Shen, Y.; Liu, Z.; Rinderknecht, S. Modelling of Power Losses of Transmission Synchronizers in Neutral Position. *SAE Tech. Pap.* 2018. [CrossRef]
16. Fernandes, C.M.; Marques, P.M.; Martins, R.C.; Seabra, J.H. Gearbox power loss. Part I: Losses in rolling bearings. *Tribol. Int.* **2015**, *88*, 298–308. [CrossRef]
17. Seetharaman, S.; Kahraman, A.; Moorhead, M.D.; Petry-Johnson, T.T. Oil Churning Power Losses of a Gear Pair: Experiments and Model Validation. *J. Tribol.* **2009**, *131*, 022202. [CrossRef]
18. Hu, X.; Jiang, Y.; Luo, C.; Feng, L.; Dai, Y. Churning power losses of a gearbox with spiral bevel geared transmission. *Tribol. Int.* **2019**, *129*, 398–406. [CrossRef]
19. Diab, Y.; Ville, F.; Velex, P. Prediction of Power Losses Due to Tooth Friction in Gears. *Tribol. Trans.* **2006**, *49*, 260–270. [CrossRef]
20. Fernandes, C.M.; Marques, P.M.; Martins, R.C.; Seabra, J.H. Gearbox power loss. Part II: Friction losses in gears. *Tribol. Int.* **2015**, *88*, 309–316. [CrossRef]
21. Vacca, F.; De Pinto, S.; Karci, A.E.H.; Gruber, P.; Viotto, F.; Cavallino, C.; Rossi, J.; Sorniotti, A. On the Energy Efficiency of Dual Clutch Transmissions and Automated Manual Transmissions. *Energies* **2017**, *10*, 1562. [CrossRef]
22. Habermehl, C.; Jacobs, G.; Neumann, S. A modeling method for gear transmission efficiency in transient operating conditions. *Mech. Mach. Theory* **2020**, 153. [CrossRef]
23. Strapasson, L.; Zimmermann, G.G.; Jasper, S.P.; Savi, D.; Sobenko, L.R. Energy efficiency of agricultural tractors equipped with continuously variable and full powershift transmission systems. *Eng. Agricola* **2022**, *42*. [CrossRef]
24. Molari, G.; Sedoni, E. Experimental evaluation of power losses in a power-shift agricultural tractor transmission. *Biosyst. Eng.* **2008**, *100*, 177–183. [CrossRef]
25. Moon, S.P.; Moon, S.G.; Kim, J.S.; Sohn, J.H.; Kim, Y.J.; Kim, S.C. Transmission efficiency of dual-clutch transmission in agricultural tractors. *J. Drive Control* **2022**, *19*, 43–50.

26. ISO/TR 14179-1; Gears-Thermal Capacity-Part 1: Rating Gear Drives with Thermal Equilibrium at 95 °C Sump Temperature. International Standard: Geneva, Switzerland, 2001.
27. Park, K.; Kang, M.; Lee, J.; Son, W.C.; Harianto, J.; Kahraman, A. Development of an Analysis Program to Predict Efficiency of Automotive Power Transmission and Its Applications. *SAE Tech. Pap.* 2018. [CrossRef]

**Disclaimer/Publisher's Note:** The statements, opinions and data contained in all publications are solely those of the individual author(s) and contributor(s) and not of MDPI and/or the editor(s). MDPI and/or the editor(s) disclaim responsibility for any injury to people or property resulting from any ideas, methods, instructions or products referred to in the content.

## Article

# Bucket Size Optimization for Metering Device in Garlic Planter Using Discrete Element Method

Dongu Im <sup>1</sup>, Ho-Seop Lee <sup>2</sup>, Jae-Hyun Kim <sup>1</sup>, Dong-Joo Moon <sup>1</sup>, Tae-Ick Moon <sup>3</sup>, Seung-Hwa Yu <sup>4</sup>  
and Young-Jun Park <sup>1,2,5,\*</sup>

- <sup>1</sup> Department of Biosystems Engineering, College of Agriculture and Life Sciences, Seoul National University, 1 Gwanak-ro, Gwanak-gu, Seoul 08826, Republic of Korea; ehddn0112@snu.ac.kr (D.I.); kjh3tt@snu.ac.kr (J.-H.K.); 98dongdong@snu.ac.kr (D.-J.M.)
- <sup>2</sup> Research Institute of Agriculture and Life Sciences, College of Agriculture and Life Sciences, Seoul National University, 1 Gwanak-ro, Gwanak-gu, Seoul 08826, Republic of Korea; ghtjqdlek@snu.ac.kr
- <sup>3</sup> Taeung Farm Machinery, Hanseong-ro, Isan-myeon, Yeongju-si 36170, Republic of Korea; 0175010751@hanmail.net
- <sup>4</sup> Department of Agricultural Engineering, Upland Mechanization Team, National Institute of Agricultural Sciences, Nongsaeangmyeong-ro, Deokjin-gu, Jeonju-si 54875, Republic of Korea; yush6210@korea.kr
- <sup>5</sup> Convergence Major in Global Smart Farm, College of Agriculture and Life Sciences, Seoul National University, 1 Gwanak-ro, Gwanak-gu, Seoul 08826, Republic of Korea
- \* Correspondence: yjpark95@snu.ac.kr

**Abstract:** In this study, the discrete element method was used to optimize the bucket size for the metering device in a garlic planter for enhancing the productivity of garlic farming according to the garlic size. Statistical information concerning the actual shape of garlic cloves was incorporated, and the mechanical properties of garlic were determined using the bulk density, sliding test, and repose angle test for enhancing the fidelity of the simulation model. The optimal bucket size achieving the target plant rate of 97.5% was determined using the developed discrete element model for the three garlic size groups. The linear search method was used for optimization, and batch simulation was performed to validate the optimized results and confirm the performance index of the metering device. A Gaussian distribution based on statistical information accounted for the various garlic sizes in each group. Finally, a metering test verified the reliability of the optimization technique. The differences between the simulation and test results were within 10% for all performance indices, including missing plant rate, multi-plant rate, and planting rate, indicating the high reliability of the analysis model. Subsequently, the larger garlic groups (Groups 2 and 3) exhibited metering performance close to the target plant rate.

**Keywords:** garlic planter; metering device; size optimization; discrete element method

**Citation:** Im, D.; Lee, H.-S.; Kim, J.-H.; Moon, D.-J.; Moon, T.-I.; Yu, S.-H.; Park, Y.-J. Bucket Size Optimization for Metering Device in Garlic Planter Using Discrete Element Method. *Agriculture* **2023**, *13*, 1199. <https://doi.org/10.3390/agriculture13061199>

Academic Editor: Mustafa Ucgul

Received: 15 May 2023

Revised: 1 June 2023

Accepted: 2 June 2023

Published: 5 June 2023



**Copyright:** © 2023 by the authors. Licensee MDPI, Basel, Switzerland. This article is an open access article distributed under the terms and conditions of the Creative Commons Attribution (CC BY) license (<https://creativecommons.org/licenses/by/4.0/>).

## 1. Introduction

The United Nations has identified zero hunger as one of the sustainable development goals to be achieved by 2030. Consequently, global interest in enhancing agricultural production rates has been growing [1]. However, in countries such as South Korea, the aging population and decreasing rural population pose challenges to these goals. One potential solution is the automation and mechanization of agriculture, which is particularly effective for labor-intensive crops. Garlic, a typical such crop, is a case in point; garlic planting is particularly strenuous and accounts for 15% of the total labor in garlic farming [2]. The mechanization of garlic planting could alleviate the manpower shortage, enhance the planting rate per hour, and increase overall production.

Garlic planters can be classified based on their power source and divided into self-propelled and tractor-attached types. They can also be categorized based on the posture of the garlic cloves to be planted, including upright planting, in which the root of the garlic cloves faces downwards, and lie-down planting, in which the garlic cloves are placed

horizontally on the ground using free fall [3]. One planter component, the metering device, transfers garlic cloves from the hopper to the planting unit, which then plants them in the field based on the planting method. This is followed by soil covering and mulching. The metering device is a crucial component of the garlic planter. It plays a significant role in controlling the missing plant and multi-plant rates, key performance indicators of the garlic planter [4]. The missing plant rate refers to the frequency at which garlic cloves fail to be transferred to the planting unit, while the multi-plant rate indicates the frequency at which two or more garlic cloves are transferred to the planting unit simultaneously. Both performance indicators can cause significant losses for farmers and must be minimized. A high missing plant rate can result in a reduction in total production and/or additional labor required to replant in the missed area, while a high multi-plant rate leads to unnecessary waste of garlic cloves and can result in interference of the growth between several garlic cloves planted in a limited space, leading to reduced total production.

To reduce the rates of missing plants and multiple plants, an optimal design that considers the performance index of the metering device is necessary. It is imperative to anticipate the missing plant and multi-plant rates of the metering device during the development stage and supplement the design accordingly based on the results to achieve the optimal design of the metering device. Performance indicators of metering devices can be predicted through experimental methods using test devices and simulation methods. While performance prediction through experimentation offers the advantage of high accuracy when performed under the same conditions as the actual operation, it requires a significant amount of time and resources to build a test device, thereby limiting the production of samples that cover a wide range of design variables. Conversely, simulation-based methods offer high accuracy when using validated analysis models and, as there is no limit on the design range, can predict the performance of the metering device across a wide range of design parameters. Therefore, an analytical method that employs simulation is appropriate for optimal design beyond simple performance comparison.

To analyze the performance of garlic planters, various studies have been conducted utilizing both experimental and simulation methods. Kang et al. [5] conducted a yield comparison experiment as a testing method to determine the effects of planting angle and planting depth on garlic growth. The results confirmed that garlic yield was highest at planting angles of 45° or 90° and planting depths of 2–4 cm. Additionally, to improve the performance of the metering device, Kang et al. [3] experimentally determined the missing plant rate based on the bucket size. The results indicated that the bucket size of the metering device significantly affects the performance index. Zilpilwar et al. [6] determined the optimal cup size and operating speed of a cup-feed-type metering device through an experimental method similar to that in the aforementioned study. The authors considered the planting rate, planting interval, and clove damage rate. Zhang et al. [7] conducted one-factor and multifactor experiments to optimally design key components of a spoon-clamping type planter and optimize working parameters. As mentioned above, experimental studies offer high prediction accuracy using actual metering devices. However, these studies have limited applicability of predictive models depending on the sample range and expense of test equipment. Additionally, due to the restricted selection range of design variables, the scope for optimal design is limited.

In addressing the limitations of the experimental method, studies have been conducted using simulations to predict the performance of garlic planters. Im et al. [8] classified garlic samples into four groups based on size and developed a 3D computer-aided design (CAD) model using statistical results on garlic clove shape. The optimal bucket size of the metering device was then determined using the developed CAD model and multi-body dynamics model according to the size of the garlic cloves. Although the fidelity of the model was increased by incorporating the shape of actual garlic cloves in the analysis, validation of the determined optimal bucket size and simulation model was not performed. Guo et al. [9] analyzed the single seed rate, multiple seed rate, and missing seed rate of the metering device according to the adjustment size and operation speed using the discrete element

method (DEM). This resulted in a single-seed metering performance qualification rate of over 80%. An actual field test was performed to validate the applicability of the optimal design, and the performance of the metering device met the required standards. While the authors derived the optimal design value using DEM, they did not consider the various sizes of garlic in the analysis model nor incorporate the actual shape of garlic cloves.

To minimize the missing seed rate of a finger clip plate garlic seed-metering device, Wang & Sun et al. [4] utilized the commercial software EDEM as a further investigation that executed optimal design using the DEM. The study scrutinized the missing seed and single seed rates based on the opening diameter of the device, operating speed, and the population number of garlic cloves. Moreover, a regression model was constructed via a Box–Behnken center combination test. However, the analysis model did not consider the actual shape of the target garlic, which was the garlic grown in Pizhou, and cloves were depicted as multi-spheres. The low accuracy of the resulting contact force calculation limits the validity of the study, similar to Guo et al. [9].

As another machine for the mechanization of garlic farming, Yu et al. [10] optimized the parameters for the root-cutting operation of the garlic harvester to minimize the root clearance rate and bulb damage. To achieve this optimization, they developed a mathematical model for assessing the root clearance rate and bulb damage.

Research has been conducted to enhance planting performance not only in garlic but also in other crops [11–17]. However, studies that utilized experimental approaches have limitations in design variables or operating conditions and are applicable only within specific sample ranges [3,5–7]. Previous studies that used simulation models executed optimal designs without design variable constraints; however, in some cases, the analysis model was not validated [8], and the actual shape of garlic cloves was not considered in the analysis model, constraining its reliability [10,11].

In this investigation, we aimed to surpass the limitations of prior research by incorporating the actual shape of garlic cloves into the discrete element model to determine the optimal bucket size of the metering device. We optimized by categorizing the garlic cloves into three groups, considering their size distribution. Furthermore, we conducted a metering simulation to validate the optimization results and validated the reliability of the optimization technique by comparing the outcomes with the actual test results. To incorporate the actual shape of garlic cloves, we adopted the statistical data proposed by Im et al. [8] into the discrete element model. We performed angle of repose and sliding tests to identify the mechanical parameters of the analysis model. Using the developed discrete element model, we determined the optimal bucket size to meet the target planting rate under the same operating conditions as the actual planter. We employed the sequential search method as the optimization technique and found the optimal solution by gradually reducing the bucket size. We conducted a metering simulation to validate that the determined bucket size satisfied the required performance index, we conducted a metering simulation and validated the optimization technique through a metering test. As a result of the metering simulation, the performance index of the required level was nearly achieved, and the reliability of the optimization technique was confirmed as the difference between the test result and simulation result in all performance indexes was within 10%.

Thus, in this study, we developed a discrete element model with high fidelity and executed the optimal design of the garlic planter metering device using the developed model. During actual metering operation, the optimization result of each group almost satisfied the target plant rate, and the proposed methodology can be used to optimize metering devices for other crops.

## 2. Materials and Methods

In this study, the DEM was employed to optimize the bucket size of the metering device of the garlic planter. To accurately represent the actual shape of garlic cloves in the analysis model, a 3D mesh model was created using the 3D CAD model for each of the three garlic size groups, which was previously developed by Im et al. [8]. Subsequently, the

discrete element model parameters were determined through bulk density measurement, sliding test, and repose angle test. The optimal bucket size for each group was determined using the developed discrete element model, and a metering simulation was conducted to validate the optimal bucket size. Finally, an actual metering experiment was conducted to validate the optimization technique.

### 2.1. Metering Device Working Principle

The finger-type bucket metering device utilized in this study comprises the components illustrated in Figure 1. The finger-type bucket is affixed to the chain and derives its power from the sprocket. The lower sprocket is connected to the support wheel of the planter, and as the vehicle advances, it rotates in a clockwise direction owing to the frictional force on the ground. The bucket moves in unison with the rotation of the sprocket, collects the garlic cloves from the hopper in the carrying area, and transports them to the planting area. Throughout this process, the bucket size is determined based on the bucket guide setting, and according to the bucket size, any excess garlic cloves in the sorting area fall back into the hopper. The garlic that passes through the sorting area without falling rotates along the pitch diameter of the sprocket and undergoes a  $180^\circ$  phase shift as the bucket moves. As the phase shifts, gravity causes the garlic to fall onto the back of the finger-type bucket, which is one cycle ahead, and it is then planted through free fall while the planter traverses the planting area.

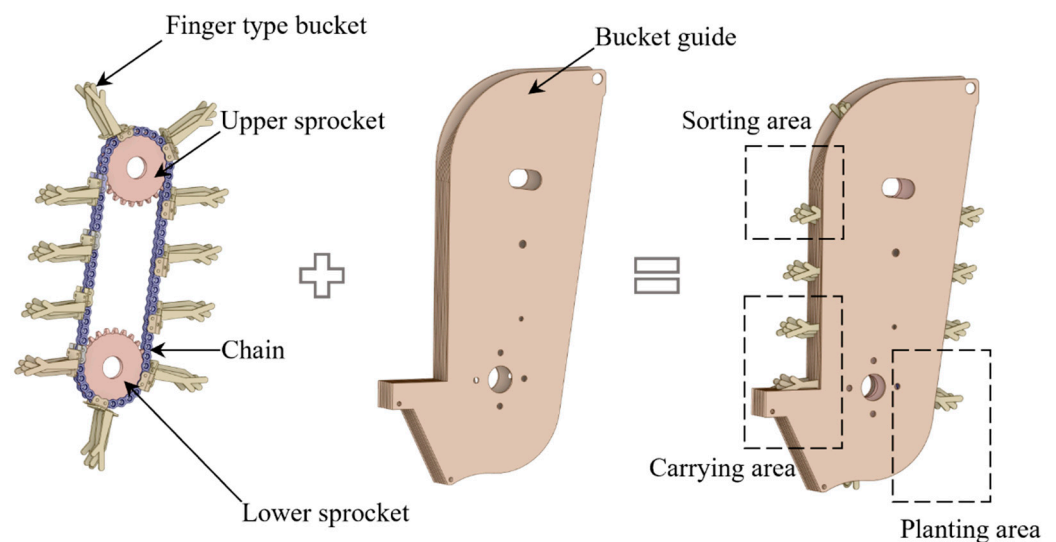


**Figure 1.** Configuration of metering device.

The bucket size varies based on the setting angle ( $\alpha$ ) of the bucket guide, as illustrated in Figure 2a, and the bucket guide rotates around the same rotation center as the lower sprocket, as shown in the figure. The position of the chain and sprocket does not change in accordance with the bucket guide settings, and the buckets affixed to the chain always follow the same trajectory. The bucket trajectory can be defined as the combination of the outermost points traced while the bucket moves, as indicated by the dotted line in Figure 2b. As the trajectory of the bucket is consistent, the bucket size ( $l$ ) changes as the relative position of the guide changes. The bucket size can be defined as the minimum distance between the bucket trajectory and bucket guide, as shown in Figure 2b. When the center of gravity of the placed garlic cloves surpasses the bucket trajectory by a specific distance, the cloves fall under the influence of their weight.



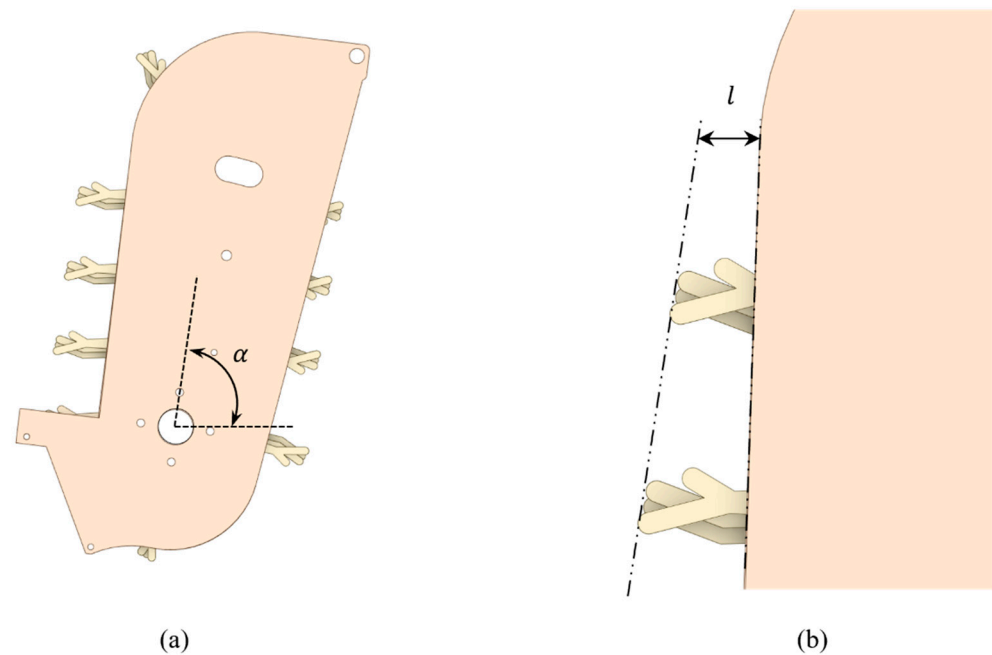


**Figure 2.** Mechanism of bucket size control in metering device. (a) Rotatable bucket guide. (b) Bucket size.

### 2.2. 3D Mesh Modeling

In this investigation, as the target garlic, we used garlic from the cold Uiseong region, identical to the sample used by Im et al. [8], and produced a 3D mesh model of garlic cloves using the 3D CAD model proposed in that study. Figure 3 displays samples of the actual garlic cloves of each group alongside the corresponding 3D CAD and mesh models for contact force calculation. The commercial software ANSYS Rocky can accommodate the actual particle shape in the analysis model by importing the mesh file (in STL format) to define the nodes required for contact force calculation (ANSYS Rocky, [18]). Excessively refined nodes demand a significant amount of computation and the analysis time can increase exponentially. Conversely, excessively coarse nodes can produce numerical errors during calculation. Therefore, selecting the appropriate number of nodes is critical. To ensure the accuracy and convergence of contact calculation, we utilized 3912 nodes for Group 1, 4730 nodes for Group 2, and 4497 nodes for Group 3 in the model, determined through trial-and-error procedures.

The 3D CAD model of garlic cloves used in this study comprises the elongated model, as presented in Figure 4a, and the average model, as shown in Figure 4b. To obtain statistical information about the shape of garlic cloves, Im et al. [8] measured the height and length of 160 garlic samples and developed a 3D CAD model to represent the shape of each group based on the statistical results. Similarly, we used an elongated model with an elongated length ( $\mu_L + 2\sigma_L$ ) and average height ( $\mu_H$ ) was used to determine the optimal bucket size, as was executed by Im et al. [8]. For the metering simulation, an average model with an average length ( $\mu_L$ ) and average height ( $\mu_H$ ) of the groups was employed. During metering work, mechanical vibration aligns the garlic cloves parallel to the finger-type bucket, and the length of the garlic cloves determines the location of their center of gravity. The length of the garlic clove model was set to  $\mu_L + 2\sigma_L$ , and the minimum bucket size allowing the clove to pass through the sorting area was determined to achieve the target planting rate of 97.5%. Further details are excluded as they are beyond the scope of this thesis. The average model presented in Figure 4b was utilized for the metering simulation described in Section 2.6. To validate that the optimal bucket size indeed satisfies the plant rate of 97.5%, we conducted a metering simulation. At this juncture, the average model was scaled up and down according to the Gaussian distribution to test the optimal bucket size for various garlic sizes.

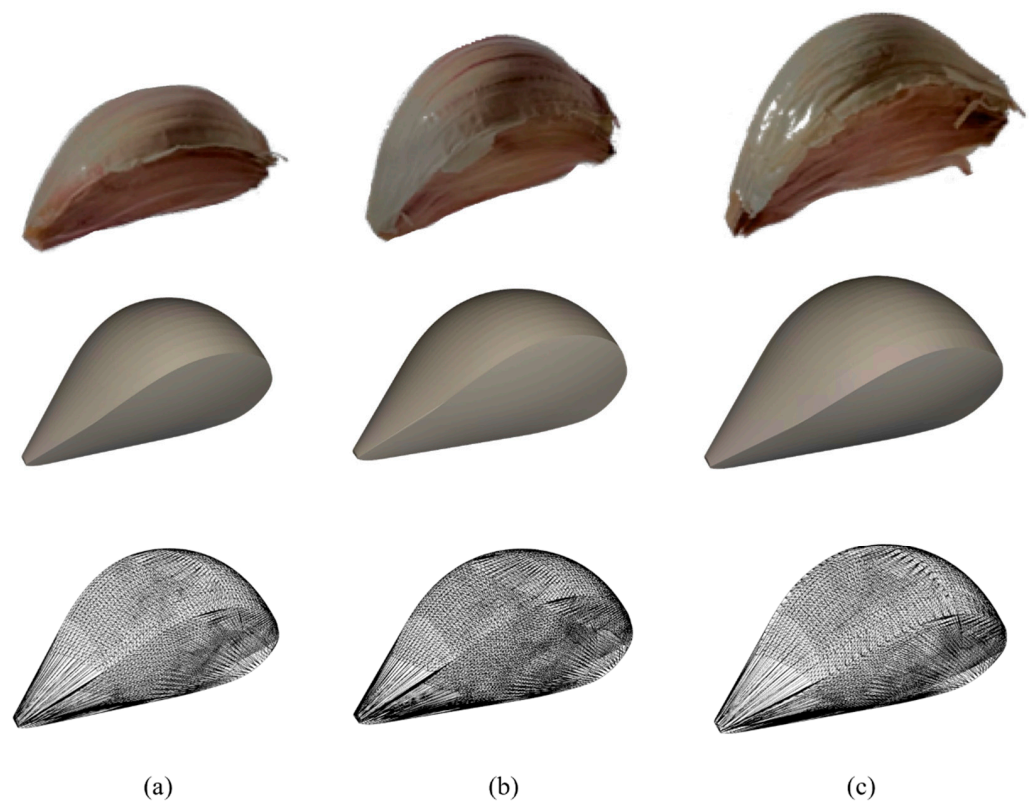


**Figure 3.** Contact calculation node for garlic clove. (a) Group 1. (b) Group 2. (c) Group 3.

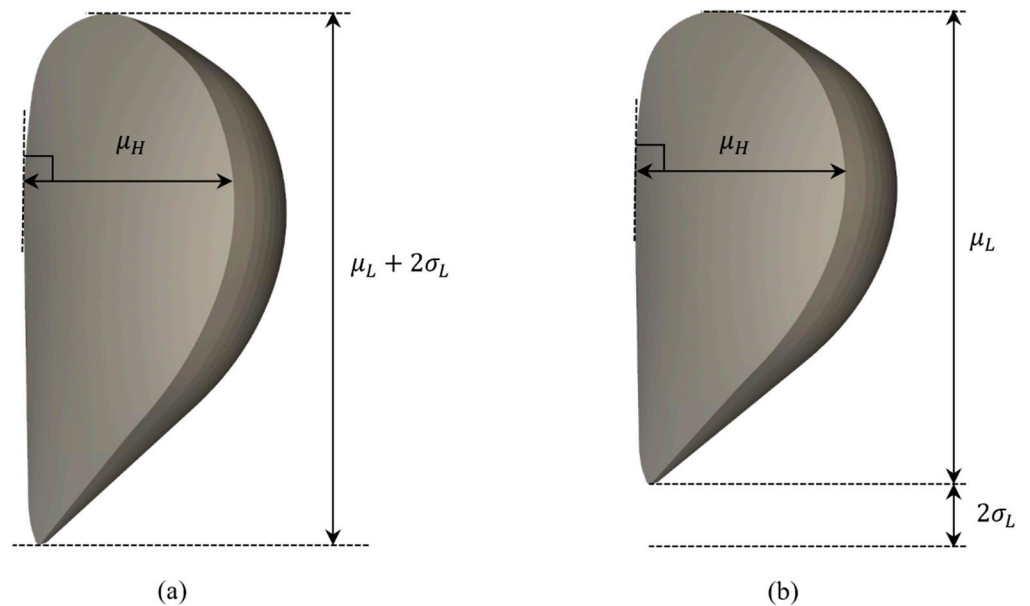


**Figure 4.** Garlic 3D models. (a) Elongated model. (b) Average model.

When constructing a discrete element model, it is necessary to define a mesh as a calculation node for the garlic cloves and the mechanical device with which they come into contact during planting. The garlic cloves come into contact with finger-type buckets and bucket guides, as shown in Figures 5 and 6. For this component, 8166 computational nodes were defined, as depicted in Figure 5b. Similarly, Figure 6a illustrates the 3D model of the bucket guide with 37,268 computational nodes, as shown in Figure 6b. The bucket guide consists of several plates, and contact with the garlic occurs in the anterior part, which

is enlarged in Figure 6b. Therefore, a denser mesh was constructed in the contact area to efficiently calculate contact forces.

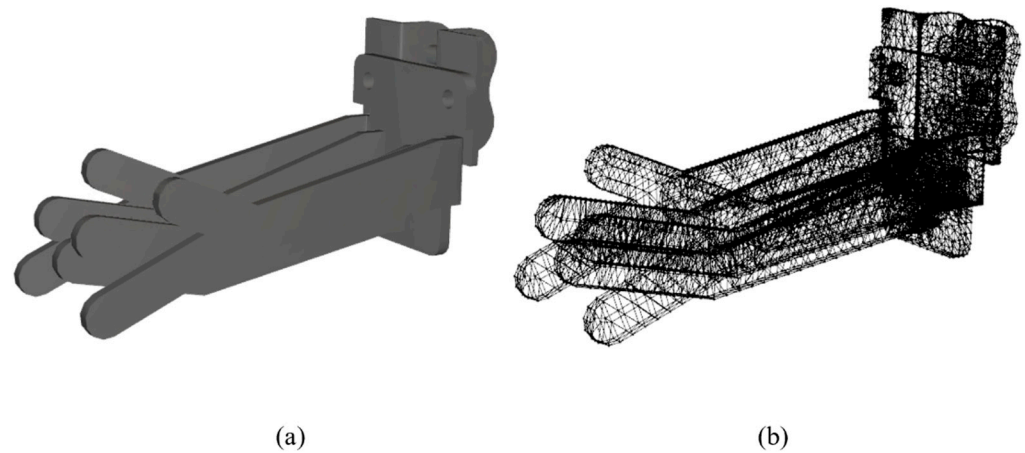


**Figure 5.** Contact calculation node for the bucket. (a) Finger-type bucket. (b) Contact calculation node for bucket.

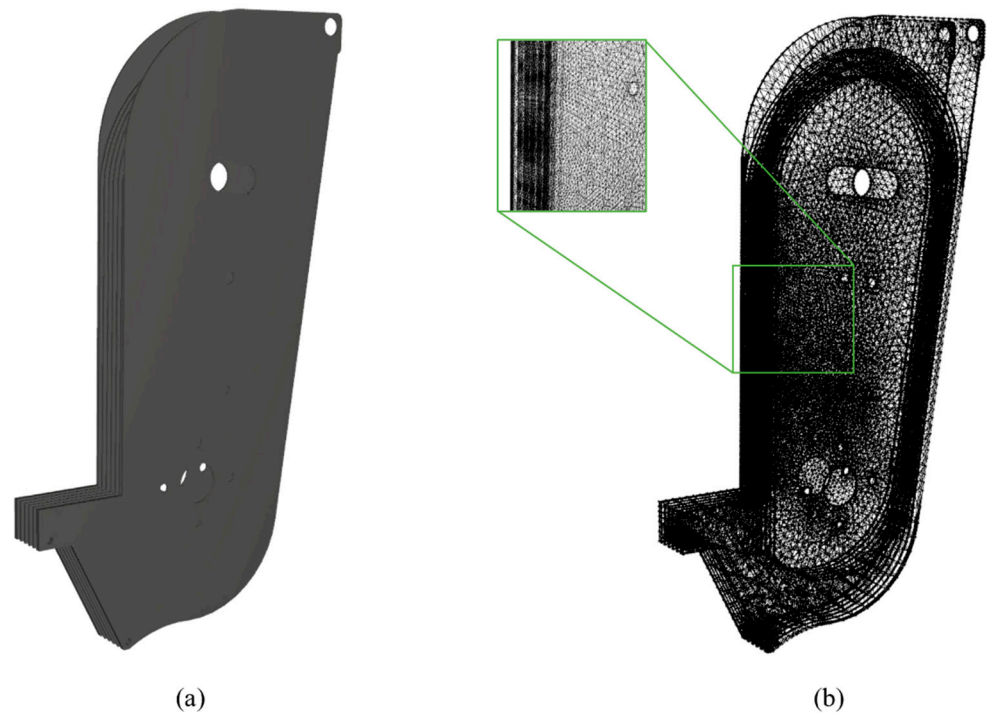


**Figure 6.** Contact calculation node for the guide. (a) Bucket guide. (b) Contact calculation node for guide.

### 2.3. DEM Parameter Determination

It is essential to define discrete element parameters that precisely reflect the mechanical properties of actual garlic cloves to ensure the high accuracy of the discrete element model. These parameters include properties that reflect the mechanical characteristics of the particle itself, such as bulk density, Young's modulus, and Poisson's ratio, as well as parameters related to interactions with other mechanical devices, such as static friction coefficient and restitution coefficient. The parameters for the interaction between garlic and steel were determined to simulate the mechanical interaction with an actual steel device. We also determined the parameters for the interaction between acrylic and garlic to calibrate the repose angle. For visualization, we used an acrylic cylinder for the repose angle test and

for the discrete element model for calibration. Table 1 summarizes the discrete element parameters and methods used to determine these parameters.

**Table 1.** DEM parameter determination.

Category	Property	Value	Unit	Determination
Garlic	Bulk density	605.45	kg/m <sup>3</sup>	Directly measured
	Young's modulus	13.38	MPa	Park et al. [19]
	Poisson's ratio	0.16	-	Park et al. [19]
Garlic-garlic	Static friction coefficient	0.46	-	Repose angle calibration
	Tangential ratio	1	-	Default
	Restitution coefficient	0.50	-	Park et al. [19]
Acryl-garlic	Static friction coefficient	0.4	-	Sliding test
	Tangential ratio	1	-	Default
	Restitution coefficient	0.65	-	Yu et al. [20]
Steel-garlic	Static friction coefficient	0.31	-	Sliding test
	Tangential ratio	1	-	Default
	Restitution coefficient	0.65	-	Yu et al. [20]

The bulk density of garlic was directly measured using an acrylic cylinder, as depicted in Figure 7. In this study, the garlic cloves were used with their peels intact, resembling their natural state for planting. However, this preservation of the peels led to a notable disparity in true density. The presence of a gap between the garlic (white part) and the peel resulted in an overestimation of the clove's volume, consequently leading to imprecise measurements. By determining the bulk density of a specific set of garlic cloves, it becomes feasible to obtain a representative parameter more effortlessly. The values for Young's modulus and Poisson's ratio proposed by Park et al. [19] were employed. The value suggested by Yu et al. [20] for the restitution coefficient was used as an interaction parameter. The static friction coefficients and friction angle between steel–garlic, and acryl–garlic were determined via a sliding test, as shown in Figure 8. The garlic clove was placed on a plate made of the material to be measured, which was then slowly tilted; the angle at which the garlic clove began to move was considered the friction angle ( $\phi$ ) and the static friction coefficient was defined as  $\tan(\phi)$ . Guo et al. [9] applied the same method to determine the static friction coefficient between garlic and steel plate. Finally, since fabricating a garlic plate is infeasible, the garlic–garlic static friction coefficient was determined through repose angle calibration.



**Figure 7.** Bulk density measurement.



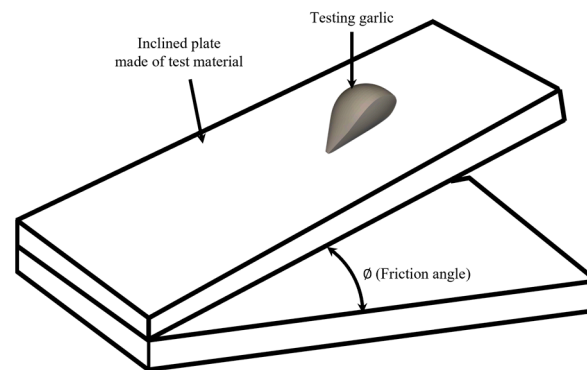


**Figure 8.** Sliding test for the determination of friction coefficient.

The repose angle calibration refers to the process of adjusting the garlic–garlic friction coefficient of the model such that the same value as the repose angle obtained through the actual test is obtained in the simulation result. For accurate calibration, fixed values should be used for the rest of the parameters except for the friction coefficient [21]. In this study, as shown in Table 1, calibration was performed after fixing the remaining values except for the garlic–garlic static friction coefficient. For the repose angle test, a cylinder lifting test (CLT) was performed, as shown in Figure 9 [22]. A total of eight repose angles were measured at 45° intervals in one test, and the reliability of the test results was improved by repeating the test three times. The measurement of the repose angle involved using a digital protractor attached to a steel plate. The steel plate was adjusted to be parallel to the pile of garlic cloves, and the angle of the steel plate was measured. When using large-sized garlic, the reproducibility of test results may not be secured owing to limited boundary conditions; hence, Group 1, which has the smallest size, was used. In addition, the CLT method can be affected by the lifting velocity according to the friction coefficient between the cylinder and the garlic [23]. Therefore, the dynamic effect was removed by performing CLT at a speed of 5 mm/s [22]. Consequently, an average of 30.53° and a standard deviation of 1.26° were obtained.



**Figure 9.** Repose angle test.

Figure 10a shows the actual repose angle test, and Figure 10b illustrates the response angle simulation for calibration purposes. An analysis was conducted by incrementally increasing the garlic–garlic friction coefficient by 0.1 from 0.3 to match the repose angle obtained from the test. Figure 11 shows the simulation results. Using data interpolation, it was confirmed that when the friction coefficient was 0.46, the angle of repose of 30.53° matched the test results.

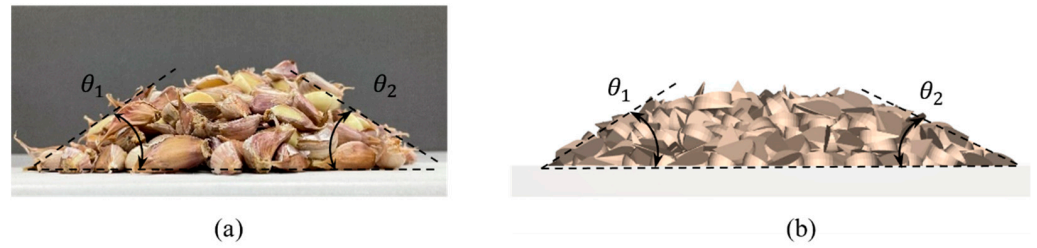


**Figure 10.** DEM parameter calibration using repose angle test. (a) Repose angle (test). (b) Repose angle (simulation).

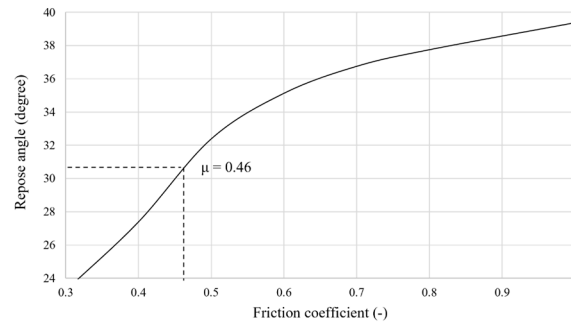


**Figure 11.** Repose angle according to the friction coefficient of garlic-garlic.

#### 2.4. DEM Contact Model

##### 2.4.1. Normal Force Model: Hysteretic Linear Spring Model

The study employed the hysteretic linear spring model proposed by Walton and Braun [23] to define contact in the normal direction of the discrete element model. This model is characterized by a rapid computation speed of plastic energy dissipation and is suitable as a model for compressible materials, such as garlic (ESSS Rocky [24]). The formula used to calculate the contact force in the normal direction is as follows.

$$F_n^t = \begin{cases} \min(K_{nl}s_n^t, F_n^{t-\Delta t} + K_{nu}\Delta s_n) & \text{if } \Delta s_n \geq 0 \\ \max(F_n^{t-\Delta t} + K_{nu}\Delta s_n, \lambda K_{nl}s_n^t) & \text{if } \Delta s_n < 0 \end{cases} \quad (1)$$

$$\Delta s_n = s_n^t - s_n^{t-\Delta t}, \quad (2)$$

where:

- $F_n^t$  is the normal elastic-plastic contact force at the current time  $t$  (N)
- $F_n^{t-\Delta t}$  is the normal elastic-plastic contact force at the previous time  $t - \Delta t$  (N)
- $\Delta s_n$  is the change in the contact normal overlap during the current time (mm)
- $K_{nl}$  is the loading contact stiffness (N/mm)
- $K_{nu}$  is the unloading contact stiffness (N/mm)
- $\lambda$  is a dimensionless small constant (its value in Rocky is 0.001) (-).

$$\frac{1}{K_{nl}} = \begin{cases} \frac{1}{K_{nl,p1}} + \frac{1}{K_{nl,p2}} & \text{for particle - particle contact} \\ \frac{1}{K_{nl,p}} + \frac{1}{K_{nl,p}} & \text{for particle - boundary contact} \end{cases} \quad (3)$$

$$K_{nu} = \frac{K_{nl}}{\varepsilon^2} \quad (4)$$

Here:

- $K_{nl,p1}$  is the loading contact stiffness of particle one (N/mm)
- $K_{nl,p2}$  is the loading contact stiffness of particle two (N/mm)
- $\varepsilon$  is the coefficient of restitution (-)

$$K_{nl,p} = E_p L \quad (5)$$

$$K_{nl,b} = E_b L \tag{6}$$

Here:

$E_p$  is the particle material’s bulk Young’s modulus (Pa)

$E_b$  is the boundary’s bulk Young’s modulus (Pa)

$L$  is the particle size (mm)

#### 2.4.2. Tangential Force Model: Linear Spring Coulomb Limit Model

Calculating the contact force in the tangential direction utilizes a linear spring Coulomb limit model. This model is categorized as an elastic-frictional model; the tangential force for purely elastic contact is computed using Equations (7) and (8), while the final tangential force uses Equation (9). This step is necessary as the tangential contact force must not surpass the Coulomb friction force.

$$F_{\tau,e}^t = F_{\tau}^{t-\Delta t} - K_{\tau} \Delta s_{\tau} \tag{7}$$

Here:

$F_{\tau,e}^t$  is the value of the tangential force at the current time (N)

$F_{\tau}^{t-\Delta t}$  is the value of the tangential force at the previous time (N)

$\Delta s_{\tau}$  is the tangential relative displacement of the particles during the timestep (mm)

$K_{\tau}$  is the tangential stiffness, which is defined as:

$$K_{\tau} = r_K K_{nl}, \tag{8}$$

where:

$r_K$  is the tangential stiffness ratio (-).

$$F_{\tau}^t = \min(|F_{\tau,e}^t|, \mu F_n^t) \frac{F_{\tau,e}^t}{|F_{\tau,e}^t|}, \tag{9}$$

where:

$\mu$  is the friction coefficient (-).

#### 2.5. Bucket Size Optimization Using DEM

A simulation model was created to optimize the bucket size of the metering device using the commercial software ANSYS Rocky for the DEM [18]. The bucket optimization method proposed by Im et al. [8] was employed to determine the optimal bucket size for each group. There exists a linear relationship between garlic size and optimal bucket size, and the sequential search method was used to optimize the design parameter by linearly decreasing the bucket size [8,25]. In the sorting process of the metering device, excess garlic cloves, which are more than one clove, are preferable to fall into the hopper via the guide. The rate at which the bucket was exhibited to be too small to contain a clove was defined as the missing plant rate. The target metering device is required to achieve a plant rate of 97.5% or more while simultaneously minimizing the multi-plant rate, as described in Equation (13). Although a bucket size larger than necessary is advantageous for achieving a plant rate of 97.5% or more, it may increase the multi-plant rate. Therefore, it is desirable to determine the smallest bucket size that satisfies the target plant rate.

$$Q = \left(1 - \frac{N_2}{N}\right) \times 100, \tag{10}$$

$$M = \frac{N_1}{N} \times 100, \tag{11}$$

$$C = \frac{N_2}{N} \times 100, \tag{12}$$



where:

$Q$  is plant rate (%)

$M$  is multi-plant rate (%)

$C$  is missing plant rate (%)

$N$  is the total number of trials (-)

$N_1$  is the number of metering trials with multiple cloves (-)

$N_2$  is the number of metering trials with empty bucket (-)

$$\begin{aligned} & \text{minimize : } M \\ & \text{subject to : } Q \geq 97.5 \end{aligned} \quad (13)$$

The elongated model depicted in Figure 4a was utilized to achieve the target plant rate. The model was constructed by setting the length that determines the center of gravity of garlic cloves as  $\mu_L + 2\sigma_L$ . Assuming a normal distribution of garlic clove lengths, all cloves, except for the top 2.5% of the group, are successfully planted if they pass safely through the metering device [8]. Figure 12 illustrates the bucket size optimization simulation and displays the initial posture of the garlic clove for simulation purposes. The most unfavorable condition for the metering operation was selected as the initial location of the garlic clove to attain the target plant rate. The mechanical vibration and geometrical characteristics of the finger-type bucket ensure that garlic cloves are always positioned parallel to the bucket; when the center of gravity faces outward, it is disadvantageous for planting. Furthermore, due to the rolling phenomenon, when the round side of the garlic clove faces the bottom, the center of gravity moves inside the bucket trajectory, which can be beneficial for metering. Therefore, the flat side was arranged to face the bottom for the most unfavorable condition.

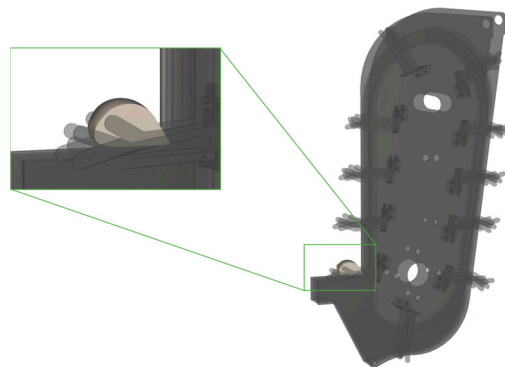


**Figure 12.** DEM simulation for the determination of optimal bucket size.

The dynamics model provided by ANSYS Rocky was utilized, and a rotational motion of 30 rpm was set on the lower sprocket, consistent with the actual operating conditions to establish the operation of the metering device. To carry out the sequential search method, the garlic clove model was positioned in the initial location in the most unfavorable orientation for planting, and multiple simulations were conducted while incrementally increasing the metering device guide angle ( $\alpha$ ) depicted in Figure 2a by  $0.1^\circ$ . The optimal bucket size was determined as the size immediately prior to the garlic clove of each group falling into the hopper via the guide. The design parameter interval was established to ensure applicability to the actual system as  $0.1^\circ$ , adjustable by the user.

### 2.6. Metering Simulation Using DEM

To validate the optimal bucket size of each group obtained through Section 2.5, a metering simulation was conducted using the DEM. The bucket size of the metering device was set to the optimum value obtained earlier, and the lower sprocket was rotated at 30 rpm, identical to the actual operating condition. Figure 13 depicts the metering simulation, demonstrating the sorting process that garlic cloves go through after being

placed in the hopper. By incorporating the virtual sensor into the simulation model, as shown in Figure 13, the number of garlic cloves in the bucket that passed through the sorting area was analyzed in the time domain. The garlic clove model for metering simulation was based on statistical information on the shape of garlic cloves and used the average model illustrated in Figure 4b. Furthermore, for various sizes, garlic clove models were scaled up or down based on a Gaussian distribution and randomly placed in the hopper to perform metering simulations for various sizes. The software provides a scale distribution method to consider different sizes when the mean and standard deviation information is available [18]. The morphological statistical information of garlic cloves to define the Gaussian distribution was based on the values provided by Im et al. [8].

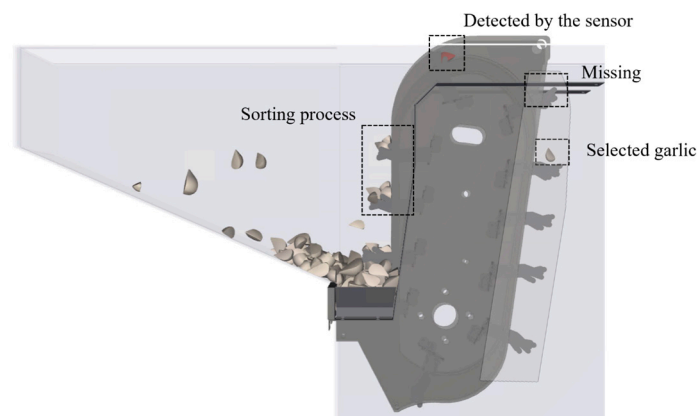


**Figure 13.** Metering simulation using DEM.

### 2.7. Metering Experiment

An actual metering experiment was conducted using a real metering device to validate the reliability of the discrete element analysis model and optimization technique. Figure 14a illustrates the actual garlic planter, while Figure 14b depicts the 1-row metering test machine. A boundary plate was installed on a 7-row metering device to create a 1-row metering test, establishing the same boundary conditions as the simulation model. Fifty garlic cloves were selected from each group, and a metering test was conducted with the sprocket rotating at 30 rpm, using the optimal bucket size as in the metering simulation. The test verified the plant rate (Q), multi-plant rate (M), and missing plant rate (C), and to ensure the reliability of the test results, it was repeated five times. The average value of each result was compared to the simulation result to validate the optimization methodology.

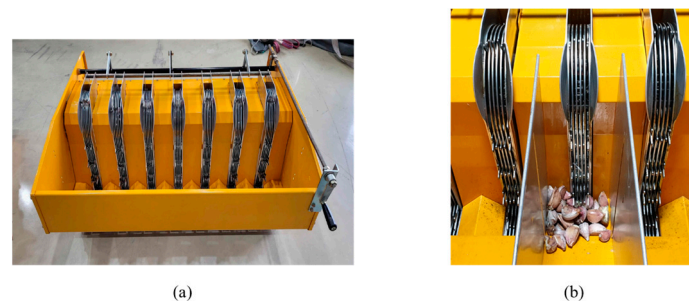


**Figure 14.** Metering experiment equipment. (a) Metering device. (b) 1-row metering test.

## 3. Results and Discussions

### 3.1. Bucket Size Optimization & Metering Simulation

This study aimed to optimize the bucket size of the metering device by initially positioning the garlic clove model under the most unfavorable conditions for metering. The optimal solution was then determined by gradually reducing the bucket size using the sequential search method. The design parameter interval was set at  $0.1^\circ$ , which the user can

adjust to ensure system applicability. The optimization process revealed that the optimal bucket size increased with the size of the garlic clove, and it was found that Group 1 had an optimal bucket size of 16.11 mm, Group 2 had 22.75 mm, and Group 3 had 23.64 mm. Table 2 summarizes the results of the bucket size optimization. A batch simulation of the metering operation was conducted to validate the accuracy of optimization results. Once the optimal bucket size was obtained through the sequential search method, a metering simulation at the optimal setting was conducted for garlic of various sizes in each group, and the results are shown in Table 3. Some 40 metering operations were performed for Group 1, 37 for Group 2, and 43 for Group 3 to enhance the reliability of the metering performance results.

**Table 2.** Optimal bucket size for each group of garlic.

Group	Optimum Bucket Size <i>l</i> (mm)
Group 1	16.11
Group 2	22.75
Group 3	23.64

**Table 3.** Results of metering simulation.

Group	No. Trials	Plant Rate ( <i>Q</i> )	Multi-Plant Rate ( <i>M</i> )	Missing Plant Rate ( <i>C</i> )
Group 1	40	92.50%	10.00%	7.50%
Group 2	37	97.30%	2.70%	2.70%
Group 3	43	97.70%	2.30%	2.30%

Except for Group 1, all groups were able to nearly achieve the target plant rate of 97.5%. Moreover, the multi-plant rate demonstrated a low level of under 3%. Group 1, being the smallest in size, exhibited the highest multi-plant rate at 10% and demonstrated poor metering performance. It is believed that the overlapping planting of more than one garlic clove occurred in the width direction of the finger-type bucket for Group 1, as shown in Figure 15. Conversely, in the case of Groups 2 and 3, this phenomenon did not occur because the thickness of the garlic clove was large, considering the bucket width. As such, they were deemed the most suitable groups for applying the metering device.

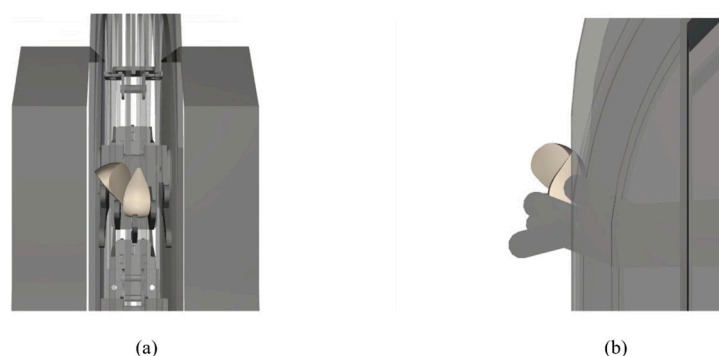


**Figure 15.** Overlapped garlic cloves causing multi plant. (a) Front view. (b) Side view.

### 3.2. Experimental Result

To validate the bucket size optimization technique, an actual metering test was conducted, as depicted in Figure 14, and the results are illustrated in Table 4. The test was executed under conditions identical to the analysis model, including bucket size and rotational speed, to validate the optimization process using simulation. The test was repeated five times using 50 garlic cloves in each group to enhance the reliability of the test results. Average plant rates of 90.44% for Group 1, 97.97% for Group 2, and 94.95% for Group 3 were confirmed. It was observed that all groups except Group 1 came close to the target

plant rate of 97.5%. Additionally, it was confirmed that Group 1 had a multi-plant rate of 1.47%, Group 2 had a rate of 2.85%, and Group 3 had a rate of 0.49%. These findings demonstrate significantly improved metering performance compared to the test results of Kang et al. [3].

**Table 4.** Results of the metering experiment.

Group	Test No	Plant Rate (Q)	Multi-Plant Rate (M)	Missing Plant Rate (C)
Group 1	1	89.29%	0.00%	10.71%
	2	89.09%	1.82%	10.91%
	3	90.91%	0.00%	9.09%
	4	89.29%	0.00%	10.71%
	5	94.00%	6.00%	6.00%
	Average	90.44%	1.47%	9.56%
Group 2	1	100.00%	2.04%	0.00%
	2	97.92%	6.25%	2.08%
	3	97.96%	4.08%	2.04%
	4	95.92%	2.04%	4.08%
	5	98.04%	0.00%	1.96%
	Average	97.97%	2.85%	2.03%
Group 3	1	97.56%	2.44%	2.44%
	2	97.62%	0.00%	2.38%
	3	93.18%	0.00%	6.82%
	4	93.18%	0.00%	6.82%
	5	93.18%	0.00%	6.82%
	Average	94.95%	0.49%	5.05%

Table 5 presents the simulation and test results for the plant rate, multi-plant rate, and missing plant rate. It was confirmed that the plant rate for both results had a maximum error of 2.8% for Group 3. The difference between the two results for the multi-plant rate was 8.5% for Group 1, 0.2% for Group 2, and 1.8% for Group 3. Lastly, for the missing plant rate, a relatively low level of error was confirmed, with a maximum error of 2.8% for Group 3. For Group 1, due to the relatively narrow width of cloves, multiple garlic cloves could be stacked in the bucket, as shown in Figure 15, and the metering performance was affected by both the width of the bucket and the length of the garlic cloves. The bucket size optimization technique applied in this study considered the length of garlic cloves as the only independent variable and not the effect of bucket width. Consequently, both simulation and test results displayed poor metering performance, and the reliability of the optimal solution was not fully guaranteed for Group 1. As a result, there was a relatively significant difference between the analysis and test results in Group 1 compared to those of Groups 2 and 3. Upon comparing the analysis and test results, it was determined that the analysis model predicted the metering performance of the actual metering device within 10% of all performance indicators, including plant rate, multi-plant rate, and missing plant rate. Particularly for Groups 2 and 3, the high reliability of the analysis model was confirmed, showing a difference in the metering performance of a maximum of 2.8% (plant rate of Group 3).

**Table 5.** Comparison between simulation and experiment results.

Group	Index	Simulation	Experiment	Difference
Group 1	Plant rate (Q)	92.50%	90.44%	2.10%
	Multi-plant rate (M)	10.00%	1.50%	8.50%
	Missing plant rate (C)	7.50%	9.60%	−2.10%
Group 2	Plant rate (Q)	97.30%	97.97%	−0.70%
	Multi-plant rate (M)	2.70%	2.90%	−0.20%
	Missing plant rate (C)	2.70%	2.00%	0.70%
Group 3	Plant rate (Q)	97.70%	94.95%	2.80%
	Multi-plant rate (M)	2.30%	0.50%	1.80%
	Missing plant rate (C)	2.30%	5.10%	−2.80%

#### 4. Conclusions

In this investigation, the bucket size of the garlic planter metering device was optimized by utilizing the DEM, considering the size of various garlic cloves. To enhance the precision of the analysis model, the actual shape of the garlic cloves was incorporated using a 3D mesh, and the mechanical properties of garlic were found through various tests, such as the angle of repose test and sliding test. Subsequently, the optimal bucket size was determined for the three garlic size groups using the sequential search method based on the developed model. A metering simulation was carried out to validate the optimal value, and finally, a physical test was conducted under the same conditions to ensure the reliability of the optimization technique. The primary findings of the study are summarized as follows.

- (1) Calibration was executed by conducting a repose angle test to establish the garlic-garlic friction coefficient. It was ascertained that the simulation model and the test produced the same repose angle when the garlic-garlic friction coefficient was 0.46.
- (2) Bucket size optimization was carried out to achieve the target metering rate of 97.5%. Subsequently, it was determined that Group 1 had an optimal bucket size of 16.11 mm, Group 2 had that of 22.75 mm, and Group 3 had that of 23.64 mm.
- (3) To validate the reliability of the determined optimal bucket size, a metering simulation was conducted, which showed that the plant rate was 90.44% for Group 1, 97.97% for Group 2, and 94.95% for Group 3. The results indicate that Groups 2 and 3 achieved a seeding rate close to the target value of 97.5%.
- (4) To validate the reliability of the optimization methodology, an actual metering test was conducted under identical conditions. Upon comparing the metering performance, it was confirmed that all metering performances exhibited differences of less than 10%. Notably, in Groups 2 and 3, the difference in metering performance was within 2.8%, thus confirming the reliability of the optimization technique.
- (5) Regarding Group 1, as depicted in Figure 15, the garlic clove widths were relatively narrow, leading to an overlap phenomenon. Consequently, the metering performance prediction exhibits low accuracy, and the metering performance is inferior to Groups 2 and 3.

The DEM was employed to confirm the optimal bucket size for each garlic group, and during actual metering work, the optimal bucket size resulted in nearly satisfactory target plant rates. Moreover, the proposed methodology enables the optimal design of various agricultural implements with similar mechanisms. Notably, this study solely considered the length of the finger-type bucket in the bucket optimization process, while the width was not taken into account. As a result, while Groups 2 and 3 met the target plant rate, Group 1 did not. Future studies will enhance the optimization completeness by incorporating the width as well as the bucket size.

**Author Contributions:** Conceptualization, D.I.; methodology, D.I.; software, J.-H.K. and D.-J.M.; validation, D.I. and H.-S.L.; resources, T.-I.M.; supervision, Y.-J.P.; project administration, S.-H.Y. All authors have read and agreed to the published version of the manuscript.

**Funding:** This work was carried out with the support of the “Cooperative Research Program for Agriculture Science & Technology Development (Project No. PJ016061)” Rural Development Administration, Republic of Korea.

**Institutional Review Board Statement:** Not available.

**Data Availability Statement:** No new data were created or analyzed in this study. Data sharing is not applicable to this article.

**Acknowledgments:** This work was carried out with the support of the “Cooperative Research Program for Agriculture Science & Technology Development (Project No. PJ016061)”, Rural Development Administration, Republic of Korea.

**Conflicts of Interest:** The authors declare no conflict of interest.

## References

- Walsh, P.P.; Murphy, E.; Horan, D. The role of science, technology and innovation in the UN 2030 agenda. *Technol. Forecast. Soc. Change* **2020**, *154*, 119957.
- Choi, D.K.; Cho, S.C.; Lee, C.S.; Park, S.H.; Kim, H.J.; Kang, T.K.; Kim, C.K.; Kwak, T.Y. Development of a Metering Device for the Garlic Planter. *Biosyst. Eng.* **2001**, *26*, 525–534.
- Kang, T.G.; Lee, S.H.; Kim, J.G.; Kim, Y.K.; Choi, Y.; Choi, I.S.; Lim, J. A factor analysis of garlic metering device for development of a garlic planter. *J. Agric. Sci.* **2018**, *52*, 143–151.
- Wang, H.; Sun, X.; Li, H.; Fu, J.; Zeng, X.; Xu, Y.; Wang, Y.; Liu, H.; Lü, Z. Design and parameter optimization of a finger clip plate garlic seed-metering device based on EDEM. *Agronomy* **2022**, *12*, 1543.
- Kang, T.G.; Lee, S.H.; Choi, Y.; Kwon, Y.S.; Kim, T.H. Study on the optimum condition of mechanical sowing of a garlic. *J. Korea Acad.-Ind. Coop. Soc.* **2021**, *22*, 360–366.
- Zilpilwar, S.; Yadav, R.; Gajjar, P.; Jakasania, R. Development and performance evaluation of metering mechanism for planting garlic cloves. *Agric. Res.* **2021**, *10*, 274–284.
- Zhang, X.; Yi, S.; Tao, G.; Zhang, D.; Chong, J. Design and experimental study of spoon-clamping type garlic precision seeding device. *Wirel. Commun. Mob. Comput.* **2022**, *2022*, 5222651.
- Im, D.; Kim, J.H.; Moon, D.J.; Moon, T.I.; Yu, S.H.; Park, Y.J. Optimization of bucket size of garlic metering device using multibody dynamics simulation. *Biosyst. Eng.* **2022**, *47*, 480–488.
- Guo, H.; Cao, Y.; Song, W.; Zhang, J.; Wang, C.; Wang, C.; Zhu, L. Design and simulation of a garlic seed metering mechanism. *Agriculture* **2021**, *11*, 1239.
- Yu, Z.; Yang, K.; Hu, Z.; Peng, B.; Gu, F.; Yang, L.; Yang, M. Parameter optimization and simulation analysis of floating root cutting mechanism for garlic harvester. *Comput. Electron. Agric.* **2023**, *204*, 107521.
- Wang, J.; Tang, H.; Wang, J.; Li, X.; Huang, H. Optimization design and experiment on ripple surface type pickup finger of precision maize seed metering device. *Int. J. Agric. Biol.* **2017**, *10*, 61–71.
- Kang, J.; Peng, Q.; Zhang, C.; Zhang, N.; Fang, H. Design and testing of a punching-on-film precision hole seeder for peanuts. *Trans. ASABE* **2020**, *63*, 1685–1696. [CrossRef]
- Singh, R.C.; Singh, G.; Saraswat, D.C. Optimisation of design and operational parameters of a pneumatic seed metering device for planting cottonseeds. *Biosyst. Eng.* **2005**, *92*, 429–438. [CrossRef]
- Wang, M.; Liu, Q.; Ou, Y.; Zou, X. Numerical simulation and verification of seed-filling performance of single-bud billet sugarcane seed-metering device based on EDEM. *Agriculture* **2022**, *12*, 983. [CrossRef]
- Ryu, I.H.; Kim, K.U. Design of roller type metering device for precision planting. *Trans. ASABE* **1998**, *41*, 923. [CrossRef]
- Han, D.; Zhang, D.; Jing, H.; Yang, L.; Cui, T.; Ding, Y.; Zhang, T. DEM-CFD coupling simulation and optimization of an inside-filling air-blowing maize precision seed-metering device. *Comput. Electron. Agric.* **2018**, *150*, 426–438. [CrossRef]
- Sun, X.; Li, H.; Qi, X.; Nyambura, S.M.; Yin, J.; Ma, Y.; Wang, J. Performance parameters optimization of a three-row pneumatic precision metering device for brassica chinensis. *Agronomy* **2022**, *12*, 1011. [CrossRef]
- ANSYS Rocky. 2023. Available online: <https://www.ansys.com/products/fluids/ansys-rocky> (accessed on 1 January 2023).
- Park, D.; Lee, C.G.; Park, H.; Baek, S.H.; Rhee, J.Y. Discrete element method analysis of the impact forces on a garlic bulb by the roller of a garlic harvester. *Biosyst. Eng.* **2019**, *44*, 208–217. [CrossRef]
- Yu, Z.; Hu, Z.; Peng, B.; Gu, F.; Yang, L.; Yang, M. Experimental determination of restitution coefficient of garlic bulb based on high-speed photography. *Int. J. Agric. Biol. Eng.* **2021**, *14*, 81–90. [CrossRef]
- Chen, J.; Gao, R.; Liu, Y. Numerical study of particle morphology effect on the angle of repose for coarse assemblies using DEM. *Adv. Mater. Sci. Eng.* **2019**, *2019*, 8095267. [CrossRef]
- Zeng, Y.W.; Jin, L.; Du, X.; Gao, R. Refined modeling and movement characteristics analyses of irregularly shaped particles. *Int. J. Numer. Anal. Methods* **2015**, *39*, 388–408. [CrossRef]
- Walton, O.R.; Braun, R.L. Viscosity, granular-temperature, and stress calculations for shearing assemblies of inelastic, frictional disks. *J. Rheol.* **1986**, *30*, 949–980. [CrossRef]
- ESSS Rocky, Release 2021 R2.2, DEM Technical Manual, ESSS Rocky DEM, S.R.L. 2021. Available online: <https://rocky.esss.co/technical-library/> (accessed on 1 January 2023).
- Kiefer, J. Sequential minimax search for a maximum. *Proc. Am. Math. Soc.* **1953**, *4*, 502–506. [CrossRef]

**Disclaimer/Publisher’s Note:** The statements, opinions and data contained in all publications are solely those of the individual author(s) and contributor(s) and not of MDPI and/or the editor(s). MDPI and/or the editor(s) disclaim responsibility for any injury to people or property resulting from any ideas, methods, instructions or products referred to in the content.

Communication

# Methodology for Assessing Tractor Traction Properties with Instability of Coupling Weight

Anatoliy Lebedev <sup>1</sup>, Mykhailo Shuliak <sup>1</sup>, Stanislav Khalin <sup>2</sup>, Sergei Lebedev <sup>2</sup>, Katarzyna Szwedziak <sup>3,\*</sup>, Krzysztof Lejman <sup>3</sup>, Gniewko Niedbała <sup>4,\*</sup> and Tomasz Łusiak <sup>5</sup>

<sup>1</sup> Agroengineering Department, Sumy National Agrarian University, 160 Herasyma Kondratieva Street, 4000 Sumy, Ukraine

<sup>2</sup> Leonid Pogorilyy Ukrainian Scientific Research Institute, 08654 Doslidnitske, Ukraine

<sup>3</sup> Institute of Agricultural Engineering, Wrocław University of Environmental and Life Sciences, 37b Chełmońskiego Street, 51-630 Wrocław, Poland

<sup>4</sup> Department of Biosystems Engineering, Faculty of Environmental and Mechanical Engineering, Poznań University of Life Sciences, Wojska Polskiego 50, 60-627 Poznań, Poland

<sup>5</sup> Department of Thermodynamics, Fluid Mechanics and Aviation Propulsion Systems, Lublin University of Technology, Nadbystrzycka 38 D, 20-618 Lublin, Poland

\* Correspondence: katarzyna.szwedziak@upwr.edu.pl (K.S.); gniewko.niedbala@up.poznan.pl (G.N.)

**Abstract:** The purpose of the study is to increase the efficiency of using the tractor hitch weight in traction mode by reducing the uneven distribution of vertical reactions between the wheels. This work is grounded on a methodology that involves summarizing and analyzing established scientific findings related to the theory of tractors operating in traction mode. The analytical method and comparative analysis were employed to establish a scientific problem, define research objectives, and achieve the goal. The key principles of probability theory were applied in developing the empirical models of the tractor. The main provisions of the methodology for evaluating the traction properties of the tractor with the instability of the coupling weight were formulated. The method of evaluating the vertical reactions on the wheels of the tractor is substantiated, which is based on the measurement of the vertical reaction on one of the four wheels. It was proven that tractors with a center of mass offset to the front or rear axles have the greatest probability of equal distribution of vertical reactions between the wheels of one axle, and tractors with a center of mass in the middle between the axles have the lowest probability. It is theoretically substantiated and experimentally confirmed that when the tractor performs plowing work with uneven distribution of loads on the sides, its operation with maximum traction efficiency is ensured by blocking the front and rear axle drivers.

**Keywords:** tractor; traction properties; coupling weight; center of mass; vertical reactions; driving bridges; blocking

**Citation:** Lebedev, A.; Shuliak, M.; Khalin, S.; Lebedev, S.; Szwedziak, K.; Lejman, K.; Niedbała, G.; Łusiak, T. Methodology for Assessing Tractor Traction Properties with Instability of Coupling Weight. *Agriculture* **2023**, *13*, 977. <https://doi.org/10.3390/agriculture13050977>

Academic Editors: Ju-Seok Nam and Yongjin Cho

Received: 26 March 2023

Revised: 22 April 2023

Accepted: 26 April 2023

Published: 28 April 2023



**Copyright:** © 2023 by the authors. Licensee MDPI, Basel, Switzerland. This article is an open access article distributed under the terms and conditions of the Creative Commons Attribution (CC BY) license (<https://creativecommons.org/licenses/by/4.0/>).

## 1. Introduction

The classic approach to the tractor as an object of design and management [1] consists of imagining it as a traction machine that has one connection with the external environment (running gear). Such an idea leads to the setting of tasks for optimizing the properties of the tractor, including traction force and efficiency, movement resistance, load on the axles, etc. These tractor parameters are regulated during their tests in NTTL laboratories [2] in the United States of America and Germany [3].

When the tractor is working in traction mode, its connection with the soil is carried out through two channels (running gear, working implement), which lead to the instability of the traction force of the tractor and the resistance of the aggregated agricultural machine [4–6]. At the same time, the reactions between the wheels of the front and rear axles are assumed to be uniform, although due to different rolling resistance of the wheels, for example, when the tractor performs certain tasks, the reactions between the wheels



are unevenly distributed [7–9]. The movement of the tractor during the execution of the technological process leads to longitudinal, lateral, and vertical oscillations of sprung and unsprung masses and tractor wheels. Longitudinal and lateral oscillations of the tractor lead to an increase in the dynamic tension of the soil due to skidding, which reduces its traction force, and vertical oscillations are the main cause of dynamic soil compaction [10,11]. At the same time, an uneven distribution of vertical reactions between the wheels of the tractor is noted, which affects the efficiency of using the coupling weight in traction mode [12,13]. The essential feature of the tractor's movement in the traction mode was not adequately covered in the technical literature when evaluating its support and traction properties.

The solution to the problem of the influence of a mobile machine's center of mass is considered in a number of foreign publications [14], which note the perspective of research in the direction of machine operation in traction mode. It is proposed to determine the energy parameters of the machine by differentiating its mass.

Practice presents science with the need to solve the problem of developing a methodology for assessing the uneven distribution of vertical reactions between the tractor wheels in traction mode.

The efficiency of using the towing weight of the tractor in traction mode is increased by reducing the uneven distribution of vertical reactions between the wheels.

The following tasks were set in this work:

- Justify the dependence of the tractor's traction properties on the use of the coupling weight of the driving axles.
- Estimate the distribution of vertical reactions between the wheels of one driving axle of a tractor.
- Justify the zone of the most likely reduction in the use of the towing weight of the four-wheel drive tractor.

## 2. Materials, Method and Results

This work is based on a methodology that summarizes and examines existing scientific findings on the theory of tractors in traction mode. The analytical method and comparative analysis were utilized to formulate the scientific problem, establish research objectives, and achieve the goal. The fundamental principles of probability theory were incorporated in developing the empirical tractor models.

Let us assume that the tractor, being on a flat horizontal surface, moves at a constant speed with the power take-off shaft turned off (Figure 1). Traction efficiency of the tractor can be expressed [1] by the following equation:

$$\eta_T = \frac{N_T}{N_e} = \frac{P_{KP}v_d}{M_d n_d} \frac{716.2}{270} = 2.65 \frac{P_{KP}v_d}{M_d n_d}, \quad (1)$$

where  $N_T$ —traction power of the tractor, kW;  $N_e$ —effective engine power, kW;  $P_{KP}$ —traction force on the hook, kN;  $v_d$ —actual driving speed, km/h.;  $M_d$ —engine torque, kN•m;  $n_d$ —engine crankshaft rotation frequency (engine speed), r/min.

Let us imagine that the traction forces on the hook and the actual speed of movement, which are included in Equation (1) of the traction efficiency of the tractor, are functions of the dimensionless coefficients  $\varphi_{1,2}$  of the use of the coupling weight of the driving axles in the following equation:

$$\varphi_{1,2} = \frac{P_{K1,2}}{Y_{1,2}}, \quad (2)$$

where  $P_{K1,2}$ —tangential traction force of the driving axle, kN;  $Y_{1,2}$ —soil reaction, numerically equal to the towed weight of the tractor, which is distributed to the drive axle ( $Y_{1,2} = G_{1,2}$ ), kN. Here, and further, the index "1" refers to the front, and the index "2" refers to the rear axles.

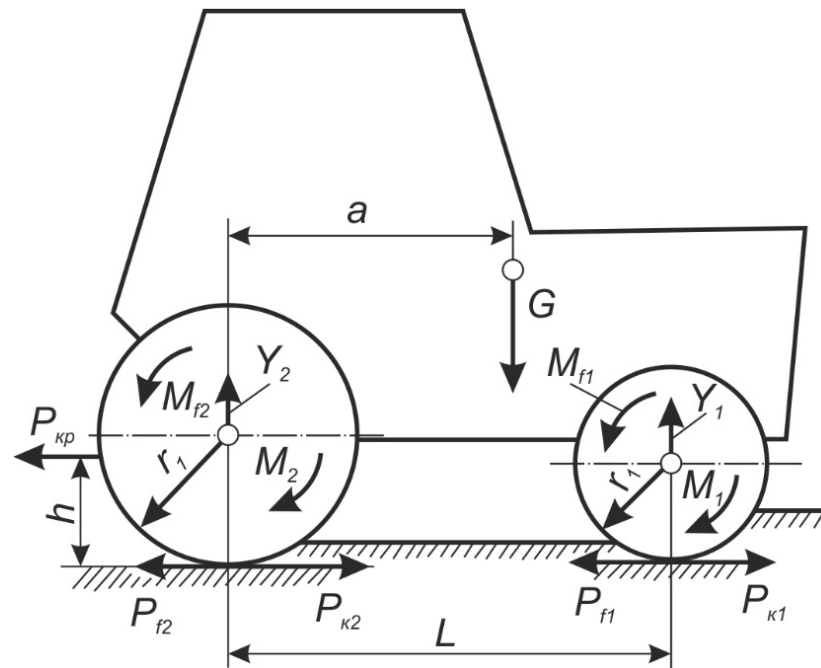


Figure 1. Diagram of the forces acting on the tractor.

To obtain the dependency  $P_{kp} = f(\varphi_1, \varphi_2)$  we express  $P_{kp} = P_{kp1} + P_{kp2} - P_{f1} - P_{f2}$ ;  $P_{k1,2} = G_{1,2}\varphi_{1,2}$ ;  $P_{f1,2} = G_{1,2}f_{1,2}$ , where  $P_{f1,2}$ —force of resistance to rolling of driving axles;  $f_{1,2}$ —coefficient of resistance to rolling of driving axles.

Taking into account the redistribution of the coupling weight depending on the traction force, we obtain the following equation:

$$P_{kp} = \frac{G[A_1(\varphi_1 - f_1) + A_2(\varphi_2 - f_2)]}{A_3 + h(\varphi_1 - \varphi_2)}, \tag{3}$$

where  $A_1 = a - f_2r_2$ ;  $A_2 = L - a - f_1r_1$ ;  $A_3 = L - h(\varphi_1 - \varphi_2) + f_1r_1 - f_2r_2$ ;  $G$ —the weight of the tractor, kN;  $L$ —longitudinal base of the tractor, m;  $h$ —trailer point height, m;  $r_1r_2$ —rolling radii of the wheels, m.

Traction-supporting properties of the tractor depend mainly on its operating weight  $G_e$ , the conversion of which into traction force  $P_{kp}$  is estimated by the coefficient of use of the towing weight  $\varphi_{kp} = P_{kp}/G_e$ . When moving a wheeled tractor on a flat agricultural background, with the coefficients of traction of the driving wheels with the soil  $\varphi_{3\psi}$ , rolling resistance  $f$ , and the share of weight falling on the driving wheels  $\lambda_k$ , the support and traction properties of a tractor with one driving axle are estimated according to the dependence  $\varphi_{kp} = \varphi_{3\psi}\lambda_k - f$ , and for all-wheel drive tractors— $\varphi_{kp} = \varphi_{3\psi} - f$ . An analysis  $\varphi_{kp}$  of tractors with one drive axle and four-wheel drive tractors shows that the greater the coefficient of traction in comparison with the coefficient of rolling resistance, the greater the tractor’s margin of traction force.

In operating conditions, the traction force of the tractor varies from zero to the maximum value  $P_{kp} = P_{kpmax}$ , which is determined by the traction properties at  $G_e = const$ .

Therefore, the coefficient  $\varphi_{kp}$  changes from zero to  $\varphi_{kpmax}$ . The nominal traction force corresponds to a certain value  $\varphi_{kpH}$ . This statement was confirmed when the John Deere 8335 R tractor was moving in traction mode (Figure 2) [7,9,10,12].

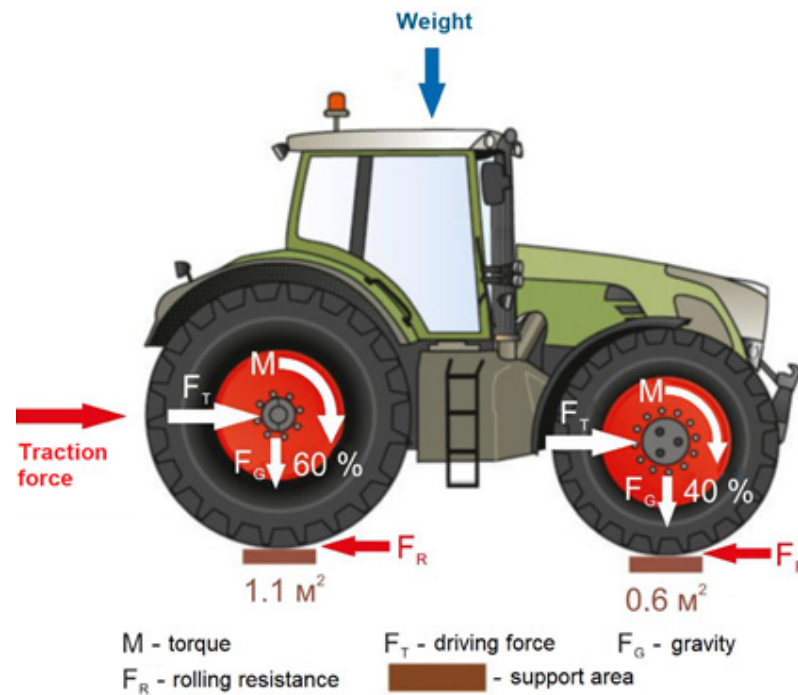


Figure 2. Diagram of the forces acting on the John Deere 8335 R tractor in traction mode.

Technical characteristics of the tractor John Deere 8335 R:

Nominal power of the engine,  $N_e$ , kW—246;

Nominal specific fuel consumption,  $g_e$ , g/kWh—224;

Engine torque reserve, %—41.4;

Traction power,  $N_e$ , kW—212;

Operating mass,  $m_e$ , kg—13,820;

Axle load, front/rear, kg—5528/8292;

Energy saturation,  $E = N_e/m_e$ —1.81;

Conditional traction efficiency,  $\eta_T = N_T/N_e$ —0.86.

Comparing the values of the loads acting on the front  $y_n$  and rear  $y_3$  wheels of the tractor show that they do not remain constant. If the traction resistance line is parallel to the road surface, then the loads  $y_n$  and  $y_3$  change due to the redistribution of the tractor's weight between the front and rear wheels. Reducing the load on the front wheels causes the same increase in the load on the rear wheels, and vice versa. The amount  $y_n + y_3$  is equal to the weight of the tractor  $G_T$ . Instability in  $y_n$  and  $y_3$  leads to an uneven distribution of vertical reactions between the wheels of the tractor, and a decrease in the efficiency of using its hitch weight in traction mode. At the same time, even when the center of mass of the tractor is located strictly in the longitudinal plane of symmetry, inequality of vertical reactions on the left and right wheels of the same axle is possible. This is due to the static uncertainty of the four-wheeled tractor as a spatial structure that has four supports (connections) and, accordingly, four vertical reactions of the connection. A well-founded methodology for solving this problem is based on the interrelationship of dimensionless (specific) forces on the wheels of the tractor as follows:

$$\gamma_{zi} = R_{z1}/G; \gamma_{z2} = b/L - \gamma_{zi}; \gamma_{z3} = 0.5 - \gamma_{zi}; \gamma_{z4} = \frac{a}{L} - 0.5 + \gamma_{zi}, \quad (4)$$

where  $R_{z1}$ —vertical reaction on the front wheel;  $G$ —total weight of the tractor;  $a$ ,  $b$ ,  $L$ —distances from the projection of the center of mass on the horizontal plane to the front and rear axles, the longitudinal wheel base of the tractor.

By specifying and measuring the vertical reaction on one of the four tractor wheels, the vertical reactions on the last three wheels can be accurately determined. Developed at the

Kharkiv branch of L. Pogorilyy UkrNDIPVT, the method for determining vertical reactions of tractor wheels involves determining two components: the position of the tractor frame in space and the vertical reaction to any of the four tractor wheels. In this case, the frame of the tractor is taken as a completely solid body and the vertical reaction is determined experimentally; the other three vertical reactions with the known weight of the tractor are determined analytically. For further modeling in this article, it was assumed that the tractor is installed on a perfectly flat surface, that is, the angles of inclination of the frame are equal to zero. In real operation, the position of the frame can be determined using acceleration sensors [15] and calculated analytically or using a digital gyroscope. At the stage of tractor design, it is advisable to imagine the vertical reaction on one of the wheels as a random variable, the distribution of which is subject to a normal law. Let us assume that such an independent random variable will be  $\gamma_{z2}$ , the changes of which are theoretically possible within the limits of  $[0, b/L]$ . With a decrease in  $\gamma_{zi}$  there is a decrease in  $\gamma_{z4}$ , which cannot take negative values, because this leads to a violation of the system equilibrium.

Thus, when  $\gamma_{zi} = 0$  the following must be performed:

$$\gamma_{z4min} = \frac{a}{L - 0.5} \geq 0 \text{ or } b/L \leq 0.5. \tag{5}$$

Therefore, when  $b/L \leq 0$ , the value  $\gamma_{zi}$  can vary within the following limits:

$$\frac{b}{L} - 0.5 \leq \gamma_{zi} \leq 0.5. \tag{6}$$

With the normal distribution law of vertical reactions on the wheels of the tractor, the density of the distribution of the specific load on one front wheel is estimated by the following equation:

$$f(\gamma_{zi}) = \left\{ \begin{array}{l} \frac{2394}{b/L} \mu_{\sigma} \exp \left[ -\frac{1}{2} \left( \frac{6}{b/L} \gamma_{zi} - 3 \right)^2 \right] \text{ at } \frac{b}{L} \leq 0.5; \\ \frac{2394}{1-b/L} \mu_{\sigma} \exp \left[ -\frac{1}{2} \left( \frac{6}{1-b/L} \gamma_{zi} - \frac{3b/L}{1-b/L} \right)^2 \right] \text{ at } \frac{b}{L} > 0.5 \end{array} \right\} \tag{7}$$

where  $\mu_{\sigma}$ —the selected scale of the root means square deviation, i.e., the value is conventionally taken as a unit during the analysis.

Figure 3 shows graphs of Function (7) at different positions of the tractor’s center of mass (parameter  $b/L$ ), taking into account the possible range of changes of  $\gamma_{zi}$ .

Analysis of the calculation results shows that tractors with an offset to the front or rear axle of the center of mass have the greatest probability of equal distribution of vertical reactions between the wheels of one axle. Tractors with a center of mass located in the middle between the axles have the lowest probability of equal distribution of vertical reactions at  $b/L = 0.5$ , and the largest—at  $b/L = 0.9$  and  $b/L = 0.1$ .

If at  $b/L = 0.1$ , this probability is 0.4, then at  $b/L = 0.5$ , it is equal to 0.1.

When the tractor is working in the traction mode, the uneven distribution of vertical reactions leads to the deterioration of its traction–speed characteristics, since the total tangential traction force is determined by the wheel, which is in worse grip conditions. If we consider the specific vertical reactions on the wheels (the ratio of the corresponding reaction on the  $j$ -th wheel to the total weight of the tractor), taking into account their possible changes within the rms deviation, then the dependencies for their calculation are written in the following form:

$$\gamma_{z1} = m_{\gamma1} + \sigma_{\gamma1}; \gamma_{z2} = m_{\gamma2} - \sigma_{\gamma2}; \gamma_{z3} = m_{\gamma3} - \sigma_{\gamma3}; \gamma_{z4} = m_{\gamma4} + \sigma_{\gamma4}, \tag{8}$$

where  $m_{\gamma1}, m_{\gamma2}, m_{\gamma3}, m_{\gamma4}$ —mathematical expectation of specific vertical reactions on the corresponding wheels (1, 2—front wheels; 3, 4—rear wheels; 1, 3—left side wheels; 2, 4—starboard wheels);  $\sigma_{\gamma1}, \sigma_{\gamma2}, \sigma_{\gamma3}, \sigma_{\gamma4}$ —root mean square deviations of the specific vertical reactions on the specified wheels.

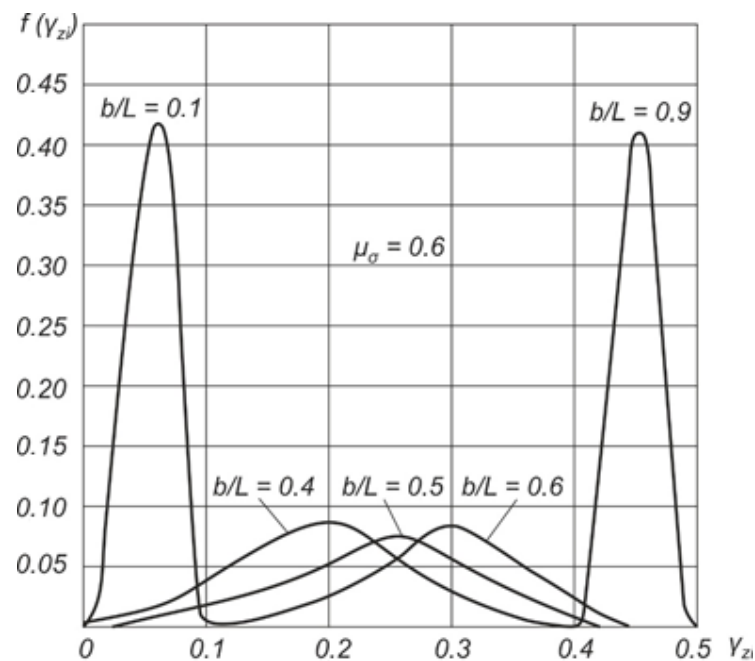


**Figure 3.** The density of the distribution of the specific load on one front wheel at the cut-off position of the tractor’s center of mass.

It is obvious that

$$m_{\gamma 1} = m_{\gamma 1} = \frac{1}{2} \frac{b}{L}; m_{\gamma 3} = m_{\gamma 4} = \frac{1}{2} \left(1 - \frac{b}{L}\right). \tag{9}$$

At  $b/L \leq 0.5$  we have

$$\sigma_{\gamma} = \sigma_{\gamma 1} = \sigma_{\gamma 2} = \sigma_{\gamma 3} = \sigma_{\gamma 4} = \frac{1b}{6L}. \tag{10}$$

At  $b/L > 0.5$  we have

$$\sigma_{\gamma} = \sigma_{\gamma 1} = \sigma_{\gamma 2} = \sigma_{\gamma 3} = \sigma_{\gamma 4} = \frac{1}{6} \left(1 - \frac{b}{L}\right). \tag{11}$$

The acceleration that occurs when the tractor accelerates in the absence of wheel slippage is determined by the wheel that is in worse grip conditions, that is, having a lower vertical load, as follows:

$$a = g\varphi\varphi_{KP}, \tag{12}$$

where  $g$ —free fall acceleration,  $g = 9.81 \text{ m/s}^2$ ;  $\varphi$ —coefficient of adhesion of the wheels to the road;  $\varphi_{KP}$ —the coefficient of use of the coupling weight in traction mode for a four-wheel drive tractor.

$$\varphi_{KP} = 2(\gamma_{z2} + \gamma_{z3}) = 2(m_{\gamma 2} + m_{\gamma 3} - 2\sigma_{\gamma}) = \begin{cases} 1 - \frac{2b}{3L} & \text{at } \frac{b}{L} \leq 0.5 \\ \frac{1}{3} - \frac{2b}{3L} & \text{at } \frac{b}{L} > 0.5 \end{cases} \tag{13}$$

Figure 4 presents a graph illustrating the dependence of  $\varphi_{KP}$  on the parameter  $b/L$ .

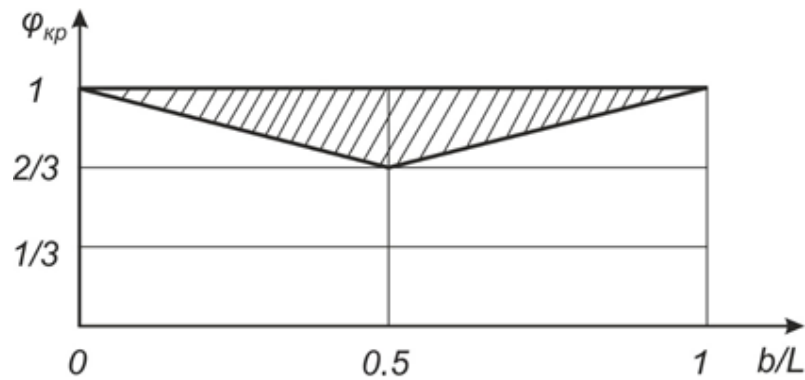


**Figure 4.** The zone of the most probable values of the reduction in the coefficient of use of the drawbar weight of a two-axle four-wheel drive tractor in traction mode (shaded).

Analysis of the graph in Figure 4 shows that the greatest decrease in the coupling weight coefficient of a two-axle four-wheel drive tractor in traction mode occurs when  $\frac{b}{L} > 0.5$ . This decrease can reach 33%.

In case of asymmetric application of the traction force on the tractor hook, for example, the resistance force of the plow, which is characterized by the distance  $\alpha$  from the tractor axis to the point of application  $P_{n,l}$  and different rolling resistance of the wheels  $P_{fi}$ , the traction force required to overcome  $P_{fi}$  will be different for each wheel  $P_{ki}$  (Figure 5).

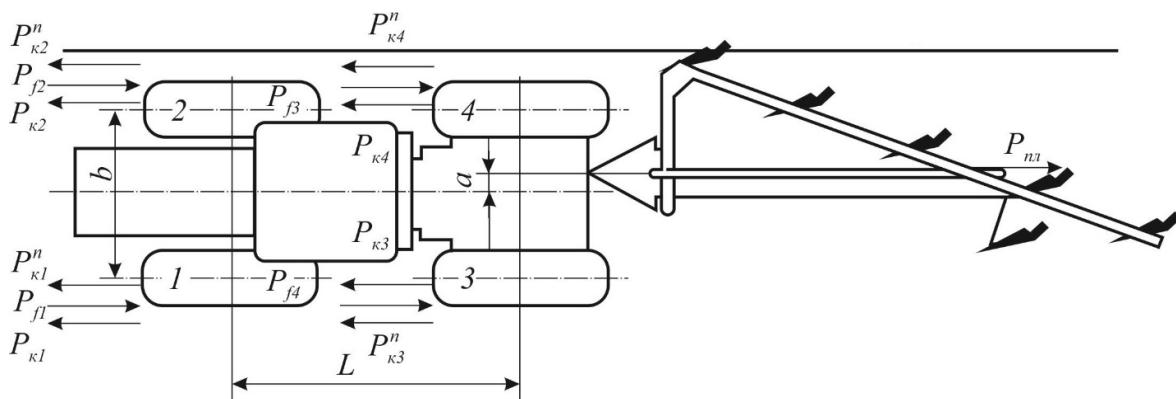


**Figure 5.** Diagram of the action of forces on the tractor's wheels during plowing operations.

To ensure uniform straight-line movement of the tractor, it is necessary to fulfill the condition  $P_{ki} = P_{fi} + P_{ki}^n$ , where  $P_{ki}^n$ —the traction force required to overcome the drag force of the plow.

For this case, the tangent of the traction force of the wheels is written in the following form:

$$\left. \begin{aligned} P_{k1} &= P_{n,l} \frac{(b/2-a)}{b} + P_{k3} + \sum (P_{f1,3} + P_{k1,3}^n) \\ P_{k2} &= P_{n,l} \frac{(b/2-a)}{b} + P_{k4} + \sum (P_{f2,4} + P_{k2,4}^n) \\ P_{k3} &= P_{n,l} \frac{(b/2-a)}{b} + P_{k1} + \sum (P_{f1,3} + P_{k1,3}^n) \\ P_{k4} &= P_{n,l} \frac{(b/2-a)}{b} + P_{k2} + \sum (P_{f2,4} + P_{k2,4}^n) \end{aligned} \right\} \quad (14)$$

The analysis of this system of equations shows that at  $P_{f1,3} \neq P_{f2,4}$  caused by different wheel rolling conditions when the tractor plows ( $P_{f2} > P_{f4}, P_{f1} > P_{f3}, P_{f2} > P_{f1}, P_{f4} > P_{f3}$ ) has  $P_{k2} > P_{k4}, P_{k1} > P_{k3}, P_{k2} > P_{k1}, P_{k4} > P_{k3}$ .

In the Kharkiv branch of L. Pogorilyy UkrNDIPVT, in order to evaluate the dependence of the traction force of the tractor on the coupling weight with an uneven distribution of reactions between the axles, experimental studies of the HTZ-17021 tractor when aggregated

with a PLN-5.35 plow were carried out. The results of these experimental studies are shown in Table 1.

**Table 1.** Torques ( $M_{kp}$ ) on the sun gears of the wheel gearboxes of the HTZ-17021 tractor with the PLN-5-35 plow (plowing winter wheat stubble to a depth of 25–27 cm).

$y, m$	$a, m$	$M_{kp}, Nm$			
		$M_{kp1}$	$M_{kp2}$	$M_{kp3}$	$M_{kp4}$
0.150	0.36	947	2222	875	2150

$y$ —the distance from the edge of the furrow to the outer edge of the wheel;  $a$ —asymmetry of traction load application;  $M_{kp1}, M_{kp2}, M_{kp3}, M_{kp4}$ —torques on the sun gears of the wheel gearboxes of the front left and right wheels, and the rear left and right wheels, respectively.

The analysis of this table shows that the front right wheel is the most loaded during plowing of the HTZ tractor, and the rear left wheel is the least loaded. Behind the sides of the tractor, the front wheels are 3–5% more loaded than the rear wheels. Let us take it for simplification that  $P_{K1}^n = P_{K3}^n$  and  $P_{K2}^n = P_{K4}^n$ . In this case, the load on the wheels of the right  $P_{II}^n$  and left  $P_{I}^n$  sides of the tractor, which is necessary to overcome the resistance of the plow, from the system of Equation (14), is written in the following form:

$$\left. \begin{aligned} P_{II}^n &= P_{II.I} \left( \frac{1}{2} + \frac{a}{b} \right), \\ P_{I}^n &= P_{II.I} \left( \frac{1}{2} - \frac{a}{b} \right) \end{aligned} \right\} \quad (15)$$

The asymmetrical connection of the plow, characterized by parameter  $a$ , leads to a greater load on the right side of the tractor compared to the left side. For a tractor of the HTZ type in plowing operations with a PLN-5-35 plow, this excess is 50–60%. In this case, to ensure stable rectilinear movement of the plow unit, it is necessary to fulfill the condition  $M_2 \approx 1.5M_1, \omega_1 \approx 1.5\omega_2$ .

For example, Figure 6 shows the universal characteristics of the traction efficiency of the HTZ-170 tractor when plowing winter wheat stubble with a PLN-5-35 plow to a depth of 25–27 cm (operating weight of the tractor 8.0 t, engine power 121.1 kW, speed 2.37 m/s).

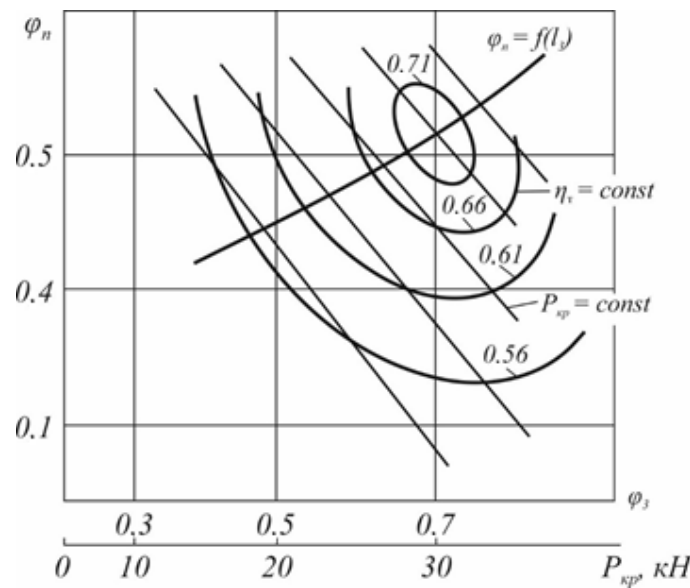


**Figure 6.** Universal characteristics of traction efficiency of the HTZ-170 tractor in plowing.

The universal characteristics show the traction range of the tractor in the form of a series of straight lines,  $P_{kp} = const$ , on which the graph of the function is plotted  $\varphi_{II} = f(\varphi_3)$  at  $\eta_{T max}$ . This is the optimal combination of coefficients of the use of the driving



axles' coupling weight, which leads to the operation of the tractor with maximum traction efficiency.

The analysis of the universal characteristics shows that  $\eta_{T \max} = 0.71$  of the KhTZ-17021 tractor during plowing will be in the case of blocked front and rear drive axles. All  $\eta_T$  points are located on the abscissa axis (because  $\varphi_{\Pi} = 0$ ). At the same time,  $\eta_T$  on the universal characteristics will be below  $\eta_{T \max}$ .

According to this characteristic, it is possible to estimate  $\eta_T$  when unlocking the differentials and simultaneously turning on the front and rear axles.

### 3. Discussion

The results of this research are mainly aimed at solving the scientific problem of increasing the efficiency of using the tractor hitch weight in traction mode by reducing the uneven distribution of vertical reactions between the wheels. New dependencies of the traction properties of the tractor on the use of its drawbar weight and a method of estimating the vertical reactions on the tractor's wheels from its drawbar weight are proposed. It was proven that the greatest efficiency of using the hitch weight of an all-wheel drive tractor in traction mode is achieved when its center of mass is located between the driving axles. At the same time, during plowing operations, the most energy-intensive technological process ensures its operation with maximum traction efficiency when the front and rear axle drivers are blocked.

Domestic and foreign scientists pay attention to the fact that the efficiency of tractors significantly depends on the position of its center of mass and the distribution of vertical reactions between the wheels. Domestic regulatory documents and methods of testing tractors according to the OECD Code 2 procedure in NTTL laboratories [2] in the United States of America and in Germany [3] do not provide for evaluating the efficiency of the tested tractors from the position of the center of its masses during the execution of the technological process. This is mainly a consequence of the lack of methods and instrumentation for evaluating the traction properties of the tractor during its unsteady movement.

The solution to this problem is possible using the method of partial accelerations [10], which is implemented at the standard L. Pogorilyy UkrNDIPVT, and the measuring and registration complex developed at the Kharkiv branch of L. Pogorilyy UkrNDIPVT, who has no analogues in the world. The presence of a solid underlying layer in the form of permafrost and the heavy precipitation typical of this period drastically reduce the load-bearing capacity of soils [16–20]. The increase in the tractor's weight under these conditions results in breaking of the upper layer of the soil down to permafrost, degradation of traction, and coupling properties and slippage, which, in turn, causes the increase in the man-made (technogenic) impact, and bad flotation even with small hook loads [21–24]. Numerous scientists worldwide have investigated this problem and proposed various solutions. One such study [2] examines the relationship between the load-carrying capacity and the speed of transport aggregate movement. The optimal ratio of these two factors helps to reduce the vertical load on the soil. The sustainable dead weight loading is also an efficient way to reduce the impact of the ground drive system on the soil when the tractor is in motion [25–28]. However, the dead weight loading increases metal consumption, fuel consumption, and the cost of the tractor. After analyzing both the foreign and domestic scientific literature, it was found that the established techniques used to enhance the traction and coupling properties of wheeled tractors [29,30] are not efficient when one needs to reduce the man-made (technogenic) impact of the ground drive system on the soil and simultaneously achieve sufficient traction properties of the machine-tractor units (MTA) or tractor-transport units (TTA). Therefore, the aim of this research is to determine new methods of improving the traction and coupling properties and reducing the anthropogenic (technogenic) impact on the arable soil of the drive system of a moving wheeled tractor, which are important components of increasing the productivity and efficiency of labor and mechanized work, as well as the rational use of natural resources and long-term conservation of soil horizons [11,31]. In their research, the authors of [16] determined that

the optimal way to achieve this goal is to rationally distribute the weight of the coupling to the tractor propellers. For non-wheel drive modifications, the weight is redistributed from the non-driving front wheels to the driving rear wheels, with the front wheels pre-loaded to provide longitudinal stability if necessary.

#### 4. Conclusions

Based on the results of this research, the methodology for evaluating the impact of the position of the tractor's center of mass on its traction properties is substantiated. The results of this research made it possible to form the main theoretical and scientific-practical conclusions:

1. The formulated methodology for evaluating the traction properties of a tractor with instability of the vertical reactions on its wheels. It was proven that when the tractor's center of mass is located in the longitudinal plane of symmetry, an uneven distribution of vertical reactions on the wheels of one axle of the tractor is possible.
2. The method of evaluating the vertical reactions on the wheels of the tractor, which is based on the measurement of the vertical reaction on one of the four wheels, is substantiated.
3. It was proven that tractors with the center of mass shifted to the front or rear axle have the greatest probability of equal distribution of the vertical reactions between the wheels of one axle, and tractors with the center of mass in the middle, between the axles, have the lowest probability.
4. It is theoretically substantiated and experimentally confirmed that when the tractor performs plowing work with an uneven distribution of the load on the sides, it is ensured that it works with maximum traction efficiency with the front and rear axles locked.
5. The issue of evaluating the influence of the tractor's center of mass on its traction properties when aggregated with mounted, trailed, and combined agricultural machines remains open. It is necessary to carry out theoretical and experimental research in this direction.

**Author Contributions:** Conceptualization, A.L., S.L. and S.K.; methodology, M.S. and T.L.; formal analysis, A.L., M.S., S.K., K.S. and T.L.; investigation, A.L., M.S., S.K., K.S. and T.L.; resources, A.L., S.L., M.S. and T.L.; writing—original draft preparation, A.L., M.S., S.K., K.S. and G.N.; writing—review and editing, K.S., K.L. and G.N.; visualization, K.S. and T.L.; supervision, K.L. and G.N.; project administration, K.S. and G.N.; funding acquisition, A.L., S.K. and K.S. All authors have read and agreed to the published version of the manuscript.

**Funding:** This research received no external funding.

**Institutional Review Board Statement:** Not applicable.

**Data Availability Statement:** Not applicable.

**Conflicts of Interest:** The authors declare no conflict of interest.

#### References

1. Guskov, V.V.; Velev, N.N.; Atamanov, Y.E.; Bocharov, N.F.; Ksenevich, I.P.; Solonsky, A.S. *Tractors: Theory: Manual for Students "Car & Tractor"*; Guskova, V.V., Ed.; Mashinostroenie: Moscow, Russia, 1988; 376p.
2. Nebraska Tractor Test Laboratory. Available online: <https://tractortestlab.unl.edu/test-page-nttl> (accessed on 16 April 2023).
3. DLG—Deutsche Landwirtschafts-Gesellschaft. Available online: <https://www.dlg.org/de/landwirtschaft/tests> (accessed on 16 April 2023).
4. Kalinin, E.; Shuliak, M.; Koliesnik, I. Optimization of machinery operation modes from the point of view of their dynamics. In Proceedings of the ICCPT 2019: Current Problems of Transport: Proceedings of the 1st International Scientific Conference, Ternopil, Ukraine, 28–29 May 2019; pp. 211–222.
5. Szwedziak, K.; Lusiak, T.; Grzywacz, Z.; Drozd, K. Numerical CFD Analysis of an Aerodynamic Head Cover of a Rotorcraft Motor. *Commun Sci. Lett. Univ. Zilina* **2018**, *20*, 42–47. [CrossRef]
6. Szwedziak, K.; Lusiak, T.; Bąbel, R.; Winiarski, P.; Podsedek, S.; Doležal, P.; Niedbała, G. Wind Tunnel Experiments on an Aircraft Model Fabricated Using a 3D Printing Technique. *J. Manuf. Mater. Process.* **2022**, *6*, 12. [CrossRef]

7. Lebedev, A.T.; Artjomov, N.P.; Grinenko, A.A. Traction efficiency of the tractor with uneven distribution of reactions between the wheels. In *Tractor Power Engineering in Crop Production*; Collection of Scientific Articles; KhNTUA: Kharkiv, Ukraine, 2003; pp. 49–56.
8. Fluck, R.C. Energy analysis for agricultural systems. In *Energy in Farm Production*; Elsevier: Amsterdam, The Netherlands, 2014; pp. 45–51.
9. Lebedev, S. The technical level of agricultural tractors on the market of Ukraine. *Tech. Technol. APK* **2014**, *11*, 8–12.
10. Lebedev, A.T.; Lebedev, S.A.; Korobko, A.I. *Qualimetry and Metrological of Tractors Testing*; Lebedev, A.T., Ed.; Miskdruk: Kharkiv, Ukraine, 2018; 394p.
11. Brouwer, F.M.; van Ittersum, M. (Eds.) *Environmental and Agricultural Modelling: Integrated Approaches for Policy Impact Assessment*; Springer: Dordrecht, The Netherlands, 2010; 322p.
12. Aleksandrov, E.E.; Volontsevych, D.O.; Karpenko, V.A.; Lebedev, A.T.; Peregon, V.A.; Samorodov, V.B.; Turenko, A.N. *Dynamics of Transport and Traction Wheeled and Tracked Vehicles*; KHNADU (KHADI): Kharkiv, Ukraine, 2001; 642p.
13. Maharjan, K.L.; Joshi, N.P. *Climate Change, Agriculture and Rural Livelihoods in Developing Countries*; Series: Advances in Asian Human-Environmental Research; Springer: Berlin/Heidelberg, Germany, 2013; 176p.
14. Hunt, D. *Farm Power and Machinery Management*; Wiley-Blackwell: Hoboken, NJ, USA, 2001; 368p.
15. Shuliak, M.; Klets, D.; Kalinin, Y.; Kholodov, A. Selecting a rational operation mode of mobile power unit using measuring and control complex. *CEUR Workshop Proc.* **2019**, *2387*, 141–151. Available online: <https://ceur-ws.org/Vol-2387/20190141.pdf> (accessed on 25 April 2023).
16. Kuznetsov, E.E. *The Use of the Multi-Axis Energy Devices of Class 1.4: Monograph*; FESAU: Blagoveschensk, Russia, 2013; 153p.
17. Kuznetsov, E.E.; Kuznetsova, O.A.; Polikutina, E.S. Energy consumption dependencies of an experimental machine-tractor aggregate equipped with a trailing weight distribution device. In Proceedings of the International Applied Research Conference, Samara, Russia, 11 April 2017; Current Issues in Science and Technology. pp. 26–29.
18. Kuznetsov, E.E.; Schitov, S.V. Hydro-Chain Regulating Device. Utility Model Patent No. 164794, 20 September 2016.
19. Kuznetsov, E.E.; Schitov, S.V.; Polikutina, E.S. Methodological Validation of the Design For Rational Trailing Weight Distribution Devices. *AgroEcoInfo*, no. 2. 2016. Available online: <http://agroecoinfo.narod.ru/iournal/STATYI/2016/2/st209.doc> (accessed on 25 April 2023).
20. Pentoś, K.; Mbah, J.T.; Pieczarka, K.; Niedbała, G.; Wojciechowski, T. Evaluation of Multiple Linear Regression and Machine Learning Approaches to Predict Soil Compaction and Shear Stress Based on Electrical Parameters. *Appl. Sci.* **2022**, *12*, 8791. [CrossRef]
21. Behnassi, M.; Syomiti Muteng'e, M.; Ramachandran, G.; Shelat, K.N. (Eds.) *Vulnerability of Agriculture, Water and Fisheries to Climate Change: Toward Sustainable Adaptation Strategies*; Springer: Dordrecht, The Netherlands, 2014; 336p.
22. Bulinski, J. Effect of Moisture Content in Soil on Its Compaction Caused by Multiple Running of Agricultural Vehicles. In *Annals of Warsaw University of Life Sciences*; Bulinski, J., Niemczyk, H., Eds.; SGGW: Warsaw, Poland, 2007; pp. 3–8.
23. Belyaev, V.I. Ecological Consequences of Conversion of Steppe to arable Land in Western Siberia. *Eur. Reg.* **2004**, *1*, 13–21.
24. Zakharov, N.S. Laws of change of quality of machines during use. In *Operation Efficiency Increase of Wheel and Track Machines under Severe Operating Conditions, Proceedings of the International Scientific and Technical Conference, Evanston, IL, USA, 25–27 July 1996*; Tyumen State Oil and Gas University: Tyumen, Russia, 1996; pp. 110–116.
25. Vorokhobin, A.V.; Vysotskaya, E.A.; Skuryatin, N.F. The reduction in the soil-packing impact caused by ground drive systems of the mobile energy devices. In *Modern Scientific and Practical Solutions for the 21st Century*; Materials of the International Applied Research Conference; OECD: Voronezh, Russia, 2016; pp. 15–19.
26. Selivanov, N.I. Improvement of Classification and Use of Energy-Packed Tractors. In *Krasnoyarsk State Agrarian University Bulletin*; Krasnoyarsk State Agrarian University: Krasnoyarsk Krai, Russia, 2016; Volume 4, pp. 113–119.
27. Selivanov, N.I.; Makeeva, Y.N. Dead Weight Loading of Wheeled Tractors during Soil Cultivation. In *Krasnoyarsk State Agrarian University Bulletin*; Krasnoyarsk State Agrarian University: Krasnoyarsk Krai, Russia, 2015; pp. 77–81.
28. Selivanov, N.I.; Makeeva, Y.N. Adaptation of wheeled tractors to soil cultivation technologies. *Mod. Issues Sci. Educ.* **2015**, 344.
29. Milan, J. *Advanced Transport Systems: Analysis, Modeling, and Evaluation of Performances*; Springer: Berlin/Heidelberg, Germany, 2014; 408p.
30. Mendes, A.; da Silva, E.L.S.; Santos, J.M.A. (Eds.) *Efficiency Measures in the Agricultural Sector: With Applications*; Springer Science & Business Media: Berlin/Heidelberg, Germany, 2012; 197p.
31. Lichtfouse, E. (Ed.) *Sustainable Agriculture Reviews*; Springer: Berlin/Heidelberg, Germany, 2015; Volume 15, p. 407.

**Disclaimer/Publisher's Note:** The statements, opinions and data contained in all publications are solely those of the individual author(s) and contributor(s) and not of MDPI and/or the editor(s). MDPI and/or the editor(s) disclaim responsibility for any injury to people or property resulting from any ideas, methods, instructions or products referred to in the content.

## Article

# Comparison of Consumed Power and Safety of Two Types of Semi-Automatic Vegetable Transplanter: Cam and Four-Bar Link

Sri Markunningsih<sup>1,2</sup>, Seok-Joon Hwang<sup>1,3</sup>, Jeong-Hun Kim<sup>1,3</sup>, Moon-Kyeong Jang<sup>1,3</sup>, Chang-Seop Shin<sup>4,\*</sup> and Ju-Seok Nam<sup>1,3,\*</sup>

<sup>1</sup> Department of Biosystems Engineering, Kangwon National University, 1 Kangwondaehak-gil, Chuncheon 24341, Republic of Korea

<sup>2</sup> Department of Agricultural and Biosystems Engineering, Faculty of Agricultural Technology, Universitas Gadjah Mada, Jl. Flora No. 1, Bulaksumur, Yogyakarta 55281, Indonesia

<sup>3</sup> Interdisciplinary Program in Smart Agriculture, Kangwon National University, 1 Kangwondaehak-gil, Chuncheon 24341, Republic of Korea

<sup>4</sup> Department of Biosystems Engineering, Chungbuk National University, Chungdae-ro 1, Cheongju 28644, Republic of Korea

\* Correspondence: shinchang7@cbnu.ac.kr (C.-S.S.); njsg1218@kangwon.ac.kr (J.-S.N.); Tel.: +82-43-261-2584 (C.-S.S.); +82-33-250-6497 (J.-S.N.)

**Abstract:** The consumed power and safety of cam and four-bar-link semi-automatic vegetable transplanters were analyzed and compared according to the engine speed and planting distances. A measurement system was constructed to obtain the torque, rotational speed, and strain at the corresponding locations of both transplanters. Field tests were conducted at three engine speeds and three planting distances for each type of transplanter. The torque and rotational speed data of the input shaft of the transplanting devices were used to calculate the power consumed during transplanting. The strain data were converted into stress values to calculate the static safety factor and fatigue life. The results show that the torque and consumed power of the cam transplanter were greater than those of the four-bar-link transplanter under similar operational conditions, owing to its rigid and heavier design. The consumed power increased as the engine speed increased for both types. The static safety factor and fatigue life exhibited different values depending on the measurement location with a sufficient safety margin. Although more skill is required in planting distance control owing to its manual adjustment, the four-bar-link type is more economical under similar operating conditions because of its smaller power requirement.

**Keywords:** cam type; consumed power; torque; vegetable transplanter; four-bar-link type

**Citation:** Markunningsih, S.; Hwang, S.-J.; Kim, J.-H.; Jang, M.-K.; Shin, C.-S.; Nam, J.-S. Comparison of Consumed Power and Safety of Two Types of Semi-Automatic Vegetable Transplanter: Cam and Four-Bar Link. *Agriculture* **2023**, *13*, 588. <https://doi.org/10.3390/agriculture13030588>

Academic Editor: Massimo Cecchini

Received: 10 February 2023

Revised: 23 February 2023

Accepted: 27 February 2023

Published: 28 February 2023



**Copyright:** © 2023 by the authors. Licensee MDPI, Basel, Switzerland. This article is an open access article distributed under the terms and conditions of the Creative Commons Attribution (CC BY) license (<https://creativecommons.org/licenses/by/4.0/>).

## 1. Introduction

A vegetable transplanter is an agricultural machine used to transplant vegetable seedlings from a nursery to a field [1,2]. There are two types of vegetable transplanters based on the seedling supply method: semi-automatic and fully automatic. For semi-automatic vegetable transplanters, the operator manually places the seedlings into the seedling cylinder. For fully automatic ones, the seedlings are automatically placed in the seedling cylinder using additional mechanical systems [3–5]. Fully automatic vegetable transplanters have high operational speeds with continuous operation, which saves labor. However, their working mechanism is more complicated and has special requirements, such as seedlings of a specific size and the use of special pot trays [6,7]. Although semi-automatic vegetable transplanters have limited speed, there are no restrictions on seedling size or pot tray type, and the working mechanism is more straightforward [8]. Both types are equally important, depending on the type of vegetable cultivation [9].

Vegetable transplanters are also classified based on the working mechanism of the transplanting device, which is an important component for planting seedlings in soil.

Four types of transplanting devices have been developed: wheel, rotary, four-bar-link, and cam types [10]. The most widely used are the cam and four-bar-link transplanters because of their relatively simple structures and ease of use [11]. The four-bar-link transplanting device uses four-bar-link mechanisms for planting seedlings, whereas the cam transplanter is characterized by a cam that opens and closes the hopper through contact with the bearing [10].

Several studies on both types of transplanting devices have been conducted, including analyses of working mechanisms and operational characteristics [12–14], modification of the transplanting device to improve performance through simulations [2,9], and safety analyses [11,15]. In contrast, research on the consumed power for both semi-automatic transplanting devices has yet to be conducted.

Research on the consumed power and load characteristics of agricultural machinery, such as tractors [16–22], potato harvesters [23], plows and rotavators [24–27], and other types of transplanters (including two-row riding fully automatic vegetable transplanters [28–30] and electric semi-automatic vegetable transplanters [31,32]), has been performed. Several studies on the consumed power and load characteristics of two-row riding fully automatic vegetable transplanters have been conducted, including one by Kim et al. [28], who measured the PTO (Power Take-Off) torque during field operation based on the planting distance. Kim et al. [29] analyzed the PTO shaft load with respect to the planting distance through load spectra and damage-level calculations. Then, Kim et al. [30] studied the PTO load spectrum under various working conditions, not only with various planting distances but also with different planting depths. Another type of vegetable transplanter studied for its power requirements is the electric semi-automatic vegetable transplanter. This machine is a modification of the conventional transplanting machine in which the power source, which was initially a conventional internal combustion engine, is changed into an electric motor. Lee et al. [31] measured the current to calculate and analyze the consumed power according to the planting distance and travel speed. Lim et al. [32] studied the power requirements of this machine based on the torque and rotational speed of the transplanting axle. Despite all the studies on the power consumed by various types of vegetable transplanters, none have been carried out for conventional semi-automatic cam- and four-bar-link transplanters. Therefore, comparative studies on the consumed power and safety of the two transplanting devices are needed for effective transplanting operations.

The purpose of this study was to analyze and compare the consumed power and safety of cam and four-bar-link semi-automatic vegetable transplanters according to engine speed and planting distance. The specific objectives were (1) to measure the torque, rotational speed, and strains on the corresponding spots of both transplanters, (2) to calculate the consumed power, static safety factor, and fatigue life from the measured data, and (3) to compare the torque and consumed power, static safety factor, and fatigue life for the two transplanters under similar operating conditions.

## 2. Materials and Methods

### 2.1. Test Equipment

Two types of vegetable transplanters were used in this study: cam and four-bar-link semi-automatic transplanters, which are mainly used on small farms. Figure 1 and Table 1 show the shapes and main specifications, respectively, of the cam semiautomatic vegetable transplanter. The shape and main specifications of the four-bar-link semi-automatic vegetable transplanter are shown in Figure 2 and Table 2, respectively. Both types of vegetable transplanters consist of engines, transmissions, control sections, wheels, seeding cylinders, transplanting devices, and molding wheels.

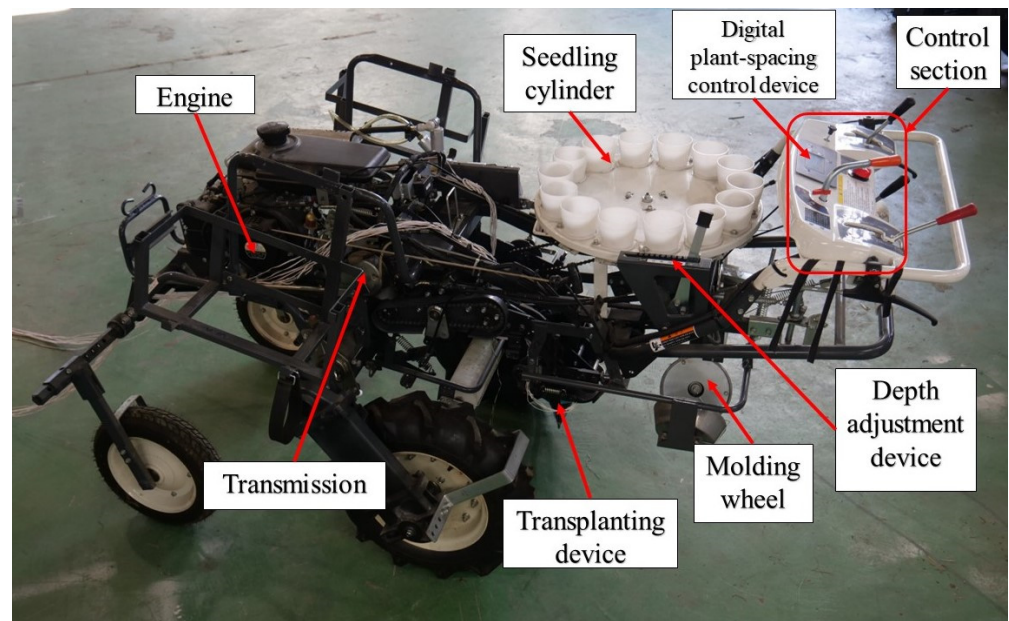


Figure 1. View of cam semi-automatic vegetable transplanter.

Table 1. Main specifications of the cam semi-automatic vegetable transplanter.

Items		Specification
Model		KP-100KR
Manufacturer, nation		KUBOTA, Japan
Length/width/height	mm	2150/1360/1130
Weight	kg	280
Engine	Rated power (kW)	2.6
	Rated speed (rpm)	1550
Wheel adjustment (inner/outer)	mm	750–1000/1100–1500
Planting distance	mm	350–900
Maximum working speed	m/s	0.57
Working efficiency	h/10a	1.5–2.5
Price	KRW	13,000,000

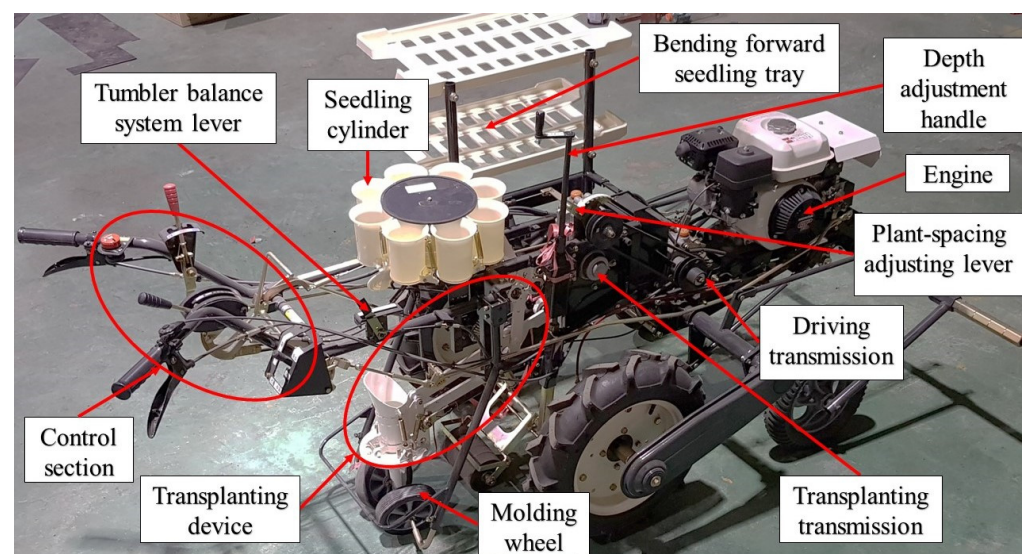


Figure 2. View of four-bar-link semi-automatic vegetable transplanter.



**Table 2.** Main specifications of the four-bar-link semi-automatic vegetable transplanter.

Items	Specification	
Model	KTP-30	
Length/width/height	mm	2125/1180/1510
Weight	kg	199
Engine	Rated power (kW)	3.4
	Rated speed (rpm)	1800
Wheel adjustment (inner/outer)	mm	360–750/1170–1550
Planting distance	mm	300–500
Maximum working speed	m/s	0.4
Working efficiency	h/10a	1.5–2.0
Price	KRW	4,900,000

The main difference between the two types is the design and working mechanism of the transplanting device. Figure 3 shows the transplanting device of cam and four-bar-link types. The four-bar-link type of transplanting device consists of several linkages and a transplanting hopper. In the cam type, the transplanting device consists of a frame, cam, bearing, crank, transplanting hopper, and some linkages. Additional differences exist in the transmission part and plant-spacing control device. The cam type has only one transmission to transmit the power from the engine to the wheel and transplanting device, while the four-bar-link type has (a) a driving transmission to transmit the engine power to the wheel and the planting unit and (b) a transplanting transmission to transmit the power received from the driving transmission to the crank of the four-bar-link mechanism of the transplanting device. The planting distance in the cam type is determined from the set value of the digital plant-spacing control device. The cam transplanter has a distance sensor that can measure the traveling distance of the transplanter. If the travel distance reaches the set planting distance in the digital plant-spacing control device, the transplanting device input shaft operates at a constant rotational speed so that it remains constant for various planting distances. In contrast, in the four-bar-link transplanter, the planting distance is determined by adjusting the number of shift stages of the transplanting transmission using a manual lever, which requires empirical skill to adjust the planting distance precisely. At a constant working speed, if the rotational speed of the input shaft of the transplanting device increases, the transplantation distance decreases.

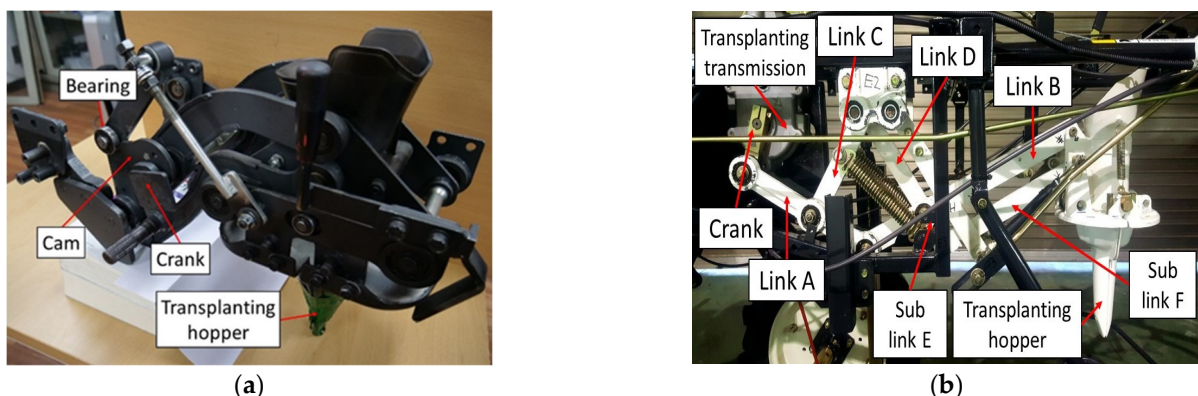


**Figure 3.** Shapes of the transplanting devices of the semi-automatic vegetable transplanter types: (a) cam and (b) four-bar link.

In general, the working mechanism of a semi-automatic vegetable transplanter is as follows. The operator starts the engine and sets the desired planting distance digitally in the control section (for the cam type) or manually using the lever (for the four-bar-link type). The transplanter moves forward, and the transplanting device moves up and down. The operator places the seedlings manually in the seedling cylinder. The seedling cylinder



is opened when the transplanting hopper of the transplanting device is in the top position to place the seedling into the hopper. Then, the transplanting device moves down, and the hopper is opened when it is in the bottom position to plant the seedling in the soil. The transplanting device moves up again, while the molding wheel covers both sides of the planted seedling with soil.

## 2.2. Work Conditions

Field tests were conducted by considering the primary operational conditions for vegetable transplanting. Semi-automatic vegetable transplanters usually work on ridges with soft tilled soil; therefore, the effect of soil strength can be ignored. The variables of the working conditions in this study were engine speed and planting distance. For the cam vegetable transplanter, the engine speeds were set to 1100, 1250, and 1550 rpm, and the planting distances were 0.35, 0.40, and 0.45 m; for the four-bar-link vegetable transplanter, the engine speeds were 1000, 1250, and 1500 rpm, and the planting distances were 0.35, 0.41, and 0.45 m. There are few differences in the engine speed and planting distance conditions between the cam and the four-bar-link types because fine adjustment is difficult. However, the difference is small and can be ignored when comparing the overall trend or tendency of consumed power and safety. The planting depth was set at 70 mm. The test was repeated three times for each working condition, and the data were analyzed using the average value. The experimental field was located in Sinbuk-eup, Chuncheon, Gangwon Province, in South Korea ( $37^{\circ}56'24.0''$  North and  $127^{\circ}46'59.1''$  East with an altitude of 111.00 m.a.s.l.). The field consisted of ridges with a width and height of 0.6 and 0.3 m, respectively.

## 2.3. Measurement and Analysis

The torque and rotational speed of the input shaft of the transplanting device were derived to investigate the power consumed by the transplanting work of each type of vegetable transplanter. In addition, the operational stress of the transplanting device was measured for the safety analysis. The measurement system consisted of a torque sensor, an RPM sensor, strain sensors, a data acquisition device (DAQ), and a laptop. Figure 4 shows the instrument setup for the measurement system of the cam vegetable transplanter, whereas the measurement system of the four-bar-link type is shown in Figure 5. The signal from the sensors was transmitted to the DAQ through a telemetry system, and the data were stored on a laptop. The sampling frequency was set to 100 Hz after preliminary testing.

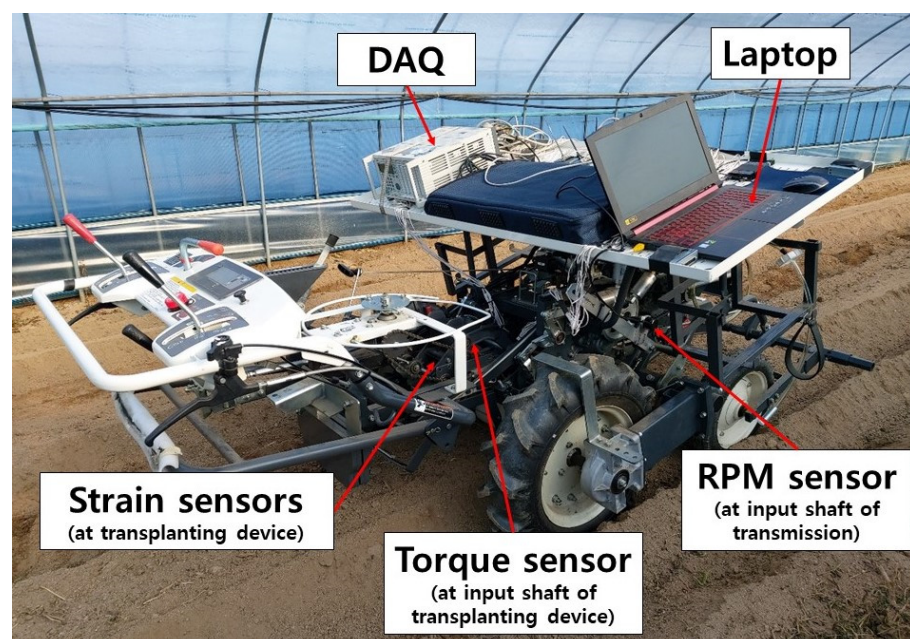


**Figure 4.** Measurement system for the cam vegetable transplanter.

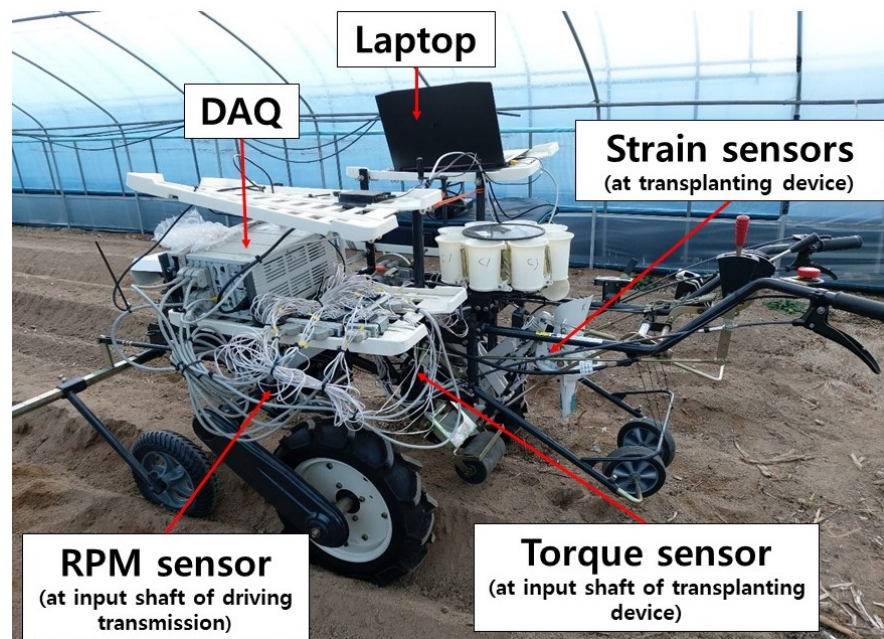


Figure 5. Measurement system for the four-bar-link vegetable transplanter.

Figures 6 and 7, respectively, show the locations of the torque sensor and rpm sensor for the cam and four-bar-link types. A torque sensor was installed at the input shaft of the transplanting device, and the rpm sensor was attached to the transmission input shaft. The rotational speed of the input shaft of the transplanting device was derived from the rotational speed of the transmission input shaft and the reduction gear ratio between the two shafts (Figure 8). The power consumed by the transplanting work was then calculated using Equation (1) [23].

$$P = \frac{2\pi \times T \times N}{60,000} \quad (1)$$

where  $P$  is the power consumed by the transplanting work (kW),  $T$  is the torque at the transplanting device input shaft (Nm), and  $N$  is the rotational speed of the transplanting device input shaft (rpm).

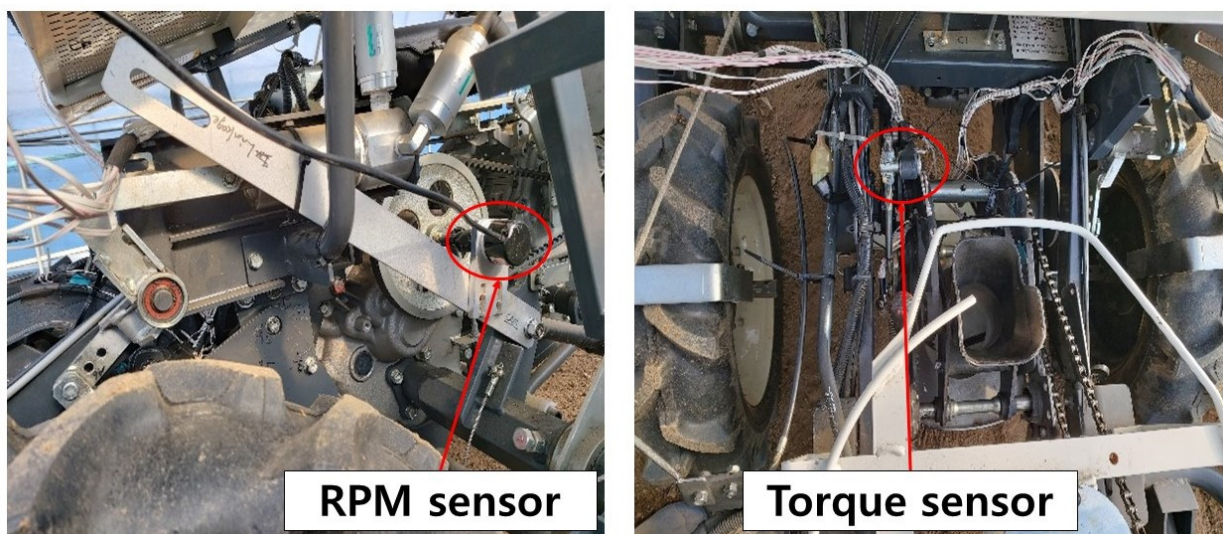


Figure 6. Location of torque and rpm sensors installed on cam vegetable transplanter.



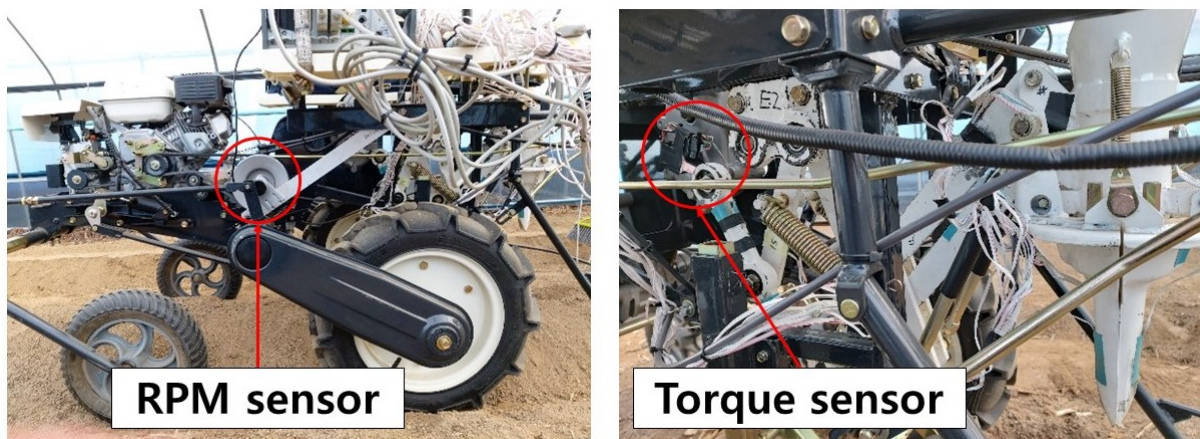
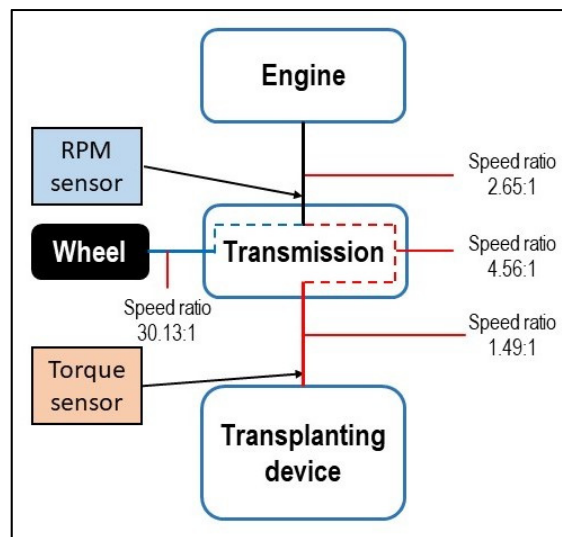
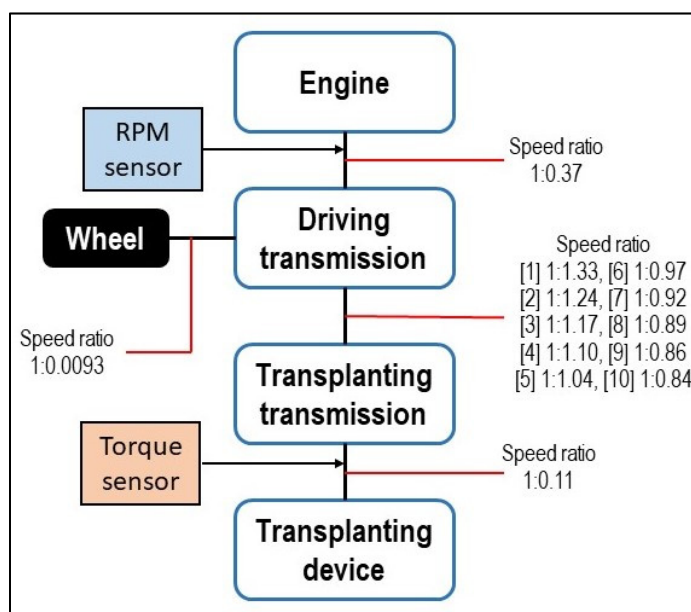


Figure 7. Location of torque and rpm sensor installed on four-bar-link vegetable transplanter.



(a)



(b)

Figure 8. Reduction gear ratio of the transmission system: (a) cam and (b) four-bar-link types.

The strain sensors comprised 15 strain gauges attached to the main loading paths of the transplanting device to measure the stress during transplanting. Two types of strain gauges were used: a uniaxial strain gauge (KFGS-5-350-C1-11 L10M3R, KYOWA) to measure one-directional strain in the main loading direction, such as at linkages, and a triaxial strain gauge or rosette (KFGS-1-350-D17-11 L5M3S, KYOWA) to measure the strain in three directions in the main loading direction, such as at the surface of the transplanting hopper. The detailed attachment locations of the strain gauges are shown in Figure 9 and Table 3.

The measured strain data were converted into stress data for the safety analysis. Two types of safety analysis were conducted: static safety and dynamic safety (or fatigue life). For the static safety analysis, the static safety factor was calculated using the yield strength of the transplanting device material and the maximum stress that occurred during operation—see Equation (2). As for the maximum stresses, the maximum normal stress was used for uniaxial strain gauges, while the maximum von Mises stress was used for triaxial strain gauges. If the static safety factor is greater than 1.0, the design is considered statically safe. If the static safety factor is less than 1.0, this implies that the design is unsafe or that the part may fail.

$$SF = \frac{S_y}{\sigma_{max}} \quad (2)$$

where  $SF$  is the static safety factor,  $S_y$  is the yield strength of the transplanting device material (Pa), and  $\sigma_{max}$  is the maximum operational stress (Pa).

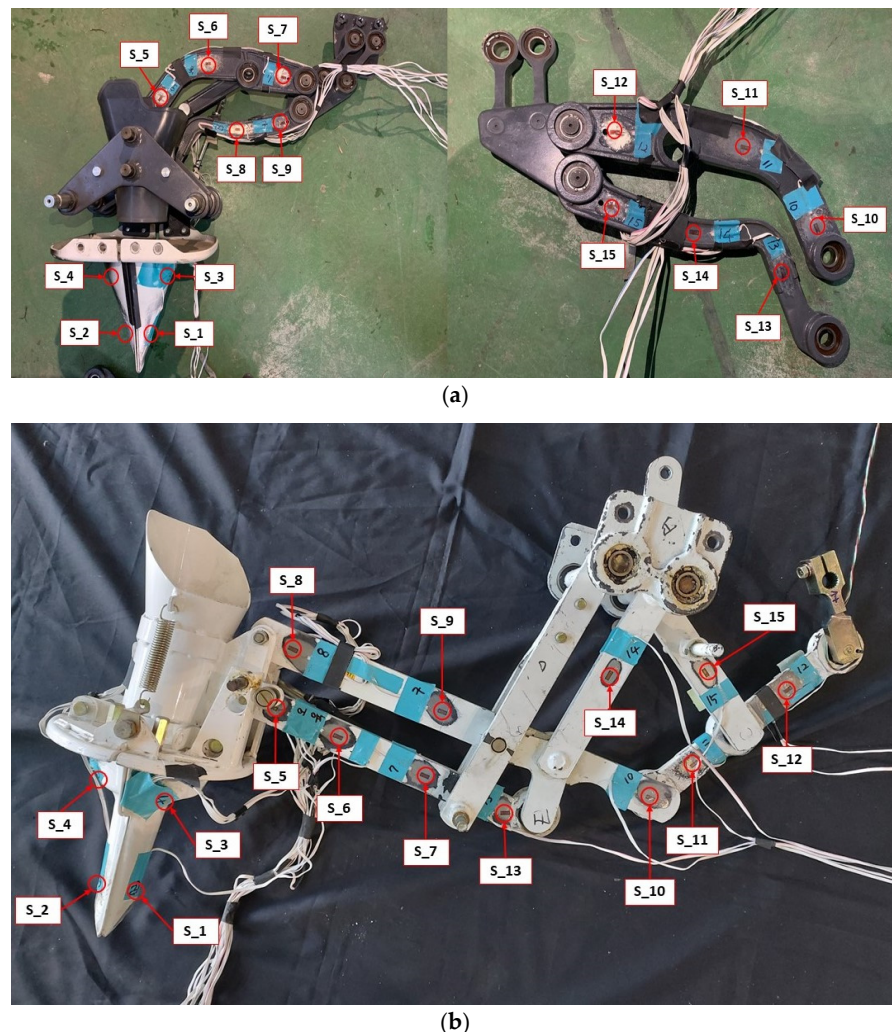


**Figure 9.** Location of the strain gauge on the transplanting device: (a) cam and (b) four-bar-link types.

**Table 3.** Detailed description of strain measurement location.

Strain Gauge Number	Locations	
	Cam Type	Four-Bar-Link Type
S_1	front lower side of transplanting hopper	front lower side of transplanting hopper
S_2	back lower side of transplanting hopper	back lower side of transplanting hopper
S_3	front upper side of transplanting hopper	front upper side of transplanting hopper
S_4	back upper side of transplanting hopper	back upper side of transplanting hopper
S_5	left side of left upper link	left side of sublink F
S_6	middle side of left upper link	middle side of sublink F
S_7	right side of left upper link	right side of sublink F
S_8	middle side of left bottom link	left side of link B
S_9	right side of left bottom link	right side of link B
S_10	right side of right upper link	right side of link B
S_11	middle side of right upper link	left side of link A
S_12	left side of right upper link	right side of link A
S_13	right side of right bottom link	right side of sublink F
S_14	middle side of right bottom link	middle side of link D
S_15	left side of right bottom link	middle side of link C

Fatigue life analysis is also required because the transplanting device is subjected to repeated cyclic loads when the vegetable transplanter is working. Figure 10 shows the fatigue life analysis procedure.

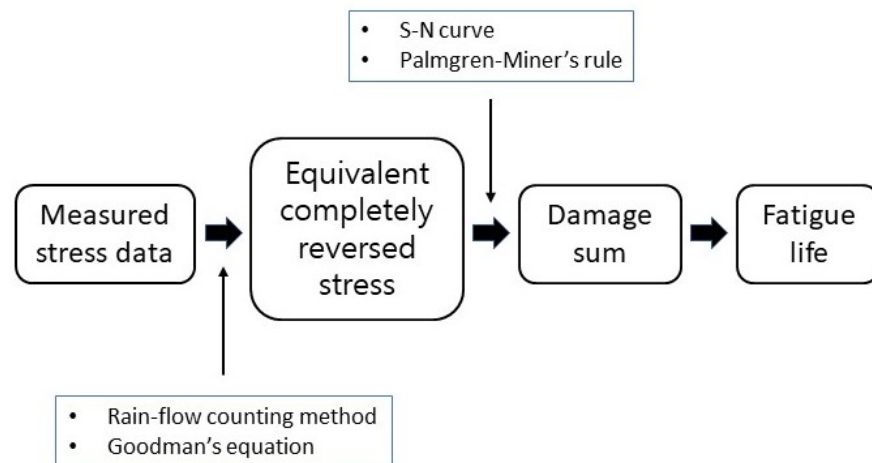


**Figure 10.** Fatigue life calculation procedure.

The measured stress was converted into equivalent, completely reversed stresses and their corresponding loading cycles by applying the rain-flow counting method and Goodman’s equation [33,34]. The rain-flow counting method is used to obtain the loading cycles for each mean stress and stress amplitude from time-series stress data. Then mean stress and amplitude were used to derive the equivalent completely reversed stress using Goodman’s equation—see Equation (3). The actual applied loading cycle ( $n_i$ ) can be derived from the rain-flow counting. The life cycles ( $N_i$ ) were determined from the S–N curve using the equivalent completely reversed stresses [35]. The ratio between the actual applied loading cycles and the life cycles is called “partial damage”. The damage sum was calculated by summing the partial damages from all stresses that occurred during the operation using the Palmgren–Miner rule—see Equation (4) [36]. Fatigue failure occurs when the damage sum reaches 1.0 [37]. The damage sum and working time were used to calculate the fatigue life of the transplanting device, as shown in Equation (5). The 25.5 h of average annual usage time of vegetable transplanters was considered to determine the fatigue life in years [11].



$$\sigma_{eq} = \frac{S_u \sigma_a}{S_u - \sigma_m} \tag{3}$$

$$D = \sum_i \frac{n_i}{N_i} \tag{4}$$

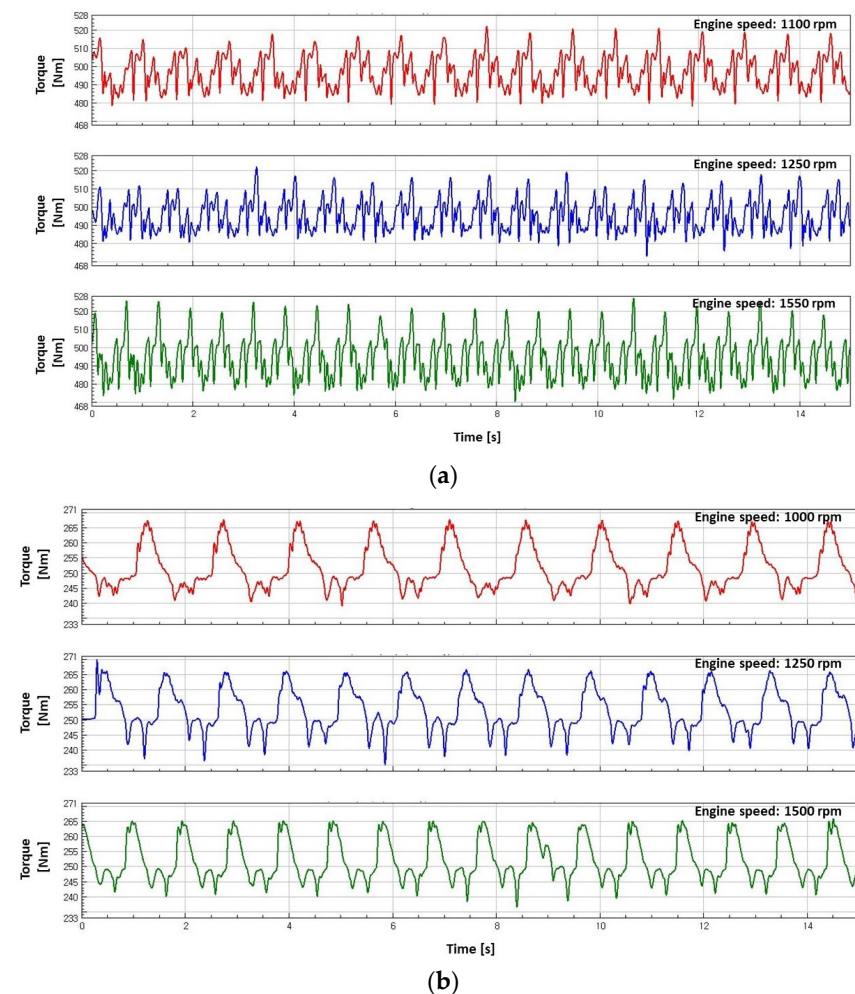
$$L_f = \frac{1}{D} \times t \tag{5}$$

where  $\sigma_{eq}$  is the equivalent completely reversed stress (Pa),  $S_u$  is the ultimate strength (Pa),  $\sigma_a$  is the stress amplitude (Pa),  $\sigma_m$  is the mean stress (Pa),  $D$  is the cumulative damage sum,  $n_i$  is the number of applied loading cycles for the equivalent completely reversed stress  $i$  (cycles),  $N_i$  is the life cycles for the equivalent completely reversed stress  $i$  (cycles),  $L_f$  is the fatigue life (s), and  $t$  is the working time that generates the cumulative damage sum (s).

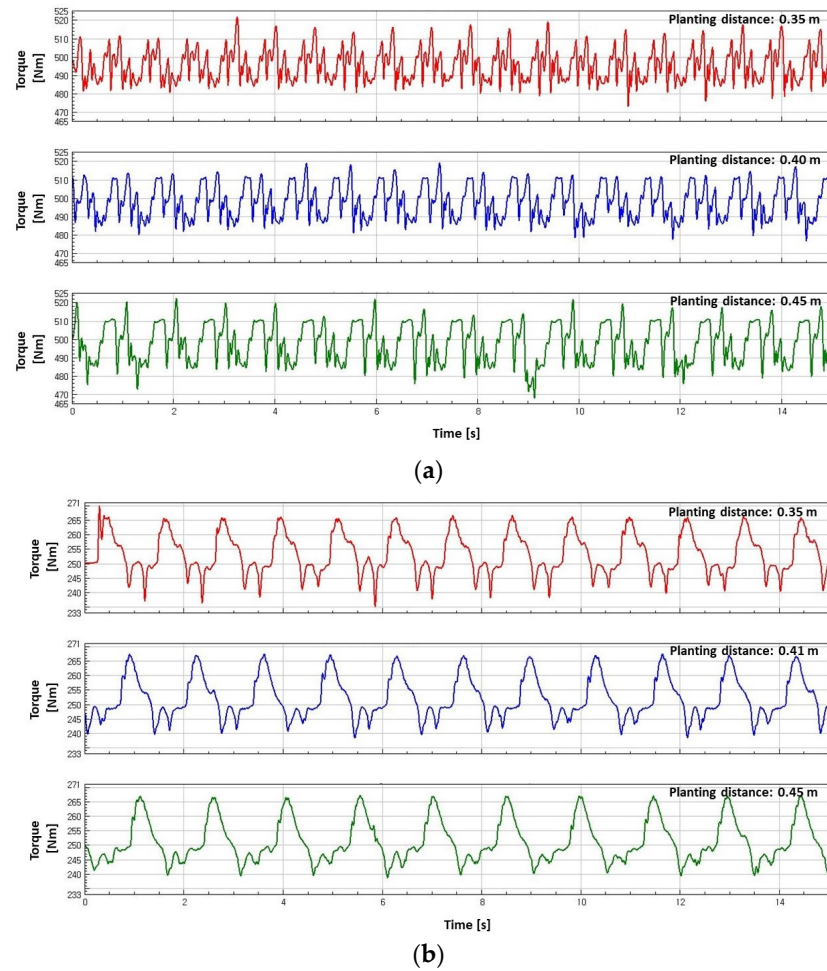
### 3. Results

#### 3.1. Torque and Consumed Power

Figure 11 shows the time series torque data on the transplanting device input shaft according to the three engine speed conditions at a planting distance of 0.35 m, while Figure 12 shows the torque data according to the three planting distances at an engine speed of 1250 rpm. The shape and magnitude of the operational torque between the cam and the four-bar-link types are different because they have different designs and movement mechanisms. However, both have similarities in a regular fluctuation pattern because of the repeated up and down motions of the transplanting device.

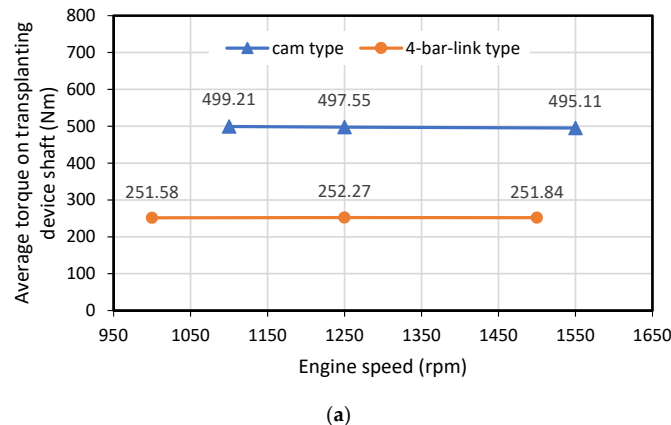


**Figure 11.** Measured torque of transplanting device input shaft at a planting distance of 0.35 m: (a) cam and (b) four-bar-link types.



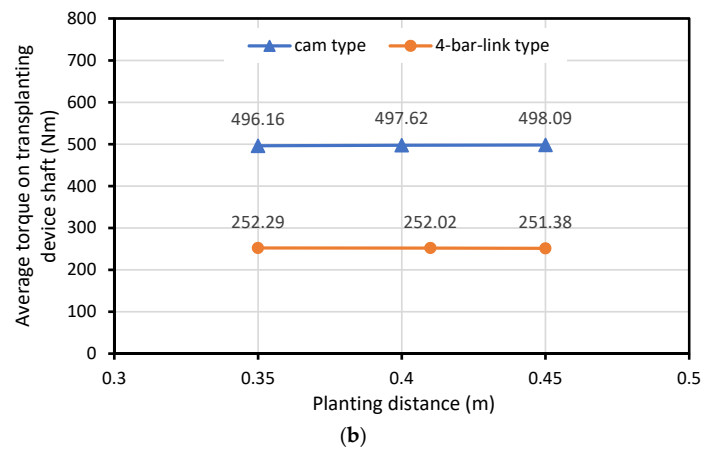
**Figure 12.** Measured torque of the transplanting device input shaft at an engine speed of 1250 rpm: (a) cam and (b) four-bar-link types.

Table 4 lists the average torque, rotational speed, and consumed power of the transplanting device input shaft of the two vegetable transplanters under different working conditions. Figure 13 shows a comparison of the average torque on the input shaft of the transplanting device. The cam type had a greater torque than the four-bar-link type under similar operating conditions. For the same type, the average torque showed no significant differences according to the engine speed and planting distance because the transplanting work was conducted under uniformly soft soil conditions.



**Figure 13.** Cont.





**Figure 13.** Comparison of torque on the transplanting device input shaft between cam and four-bar-link types according to working conditions: (a) engine speed and (b) planting distance.

**Table 4.** Torque, rotational speed, and consumed power of the transplanting device input shaft under different working conditions.

Type of Vegetable Transplanter	Engine Speed (rpm)	Planting Distance (m)	Torque of Transplanting Device Input Shaft (Nm)	Rotational Speed of Transplanting Device Input Shaft (rpm)	Consumed Power of the Transplanting Device Input Shaft (kW)
Cam	1100	0.35	497.55	66.3	3.45
		0.4	499.94	67.15	3.4
		0.45	500.15	63.44	3.32
	1250	0.35	496.1	73.64	3.83
		0.4	497.94	73.61	3.84
		0.45	498.61	73.56	3.84
	1550	0.35	494.83	89.94	4.66
		0.4	494.98	90.04	4.67
		0.45	495.51	90.23	4.68
Four-bar-link type	1000	0.35	251.66	41.24	1.09
		0.41	251.72	36.29	0.96
		0.45	251.36	31.83	0.84
	1250	0.35	253.2	50.78	1.35
		0.41	252.19	44.4	1.17
		0.45	251.41	42.38	1.12
	1500	0.35	252.01	63.02	1.66
		0.41	252.14	51.92	1.37
		0.45	251.37	48.01	1.26

Figure 14 shows a comparison of the consumed power of the transplanting device inputs for the two types. The consumed power based on engine speed is shown in Figure 14a, obtained from the average consumed power for three variations in planting distance. The consumed power according to the planting distance shown in Figure 14b is obtained from the average consumed power for three variations in engine speed. The consumed power of the cam type is almost three times greater than that of the four-bar-link type. The higher torque and consumed power of the cam type result from the rigid and heavier design of the transplanting device when compared to the four-bar-link type. The total weight of the

cam type, including the transplanting device, is more than 1.4 times greater than that of the four-bar-link type, as shown in Tables 1 and 2.

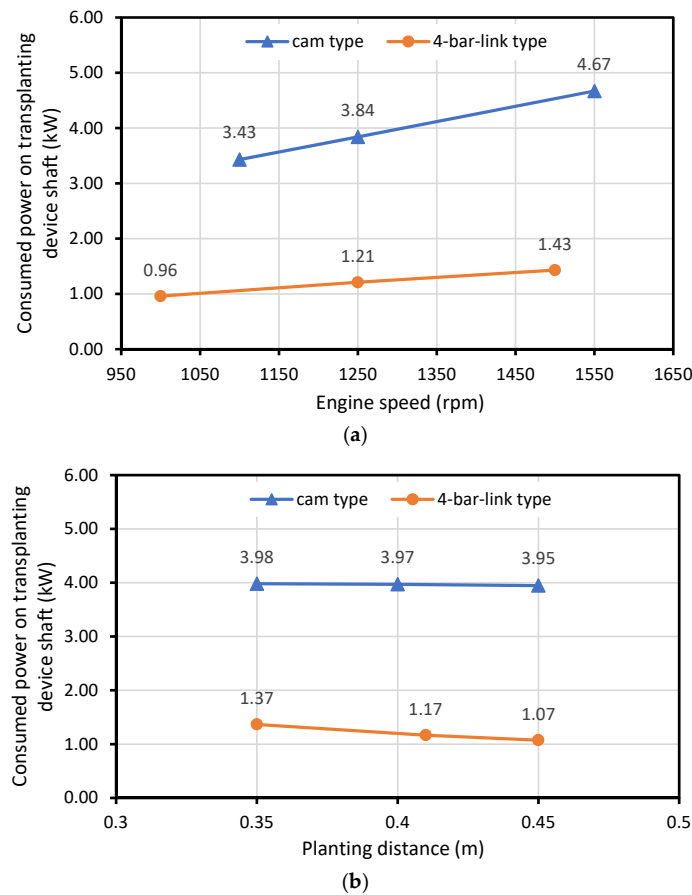


**Figure 14.** Comparison of consumed powers on transplanting device input shafts between cam and four-bar-link types according to working conditions: (a) engine speed and (b) planting distance.

The consumed power for both types showed a tendency to increase when the engine speed increased and planting distance decreased. The engine speed is directly proportional to the rotational speed of the input shaft of the transplanting device. The higher the engine speed, the higher the rotational speed of the transplanting device input shaft; thus, the consumed power also increases—see Figure 14a.

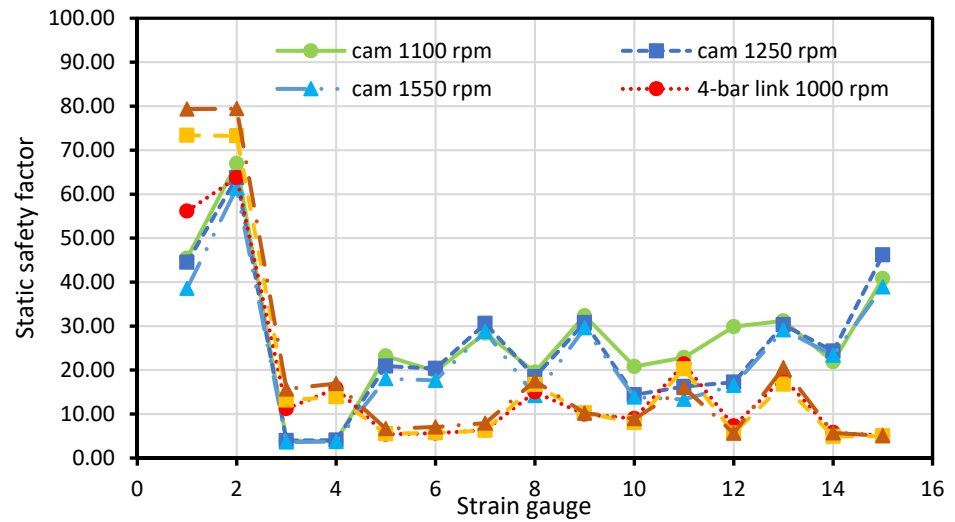
When the machine operates at the same engine speed, the difference in planting distance causes the period of one transplanting cycle to be different. The shorter the planting distance, the faster the period, and the higher the frequency. The mechanism for determining the planting distance of the cam transplanter uses a digital plant-spacing controller, which makes the rotational speed of the transplanting device input shaft constant for various planting distances. The torque of the shaft is similar according to the planting distance (Figure 13b). Therefore, the consumed power for cam transplanters based on planting distance showed no significant differences. However, the four-bar-link type determines the planting distance by adjusting the stages of the transplanting transmission, which makes the rotational speed of the input shaft of the transplanting device different for each planting distance. When the planting distance increases, the rotational speed decreases but the torque remains constant (Figure 13b); thus, the consumed power decreases—see Figure 14b.

### 3.2. Static Safety Factor

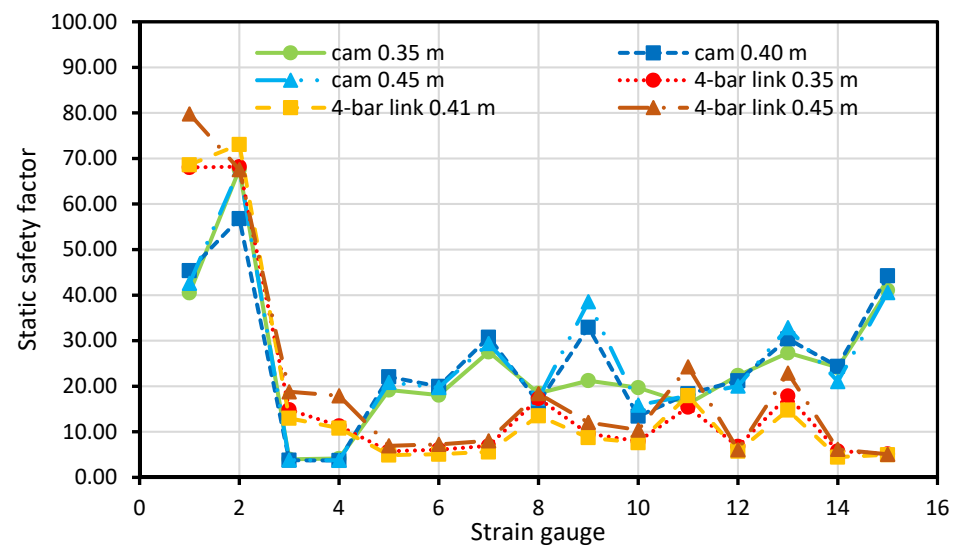
The static safety factors for each strain measurement spot in the transplanting devices are listed in Table 5. The results show that the static safety factor is greater than 1.0 for all

locations and working conditions. This indicates that both types of vegetable transplanters are designed to be safe for static loads. The minimum static safety factor for the cam type was 3.35 at location S\_4 at an engine speed of 1550 rpm and a planting distance of 0.35 m. For the four-bar-link type, it was 4.05 at location S\_14 under an engine speed of 1500 rpm and a planting distance of 0.41 m. Location S\_4 of the cam type, on the upper side of the hopper, has the minimum static safety factor because it receives a high reaction force when the hopper hits the soil and is subjected to a significant peak load. Location S\_14 (link D) of the four-bar-link type is on the linkage connected to the body-fixing frame; therefore, it receives high reaction forces when the transplanting device is operated. In the four-bar-link type, the linkages are relatively thin and flexible compared with the cam type. Therefore, the location of the minimum static safety factor is one of the linkages of the four-bar-link type.

Figure 15 shows the tendency of static safety factor for both types. The four-bar-link type has a smaller static safety factor for many parts than the cam type. This is because of the thin and flexible linkage structure of the four-bar-link type.



(a)



(b)

**Figure 15.** Comparison of static safety factor between cam and four-bar-link types on every strain gauge location in the transplanting device according to working conditions: (a) engine speed and (b) planting distance.

**Table 5.** Static safety factor on every spot of strain gauge in cam and four-bar-link types of vegetable transplanters under each working condition.

Type of Vegetable Transplanter	Engine Speed (rpm)	Planting Distance (m)	S_1	S_2	S_3	S_4	S_5	S_6	S_7	S_8	S_9	S_10	S_11	S_12	S_13	S_14	S_15
Cam Type	1100	0.35	39.21	73.85	4.41	4.18	23.25	20.07	28.3	22.29	20.84	20	19.51	28.29	28.22	20.43	38.96
		0.4	49.14	67.18	3.79	3.78	22.53	19.55	30.24	17.79	34.83	18.69	23.14	34.89	30.58	26.24	43.23
		0.45	47.99	59.81	3.84	3.37	23.81	19.7	26.58	18.54	41.35	23.74	25.88	26.44	34.74	18.96	40.26
	1250	0.35	45.94	68.86	3.83	4.89	17.69	17.24	26.08	17.47	15.79	21.02	14.07	18.46	27	30.45	47.71
		0.4	45.77	55.69	3.91	3.73	23.83	22.77	34.03	17.78	31.16	9.85	18.13	14.36	32.78	24.12	50.16
		0.45	41.75	66.64	4.08	3.6	21.15	21.03	31.62	20.12	45.41	12.16	16.56	18.85	31.09	18.31	40.62
	1550	0.35	36.31	60.12	3.7	3.35	16.62	16.87	28.26	15.66	27.09	18.04	14.86	20.33	26.79	21.51	36.53
		0.4	41.21	47.58	3.59	3.61	19.89	17.6	27.99	13.51	32.8	11.74	13.78	14.37	27.87	22.74	39.35
		0.45	38.12	76.39	3.52	4.28	17.56	18.44	30.02	13.32	28.9	11.74	11.36	14.82	32.75	25.83	40.83
Four-Bar-Link Type	1000	0.35	61.42	72.83	8.12	15.52	5.03	5.33	6.09	15.66	8.61	8.49	19.12	8.81	18.67	6.55	5.23
		0.41	60.7	62.83	8.28	13.65	4.41	4.67	5.26	10.83	7.54	8.17	16.97	6.79	13.98	4.29	4.95
		0.45	46.29	55.6	17.23	18.25	6.73	6.95	7.67	18.54	13.7	10.29	28.01	6.28	21.95	6.54	5.11
	1250	0.35	60.46	62.32	9.58	10.38	4.43	4.67	5.15	15.82	8.41	6.4	15.19	5.53	12.32	4.47	5.05
		0.41	88.82	67.85	14.3	14.82	5.67	5.83	6.33	16.78	10.27	8.2	22.91	5.56	17.58	5.02	5.02
		0.45	70.81	89.57	15.55	16.44	6.48	6.68	7.35	17.41	12.06	9.49	22.61	5.88	20.43	5.24	5.04
	1500	0.35	82.72	68.91	16.21	18.62	7.78	8.26	9.5	20.46	11.75	8.97	11.88	6.03	22.58	6.36	5.19
		0.41	69.72	75.16	9.89	10.46	4.63	4.76	5.17	12.94	8.37	6.42	13.94	4.89	12.72	4.05	4.95
		0.45	85.58	94.2	20.95	21.66	7.61	8.13	9.12	19.21	10.45	11.38	22.18	6	26.31	6.68	5.02

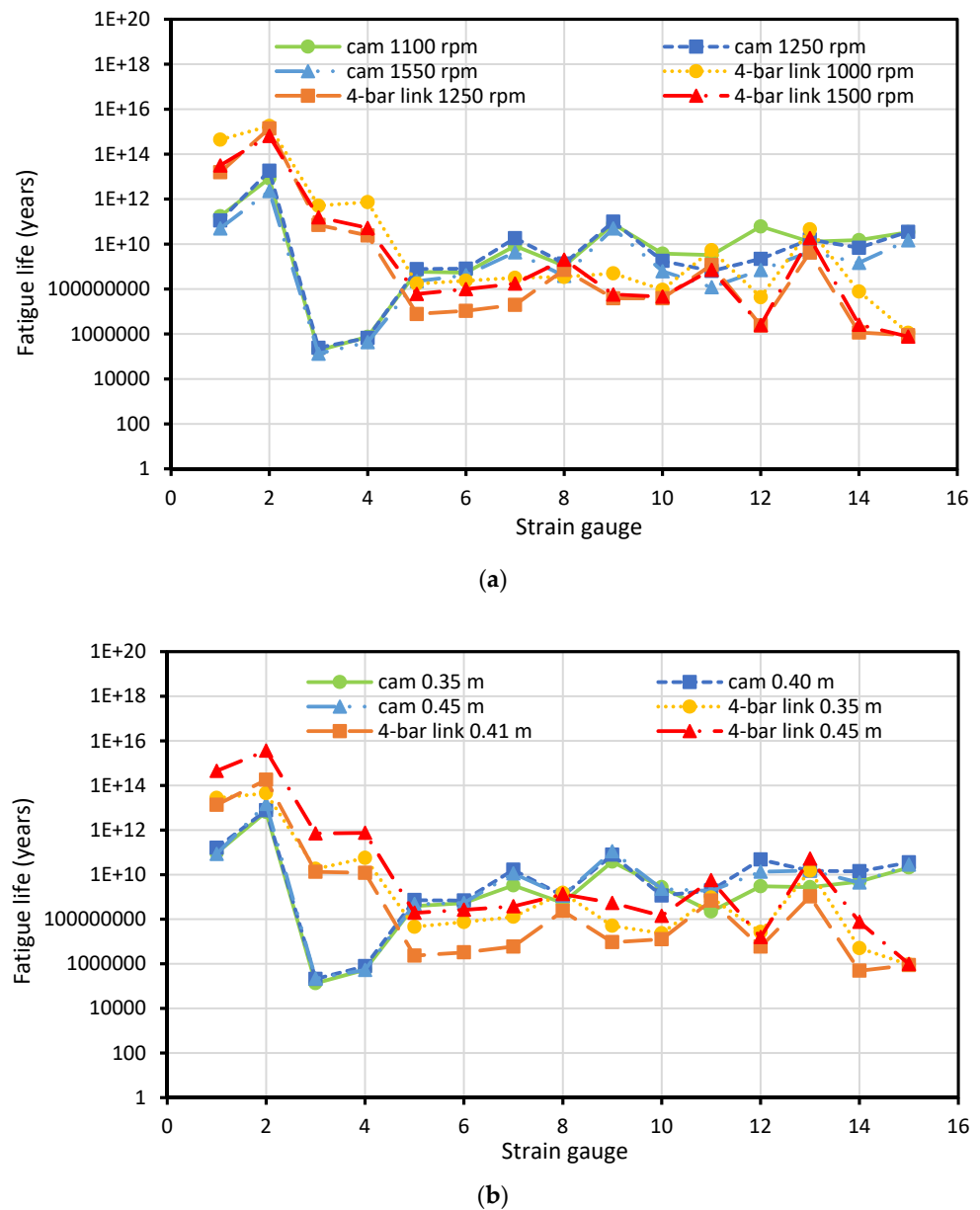
### 3.3. Fatigue Life

Table 6 lists the fatigue life data for every strain measurement point on the transplanting devices. The minimum fatigue life for the cam type was 95,603 years at location S\_3 at an engine speed of 1550 rpm and a planting distance of 0.35 m. However, the minimum fatigue life for the four-bar-link type was 196,000 years at location S\_14 under an engine speed of 1500 rpm and a planting distance of 0.41 m. Location S\_3 on the cam type is on the upper side of the hopper and receives a large load when hitting the ground, so that these parts have the minimum fatigue life. However, the maximum stress value on S\_3 is slightly lower than that at location S\_4; therefore, there are differences in locations that have the minimum static safety factor and minimum fatigue life on the cam type. For the four-bar-link type, the minimum static safety factor and fatigue life occur at the same location (S\_14).

Figure 16 shows the fatigue life tendency for both types. The cam type has more parts with a longer fatigue life than the four-bar-link type. However, for the transplanting device, the four-bar-link type exhibited a longer fatigue life. This is because the many linkages in the four-bar-link transplanting device can distribute the cyclic transplanting load more efficiently from the hopper to the linkages.

**Table 6.** Fatigue life (years) on every spot of strain gauge in cam and four-bar-link types of vegetable transplanters under each working condition.

Type of Vegetable Transplanter	Engine Speed (rpm)	Planting Distance (m)	S_1	S_2	S_3	S_4	S_5	S_6	S_7	S_8	S_9	S_10	S_11	S_12	S_13	S_14	S_15		
Cam Type	1100	0.35	1.60E+11	1.10E+13	1.63E+05	4.52E+05	8.00E+08	4.00E+08	2.00E+09	7.00E+08	5.80E+10	3.00E+09	4.00E+08	4.00E+09	5.00E+09	2.00E+09	7.90E+09	1.70E+10	
		0.4	2.30E+11	7.70E+12	2.28E+05	1.00E+06	5.00E+08	6.00E+08	1.00E+10	1.00E+10	1.00E+09	8.10E+10	3.00E+09	4.00E+09	1.00E+11	1.30E+10	3.00E+10	5.30E+10	
		0.45	1.30E+11	6.30E+12	1.66E+05	3.87E+05	5.00E+08	6.00E+08	9.00E+09	1.00E+09	1.00E+09	9.40E+10	6.00E+09	5.00E+09	4.00E+10	2.30E+10	7.00E+09	3.10E+10	
	1250	0.35	7.70E+10	6.50E+12	1.48E+05	8.69E+05	2.00E+08	2.00E+08	5.00E+08	4.00E+09	6.00E+08	5.70E+09	5.00E+09	2.00E+08	3.00E+09	4.60E+09	5.40E+09	3.40E+10	
		0.4	1.90E+11	1.30E+13	3.03E+05	4.41E+05	1.00E+09	1.00E+09	1.00E+09	3.00E+10	2.00E+09	1.10E+11	1.00E+08	1.00E+09	1.00E+09	2.60E+10	1.10E+10	3.70E+10	
		0.45	6.90E+10	3.50E+13	2.79E+05	7.00E+05	8.00E+08	8.00E+08	8.00E+08	2.00E+10	2.00E+09	1.80E+11	6.00E+08	5.00E+08	3.00E+09	1.70E+10	4.10E+09	3.40E+10	
	1550	0.35	4.30E+10	1.90E+12	9.56E+04	3.10E+05	2.00E+08	7.00E+08	7.00E+08	4.00E+09	3.00E+08	5.00E+10	1.00E+09	1.00E+08	1.00E+09	1.60E+09	1.30E+09	1.10E+10	
		0.4	5.30E+10	2.10E+12	9.72E+04	4.80E+05	4.00E+08	4.00E+08	3.00E+08	4.00E+09	4.00E+08	4.00E+10	4.00E+08	2.00E+08	4.00E+08	5.60E+09	1.10E+09	1.50E+10	
		0.45	5.40E+10	2.90E+12	2.08E+05	5.08E+05	1.00E+08	3.00E+08	3.00E+08	5.00E+09	5.00E+08	5.80E+10	4.00E+08	4.00E+07	3.00E+08	6.20E+09	2.00E+09	1.80E+10	
	Four-Bar-Link Type	1000	0.35	3.60E+13	1.30E+14	2.00E+09	9.00E+10	1.00E+07	2.00E+07	5.00E+07	9.00E+08	4.00E+07	4.00E+07	2.00E+09	8.00E+07	1.30E+10	1.30E+07	1.25E+06	
			0.41	4.20E+12	1.50E+13	1.00E+09	1.00E+10	1.00E+06	2.00E+06	4.00E+06	4.00E+06	1.00E+08	5.49E+06	1.00E+07	8.00E+08	1.00E+07	7.70E+08	6.22E+05	9.89E+05
			0.45	1.30E+15	5.20E+15	2.00E+12	2.00E+12	5.00E+08	7.00E+08	7.00E+08	9.00E+08	1.00E+07	1.50E+09	2.00E+08	1.00E+10	4.00E+07	1.20E+11	2.20E+08	1.13E+06
		1250	0.35	5.90E+12	3.50E+12	5.00E+09	4.00E+09	7.79E+05	1.00E+06	1.00E+06	2.00E+06	2.00E+08	5.49E+06	7.00E+06	2.00E+08	1.00E+06	2.30E+08	3.05E+05	7.83E+05
			0.41	3.20E+13	5.20E+14	3.00E+10	2.00E+10	5.00E+06	6.00E+06	6.00E+06	1.00E+07	5.00E+08	1.80E+07	2.00E+07	2.00E+09	1.00E+09	2.00E+06	6.48E+05	9.36E+05
			0.45	9.40E+12	3.70E+15	2.00E+11	5.00E+10	2.00E+07	2.00E+07	2.00E+07	5.00E+07	1.00E+09	9.30E+07	9.00E+07	2.00E+09	4.00E+06	1.00E+10	2.54E+06	9.29E+05
1500		0.35	4.00E+13	4.00E+12	5.00E+10	8.00E+10	1.00E+08	2.00E+08	2.00E+08	3.00E+08	3.00E+09	1.10E+08	2.00E+07	2.00E+08	2.00E+06	3.20E+10	1.74E+06	7.17E+05	
		0.41	4.50E+12	3.70E+12	9.00E+09	3.00E+09	1.00E+06	1.00E+06	1.00E+06	3.00E+06	1.00E+08	4.51E+06	7.00E+06	2.00E+08	1.00E+06	2.60E+08	1.96E+05	6.85E+05	
		0.45	5.00E+13	1.90E+15	4.00E+11	8.00E+10	6.00E+07	9.00E+07	9.00E+07	2.00E+08	3.00E+09	6.20E+07	1.00E+08	2.00E+09	4.00E+06	2.30E+10	5.88E+06	8.97E+05	



**Figure 16.** Comparison of fatigue life between cam and four-bar-link types on every strain gauge location on the transplanting device according to working conditions: (a) engine speed and (b) planting distance.

#### 4. Conclusions

The torque, rotational speed, and strain were measured for cam and four-bar-link semi-automatic transplanting devices. The field test was conducted under various working conditions. The cam type has three engine speeds (1100, 1250, and 1550 rpm) and three planting distances (0.35, 0.40, and 0.45 m). The four-bar-link type has three engine speeds (1000, 1250, and 1500 rpm) and three planting distances (0.35, 0.41, and 0.45 m). The measured data were used to calculate and analyze the consumed power, static safety factor, and fatigue life of both types of transplanting devices.

The main results of this research are as follows:

1. Under similar operating conditions, the cam type had a greater torque and consumed more power than the four-bar-link type owing to its rigid and heavier design. The range of the consumed power on the transplanting device input shaft of the cam type was 3.32–4.68 kW, while it was 0.84–1.66 kW for the four-bar-link type. The

- consumed power on the transplanting device input shaft increased when the engine speed increased and the planting distance decreased for both types.
2. The static safety factor was greater than 1.0 for both types at all measurement locations and under all working conditions. The minimum static safety factor for the cam type was 3.35 on the upper side of the transplanting hopper (S\_4) at an engine speed of 1550 rpm and a planting distance of 0.35 m. For the four-bar-link type, the minimum static safety factor was 4.05 at one of the linkages (link D) at an engine speed of 1500 rpm and a planting distance of 0.41 m.
  3. The minimum fatigue life for the cam type was 95,603 years at the upper side of the transplanting hopper (S\_3) at an engine speed of 1550 rpm and a planting distance of 0.35 m. The minimum fatigue life for the four-bar-link type was 196,000 years at the same location with the minimum static safety factor (link D) at an engine speed of 1500 rpm and a planting distance of 0.41 m.
  4. The rated work efficiencies of the cam and four-bar-link vegetable transplanters are similar. The cam type had a digital plant-spacing control device so that workers could work comfortably. However, considering the power consumption and price of the machine, the four-bar-link vegetable transplanter is highly economical.

**Author Contributions:** Data curation and formal analysis, S.M., S.-J.H., J.-H.K. and M.-K.J.; writing—original draft, S.M. and S.-J.H.; writing—review and editing, J.-S.N. and C.-S.S. All authors have read and agreed to the published version of the manuscript.

**Funding:** This work was supported by Korea Institute of Planning and Evaluation for Technology in Food, Agriculture and Forestry (IPET) through Agriculture, Food and Rural Affairs Convergence Technologies Program for Educating Creative Global Leader, funded by Ministry of Agriculture, Food and Rural Affairs (MAFRA) (320001-4), Republic of Korea. This research was also supported by Basic Science Research Program through the National Research Foundation of Korea (NRF) funded by the Ministry of Education (NRF-2020R1I1A3054353).

**Institutional Review Board Statement:** Not applicable.

**Informed Consent Statement:** Not applicable.

**Data Availability Statement:** Not applicable.

**Conflicts of Interest:** The authors declare no conflict of interest.

## References

1. Kim, S.K.; Park, S.; Kwak, J.-H.; Choi, S.-K.; Chae, W.B.; Yang, E.Y.; Lee, M.J.; Jang, Y.; Seo, M.H.; Lee, S.H.; et al. Proper Plant Density for Mechanical Transplanting of Several Leafy Vegetables Under Korean Agricultural Condition. *J. Biosyst. Eng.* **2019**, *44*, 276–280. [CrossRef]
2. Hwang, S.-J.; Park, J.-H.; Lee, J.-Y.; Shim, S.-B.; Nam, J.-S. Optimization of Main Link Lengths of Transplanting Device of Semi-Automatic Vegetable Transplanter. *Agronomy*. **2020**, *10*, 1938. [CrossRef]
3. Khadatkar, A.; Mathur, S.M.; Gaikwad, B.B. Automation in Transplanting: A Smart Way of Vegetable Cultivation. *Curr. Sci.* **2018**, *115*, 1884–1892. [CrossRef]
4. Rasool, K.; Islam, N.; Ali, M.; Jang, B.-E.; Khan, N.A.; Chowdhury, M.; Chung, S.-O.; Kwon, H.-J. Onion transplanting mechanisms: A review. *Precis. Agric. Sci. Technol.* **2020**, *2*, 196. [CrossRef]
5. Kang, D.H.; Kim, D.E.; Lee, G.I.; Kim, Y.H.; Lee, H.J.; Min, Y.B. Development of a Vegetable Transplanting Robot. *J. Biosyst. Eng.* **2012**, *37*, 201–208. [CrossRef]
6. Moon, S.D.; Min, Y.B.; Park, J.C. Analysis of working capacity of a hand-fed transplanter. *J. Bio. Fac. Environ.* **1997**, *6*, 159–167. Available online: <https://www.koreascience.or.kr/article/JAKO199711922405384.pdf> (accessed on 18 December 2022).
7. Shao, Y.; Liu, Y.; Xuan, G.; Hu, Z.; Han, X.; Wang, Y.; Chen, B.; Wang, W. Design and Test of Multifunctional Vegetable Transplanting Machine. *IFAC-PapersOnLine* **2019**, *52*, 92–97. [CrossRef]
8. Kumar, G.V.P.; Raheman, H. Vegetable Transplanters for Use in Developing Countries—A Review. *Int. J. Veg. Sci.* **2008**, *14*, 232–255. [CrossRef]
9. Jo, J.S.; Okyere, F.G.; Jo, J.M.; Kim, H.T. A Study on improving the performance of the planting device of a vegetable trans-planter. *J. Biosyst. Eng.* **2018**, *43*, 202–210. [CrossRef]
10. Min, Y.B.; Kang, J.K.; Ryu, C.S. Development Onion Transplanter: Analysis a Transplanting Locus on The Type of Transplanting Devices for a Vegetable Transplanter. *J. Agric. Life Sci.* **2015**, *49*, 289–294. [CrossRef]



11. Sri, M.; Hwang, S.-J.; Nam, J.-S. Experimental Safety Analysis for Transplanting Device of the 4-Bar Link Type Semi-Automatic Vegetable Transplanter. *Agronomy* **2022**, *12*, 1890. [CrossRef]
12. Park, J.-H.; Hwang, S.-J.; Nam, J.-S. Operational Characteristics of a Domestic Commercial Semi-automatic Vegetable Transplanter. *J. Agric. Life Sci.* **2018**, *52*, 127–138. [CrossRef]
13. Park, J.-H.; Hwang, S.-J.; Nam, J.-S. Operational Characteristics of a Cam-type Vegetable Transplanter and Mechanism of a Transplanting Device. *J. Agric. Life Sci.* **2019**, *53*, 113–124. [CrossRef]
14. Iqbal, Z.; Islam, N.; Ali, M.; Kiraga, S.; Kim, Y.-J.; Chung, S.-O. Theoretical Overturning Analysis of a 2.6-kW Two-Row Walking-Type Automatic Pepper Transplanter. *J. Biosyst. Eng.* **2022**, *47*, 79–91. [CrossRef]
15. Sri, M.; Hwang, S.-J.; Nam, J.-S. Experimental safety analysis of transplanting device of the cam-type semi-automatic vegetable transplanter. *J. Terramechanics* **2022**, *103*, 19–32. [CrossRef]
16. Kim, Y.-J.; Chung, S.-O.; Park, S.-J.; Choi, C.-H. Analysis of Power Requirement of Agricultural Tractor by Major Field Operation. *J. Biosyst. Eng.* **2011**, *36*, 79–88. [CrossRef]
17. Lee, D.-H.; Kim, Y.-J.; Chung, S.-O.; Choi, C.-H.; Lee, K.-H.; Shin, B.-S. Analysis of the PTO load of a 75kW agricultural tractor during rotary tillage and baler operation in Korean upland fields. *J. Terramechanics* **2015**, *60*, 75–83. [CrossRef]
18. Choudhary, S.; Upadhyay, G.; Patel, B.; Naresh; Jain, M. Energy Requirements and Tillage Performance Under Different Active Tillage Treatments in Sandy Loam Soil. *J. Biosyst. Eng.* **2021**, *46*, 353–364. [CrossRef]
19. Koo, Y.M.; Kang, Y. Characteristics of Power and Fuel Use of a Tractor-Mounted Integrated Implement for Round Ridge Preparation. *J. Biosyst. Eng.* **2021**, *46*, 496–507. [CrossRef]
20. Swe, K.M.; Islam, N.; Chowdhury, M.; Ali, M.; Wing, S.; Jun, H.-J.; Lee, S.-H.; Chung, S.-O.; Kim, D.-G. Theoretical Analysis of Power Requirement of a Four-Row Tractor-Mounted Chinese Cabbage Collector. *J. Biosyst. Eng.* **2021**, *46*, 139–150. [CrossRef]
21. Shafaei, S.M.; Loghavi, M.; Kamgar, S. On the Reliability of Intelligent Fuzzy System for Multivariate Pattern Scrutinization of Power Consumption Efficiency of Mechanical Front Wheel Drive Tractor. *J. Biosyst. Eng.* **2021**, *46*, 1–15. [CrossRef]
22. Koo, Y.M. PTO Torque and Draft Analyses of an Integrated Tractor-Mounted Implement for Round Ridge Preparation. *J. Biosyst. Eng.* **2022**, *47*, 330–343. [CrossRef]
23. Lee, J.-Y.; Hwang, S.-J.; Nam, J.-S.; Kim, J.-G. Consumed-Power and Load Characteristics of Potato Harvesting Operation in Dry Field. *Korean Soc. Manuf. Process. Eng.* **2020**, *19*, 89–99. [CrossRef]
24. Nam, J.-S.; Kang, D.-S.; Kang, Y.-S.; Kim, K.-U.; Kim, D.-C. Comparison of Work Performance of Crank-type and Rotary-type Rotavators in Korean Farmland Conditions. *J. Biosyst. Eng.* **2012**, *37*, 140–147. [CrossRef]
25. Kim, M.-H.; Nam, J.-S.; Kim, D.-C. Comparison of Tillage and Loads Characteristics of Three Types of Rotavators: Rotary-type, Crank-type, and Plow-type. *J. Biosyst. Eng.* **2013**, *38*, 73–80. [CrossRef]
26. Kim, J.G.; Kim, Y.J.; Kim, J.H.; Shin, B.S.; Nam, J.S. Consumed-power and load characteristics of a tillage operation in an upland field in Republic of Korea. *J. Biosyst. Eng.* **2018**, *43*, 83–93. [CrossRef]
27. Lee, J.-Y.; Nam, J.-S. Load and Safety Analysis for Plow Operation in Dry Fields. *Korean Soc. Manuf. Process. Eng.* **2019**, *18*, 9–18. [CrossRef]
28. Kim, W.S.; Chung, S.O.; Choi, C.H.; Cho, J.S.; Choi, D.S.; Kim, Y.J.; Lee, S.D.; Hong, S.J.; Koo, S.M. Analysis of the PTO Torque of a Transplanter by Planting Condition. *J. Biosyst. Eng.* **2016**, *41*, 313–318. [CrossRef]
29. Kim, W.; Kim, Y.; Kim, Y.; Choi, C.; Inoue, E.; Okayasu, T. Analysis of the Load of a Transplanter PTO Shaft Based on the Planting Distance. *J. Fac. Agric. Kyushu Univ.* **2018**, *63*, 97–102. [CrossRef]
30. Kim, W.-S.; Kim, Y.-S.; Kim, T.-J.; Nam, K.-C.; Kim, T.-B.; Han, T.-H.; Im, R.-G.; Kim, Y.-H. Effects of planting distance and depth on PTO load spectrum of a small riding-type transplanter. *Int. J. Agric. Biol. Eng.* **2020**, *13*, 57–63. [CrossRef]
31. Lee, P.U.; So, J.H.; Nam, Y.S.; Choi, C.H.; Noh, H.S.; Shim, J.Y.; Hong, S.J. Power analysis of electric transplanter by planting distances. *Korean J. Agric. Sci.* **2018**, *45*, 290–297. [CrossRef]
32. Lim, S.-J.; Kwon, H.-J.; Kang, Y.-S.; Lee, P.-U.; Kim, T.-J.; Kim, Y.-J.; Kim, Y.-S. Power Analysis of a 3-kW Class Motor-Driven Multipurpose Walking-Type Transplanter. *J. Biosyst. Eng.* **2019**, *44*, 135–145. [CrossRef]
33. Downing, S.; Socie, D. Simple rainflow counting algorithms. *Int. J. Fatigue* **1982**, *4*, 31–40. [CrossRef]
34. Rychlik, I. A new definition of the rainflow cycle counting method. *Int. J. Fatigue* **1987**, *9*, 119–121. [CrossRef]
35. Juvinall, R.C.; Marshek, K.M. *Machine Component Design*, 5th ed.; John Wiley & Sons, Inc.: New York, NY, USA, 2020; pp. 338–340.
36. Paraforos, D.S.; Griepentrog, H.W.; Vougioukas, S.G.; Kortenbruck, D. Fatigue life assessment of a four-rotor swather based on rainflow cycle counting. *Biosyst. Eng.* **2014**, *127*, 1–10. [CrossRef]
37. Mattetti, M.; Molari, G.; Sereni, E. Damage evaluation of driving events for agricultural tractors. *Comput. Electron. Agric.* **2017**, *135*, 328–337. [CrossRef]

**Disclaimer/Publisher’s Note:** The statements, opinions and data contained in all publications are solely those of the individual author(s) and contributor(s) and not of MDPI and/or the editor(s). MDPI and/or the editor(s) disclaim responsibility for any injury to people or property resulting from any ideas, methods, instructions or products referred to in the content.

## Article

# Investigating the Effect of Tractor's Tire Parameters on Soil Compaction Using Statistical and Adaptive Neuro-Fuzzy Inference System (ANFIS) Methods

Gholamhossein Shahgholi <sup>1,\*</sup>, Abdolmajid Moinfar <sup>1</sup>, Ali Khoramifar <sup>1</sup>, Sprawka Maciej <sup>2,\*</sup> and Mariusz Szymanek <sup>2</sup>

<sup>1</sup> Department of Biosystems Engineering, University of Mohaghrgh Ardabili, Ardabil 56199-11367, Iran

<sup>2</sup> Department of Agricultural, Forest and Transport Machinery, University of Life Sciences in Lublin, 20-950 Lublin, Poland

\* Correspondence: shahgholi@uma.ac.ir (G.S.); maciej.sprawka@up.lublin.pl (S.M.)

**Abstract:** Many factors contribute to soil compaction. One of these factors is the pressure applied by tires and tillage tools. The aim of this study was to study soil compaction under two sizes of tractor tire, considering the effect of tire pressure and traffic on different depths of soil. Additionally, to predict soil density under the tire, an adaptive neuro-fuzzy inference system (ANFIS) was used. An ITM70 tractor equipped with a lister was used. Standard cylindrical cores were used and soil samples were taken at four depths of the soil inside the tire tracks. Tests were conducted based on a randomized complete-block design with three replications. We tested two types of narrow and normal tire using three inflation pressures, at traffic levels of 1, 3 and 5 passes and four depths of 10, 20, 30 and 40 cm. A grid partition structure and four types of membership function, namely triangular, trapezoid, Gaussian and General bell were used to model soil compaction. Analysis of variance showed that tire size was significant on soil density change, and also, the binary effect of tire size on depth and traffic were significant at 1%. The main effects of tire pressure, traffic and depth were significant on soil compaction at 1% level of significance for both tire types. The inputs of the ANFIS model included tire type, depth of soil, number of tire passes and tire inflation pressure. To evaluate the performance of the model, the relative error ( $\epsilon$ ) and the coefficient of explanation ( $R^2$ ) were used, which were 1.05 and 0.9949, respectively. It was found that the narrow tire was more effective on soil compaction such that the narrow tire significantly increased soil density in the surface and subsurface layers.

**Keywords:** inflation pressure; bulk density; ANFIS; tire

**Citation:** Shahgholi, G.; Moinfar, A.; Khoramifar, A.; Maciej, S.; Szymanek, M. Investigating the Effect of Tractor's Tire Parameters on Soil Compaction Using Statistical and Adaptive Neuro-Fuzzy Inference System (ANFIS) Methods. *Agriculture* **2023**, *13*, 259. <https://doi.org/10.3390/agriculture13020259>

Academic Editors: Ju-Seok Nam and Yongjin Cho

Received: 29 December 2022

Revised: 16 January 2023

Accepted: 19 January 2023

Published: 20 January 2023



**Copyright:** © 2023 by the authors. Licensee MDPI, Basel, Switzerland. This article is an open access article distributed under the terms and conditions of the Creative Commons Attribution (CC BY) license (<https://creativecommons.org/licenses/by/4.0/>).

## 1. Introduction

Soil is a resource with a potentially rapid degradation rate and a very slow regeneration and formation process [1]. Thus, sustainable soil use is the only solution to global problems such as food security, energy and water demands, climate change and biodiversity [2]. In order to increase productivity in the agricultural sector, farms should be a large size, in which productivity can be increased by the use of more efficient machines [3]. For many years, the agricultural sector has tended to increase the size and weight of the tractor, which increases the risk of severe soil compaction [4].

One of the causes of soil compaction in mechanized agriculture is the passage of agricultural implements and tools. Soil compaction as a form of reducing the pore space between soil particles can significantly reduce soil production capacity [5]. According to data from seven countries in Europe and North America, a 14% drop in crop yield was reported in the first year after machine traffic [6]. Soil compaction is a form of physical degradation of soil that causes compacted soil particles to be closer to each other and the disappearance of voids in the soil, reducing porosity and soil permeability. This manifests as

an increase in soil bulk density [7]. One method of assessing soil compaction is to measure its bulk density. When soil compaction occurs, the bulk density of the soil increases as the mass remains constant and the volume decreases. Density reduction decreases hydraulic conductivity and thus causes surface runoff and soil erosion by water. This induces forced currents in the soil pores, thus facilitating the transport of absorbable colloidal nutrients and pesticides to deeper horizons and groundwater, thereby reducing root growth and causing a loss of nitrogen and production of greenhouse gases through nitrogenization by anaerobic processes. As a result, soil compaction is one of the main causes of environmental and agricultural problems, and as a result causes significant economic damage to society and agriculture [8].

Increasing the load on the wheels of agricultural machinery is the most important cause of soil compaction created in deeper soil layers. The topsoil of arable lands is loosened every year by plowing operations, however, the subsoil often remains intact, which means that whenever the maximum load capacity is exceeded, additional soil compaction will occur deep in the soil. In addition, these effects are lasting, and the results of natural and artificial soil loosening are disappointing [9]. Excessive movement of agricultural machinery on the field and plowing at a constant depth gradually causes soil compaction, and this compaction restricts plant root growth and reduces crop yield [10]. To remove this hard layer created in the subsoil, which limits the longitudinal growth of roots and proper soil drainage, deep plowing is required, which greatly increases the required energy [11]. Another solution is to use energy-efficient combined (active-passive or passive-passive) tillage implements in place of conventional ones to reduce soil compaction, labor, and fuel cost as well as to save time in preparing the seedbed [12]. Another aspect affecting the protection of soil structure from compaction is the evolution of tires [13]. In this article we compare the effects of five tractor tires introduced between the 1970s and 2017 on soil stress and soil structure. Soil physical properties before and after one pass of each of the five tires were measured on undisturbed soil. The results of stress measurements showed the lowest mean normal stress at all depths with newer tires, both below the center of the tire and at the edge, even though the effect decreased with increasing depth. The results indicate that tire design can play an important role in reducing soil stress for a given wheel load. Tire design might then also help to reduce the compaction risk for larger wheel loads and other soil conditions which were tested in the study.

Maintaining proper ratios between solid, liquid and gas phases is of particular importance, because increasing the solid phase (i.e., reducing the liquid and gas phases) increases the mechanical strength of the soil and consequently reduces the growth and development of plant roots inside the soil. Reducing the development of root growth causes less water and nitrogen to be available to the plant. When the machine enters the field, the solid phase of the soil increases by a certain volume and the gas phase decreases. Soil density is one of the indicators of the destruction of the physical structure of the soil, which is defined as an increase in soil bulk density (solid phase mass to total volume), or a decrease in porosity [14]. Wheel load, tire type, and inflation pressure can increase soil bulk density and play an important role in soil compaction [15]. Almost all tires significantly increase soil compaction along the wheel track, while only some increase soil compaction near the track [15]. As the distance from the wheel path increases, a general decrease in soil density occurs, especially in the subsoil. Many researchers have reported that working with low-pressure tires can significantly reduce soil compaction and increase crop yield [16,17], while high tire pressure increases soil compaction [18]. Tire pressure control is an important factor in the control of and in soil compaction. A new tire pressure control system in forest machines was developed using a PressurePro solution. It was found that the installation of an automatic tire pressure control system leads to compaction reduction by 20%. Additionally, reduced tire pressure and its automatic control contribute to a minimal reduction in humus content and soil compaction over time [19]. Another researchers have investigated the effect of different tire inflation pressures of 100 and 200 kPa on selected physical soil properties by conducting field tests. The undisturbed samples were collected

both in and between the tracks at depths of 0 to 0.5 m. The results indicated that fewer negative changes were found in the variant with a lower inflation pressure for all of the soil properties. Change in soil physical properties caused by the passage of the tractor were statistically significant for both tire pressures only at depths ranging from 0 to 0.1 m [20]. The effect of three types of wide, low-inflation pressure tires with similar dimensions on mean normal stress on the soil profile was also investigated. The results revealed a very limited effect of tire construction on mean normal stress. No differences were measured beneath the center, and differences at +0.3 m were found only at 0.2 m depth for the tires at the rear axle. The effect of low tire inflation pressure was limited to the upper parts of the soil profile for beneath the center of the tire, which was significant at depths of 0.2 m and 0.4 m. It was found that in order to reduce soil stress, tire design should allow for a large contact area and low inflation pressure [21].

Machine traffic plays an important role in soil compaction. Experiments have been carried out to study the effect of multiple passes of tillage operation on soil compaction beneath the tillage depth with three different tillage systems. The authors observed that active tillage machinery generally caused more compaction compared to passive tillage machinery for the same number of passes. However, active machinery required fewer vehicular passes [22]. In plowed soils, the first pass can dramatically increase soil compaction and cause soil degradation, while in firm soil and deep areas soil compaction occurs over time and with large numbers of tire passes [23]. Research has also shown that if the traffic exceeds 10 times, the benefits of using light tractors are lost and soil compaction is greatly increased. These studies have suggested that heavy tractors with less traffic should be used as much as possible because high traffic leads to compaction in the subsoil [24,25].

One method of assessing soil compaction is to measure its bulk density. When soil compaction occurs, the bulk density of the soil increases as the mass remains constant and the volume decreases. In this method, after determining soil bulk density at different depths and, based on the soil texture, measured data are compared with the standard values to determine the level of soil compaction. For example, soil compaction is considered significant for loamy clay soil when bulk density reaches more than 1.5 g/cm<sup>3</sup>, and for sandy and loamy soil more than 1.6 g/cm<sup>3</sup> [26].

In recent years, the artificial intelligence approach has shown that it has great power to model and predict complex systems, thus it can be an alternative method to physical models that do not respond well to a large number of input variables [26]. Because agricultural systems such as soil are so complex, most researchers have focused on artificial intelligence to model different components of agricultural systems. The fuzzy neural adaptive inference system (ANFIS) is a multi-layered adaptive network consisting of the main elements and functions of fuzzy logic systems developed by Jang [27]. Each of the fuzzy systems and artificial neural networks (ANNs) has advantages and disadvantages. The fuzzy system is able to use human language and can use human experiences and experts while it is not able to learn [28]. In other words, the fuzzy system cannot be trained using observational data and it should be noted that this method does not provide good results in unpredictable conditions [29]. However, neural networks are self-learning using data sets. At the same time, neural networks are implicit and unable to use human language. They require a wide range of tested input and output data for successful modeling [30]. Although ANN is a powerful technique for modeling various problems in the real world, it has its own weaknesses. If the input data is vague or the uncertainty is relatively high, a fuzzy system such as ANFIS may be a better option [31].

In order to evaluate the potential of ANFIS in predicting the energy efficiency indicators of the drive wheel, experiments were performed in the soil reservoir. Input parameters included tire load, wheel speed and slip, each at three different levels. ANFIS was used with a combined method of descending gradient and least squares to find the optimum learning parameters using different membership functions (MFS). The results of this study showed high accuracy (MSE = 0.0166 and R<sup>2</sup> = 0.98) in prediction [31]. A fuzzy logic model was developed to describe soil fragmentation for seedbed preparation in a combination

of primary and secondary tillage tools from subsoil, moldboard plow and disc. In this research, an intelligent model based on the Mardani fuzzy modeling principles approach was developed to predict soil fragmentation during tillage operations. Model inputs were: soil moisture, tractor speed and sampling depth. The fuzzy model consisted of 50 rules in which the three parameters of mean root mean square error (RMSE), relative error ( $e$ ), and coefficient of determination ( $R^2$ ) were used to evaluate fuzzy models. These parameters were calculated to be 0.17%, 3.95% and 0.99%, respectively. According to the results of this study, the fuzzy model can be used as a method to predict soil fragmentation during tillage operations [32]. In the study, the ANFIS model was used to predict soil compaction under tractor wheels. Model inputs included four factors: manure rate, number of passes, moisture and depth. The network structure was selected from the network segmentation type. The number of membership functions for each input was considered to be three and the membership functions of bell, triangle, trapezoid and Gaussian were tested for best performance. The results of this study showed that the ANFIS model has a higher accuracy in predicting soil density than the regression model [33].

The main objectives of this research are as follows:

1. Investigating the density created in different depths of the soil due to the passage of tractor wheels of different size;
2. Investigating the effect of inflation pressure changes of drive wheel and machine traffic on the soil density created at different depths;
3. Modelling the effect of tire size, tire pressure, and machine traffic on soil density at different depths using statistical and adaptive neuro-fuzzy inference system (ANFIS) methods

## 2. Materials and Methods

Field experiments were performed to measure the bulk density of the soil under two common and narrow radial tires. The first type of tire was a standard 8 layer tire with a size of 14–38. Three inflation pressures of 80, 120 and 160 kPa were used to evaluate the effect of tire pressure on soil compaction. The second type of tire was a 10 layer radial narrow tire with a size of 9.5–48. Inflation pressures of 240, 275 and 310 kPa were investigated. For each of these tire pressures, three traffics of 1, 3 and 5 were tested. In all tests, soil samples were obtained from four depths of 10, 20, 30 and 40 cm. The farm had been plowed already, and an ITM70 tractor equipped with a bedder-ridger on a three-point hitch was used for conducting tests. In this case, the weight measured on the rear axle was 2740 kg, and on the front axle 770 kg. In all experiments, the tractor speed was constant, equal to 3 km/h. The process of adjusting the desired speed was done in such a way that the tractor was moved to a distance of 30 m on the field to achieve a speed of 3 km/h with two gears and at engine speed of 1400 and 1600 rpm. the desired speed was obtained using a calibration diagram.

A hydrometric test (ASTM D-422) was used to determine the soil texture by determining the relative amount of sand, silt and clay. It was found that there were 43.92, 32.06 and 24.02% sand, silt and clay, respectively. According to the soil texture triangle, the soil texture was loamy. A standard proctor test was used to determine the soil critical moisture. According to Figure 1, a moisture level of 25% is the critical moisture content, and the highest value of compaction occurs at this humidity.

To measure the bulk density after the tire passes, standard cylinders were placed in groups of 3 at different depths of 10, 20, 30 and 40 cm measured from the center of the cylinders to the soil surface and in line with tire path direction in the center line of the tire track (Figure 2). In order that the cylinders were placed exactly at the desired height and in one direction inside the profile, a string was drawn from the middle of the profile and from the beginning to the end. Figure 3 shows how the cylinders were exerted inside the soil vertically in the direction of the string. Each group of cylinders was about 40 cm apart so that there were no problems when removing the cylinders. It should be noted that the soil surface appears loose in Figure 3; this is because the soil had been dug to place the cylinder at a predetermined depth.

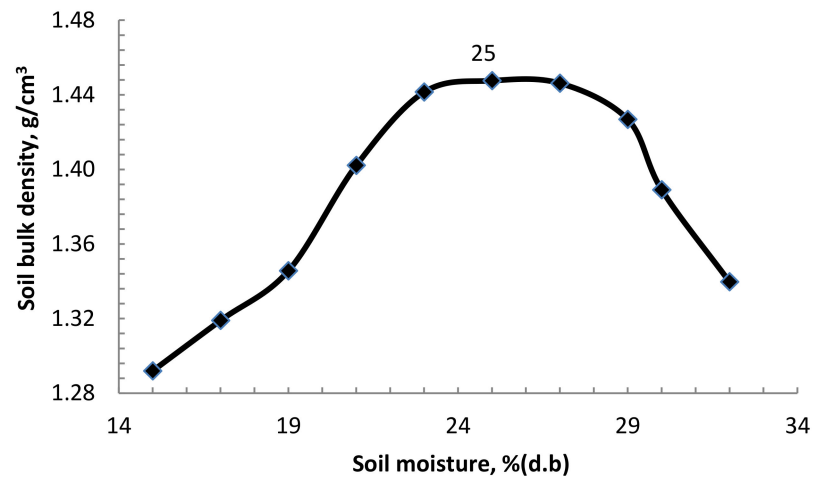


Figure 1. Determining the critical soil moisture using the proctor test.



Figure 2. Passing the tractor with two types of tires on the field.

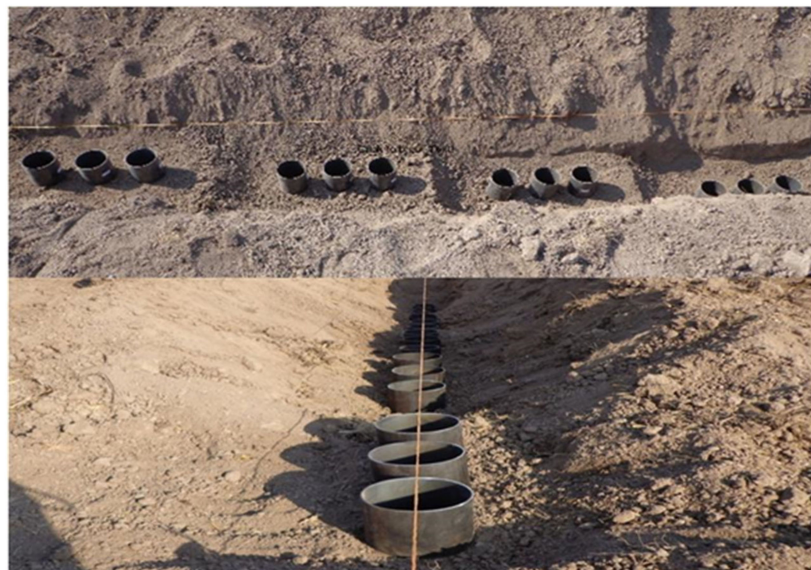


Figure 3. Placement of the cylinders inside the soil profile.



To implement the fuzzy neural adaptive model, MATLAB 2014a software toolbox under Windows was used. According to the performed experiments, soil density was defined as system output, while tire type, tire inflation pressure, traffic and soil depth were independent inlet parameters (Figure 4). The data is usually divided into three categories: training data, validation data, and test data. The training data were used in the training process to calculate the gradient and optimize the parameters. One of the points that should be considered during the training is aiming to prevent the network from becoming specialized and the occurrence of over-fitting phenomena. For this purpose, a series of data was considered for validation during the training of the network. These data are actually part of the training data. In this way, in the regular intervals of the optimization process, the data obtained from the network were checked using the validation data. In this case, network training continued until the optimization error related to the evaluation data began to increase, and as soon as this error increased to a certain value or a certain number of repetition, network training was stopped. Finally, the test data was used to test the performance of the network after training. The test data was not used during network training, but it was used to compare the error rate. Accordingly, in this research, 70% of the data were considered for training, 15% for evaluation, and 15% for testing the network.

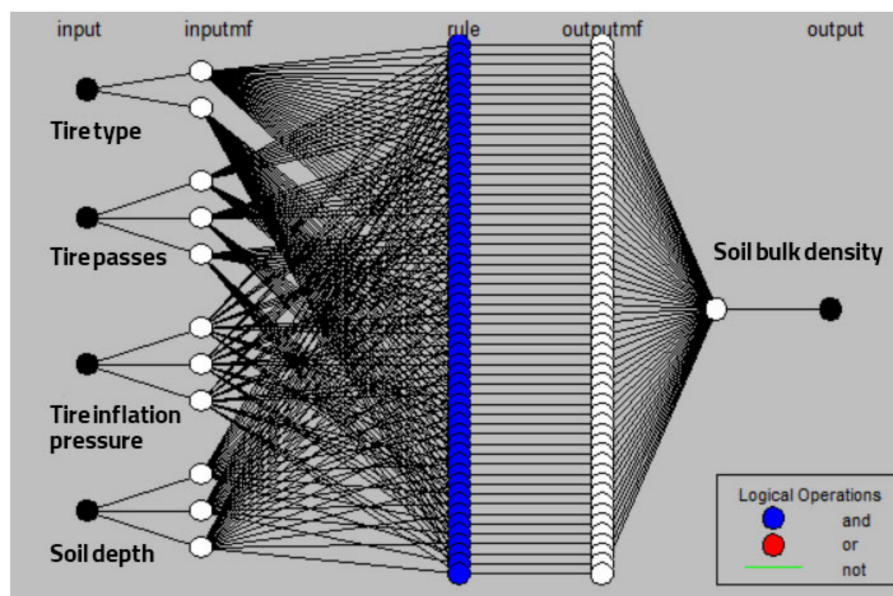


Figure 4. Structure topology of the neural-fuzzy adaptive fuzzy inference system (ANFIS).

A network separation structure was considered to create the network. Four commonly used membership functions, namely triangular, trapezoidal, Gaussian, and bell, were considered as membership functions to represent the inputs (Figure 5), and four different models were constructed using these membership functions.

The number of membership functions for each variable was considered proportional to the levels tested for that variable. Table 1 shows the membership functions for each variable.

The output membership function in this network is linear. A hybrid optimization method was used for network training. The number of rules created by the network was 54. Given that the number of rules created was very high, only a few of them are presented in Table 2.



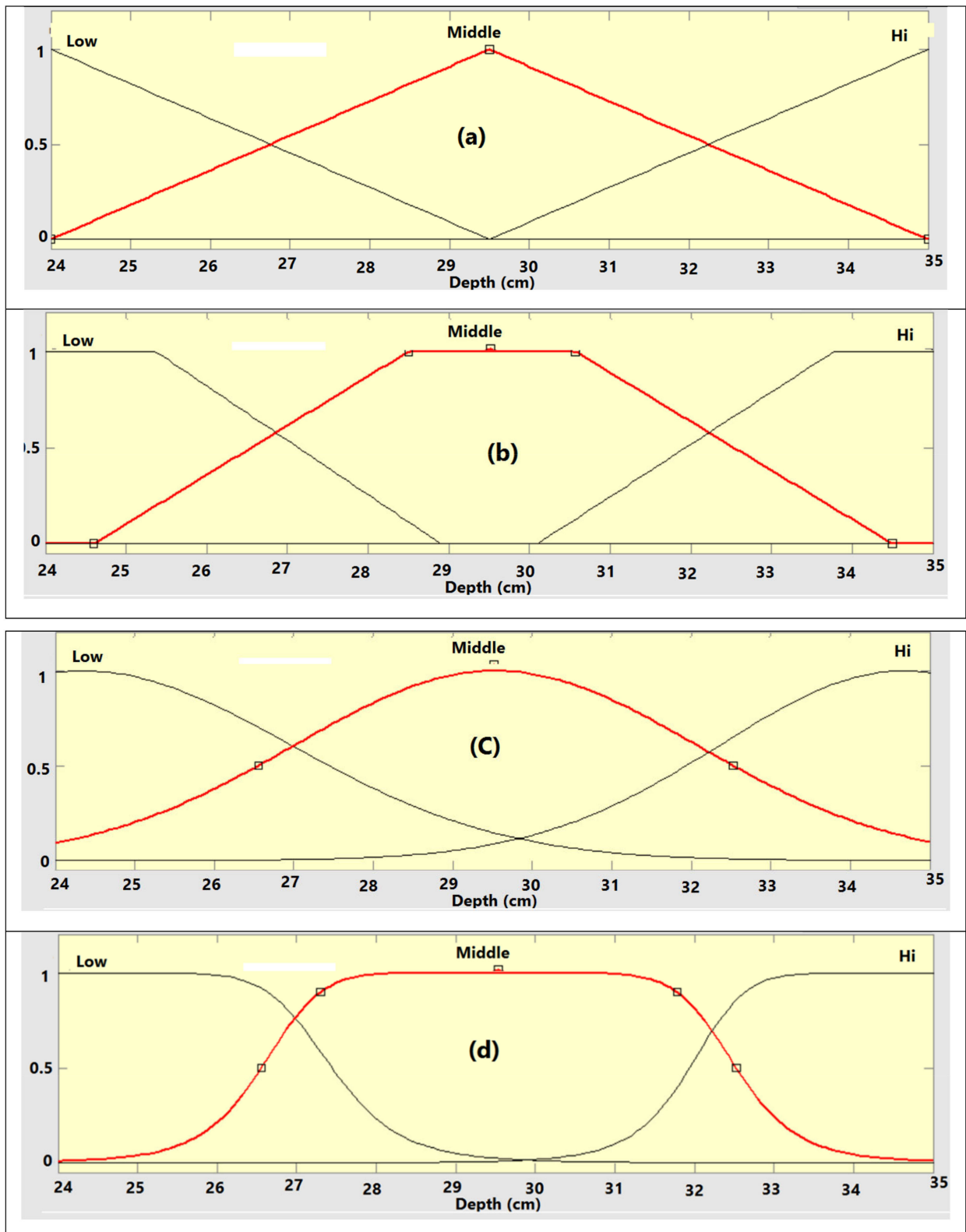


**Figure 5.** Membership functions used to represent inputs (a) Triangular, (b) Trapezoidal, (c) Gaussian, (d) Bell-shaped.

**Table 1.** Membership functions of input variables.

Input Variable	Membership Function		
Tire Type	Narrow		Wide
Traffic	max	ave	min
Tire pressure	high	normal	low
Depth	subsoil	mid soil	topsoil

**Table 2.** Some rules created in the ANFIS model.

Rules	Input Parameters				Output Variable
	Tire Type(T)	Traffic (P)	Tire Inflation (IP)	Soil Depth (D)	Special Mass
1	Wide	Min	Low	Topsoil	BD = 0.09035T + 0.06862P + 0.09035IP + 0.09035D + 0.09035
8	Wide	Min	High	Middle soil	BD = 0.01578T + 0.06565P + 0.07889IP + 0.03156D + 0.01578
16	Wide	Ave	High	Topsoil	BD = -0.00517T + 0.04506P - 0.02585IP - 0.00517D - 0.00517
24	Wide	Max	Normal	Subsoil	BD = 0.00329T + 0.0256P + 0.009871IP + 0.009871D + 0.00329
32	Narrow	Min	Normal	Middle soil	BD = 0.05436T + 0.07231P + 0.08154IP + 0.05436D + 0.02718
40	Narrow	Ave	Normal	Topsoil	BD = -0.02717T + 0.04873P - 0.04075IP - 0.01358D - 0.01358
48	Narrow	Max	Low	Subsoil	BD = 0.009582T + 0.02666P + 0.004791IP + 0.01437D + 0.004791
56	Narrow	Max	High	Subsoil	BD = 0.004228T + 0.02739P + 0.01057IP + 0.006341D + 0.002114

Finally, the performance of the models was evaluated based on the statistical criteria presented in Equations (1) and (2).

$$MAPE = \frac{100\%}{N} \sum_{i=1}^n \frac{Y_{measured} - Y_{predicted}}{Y_{measured}}, \tag{1}$$

$$R^2 = 1 - \frac{\sum_{i=1}^N (Y_{measured} - Y_{predicted})^2}{\sum_{i=1}^N (\bar{Y}_{measured} - Y_{predicted})^2}, \tag{2}$$

where:

MAPE: the absolute mean percentage of system error

R<sup>2</sup>: is the coefficient of determination

N: the number of samples

Y<sub>predicted</sub>: the predicted values

Y<sub>measured</sub>: the measured values

$\bar{Y}_{measured}$ : the average of measured values.

### 3. Results and Discussion

Table 3 shows the analysis of variance of soil bulk density for two types of ordinary and narrow tire. Data were analyzed in a 4 × 3 × 4 factorial design based on a randomized complete block design. The data coefficient of variation (CV) was 0.44%. Average initial soil bulk density was 1.017 g/cm<sup>3</sup>, and based on data of initial bulk density it was uniform in all plots. In comparison with initial bulk density, statistical analysis showed that the main effects of tire type, traffic and depth on soil density change were significant at the

level of 1% probability. The interactions of depth with traffic, depth with tire type, and traffic with tire type on soil bulk density were found to be significant at the 1% probability level. However, the combined interaction of depth, tire type and traffic on soil bulk density was not found to be significant at the 1% probability level.

**Table 3.** Analysis of variance of soil bulk density change due to tire type, traffic and depth.

Source of Variation	Df	Sum of Squares	Mean Squares	F
Soil depth	3	0.054	0.018	715.6 **
Traffic	2	0.015	0.008	302.1 **
Tire type	1	0.113	0.113	4490 **
Depth × pass	6	0.001	0.00016	5.5 **
Depth × tire type	3	0.002	0.00067	25.6 **
Pass × tire type	2	0.001	0.0005	13.5 **
Depth × pass × tire type	6	0	0	1.6 ns
Error	46	0.001	0	-

\*\* : Highly significant, ns: Not significant.

### 3.1. The Binary Effect of Tire Type and Depth on Soil Bulk Density

The binary effect of tire type and depth on soil bulk density was evaluated using a Duncan test at 1% probability level, and is presented in Figure 6. According to the results, the maximum value of bulk density was 1.217 g/cm<sup>3</sup> for narrow tire at a depth of 10 cm, and the lowest value was 1.061 g/cm<sup>3</sup> which occurred for common tires at a depth of 40 cm. For both tires, a significant decrease in the soil bulk density was seen with increasing depth, but the intensity of these changes in the narrow tire and especially in shallow depths was greater than for the common tire. The bulk density of soil for the narrow tire, even at a depth of 40 cm, was greater than the bulk density of soil for a normal tire at a depth of 10 cm. The effect of tire size on stress applied to different soil layers was examined [34]. Their results showed that a narrow tire created much more stress in different layers of soil than a common tire, and as a result, it compacted the soil more. Stress for a narrow tire at a depth of 50 cm was higher than the stress of a common tire at depth of 30 cm.

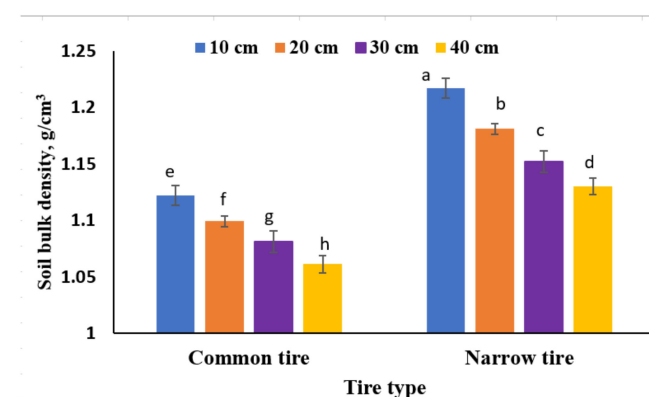


**Figure 6.** The main effect of tire type and depth on soil bulk density (different English alphabets shows significant difference between treatments).

### 3.2. The Binary Effect of Tire Type and Traffic on Soil Bulk Density

The results of comparing the mean interaction of tire type and depth on soil bulk density using a Duncan test at 1% probability level are presented in Figure 7. In both tires, the soil bulk density increased with increasing traffic. According to the results, the highest mean value of soil density was found for the narrow tire after five passes with a value of

1.185 g/cm<sup>3</sup> and the lowest for a normal tire after one pass with a value of 1.112 g/cm<sup>3</sup>. It is noteworthy that the bulk density of soil for a narrow tire, even at one pass, is more than the bulk density of soil for a normal tire in five passes.

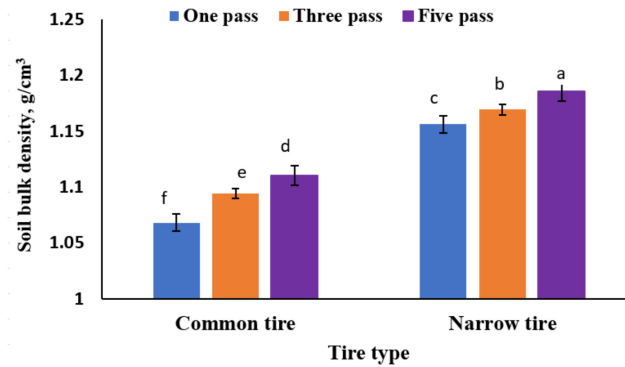


**Figure 7.** The main effect of tire type and traffic on soil bulk density (different English alphabets shows significant difference between treatments).

### 3.3. Results of Modeling Soil Bulk Density Using ANFIS

Four different models were developed to predict soil bulk density. Table 4 presents the structural parameters of the models along with their statistical criteria to evaluate their performance. According to the results presented in Table 4, it is clear that all models have a high ability ( $R^2 \geq 0.99$  and  $\epsilon (\%) \leq 2$ ) to predict. The best model for predicting soil bulk density is a model that uses the bell membership function (Gbellmf) ( $R^2 = 0.9949$  and  $\epsilon (\%) = 1.05$ ).

**Table 4.** Specifications and evaluation results of adaptive fuzzy-neural inference system models (ANFIS).

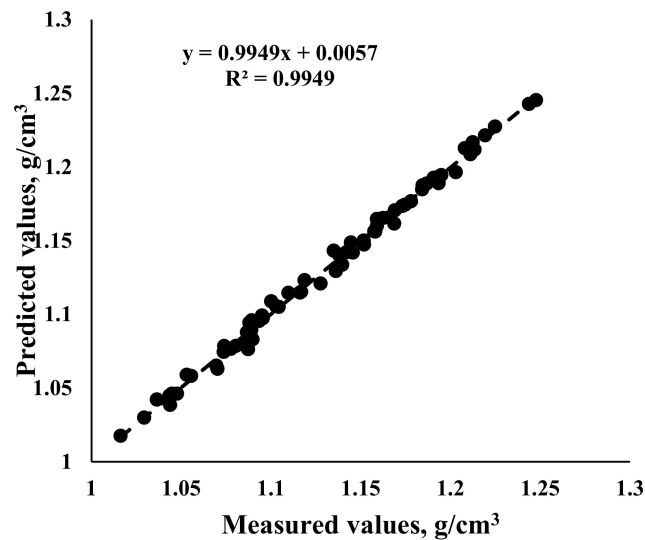
Network Structure	Membership Function Type		Number of Membership Functions		Optimization Method	Test Result	
	Input	Output	Input	Epochs		Coefficient of Determination ( $R^2$ )	Relative Error (e)
Grid Partition	Triangular	Linear	2-3-3-3	20	hybrid	0.992	1.5
Grid Partition	Trapezoidal	Linear	2-3-3-3	20	hybrid	0.99	1.75
Grid Partition	Gaussian	Linear	2-3-3-3	20	hybrid	0.982	2.2
Grid Partition	Bell-shaped	Linear	2-3-3-3	20	hybrid	0.995	1.05

Table 5 presents the statistical characteristics of the stepwise regression model for predicting soil bulk density. The ANFIS models have poorer performance than the regression model due to a low coefficient determination of 0.96. However, regression models have valuable advantages, such as the fact that ANFIS models do not provide any information about the internal structure of the model and the relationships between independent and dependent variables, while the regression model directly deals with the impact of each factor and tries to provide a model in which the importance and impact of each factor is clear. According to Table 5 and the standard coefficients mentioned therein, type of tire, soil depth, inflation pressure, and finally the number of passes have the greatest impact on the bulk density.

**Table 5.** Statistical characteristics of stepwise regression model for predicting soil bulk density.

Model	Unstandardized Coefficients		Standardized Coefficients	t	Sig
	Beta	Std. Error	B		
Constant	0.98	0.006		154.528	<0.0001
Tire type	0.08	0.003	0.705	30.916	<0.0001
Depth	−0.002	0.001	−0.458	−20.091	<0.0001
Inflation pressure	0.031	0.002	0.444	19.452	<0.0001
Traffic	0.008	0.001	0.245	10.748	<0.0001

Figure 8 shows the relationship between measured and predicted values using ANFIS models under different operating conditions. In addition, the deviation between the measured values and the predicted values was calculated and plotted by ANFIS and multiple regression models. Figure 9 shows that the deviation distance of the predicted values of the ANFIS model (−0.011 to 0.0085) was much less than the deviation distance of the predicted values of the multiple regression model (−0.021 to 0.033).



**Figure 8.** Relationship between measured and predicted values of soil bulk density.

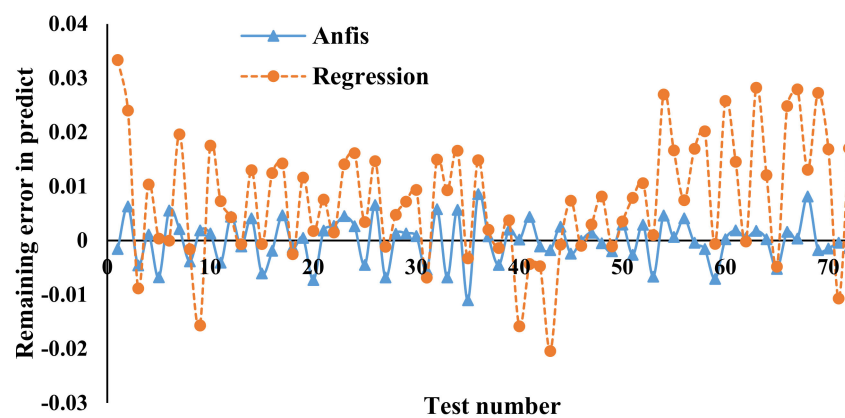


**Figure 9.** Deviation distance of predicted values of ANFIS and regression models from measured values.

Figure 10 shows the three-dimensional variation of soil bulk density with the interaction of tire type and soil depth. It indicates that with increasing depth, the bulk density of the soil decreased, indicating that the compaction created by the tire traffic of the tractor in the

topsoil was higher than in the sub layers. It was found that at all depths the density change by the passage of common tire was less than the density created by the narrow tire. Such a low pressure at the soil surface and soil behavior was investigated using a flat tire [3].

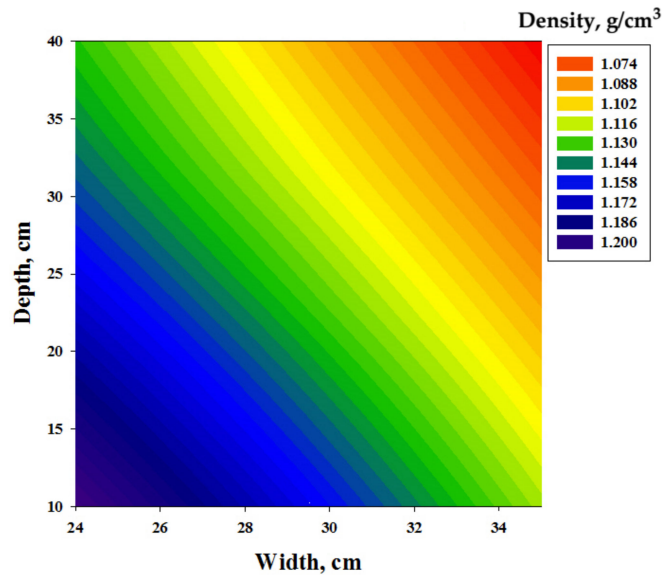


Figure 10. Binary effect of tire type and soil depth on the soil bulk density.

Figure 11 shows the binary effect of tire pressure and tire traffic on the soil bulk density. As the tire pressure decreases, the bulk density of the soil decreased. As the pressure decreased, the contact area between the tire and the soil increased, which reduces the pressure on the soil, resulting in decreased soil compaction and this was reported by other researchers [35–37]. With increasing traffic, the bulk density of the soil increased [33,38,39].

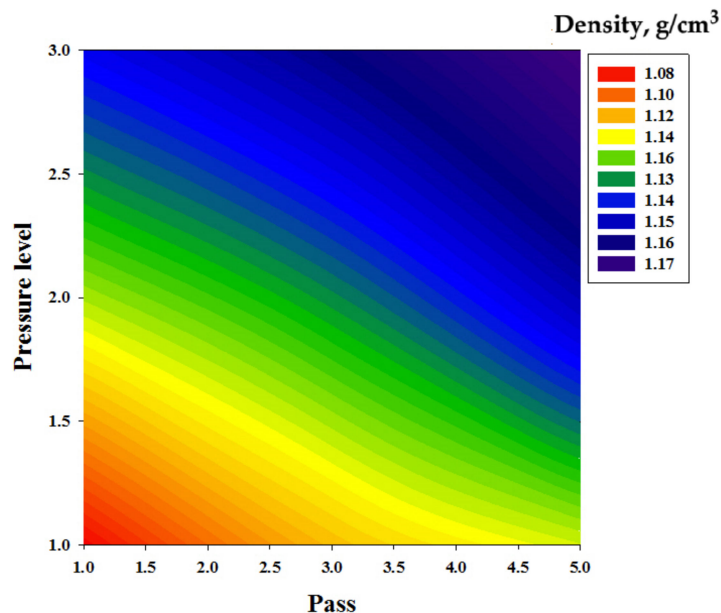


Figure 11. Binary effect tire inflation pressure and traffic on the soil bulk density.

Figure 12 illustrates with a surface plot of the interaction of tire type and traffic on the bulk density of the soil. With increasing traffic, when using a narrow tire, the soil bulk density increased sharply, but using a common tire was less effective on soil bulk density increment. This indicates that narrow tires are very destructive on soil structure.

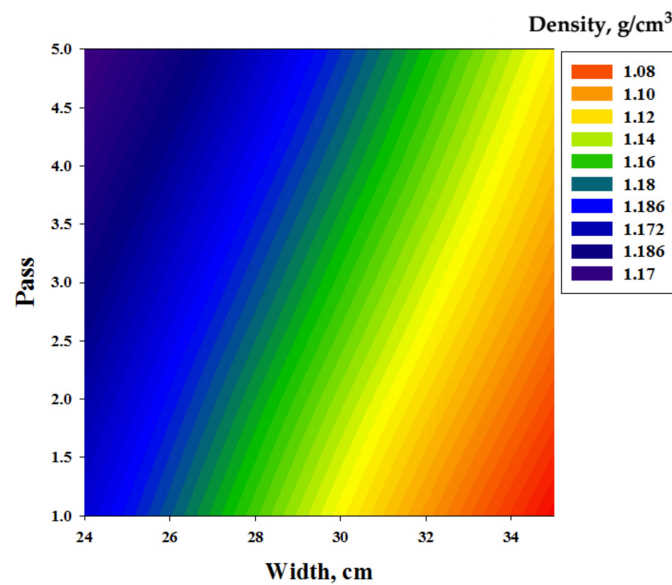


Figure 12. Tire type and traffic effect on the soil bulk density.

Figure 13 shows the interactive effect of tire type and tire inflation pressure on soil compaction. The soil bulk density changed strongly with increasing pressure when using a narrow tire, but less changes occurred when using a wide tire with increasing pressure.

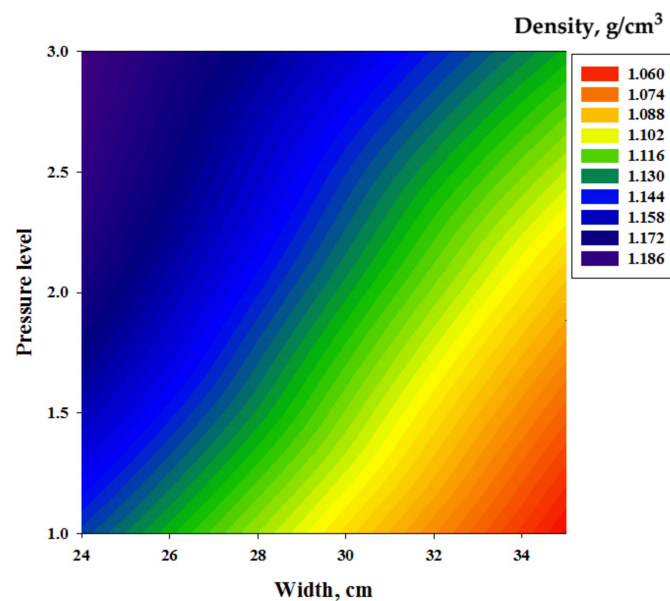


Figure 13. Three-dimensional surface curve of the main effect of tire type pressure and tire pressure on the soil bulk density of the soil.

#### 4. Conclusions

1. The results showed that using a narrow tire increased the soil bulk density in different layers of soil much more in comparison with a common tire. A narrow tire compacted the soil more and increased the soil density, even at a depth of 50 cm, more than a common tire at a depth of 30 cm. Additionally, the soil bulk density of soil for a narrow tire at a depth of 40 cm was greater than that of a normal tire at a depth of 10 cm.
2. In both tires, the soil bulk density of the soil increased with increasing tire wheeling. According to the results, the highest mean value of soil density for narrow tire was after five passes, with a value of 1.185 g/cm<sup>3</sup>. The lowest value was for a common



tire after one pass, with a value of 1.112 g/cm<sup>3</sup>. It is noteworthy that the bulk density of soil for a narrow tire after one pass was more than the bulk density of soil for a common tire after five passes.

3. Using a narrow tire with tire wheeling increased the soil bulk density very sharply, but when using a wide tire, with increasing passes, fewer changes in the bulk density of the soil occurred. This indicates that using narrow tires should be considered to be very destructive on the soil structure. Additionally, with increasing tire pressure, and when using a narrow tire, the soil bulk density changed much more than when the common tire's pressure changed.

**Author Contributions:** Conceptualization, G.S. and A.M.; formal analysis, A.K., M.S.; investigation, A.M. and A.K.; methodology, G.S., A.M. and A.K.; resources, G.S., A.M. and A.K.; supervision, G.S.; visualization, G.S., A.M., A.K. and M.S.; writing—original draft, A.M. and A.K.; writing—review and editing, G.S., A.M., A.K., M.S. and S.M. All authors have read and agreed to the published version of the manuscript.

**Funding:** This research received no external funding.

**Institutional Review Board Statement:** Not applicable.

**Data Availability Statement:** Not applicable.

**Conflicts of Interest:** The authors declare no conflict of interest.

## References

1. Van-Camp, L.; Bujarrabal, B.; Gentile, A.R.; Jones, R.J.; Montanarella, L.; Olazabal, C.; Selvaradjou, S.K. *Reports of the Technical Working Groups Established under the Thematic Strategy for Soil Protection*; Office for Official Publications of the European Communities: Luxembourg, 2004.
2. Lal, R. Soils and food sufficiency: A review. In *Sustainable Agriculture*; Springer: Dordrecht, The Netherlands, 2009; pp. 25–49.
3. Ansoorge, D.; Godwin, R.J. The effect of tyres and a rubber track at high axle loads on soil compaction, Part 1: Single axle-studies. *Biosyst. Eng.* **2007**, *98*, 115–126. [CrossRef]
4. Arvidsson, J.; Westlin, H.; Keller, T.; Gilbertsson, M. Rubber track systems for conventional tractors—Effects on soil compaction and traction. *Soil Tillage Res.* **2011**, *117*, 103–109. [CrossRef]
5. Li, H.; Schindler, C. Analysis of soil compaction and tire mobility with finite element method. Proceedings of the Institution of Mechanical Engineers, Part K. *J. Multi-Body Dyn.* **2013**, *227*, 275–291.
6. Hakansson, I.; Reeder, R.C. Subsoil compaction by vehicles with high axle load-extent, persistence and crop response. *Soil Tillage Res.* **1994**, *29*, 277–304. [CrossRef]
7. Veronesi, F.; Corstanje, R.; Mayr, T. Mapping soil compaction in 3D with depth functions. *Soil Tillage Res.* **2012**, *124*, 111–118. [CrossRef]
8. Keller, T.; Lamandé, M.; Peth, S.; Berli, M.; Delenne, J.Y.; Baumgarten, W.; Or, D. An interdisciplinary approach towards improved understanding of soil deformation during compaction. *Soil Tillage Res.* **2013**, *128*, 61–80.
9. Voorhees, W.B. Long-term effect of subsoil compaction on yield of maize. *Adv. GeoEcol.* **2000**, *32*, 331–338.
10. Taylor, H.M.; Roberson, G.M.; Parker, J.J., Jr. Soil strength-root penetration relations for medium-to coarse-textured soil materials. *Soil Sci.* **1966**, *102*, 18–22. [CrossRef]
11. Barik, K.; Aksakal, E.L.; Islam, K.R.; Sari, S.; Angin, I. Spatial variability in soil compaction properties associated with field traffic operations. *Catena* **2014**, *120*, 122–133. [CrossRef]
12. Sarkar, P.; Upadhyay, G.; Raheman, H. Active-passive and passive-passive configurations of combined tillage implements for improved tillage and tractive performance: A review. *Span. J. Agric. Res.* **2021**, *19*, e02R01. [CrossRef]
13. Damme, L.; Stettler, M.; Pinet, F.; Vervaeet, P.; Keller, T.; Munkholm, L.J.; Lamandé, M. The contribution of tyre-evolution to the reduction of soil compaction risks. In Proceedings of the 21th ISTRO Conference, Paris, France, 25–27 September 2018.
14. Hakansson, I. *Machinery-Induced Compaction of Arable Soils; Incidence–Consequences–Counter-Measures*; Reports from the Division of Soil Management; FAO: Québec City, QC, Canada, 2005; Volume 109.
15. Horn, R.; Way, T.; Rostek, J. Effect of repeated wheeling on stress/strain properties and ecological consequences in structured arable soils. *Rev. Cienc. Suelo Nutr. Veg.* **2001**, *1*, 34–40.
16. Boguzas, V.; Hakansson, I. Barley yield losses simulation under Lithuanian conditions using the Swedish soil compaction model. In Proceedings of the Conference on Sustainable Agriculture in Baltic States, Tartu, Estonia, 28–30 June 2001; Tartumaa Ltd.: Tartu, Estonia, 2001.
17. Ridge, R. Trends in sugar cane mechanization. *Int. Sugar J.* **2002**, *103*, 164–166.
18. Soane, B.D.; Dickson, J.W.; Campbell, D.J. Compaction by agricultural vehicles: A review III. Incidence and control of compaction in crop production. *Soil Tillage Res.* **1982**, *2*, 3–36. [CrossRef]

19. Kunickaya, O.; Hertz, E.; Kruchinin, I.; Tikhonov, E.; Ivanov, N.; Dolmatov, N.; Zorin, M.; Grigorev, I. Pressure control systems for tyre preservation in forestry machinery and forest soils. *Asian J. Water Environ. Pollut.* **2021**, *18*, 95–102. [CrossRef]
20. Šimečková, J.; Polcar, A.; Hammerová, A.; Votava, J.; Kumbár, V. Changes to the physical properties of the soil after the passage of an agricultural tractor. *Int. Agrophysics* **2021**, *35*, 97–105. [CrossRef]
21. Damme, L.; Stettler, M.; Pinet, F.; Vervaet, P.; Keller, T.; Munkholm, L.J.; Lamandé, M. Construction of modern wide, low-inflation pressure tyres per se does not affect soil stress. *Soil Tillage Res.* **2020**, *204*, 104798.
22. Upadhyay, G.; Raheman, H. Comparative analysis of tillage in sandy clay loam soil by free rolling and powered disc harrow. *Eng. Agric. Environ. Food* **2019**, *12*, 118–125. [CrossRef]
23. Chygarev, Y.; Lodyata, S. Research of tyre rigidity in terms of ecological safety of agricultural landscapes. In Proceedings of the VII Międzynarodowe Sympozjum Ekologiczne Aspekty Mechanizacji Nawożenia, Ochrony Roślin Uprawy Gleby i Zbioru Roślin Uprawnych, Warsaw, Poland, 18–19 September 2000; pp. 171–176.
24. Balbuena, R.H.; Terminiello, A.M.; Claverie, J.A.; Casado, J.P.; Marlats, R. Soil compaction by forestry harvester operation: Evolution of physical properties. *Rev. Bras. Eng. Agric. Ambient.* **2000**, *4*, 453–459. [CrossRef]
25. Seker, C.J.S.I.I.; Isildar, A.A. Effects of wheel traffic porosity and compaction of soil profile. *Turk. J. Agric. For.* **2000**, *24*, 71–78.
26. Abbaspour-Gilandeh, Y.; Rahimi-Ajdadi, F.; Asli-Ardeh, E.A.; Sharabiani, V.R.; Ardabili, M. Application of artificial neural network for predicting fuel consumption of tractor. In Proceedings of the International Agricultural Engineering Conference, Bangkok, Thailand, 7–10 December 2009.
27. Jang, J.S. ANFIS: Adaptive-network-based fuzzy inference system. *IEEE Trans. Syst. Man Cybern.* **1993**, *23*, 665–685. [CrossRef]
28. Buragohain, M.; Mahanta, C. A novel approach for ANFIS modelling based on full factorial design. *Appl. Soft Comput.* **2008**, *8*, 609–625. [CrossRef]
29. Dehnavi, A.; Aghdam, I.N.; Pradhan, B.; Varzandeh, M.H.M. A new hybrid model using step-wise weight assessment ratio analysis (SWARA) technique and adaptive neuro-fuzzy inference system (ANFIS) for regional landslide hazard assessment in Iran. *CATENA* **2015**, *135*, 122–148. [CrossRef]
30. Ertunc, H.M.; Hosoz, M. Comparative analysis of an evaporative condenser using artificial neural network and adaptive neuro-fuzzy inference system. *Int. J. Refrig.* **2008**, *31*, 1426–1436. [CrossRef]
31. Taghavifar, H.; Mardani, A. On the modeling of energy efficiency indices of agricultural tractor driving wheels applying adaptive neuro-fuzzy inference system. *J. Terramech.* **2014**, *56*, 37–47. [CrossRef]
32. Abbaspour-Gilandeh, Y.; Sedghi, R. Predicting soil fragmentation during tillage operation using fuzzy logic approach. *J. Terramech.* **2015**, *57*, 61–69. [CrossRef]
33. Ghadernejad, K.; Shahgholi, G.; Mardani, A.; Chiyaneh, H.G. Prediction effect of farmyard manure, multiple passes and moisture content on clay soil compaction using adaptive neuro-fuzzy inference system. *J. Terramech.* **2018**, *77*, 49–57. [CrossRef]
34. Lamandé, M.; Schjøning, P. Transmission of vertical stress in a real soil profile. Part II: Effect of tyre size, inflation pressure and wheel load. *Soil Tillage Res.* **2011**, *114*, 71–77. [CrossRef]
35. Mohsenimanesh, A.; Ward, S.M. On-the-move monitoring of soil-tire interaction on soft soil using wireless data acquisition. *Trans. ASABE* **2007**, *50*, 1919–1925. [CrossRef]
36. Mohsenimanesh, A.; Ward, S.M. Estimation of a three-dimensional tyre footprint using dynamic soil–tyre contact pressures. *J. Terramech.* **2010**, *47*, 415–421. [CrossRef]
37. Sohne, W. Fundamentals of pressure distribution and soil compaction under tractor tires. *Agric. Eng.* **1958**, *39*, 290.
38. Keller, T.; Défossez, P.; Weisskopf, P.; Arvidsson, J.; Richard, G. SoilFlex: A model for prediction of soil stresses and soil compaction due to agricultural field traffic including a synthesis of analytical approaches. *Soil Tillage Res.* **2007**, *93*, 391–411. [CrossRef]
39. Zink, A.; Fleige, H.; Horn, R. Load risks of subsoil compaction and depths of stress propagation in arable Luvisols. *Soil Sci. Soc. Am. J.* **2010**, *74*, 1733–1742. [CrossRef]

**Disclaimer/Publisher’s Note:** The statements, opinions and data contained in all publications are solely those of the individual author(s) and contributor(s) and not of MDPI and/or the editor(s). MDPI and/or the editor(s) disclaim responsibility for any injury to people or property resulting from any ideas, methods, instructions or products referred to in the content.

Technical Note

# Development of Autofeeding Device Applicable to a Biodegradable Pot Tray

Seok-Joon Hwang<sup>1,2</sup>, Moon-Kyeong Jang<sup>1,2</sup> and Ju-Seok Nam<sup>1,2,\*</sup>

<sup>1</sup> Department of Biosystems Engineering, Kangwon National University, 1 Kangwondaehak-gil, Chuncheon 24341, Gangwon-do, Republic of Korea

<sup>2</sup> Interdisciplinary Program in Smart Agriculture, Kangwon National University, 1 Kangwondaehak-gil, Chuncheon 24341, Gangwon-do, Republic of Korea

\* Correspondence: njsg1218@kangwon.ac.kr; Tel.: +82-33-250-6497

**Abstract:** In this study, a pot autofeeding device for a biodegradable pot tray was developed. The tensile strength and bending strength were measured to identify the physical properties of the biodegradable pot tray. As a result of the measurement, the tensile strength and bending strength of the biodegradable pot tray were 0.06 and 0.17 times smaller than those of the plastic pot tray. Therefore, a new type of pot tray extraction mechanism was designed, considering the physical properties, dimensions, and geometry of the biodegradable pot tray, and it was applied to the pot autofeeding device. The developed pot autofeeding device consists of a pot slot, pot-separating blades, pot holders, air cylinders, and a conveyor device. It can supply 240 pot trays per hour to the seeding process without deformation or damage to the biodegradable pot tray.

**Keywords:** autofeeding device; biodegradable; pot tray; separating blade; tensile strength

**Citation:** Hwang, S.-J.; Jang, M.-K.; Nam, J.-S. Development of Autofeeding Device Applicable to a Biodegradable Pot Tray. *Agriculture* **2022**, *12*, 2097. <https://doi.org/10.3390/agriculture12122097>

Academic Editor: Vadim Bolshev

Received: 15 November 2022

Accepted: 6 December 2022

Published: 7 December 2022

**Publisher's Note:** MDPI stays neutral with regard to jurisdictional claims in published maps and institutional affiliations.



**Copyright:** © 2022 by the authors. Licensee MDPI, Basel, Switzerland. This article is an open access article distributed under the terms and conditions of the Creative Commons Attribution (CC BY) license (<https://creativecommons.org/licenses/by/4.0/>).

## 1. Introduction

As of 2019, 412,457 kilotons of paper and 183,031 kilotons of pulp were produced worldwide [1]. During the production of paper and pulp, various wastes are inevitably generated, including foreign matter, wastewater, and additives [2]. Paper sludge refers to the solid waste generated from the wastewater treatment process [3]. The amount of paper sludge generated accounts for approximately 50% of the total waste generated from the papermaking process [4]. Previously, paper sludge was treated using such methods as ocean dumping, landfill, and incineration. However, ocean dumping has been prohibited since 2014 owing to the London Convention and the Marine Pollution Prevention Act [5,6].

Under the influence of these policies, studies have been conducted to recycle paper sludge as a substitute for cement or to develop ecofriendly treatment measures [7–10]. In the agricultural sector, studies have been conducted to manufacture biodegradable pot trays that can replace the existing plastic pot trays using paper sludge [11,12]. When the hot pepper seedlings grown in the existing plastic pot trays and biodegradable pot trays were compared, there were no differences in plant length, leaf length, and the number of leaves, confirming the applicability of biodegradable pot trays [13,14]. Recently, studies have been conducted to improve the tensile and bursting strengths of biodegradable pot trays by mixing paper sludge with waste newspaper, wet strength agents, and water repellents [15,16]. Biodegradable pot trays can replace plastic pot trays, which are discarded through such methods as incineration after use, and they also have an advantage of being ecofriendly because they decompose in soil naturally [17]. In the case of transplanting using plastic pot trays, seedlings are removed from the pot trays and transplanted to the field. This extraction process may have a negative effect on the growth of crops because it can damage the roots of the seedlings [18]. In contrast, biodegradable pot trays can preserve the roots of seedlings because they are transplanted to the field together with the seedlings without an extraction process, and thus they are favorable for the growth of seedlings [16].

Owing to these benefits, biodegradable pot trays have been used for growing the seedlings of crops, such as tomatoes, cucumbers, lettuce, and hot peppers [19]. In this regard, there is a growing need for studies on the application of biodegradable pot trays to agricultural machines [18]. As a research case for applying biodegradable pot trays to agricultural machinery, a transplanter that can apply chain paper pots was developed [20,21]. Nambu and Tanimura (1992) developed the Ferris-type transplanting mechanism for biodegradable pot trays connected in a single line with applying the planting fingers to the transplanting device of the vegetable transplanter. The planting fingers gripped a cell of the biodegradable pot tray, then it rotated similarly to a Ferris wheel, and released the cells into the ground [20]. As a result of the performance evaluation, the work efficiency of the transplanter with the Ferris-type transplanting mechanism was 100 cells per minute [21]. Kumar and Raheman (2011) developed a transplanter that can transplant a biodegradable pot tray with multiple rows and columns. A supplied biodegradable pot tray was cut into multiple cells by circular blades with left–right movement. Then, each cell was dropped into the ground by the seedling drop tube [22]. Recently, a study has been conducted to shorten the time required for the cutting and extraction of biodegradable pot trays to less than one second for high-speed machine transplanting with circular blades [23].

On the other hand, there has been no prior study on the development of a pot-seeding machine capable of seeding in biodegradable pot trays. Pot-seeding machines significantly affect the increase in the mechanization rate of seeding and transplanting because they have high work efficiency and require less manpower, and pot trays that complete seeding using them are compatible with transplanters [24,25]. Therefore, studies on pot-seeding machines that can perform seeding in biodegradable pot trays are required.

A pot-seeding machine commonly used in agriculture consists of a pot autofeeder device, soil feeder, compressing device, seeding device, and covering soil feeder [26]. Among them, the pot autofeeder device is the important device which separates multi-stacked pot trays one by one and supplies them to the seeding process [27]. The mechanical operation of the pot autofeeder device continuously causes a load on pot trays during the pot tray extraction process. Biodegradable pot trays can be easily deformed and destroyed under load because their tensile strength (approximately  $0.69 \text{ N/mm}^2$ ) is lower than that of polypropylene, which is used as the main material of existing pot trays ( $34 \text{ N/mm}^2$ ) [16,17,28]. Biodegradable pot trays are also exposed to continuous contraction and expansion in the manufacturing and storage processes because their materials are vulnerable to deformation by moisture. It is difficult to apply manufactured biodegradable pot trays to machinery because their uniformity and firmness are low [22]. To apply biodegradable pot trays to pot-seeding machines, the machines need to be designed so that biodegradable pot trays cannot be deformed or destroyed by minimizing the load caused by the mechanical operation. To this end, the physical properties of biodegradable pot trays must be considered in the design process of the pot autofeeder device.

This study is a preliminary study for the development of a pot-seeding machine that can be applied to biodegradable pot trays, and a pot autofeeder device for a biodegradable pot tray was developed. The tensile and bending strengths of the biodegradable pot tray were measured and reflected in the design of the pot autofeeder device. It is expected that the development of the pot autofeeder device will contribute to an improvement in the mechanization rate of seeding and the development of pot-seeding machines for biodegradable pot trays.

## 2. Materials and Methods

### 2.1. Biodegradable Pot Tray

Figure 1 shows the biodegradable pot tray. The biodegradable pot tray consists of paper sludge, a strength resin that increases the strength of paper, and a size agent for water resistance reinforcement. Their proportions are shown in Table 1 [16]. The total weight of the biodegradable pot tray is 227.17 g. As shown in Figure 2, the biodegradable pot tray has a characteristic of being bent by its own weight. The pot tray has a length of 440 mm, a

width of 300 mm, and a height of 45 mm. Twelve cells are arranged in the lateral direction and eight cells in the longitudinal direction. Thus, the pot tray has a total of 96 cells. The shape of each cell is a truncated pyramid with square bases, and the lengths of upper base and lower base were 28.5 mm and 20.5 mm, respectively. At the bottom of the pot tray, there are empty spaces between the cells. The empty spaces are arranged at an interval of 36.5 mm.

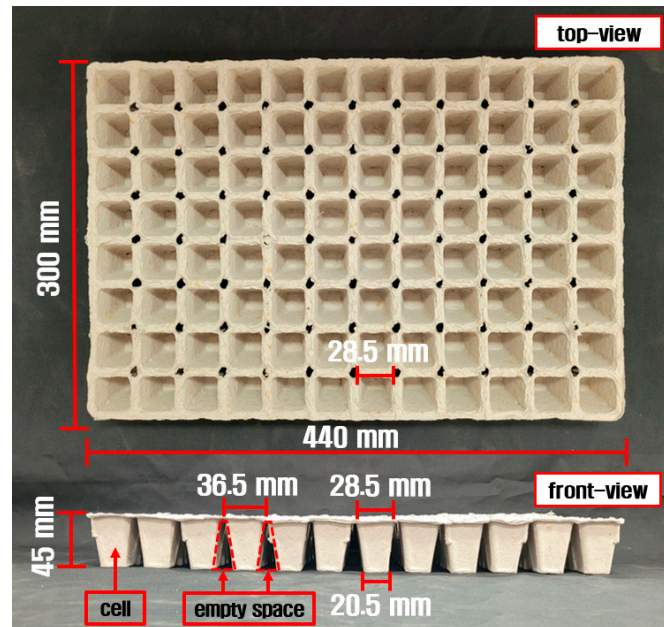


Figure 1. Dimensions of the biodegradable pot tray.

Table 1. Component ratio of the biodegradable pot tray ingredients.

Items	Ingredients of Biodegradable Pot Tray		
	Paper Sludge	Strength Agent	Sizing Agent
Component ratio	90.90%	4.55%	4.55%

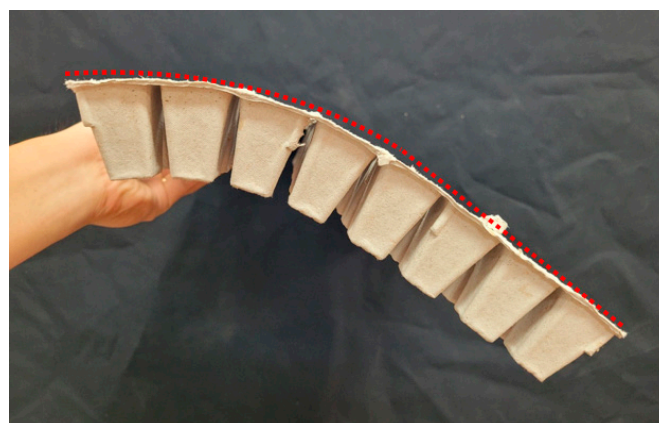


Figure 2. Deflection shape of biodegradable pot tray caused by its self-weight.

### 2.2. Characteristics of Current Pot Autofeeding Device

A pot-seeding machine commonly used in agriculture consists of a pot autofeeding device, soil feeder, compressing device, seeding device, and covering soil feeder (Figure 3). When multi-stacked pot trays are inserted into the autofeeding device, the pot trays are



separated one by one by the pot tray extraction mechanism of the pot autofeeding device and transported to the soil feeder. The soil feeder fills each cell of the pot tray with soil. The compressing device then presses the soil filled in each cell into a conical shape to create a space for seeding. Subsequently, seeding is performed on the pressed soil by the seeding device. Finally, each cell of the pot tray is filled with covering soil by the covering soil feeder. The pot autofeeding device applied to a pot-seeding machine is an important device that significantly affects the improvement in the work efficiency of the pot-seeding machine because it automatically separates the inserted pot trays one by one and supplies them to the seeding process without requiring manpower. The commercial pot autofeeding devices have different pot tray extraction mechanisms. For representative pot tray extraction mechanisms, the hook-type, roller-type, and flat-type separators were applied. Each extraction mechanism operates as follows.

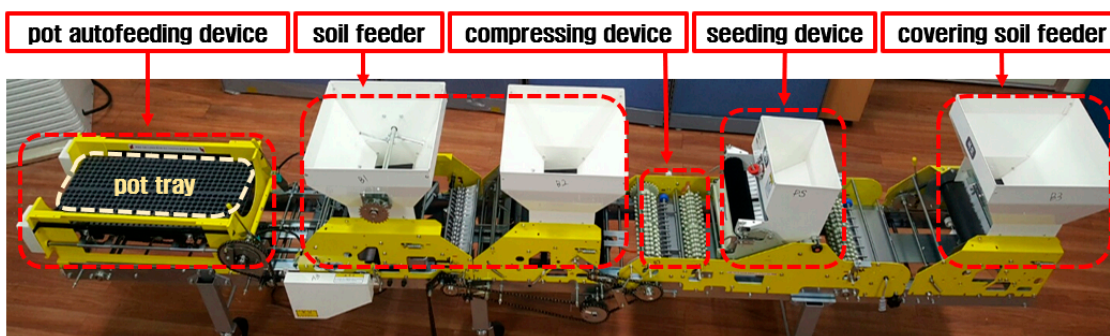


Figure 3. Picture of the mechanical pot tray seeding machine commonly used in agriculture.

A pot autofeeding device that extracts pot trays using the hook-type separator is shown in Figure 4. For this pot tray extraction mechanism, when stacked pot trays are placed in the pot autofeeding device, they are supported by pot holders. The hook-type separator is mounted on a cylindrical rod with rotational motion. Therefore, whenever the rod rotates, the hook-type separator also rotates. When the rotating hook-type separator contacts the top edge of the pot tray, it pulls down the pot tray in the direction of gravity to drop it. The separated pot tray is sent to the seeding process through the transport system.

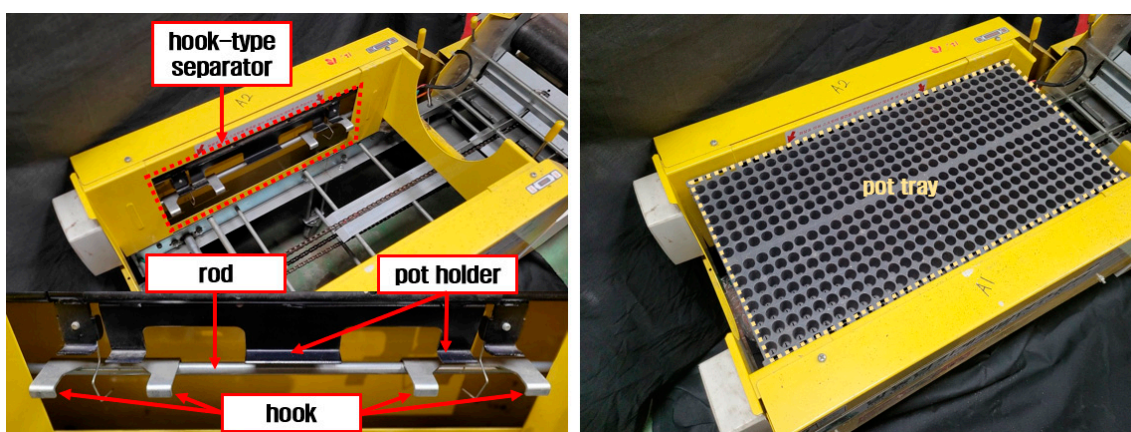


Figure 4. View of the pot autofeeding device with a hook-type separator applied.

Figure 5 shows the operation of the pot tray extraction mechanism using the flat-type separator. When stacked pot trays are placed in the pot autofeeding device, they are supported by pot holders. The flat-type separator can be moved in the vertical and horizontal directions because it is equipped with two air cylinders. The flat-type separator moves in the horizontal direction to contact the hollow between the pot trays and then

moves in the vertical downward direction to separate the pot tray at the bottom. The separated pot tray is sent to the seeding process through the transport system.

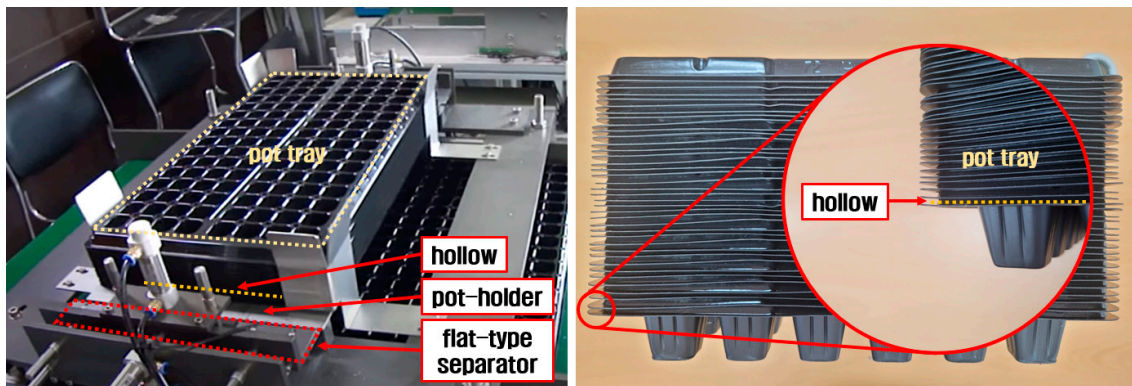


Figure 5. View of the pot autofeeding device with a flat-type separator applied.

Figure 6 shows the pot autofeeding device that extracts pot trays through the roller-type separator. For this pot tray extraction mechanism, when obliquely stacked pot trays are inserted into the pot autofeeding device, the top edge of the pot tray located at the bottom comes into contact with the roller-type separator. The roller-type separator then rotates to separate the pot tray and sends it to the seeding process.

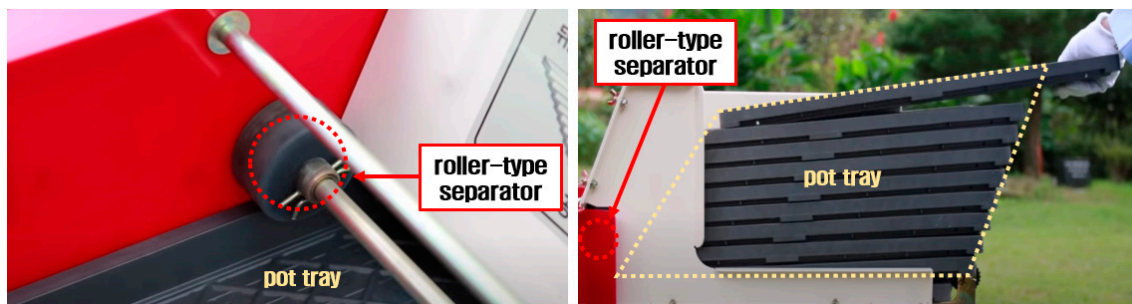


Figure 6. View of the pot autofeeding device with a roller-type separator applied.

### 2.3. Requirements for Pot Autofeeding Device

The following requirements must be considered for the design of a pot autofeeding device applicable to biodegradable pot trays.

1. To minimize the manpower required in the pot tray separation process and improve work efficiency, the pot autofeeding device must be designed so that multi-stacked biodegradable pot trays can be automatically separated one by one and sent to the seeding process.
2. The components of the pot autofeeding device must be designed considering the strength, dimensions, and geometry of biodegradable pot trays.
3. The components of the pot autofeeding device must be designed to prevent the bending of the biodegradable pot tray during the pot tray extraction process for the smooth operation of the pot autofeeding device.
4. The pot autofeeding device must be designed so that biodegradable pot trays cannot be deformed or destroyed by minimizing the load applied to the pot trays by the pot tray extraction mechanism.

As shown in Figures 4–6, plastic pot tray extraction methods that applied the hook-type, flat-type, and roller-type separators extract a pot tray by applying a load while the separator is in contact with the edge of the pot tray through mechanical behavior. Plastic pot trays are separated without deformation or destruction even if stress is concentrated on



a small area, such as an edge. This is because the physical properties of the plastic material are considered, and an appropriate load is transferred to the edge of the pot tray within a range that does not exceed the tensile strength of the material.

However, biodegradable pot trays are unfavorable for application to machines because their firmness is lower than that of plastic materials, and thus, they are easily deformed and destroyed under a relatively small load [17,22,28].

Therefore, the applicability of the existing plastic pot tray extraction mechanisms must be examined to select a mechanism for the pot autofeeding device applicable to biodegradable pot trays. If the existing mechanisms are not applicable, a new-type pot tray extraction mechanism that can prevent deformation or destruction to biodegradable pot trays needs to be studied. For such a decision, the physical properties of biodegradable and plastic pot trays must be analyzed and compared first.

Accordingly, it is necessary to select a pot extraction mechanism that suitable with the biodegradable pot tray in order to develop a pot autofeeding device. In addition, the performance evaluation should be performed to confirm deformation or damage of the biodegradable pot tray using the developed pot autofeeding device.

## 2.4. Experimental Design

### 2.4.1. Tensile and Bending Strength

The tensile and bending strengths of biodegradable and plastic pot trays were measured. The tensile and bending strengths are important indicators of the physical properties of pot trays [16]. They were measured using a universal testing machine (AGS-50kNX, Scientific, Japan) (Figure 7 and Table 2). The measurements were obtained using three specimens for each experiment. The specimens were extracted from the outer walls of the pot trays (Figure 8). For tensile strength measurement, both ends of the specimen were fixed with two jigs and the load at the time of fracture was measured by pulling the specimen. As for the test conditions, the gauge length and tensile speed were 30 mm and 5 mm/min, respectively. The tensile strength was derived by dividing the measured load by the cross-sectional area of the specimen before measurement. The tensile strength of a pot tray can be determined through Equation (1) [29].

$$\sigma_t = \frac{W_{max}}{A_0} \quad (1)$$

where  $\sigma_t$ : tensile strength, N/mm<sup>2</sup>;  $W_{max}$ : maximum tensile load, N and  $A_0$ : area of cross section, mm<sup>2</sup>.

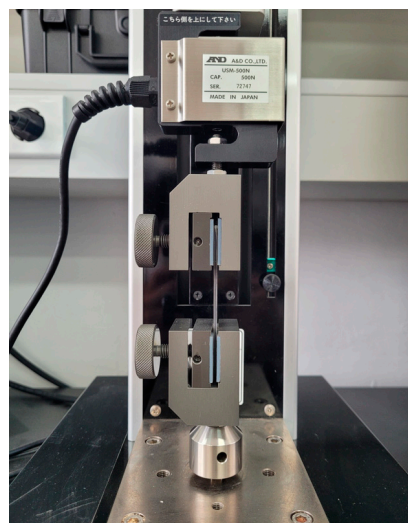


Figure 7. View of the universal testing machine used.

**Table 2.** Specifications of the universal testing machine.

Items	Specifications
Model/Company/Nation	AGS-50kNX/Scientific/Japan
Max. Load Capacity (kN)	50
Crosshead Speed Accuracy	0.1
Speed Range (mm/min)	0.001 to 1600
Max. Return Speed (mm/min)	2200

**(a)** biodegradable pot tray**(b)** plastic pot tray**Figure 8.** View of the specimen for measuring the tensile and bending stresses.

The bending strength was measured using the three-point bending method. While the specimen remained parallel to the ground, its bottom was supported with two jigs. The top of the specimen was pressed using a crosshead, and the generated load was measured. The distance between the jigs was 30 mm, and the crosshead speed was set to 2.8 mm/min. The bending strength of a pot tray can be determined through Equation (2) [30].

$$\sigma_b = \frac{3PL}{2BD^2} \quad (2)$$

where  $\sigma_b$ : bending strength, N/mm<sup>2</sup>;  $P$ : maximum bending load, N;  $L$ : length between jigs, mm;  $B$ : width of the specimen, mm and  $D$ : depth of the specimen, mm.

#### 2.4.2. Performance Evaluation

A pot extraction mechanism was selected for use with biodegradable pot trays, and a performance evaluation was performed using the pot autofeeding device developed by reflecting the selected pot extraction mechanism. The method of performance evaluation is as follows. The developed autofeeding device was operated with inserting the stacked biodegradable pot trays continuously. During the pot extraction process, it was confirmed that the components of the pot extraction mechanism were working normally. In addition, after the pot extraction process, the biodegradable pot trays supplied to the seeding process were collected, and then damage and deformation of the biodegradable pot trays were observed. The performance evaluation time was set to 1 h. The work efficiency of the pot autofeeding device was derived by counting the number of extracted biodegradable pot trays.

### 3. Results and Discussion

#### 3.1. Result of Experiment

The results of the tensile strength and bending strength tests conducted on the biodegradable and plastic pot trays are as follows. The tensile strength was determined to be  $12.66 \pm 0.87$  N/mm<sup>2</sup> for the plastic pot tray and  $0.70 \pm 0.03$  N/mm<sup>2</sup> for the biodegradable pot tray (Table 3). The tensile strength of the biodegradable pot tray was 0.06 times that of the plastic pot tray. The bending strength was measured to be  $22.26 \pm 0.28$  N/mm<sup>2</sup> for the plastic pot tray and  $3.89 \pm 0.54$  N/mm<sup>2</sup> for the biodegradable pot tray (Table 4). The bending strength of the biodegradable pot tray was 0.17 times that of the plastic pot tray. It is judged that this difference occurred due to the characteristics of the main ingredient constituting the biodegradable pot tray and the plastic pot tray.

**Table 3.** Tensile strength of the biodegradable pot tray.

Items	Tensile Strength (N/mm <sup>2</sup> )	
	Plastic Pot Tray	Biodegradable Pot Tray
1st Specimen	12.91	0.69
2nd Specimen	13.57	0.74
3rd Specimen	11.49	0.66
Average	12.66	0.70
Standard deviation	0.87	0.03

**Table 4.** Bending strength of the biodegradable pot tray.

Items	Bending Strength (N/mm <sup>2</sup> )	
	Plastic Pot Tray	Biodegradable Pot Tray
1st Specimen	22.62	3.61
2nd Specimen	22.20	4.65
3rd Specimen	21.95	3.41
Average	22.26	3.89
Standard deviation	0.28	0.54

The results of the tensile and bending strength measurements show that the strength of the biodegradable pot tray is significantly lower than that of the plastic pot tray. Accordingly, it is judged that the hook-type, roller-type, and flat-type separators, which were developed for plastic pot trays, are not suitable for extracting biodegradable pot trays. Therefore, a pot autofeeding device with a new-type mechanism that can minimize deformation or damage to pot trays was developed considering the physical properties of the biodegradable pot tray.

#### 3.2. Development of Pot Autofeeding Device

A pot autofeeding device with a new-type mechanism that can prevent deformation or destruction to the biodegradable pot tray in the pot tray extraction process was designed and fabricated considering the physical properties, dimensions, and geometry of the biodegradable pot tray.

##### 3.2.1. Design of Main Components

The characteristics of each main component which constituting the pot autofeeding device are as follows.

1. Pot slot: the pot slot is the position where the biodegradable pot tray is inserted in the pot autofeeding device, and its geometry is shown in Figure 9. The length and width of the pot slot were designed to be 440 mm and 300 mm, respectively, considering the size of the biodegradable pot tray. The height of the pot slot is 240 mm, facilitating the input of 13 pot trays at a time.

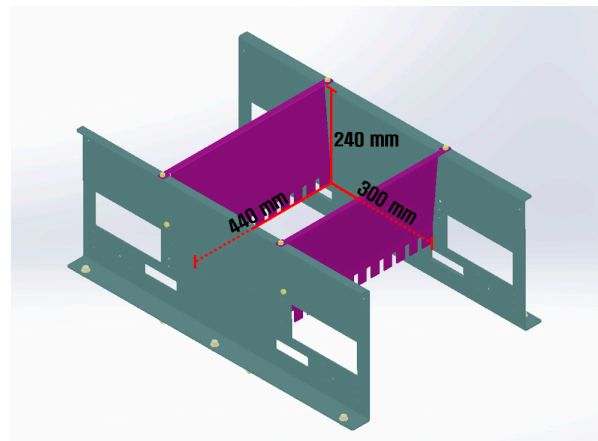


**Figure 9.** Shape of the pot slot.

2. Pot-separating blades: Figure 10 shows the geometry of the pot-separating blades. The blades are inserted into the spaces between the cells of the biodegradable pot tray to support or separate the pot tray. The biodegradable pot tray has a low bending strength, and thus, deflection occurs owing to its own weight. To prevent this, the number of pot-separating blades was maximized so that the entire pot tray could be supported. Therefore, 11 pot-separating blades were arranged at intervals of 36.5 mm to form an assembly. This interval is the same as the interval of the spaces located between the cells of the biodegradable pot tray. Each assembly is distinguished as either upper or lower pot-separating blades depending on its position. As the upper/lower pot-separating blades are located at both sides of the pot autofeeding device, 44 pot-separating blades were used in the pot autofeeding device. The thickness of the pot-separating blades was set to 4.5 mm, which was smaller than the width of the spaces located between the cells of the biodegradable pot tray (8 mm). Among the components of the pot autofeeding device, the pot-separating blades generate relatively large loads on the biodegradable pot tray during their operation. Such loads can be dispersed and geometry deformation can be minimized by designing the area in which the pot-separating blades are in contact with the biodegradable pot tray to be larger. The area can be increased by maximizing the length of the pot-separating blades. Considering that the width of the biodegradable pot tray is 300 mm, the length of the pot-separating blades was set to 150 mm. Therefore, the total length of contact between a pair of pot-separating blades and the biodegradable pot tray is 300 mm.

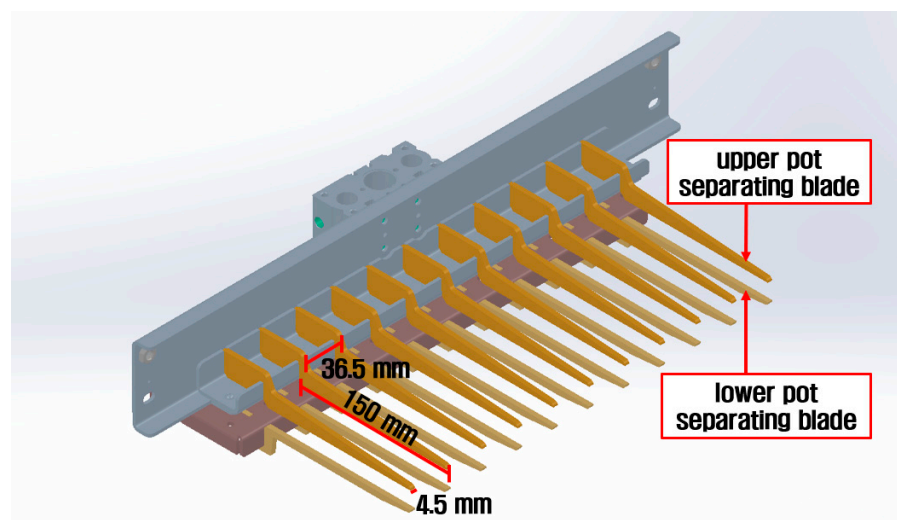


**Figure 10.** Shape of the pot-separating blade.

3. Pot holders: the pot holders support the inserted biodegradable pot tray, and their geometry is shown in Figure 11. The pot holders are located on both sides of the pot autofeeding device. Their width and height were set to 80 and 30 mm, respectively. Their length was set to 440 mm, which is the same as the length of the biodegradable pot tray.

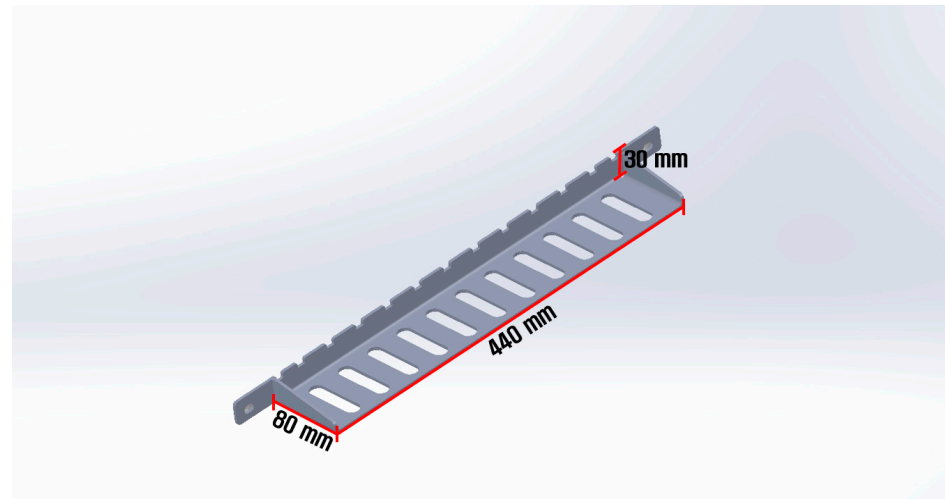


**Figure 11.** Shape of the pot holder.

4. Air cylinders: the air cylinders drive the pot-separating blades and pot holders, and their geometry is shown in Figure 12. Three types of air cylinders were used in the pot autofeeding device. Table 5 shows their specifications. The length of the pot-separating blades was set to 150 mm in Figure 10. During the pot tray extraction process, the blades need to insert 150 mm into the empty spaces of the biodegradable pot tray. Therefore, an air cylinder-Ⓐ which has a stroke of 150 mm, was used for operating the pot-separating blades. The body of air cylinder-Ⓐ is attached to the center of the frame outer wall, and the end of the piston rod is fixed to the pot-separating blades. When compressed air is supplied through position ①, the piston rod moves into the air cylinder body and pulls the pot-separating blades to the inside of the pot slot. Conversely, when compressed air is supplied through position ②, the piston rod protrudes and the pot-separating blades return to the outside of the pot slot. The width of the pot holders was set to 80 mm in Figure 11. The pot holders need to move 80 mm to support the biodegradable pot tray. Therefore, an air cylinder-Ⓑ which has a stroke of 80 mm, was selected for operating the pot holders. The operation mechanism of air cylinder-Ⓑ is the same as that of air cylinder-Ⓐ. The body of air cylinder-Ⓑ is attached on the frame outer wall, and the end of the piston rod of the air cylinder-Ⓑ is fixed to the pot holders. Therefore, when compressed air is supplied to position ③, the pot holders move to the outside of the pot slot. When compressed air is supplied to position ④, they return to the inside of the pot slot. An air cylinder-Ⓒ was designed to operate the lower pot-separating blade in Figure 10. The body of air cylinder-Ⓒ and the end of the piston rod are fixed to the upper and lower pot-separating blades, respectively. At the beginning of the operation of the pot autofeeding device, compressed air is supplied to position ⑥, and the upper/lower pot-separating blades are in contact with each other. However, when compressed air is supplied to position ⑤, the lower pot-separating blade moves downward and is separated from the upper pot-separating blade. Air cylinder-Ⓒ has a stroke of 20 mm. Therefore, the lower pot-separating blade moves 20 mm downward from the upper pot-separating blade. The proper pressure of all air cylinders was set to 0.6 bars.

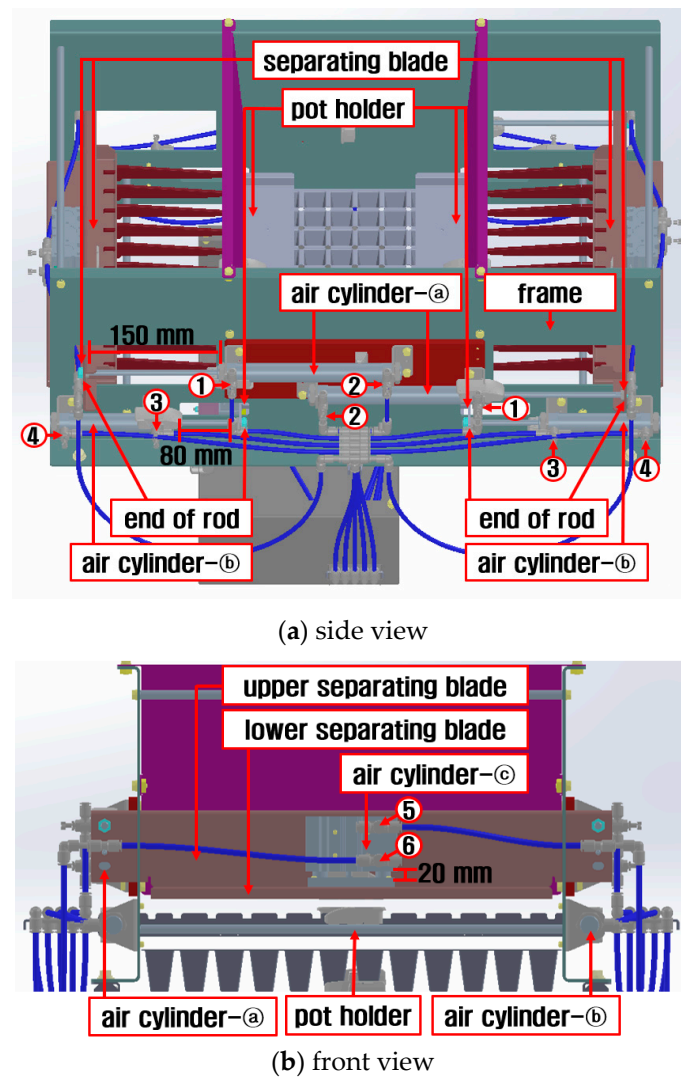


Figure 12. Shape of 3D model that the air cylinders applied to the pot autofeeding device.

Table 5. Specifications of the air cylinders used.

Items		Specifications		
Model/Company/Nation		ACS4-N LB20-S150 /KCC company/ South Korea	ACS4-N LB20-S80 /KCC company/ South Korea	ANGM 25-S20 /KCC company/ South Korea
Fluid type used		Air	Air	Air
Pressure (MPa)	Max.	1.0	1.0	1.0
	Min.	0.05	0.05	0.12
Piston speed (mm/s)	Max.	1000	1000	500
	Min.	750	750	50
Stroke (mm)		150	80	20
Inner diameter of rod (mm)		20	20	20

5. Conveyor device: The conveyor device transports the extracted biodegradable pot tray to the seeding process, and its geometry is shown in Figure 13. It has a length of 1800 mm and a height of 700 mm. Its width was set to 440 mm, which is the same as the length of the biodegradable pot tray. The conveyor device transports the biodegradable pot tray to the seeding process at a speed of 18.16 mm/s.



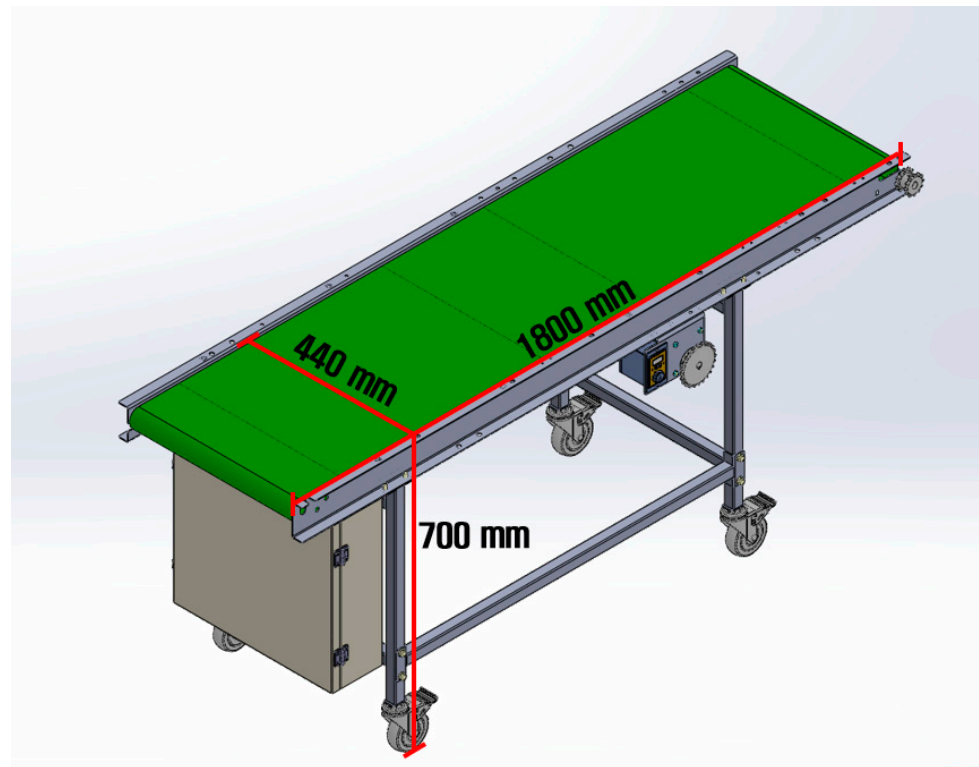
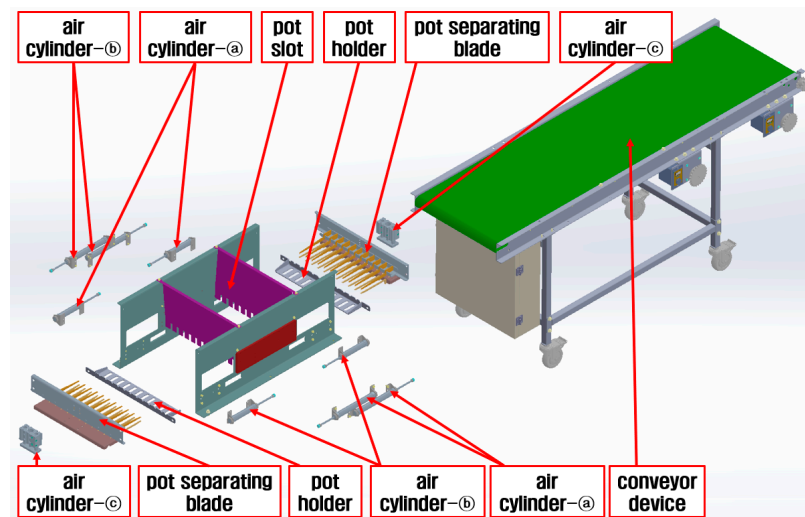


Figure 13. Shape of the conveyor device.

### 3.2.2. Operating Procedure of Developed Pot Autofeeding Device

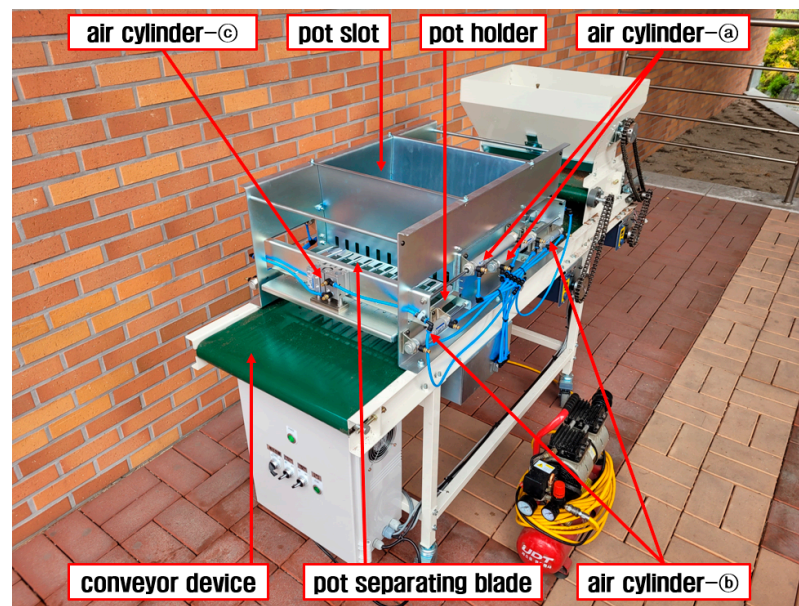
Figure 14 shows the overall geometry of the pot autofeeding device that was designed considering the dimensions, geometry, and physical properties of the biodegradable pot tray. The main components of the pot autofeeding device are a pot slot, pot-separating blades, pot holders, air cylinders, and a conveyor device.



(a) 3D model

Figure 14. Cont.

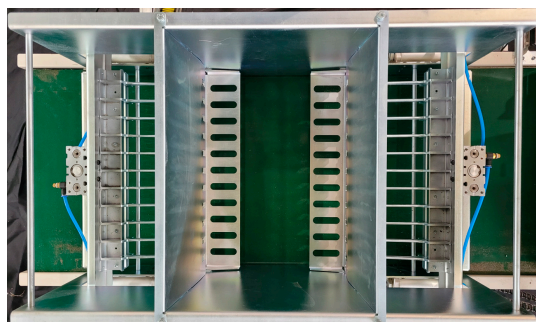




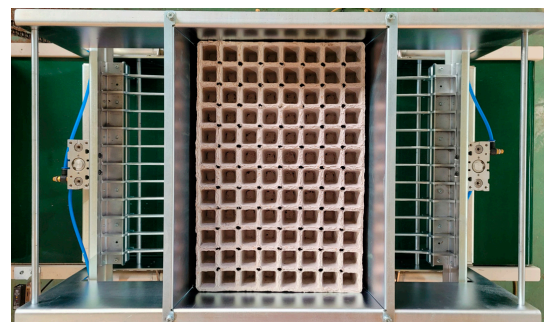
(b) picture

Figure 14. Shape of the pot autofeeding device.

Figure 15 shows the operating procedure of the developed pot autofeeding device for the biodegradable pot tray. The operator places the biodegradable pot trays stacked in 13 layers into the pot slot. The lower part of the first biodegradable pot tray located at the bottom is supported by the pot holders located inside the pot slot (Figure 15a,b). Subsequently, air cylinder-Ⓐ operates to insert the upper/lower pot-separating blades into the empty spaces between each cell of the second biodegradable pot tray (Figure 15c–e). In this instance, the upper pot-separating blade supports the lower part of the second biodegradable pot tray. Air cylinder-Ⓑ operates to move the pot holders to the outside of the pot slot (Figure 15f). The first biodegradable pot tray does not drop vertically owing to the friction with the second biodegradable pot tray. Subsequently, air cylinder-Ⓒ operates to move the lower pot-separating blade with the down-up motion (Figure 15g). The first biodegradable pot tray is separated from the second biodegradable pot tray as the lower pot-separating blade comes into contact with the upper part of the first biodegradable pot tray. The first biodegradable pot tray then drops onto the conveyor device to be transported to the seeding process (Figure 15h). Subsequently, the pot holders again move to the inside of the pot slot (Figure 15i), and the upper/lower pot-separating blades again move toward the outside of the pot slot (Figure 15j). Through this pot tray extraction mechanism, the biodegradable pot trays are sequentially extracted and transported to the seeding process one by one.



(a)



(b)

Figure 15. Cont.

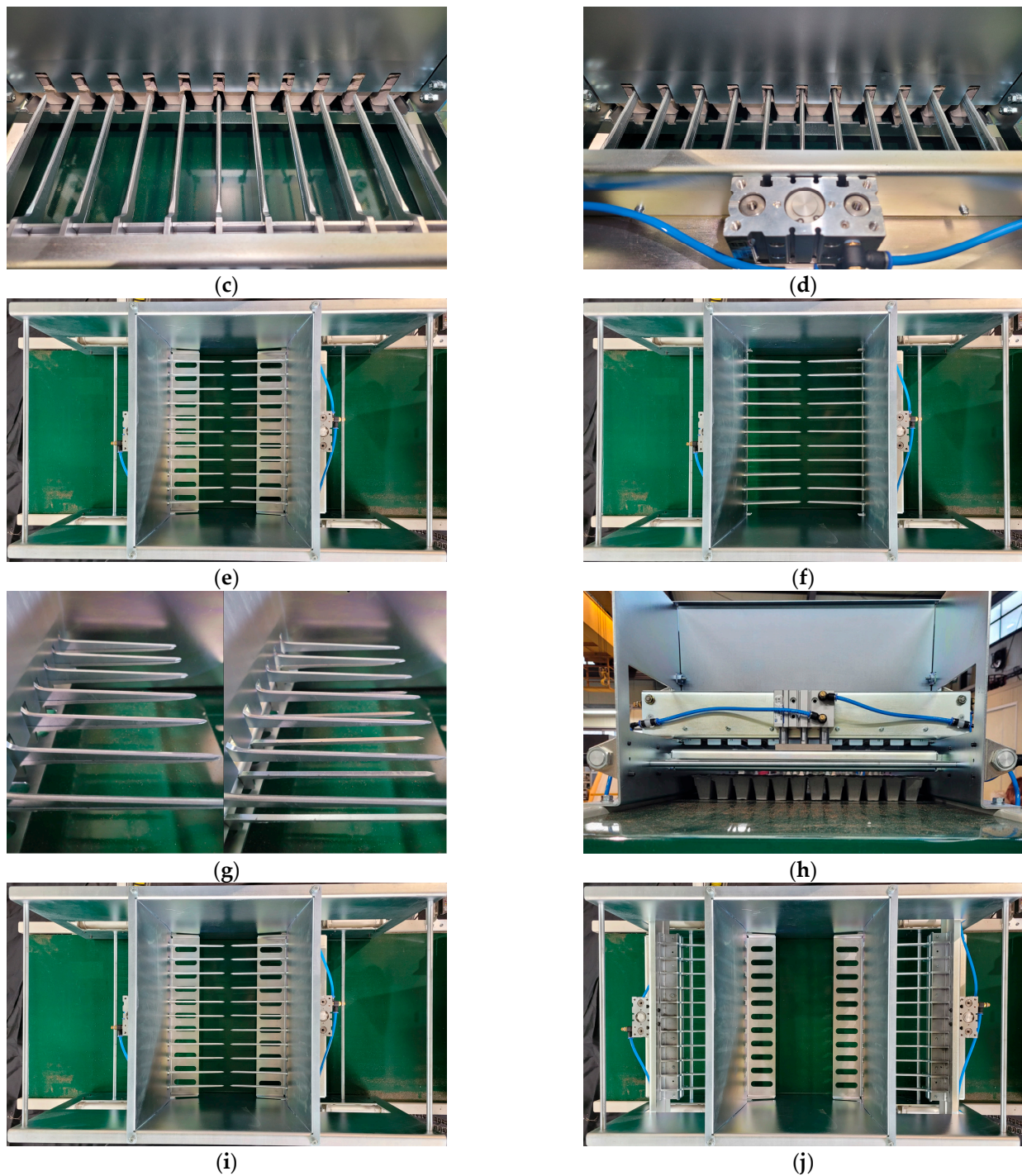
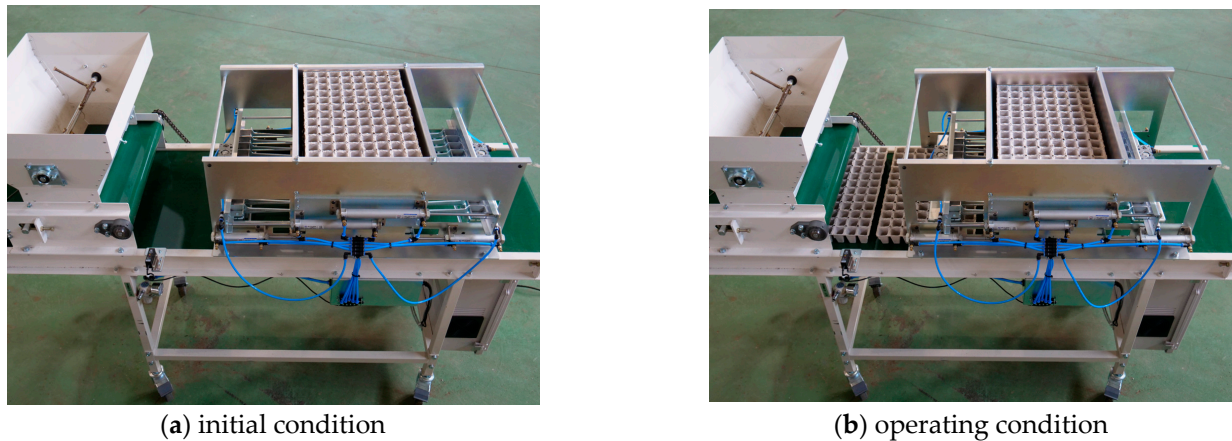


**Figure 15.** Operating procedure of the pot autofeeder device for the biodegradable pot tray: (a) an initial condition; (b) supplying the biodegradable pot tray into the pot slot; (c) the shape of the pot separating blades before inserting; (d) inserting of pot separating blades into the spaces of biodegradable pot tray; (e) the shape of pot separating blades after inserting; (f) the pot holders move to the outside of the plot slot; (g) the lower pot-separating blade moves downward for separating the bottom biodegradable pot tray; (h) separated biodegradable pot tray drops onto the conveyor belt to be transported to the seeding process; (i) the pot holders return to the inside of the pot slot; (j) the pot-separating blades return toward the outside of the pot slot.



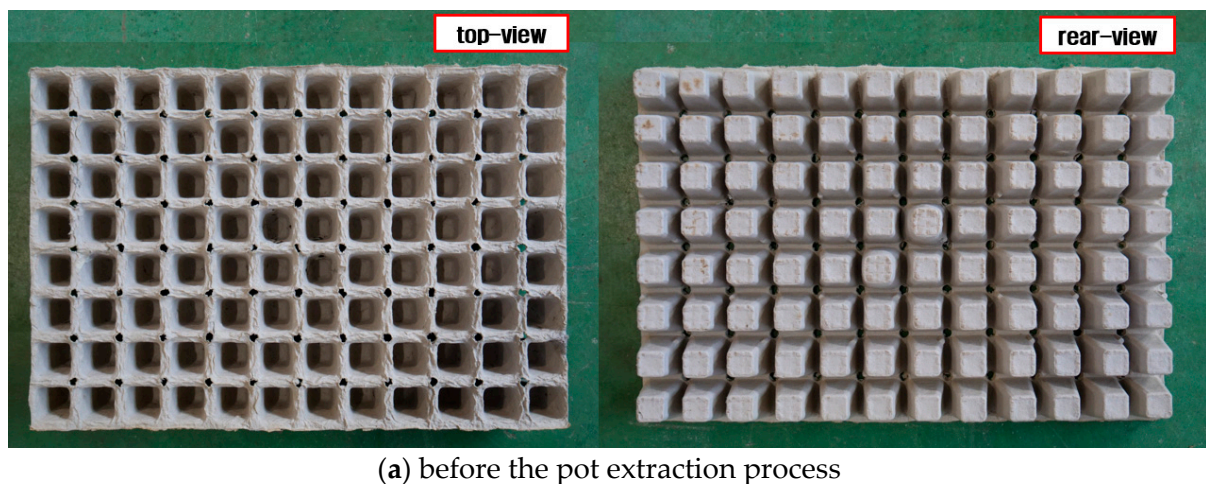
### 3.3. Result of Performance Evaluation

Figure 16 shows that conducting the performance evaluation of the pot autofeeding device. As a result of observing whether the pot autofeeding device operates normally under the condition that the biodegradable pot tray was inserted into the pot slot continuously, it was confirmed that the pot autofeeding device can automatically separate the stacked biodegradable pot trays one by one and send them to the seeding process without malfunction occurred. In addition, the result of counting the number of the biodegradable pot trays supplied for 1 h through the pot autofeeding device, it was observed that 240 biodegradable pot trays were supplied to the seeding process per hour.

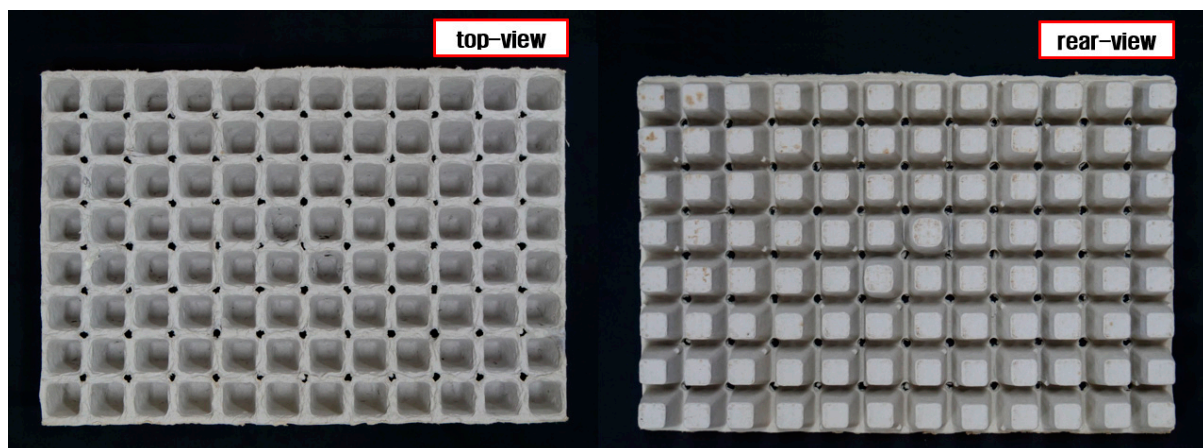


**Figure 16.** The picture of conduction the performance evaluation.

As a result of a complete enumeration survey regarding to the 240 biodegradable pot trays supplied to the seeding process, it was confirmed that no deformation or damage occurred in all biodegradable pot trays (Figure 17). This indicates that the new-type pot extraction mechanism is suitable for supplying the separating biodegradable pot trays. In particular, it was judged that the developed pot autofeeding device prevents the bending of the biodegradable pot tray due to its own weight in the pot extraction process by applying the pot separating blades, and it also prevents the deformation or destruction of the biodegradable pot tray by dispersing the load generated by the mechanical behavior of the components.



**Figure 17.** Cont.



(b) after the pot extraction process

**Figure 17.** Picture of the biodegradable pot tray used for confirming the deformation and damage.

#### 4. Conclusions

In this study, a pot autofeeding device for a biodegradable pot tray was developed considering the physical properties, dimensions, and geometry of the pot tray.

The pot tray extraction mechanisms commercialized for plastic pot trays were investigated, and their applicability to biodegradable pot trays was examined. To this end, specimens were secured from actual biodegradable and plastic pot trays, and their tensile and bending strengths were measured using a universal testing machine. The tensile and bending strengths of the biodegradable pot tray were derived as  $0.70 \pm 0.03$  and  $3.89 \pm 0.54$  N/mm<sup>2</sup>, respectively, whereas those of the plastic pot tray were  $12.66 \pm 0.87$  and  $22.26 \pm 0.28$  N/mm<sup>2</sup>, respectively. As a result of the measurement, the tensile strength and bending strength of the biodegradable pot tray were 0.06 and 0.17 times smaller than those of the plastic pot tray. It is judged that this difference occurred due to the material property of the biodegradable pot tray and the plastic pot tray.

As the strength of the biodegradable pot tray was lower than that of the plastic pot tray, a new-type pot tray extraction mechanism was developed considering the physical properties, dimensions, and geometry of the biodegradable pot tray.

The developed pot autofeeding device consists of a pot slot, pot-separating blades, pot holders, air cylinders, and a conveyor device. The pot holders support the stacked biodegradable pot trays inserted into the pot slot. The pot separating blades insert into the stacked biodegradable pot trays and extract them one by one. Then, the separated biodegradable pot tray is transferred to the seeding process by a conveyor device. A performance evaluation was conducted to confirm that the components of the pot autofeeding device operate normally during the operation procedure. In addition, the biodegradable pot tray supplied to the seeding process was collected, and then damage and deformation occurring in the biodegradable pot tray were observed. As a result of observing whether the pot autofeeding device works normally, it was checked that the stacked biodegradable pot trays were extracted one by one automatically without malfunction occurred. The work efficiency of the pot autofeeding device was 240 pot trays per hour. As a result of a complete enumeration survey regarding to the 240 biodegradable pot trays supplied to the seeding process, it was confirmed that no deformation or damage occurred in all biodegradable pot trays. This indicates that the new-type pot extraction mechanism is suitable for supplying the separating biodegradable pot trays. Especially, it judged that the developed pot autofeeding device prevents the bending of the biodegradable pot tray due to its own weight in the pot extraction process by applying the pot separating blades, and it also prevents the deformation or destruction of the biodegradable pot tray by dispersing the load generated by the mechanical behavior of the components.

It is expected that the development of the pot autofeeding device for the biodegradable pot tray will reduce the manpower and labor load of seeding and improve the applicability of biodegradable pot trays.

**Author Contributions:** Investigation, S.-J.H., M.-K.J.; writing—original draft preparation, S.-J.H.; writing—review and editing, J.-S.N. All authors have read and agreed to the published version of the manuscript.

**Funding:** This work was supported by Korea Institute of Planning and Evaluation for Technology in Food, Agriculture and Forestry (IPET) through Agriculture, Food and Rural Affairs Convergence Technologies Program for Educating Creative Global Leader Program, funded by Ministry of Agriculture, Food and Rural Affairs (MAFRA)(716001-7).

**Institutional Review Board Statement:** Not applicable.

**Data Availability Statement:** Not applicable.

**Conflicts of Interest:** The authors declare no conflict of interest.

## References

1. Korea Paper Association: Paper production by region. Available online: [http://www.paper.or.kr/sub\\_5/5\\_1\\_3.php](http://www.paper.or.kr/sub_5/5_1_3.php) (accessed on 10 October 2022).
2. Skinner, H.J. Waste problems in the pulp and paper industry. *Ind. Eng. Chem.* **1939**, *31*, 1331–1335. [CrossRef]
3. Boni, M.R.; D’Aprile, L.; De Casa, G. Environmental quality of primary paper sludge. *J. Hazard. Mater.* **2004**, *108*, 125–128. [CrossRef]
4. Lee, Y.H.; Jo, H.M.; Kim, S.H.; Lee, J.Y. Fundamental study of the production of paper ash made from paper sludge I: Evaluation of the characteristics of paper ash made from paper sludge in a specialty paper mill. *J. Korea TAPPI* **2020**, *52*, 113–119. [CrossRef]
5. Ko, J.C.; Kim, S.H.; Park, Y.K.; Jeon, J.Y.; Kim, J.H.; Park, J.S. Pyrolysis characteristics of sludge discharged from paper mill process. *J. Korra* **2009**, *17*, 80–87.
6. Song, D.B.; Lim, K.H.; Jung, D.H.; Yoon, J.H. Analysis of drying performance and cost of large-capacity sewage sludge dryer. *J. Biosyst. Eng.* **2021**, *46*, 105–111. [CrossRef]
7. Takizawa, S.; Baba, Y.; Tada, C.; Fukuda, Y.; Nakai, Y. Pretreatment with rumen fluid improves methane production in the anaerobic digestion of paper sludge. *Waste Manag.* **2018**, *78*, 379–384. [CrossRef]
8. Bui, N.K.; Satomi, T.; Takahashi, H. Influence of industrial by-products and waste paper sludge ash on properties of recycled aggregate concrete. *J. Clean. Prod.* **2019**, *214*, 403–418. [CrossRef]
9. Chen, M.; Zheng, Y.; Zhou, X.; Li, L.; Wang, S.; Zhao, P.; Lu, L.; Cheng, X. Recycling of paper sludge powder for achieving sustainable and energy-saving building materials. *Constr. Build. Mater.* **2019**, *229*, 116874. [CrossRef]
10. Kang, I.K.; Oh, H.Y.; Han, D.Y.; Lim, Y.T.; Jang, M.M.; So, S.Y. An analysis of characteristics of asphalt concrete using paper sludge. *Conf. AIK* **2020**, *40*, 461.
11. Schrader, J.A.; Srinivasan, G.; Grewell, D.; McCabe, K.G.; Graves, W.R. Fertilizer effects of soy-plastic containers during crop production and transplant establishment. *Hortscience* **2013**, *48*, 724–731. [CrossRef]
12. Nandede, B.M.; Raheman, H.; Kumar, G.V.P. Standardization of potting mix and pot volume for the production of vegetable seedlings in paper pot. *J. Plant Nutr.* **2014**, *37*, 1214–1226. [CrossRef]
13. Seo, T.C.; An, S.W.; Jang, H.W.; Nam, C.W.; Chun, H.; Kim, Y.C.; Kang, T.K.; Lee, S.H. An approach to determine the good seedling quality of grafted tomatoes (*Solanum lycopersicum*) grown in cylindrical paper pot through the relation analysis between DQI and short-term relative growth rate. *J. Bio-Env. Control* **2018**, *27*, 302–311. [CrossRef]
14. Lee, J.H.; Lee, D.H.; Choi, G.M.; Kim, E.G.; Kim, T.H.; Kim, H.T. Analysis of plant guarding characteristics of biodegradable pot for transplant. *Proc. Conf. Korean Soc. Agric.* **2019**, *24*, 494–495.
15. Lee, J.Y.; Kim, C.H.; Lee, G.S.; Jo, H.S.; Nam, H.G.; Park, H.H.; Moon, S.O. Physico-chemical characteristics of biodegradable seedling pots made of paper mill sludges. *J. Korea TAPPI* **2014**, *46*, 9–18. [CrossRef]
16. Park, J.H.; Lee, G.H.; Lee, H.M.; Madhavi, B.G.K.; Arulmozhi, E.; Bhujel, A.; Moon, B.E.; Kim, H.T. Physical properties and plant growth according to the content of additives in the biodegradable pot for mechanical transplanter. *JALS* **2022**, *56*, 129–134. [CrossRef]
17. Park, H.S.; Son, K.Y.; Kang, J.R.; Seo, W.J.; Lee, S.J.; Lee, W.K. Study on properties of eco-friendly pot with biodegradable PLA/PBAT blend film. *J. Environ. Sci. Int.* **2015**, *24*, 1037–1043. [CrossRef]
18. Jang, Y.N.; An, S.W.; Chun, H.; Lee, H.J.; Wi, S.H. The growth of cucumber seedlings grown in paper pot trays affected by nutrient management during seedling period, seedling age, and night temperature after transplanting. *J. Bio-Env. Control* **2019**, *28*, 396–403. [CrossRef]
19. Seo, T.C.; An, S.W.; Kim, S.M.; Nam, C.W.; Chun, H.; Kim, Y.C.; Kang, T.K.; Kim, S.W.; Jang, K.S. Effect of the seedlings difference in cylindrical paper pot trays on initial root growth and yield of pepper. *J. Bio-Env. Control* **2017**, *26*, 368–377. [CrossRef]

20. Nambu, T.; Tanimura, M. Development of automatic transplanter using chain pot for vegetable crops. *Int. Symp. Transpl. Prod. Syst.* **1992**, *319*, 541–546.
21. Suggs, C.W.; Thomas, T.N.; Eddington, D.L.; Peel, H.B.; Seaboch, T.R.; Gore, J.W. Self feeding transplanter for tobacco and vegetable crops. *Appl. Eng. Agric.* **1987**, *3*, 148–152. [CrossRef]
22. Kumar, G.V.P.; Raheman, H. Development of a walk-behind type hand tractor powered vegetable transplanter for paper pot seedlings. *Biosyst. Eng.* **2011**, *110*, 189–197. [CrossRef]
23. Lee, M.H.; Moon, B.E.; Jo, J.M.; Choi, T.H.; Kim, H.T. Development of Automatic type transplanter for biodegradable seedling pot. *Proc. Conf. Korean Soc. Agric.* **2017**, *22*, 136.
24. Jun, H.J.; Yu, S.H.; Choi, I.S.; Kim, J.G.; Lee, S.H.; Kang, T.G.; Kim, Y.K.; Choi, Y. Study on compatibility between plug tray sowing, seedlings and transplanters for planting mechanization of sesame. *Proc. Conf. Korean Soc. Agric.* **2018**, *23*, 155.
25. Choudhary, V.; Machavaram, R. Need of automation in paddy nurseries for raising paddy seedlings in India: A Review. *J. Biosyst. Eng.* **2022**, *47*, 209–222. [CrossRef]
26. Hwang, S.J.; Lee, J.Y.; Nam, J.S. Irrigation System for a Roller-Type Onion Pot Seeding Machine. *Appl. Sci.* **2019**, *9*, 430. [CrossRef]
27. Hwang, S.J.; Nam, J.S. Development of automatic accumulating equipment for roller-type onion pot-seeding machine. *Appl. Sci.* **2019**, *9*, 2139. [CrossRef]
28. Juvinall, R.C.; Marshek, K.M. *Machine Component Design*, 5th ed.; WILEY (John Wiley & Sons): Hoboken, NJ, USA, 2015; pp. 338–340.
29. Malik, G.K.; Khuntia, A.; Mitra, J. Comparative effect of different plasticizers on barrier, mechanical, optical, and sorption properties of hydroxypropyl methylcellulose (HPMC)-based edible film. *J. Biosyst. Eng.* **2022**, *47*, 93–105. [CrossRef]
30. Sim, J.H.; Lee, J.B.; Hwang, S.S. Effect of glazing on the flexural strength of lithium disilicate glass ceramics. *Korean J. Dent. Mater.* **2019**, *46*, 185–194. [CrossRef]

MDPI AG  
Grosspeteranlage 5  
4052 Basel  
Switzerland  
Tel.: +41 61 683 77 34

*Agriculture* Editorial Office  
E-mail: [agriculture@mdpi.com](mailto:agriculture@mdpi.com)  
[www.mdpi.com/journal/agriculture](http://www.mdpi.com/journal/agriculture)



Disclaimer/Publisher's Note: The statements, opinions and data contained in all publications are solely those of the individual author(s) and contributor(s) and not of MDPI and/or the editor(s). MDPI and/or the editor(s) disclaim responsibility for any injury to people or property resulting from any ideas, methods, instructions or products referred to in the content.



